Volcano-Tectonic Evolution of the Christiana-Santorini-Kolumbo Volcanic Field, Central Aegean Sea

DISSERTATION

with the aim of achieving a doctoral degree
at the Faculty of Mathematics, Informatics and Natural Sciences
Department of Earth Sciences
at Universität Hamburg

submitted by:
Jonas Preine

Hamburg, 2022

Department of Earth Sciences

Date of Oral Defence: 17.11.2023
Reviewers: Prof. Dr. Christian Hübscher
                                                    Prof. Dr. Paraskevi Nomikou

Members of the examination commission: Prof. Dr. Christian Hübscher
                                                    Prof. Dr. Matthias Hort
                                                 Prof. Dr. Paraskevi Nomikou
                                                    Prof. Dr. Conny Hammer
                                                    Dr. Sebastian Lindhorst

Chair of the Subject Doctoral Committee
Earth System Sciences: Prof. Dr. Hermann Held

Dean of Faculty MIN: Prof. Dr.-Ing. Norbert Ritter

Abstract

The Christiana-Santorini-Kolumbo volcanic field (CSKVF) in the southern Aegean Sea lies in an active continental rift zone and is one of the most hazardous volcano-tectonic regions in the world. Here, the historic eruption of the submarine Kolumbo Volcano occurred in 1650 CE, as well as the iconic Minoan eruption in 1600 BCE, which is thought to have contributed to the fall of the great Minoan civilization. Extensive research in the last decades has led to a detailed understanding of the onshore volcanic history of Santorini. However, since most of the volcanic edifices and their deposits lie offshore, critical observation gaps regarding the volcano-tectonic evolution of the CSKVF remain. In this thesis, I exploit a dense array of high-resolution seismic reflection profiles to address the following questions: How did the CSKVF evolve in time and space, and how did volcanism and crustal tectonics interact? What is the volume of the Minoan eruption and how did the eruption shape the seafloor morphology of Santorini? What processes led to the tsunamigenic eruption of the Kolumbo volcano? Can seismic diffractions support the depth conversion and interpretation of offset-limited seismic data?

By linking the marine stratigraphy to onshore volcanic sequences, I present the first consistent seismostratigraphic framework for the CSKVF that allows linking the tectonic evolution of the rift basins to the evolution of the volcanic centers. I demonstrate that the CSKVF evolved from a volcanic field with local centers, and only matured in the last ∼350,000 years to form the vast Santorini edifice. Volcanism emerged in the Late Pliocene when an ESE-WNW-oriented tectonic regime was over-printed by a newly emerging NE-SW-directed rift system. Thereafter, all volcanic centers aligned parallel to this trend and evolved above distinct NE-SW-directed faults that cross-cut present-day Santorini. A major tectonic pulse occurred at ∼0.7 Ma, triggering a large mass-wasting cascade on the flanks of Santorini and Christiana, while another rift pulse at ∼0.35 Ma led a focus of volcanic activity on Santorini with increasing explosivity. In addition, the seismic reflection data enable the Minoan ignimbrites to be identified and mapped in the offshore domain. Combining these data with a multidisciplinary dataset comprising sediment cores and P-wave tomography data, allowed the calculation of the volume of the Minoan eruption, which is estimated to 31.4 ± 5.2 km^3. This estimate is significantly smaller than previously assumed but consistent with an independent caldera collapse reconstruction. The emplacement of vast amounts of ignimbrites, as well as major slumping events during the Minoan eruption, caused the formation of large-scale undulating seafloor bedforms around Santorini. Further, high-resolution 3D seismic and bathymetry data show that the 1650 CE Kolumbo eruption was triggered by a major slumping event of its NW flank that depressurized the magma system, leading to a catastrophic explosion. This chain of events is supported by tsunami models that reproduce historic eyewitness accounts. Finally, I show that diffraction-based wavefront tomography, in combination with an interpretation-driven refinement, enables depth migration of offset-limited seismic data and that the focussed diffracted wavefield is a valuable tool for the interpretation of small-scale heterogeneities, e.g. faults and unconformities.

Combining all results, this thesis highlights that tectonics, volcanism, and mass-wasting are fundamentally interconnected at the CSKVF and can trigger each other as hazardous disaster cascades. Shoreline crossing monitoring and early warning systems are urgently needed on the flanks of Santorini and Kolumbo to prevent the next major event from becoming a disaster.

Kurzfassung

Das Christiana-Santorini-Kolumbo-Vulkanfeld (CSKVF) in der südlichen Ägäis liegt in einer aktiven kontinentalen Riftzone und ist eine der gefährlichsten Vulkanregionen der Welt. Hier ereignete sich vor ca. 400 Jahren der historische Ausbruch des submarinen Kolumbo-Vulkans sowie vor ca. 3600 Jahren die minoische Eruption, die vermutlich zum Untergang der minoischen Zivilisation beigetragen hat. Die Land-Stratigrafie des CSKVF ist eine der am besten untersuchten der Welt, jedoch bestehen große Wissenslücken bezüglich der submarinen Ablagerungen. In dieser Arbeit nutze ich hochauflösende reflexionsseismische Profile, um folgende Fragen zu beantworten: Wie hat sich das CSKVF zeitlich und räumlich entwickelt? Wie haben Vulkanismus und Tektonik interagiert? Wie groß ist das Volumen der minoischen Eruption und wie hat diese Eruption die Morphologie des Meeresbodens von Santorini beeinflusst? Welche Prozesse haben zur tsunamigenen Eruption des Kolumbo-Vulkans geführt? Zudem untersuche ich, wie Diffraktionen die Tiefenkonversion und Interpretation von Offset-begrenzten seismischen Daten unterstützen können.

Durch die Verknüpfung der marinen Stratigrafie mit vulkanischen Sequenzen an Land präsentiere ich das erste konsistente seismostratigrafische Modell für das CSKVF, das es ermöglicht, die tektonische Entwicklung der Riftbecken mit der Entwicklung der vulkanischen Zentren in Verbindung zu bringen. Ich zeige, dass sich das CSKVF aus einem Vulkanfeld mit lokalen Zentren entwickelt hat, das erst in den letzten ca. 350.000 Jahren zu dem großen Santorini-Vulkankomplex heranreifte. Der Vulkanismus begann im späten Pliozän, als ein ESE-WNW-orientiertes tektonisches Regime von einem neu entstehenden NE-SW-gerichteten Riftsystem überlagert wurde. Danach entstanden alle Vulkane parallel zu diesem Trend entlang von NE-SW-streichenden Verwerfungen. Im Pleistozän kam es zu zwei tektonischen Pulsen, die an den Flanken von Santorini eine Kaskade von großen Hangrutschungen auslösten und zu einer Fokussierung der vulkanischen Aktivität auf Santorini führten. Darüber hinaus ermöglichen die seismischen Daten die Identifizierung und Kartierung des minoischen Ignimbrits im submarinen Bereich. Die Kombination dieser Daten mit einem multidisziplinären Datensatz, der Sedimentkerne und P-Wellen-Tomografiedaten umfasst, ermöglichte die Berechnung des Volumens der minoischen Eruption, welches $31,4 \pm 5,2 \text{ km}^3$ beträgt und damit deutlich kleiner ist als bisher angenommen, aber mit einer unabhängigen Rekonstruktion des Caldera-Kollapses übereinstimmt. Die rapide Ablagerung großer Mengen von Ignimbrit sowie Hangrutschungen während der minoischen Eruption führten zur Bildung großflächiger, wellenförmiger Meeresbodenstrukturen um Santorini. Außerdem zeigen hochauflösende seismische 3D-Daten, dass der historische Ausbruch des Kolumbo durch eine Flankenrutschung ausgelöst wurde, die zu einer Druckentlastung im Magmasystem und damit zu einer katastrophalen Explosion führte. Diese Kette von Ereignissen wird durch Tsunami-Modelle gestützt, die historische Augenzeugenberichte reproduzieren können. Schließlich zeige ich anhand einer seismischen Linie, dass Diffraktions-basierte Wellenfronttomografie die Tiefenmigration seismischer Daten ermöglicht und, dass fokussierte Diffraktionen ein wertvolles Werkzeug für die Interpretation von kleinskaligen Strukturen darstellen.

Insgesamt verdeutlicht diese These, dass Tektonik, Vulkanismus und Massenbewegungen am CSKVF grundlegend miteinander verbunden sind und sich gegenseitig als gefährliche Katastrophenkaskaden auslösen können. Überwachungs- und Frühwarnsysteme an den Flanken von Santorini und Kolumbo sind dringend erforderlich, damit das nächste Ereignis nicht zu einer Katastrophe wird.

Contents

List of Figures

List of Tables

List of Publications

Preine, J., Karstens, J., Hübscher, C., Nomikou, P., Schmid, F., Crutchley, G. J., Druitt, T. H., Papanikolaou, D. (2022a). Spatio-temporal evolution of the Christiana-Santorini-Kolumbo volcanic field, Aegean Sea. Geology, 50(1), 96-100. DOI: 10.1130/G49167.1.

Preine, J., Karstens, J., Hübscher, C., Crutchley, G. J., Druitt, T. H., Schmid, F., Nomikou, P. (2022b). The Hidden Giant: How a rift pulse triggered a cascade of sector collapses and voluminous secondary mass-transport events in the early evolution of Santorini. Basin Research. DOI: 10.1111/bre.12667.

Preine, J., Hübscher, C., Karstens, J., Nomikou, P. Volcano-Tectonic evolution of the Christiana-Santorini-Kolumbo Rift Zone (2022c). Tectonics. DOI: 10.1029/2022TC0-07524.

Preine, J., Hübscher, C., Karstens, J., Crutchley, G. J., Nomikou, P., Spatio-temporal evolution of the Kolumbo Volcanic Chain and its link to the volcanic plumbing system of Santorini. Submitted to Geochemistry, Geophysics, Geosystems. DOI: 10.10-02/essoar.10512943.2.

Karstens, J., **Preine, J.**, Crutchley, G. J., Kutterolf, S., van der Bilt, W. G. M., Hooft, E. E. E., Druitt, T. H., Schmid, F., Cederstrøm, J. M., Hübscher, C., Nomikou, P., Carey, S., Kühn, M., Elger, J., Berndt, C. Revised Minoan eruption volume as benchmark for large volcanic eruptions. In Revision in Nature Communications.

Karstens, J., **Preine, J.**, Carey, S., Bell, K. C., Nomikou, P., Hübscher, C., Lampridou, D., Urlaub, M. Formation of undulating seafloor bedforms during the Minoan eruption and their implications for eruption dynamics and slope stability at Santorini. Submitted to Earth and Planetary Science Letters.

Karstens, J., Crutchley, G. J., Hansteen, T., **Preine, J.**, Carey, S., Elger, J., Kühn, M., Nomikou, P., Schmid, F., Dalla Valle, G., Kelfoun, K., Berndt, C. Set up to fail – cascading events during the 1650 tsunamigenic eruption of Kolumbo volcano. In Review by Nature Communications.

Preine, J., Schwarz, B., Bauer, A., Hübscher, C. (2020). When There Is No Offset: A Demonstration of Seismic Diffraction Imaging and Depth-Velocity Model Building in the Southern Aegean Sea. Journal of Geophysical Research: Solid Earth, 125(9). DOI: 10.1029/2020JB019961.

Chapter 1

Introduction

1.1 Motivation

Volcanic eruptions have caused more than 250,000 fatalities since the late 16th century, and large events even affect global climate (Auker et al., 2013; Brown et al., 2017). Today, about one-tenth of the world's population lives within the potential impact zone of volcanic eruptions, while 29 million people live just 10 km away from active volcanoes (Brown et al., 2015). In a world where population growth and anthropogenic climate change are putting increasing stress on societies that are heavily dependent on global supply chains, the global vulnerability to volcanic eruptions, especially in coastal areas, has never been greater (Kopp et al., 2021; Cassidy and Mani, 2022; Pörtner et al., 2022). The impact of a major eruption today would be devastating and would hit the world largely unprepared (Cassidy and Mani, 2022).

As demonstrated by the massive eruption of the Hunga Tonga–Hunga Ha'apai volcano in early 2022, seawater interaction during shallow eruptions is capable of producing violent phreatomagmatic explosions sending ash over distances of hundreds of kilometers affecting communities, infrastructures, and agriculture (Cassidy and Mani, 2022). The blast of this eruption created a shockwave that circled several times across the globe and tsunamis that reached the coastlines of North and South America more than 10,000 km away (Lynett et al., 2022). With a magnitude of 5-6 on the volcanic explosivity index (VEI), the eruption of Hunga Tonga–Hunga Ha'apai was the largest eruption of the 21st century so far (Poli and Shapiro, 2022). However, recent data from ice cores suggest that the probability of an eruption with a magnitude 10-100 times larger or more than of Hunga Tonga–Hunga Ha'apai is 1 in 6 in this century (Cassidy and Mani, 2022; Lin et al., 2022). The last event of such magnitude occurred in 1815 during the Tambora eruption in Indonesia and the death toll from this event is estimated to be as high as 100,000 on nearby islands (Reid and Mountain, 2015). In the following year, global temperatures dropped by 1 °C causing famines, violent upheavals, and the uprising of epidemics in Europe and the United States (Cassidy and Mani, 2022; Stothers, 1984).

Since reliable predictions of eruptions are still a distant goal, in addition to improving and expanding monitoring systems, it is imperative to advance our understanding of the history of volcanic systems to be better prepared for the next big eruption (Cassidy and Mani, 2022). For this, we need to know: What are the volumes and reoccurrence rates of large-scale eruptions? How do volcanic plumbing systems develop in time and space? How are volcanic systems related to tectonic systems? How do extreme events such as volcanic eruptions, earthquakes, and tsunamis interact?
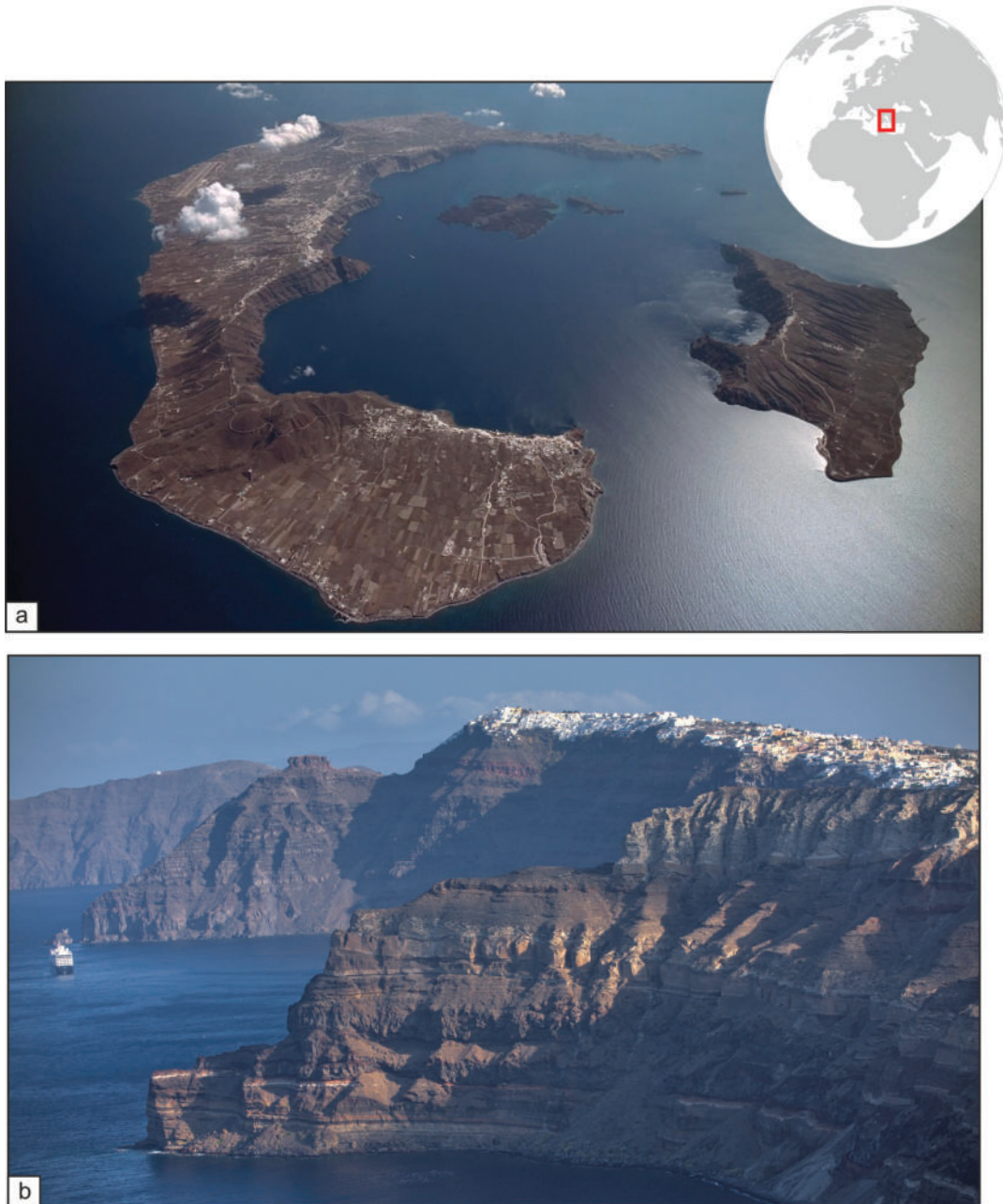
FIGURE 1.1: (a) Aerial photograph of Santorini Caldera from the north (Druitt et al., 2019b) (b) Photograph of the eastern caldera cliff of Santorini with the town of Firá at the top (photo: J. Preine). The layers exposed on the cliffs contain the eruption products from Santorini dating back more than 300,000 years.

A particularly well-suited region for studying the history of large-scale eruptions is the Hellenic Volcanic Arc in the southern Aegean Sea, which poses a major hazard to the densely populated eastern Mediterranean. At the center of this arc lies the Santorini archipelago, which is visited by over 2 million tourists per year and is considered one of the most popular island destinations in the world (Smith, 2017). In the center of the Santorini archipelago lies the Kameni volcano, the activity of which was last highlighted by a period of ground inflation due to magma intrusion underneath Santorini in 2011-2012 (Parks et al., 2015).
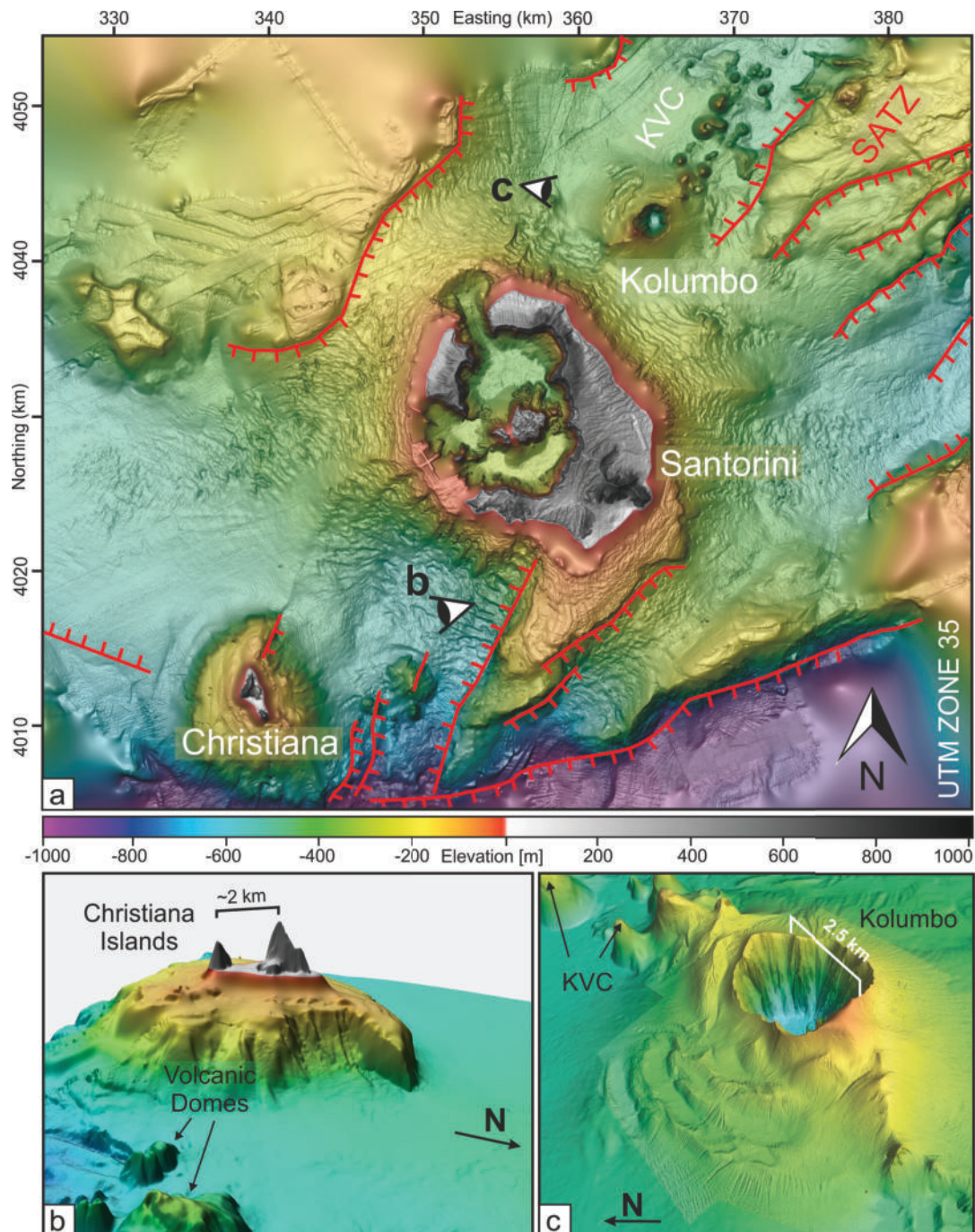
FIGURE 1.2: (a) Morphological map of the Christiana-Santorini-Kolumbo volcanic field. Red lines indicate faults. KVC: Kolumbo Volcanic Chain. SATZ: Santorini-Amorgos Tectonic Zone. Modified from Preine et al. (2022a). (b) Three-dimensional view of the Christiana Volcano and the (c) Kolumbo Volcano. Viewpoints are illustrated in (a). Modified from Preine et al. (2022b) and (Karstens et al., In Review_B). Five-times vertical exaggeration.

Santorini has a history of violent volcanic eruptions, and 3,600 years ago, it was the site of one of the largest eruptions of the Holocene (Sigurdsson et al., 2006; Johnston

et al., 2014). The so-called Minoan eruption released vast amounts of gas-charged magma within hours to days sending tephra, aerosols, and tsunamis across the eastern Mediterranean (e.g. Druitt et al., 2019a). After the eruption, major parts of the island collapsed into the sea, leaving behind a large caldera (Fig. 1.1a). The eruption had disastrous consequences for the people who populated the islands of the Aegean Sea in the late Bronze Age and possibly contributed to the decline of the great Minoan civilization (Marinatos, 1939; Druitt et al., 2019a).

The Minoan eruption was one of many large-scale eruptions on Santorini, which are well documented on the caldera cliffs where the deposits of over 100 explosive eruptions are exposed (Druitt et al., 1999) (Fig. 1.1b). Since the 19th century, volcanological studies have been carried out on Santorini, and the work of Fouqué (1879) is considered an early masterpiece of volcanological research (Druitt et al., 1999). It described the stratigraphy of the caldera wall, recognized the true volcanic origin of the caldera depression, and discovered buildings of an ancient civilization beneath the uppermost volcanic layers (Fouqué, 1879; Druitt et al., 1999). Thanks to the diligent work of volcanologists since the 1980s, the onshore volcanic products of Santorini are now one of the best-studied volcanic sequences worldwide (e.g. Druitt et al., 1999). However, large amounts of the volcanic products from Santorini lie in the offshore realm, which is difficult to access and has only recently started to be systematically explored (e.g. Hübscher et al., 2006; Carey et al., 2011; Johnston et al., 2015; Nomikou et al., 2019). Thus, the early evolution of Santorini, as well as the nature and volume of deposits within and outside the caldera are still largely unknown.

In addition to the volcanism on Santorini, the neighboring Kolumbo volcano poses a major hazard to the southern Aegean (Fig. 1.2b) (e.g. Nomikou et al., 2019). It is part of the Christiana-Santorini-Kolumbo (CSK) volcanic field, which extends over 100 km in a NE-SW direction with Santorini at its center (e.g. Nomikou et al., 2019). The Christiana Volcano SW of Santorini is a large but inactive edifice of which only a small part is exposed above the seafloor, forming three uninhabited islets (Fig. 1.2b). About 8 km NE of Santorini lies the submarine Kolumbo volcano as well as the Kolumbo Volcanic Chain (KVC), which consists of more than 20 additional submarine volcanoes (Fig. 1.2c) (Nomikou et al., 2012; Hübscher et al., 2015; Hooft et al., 2017). The historic eruption of Kolumbo in 1650 caused over 70 fatalities on Santorini and generated damaging tsunamis that inundated the nearby islands (Dominey-Howes, 2004; Cantner et al., 2014). However, none of the earlier eruptions of Kolumbo have been dated, and also the volcanism of Christiana is completely undated, leaving important questions about the chronological and structural evolution of the CSK volcanic field unanswered.

In addition to the volcanic hazard, Santorini is part of the Santorini-Amorgos Tectonic Zone (SATZ), one of the seismically most active regions of the Mediterranean (Fig. 1.2) (Bohnhoff et al., 2006). The largest earthquake of the 20th century in the Aegean sea occurred on 9 July 1956 SW of the island of Amorgos with a magnitude of $MS = 7.4$ and a second earthquake with a magnitude of $MS = 7.2$ occurred only 13 minutes later (Brüstle et al., 2014). Both earthquakes generated a major tsunami and caused severe damage on the surrounding islands, killing 54 people and collapsing more than 3,200 buildings, most of which were located on Santorini. While the most accepted fault-plane solution indicates normal faulting to be the main tectonic movement in the SATZ (Brüstle et al., 2014), there is an ongoing debate about the role of strike-slip tectonics (Sakellariou et al., 2010; Hübscher et al., 2015; Nomikou et al., 2018b). So far, a detailed analysis of the internal fault patterns and how they

continue underneath Santorini as well as a reconstruction of the tectonic evolution of the SATZ are missing, which are essential to help resolve the debate over the role of strike-slip faulting and to better understand the acting tectonic forces.

A detailed understanding of the tectonic system is also imperative since volcanism and tectonics are often linked in complex ways (Acocella, 2021). Regional tectonics can weaken the crust through increased faulting and fracturing creating pathways for magmatic fluids to ascent to the surface, although the controlling mechanisms remain elusive (Hill et al., 2002; Manga and Brodsky, 2006). In turn, volcanism can alter the stress of the crust by accommodating extensional strain and inhibiting the formation of faults (Faulds and Varga, 1998) or by inducing unrest or eruptions in volcanic systems that are situated up to several hundreds of km from the epicenter (Hill et al., 2002; Manga and Brodsky, 2006). At Santorini, such sensitive volcano-tectonic feedback links were highlighted during the phase of magmatic inflation in 2011-12, during which the stress changes induced by the magma intrusion below the caldera of Santorini triggered earthquakes ∼60 km to the SW at the margin of the Cretan Basin (Feuillet, 2013; Kiratzi, 2013). However, the dynamics of long-term interaction (> 100 ka) between tectonics and magmatism are yet underexplored, since they require knowledge of the past dynamics of the tectonic stress field and the volcanic behavior, which are rarely available (Giba et al., 2013).

It is evident that the islands of the Aegean and the broader eastern Mediterranean are threatened by a wide range of geohazards from the CSK volcanic field (Hübscher et al., 2006). To improve the understanding of these hazards, this work provides detailed insights into the history of the interplay between volcanism, tectonics, and mass-wasting at the CSK volcanic field, which is poorly understood at this point. A major reason for this knowledge gap is that most of the deposits and tectonic features are submarine and thus difficult to assess for direct observation and sampling. However, modern marine seismic reflection surveys offer the unique opportunity to produce high-resolution images of the subsurface that allow detailed insights into the internal structure of the basins, fault systems, volcanoes, eruptive products, and mass-wasting deposits and, thus, enable a reconstruction of the volcano-tectonic history (e.g. Hübscher et al., 2015; Reynolds et al., 2018; Karstens et al., 2019). The field of seismic interpretation of volcanic structures is comparatively young (e.g. Bischoff et al., 2021), but is capable of providing crucial information on the evolution of volcanic systems (e.g. Hübscher et al., 2015; Reynolds et al., 2018; Karstens et al., 2019). For example, seismic imagery can be used to resolve the internal structure of volcanoes (e.g. Magee et al., 2013; Reynolds et al., 2018; Romer et al., 2021), to image sills as storage and transport systems of magma (e.g. Planke et al., 2005; Schofield et al., 2012; Galland et al., 2018), to identify and map the eruptive products of volcanoes, (e.g. Karstens et al., 2013; Pope et al., 2018; Casalbore et al., 2021), or to reconstruct the disintegration processes of volcanic edifices (e.g. Watt et al., 2012; Karstens et al., 2019; Kühn et al., 2021).

In this thesis, I use an extensive collection of seismic reflection data consisting of more than 170 seismic profiles covering a distance of over 3,300 km to reconstruct the history of volcanism and tectonics at Santorini and its neighboring rift system. In the course of this PhD thesis, I have processed all of these profiles to produce the best possible seismic images for interpretation and, since the data were acquired during six different research expeditions, homogenized the dataset to enable a joint interpretation. The resulting seismic images provide high-resolution insights into the subsurface and internal architecture of the basins and volcanic edifices, which

enables a detailed reconstruction of the spatio-temporal interplay of volcanism, tectonics, and mass-wasting. In this thesis, I seek to provide insights into the following questions:

- How did the main volcanic centers of the CSK volcanic field evolve in time and space?

- How did the rift basins evolve and is there a link to the activity of the volcanic centers?

- Are there any large-scale mass-wasting deposits around the CSK volcanic field, as known from other volcanic islands?

- Are there unknown volcanoes in the CSK region that lie hidden beneath the seafloor?

- Can the Minoan deposits be distinguished in the seismic data and how large is their volume?

- How do caldera-forming eruptions influence the surrounding seafloor morphology?

- What series of events led to the 1650 eruption of Kolumbo occur and what caused the tsunami?

Answering these questions will allow to reconstruct the history of the CSK volcanic field and provide new insights into the frequency, impact, and interplay of marine hazards in this region. The lessons learned from this will help to improve the required action knowledge for addressing these hazards. Therefore, it is necessary to pave the way from these newly gained geological insights to the last mile and support local stakeholders and policymakers in a holistic hazard assessment for the southern Aegean Sea to be better prepared for the next big event.

1.2   Structure of the Thesis

This thesis is divided into 12 chapters. Chapters 4-11 represent scientific articles that were written as part of this doctoral thesis and have been peer-reviewed and published in international journals (Chapters 4, 5, 6, 11), as well as articles that have been submitted and are under review (Chapters 7, 8, 9, 10). Chapters 4-7, as well as Chapter 11, represent scientific articles, which I led as the first author. Chapters 8-10 are scientific articles led by Dr. Jens Karstens as the first author, to which I contributed significantly as part of my PhD project and am therefore listed as either second (Chapters 8, 9) or fourth author (Chapter 10). All chapters are largely based on the seismic database processed and homogenized as part of this thesis as well as the seismostratigraphic framework established in this thesis.

Chapter 1 provides an introduction to the motivation and objectives of this doctoral thesis, gives an overview of the structure of this thesis, and lists the author contributions to Chapters 4-11.

Chapter 2 gives an overview of the geological framework of the study area.

Chapter 3 provides an overview of the basic concept of the seismic imaging method and gives an overview of the database, the applied seismic processing workflow, as well as the basic concepts of seismic interpretation relevant to this thesis.

Chapter 4 is based on an article published in the journal **GEOLOGY**:
Preine, J., Karstens, J., Hübscher, C., Nomikou, P., Schmid, F., Crutchley, G. J., Druitt, T.H. & Papanikolaou, D. (2022a). Spatio-temporal evolution of the Christiana-Santorini-Kolumbo volcanic field, Aegean Sea. Geology, 50(1), 96-100.
This chapter focuses on the relative chronology of the evolution of the volcanic centers of the CSK volcanic field. It presents for the first time a consistent chronostratigraphic framework linking the volcanic centers of Christiana, Santorini, and Kolumbo based on high-resolution seismic reflection data. It shows how volcanic activity migrated over time from one center to the other. Further, this chapter presents several previously unknown volcanic edifices, eruption products, and mass-transport deposits, which close major gaps in volcanic chronology of the CSK volcanic field.

Chapter 5 is based on an article published in the journal **Basin Research**:
Preine, J., Karstens, J., Hübscher, C., Crutchley, G. J., Druitt, T. H., Schmid, F., & Nomikou, P. (2022b). The Hidden Giant: How a rift pulse triggered a cascade of sector collapses and voluminous secondary mass-transport events in the early evolution of Santorini. Basin Research.
This chapter unravels the nature of seismostratigraphic Unit 4, which was identified in Chapter 4. Using high-resolution seismic reflection profiles, it shows that this unit is the result of a complex disaster cascade that occurred at Santorini approx. 700 ka. Triggered by crustal extension, this cascade involved catastrophic sector collapse events at Christiana and Santorini that led to large-scale secondary sediment failures, which coincide with the advent of increasing volcanism along the Christiana-Santorini-Kolumbo volcanic field. The deposits of this cascade are identified in all basins surrounding Santorini and with a volume of up to 125 km^3, it represents one of the largest mass-transport deposits in the Mediterranean Sea.

Chapter 6 is based on an article published in the journal **Tectonics**:
Preine, J., Hübscher, C., Karstens, J., & Nomikou, P. (2022c). Volcano-Tectonic Evolution of the Christiana-Santorini-Kolumbo Rift Zone, Aegean Sea.
In this chapter, the tectonic evolution of the Christiana-Santorini-Kolumbo Rift Zone is reconstructed since the Early Pliocene using high-resolution seismic reflection profiles. The evolution of the tectonic faults had a major influence on the emplacement of volcanic edifices along the volcanic field, and vice versa. Volcanism initiated as an emerging NE-SW-directed fault trend overprinted an older NNE-SSW-oriented fault regime. In addition, this chapter shows that two major tectonic pulses preceded major changes in the behavior of the volcanic field and, thus, highlight distinct volcano-tectonic feedback links. These tectonic pulses are related to changes in the broader stress regime of the eastern Hellenic Arc and volcano-tectonic events are compared with studies of the Kos-Nisyros-Yali field and the island of Rhodos.

Chapter 7 is based on an article submitted to the journal **Geochemistry, Geophysics, Geosystems**:
Preine, J., Hübscher, C., Karstens, J., Crutchley, G. J., & Nomikou, P. (Submitted). Spatio-temporal evolution of the Kolumbo Volcanic Chain and its link to the volcanic plumbing system of Santorini

This chapter focuses on the Kolumbo Volcanic Chain (KVC) and its link to the tectonic system and the volcanism of Santorini. Using an extensive framework of seismic reflection profiles, the evolution of the KVC in space and time and its link to the volcanic plumbing system of Santorini is reconstructed. The KVC evolved during two episodes evolving from largely effusive to more explosive volcanism. An analysis of the NE part of the KVC shows that two normal fault systems continue the linear trend of the KVC indicating that the formation of the volcanic edifices was controlled by distinct tectonic lines. In addition, seismic profiles are used to investigate the area between the Kolumbo Volcano and the Santorini Caldera, which reveal a volcanic ridge that connects the NE flank of Santorini with Kolumbo, highlighting a deep-seated connection between both systems.

Chapter 8 is based on an article in revision in the journal **Nature Communications**:
*Karstens, J., **Preine**, J., Crutchley, G. J., Kutterolf, S., van der Bilt, W. G. M., Hooft, E. E. E., Druitt, T. H., Schmid, F., Cederstrøm, J. M., Hübscher, C., Nomikou, P., Carey, S., Kühn, M., Elger, J., Berndt, C. (In Review). Revised Minoan eruption volume as benchmark for large volcanic eruptions.*
In this chapter, a unique multi-disciplinary dataset is used to constrain the volume of the Minoan volcanic eruption, which is estimated to be much smaller than previously suggested. By integrating high-resolution seismic reflection and seismic P-wave tomography datasets with sediment core analysis, the bulk volume of distal ash-fall, proximal ignimbrite, and intra-caldera deposits is estimated. Computed-Tomography-derived porosity estimates enable the calculation of the dry-rock equivalent volume, which corresponds well to an independent reconstruction of the caldera collapse volume, indicating an internal consistency of these estimates.

Chapter 9 is based on an article submitted to the journal **Earth and Planetary Science Letters**:
*Karstens, J., **Preine, J.**, Carey, S., Bell, K. C., Nomikou, P., Hübscher, C., Lampridou, D., Urlaub, M. (Submitted). Formation of undulating seafloor bedforms during the Minoan eruption and their implications for eruption dynamics and slope stability at Santorini.*
This chapter uses a combination of high-resolution seismic reflection data, combined with multibeam echosounder bathymetry to study the formation of undulating seafloor bedforms around the flanks of Santorini. These bedforms occur up to 25 km away from Santorini and differ significantly in wavelength and wave heights (several meters vs tens to hundreds of meters). This chapter shows that all of these deposits are mass-transport deposits but differ in composition or formation mechanisms. Three different types of USBs are distinguished, the first type being flow-derived ignimbrites that occur north of Santorini, where the undulating topography is the result of syn-depositional thrusting. The second type of undulating seafloor bedforms occurs east, west, and south of Santorini and are the result of slope failures that affect also pre-Minoan deposits. The third type is found in the SW of Santorini, where the activity of the rift system controlled deep-seated deformation of the flank of Santorini leading to a steepened slope and multiple mass-wasting events. For the last two types, undulating topography is caused by block rotation in the upslope domain and thrusting in the downslope domain.

Chapter 10 is based on an article in review by the journal **Nature Communications**:
*Karstens, J., Crutchley, G. J., Hansteen, T., **Preine, J.**, Carey, S., Elger, J., Kühn, M., Nomikou, P., Schmid, Fl., Dalla Valle, G., Kelfoun, K., Berndt, C. Set up to fail – cascading events during the 1650 tsunamigenic eruption of Kolumbo Volcano*

In this chapter, the complex tsunami genesis during the submarine volcanic eruption of the Kolumbo Volcano in 1650 is reconstructed. Based on a combination of high-resolution 3D seismic and bathymetric data, as well as numerical tsunami simulations, it is shown that a combination of flank deformation and explosive eruption is required to explain the detailed historic eyewitness accounts of the tsunami run-up. The 3D seismic data reveal how flank deformation initiated a cascade of processes that ultimately led to the violent explosive eruption and tsunami.

Chapter 11 is based on an article published in the journal **JGR Solid Earth**:
Preine, J., Schwarz, B., Bauer, A., & Hübscher, C. (2020). When There Is No Offset: A Demonstration of Seismic Diffraction Imaging and Depth-Velocity Model Building in the Southern Aegean Sea. Journal of Geophysical Research: Solid Earth, 125(9)
In this chapter, a robust diffraction extraction scheme that models and adaptively subtracts the reflected wavefield from the seismic data is used to generate diffraction-only images of a seismic profile crossing the eastern Santorini-Anafi Basin. These diffractions allow the estimation of insightful wavefront attributes, which are used to perform wavefront tomography. Afterwards, the obtained seismic velocity model is refined by an interpretation-driven analysis to exclude out-of-plane effects before depth migration is performed. In addition, by using diffractions as physics-guided attribute maps, diffraction images are produced that support the interpretation of faults and unconformities in the Santorini-Anafi Basin revealing several distinct internal fault systems.
Although this paper has been published first, I include it as the last chapter of this thesis, as this paper is more methodological in nature. The other chapters are directly related and tell a common big story and this chapter deviates somewhat from the flow of the other chapters. In addition, the method of diffraction-based depth conversion requires verification by drilling data, which was not available in this area at the time this thesis is submitted.

Chapter 12 summarizes the results from the previous chapters, provides an outlook on upcoming projects, and draws an integrated conclusion for future research directions.

1.3   Author Contributions

Chapters 4-7 and 11 are based on articles either published or submitted to scientific journals that I was the first author on, while Chapters 8-10 are based on articles either in review or submitted to scientific journals that I was a co-author on. In the following, I briefly summarize the contributions from all (co-)authors following the CRediT Taxonomy (Allen et al., 2019).

Chapter 4: C. Hübscher supervised the PhD project. J. Karstens and C. Hübscher were responsible for organizing and designing the seismic reflection experiments during cruise POS538. J. Karstens, **J. Preine**, G. J. Crutchley, F. Schmid., and P. Nomikou acquired the seismic reflection data during cruise POS538. C. Hübscher and P. Nomikou provided additional seismic reflection data from previous cruises. **J. Preine** processed all seismic reflection data and integrated them with the previously acquired seismic reflection data. **J. Preine** established the seismostratigraphic framework. **J. Preine**, J. Karstens, and C. Hübscher interpreted the data. F. Schmidt

applied OBS-based ray-tracing analysis to estimate seismic velocities. **J. Preine** estimated the age model. **J. Preine**, J. Karstens, C. Hübscher, T. H. Druitt, and D. Papanikolaou integrated the geophysical results into the volcanological framework of Santorini. **J. Preine** drafted the manuscript, which was then initially discussed and revised with J. Karstens and C. Hübscher, while all coauthors discussed the dataset and provided comments and corrections to the manuscript.

Chapter 5: C. Hübscher supervised the PhD project J. Kastens and C. Hübscher were responsible for organizing and designing the seismic reflection experiments during cruise POS538. J. Karstens, **J. Preine**, G. J. Crutchley, F. Schmid., and P. Nomikou acquired the seismic reflection data during cruise POS538. C. Hübscher and P. Nomikou provided additional seismic reflection data from previous cruises. **J. Preine** processed all seismic reflection data and integrated them with the previously acquired seismic reflection data. **J. Preine** established the seismostratigraphic framework, mapped and gridded Unit 4. **J. Preine**, J. Karstens, and C. Hübscher established the general concept of the mass-wasting cascade. **J. Preine**, J. Karstens, C. Hübscher, and T. H. Druitt integrated the geophysical results into the volcanological framework of Santorini. **J. Preine** drafted the manuscript, which was then initially discussed and revised with J. Karstens and C. Hübscher, while all coauthors discussed the dataset and provided comments and corrections to the manuscript.

Chapter 6: C. Hübscher supervised the PhD project and provided the POS338 data. J. Karstens provided the POS538 data, and P. Nomikou provided the SCS data. **J. Preine** processed all seismic reflection data and integrated them with the previously acquired seismic reflection data. **J. Preine** established the seismostratigraphic framework, and mapped and gridded the seismic units. **J. Preine** and C. Hübscher identified tectonic pulses and linked tectonic episodes to the evolution of the Kos-Nisyros-Yali field. P. Nomikou provided additional bathymetric data from the Kos-Nisyros-Yali field. **J. Preine** drafted the manuscript, which was then initially discussed and revised with C. Hübscher and J. Karstens, while all coauthors discussed the dataset and provided comments and corrections to the manuscript.

Chapter 7: C. Hübscher supervised the PhD project and provided the POS338 data. J. Karstens provided the POS538 data, and P. Nomikou provided the SCS data. J. Karstens, **J. Preine**, G. J. Crutchley, and P. Nomikou acquired the seismic reflection data during cruise POS538. **J. Preine** processed all seismic reflection data and integrated them with the previously acquired seismic reflection data. **J. Preine** established the seismostratigraphic framework and identified the volcanic structures and their chronological formation order. **J. Preine** drafted the manuscript, which was then initially discussed and revised with C. Hübscher and J. Karstens, while all coauthors discussed the dataset and provided comments and corrections to the manuscript.

Chapter 8: J. Karstens., C. Berndt., and C. Hübscher were responsible for organizing and designing the seismic reflection experiments during cruise POS538. J. Karstens, **J. Preine**, G. J. Crutchley, F. Schmid., P. Nomikou, M. Kühn, and J. Elgers acquired the seismic reflection data during cruise POS538. C. Hübscher and P. Nomikou provided seismic reflection data from previous cruises. **J. Preine** processed the seismic reflection data and integrated them with the previously acquired seismic reflection data. J.Karstens and **J. Preine** interpreted the data, identified and mapped the Minoan deposits in and outside the caldera. S. Kutterolf collected the sediment cores,

W. G. M. van der Bilt. and J.M. Cederstrøm. performed the C-T scans and all three interpreted the sediment cores. E. E. E. Hooft provided and interpreted the P-wave tomography data. J. Karstens, **J. Preine**, T. H. Druitt, S. Kutterolf, and S. Carey integrated the geophysical results into the volcanological framework of Santorini. J. Karstens, **J. Preine**, and G. J. Crutchley drafted the manuscript, while all coauthors discussed the dataset and provided comments and corrections to the manuscript.

Chapter 9: J. Karstens., and C. Hübscher were responsible for organizing and designing the seismic reflection experiments during cruise POS538. J. Karstens, **J. Preine**, and P. Nomikou acquired the seismic reflection data during cruise POS538. C. Hübscher and P. Nomikou provided seismic reflection data from previous cruises. **J. Preine** processed the seismic reflection data and integrated them with the previously acquired seismic reflection data. **J. Preine** established the seismostratigraphic framework. J.Karstens and **J. Preine** interpreted the data, identified and mapped undulating seafloor bedforms. J. Karstens, **J. Preine** and D. Lampridou generated the morphological profiles and regression curves for selected bathymetric profiles across undulating seafloor bedforms. J. Karstens, **J. Preine**, S. Carey, P. Nomikou, and C. Hübscher integrated the geophysical results into the volcanological framework of Santorini. J. Karstens and **J. Preine** drafted the manuscript, while all coauthors discussed the dataset and provided comments and corrections to the manuscript.

Chapter 10: J. Karstens was responsible for organizing and designing the seismic reflection experiments. J. Karstens, G. J. Crutchley, **J. Preine**, F. Schmid, P. Nomikou, M. Kühn, and J. Elgers. acquired, processed, and interpreted the seismic reflection data. S. Carey provided the ROV footage from within the crater. J. Karstens and K. Kelfoun performed the numerical tsunami simulations. J. Karstens, G. J. Crutchley, T. Hansteen, **J. Preine** and S. Carey integrated the geophysical results into the volcanological framework of Santorini. J. Karstens, G. J. Crutchley, and T. Hansteen drafted the manuscript, while all coauthors discussed the dataset and provided comments and corrections to the manuscript.

Chapter 11: C. Hübscher provided the seismic reflection data and supervised the project. B. Schwarz provided the diffraction separation code, while A. Bauer provided the wavefront tomography. **J. Preine** performed the diffraction separation and the interpretation-guided velocity model refinement. A. Bauer performed the post-stack depth migration. **J. Preine** conceptualized the idea of using diffraction images for interpretation by blending focused diffraction images over the migrated full-wavefield images. **J. Preine** drafted the manuscript and the figures. All coauthors discussed the method and provided comments and corrections to the manuscript.

Chapter 2

Geological Framework

The CSK volcanic field lies on the Hellenic Arc in the southern Aegean Sea, which represents the seismically most active region in the Mediterranean Sea (Fig. 2.1, 2.2) (Bohnhoff et al., 2006). Formed as a consequence of the subduction of the African plate underneath the Eurasian plate, the Hellenic Arc is an arcuate belt reaching from the Adriatic Sea towards western Anatolia, where it transitions into the Cyprus arc (e.g. Le Pichon and Angelier, 1979; Royden and Papanikolaou, 2011). Since the Late Miocene, the Hellenic Arc has stepped southwards and increased in curvature, leading to enhanced extension and intensive internal deformation of the Aegean microplate (e.g. Veen and Kleinspehn, 2002). These processes have been attributed to the rollback of the subducted African slab induced by the downwards pull of the subducted slab (e.g. Le Pichon and Angelier, 1979; Le Pichon and Kreemer, 2010), gravitational forcing associated with overthickened Alpine crust (e.g. Jolivet, 2001), andd westward extrusion of the Anatolian plate (e.g. Taymaz et al., 1991). The complex interplay of these processes produced the neotectonic horst and graben structures of the Cycladic islands (Le Pichon and Kreemer, 2010; Royden and Papanikolaou, 2011), where crustal thicknesses range from 20 to 30 km, compared to 40-50 km under mainland Greece and Turkey (Zhu et al., 2006).

The Aegean crust consists of metamorphic rocks belonging to the Attico-Cycladic complex that formed as a result of compressional orogeny in the early Cenozoic (Piper et al., 2007). During Miocene to Pliocene, N-S directed extension led to basin subsidence in the southern Aegean forming multiple basins bounded by E-W directed listric normal faults (Anastasakis and Piper, 2005; Piper et al., 2007). Increasing curvature of the Hellenic Arc led to counterclockwise rotation of the eastern segments of the Aegean in the Pliocene, leading to higher curvature of the slab east of Crete compared to the western part (e.g. Bocchini et al., 2018). The strong curvature of the plate boundary implies an increasing obliquity of the plate convergence from west to east (Fig. 2.1). While west of Crete, plate convergence occurs perpendicular to the arc, the obliquity increases to about 40° to 50° in the region of Rhodes (Bocchini et al., 2018). This slab segmentation affects upper plate deformation, which is stronger in the eastern slab leading to the formation of major NE-SW directed fault systems. In the forearc region, this differential movement is accommodated by arc-parallel extension causing left-lateral movements between the forearc slivers along the Ptolemy, Pliny, and Strabo Trenches, and arc-normal extension in the backarc region, causing transtensional faulting along the Santorini-Amorgos Tectonic zone, which hosts the CSK volcanic field (Fig. 2.1) (Gautier et al., 1999; Meier et al., 2007; Nomikou et al., 2018b).
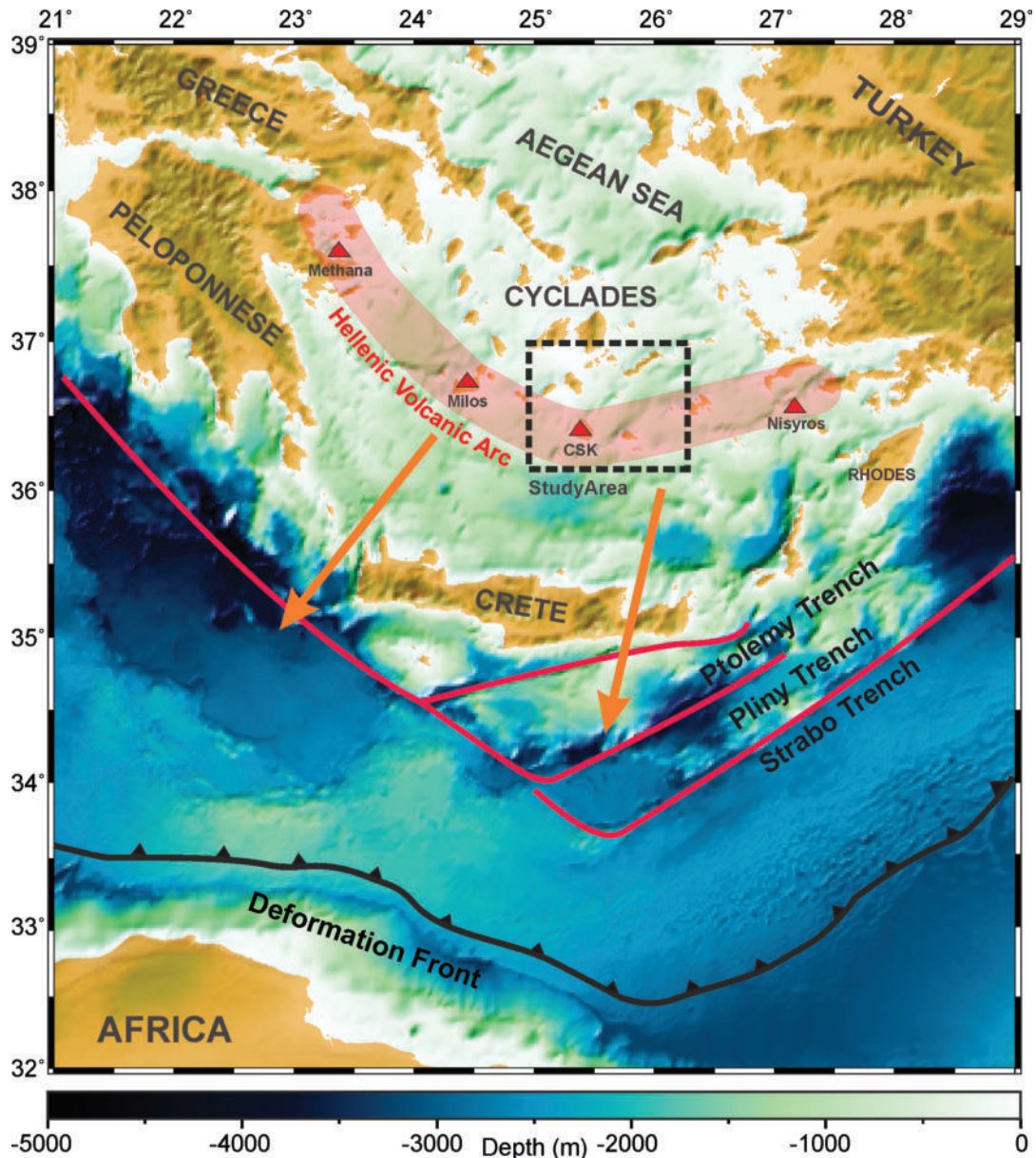
FIGURE 2.1: Southern Aegean Sea and major structural features of
the Hellenic Arc. The Hellenic Volcanic Arc is indicated by the semi-
transparent red area. The study area is highlighted by the dashed
box. Orange arrows indicate GPS-derived velocity vectors relative to
Eurasia (Reilinger et al., 2010). Modified from Jolivet et al. (2013) and
Bocchini et al. (2018).

Located in the center of the Hellenic Arc, the 100 km long and 45 km wide CSK rift
zone represents a major structural boundary separating the Hellenic Arc into a vol-
canically and seismically quiet western and an active eastern part (Fig. 2.2) (Bohn-
hoff et al., 2006). The CSK rift zone is situated on the junction of the Christiana Basin
in the west, and the Santorini-Amorgos Tectonic Zone in the east (Fig. 2.2, 2.3). The
NE basins (Anhydros, Santorini-Anafi, and Amorgos) are NE-SW striking grabens
and half-grabens with sediment infill up to 1,400 m thick that are bounded by major
extensional to transtensional faults (Fig. 2.3) (Bohnhoff et al., 2006; Hübscher et al.,
2015; Nomikou et al., 2016b; Nomikou et al., 2018b). The Anhydros Basin contains

the submarine Kolumbo Volcano and the Kolumbo Volcanic Chain (KVC) (Fig. 2.3), whereas the Santorini-Anafi and Amorgos Basins lack volcanoes (Fig. 2.3). Opening of these basins occurred in multiple episodes of enhanced rift activity, so-called 'tectonic pulses' (Hübscher et al., 2015). Both, the Anhydros and Anafi Basins contain six seismostratigraphic units separated by onlap surfaces while the Amorgos Basin only contains the uppermost four units (Hübscher et al., 2015; Nomikou et al., 2016b; Nomikou et al., 2018b; Nomikou et al., 2019). SW of Santorini lies the Christiana Basin, which hosts the Christiana Volcano and several volcanic domes (Fig. 2.3) (Nomikou et al., 2013; Hooft et al., 2017). This basin is assumed to have formed prior to the basins NE of Santorini under an older E-W striking fault system (Piper et al., 2007; Heath et al., 2019).
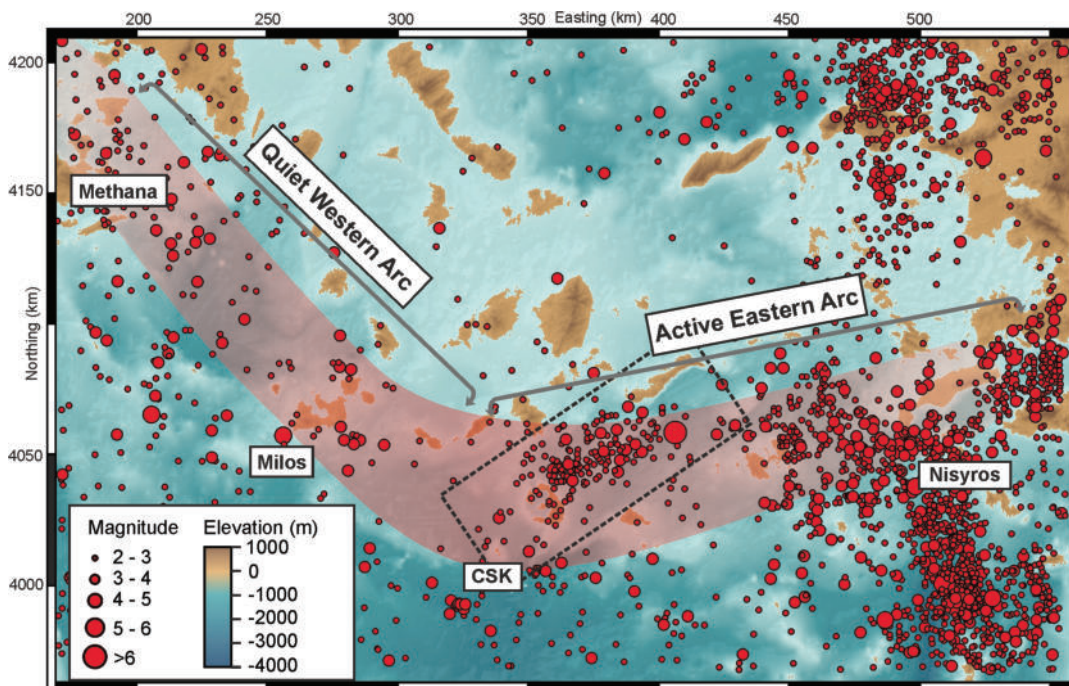
FIGURE 2.2: Seismicity along the Hellenic Volcanic Arc (semi-transparent area). Red circles indicate earthquakes recorded from 1950 to 2022 (courtesy of the U.S. Geological Survey). Bathymetry from EMODnet Bathymetry Consortium (2020). Dashed box indicates the CSK rift zone. Coordinate system is UTM Zone 35N, WGS84.

The present-day Hellenic Volcanic Arc initiated 3-4 Ma ago and stretches from Methana in the west through Milos, the CSK field, to Nisyros in the east (Fig. 2.1,2.2) (e.g. Nomikou et al., 2013) These eruptive centers are located above the subducting slab of the African plate between the Benioff zone isodepths of 100 and 160 km (Papazachos, 2019). The CSK field in the center of the Hellenic Volcanic Arc comprises the extinct Christiana Volcano, the Santorini Caldera, the polygenetic submarine Kolumbo Volcano, as well as the KVC (Fig. 1.2a, 2.3) (Nomikou et al., 2013; Nomikou et al., 2019; Hübscher et al., 2015; Hooft et al., 2017).
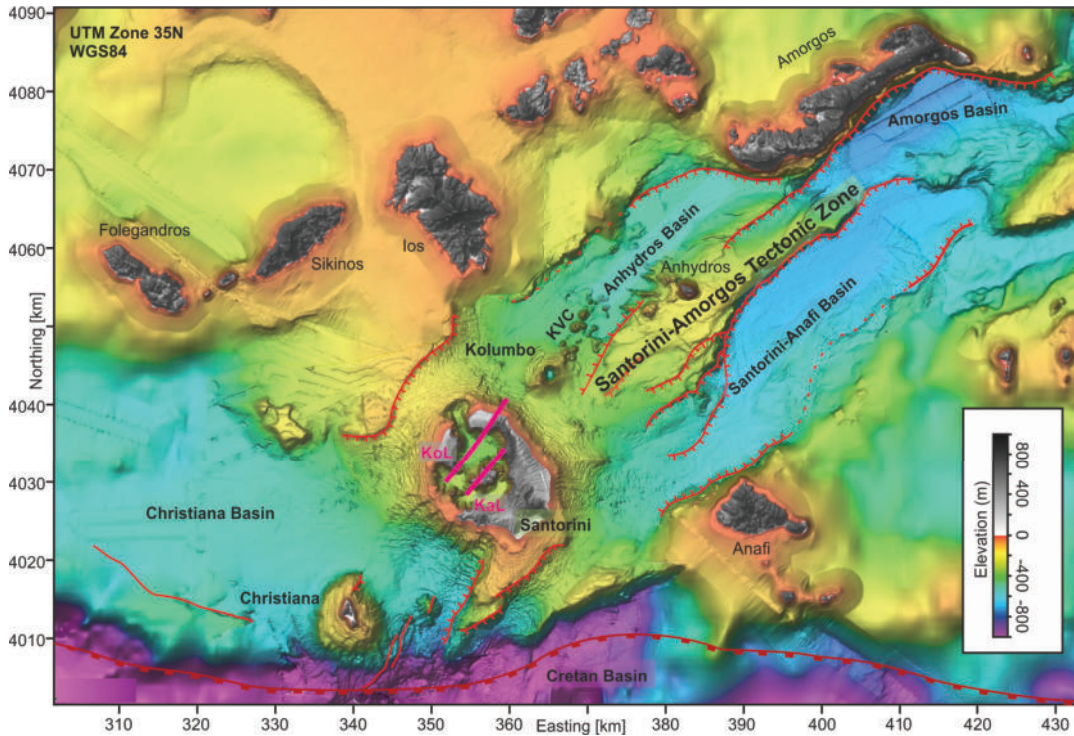
FIGURE 2.3: Morphological map of the CSK rift zone showing islands, basins, volcanic centers, major extensional structures (red lines) (Nomikou et al., 2019), and volcano-tectonic lineaments (pink lines) (Heath et al., 2019). Bathymetry from Nomikou et al. (2012, 2013, 2018, 2019) and Hooft et al. (2017). Topography from the Hellenic Military Geographic Service (HMGS). Coordinate system is UTM Zone 35N, WGS84. KVC: Kolumbo Volcanic Chain; Kol: Kolumbo Line; KaL: Kameni Line (KaL).

The earliest known eruptions of Santorini are the early Akrotiri volcanic centers in the SW of Santorini (Fig. 2.4) that have been dated to 650-550 ka (Druitt et al., 1999). The majority of these centers were presumably submarine and were subsequently uplifted above sea level. This was followed by the construction of the Peristeria stratovolcano (530-430 ka) in the NE of Thera (Fig. 2.4), and the cinder cones of the Akrotiri peninsula that formed during strombolian eruptions between 450-340 ka (Fig. 2.4) (Druitt et al., 1999). Volcanism changed from being dominantly effusive to highly explosive at Santorini at about ~360 ka, which marks the onset of the first explosive cycle that ended with the caldera-forming Lower Pumice eruption at approx. 177 ka (Fig. 2.4b) (e.g. Druitt et al., 2019b). The products of the first and second eruptive cycles are referred to as the Thera Pyroclastic Formation (TPF). At least four caldera collapses occurred during the TPF, as indicated by prominent unconformities in the caldera cliffs.
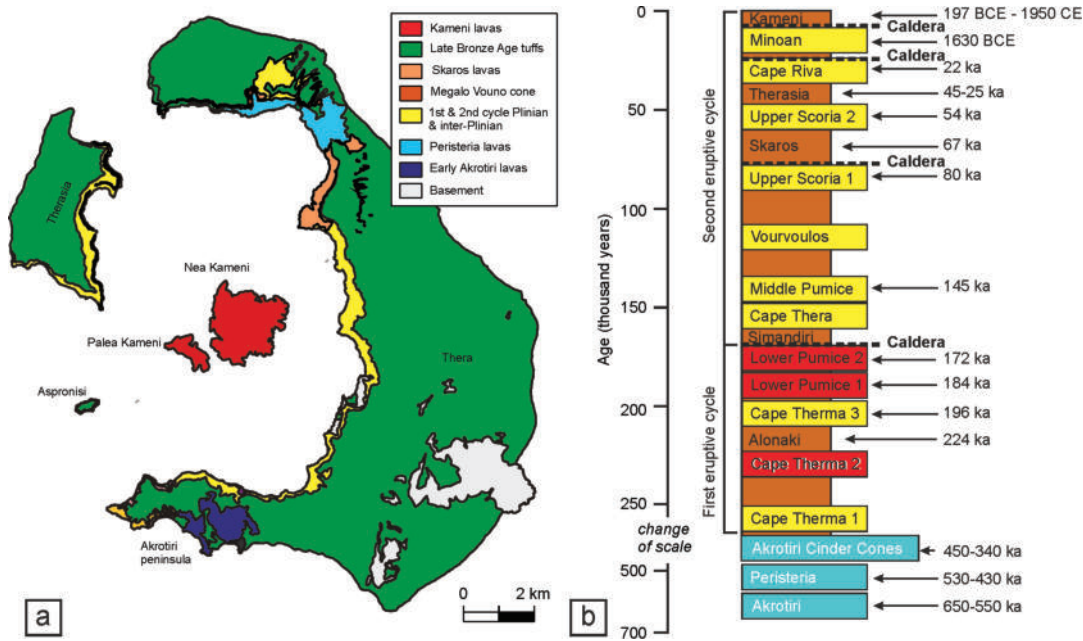
FIGURE 2.4: (a) Simplified geological map of Santorini. Modified from Druitt et al. (1999, 2019b). (b) Overview of the volcanic history of Santorini since the earliest dated activity (∼650 ka). The three earliest volcanic centers are shown in blue. Plinian eruptions are indicated in yellow (mainly magmas of intermediate compositions) and red (Mainly silicic magmas). The products of inter-Plinian periods are indicated in brown, five of which are named. Dashed black lines indicate caldera-forming eruptions. BCE: Before Common Era; CE: Common Era. Modified from Druitt et al. (1999, 2019b).

The last caldera-forming eruption was the Minoan eruption which occurred approx. 1600 BCE. This cataclysmic event started with precursory explosions some days to weeks before the onset of the main eruption sequence (Heiken and McCoy, 1984; Druitt et al., 1999; Druitt et al., 2019a), which was subdivided into four phases beginning with subaerial Plinian discharge (phase 1). After several hours, the eruption vent migrated into a pre-existing flooded caldera, where the interaction with sea water caused violent phreatomagmatic explosions (Heiken and McCoy, 1984; Druitt et al., 1999; Druitt et al., 2019a), and the emplacement of pyroclastic surges (phase 2) and low-temperature pyroclastic flows (phase 3). This phreatomagmatic activity formed a tuff cone that filled up the pre-existing caldera, allowing the low-temperature pyroclastic flows to spill over onto Santorini's flanks (Bond and Sparks, 1976; Johnston et al., 2014). Finally, after the connection to the sea was closed and water evaporated, large volumes of hot, fluidized pyroclastic flows ran over the island's slopes forming thick depositional fans (phase 4), while the caldera collapse during and after the eruption formed the island's present-day topography (Druitt and Francaviglia, 1992; Johnston et al., 2014; Druitt et al., 2019a). The entrance of the pyroclastic flows of phases 3 and 4 into the sea may have triggered tsunamis that impacted coasts around the Aegean Sea (McCoy and Heiken, 2000; Novikova et al., 2011). Thick accumulations of primary and reworked deposits from these pyroclastic flows (termed ignimbrite) occur in the submarine basins surrounding Santorini but their volume remained poorly constrained so far leading to major uncertainties regarding the volume of the Minoan eruption with estimates ranging from 19 to 86

km^3 (Heiken and McCoy, 1984; Johnston et al., 2014).

FIGURE 2.5: Photograph of the two major Christiana Islands: Askania
(left) and Christiani (right) (Photo: J. Preine).

SW of Santorini lies the extinct Christiana Volcano of which only three islets are exposed above the sea level (Fig. 2.3, 2.5). This volcano produced lavas and tuffs that have so far not been dated. The submarine Kolumbo volcano lies approx. 7 km NE of Santorini and rises approx. 500 m above the surrounding seafloor (Fig. 2.3). It is part of the KVC consisting of over 20 submarine volcanic cones that extend approx. 16 km further towards NE. Kolumbo consists of five vertically stacked circular and cone-shaped units (K1-K5) that are undated except for the historic 1650 CE eruption (K5) (Fouqué, 1879; Hübscher et al., 2015). This eruption produced vast amounts of layered pumice deposits that breached the sea surface before being destroyed by a violent explosive eruption forming an approx. 1.7 km wide crater (Nomikou et al., 2012; Cantner et al., 2014). After this eruption, a hydrothermal vent field evolved in the northern part of the Kolumbo crater, which constructed vent chimneys of up to 4 m height (Carey et al., 2011; Carey et al., 2013).
The 1650 CE eruption of Kolumbo triggered a tsunami causing major destruction on the neighboring islands of Santorini, Ios, and Skinios (Fig. 2.3). Historical eyewitness accounts reported run-up heights of 20 m on the southern coast of Ios, 240 inundation on Skinios, and flooding of up to 2 km^2 of land on the western coast of Santorini (Fouqué, 1879; Dominey-Howes et al., 2000). Onshore tsunami deposits have been identified up to 14 m above sea level on Santorini. Previous studies proposed caldera collapse, underwater explosions, or the emplacement of pyroclastic flows as potential singular source mechanisms (Ulvrova et al., 2016). However, simulations of the resulting tsunamis from these source mechanisms could reproduce neither the run-up heights on Santorini nor the initial sea retreat at the SE coast of Santorini, which was reported in eyewitness accounts (Fouqué, 1879; Dominey-Howes et al., 2000).

An important influence of the local tectonic system on the emplacement of volcanoes at the CSK field has been suggested by previous studies due to the overall linear alignment of volcanic edifices parallel to the NE-SW striking regional rift system (Druitt et al., 1999; Heath et al., 2019). The two most prominent volcano-tectonic lineaments are the Kameni and Kolumbo Lines, which strike NE-SW intersecting

the northern part of the Santorini Caldera (pink lines in Fig. 2.3) (Druitt et al., 1999; Hooft et al., 2019; Heath et al., 2019; McVey et al., 2020). While the Kameni Line is defined by a linear alignment of post-Minoan vents in the center of the caldera, the Kolumbo Line connects older volcanic centers in the northern caldera basin and extends towards Kolumbo NE of Santorini (Fig. 2.3). Both lineaments bound a region of isolated caldera collapse (Hooft et al., 2019) as well as a low-velocity anomaly interpreted as a magma body in the depth of 3 to 5 km (Heath et al., 2019; McVey et al., 2020).

Chapter 3

Methods and Database

3.1 Seismic Imaging
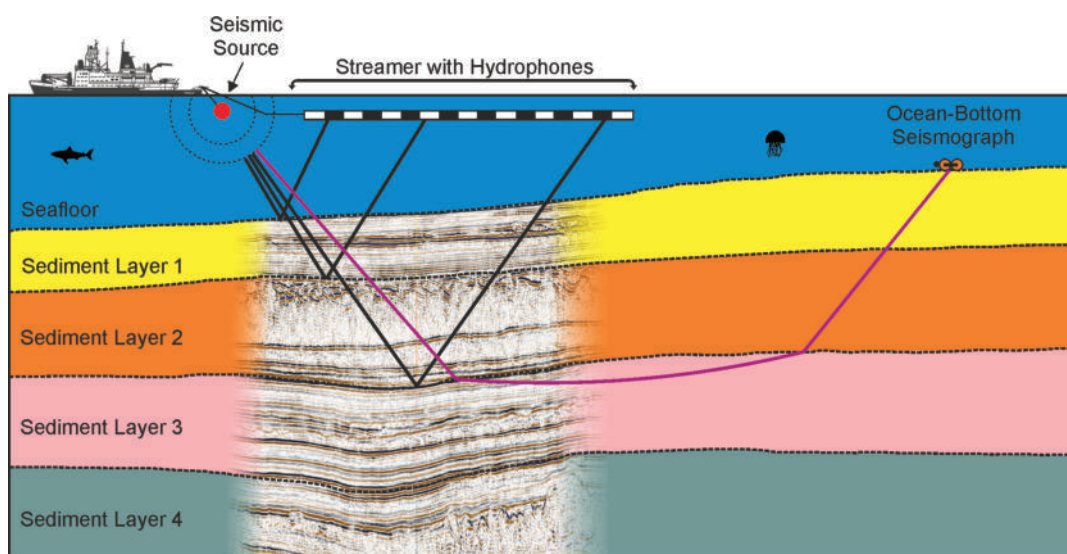
FIGURE 3.1: Schematic visualization of the marine seismic imaging principle with an example seismic image from the study area (Preine et al., 2022a). Artificially generated seismic waves propagate from the seismic source through the subsurface and are reflected at geological layer boundaries due to contrasts in the properties of the substrate. Black lines illustrate ray paths for reflected waves, which are recorded by hydrophones in the streamer that is towed behind the ship. Purple line illustrate ray paths of refracted waves that propagate along layer boundaries and are recorded at Ocean-bottom seismographs. Modified from Hübscher and Gohl (2016).

The seismic reflection method allows to create structural images of the Earth's subsurface. Artificially generated shock waves are sent through the subsurface and are reflected at geological layer boundaries as a result of contrasts in rock properties (e.g. Hübscher and Gohl, 2016) (Fig. 3.1). The returning waves are recorded and analyzed to create seismic crosssections of the subsurface. Seismic reflection acquisition is mainly designed for steep angle reflections, where the lateral distance between source and receiver is smaller than the target depth (Fig. 3.1). In contrast, wide-angle refraction seismic uses seismic waves that are refracted at layer boundaries and travel subhorizontally as diving waves through the subsurface. Throughout their propagation, parts of the wave energy is radiated back to the surface where it

can be recorded by Ocean-bottom seismographs (Fig. 3.1) (e.g. Hübscher and Gohl, 2016).

Compared to land-based acquisitions, marine seismic surveys have a major operational advantage since the equipment can be towed behind ships at sea, thus, allowing large areas to be surveyed in a comparatively short time (Fig. 3.1). In marine acquisitions, seismic signals are usually generated by using airguns. Highly compressed air is repeatedly released at intervals of a few seconds. The rapid expansion of the air bubble then generates a highly reproducible seismic signal that travels through the water column and into the subsurface (e.g. Hübscher and Gohl, 2016). Part of the downward traveling signal is reflected at layer boundaries, while the rest is transmitted and travels deeper into the subsurface, where it is reflected at subsequent layer boundaries (Fig. 3.1).

The reflected signals are recorded using a so-called streamer, which is towed behind the ship and contains either individual hydrophones or hydrophone groups, so-called channels (Figure 3.1). The length of streamers and the number of individual hydrophones can vary significantly from acquisition to acquisition. For example, in academia, acquisitions include deployments with only a single-channel group (single-channel) or with multiple hydrophone groups (multi-channel) with streamer lengths typically varying between 100-3,000 m (e.g. Hübscher and Gohl, 2016).

By towing several streamers and sources parallel to each other, 3D seismic data is acquired. The result of 3D seismic surveys is a cube of stacked reflections that allows tracing reflections in all three spatial dimensions. While 3D seismic reflection data acquisition requires a very dense grid of seismic lines and is therefore very time-consuming, it has the advantage of providing many more reflections at each point for stacking, resulting in a significantly enhanced resolution of the subsurface (e.g. Cartwright and Huuse, 2005). In the last decade, the so-called P-cable system has gained increasing importance for 3D seismic surveys, especially for academic purposes (Planke et al., 2009). With highly mobile 3D seismic arrays, this system allows imaging of the upper subsurface (1-2 km) with very high lateral and vertical resolution. A bundle of 12 short streamers with 8-16 channels is towed behind the survey vessel (Planke et al., 2009).

Having recorded the reflected seismic waves, seismic processing is necessary to produce a high-quality image of the subsurface that allows geologic interpretation (e.g. Hübscher and Gohl, 2016). To accomplish this, seismic data processing makes use of various techniques that are generally aimed at reducing or eliminating unwanted components (noise) in the data while enhancing the signals that carry the desired information about the subsurface. An overview of seismic processing techniques can be found in Yilmaz (2001). In the following, I shortly point out the two most important targets of seismic processing relevant to this thesis.
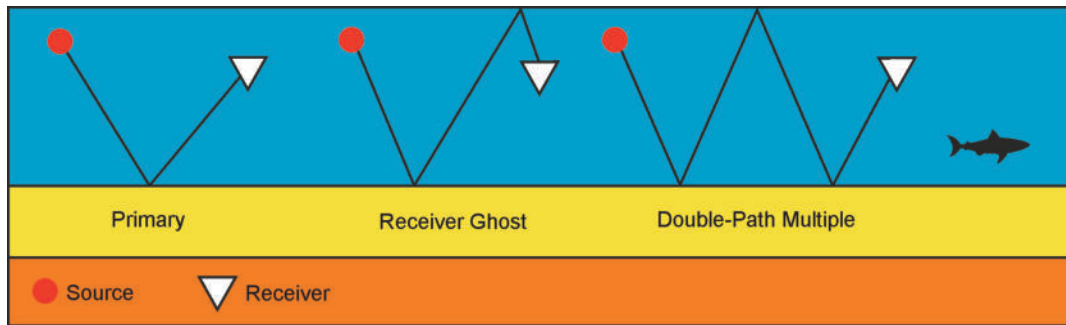
FIGURE 3.2: Schematic visualisation of ray paths from primary reflections, receiver ghost reflections, and seafloor multiple reflections. Modified from Kearey et al. (2002).

A seismic wave that has been reflected only once before being recorded is called a primary reflection (Fig. 3.2). There are many paths in a layered subsurface by which rays may return to the surface after reflections at more than one interface. Such rays are referred to as multiple reflections, reverberations, or simply multiples (Kearey et al., 2002). There is a variety of possible ray paths involving multiple reflections whereby the two most important types for the scope of this thesis are shown in Figure 3.2. A receiver ghost is created, when energy gets reflected at the sea surface on its way upwards (Fig. 3.2). Double-Path Multiples occur when the seismic energy is reflected three times, e.g., at the geological interface, at the water-air interface, and again at the geological interface. Both types of multiple reflections are usually unwanted signals since they can mask primary reflections. The third type of unwanted signal relevant to this work is the bubble signal. It is generated by the oscillation of the air bubble released by the airgun. To prevent this, airgun arrays or so-called G.I. (Generator Injector) guns are used, where a second air pulse is released shortly after the first one to stabilize the air bubble and thus minimize the bubble effect (e.g. Hübscher and Gohl, 2016). In order to eliminate multiple reflections from the data, seismic processing is necessary.

Another important step in seismic data processing is seismic migration (e.g. Yilmaz, 2001; Gray et al., 2001). It comprises a range of techniques for transforming seismic reflection data into an image of the reflecting boundaries in the subsurface similar to the geological cross-section along a seismic traverse (Yilmaz, 2001). Migration corrects for geometric effects caused by dipping reflectors and velocity effects. In addition, it focuses energy that is distributed along diffraction hyperbolas. Such diffractions occur when the seismic wave encounters an obstacle smaller or comparable to its wavelength and is scattered radially. The result of the migration strongly depends on the quality of the velocity field used. In academia, migration usually takes place in the time domain since reliable velocity information typically requires extremely expensive acquisitions with streamers of several kilometers in length. If excellent depth velocity information is available, migration into the depth domain is applied, which can be considered the ultimate goal of seismic data processing.

3.2 Seismic Database
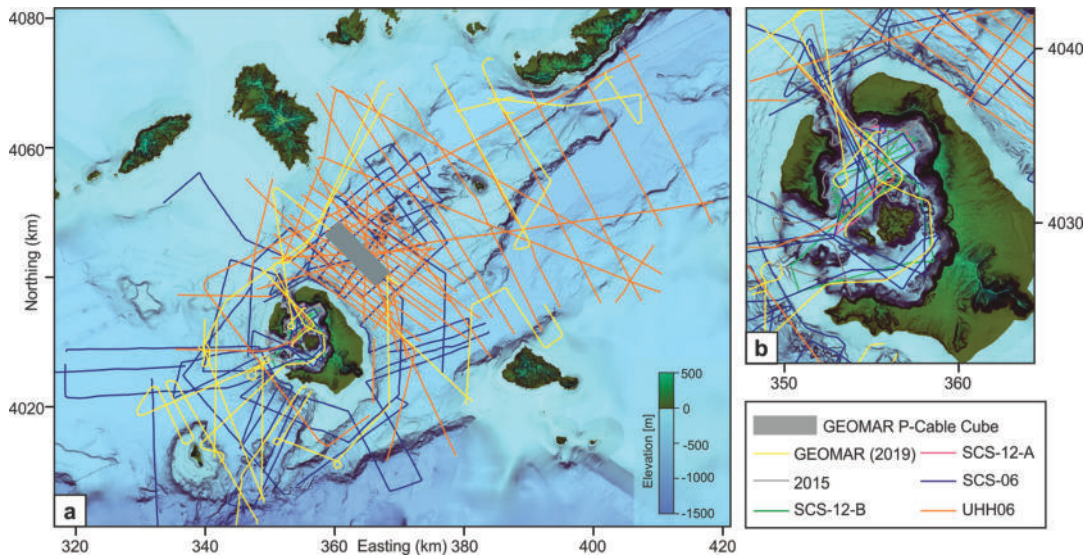
FIGURE 3.3: (a) Morphological map of the study area with all available seismic datasets. (b) Enlargement of the Santorini Caldera showing the dense grid of seismic lines within the caldera.

This study is largely based on a collection of six different 2D seismic datasets collected between 2006 and 2019 (Sigurdsson et al., 2006; Hübscher et al., 2006; Karstens et al., 2020b). In total, more than 170 seismic profiles covering over 3.300 km were processed, homogenized, and interpreted in the course of this thesis. An overview of the location of the different profiles is given in Figure 3.3 and more detailed information about acquisition parameters is provided in Table 3.1. The different datasets were acquired with different seismic sources ranging from electric sparker sources to airguns with different air volumes. They were recorded with acquisition systems comprising single-channel seismic (SCS) and multi-channel seismic (MCS) recording systems with different lengths (Table 3.1). Each acquisition system has its advantages and disadvantages in terms of resolution, penetration depth, and overprint of multiples, which meant that different processing strategies were required for each dataset.

The UHH06 MCS dataset was acquired using a single G.I. gun and streamers of 600 m or 150 m length with 24 channels respectively. With a total length of about 1,500 km, this dataset is the largest in this compilation and covers the area northeast of Santorini and the Kolumbo edifice but also crosses the Santorini Caldera and extends into the Christiana Basin (Fig. 3.3). The main processing challenges for this data were the overprint of the seafloor multiple (yellow arrows in Fig. 3.4A) and the overprint of a pronounced receiver ghost. As a result, some prominent reflections are followed by phase-reversed multiple reflections (red vs. yellow arrows in Fig. 3.4C), which decrease the vertical resolution of this data (Fig. 3.4C). The reason for this pronounced receiver ghost is a missing depth control for the streamer during the acquisition, which sagged especially towards the distal channels.

The most recent 2019 dataset was collected using a single G.I gun and consists of more than 650 km of high-resolution MCS lines crossing the Christiana Basin, the Santorini Caldera, as well as the SATZ (Fig. 3.3). With a channel spacing of 1.56

TABLE 3.1: Overview of all available seismic datasets for this thesis.
cin: Cubic inch (volume); KJ: Kilo Joule; SCS: Single-channel seismic.
Vertical resolution calculated using the $\lambda/4$ criterion (Yilmaz, 2001)
and a velocity of 2000 m/s.

Survey (Year)	No. of Profiles	Total Length (km)	Source	No. of Channels	Streamer Length (m)	Dominant Frequency (Hz)	Vertical Resolution (m)
UHH06	51	1500	1 GI-Gun (45/ 105 cin)	24	600 / 150	100	~5
SCS-06-B	47	990	1 Airgun (10 cin)	1	SCS	125	~4
SCS-12-A	19	82	1 Airgun (10 cin)	1	SCS	125	~4
SCS-12-B	13	38	1 Airgun (10 cin)	1	SCS	125	~4
2015	13	120	1 Sparker (6 kJ)	24	100	300	~1.5
GEOMAR (2019)	43	650	1 GI-Gun (75/75 cin)	160 / 130 / 122 / 32	250 / 200/ 190/ 50	150	~3

m, this dataset has a very high lateral resolution (Karstens et al., 2020b) (compare Figs. 3.4C and D). Since the signal-to-noise ratio of this data was already very good, the processing was aimed primarily at suppressing the seafloor multiple, which was challenging due to the comparatively short streamer lengths (50-250 m) (Fig. 3.4B). In addition, a P-cable cube was collected across the Kolumbo volcano during this cruise (Karstens et al., 2020b) (Fig. 3.3). The processing of these data was mainly performed at GEOMAR in Kiel and will not be described in further detail in this thesis.
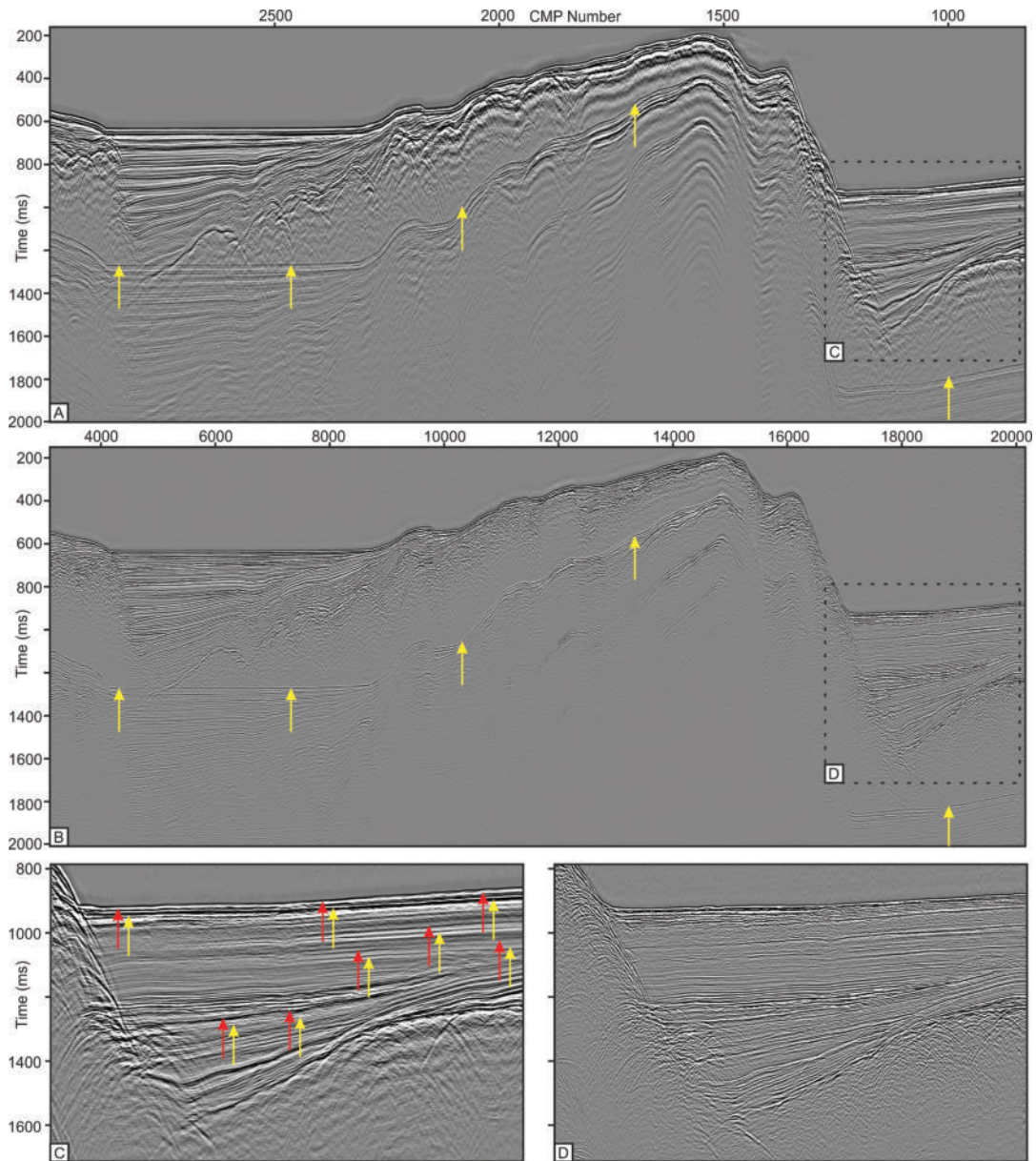
FIGURE 3.4: Comparison of seismic profile UHH06-P15 (A) and
GEOMAR-P5016 (B) that lie very close to each other. Enlargements
(C) and (D) highlight the resolution of each dataset. Yellow arrows
in A and B highlight the seafloor multiple. The receiver ghost for the
UHH06 data in C is marked by the yellow arrows, while the red ar-
rows mark the corresponding primary reflections.

The SCS-06 data, as well as the SCS-12-A and SCS-12-B data, were collected using a
single-channel acquisition system and a single airgun without bubble suppression.
The SCS-06 profiles have a total length of ~990 km and extend radially from the
Santorini edifice, covering the western Anhydros Basin and the Christiana Basin as
well as also the Santorini Caldera (Fig. 3.3). The SCS-12-A and SCS-12-B data were
collected exclusively inside the caldera (Fig. 3.3). For these three datasets, the main
processing challenges were the significant overprint of the bubble reflection as well
as the spatial regularisation of the data to perform migration. Figure 3.5A clearly
shows the overprint of the bubble reflection (yellow arrows).

Further, the 2015 data were acquired using an electrical sparker source and a short multi-channel streamer and cover the caldera as well as the northern breach of Santorini (Fig. 3.3). With a dominant frequency of approx. 300 Hz, these data are of high vertical resolution (Fig. 3.5B). However, they are also overprinted by a bubble reflection, that follows the primary signal after approx. 7 ms (yellow arrows in Fig. 3.5B).
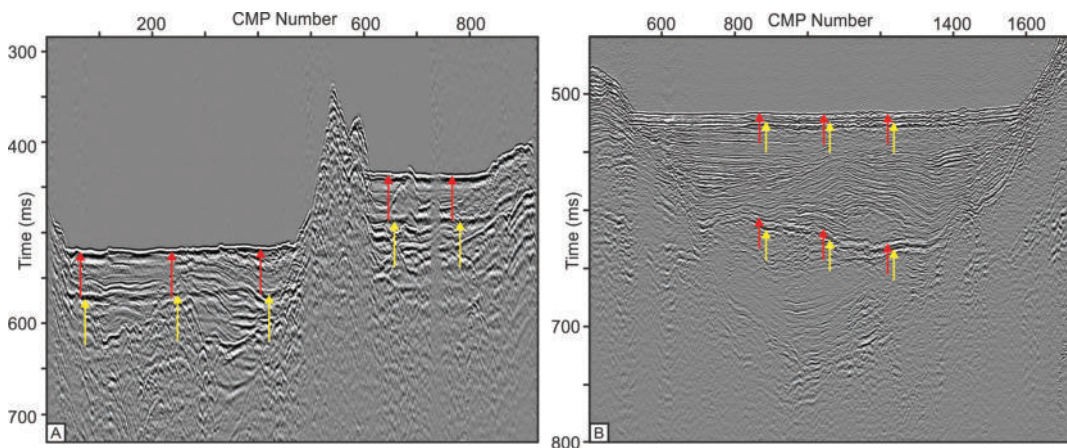
FIGURE 3.5: Single-channel profile SCS-06-21 (A) and sparker profile 05 (B) after initial bandpass-filtering. The strong bubble signals in both data are marked by the yellow arrows, while the red arrows mark the corresponding primary reflection.

3.3 Seismic Processing

As a result of the different acquisition parameters of the various datasets (Table 3.1), four different processing flows were developed for the seismic data processing, which are summarized in Figure 3.6. The goal of the data processing was to produce seismic images with minimum noise for the best possible interpretation. In each case, a tradeoff between noise reduction and preservation of primary signals was pursued to avoid over-processing. Furthermore, the processing flow was designed to achieve the best possible internal consistency within each dataset but also between all datasets.

Showing every processing step would go beyond the scope of this thesis. Therefore, in the following, I will concentrate on the most important processing steps. Since different datasets have similar challenges, I do not take a dataset-by-dataset approach, but show examples that are representative for several different datasets. One of the most important steps for the UHH06 and GEOMAR MCS datasets was the suppression of the seafloor multiple, which I addressed using surface-related multiple elimination (marked yellow in Fig. 3.6) (Verschuur et al., 1992). For the SCS-06 and the SCS-12 datasets, as well as for the 2015 Sparker data, the suppression of the bubble reflection was important, which I addressed by means of a predictive deconvolution approach (marked yellow in Fig. 3.6). An additional important processing step for the UHH06 data was the suppression of the receiver ghost, which was also tackled using predictive deconvolution. For all datasets, migration was crucial, which will be exemplarily highlighted in the following (marked red in Fig. 3.6).
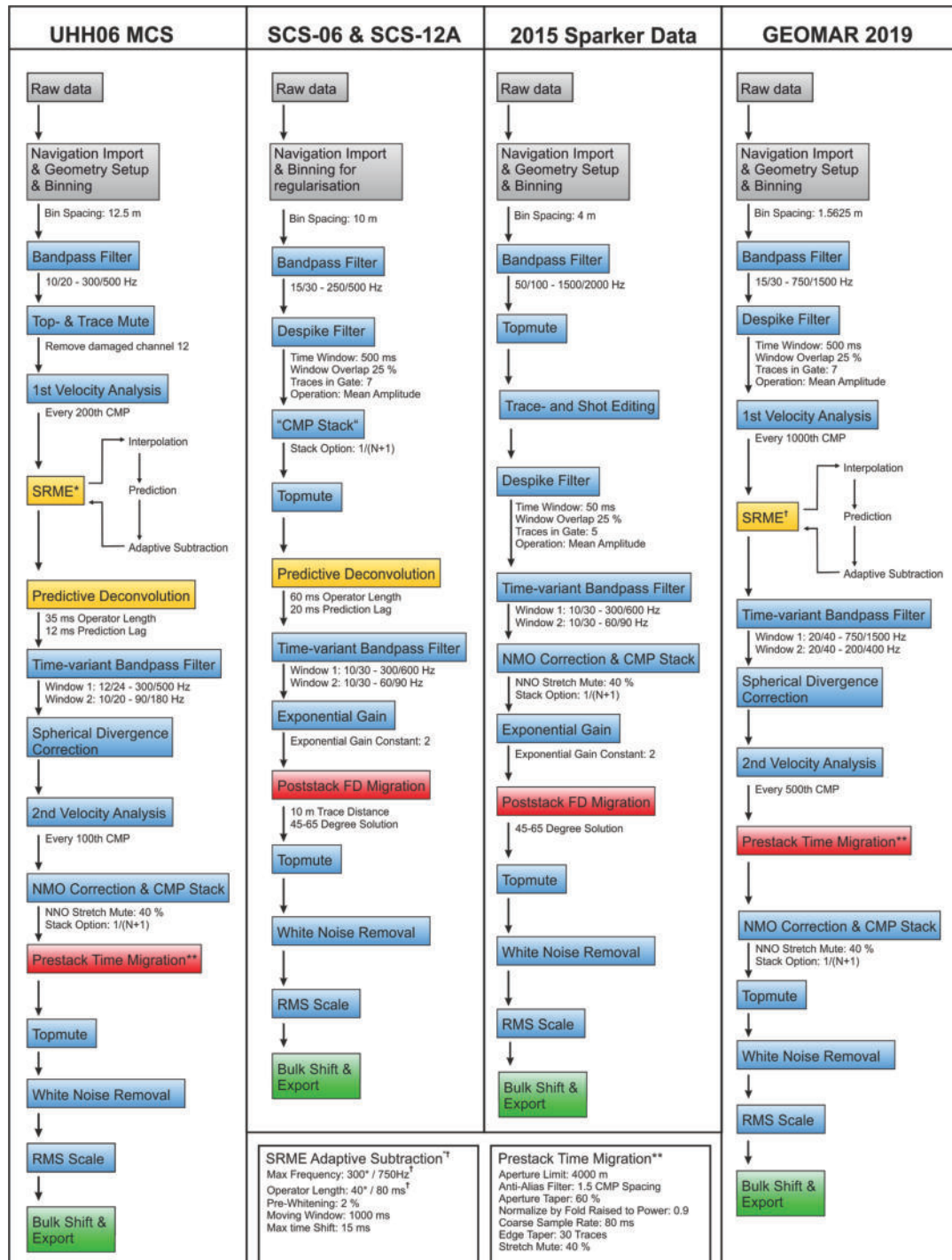
FIGURE 3.6: Visualisation of the processing workflow applied to the different datasets. Grey-colored boxes indicate initial processing steps for geometry set-up, blue-colored boxes indicate conventional processing steps, yellow-colored boxes indicate ghost-, multiple- and bubble-related processing steps, red-colored boxes indicate migration-related processing steps, and green-colored boxes indicate the final export stage.

3.3.1 Surface-Related Multiple Elimination

As shown in Figure 3.6, surface-related multiple elimination (SRME) is part of the processing flow for the UHH06 and GEOMAR MCS data. This method is a powerful algorithm to suppress multiple reflections (Verschuur et al., 1992). By predicting all surface multiples during a convolutional process, multiples are removed from the data by adaptive subtraction. SRME is carried out in three steps: interpolation, prediction, and adaptive subtraction. The former is needed because in marine acquisitions, the near offsets are not measured up to zero offset due to operational difficulties (e.g. Hübscher and Gohl, 2016). Those offsets need to be filled in before multiple prediction is carried out (Verschuur et al., 1992). Therefore, normal moveout (NMO) correction is applied in the CMP domain, and the nearest offset is repeated up to zero offset before an inverse NMO correction is applied. After resorting the data back to the shot domain, the required interpolated result can be used for multiple prediction. An example of this interpolation process for a shot gather of a seismic profile from the UHH06 data is shown in Figure 3.7. In addition, interpolation of shot gathers is carried out to ensure equal source and receiver spacing. The prediction is carried out by auto-convolution of the data and results in multiple-only shot gathers, which are subsequently subtracted from the original shots in the frequency domain using an adaptive subtraction scheme that matches the predicted traces to the original traces (for more details, see Verschuur et al. (1992)) (Fig. 3.7).

Figure 3.8 shows a CMP stack of a seismic profile from the UHH06 data before (Fig. 3.8A) and after (Fig. 3.8B) the application of SRME. The yellow arrows in A highlight the location of the seafloor multiple reflection, which is largely removed after the application of SRME, while preserving most of the primary signals (Fig. 3.8B).
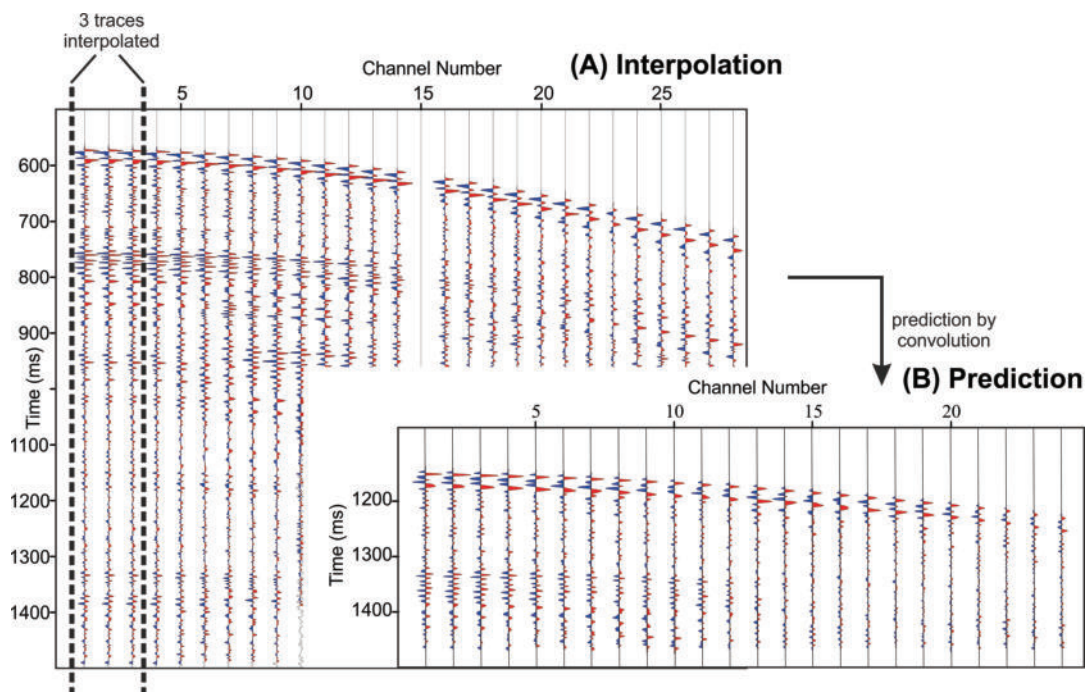
FIGURE 3.7: (A) Interpolation and (B) prediction of a single shot for SRME (Shot 1780, UHH06-P11).
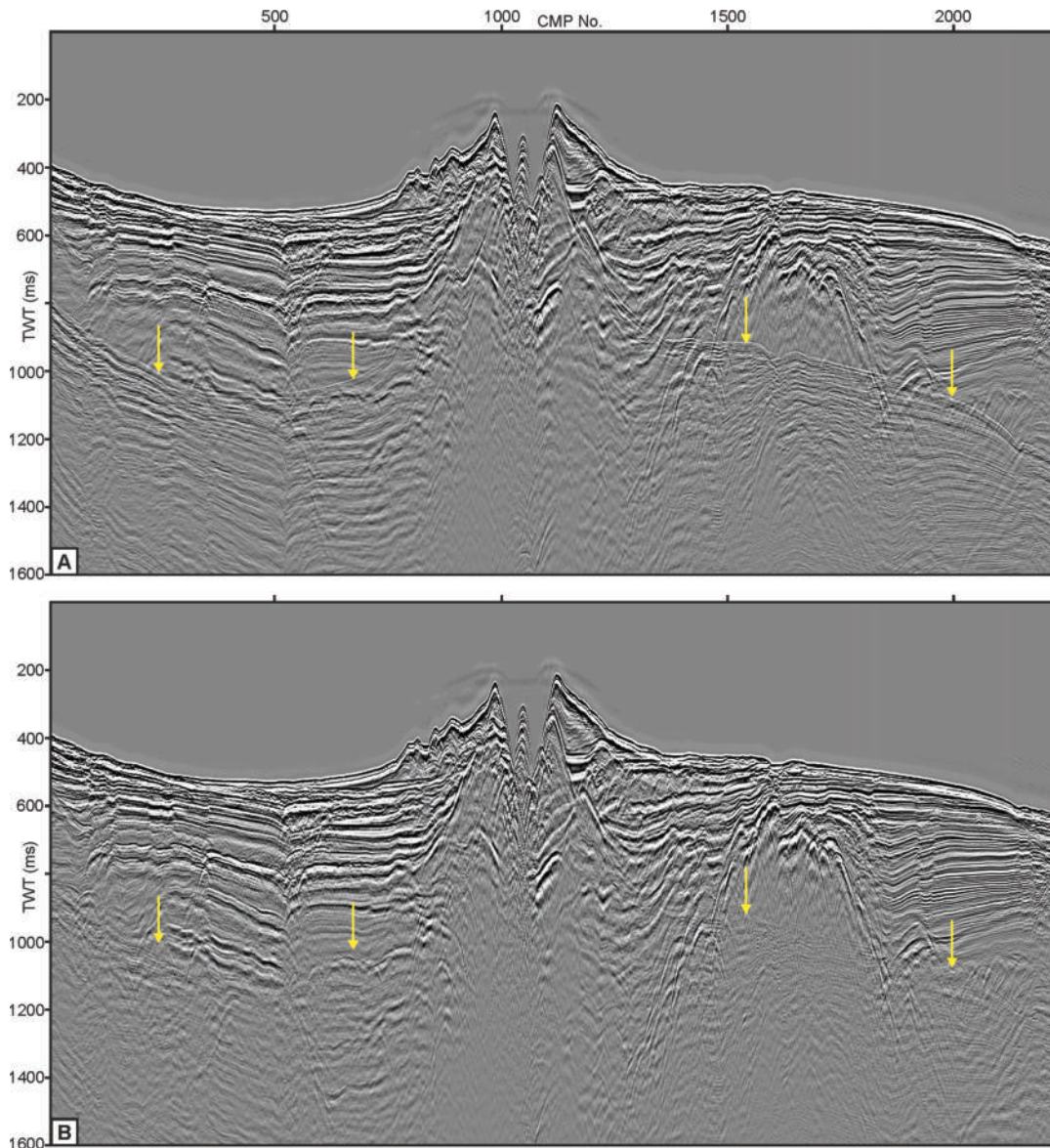
FIGURE 3.8: Stack of seismic profile UHH06-P22 before (A) and after
(B) the application of surface-related multiple elimination
.

3.3.2 Predictive Deconvolution

Deconvolution is a powerful method and an integral part of seismic processing (Yil-maz, 2001). It is based on the convolutional model, which assumes that the recorded seismic trace is the result of the convolution of the seismic source wavelet and the earth's impulse response. By applying the inverse process to convolution, deconvo-lution, the earth's impulse response is derived. In practice, this method is limited as the convolutional model is based on assumptions that are hardly ever valid for non-synthetic seismic data, i.e., the noise component of the data should be zero, the source waveform should be known, stationary, and of minimum phase, and that re-flectivity is a purely random process (Yilmaz, 2001). This means that when applying deconvolution, sophisticated parameter tests are necessary to find a good trade-off

between multiple suppression and the preservation of primary signal. The calculation of the deconvolution operator is performed using so-called Wiener filters (Yilmaz, 2001). When the desired output of deconvolution is a time-advanced form of the input series, the process is called predictive deconvolution, which aims to predict the value of the input $x(t)$ at some future form $t + a$, where a is the prediction lag (Yilmaz, 2001).

As shown in Figure 3.6, predictive deconvolution is applied to both the UHH06 MSC data, and the SCS-06/12 data. However, the purpose of predictive deconvolution differs. While predictive deconvolution for the UHH06 MCS data was designed for the suppression of the receiver ghost, it is used for the SCS data for the suppression of the bubble reflection. This is also reflected in the parameters chosen for deconvolution. In order to suppress the receiver ghost for the UHH06 MCS data, I used a short prediction lag of 12 ms, and an operator length of 35 ms (approx. three times the prediction lag), whereas for the SCS-06/12 data, I applied a prediction lag of 20 ms and an operator length of 60 ms (Fig. 3.6). In both cases, I used a time gate for the calculation of the deconvolution operator that contained the part of the data dominated by primary reflections.

Figure 3.9 illustrates the results of predictive deconvolution in a shot gather (A and B) as well as in the autocorrelation function (C and D) of an example profile from the UHH06 MCS dataset. In addition, the first channel of the shot gather, as well as the autocorrelation before and after the application of predictive deconvolution are shown in Figure 3.9E. The shot gather clearly indicates that a significant amount of the ghost energy has been removed. The black arrows in Figure 3.9 indicate the position of the receiver ghost, which has been removed completely in the first channels. Only some remnants are still visible in the distant channels with significantly reduced amplitudes. The autocorrelation function shown in Figure 3.9C and D further underlines the success of the predictive deconvolution. Figure 3.9D shows that the predictive deconvolution achieved satisfying results and the receiver-ghost indicated by the black arrows has been removed completely. On the other hand, the wavelet in the vicinity of lag zero has not been altered significantly by the deconvolution process (Fig. 3.9C and D).

Figure 3.10 underlines the success of the first pass of predictive deconvolution in a CMP stack section of a profile from the UHH06 MCS dataset. The receiver-ghost reflections are highlighted by the yellow arrows. They appear as phase-reversed low-frequency events and mask significant parts of the section (Fig. 3.10A). After predictive deconvolution, a significant amount of this energy has been removed (Fig. 3.10B). The overall resolution has been improved and many primary reflections appear much clearer. The receiver-ghost has not only been suppressed underneath the seafloor reflection but also underneath other reflections like the acoustic basement. While a loss of primary energy has not been observed, the biggest amount of the ghost energy has been removed.
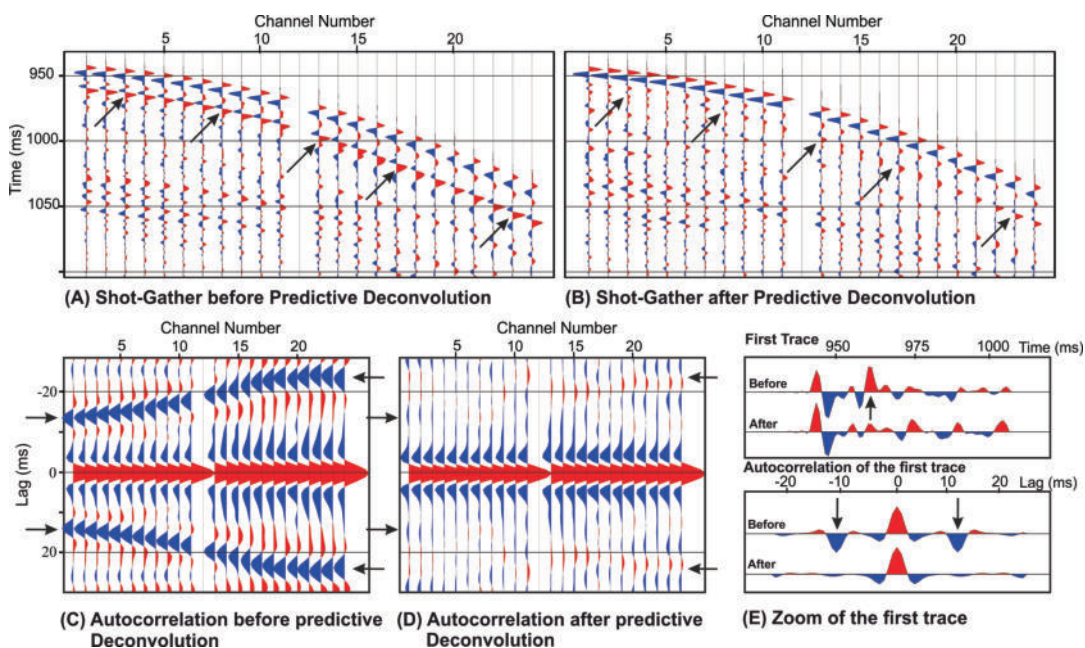
FIGURE 3.9: Comparison of a shot gather from profile UHH06-P11 before (a) and after (b) predictive deconvolution. The corresponding autocorrelation before and after predictive deconvolution as well as the first channel are illustrated in (c-e). Black arrows highlight the position of the receiver-ghost signals in each domain

.
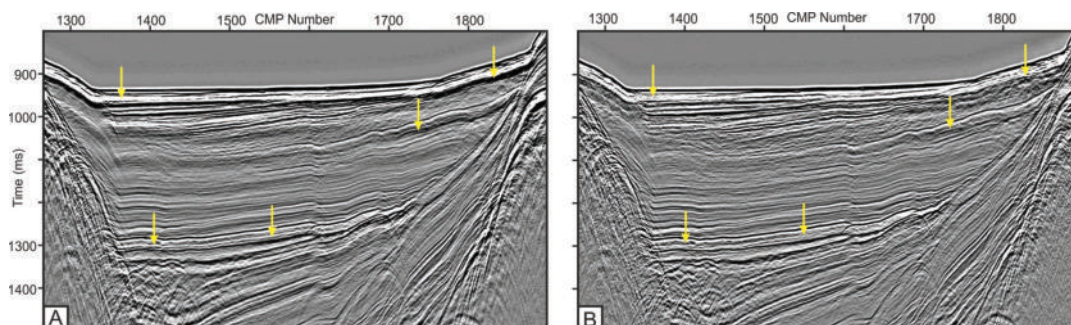
FIGURE 3.10: Stack of Profile UHH06-14 before (a) and after (b) predictive deconvolution. Yellow arrows indicate the location of the receiver ghost.

For the SCS-06 and SCS-12 SCS data, I used a slightly longer prediction lag of 20 ms since the lag of the primary signal and the bubble reflection was larger than that of the primary reflection and the receiver ghost in the UHH06 MCS data. The result of this procedure is shown in Figure 3.11, which shows the SCS data before (A) and after (B) the application of predictive deconvolution. The receiver ghost is highlighted by the arrows in A and most of it is removed after predictive deconvolution without significantly harming primary reflections (Fig. 3.11B).

In contrast, in the 2015 Sparker data, the use of predictive deconvolution to suppress the bubble signal was not satisfactory. While the bubble signal was well suppressed with different parameters, this also always led to significant degradation of the primary signal. This is probably the result of the complex signature of sparker sources

(Bellefleur et al., 2006), which is why I refrained from the application of deconvolution in this case.
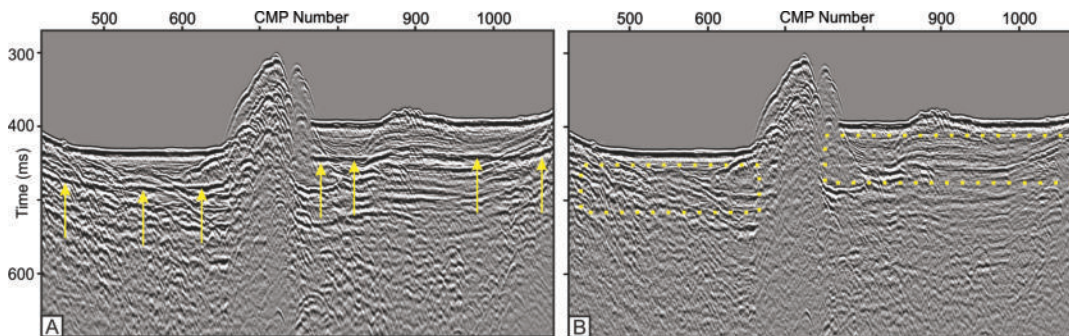
FIGURE 3.11: Section of profile SCS-06-P22 before (a) and after (b)
predictive deconvolution for bubble suppression.

3.3.3 Migration

As shown in Figure 3.6, the processing flows for all datasets contain a migration step. While I applied pre-stack time migration (PSTM) for the UHH06 and GEO-MAR MCS data, the other profiles were migrated in the post-stack domain using a finite difference (FD) migration scheme. For the UHH06 and GEOMAR MCS data, I used a velocity model based on an extensive NMO analysis for each profile, while for the SCS data and the 2015 sparker data, I used a constant velocity of 1,500 m/s (approx. water velocity).

Figure 3.12 shows a comparison of two sections of profile UHH06-02 before (A) and after (B) PSTM. The orange arrows point to a set of faults, which are sharply focused after migration (Fig. 3.12B). Figure 3.12C and D show an example from the GE-OMAR MCS data before and after PSTM. The yellow arrows highlight prominent diffractions and bow tie structures, which are focused after migration.
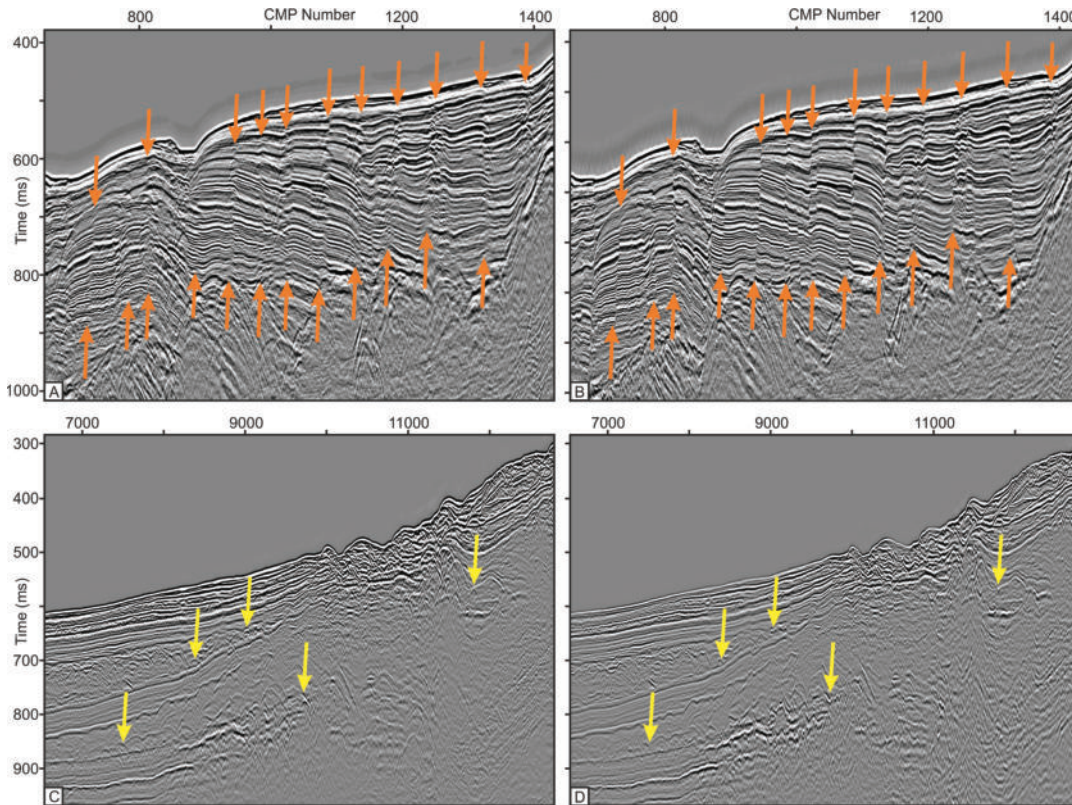
FIGURE 3.12: Section of profile UHH06-02 before (a) and after (b) PSTM. Orange arrows indicate location of prominent faults. Section of profile GEOMAR-P5009 before (c) and after (d) PSTM. Yellow arrows highlight prominent diffractions in the unmigrated section and how they are focused after migration.

3.4 Diffraction Imaging

As is the case for most academic seismic data, the seismic reflection data used in this thesis were acquired with single-channel systems or multi-channel seismic cables with an offset-depth ratio too small for velocity analysis based on common-midpoint (CMP) processing. However, in order to enable quantitative modeling, depth sections would be required, for which precise knowledge of the subsurface velocity model is needed. In recent works, it has been shown that diffractions possess unique properties which bear the potential to overcome these characteristic limitations of academic studies (e.g. Bauer et al., 2017; Schwarz and Gajewski, 2017; Fomel et al., 2007). Wave diffraction occurs at geodynamically important structures like faults, pinch-outs, erosional surfaces, or other small-scale scattering objects and encodes sub-wavelength information on the scattering geometry (Fig. 3.13a) (e.g. Landa and Keydar, 1998). Diffracted waves do not obey Snell's Law and provide superior illumination compared to reflected waves. Moreover, due to their passive-source-like radiation, they encode their full multi-channel response in prominent data subsets like the zero-offset section (e.g. Bauer et al., 2017; Schwarz and Gajewski, 2017). The last chapter of this focuses on a diffraction-based velocity inversion approach using the UHH06 data.
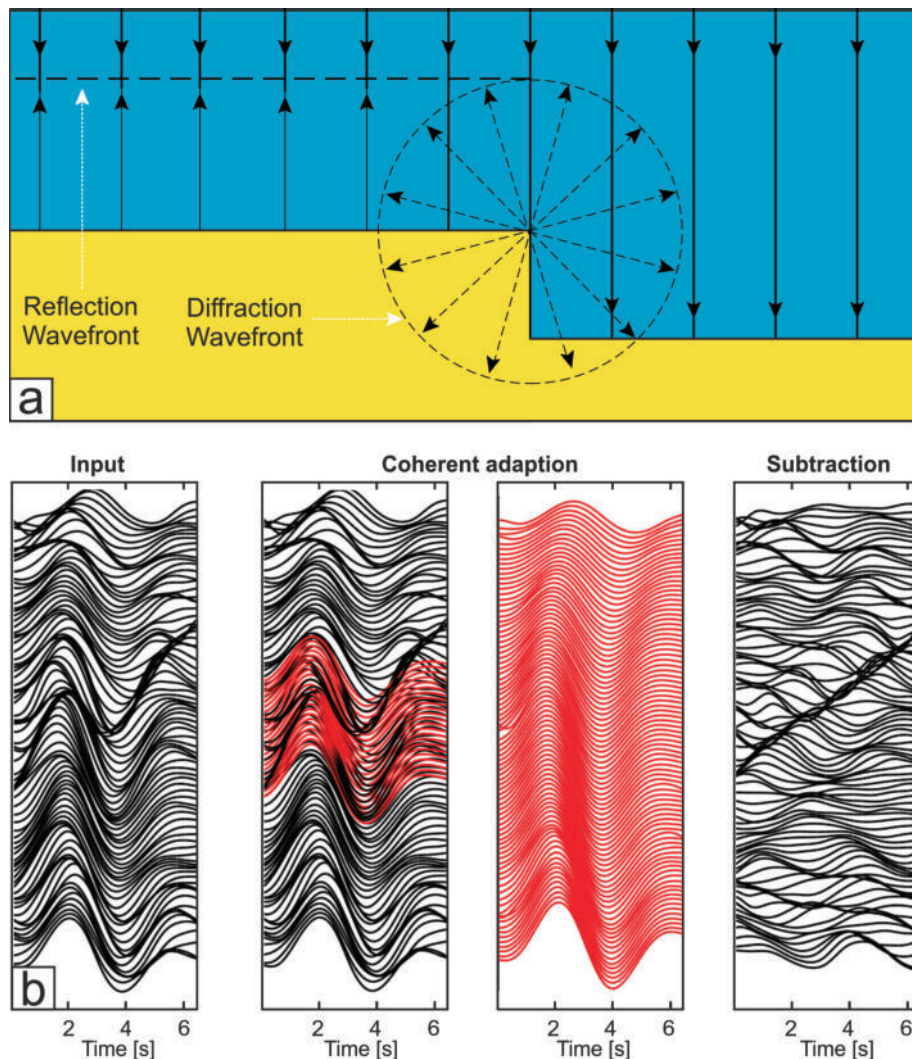
FIGURE 3.13: (a) Schematic illustration of a diffraction caused by the truncated end of a faulted layer. Adapted after Kearey et al. (2002). (b) Illustration of the coherent subtraction scheme for diffraction separation modified from Schwarz (2019b). By approximating the dominant contribution of the amplitude strong coherent events through coherent adaption and adaptively subtracting it from the input data, faint wavefields such as the diffracted wavefield are recovered.

As illustrated in Figure 3.13a, diffractions are unique in that they exclusively occur when subsurface properties change abruptly. More precisely, in contrast to reflections and diving waves, these diffractions are only caused, when the local curvature of a material contrast is comparable to or even smaller than the prevailing seismic wavelength. However, owing to the effect of geometrical spreading, diffractions are generally characterized by very low amplitudes and often remain masked by more prominent higher-amplitude reflections (Fig. 3.13a). For that reason, accessing the diffracted wavefield is a major challenge to confront.

Schwarz and Gajewski (2017) introduced an approach that specifically targets the reflected rather than the diffracted wavefield, with the potential benefit of leaving weak diffracted signatures largely unharmed in the separated result. The separation is performed directly in the un-migrated (data) domain and the first step of this strategy consists of a targeted modeling of the reflected contributions (Fig. 3.13b).

This is achieved by means of coherence analysis, in which the local fit of a curved traveltime operator

$$\Delta t(x_0, t_0) = \sqrt{\left(t_0 + 2\frac{\sin\alpha}{v_0}\Delta x \right)^2 + \frac{2t_0\cos^2\alpha}{v_0}\left(\frac{\Delta x^2}{R_{\mathrm{N}}} + \frac{h^2}{R_{\mathrm{NIP}}} \right)} - t_0 \qquad (3.1)$$

is optimized for neighboring traces (with midpoints laterally separated by Δx and half the source-receiver distance h), by repeatedly evaluating the semblance norm (Neidell and Taner, 1971). Written as above, the estimated propagation time $t_0/2$, the emergence angle α, and the curvature radius R_{NIP} represent one-way properties of a wavefront emitted by a fictitious source placed either at the normal-incidence point (NIP) or the diffractor location. While for reflections, this wavefront is fully conceptual and expresses a symmetry in the common-midpoint gather ($h \neq 0$), for diffractions and passive events ($R_{\mathrm{N}} = R_{\mathrm{NIP}}$) it describes the shape of the actual physical wavefield stemming from the localized scatterer or the passive source (Bauer et al., 2017; Diekmann et al., 2019). As a result, for reflections, sufficient offset (h) information is needed, whereas, for diffractions, wavefront curvatures can be fully determined in the zero-offset ($h = 0$) section. Forming a by-product of coherence analysis, these wavefront attributes, in addition to velocity inversion, permit the formulation of supportive diffraction filters that can additionally constrain the separation (Schwarz and Gajewski, 2017; Schwarz, 2019b).

Following this procedure of constructing a reflection model by means of local coherent data summations, a successful separation requires an adaptation step, which like the summation itself should be performed within an aperture to preserve weak interfering energy (Fig. 3.13b). Such an adaptation of the reflection stack is achieved by introducing local scaling coefficients γ_0 and time shifts τ_0. Following the superposition principle, the interference of reflections and diffractions can, in good approximation, be reversed, if the estimated coherent reflection model is reasonably accurate (Fig. 3.13b). Expressing the coherent reflection stack as C_{ref}, and the raw input data as $\mathcal{D}$, the adaptive separation procedure can thus be expressed as

$$C_{diff} \approx D(x_0, t_0) - \gamma_0 C_{ref}(x_0, t_0 + \tau_0), \qquad (3.2)$$

where $(\mathbf{x}_0, t_0)$ is the central data point under consideration and C_{diff} denotes the diffracted wavefield. More details on the estimation of the necessary amplitude weights and time shifts and applications in seismic data can be found in Schwarz (2019b).
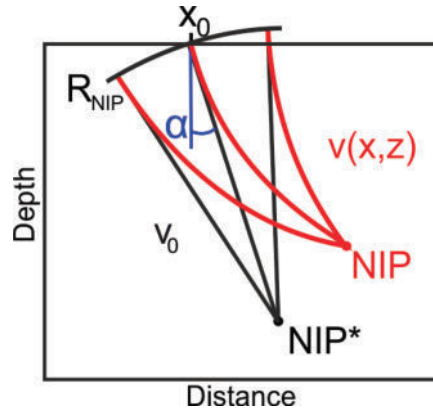
FIGURE 3.14: Illustration of the concept of wavefront tomography. Black lines indicate the optical image space with a medium of constant velocity v_0, in which the apparent location of the normal incidence point (NIP*) is obtained by straight-ray projection. Determining the true velocity model $v(x, z)$ and finding the true normal incidence point (NIP) location (red) are the objectives of wavefront tomography.

In order to obtain velocity information from the separated diffractions, the next step is to perform wavefront tomography, which represents an efficient and robust scheme for the estimation of smooth depth-velocity models (Fig. 3.14). (Duveneck, 2004). In the first step, wavefront attributes are estimated from the diffraction-only data by means of coherence analysis, during which the hyperbolic traveltime moveout approximation (11.1) is locally fitted to the data (e.g. Jäger et al., 2001). The input for wavefront tomography consists of numerous sets of wavefront attributes that can be picked in an automatic fashion in the resulting zero-offset sections based on their coherence,

$$\mathbf{d}_i = (\xi, T, \alpha, R_{\mathrm{NIP}})_i, \qquad \text{with } i = 1, \dots, n_{picks}, \tag{3.3}$$

where n_{picks} denotes the total number of picked data points, $T = t_0/2$ the one-way zero-offset traveltime and ξ the position on the recording surface. The model parameters $\mathbf{m}$ are the B-spline velocity coefficients $v(x, z)$ on a pre-defined grid of $n_x \times n_z$ knots and localisations $(x, z)_i$ and ray-takeoff angles θ_i associated with each data point. The initial localisations and ray-takeoff angles are obtained by downward kinematic ray tracing into the initial model (which in our applications merely consists of the constant near-surface velocity v_0), starting from $\tilde{\xi}_i$ under the angles α_i until the remaining traveltime vanishes. Subsequently, upwards dynamic ray tracing from $(x, z, \theta)_i$ yields the modeled data points $\tilde{\mathbf{d}}$. The misfit between the measured and modelled data points $\Delta \mathbf{d} = \mathbf{d} - \tilde{\mathbf{d}}$ defines the cost function,

$$\Psi(\mathbf{m}) = \frac{1}{2} \|\mathbf{d} - \tilde{\mathbf{d}}\|_2^2 + \Lambda \left(\partial_{xx} v(x, z) \right), \partial_{zz} v(x, z)) , \tag{3.4}$$

where Λ constitutes a regularisation term that ensures a smooth velocity model. During the inversion, the cost function is minimized iteratively in a damped-weighted least-squares sense until a velocity model and localisations $(x, z)_i$ are found that are most consistent with the measured wavefront attributes. The results of this method are shown in Chapter 11, where diffraction separation and diffraction-based wavefront tomography were tested using a profile of the UHH06 dataset.

3.5   Seismic Interpretation

3.5.1   General Principles

Seismic methods can be considered a form of remote sensing of the Earth and should, in the best case, be supported by ground truthing, i.e., calibration by drilling results through core-log seismic integration. However, this is often difficult in academia since drilling is very costly and there are usually no industry wells in young volcanic areas such as the CSK field. Therefore, purely seismic-based studies in these settings can often only provide concepts and hypotheses, especially regarding deposit thicknesses and age models, that remain to be tested by drilling.

Seismic interpretation essentially follows two steps. The first step is to describe the seismic image as objectively as possible. This involves first identifying unconformities and correlated unconformities as well as termination patterns (e.g., onlap, toplap, downlap, offlap) properties (e.g. Hübscher and Gohl, 2016; Bischoff et al., 2021). Then, internal reflection patterns are classified (e.g., divergent, parallel, undulating) and seismic attributes (e.g., instantaneous frequency, coherence) are added where appropriate. From this description, the next step is to infer processes that may have led to the described features. An interpretation is considered conclusive if it is internally consistent and can explain a maximum of observations with a minimum of assumptions (e.g. Hübscher and Gohl, 2016).

A relatively new field in seismic interpretation is seismic reflection volcanology, which is the study of buried volcanoes from seismic reflection datasets (Bischoff et al., 2021). Supported by the development of modern high-resolution 2D and 3D seismic methods (e.g. Bischoff et al., 2021), seismic reflection data provide the unique opportunity to image the internal structure of marine or buried volcanoes, which are difficult to assess by monitoring and sampling. Seismic data enable studying the entire architecture of volcanic systems, from the deep intrusive to the extrusive parts. In addition, seismic data can be used to study the role of intrusions, tectonics, host rocks, and sea-level fluctuations, as well as to map products of volcanic eruptions over wide areas (Bischoff et al., 2021).

Igneous rocks buried in sedimentary basins are often identified by the presence of anomalous high-amplitude reflections in seismic datasets (Bischoff et al., 2021). Characteristically, dense lavas and intrusions have high seismic velocities (P-waves) (>3,000 m/s), in contrast to softer sedimentary rocks that typically have lower velocities (Planke et al., 2000; Heap and Kennedy, 2016; Bischoff et al., 2021). Interpretations depend on the quality and resolution of the seismic data, especially vertical and lateral resolution, as well as the depth of penetration, which is often dampened beneath magmatic bodies. In addition, distinguishing buried volcanics from sedimentary layers can be problematic if the igneous rocks have similar physical properties and geometries to their surrounding host rocks (Bischoff et al., 2021; Rohrman, 2007). For example, it may be difficult to distinguish volcanics from basement structures or evaporites that have similar high velocities (Klarner and Klarner, 2012; Nicol et al., 2019). Alteration processes such as weathering and compaction during progressive burial, can also reduce the impedance contrast between igneous and sedimentary rocks and, moreover, mass-wasting and compaction can also significantly alter the morphology of volcanic structures. In addition, steeply inclined bodies such as dykes and highly heterogeneous subvolcanic zones are often poorly resolved in seismic reflection datasets. Thus, seismic interpretation of volcanoes must necessarily take these limitations into account to avoid misinterpretation and overinterpretation (Bischoff et al., 2021).

3.5.2 Seismic Stratigraphy of the CSK Rift

One of the most important steps of this thesis was to establish the seismo-stratigraphic classification for the infill of the sedimentary basins along the CSK rift system, which was a challenging task due to several reasons. On the one hand, the individual sedimentary basins are not connected, for example, they are interrupted by horst structures such as the Anhydros horst, or by volcanic structures such as Santorini (Fig. 2.3). Thus, jump correlations had to be applied for the establishment of the basin-spanning stratigraphy, which entails some uncertainties. On the other hand, the thickness of volcanic deposits is spatially highly variable, which means that individual stratigraphic units may be very thick in some places while being thin in other areas. The tectonic activity of the rift system had a similar effect. Subsidence along faults can locally cause significant differences in thickness that need to be taken into account when tracing seismo-stratigraphic units. This is one of the reasons why different seismo-stratigraphic interpretations have been established in previous publications, each of which, focused on a different area of the CSK rift system, e.g. the Anhydros Basin (Hübscher et al., 2015; Nomikou et al., 2016b), the eastern SATZ (Nomikou et al., 2018b; Nomikou et al., 2019) or the Christiana Basin (Tsampouraki-Kraounaki and Sakellariou, 2018). The objective of this study was to establish a consistent seismo-stratigraphic scheme applicable to all areas of the system. Therefore, I mainly used the multi-channel data, as the quality of these data was much better compared to the single-channel data. An example is illustrated in Figure 3.15, which shows a fully processed multi-channel profile and a fully processed single-channel profile that are located very close to each other in the Christiana Basin (Fig. 2.3). Especially when considering the enlargements in Figure 3.15C and D, it becomes evident that the quality of the SCS data is not suitable to identify internal structures, which is key for a reliable interpretation. Therefore, I primarily based the interpretation on the MCS data and used the SCS data mainly to trace reflections from crossing points with the MCS data.
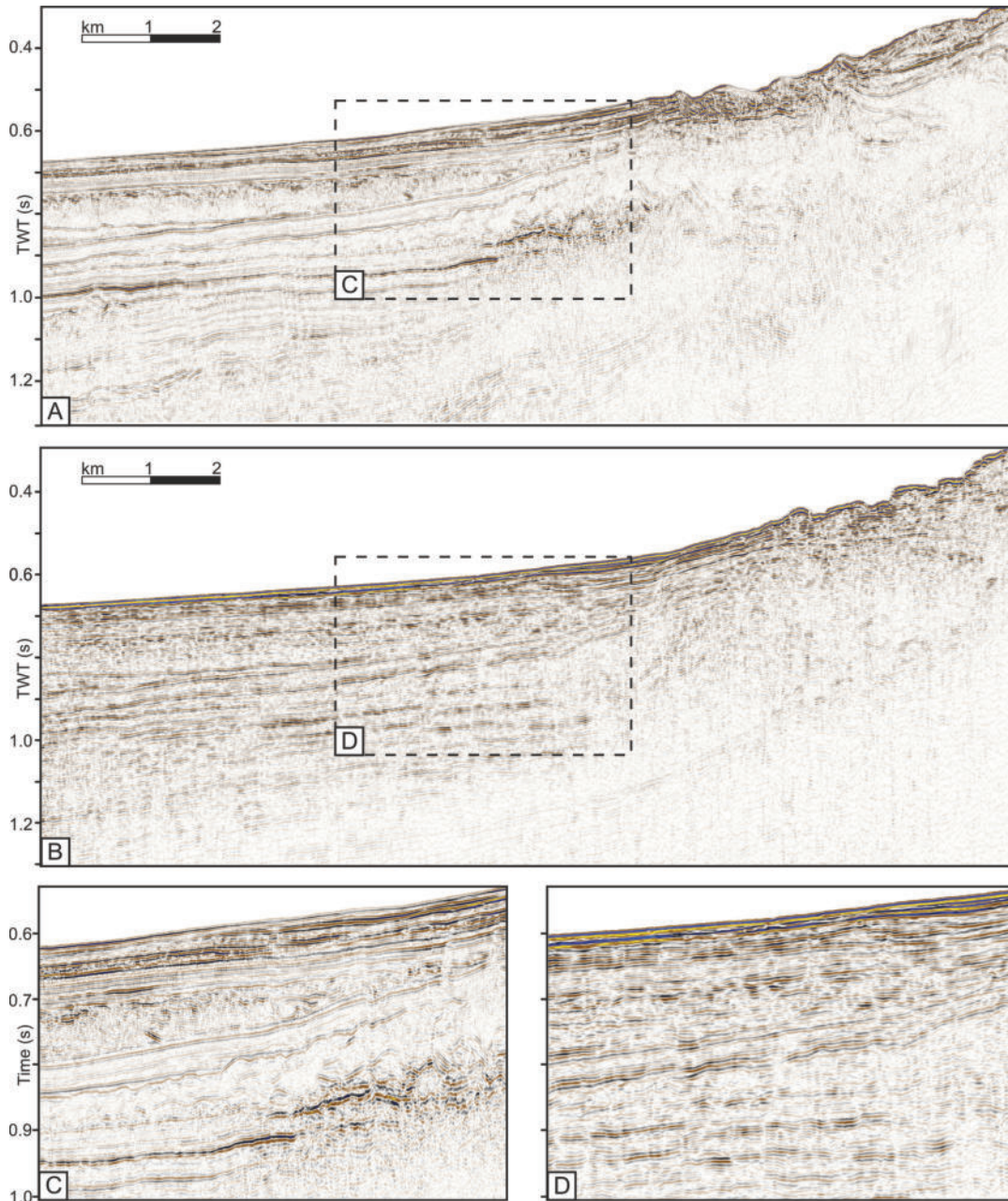
FIGURE 3.15: Comparison of fully processed seismic profiles GEOMAR-P5009 (A) and SCS-06-38 (B) that lie very close to each other. The difference in resolution is highlighted by the enlargements (C and D).

The final seismo-stratigraphic classification established in the course of this thesis has been published for the first time in Preine et al. (2022a) (Chapter 4) and will be briefly described here. In total, six seismo-stratigraphic units were identified throughout the basins of the CSK Rift System. These units (U1-U6) are separated by six key horizons h1-h6, which are major unconformities in some areas while being conformable in other areas. An overview with exemplary illustrations for each unit is shown in Figure 3.16. Table 3.2 provides a detailed comparison of how this seismo-stratigraphic framework compares to previously published classifications.

The lowermost unit (Unit 1) is characterized by weakly reflective strata with sub-parallel reflections. It is often overprinted by the seafloor multiple reflections and internal reflections are difficult to analyze 3.16. Above lies Unit 2, which comprises a series of well-stratified reflections with medium to high amplitude reflections 3.16. Unit 3 consists of a sequence of well-stratified reflections with medium amplitudes, which contrast with the weakly reflective nature of Unit 4 3.16. This Unit can be identified in all basins around Santorini and contains weakly reflective strata with some distinct high-amplitude reflections in the lower part, which sometimes onlap the base reflection. Close to Santorini, the base of this unit is strongly incised and some wavy and blocky internal reflections are visible. Away from Santorini, the base reflection is undisturbed and some internal stratification is visible. Unit 5 comprises a characteristic sequence of closely spaced parallel low- to medium-amplitude reflections, which can be traced well throughout the entire working area 3.16. The seismic signature of the uppermost unit is highly variable throughout the CSK rift. In the vicinity of Santorini, it comprises high-amplitude irregular reflections and several sequences of wavy or chaotic subunits. Towards the central Christiana Basin, Unit 6 contains closely-spaced reflections similar to those of Unit 5. In contrast, Unit 6 is very thick in the Santorini-Anafi Basin, where it comprises low-amplitude reflections that are parallel to hummocky, and show distinct onlap terminations to basal unconformity h6.

FIGURE 3.16: Summary of the seismic facies of Units 1-6. Horizons h6-h1 are the basal reflectors of the corresponding Units.

TABLE 3.2: Comparison of different seismo-stratigraphic classifications for the Christiana-Santorini-Kolumbo volcanic rift.

	This thesis	Hübscher et al. (2015)	Nomikou et al. (2016b)	Nomikou et al. (2018, 2019)	Tsampouraki-Kraounaki & Sakellariou (2018)	Piper et al. (2007)
Study Focus	Chrsitiana Basin, Anhydros Basin, Santorini-Anafi Basin	Anhydros Basin	Anhydros Basin	Anhydros Basin & Santorini-Anafi Basin	Christiana Basin	Christiana Basin, Anhydros Basin, Santorini-Anafi Basin
Seismo-stratigraphic Units	Unit 1	-	Ab1	Sab1/Ab1	Unit 5	-
	Unit 2	-	Ab2	Sab2/Ab2	Unit 4/2	-
	Unit 3	Sk1	Ab3	Sab3/Ab3	Unit 2	-
	Unit 4	Sk2	Ab4	Sab4/Ab4	Unit 1	-
	Unit 5	Sk3	Ab5	Ab5 & Sab4/Ab4	Unit 1	-
	Unit 6	Sk4	Ab6	Sab6/Ab6 & Sab5	Unit 1	-
Key reflectors / unconformities	h1	ab1	ab-0	Base Sab1/Ab1	Base Unit 5	-
	h2	ab2	ab-1	Base Sab2/Ab2	Base Unit 4	1
	h3	-	ab-2	Base Sab3/Ab3	-	C
	h4	ab7	ab-3	Base Sab4/Ab4	Base Unit 1	B
	h5	-	ab-4	-	-	-
	h6	ab10	ab-6	Base Sab5/Ab5	-	A

3.5.3 Age Estimation

An important step in this thesis was to estimate the age of the six stratigraphic units. This is a great challenge without the availability of drilling information and can therefore only be estimated with relatively large uncertainty. The approach chosen in Chapter 4 is based on the estimation of individual layer thicknesses as well as on sedimentation rates. As with any seismic interpretation, I have chosen an approach that makes as few assumptions as possible (e.g., constant sedimentation rates) and is consistent with the known onshore stratigraphy of Santorini and Christiana. Thus, it was possible to construct a consistent age model, which was first presented in Preine et al. (2022a) (Chapter 4) and is briefly introduced here.

The approach of estimating age models of seismo-stratigraphic units has been used by previous authors, who worked in the southern Aegean Sea (Piper and Perissoratis, 2003; Anastasakis and Piper, 2005; Piper et al., 2007). Piper and Perissoratis (2003) presented a large collection of sediment cores from the southern Aegean Sea and estimated a mean sedimentation rate of 10 cm/ka for the area. They further argued that, away from the volcanic centers, sedimentation rates have remained reasonably uniform in the Aegean Sea during the Quarternary. Close to the volcanic centers, however, they observed much higher sedimentation rates (> 20 cm/ka), which is in agreement with observations of the seismic data across the CSKVF in this thesis.
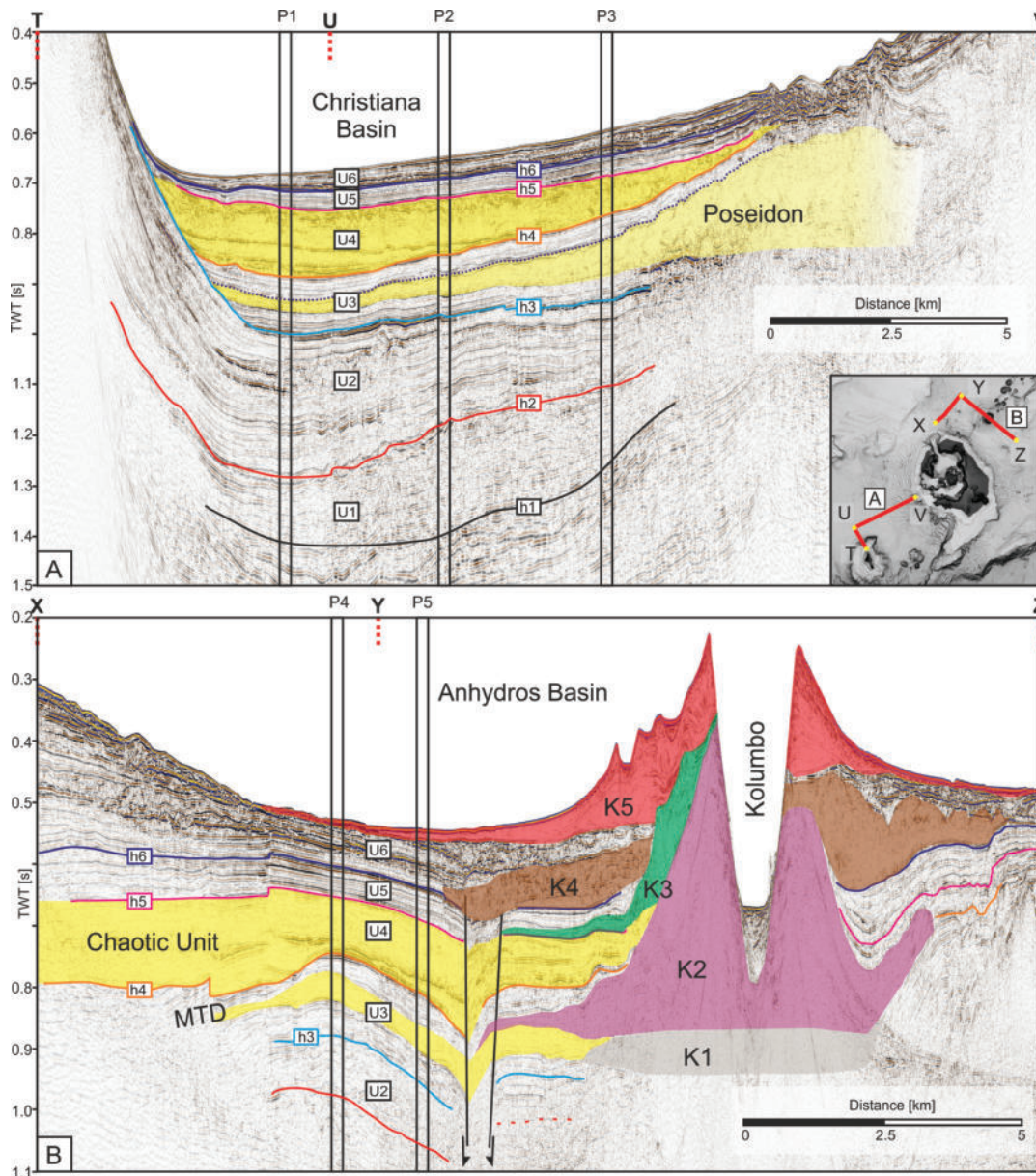
FIGURE 3.17: Seismic profile across the Christiana Basin (A) and the Anhydros Basin (B) with sample points for thickness estimation. Semi-transparent units indicate volcanic and mass-transport deposits. For location, see inlet map.

The available seismic data show that especially close to Santorini there are significant thickness variations of the uppermost unit U6, which is interpreted as the deposits from the Thera Pyroclastic Formation deposited since ~0.35 Ma. As outlined in Preine et al. (2022a) (Chapter 4), this unit has a thickness of over 350 m north of the Santorini Caldera, where it represents a wedge of alternating low-amplitude, chaotic, and wavy reflections that resemble the stratified flanks of the cliffs of the Santorini Caldera (Fig. 1.1). In contrast to that, U6 has a thickness of only ~40 m towards the Christiana basin while being less chaotic and more stratified. This thickness remains approx. constant away from Santorini across the Christiana basin indicating that the influence of volcanoclastic deposits is small here suggesting a rather constant sedimentation rate. The underlying unit U5 represents a well-stratified unit

with an approximately constant thickness across the whole working area (Fig. 3.16). Unit U4 is interpreted as a large mass-transport deposit derived from present-day Santorini and is significantly varying in thickness (Chapters 5 and 5). The thickness of Unit U3 is influenced by the presence of the Poseidon deposit and the lowermost units from Kolumbo (K1 and K2) as well as the smaller Kolumbo mass-transport deposit (MTD) (Fig. 3.17B) (Chapter 4). Apart from these volcanic units, unit U3 comprises well-stratified reflections, which generally have a constant thickness (Fig. 3.16). Unit U2 is thickening towards Christiana but has a rather constant thickness away from Christiana (Fig. 3.16). The lowermost unit U1 is hardly discernable in the Anhydros basin but represents a major unit in the Christiana basin. It is therefore imperative for age approximations based on sedimentation rates to exclude volcanoclastic formations, mass-transport deposits, and thickening strata.
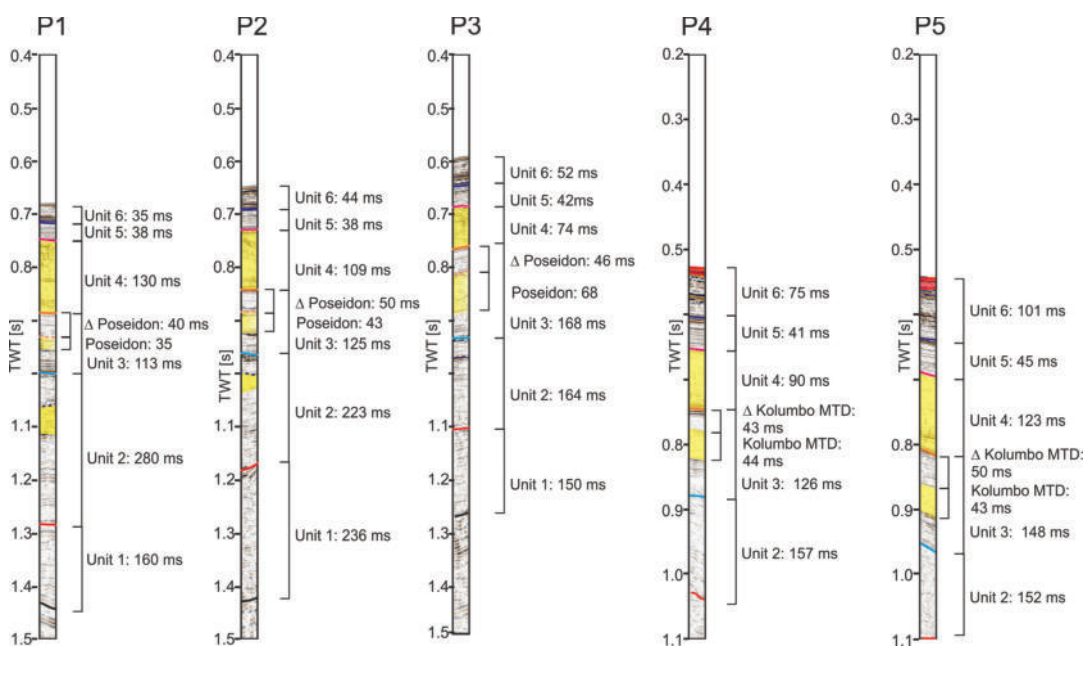
FIGURE 3.18: TWT Thicknesses of the five sample points shown in Figure 3.17.

Figures 3.17A and B show seismic profiles from the Christiana and Anhydros Basins with five sites P1-P5 for which the thickness of each stratigraphic unit is estimated. Interpreted MTDs and volcaniclastic units are highlighted by yellow semi-transparent areas. The estimated TWT thicknesses of P1-P5 are shown in Figure 3.18 and Table 3.3. In Table 3.3 it is indicated whether divergence (DIV) was observed within a unit at one of our sample sites and neglected those values for the thickness and age calculation. In addition, the thicknesses of the Poseidon deposit in the Christiana Basin and the Kolumbo MTD in the Anhydros Basin are estimated as well as their difference to the overlying unconformity h4 (Poseidon/Kolumbo MTD) in order to approximate the ages of these volcanic deposits.

Table 3.4 shows the mean TWT-thicknesses for the main units, their estimated interval velocities (as estimated from Ocean bottom seismograph-based ray-tracing analysis, see Appendix A) as well as the estimated thicknesses in meters. The age of the base of each of these units is estimated by dividing the estimated thicknesses by the approx. sedimentation rate of 10 cm/ka (Piper and Perissoratis, 2003).

TABLE 3.3: TWT-Thicknesses of the main stratigraphic units as well as volcanic units measured at the sites P1-P5. For location, see Figure 3.17.

Units Christiana	P1 [ms]	P2 [ms]	P3 [ms]	Units Anhydros	P4 [ms]	P5 [ms]
Unit 6	35	44	52 (DIV)	Unit 6	75 (DIV)	101 (DIV)
Unit 5	38	38	42	Unit 5	41	45
Unit 4	130	109	74	Unit 4	90	123
Unit 3	113	125	168 (DIV)	Unit 3	126	148 (DIV)
Poseidon	35	43	68	Kolumbo MTD	44	43
Δ Poseidon	40	50	46	Δ Kolumbo MTD	43	50
Unit 3 - Poseidon	78	82	100 (DIV)	Unit 3 - Kolumbo MTD	82	103 (DIV)
Unit 2	280 (DIV)	233 (DIV)	164	Unit 2	157	152
Unit 1	160	236 (DIV)	150	Unit 1	-	-

So far, only one scientific drilling campaign has been conducted in the vicinity of our working area: DSDP hole 378 in the Cretan Basin several kilometers southwest of Christiana (Hsu et al., 1978). Based on an old vintage seismic profile, Hsu et al. (1978) define an uppermost unit as "ponded facies" with numerous horizontal reflectors, which they correlate with hemipelagic nannofossil marls and oozes of Quaternary age with some intercalated tephra layers. Below that, they identified a "transparent facies", which was correlated to nannofossil marlstones of Pliocene age. These units overlay a unit consisting of gypsum related to the Messinian salinity crisis. The description of the "ponded facies" fits our observations of the well-stratified units U2-U6 from the CSKVF, while the "transparent facies" fits our observation of the lowermost weakly reflective unit U1 from the CSKVF. The ages would fit well since we date the uppermost units U2-U6 to approx. 0-3.4 Ma implying a mostly Pleistocene Age and unit U1 to approx. 3.4 - 5.3 Ma, which corresponds to a Pliocene Age. Since we have no direct ties to the DSDP drill site, this comparison remains speculative but shows that our age approximations generally fit with the available regional geological constraints.

TABLE 3.4:   Median TWT-Thicknesses of the main seismo-stratigraphic units and volcanic units, their interval velocities, estimated thicknesses, and approximate ages.

Units	Tickness [TWT]	Velocity [km/s]	Thickness [m]	Age at Base [Ma]
Unit 6	40	1.72 - 1.78	35 ± 1	0.35
Unit 5	41	1.90	39 ± 1	0.7
Pre-Poseidon	45	2.0 - 2.2	48 ± 3	1.2
Pre-Kolumbo	43	2.0 - 2.2	45 ± 2	1.2
Unit 3	81	2.0 - 2.2	85 ± 4	1.6
Unit 2	160	2.2 - 2.4	181 ± 8	3.4
Unit 1	155	2.4 - 2.7	198 ± 12	5.4

Chapter 4

Spatio-Temporal Evolution of the Christiana-Santorini-Kolumbo Volcanic Field, Aegean Sea

Abstract

The Christiana-Santorini-Kolumbo Volcanic Field (CSKVF) in the Aegean Sea is one of the most active volcano-tectonic lineaments in Europe. Santorini has been an iconic site in volcanology and archeology since the 19th century, and the onshore volcanic products of Santorini are one of the best-studied volcanic sequences worldwide. However, little is known about the chronology of volcanic activity of the adjacent submarine Kolumbo Volcano, and even less is known about the Christiana volcanic island. In this study, we exploit a dense array of high-resolution marine seismic reflection profiles to link the marine stratigraphy to onshore volcanic sequences and present the first consistent chronological framework for the CSKVF, enabling a detailed reconstruction of the evolution of the volcanic rift system in time and space. We identify four main phases of volcanic activity, which initiated in the Pliocene with the formation of the Christiana Volcano (Phase 1). The formation of the current SW-NE trending rift system (Phase 2) was associated with the evolution of two distinct volcanic centers, the newly discovered Poseidon Center and the early Kolumbo Volcano. Phase 3 saw a period of widespread volcanic activity throughout the entire rift. The ongoing Phase 4 is confined to Santorini Caldera and Kolumbo Volcano. Our study highlights the fundamental tectonic control on magma emplacement and shows that the CSKVF evolved from a volcanic field with local centers that matured only recently to form the vast Santorini edifice.

4.1 Introduction

Located on the Hellenic Volcanic Arc (Southern Aegean Sea), the Christiana-Santorini-Kolumbo Volcanic Field (CSKVF) is one of the most hazardous volcanic fields in the world, having produced over 100 explosive eruptions in the last 650 ky including at least four caldera-collapse events (Druitt et al., 2019b). The iconic Minoan eruption 3600 years ago may have contributed to the fall of the Minoan civilization, leaving its imprint on Greek mythology, archeology, and volcanology (Druitt et al., 2019a). The CSKVF is located in a 60-km-long, SW-NE oriented rift zone and comprises the Christiana Volcano, the Santorini Caldera, the submarine Kolumbo Volcano, and the Kolumbo Chain that consists of 24 submarine cones (Fig. 4.1B) (Nomikou et

al., 2019). The onshore geology of Santorini has been a focal point of geoscientific research for decades resulting in a detailed chronostratigraphic framework constrained by field mapping and radiometric dating (Druitt et al., 1999). In contrast, only the latest of the up to five eruptions of Kolumbo is dated by historic reports (Fouqué, 1879), and the age of the Christiana Volcano is unknown.

Our understanding of the thick volcano-sedimentary infills of the surrounding marine basins has up to now been immature. Offshore constraints on the CSKVF chronology are sparse and mainly based on analog seismic data with limited resolution and penetration, which hampers imaging and identification of the often complex nature of volcanic structures. Piper et al. (2007) suggested that volcanism of the CSKVF initiated at Christiana during the Early Pleistocene ($\sim$1.7 Ma), with a main phase of activity at $\sim$0.6 Ma. In this interpretation, the entire Kolumbo edifice represents a young volcanic episode contemporary with the Thera Pyroclastic Formation (TPF) (<0.36 Ma) at Santorini. However, later studies show that the Kolumbo Volcano is more complex than previously assumed, with five stacked volcanoclastic units from different eruptive cycles (termed K1-K5), for which two different chronologies with significantly different ages for the inception of Kolumbo volcanism (180 ka as opposed to 1.6 Ma) have been proposed Hübscher et al. (2015). This highlights large uncertainty in the chronological framework of the CSKVF and complicates the understanding of volcano-tectonic interactions in this densely populated region, which are crucial to understand for a more reliable hazard assessment.

We now have compiled the database necessary to resolve the debate over the chronology of the CSKVF. Through a regional and internally consistent seismic-reflection data interpretation linked to onshore constraints, we identify the products of some previously unknown submarine volcanic centers and unravel how CSKVF volcanism has evolved in space and time.

4.2   Data

Our seismic reflection dataset comprises over 3200 km of high-resolution multi- and single-channel profiles (Hübscher et al., 2006; Karstens et al., 2020b; Sigurdsson et al., 2006) (Fig. 4.1B). We have established the regional stratigraphy for all basins of the CSKVF by identifying and mapping six seismic units characterized by distinct seismic reflection patterns. Ocean-bottom-seismometer-based (Karstens et al., 2020b) ray-tracing analysis provided seismic velocities, which we used for thickness calculation of specific seismic units. We then estimated approximate ages assuming an average sedimentation rate of 10 cm/ky, which has been used in previous studies in this area (Piper and Perissoratis, 2003; Anastasakis and Piper, 2005). For this calculation, we excluded all mass-transport deposits, volcanoclastic formations, and areas with diverging reflections (for details see Appendix A).

4.3   Results

4.3.1   Stratigraphic Framework

A continuous seismic section across the CSKVF extends from the northern flank of Christiana through the Christiana Basin (markers T-V in Fig. 4.2A), crosses Santorini Caldera (V-X), enters the Anhydros Basin (X-Y), and covers Kolumbo Volcano (Y-Z).
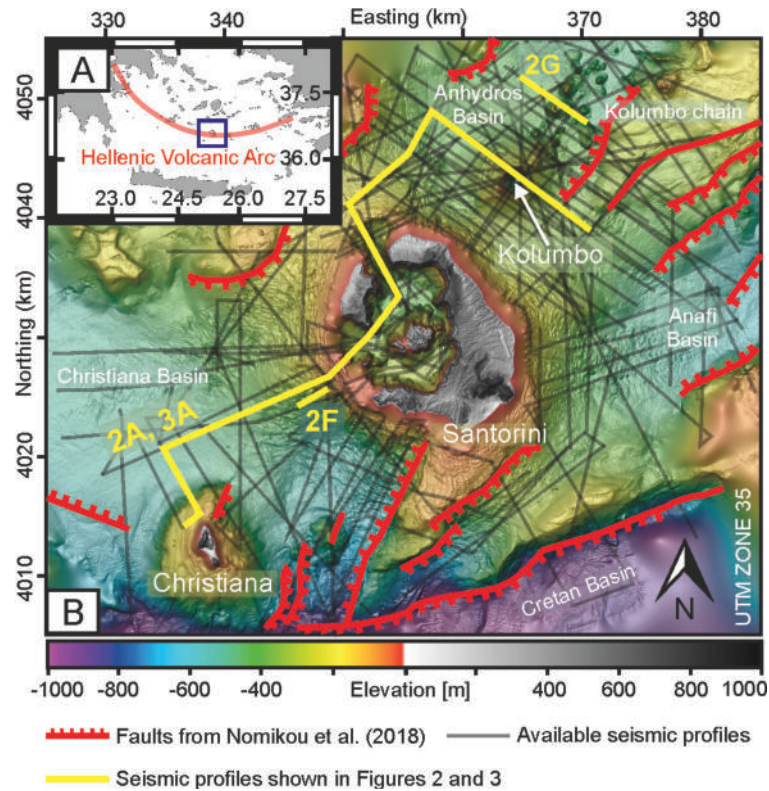
FIGURE 4.1: A) Regional setting of the Southern Aegean Sea with the study area (blue box). B) Morphological map of the CSKVF showing basins, volcanic centers, and volcanic lineaments.

Two short seismic lines show additional volcanic cones from the Christiana Basin (Fig. 4.2F) and the Kolumbo Chain (Fig. 4.2G).

We identify six marker horizons (h1- h6) in the Christiana and Anhydros basins, which define the bases of six volcano-sedimentary units (U1-U6; Fig. 4.2B-E). Figures 4.2B and C highlight the correlation between both the marker horizons and seismic facies in the Christiana and Anhydros basins. The uppermost unit (U6) comprises several high-amplitude subparallel reflections (Fig. 4.2E). While U6 is rather thin in the Christiana Basin (Fig. 4.2D), it forms a ~350 m thick wedge NE of Santorini (Fig. 4.2E), which pinches out towards the northern caldera breach and thins out toward the Anhydros Basin (Fig.4.3A). U5 is a well-stratified unit traceable throughout the whole working area with an approximately constant thickness (Fig. 4.2B and C). The underlying Unit (U4) is weakly reflective, shows wavy top-reflections in both basins, and has a distinct internal reflection in addition to some scattered reflections (Fig. 4.2B-D). U2 and U3 consist of closely spaced reflections locally interrupted by several larger chaotic or transparent subunits (Fig. 4.2D and 4.3A). The lowermost unit (U1) has low-amplitude reflections; it is thick in the Christiana Basin, but thin and hardly detectable in the Anhydros Basin (Fig. 4.3A). Deposits within Santorini Caldera are related to the Minoan Eruption and the post-Minoan activity of the Kameni Islands (Johnston et al., 2015).
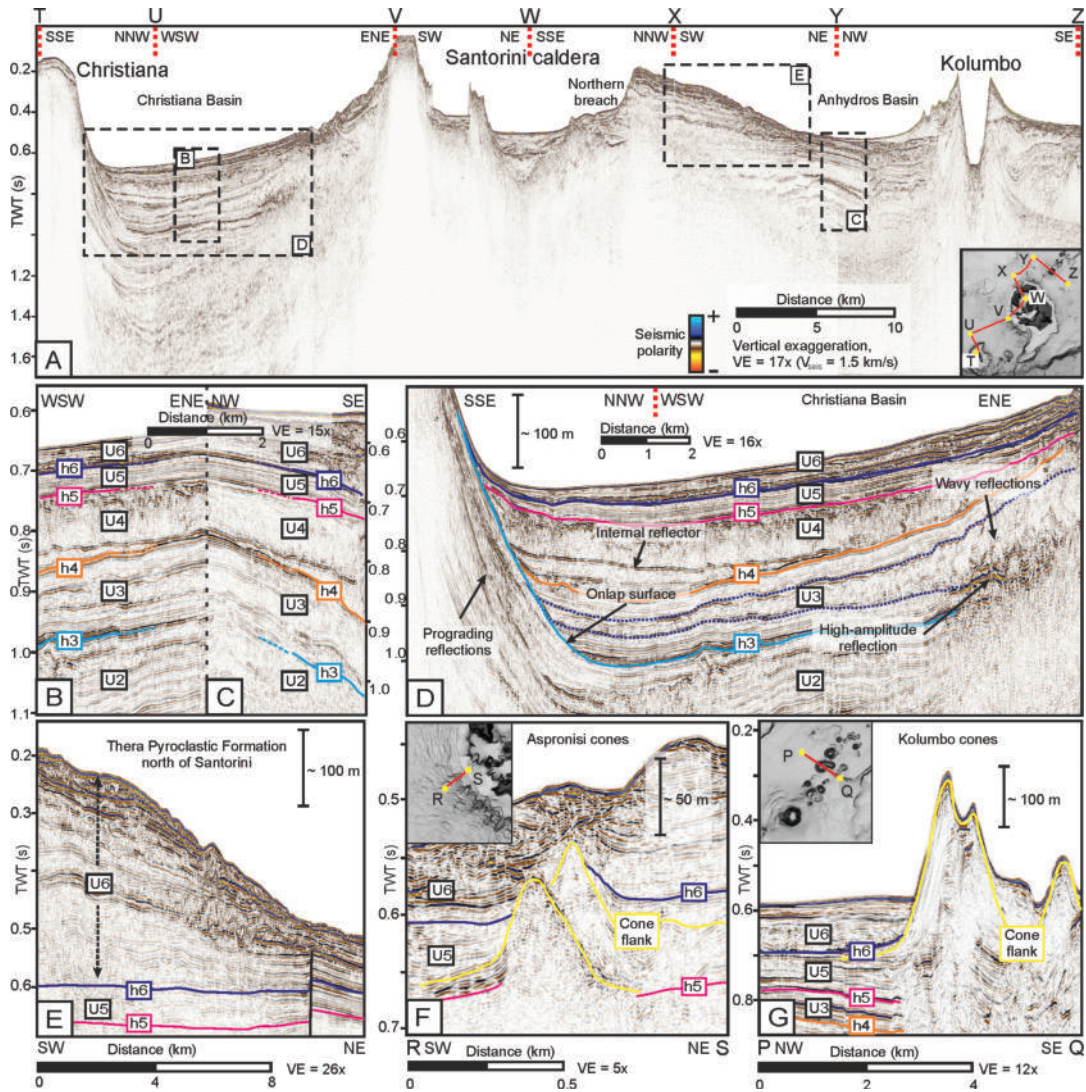
FIGURE 4.2: Seismic profile connecting the volcanic centers of the CSKVF (A). For location, see inset map and Figure 4.1. Enlargements (B-E) highlight the stratigraphic correlation of the upper units of the Christiana (B) and the Anhydros basins (C), the internal architecture of the Christiana basin (D), and the NE flank of Santorini (E). Additional seismic lines show the Aspronisi cones (F) and examples of cones from the Kolumbo Chain (G).

4.3.2 Interpretation of Volcanic Features

Our seismic data reveal an abundance of volcanic features intercalated within different stratigraphic units of the Christiana and Anhydros basins (Fig. 4.3A). In the western part of the profile, the flank of Christiana is defined by h3, which represents a major onlap surface (Fig. 4.2D). There are several prograding reflections beneath h3 that are high-amplitude and of positive polarity indicating a high acoustic impedance (Fig. 4.2D). Based on these observations, we interpret them as talus deposits or lava-flows from the Christiana edifice, which is consistent with the observation of westward dipping lava flows onshore Christiana (Puchelt et al., 1977). Within U3, we identify a large subunit in the eastern Christiana Basin of Santorini (between the dotted blue lines; Fig. 4.2D). This subunit consists of several wavy

and low-amplitude reflections (Fig. 4.2G), is ∼150 m thick at the foot of Santorini, and thins towards the Christiana Basin. The wavy top and internal reflections are typical for volcanoclastic density flow deposits, suggesting that this layer consists of volcaniclastics deposited by multiple eruptions (Pope et al., 2018). We observe anomalously high-amplitude reflections at its base (Fig. 4.2D), beneath which the reflections are very weak, implying pronounced signal attenuation. Hence, we tentatively interpret these reflections as sills or lava flows (Jackson, 2012; Bischoff et al., 2019), which form a volcanic center, hereafter referred to as Poseidon Center west of Santorini.

U4 (Fig. 4.2D and 4.3A) is a thick, widespread, and weakly reflective deposit, which has been described by Tsampouraki-Kraounaki and Sakellariou (2018) in the Christiana Basin and interpreted as a volcanoclastic density flow deposit. The chaotic internal seismic facies, however, also resembles that of debris-avalanche deposits (Watt et al., 2021). Given the distribution in both the Christiana and Anhydros basins, the source for this deposit must have been located somewhere close to present-day Santorini.

U6 comprises several pyroclastic deposits from the TPF. This is best visible at the northern caldera breach, where the thick wedge of alternating low-amplitude, chaotic, and wavy reflections are typical for pyroclastic deposits (Karstens et al., 2013; Pope et al., 2018) and resemble the stratified flanks of the caldera cliffs of the Santorini Caldera (Fig. 4.2E) (e.g. Druitt et al., 1999). Like Piper et al. (2007), we find only a comparably thin cover of TPF deposits in the Christiana Basin (Fig. 4.2D).

The Kolumbo Volcano dominates the bathymetry of the Anhydros Basin. The lowermost units K1 and K2 are within U3, with K2 making up the largest part of the entire edifice (Fig. 4.3A). We identify a small, weakly reflective subunit between K1 and K2, which we interpret as a mass-transport deposit. K3 represents a smaller unit from Kolumbo that is intercalated within the stratified unit U5. Above that, K4 is a larger unit of Kolumbo, which is located within U6. The most recent Kolumbo unit (K5), from the 1650 AD eruption, lies on top of U6 (Fig. 4.3A). Figures 4.2F and G illustrate previously unknown cones west of Santorini (Fig. 4.2F, Aspronisi Cones) and from the Kolumbo Chain (Fig. 4.2G), which strongly resemble other seismically imaged volcanic cones from different regions (e.g. Weiß et al., 2015; Bischoff et al., 2019). Onlap terminations indicate that there are relative age differences between these cones, yet all of them are within U5, as is unit K3 from Kolumbo (Fig. 4.3A).

4.4 Discussion
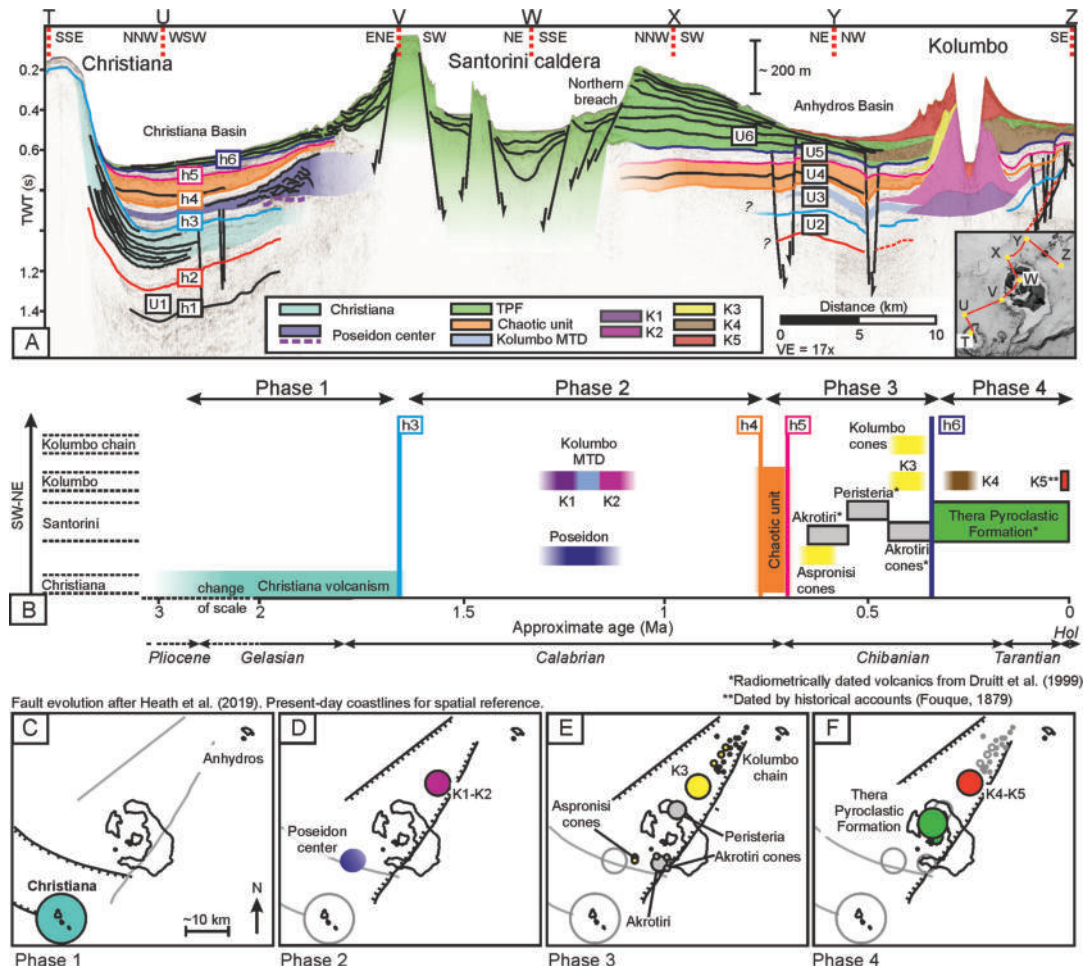
FIGURE 4.3: Interpretation of the seismic profile from Figure 4.2A. K1-K5: Kolumbo units MTD: Mass Transport Deposit; TPF: Thera Pyroclastic Formation. B) Schematic illustration of the chronology of volcanism at the CSKVF. Hol: Holocene. C-F) Sketches of the spatial distribution of the four main phases of the volcanic evolution of the CSKVF.

The detail at which we can resolve volcanic structures and deposits depends on the vertical seismic resolution (∼4-9 m), which means sub-resolution layers that would be obvious in the field cannot be resolved seismically. Further, minor volcanic centers could be missed depending on the survey layout. To overcome this limitation, extensive and costly 3D seismic surveying would be required. Nevertheless, our seismic network is sufficiently dense to identify major volcanic centers (Fig. 4.1B). Figure 4.3B illustrates the chronology of the volcanic features from the CSKVF. While the relative chronology is validated by the correlation of horizons in the Christiana and Anhydros basins (Fig. 4.2B and C), absolute ages are subject to uncertainty due to lateral thickness variations and the assumption of a constant sedimentation rate and they need to be tested by scientific drilling. Yet, our estimates are in good agreement with age constraints from previous studies. Our age estimate of ∼0.35 Ma for h6 agrees well with the onset of the TPF, while ∼0.7 Ma for h5/h4 roughly corresponds to the onset of the Akrotiri Volcano (0.65-0.55 Ma) (Druitt et al., 1999). The

estimated age of ∼1.2 Ma for the Poseidon Center roughly fits with age estimates from Seward et al. (1980) for a rhyodacitic tuff (dated at ∼1 Ma), which discordantly underlies the products of Aktoriri onshore Santorini. Horizon h1 is the only stratigraphic marker that can be correlated with DSDP Hole 378 in the Cretan Basin (Hsu et al., 1978), where it corresponds to the top of the Messinian. This is in agreement with our age estimate of ∼5.4 Ma and interpretations of previous studies (Piper et al., 2007; Hübscher et al., 2015). There are no direct age constraints for horizons h2 and h3, but our framework suggests ages of ∼4.4 Ma (h2) and ∼1.6 Ma (h3).

We define four distinct phases of volcanic activity, which we relate to the tectonic model of the CSKVF from Heath et al. (2019). Phase 1 initiated during the Late Pliocene with the formation of Christiana Volcano as a consequence of the intersection of the Miocene-Pliocene E-W oriented fault regime and an emerging SW-NE fault system (Fig. 4.3C) initiating the rifting that shaped the basin system east of Santorini (Fig. 4.1B) (Hübscher et al., 2015; Nomikou et al., 2018b). Since the volcanic deposits from Christiana are intercalated within large parts of U2, the evolution of the Christiana Volcano must have taken place over several hundreds of thousands of years. This phase terminated after h3 at roughly 1.6 Ma, which fits well with the early Christiana series from Piper et al. (2007). However, in contrast to Piper et al. (2007), we do not see evidence for a second phase of activity from Christiana.

During the next volcanic phase (Phase 2), the SW-NE-striking fault trend became the main pathway for magma ascent, which resulted in an SW-NE alignment of volcanism connecting the Poseidon Center with the center of early Kolumbo (K1/K2; Fig. 4.3D). This volcanic lineament is roughly parallel to the present-day Kameni and Kolumbo lines, which are considered to be rooted on deep-seated extensional faults focusing magma emplacement (Heath et al., 2019; McVey et al., 2020). Our results agree with the long Kolumbo chronology from Hübscher et al. (2015).

The subsequent emplacement of the chaotic Unit U4 at ∼0.7 Ma occurred prior to the third volcanic phase and is interpreted to be the result of large-scale masswasting or pyroclastic flow events or a combination of both sourced from proto-Santorini. Afterwards, volcanism occurred across the whole rift system, extending from the newly discovered Aspronisi Cones to Kolumbo Volcano (K3) and the Kolumbo Chain (Fig. 4.3E). Approximately contemporaneously, the Akrotiri rhyolitic centers (0.65 to 0.55 Ma), the Peristeria stratovolcano (0.55 to 0.45 Ma), and the monogenetic cinder cones of Akrotiri (0.45 to 0.34 ka) erupted, these being the earliest dated onshore activity on Santorini (Druitt et al., 1999). The existence of a field of monogenetic centers (cones of Aspronisi, Akrotiri, and Kolumbo Chain) in between polygenetic centers (Aktoriri, Peristeria, Kolumbo K3) is a notable feature of Phase 3.

The fourth and ongoing phase saw a distinct shift in the volcanic behavior of the CSKVF, as volcanism concentrated between the Kameni and Kolumbo Lines (Fig. 4.3F). This ongoing phase has been characterized by tomographic observations from McVey et al. (2020), who revealed a low-velocity anomaly at 2.8 to 5 km depth below the northern caldera basin, which terminates northwest of Kolumbo. McVey et al. (2020) suggested that this zone is bounded by volcano-tectonic lineaments that provide pathways for melt to reach the surface. Our results indicate that this lineament represents a long-lived feeder system that has been active for as much as ∼1.2 Ma, underlining the fundamental tectonic control of volcanism in the CSKVF.

4.4.1 Implications

For the first time, we establish the relative chronology of CSKVF volcanism, which complements onshore dating back to the Pliocene. We reconstruct the waxing and waning of volcanic centers of the CSKVF and show that these local centers matured only recently to form the vast Santorini edifice. This study highlights the potential of reflection seismic surveying to provide detailed insights into the spatio-temporal evolution of complex volcanic systems, even in an area as well studied as Santorini. Such detailed information is crucial for reconstructing eruption frequencies and for defining hazard scenarios, which are key for more reliable risk assessment. Given its comparably small extent and number of volcanic centers, the Hellenic Volcanic Arc offers the unique opportunity for a complete spatio-temporal reconstruction of an entire arc system. Extending our framework to the greater Hellenic Volcanic Arc centers should be a focus of future research.

Acknowledgements

Chapter 5

The Hidden Giant: How a rift pulse triggered a cascade of sector collapses and voluminous secondary mass-transport events in the early evolution of Santorini

Abstract

Volcanic island sector collapses have the potential to trigger devastating tsunamis and volcanic eruptions that threaten coastal communities and infrastructure. Considered one of the most hazardous volcano-tectonic regions in the world, the Christiana-Santorini-Kolumbo Volcanic Field (CSKVF) lies in the South Aegean Sea in an active rift zone. Previous studies identified an enigmatic voluminous mass-transport deposit west and east of Santorini emplaced during the early evolution of the edifice. However, the distribution and volume as well as the nature and emplacement dynamics of this deposit remained unknown up to now. In this study, we use an extensive dataset of high-resolution seismic profiles to unravel the distribution and internal architecture of this deposit. We show that it is located in all basins surrounding Santorini and has a bulk volume of up to 125 km^3, thus representing the largest known volcanic island mass-transport deposit in the entire Mediterranean Sea. We propose that the deposit is the result of a complex geohazard cascade that was initiated by an intensive rift pulse. This rifting event triggered a series of smaller precursory mass-transport events before large-scale sector collapses occurred on the northeastern flank of the extinct Christiana Volcano and on the southeastern flank of the nascent Santorini. This was followed by the emplacement of large-scale secondary sediment failures on the slopes of Santorini, which transitioned into debris and turbidity flows that traveled far into the neighboring rift basins. Following this cascade, a distinct change in the volcanic behavior of the CSKVF occurred, suggesting a close relationship between crustal extension, mass transport, and volcanism. Cascading geohazards seem to be more common in the evolution of marine volcanic systems than previously appreciated. Wider awareness and a better understanding of cascading effects are crucial for more holistic hazard assessments.

5.1 Introduction

Submarine landslides offshore volcanic islands are among the largest-volume mass movements on Earth's surface (Moore et al., 1994; Masson et al., 2002). Individual

landslide deposits can contain hundreds to thousands of cubic kilometers of material extending over distances of hundreds of kilometers (Moore et al., 1989). These collapse events are capable of generating devastating tsunamis on oceanic scales (Løvholt et al., 2008) and the associated unloading of the volcanic systems may trigger explosive volcanic eruptions (Siebert, 1984; Hunt et al., 2018). In recent years, marine geophysical surveys have revealed that sector collapses around volcanic islands are a common and important process during the evolution of volcanic edifices, and might occur in complex disaster cascades involving volcanic eruptions, tsunamis, and earthquakes (Ida and Voight, 1995; McGuire, 1996; Voight, 2000; Hunt et al., 2018; Karstens et al., 2019; Patrick et al., 2020; Watt et al., 2021). Understanding the origin, preconditions, and triggers of volcanic sector collapses, as well as their emplacement dynamics in the marine realm, is crucial for determining the magnitude of associated tsunamis and their potential influence on local volcanic systems.

Given the complexity of submarine volcanic landslides, many questions remain open regarding potential trigger mechanisms, emplacement dynamics, and the role of secondary failure processes. Recent studies have shown that landslide volumes are often much greater than the volume of the associated sector collapse scars, which implies significant incorporation of seafloor sediment into the mobilized volume (Watt et al., 2012; Watt et al., 2021; Karstens et al., 2019; Kühn et al., 2021). Watt et al. (2012) noted that many submarine landslide deposits from volcanic islands are characterized by a blocky-surfaced proximal part, which mainly comprises collapsed volcanic material, and a smoother-surfaced apron, which mainly comprises seafloor sediment. The entrainment of secondary sediment into volcanic landslides can be very widespread on low (<1°) gradients and may dominate the total landslide volume (Watt et al., 2012; Crutchley et al., 2013). At Ritter Island, for example, only 20% of the total volume that was deformed or mobilized as part of the collapse was derived from the rapid, tsunami-generating volcanic collapse (Karstens et al., 2019; Watt et al., 2019). Further, results from IODP Expedition 340 showed that the distal and medial parts of landslide deposits offshore Montserrat and Martinique lacked coarse and chaotic subaerial volcanic debris avalanche material, but comprised turbidites and hemipelagic deposits derived from secondary sediment failures (Brunet et al., 2016; Le Friant et al., 2015; Le Friant et al., 2019).

To explain the occurrence of such voluminous secondary sediment failures at volcanic islands, it has been proposed that the rapid emplacement of failed volcanic edifice material initiates the propagation of a décollement, which causes widespread failure of pre-existing low-gradient seafloor sediment (Watt et al., 2012). According to this model, the load imposed by the initial failure may generate excess pore fluid pressure and trigger additional sediment failures in slope and basin areas that would not otherwise be prone to failure (Viesca and Rice, 2012; Le Friant et al., 2015; Le Friant et al., 2019). These results have important implications for the magnitude of tsunami generation by volcanic island landslides since secondary seafloor sediment failures are likely to be much less tsunamigenic than the proximal, block-rich, mass flows (Watt et al., 2012; Le Friant et al., 2019). Therefore, the complexities within submarine volcanic landslides must be carefully considered for an accurate assessment of associated hazards (Watt et al., 2021).

Although volcanic sector collapses are fairly common in the evolution of volcanic edifices, systematic surveys of their remnants are only available for a small number of volcanic island groups and arcs (Watt et al., 2021). Examples from the Hellenic Volcanic Arc in the densely populated Aegean Sea are sparse despite the known occurrence of large-scale volcanic centers and enhanced seismicity, which make this

arc one of the major risk factors for the eastern Mediterranean (Sørensen et al., 2012). Preine et al. (2022a) reported a large mass-transport deposit within the Christiana-Santorini-Kolumbo volcanic field (CSKVF) in the central Aegean Sea. Chrono-stratigraphic relationships indicate that the deposit was emplaced during the early evolution of Santorini, approximately 0.7 Myrs ago (Preine et al., 2022a). However, the distribution, volume, trigger mechanisms, and emplacement dynamics of the deposit have not been investigated so far.
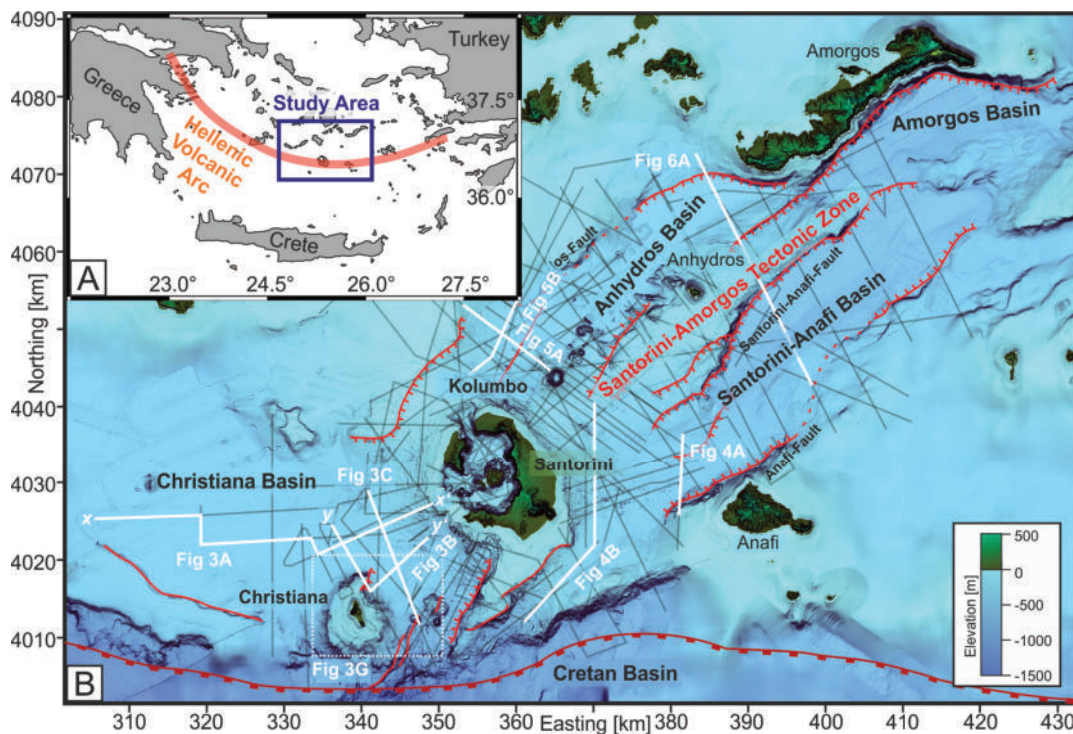
FIGURE 5.1: A) Regional setting of the Southern Aegean Sea, showing the Hellenic Volcanic Arc and the study area (blue box). B) Morphological map of the CSKVF showing islands, basins, volcanic centers, and major extensional structures (red lines) after (Nomikou et al., 2016b; Nomikou et al., 2018b; Nomikou et al., 2019). Coordinate system is UTM Zone 35N, WGS84. Grey lines show all seismic profiles, white lines indicate the locations of seismic profiles shown in this study. Dashed white rectangle indicates the location of the 3D view of Christiana shown in Fig. 5.3G. Bathymetry from Nomikou et al. (2013), Nomikou et al. (2012), Nomikou et al. (2018b), Nomikou et al. (2019), and Hooft et al. (2017). Topography from the Hellenic Military Geographic Service (HMGS).

Since 2006, we have compiled a comprehensive dataset of more than 3,200 km of high-resolution multi- and single-channel seismic reflection data (Sigurdsson et al., 2006; Karstens et al., 2020b; Hübscher et al., 2006) covering the entire basin system adjacent to Santorini (Fig. 5.1B). Using this extensive dataset, the first objective of this study is to map the distribution of the large mass-transport deposit (MTD) and estimate its volume. Our second objective is to investigate the nature of this deposit and identify kinematic indicators to determine potential sources. The third objective of this study is to reconstruct its emplacement dynamics, analyze cascading effects,

assess its impact on the shallow volcanic plumbing system of the CSKVF, and discuss implications for geohazard assessment.

5.2   Geological Framework

The marine CSKVF is one of the most hazardous volcano-tectonic fields in the world (Druitt et al., 1999). It is located on the Hellenic Volcanic Arc, which stretches from Greece in the west towards Turkey in the east and was formed as a consequence of the subduction of the Nubian underneath the Eurasian Plate (Fig. 5.1A) (Le Pichon and Angelier, 1981). Having produced over 100 explosive eruptions including at least four caldera collapses during the last 360,000 years, the CSKVF poses a major threat (eruptions, tsunamis, earthquakes) to the eastern Mediterranean region (Druitt et al., 1999; Kutterolf et al., 2021a; Kutterolf et al., 2021b; Nomikou et al., 2016a; Satow et al., 2021). The iconic Minoan Eruption ~3600 years before present may have contributed to the fall of the great Minoan civilization, leaving its imprint on Greek mythology, archeology, and volcanology (Druitt et al., 2019a).

Situated on highly stretched continental crust in an SW-NE oriented rift zone, the CSKVF comprises the extinct Christiana Volcano, the Santorini Caldera, the polygenetic submarine Kolumbo Volcano, as well as the Kolumbo Volcanic Chain (Fig. 5.1B) (Nomikou et al., 2012; Nomikou et al., 2013; Hübscher et al., 2015; Hooft et al., 2017; Hooft et al., 2019; Preine et al., 2022a). The CSKVF is located on the junction of the broad Christiana Basin to the West and the complex Santorini-Amorgos Tectonic Zone (SATZ) to the East (Fig. 5.1B) (Nomikou et al., 2018b; Nomikou et al., 2019). The Christiana Basin has been named after the Christiana Islands, a group of three highly eroded volcanic islets belonging to the same submarine edifice southwest of Santorini (Fig. 5.1B, 5.3G), which is assumed to have been dormant since the Early Pleistocene (Preine et al., 2022a). There are three larger volcanic domes (200-300 m volcanic relief) east of Christiana, which are partially cut by SW-NE trending faults (Nomikou et al., 2013). As a zone of SW-NE trending rifts, the SATZ extends from the eastern flank of Santorini towards Amorgos and separates the Cycladic Plateau to the northwest from the minor Anafi-Astypalaea Plateau to the southeast (Nomikou et al., 2018b; Nomikou et al., 2019). These complex tectonic horst and graben segments evolved during four major tectonic pulses and are bordered by SW-NE trending active extensional to transtensional faults (Hübscher et al., 2015; Nomikou et al., 2016b; Nomikou et al., 2018b; Hooft et al., 2017; Preine et al., 2020).

Besides the occurrence of pyroclastic-flow deposits from the recent (<0.36 Ma) eruptions of Santorini forming the Thera Pyroclastic Formation (Sigurdsson et al., 2006; Hübscher et al., 2015; Preine et al., 2022a), the literature of major MTDs from the basins surrounding the centers of the CSKVF is surprisingly sparse given the long history of volcanic build-up, caldera-collapse and enhanced tectonic exposure (Bohnhoff et al., 2006; Nomikou et al., 2018b; Preine et al., 2020). Bell et al. (2013) reported a surficial landslide deposit on the southeastern flank of Santorini, which contained large remobilized blocks composed of pyroclastic-flow deposits from the Minoan eruption. These authors proposed that this deposit is the result of a landslide that was triggered by a large seismic event after the Minoan eruption Bell et al. (2013). Tsampouraki-Kraounaki and Sakellariou (2018) reported several chaotic seismic units in the Christiana Basin, including a particularly thick (> 100 ms two-way traveltime (TWT)), transparent unit, which thickens towards Santorini and was interpreted to be of pyroclastic origin that might have been related to an eruption in the early phase
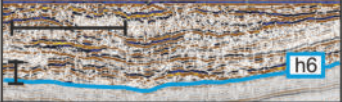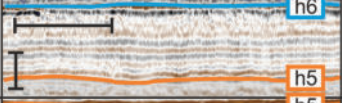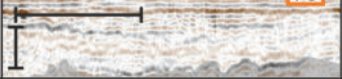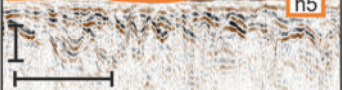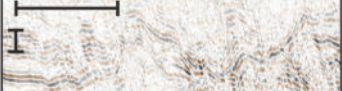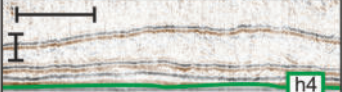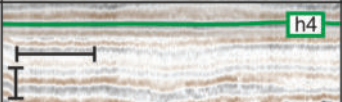
of the evolution of Santorini. In a recent study, however, it was shown that this deposit also occurs in the Anhydros Basin on the eastern side of Santorini and that the internal architecture is also consistent with that of a large MTD (Preine et al., 2022a). This deposit was emplaced after volcanism aligned southwest and northeast of Santorini, but before the emergence of enhanced, rift-wide volcanism ($\sim$0.7 – 0.36 Ma) and the onset of the explosive Thera Pyroclastic Formation (< 0.36 Ma; (Preine et al., 2022a)).

5.3   Geophysical Methods

In this study, we use a dataset of over 3,200 km of high-resolution multi- and single-channel seismic data collected during several cruises between 2006 and 2019 (Fig. 5.1B) (Sigurdsson et al., 2006; Karstens et al., 2020b; Hübscher et al., 2006). See Appendix B for details regarding the acquisition and processing of the seismic data. All processed seismic lines were combined into an interpretation project using the KingdomSuite software. Here, we established the stratigraphic framework (following the nomenclature in (Preine et al., 2022a)), mapped the seismic unit corresponding to the inferred MTD (Unit 4), and created isopach maps by interpolating between the seismic profiles. Ocean-bottom seismometer recordings and ray-tracing analysis provided seismic velocities (Preine et al., 2022a), which we then used to approximate deposit volumes. We estimated the volume of Unit 4 using an interval velocity of 1900 m/s with an uncertainty of ± 100 m/s, which accounts for errors in picking seismic reflections for the applied velocity model and the fact that the interval velocity of Unit 4 was only available at one location (Preine et al., 2022a).

5.4   Results

The stratigraphy of the basins hosting the CSKVF comprises six units (U1-U6), which are separated by six marker horizons h1-h6 at the corresponding base of each unit (following the nomenclature of (Preine et al., 2022a)). In the following, we will focus on the uppermost Units 3-6, with the potential MTD previously defined as Unit 4 (Preine et al., 2022a). Figure 5.2 gives an overview of the seismic facies within these units (based on concepts of Mitchum et al. (1977)). The internal architecture of Unit 3 and Unit 5 consists of a sequence of well-stratified reflections with generally low amplitudes that contrast with the complex architecture of Unit 4 and Unit 6. Within Unit 4 we identify four different seismic subunits (U4a-d) across our working area, highlighting the complex nature of this deposit. At the base of Unit 4, we find a sequence of subparallel to irregular high-amplitude reflections (U4a) at most locations. Only in the vicinity of Santorini, this unit is missing and we identify instead a sequence of deformed, chaotic reflections with moderate amplitudes that are occasionally interrupted by some partially layered reflection sequences (U4b). The largest part of Unit 4 is made up of incoherent strata with transparent seismic facies and some reflection patches of moderate to high amplitudes (U4c). The top of this deposit is marked by wavy reflections with moderate amplitude. Further, we identify a subunit with subparallel to incoherent low-amplitude reflections (U4d). The boundary between each of these identified internal subunits is not always distinct and individual subunits might transition into each other. The uppermost Unit 6 comprises subparallel reflections that are partially interrupted and intercalated with high-amplitude irregular reflections.

Unit	Sub-Unit	Illustration	Reflection configuration	Interpretation	Figures	
U6	-		Subparallel reflections of moderate amplitudes intercalated with hummocky, chaotic, high-amplitude reflections	Volcanic deposits from Santorini	3A,B,C 4A,B,D,E 5A,B 6A,B	7 9 10
U5	-		Parallel, low-amplitude reflections	Hemipelagic sedimentation	3A-C,E,F 4A,B,D,E 5A,B 6A,B,C	7 9 10
U4	U4d		Subparallel coherent to incoherent reflections with low amplitudes	Turbidity flow deposits	3A,B,C,F 5A,B 6A,B,C 7	
	U4c		Incoherent, transparent facies with some scattered reflection patches and wavy reflections at the top	Debris flow deposits	3A-CF 5A,B 6A,C 7	7 9 10
	U4b		Chaotic and deformed reflections with moderate amplitudes interrupted by some partially layered reflection sequences	Slump deposits	3B,C,F 4B,D,E	
	U4a		Subparallel to irregular, high-amplitude internal reflections	Stacked mass-transport deposits	3A,B,E 4A 5A,B 6A,B,C	7 9 10
U3	-		Parallel, low-amplitude reflections	Hemipelagic sedimentation	3A,B,C,E 4A,B,D,E 5A,B 6A,B,C	7 9 10

25 ms TWT   1 km

FIGURE 5.2: Summary of the seismic facies of Units 3-6 with four sub-units identified within U4. Horizons h4, h5, and h6 (green, orange, and blue lines) are the basal reflectors of the corresponding units (U4-U6) as established in Preine et al. (2022a). Seismic facies based on concepts of (Mitchum et al., 1977) and interpretation based on Bull et al. (2009) and Smit and Stemmerik (2022).

5.4.1 Christiana Basin

Figure 5.3A shows a seismic profile extending from the western flank of Santorini into the Christiana Basin to the west. Unit 3 has an approximately constant thickness while Unit 4 (orange in Fig. 5.3A) thickens significantly towards the lower slope of Santorini and is characterized by a complex internal seismic architecture. In the upper part of Unit 4, we identify wavy seismic reflections (U4c; Fig. 5.2), which become weakly reflective but stratified towards the west (U4d; Fig. 5.2, 5.3A). Further, there is a characteristic sequence of one to three internal high-amplitude reflections in the lower portion of the deposit (U4a; Fig. 5.2), with the uppermost of these reflections showing an undulating topography and onlapping the top of Unit 3 (Horizon h4) (Fig. 5.3A). Unit 4 is overlain by a sequence of closely spaced, well-stratified reflections of Unit 5, which is in turn overlain by Unit 6 (blue in Fig. 5.3A) that represents the volcanic deposits of the Thera Pyroclastic Formation according to Preine et al. (2022a).
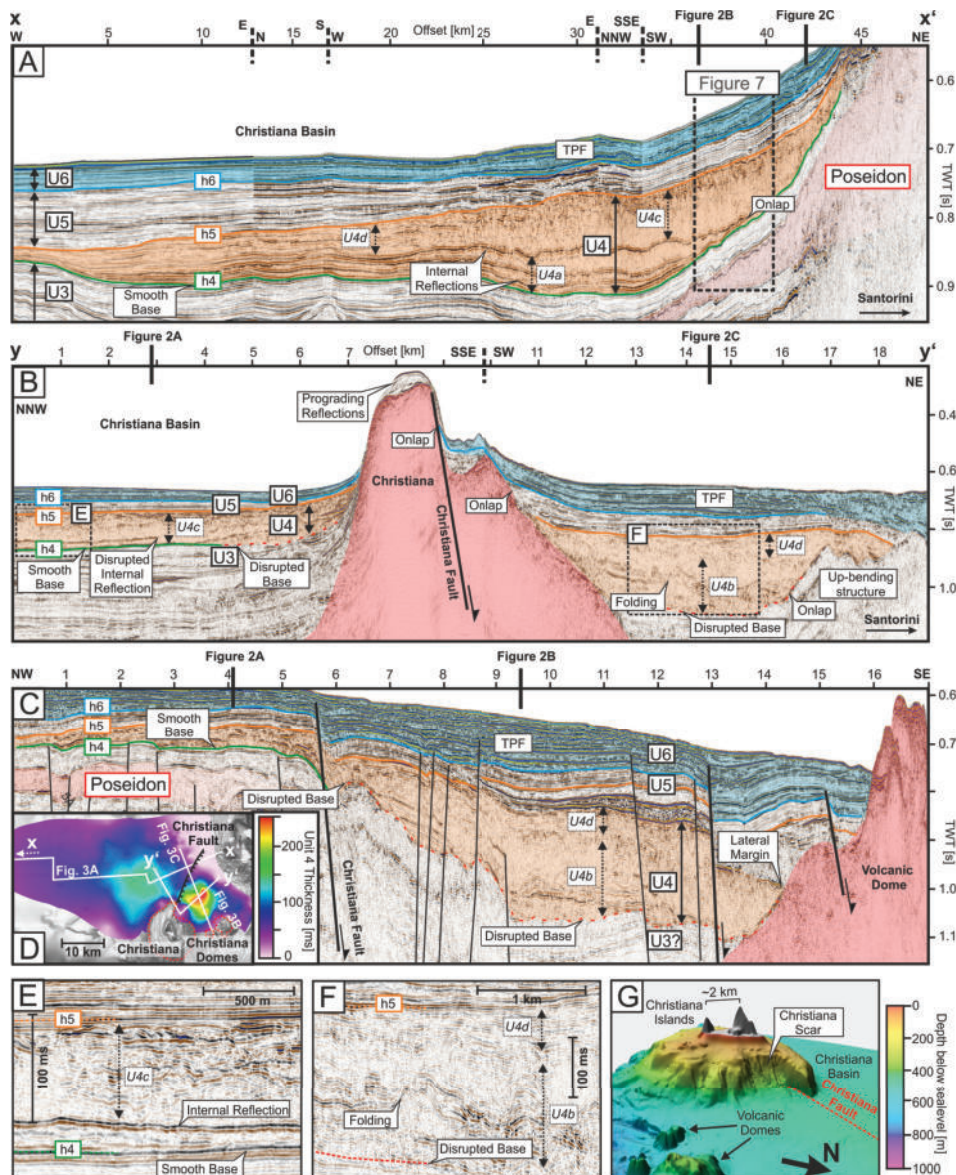
FIGURE 5.3: A) Seismic line connecting single-channel and high-resolution multichannel seismic lines across the Christiana Basin and the western flank of Santorini. Labels U3-U6 represent Units 3-6 and U4a-d represent subunits of Unit 4 as outlined in Figure 5.2. Horizons h4, h5, and h6 are the basal reflectors of the corresponding units (U4-U6). TPF = Thera Pyroclastic Formation. Poseidon indicates volcanoclastic deposits from the eponymous volcanic center according to Preine et al. (2022a). B) High-resolution multichannel seismic profile crossing the Christiana Basin and the incised northeastern flank of the Christiana Edifice. A weak and disrupted base of U4 is marked by the broken red line, as opposed to the green line (h4), which represents a distinct and continuous basal reflection. C) High-resolution multichannel seismic profile crossing the Christiana Basin, the Christiana Fault, and volcanic domes adjacent to Chrisitana. Black lines are normal faults. D) Map showing the thickness of Unit 4 and the location of the profiles. Toothed black line is the Christiana Fault. E), F) Enlargements from the seismic profile shown in B. G) 3D view of the Christiana Edifice and the Christiana Fault scar (5 times vertically exaggerated).

Figure 5.3B shows a seismic line that crosses the Christiana Edifice coming from the west and continues towards the flank of Santorini. West of Christiana, Unit 4 has the same characteristics as observed in Figure 5.3A: a generally smooth base reflection, a sequence of wavy top-reflections (U4c; Fig.5.2), and a pronounced internal reflection (U4a; Fig. 5.2, 5.3B, 5.3E). Towards Christiana, this internal reflection disappears abruptly at approximately 3 km along the profile, and the distinct base reflection (h4) is interrupted in a region, where the reflections of the underlying Unit 3 are eroded (broken red line west of Christiana in Fig. 5.3B). The Christiana Edifice is incised by the Christiana Fault scar, forming a distinct step, which is highlighted by the 3D-view in Figure 5.3G. While the slope of the edifice is smooth towards the west, it is more irregular towards the east. The edifice is covered by a thin, prograding sediment cover ($\sim$7.5-8.5 km along profile, Fig. 5.3B), while the down-faulted hangingwall of the Christiana Fault is overlain by a chaotic sedimentary cover belonging to Unit 5 and 6 (Fig. 5.3B). Further towards the northeast of Christiana, the slope of the edifice is onlapped by Unit 4, which has a much more complex internal architecture (strongly folded internal reflections, U4b, Fig. 5.2) here compared to the region northwest of Christiana (Fig. 5.3B). This deformed sequence of Unit 4 is buttressed against an irregular up-bending structure at the foot of Santorini (Fig. 5.3B). In addition, we observe that the base of Unit 4 is disrupted here (red dotted line) and that there is pronounced internal folding (Fig. 5.3F). We also identify a sequence of weak, stratified reflections (U4d; Fig. 5.2) on top of Unit 4 (Fig. 5.3B).

Figure 5.3C shows a seismic line crossing the Christiana Fault in NW-SE direction between Christiana and Santorini and ending above one of three larger volcanic domes between Christiana and Santorini. Northwest of the Christiana Fault, Unit 4 is thin (<100 ms) and is interspersed with chaotic high-amplitude reflections. The unit gradually thickens towards the Christiana Fault and then becomes much thicker to the southeast of the fault, exceeding 200 ms thickness in places (e.g. around 10 km along profile). Here, we identify a weak and disrupted base reflection and folding of the internal fabric (U4b; Fig. 5.2). Towards the southeast, Unit 4 terminates abruptly against the volcanic dome. Again, we identify weakly reflective subunits within the upper part of Unit 4 (U4d; Fig. 5.2, 5.3C).

5.4.2 Western Santorini-Anafi Basin
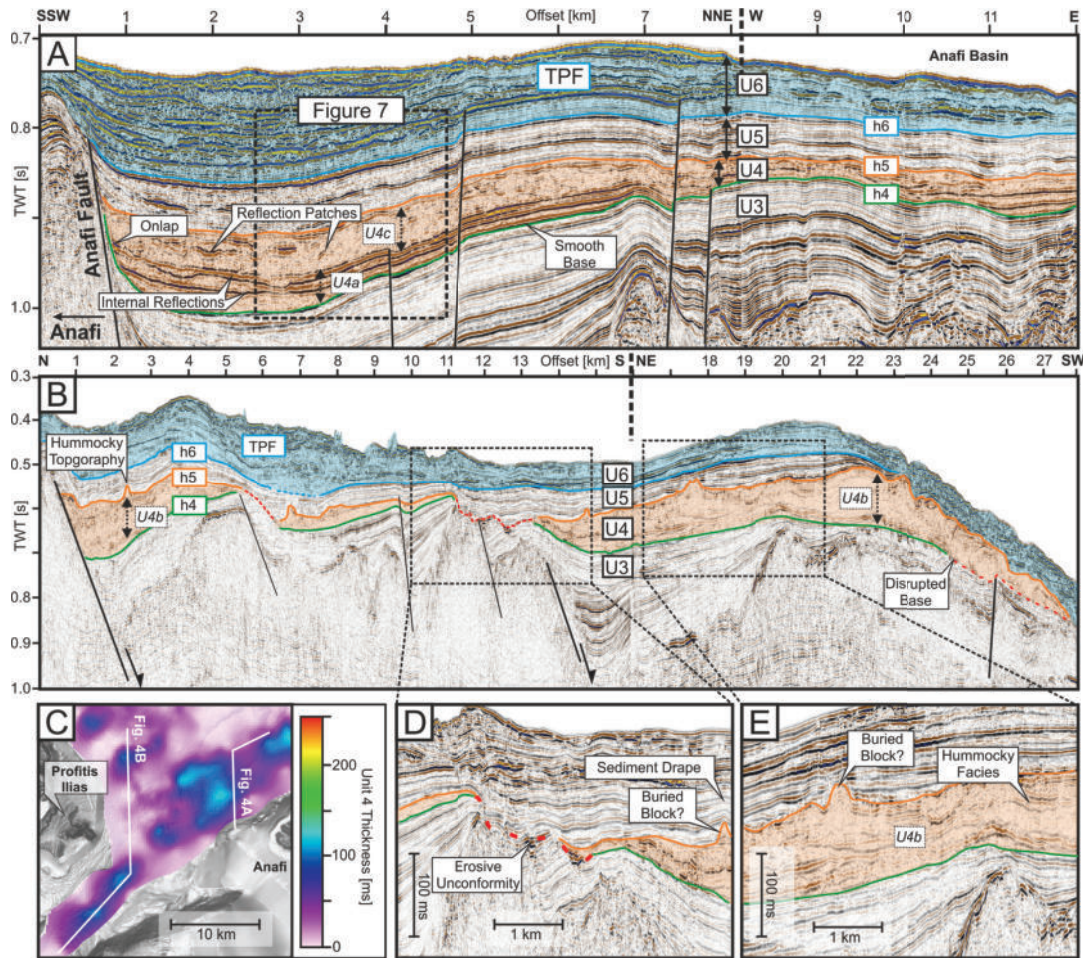
FIGURE 5.4: A) High-resolution seismic profile crossing the western Santorini-Anafi Basin. Horizon and unit labels as in Figure 5.3. TPF = Thera Pyroclastic Formation. B) High-resolution seismic profile crossing the southeastern slope of Santorini. C) Map showing the thickness of the chaotic deposit (Unit 4) and the location of the profiles. D, E) Enlargements from the seismic profile shown in B.

The Santorini-Anafi Basin extends from the southeastern flank of Santorini towards the northeast (Fig. 5.1B). Figure 5.4A shows a seismic profile that crosses the basin oblique to its rift axis. The upper part of Unit 4 is characterized by transparent seismic facies with some high-amplitude reflection patches (U4c, Fig. 5.2), while the lower part manifests itself as a sequence of high-amplitude reflections that lap onto the Anafi Fault (U4a, Fig. 5.2). The chaotic upper part thickens towards the Anafi Fault reaching a maximum thickness of ∼100 ms TWT and comprises a sequence of high-amplitude reflection patches. Unit 4 is interbedded between the generally well-stratified reflections of Units 3 and 5, which become less laterally coherent towards the Anafi Fault, where they eventually lose most of their coherency. On the eastern to the southeastern flank of Santorini, Unit 4 is not continuous but forms three separate depo-centers each separated from each other by prominent normal faults (Fig. 5.4B). Here, Unit 4 comprises transparent seismic facies interrupted by some high-amplitude, partially layered reflections (U4b, Fig. 5.2). Between the three

depo-centers, Unit 5 lies directly on top of Unit 3 with an erosive unconformity separating both units (Fig. 5.4D). Several internal reflections within the northernmost depo-center are visible but show an irregular topography, and several irregular positive structures are located at the top of the deposit (U4b, Fig. 5.2). The southernmost depo-center is fairly thick (up to 150 ms TWT in places) and is also characterized by a distinct hummocky topography, which is draped by the overlying reflections of Unit 5 (Fig. 5.4D). This irregular blocky topography (Fig. 5.4E) of the deposit contrasts with the rather smooth appearance observed at the western Santorini-Anafi Basin (Fig. 5.4A).

5.4.3   Western Anhydros Basin
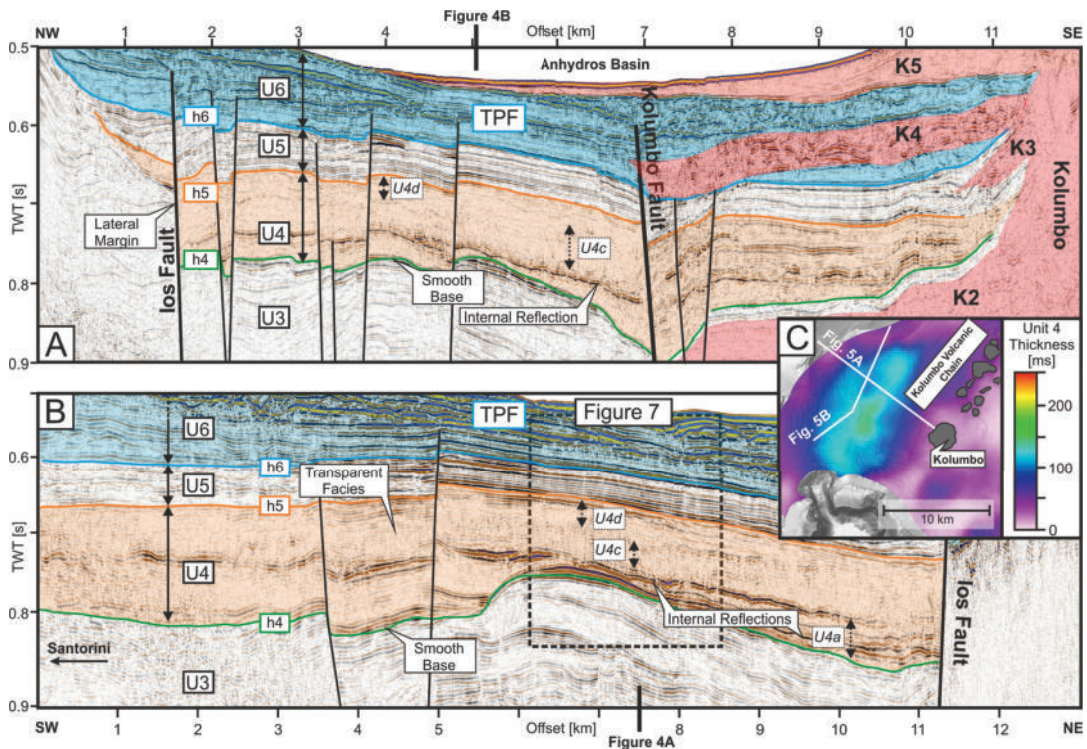
FIGURE 5.5: A) High-resolution seismic profile crossing the Anhydros Basin in NW-SE direction towards the Kolumbo Edifice. K1-K5 represent different episodes of cone growth following Hübscher et al. (2015) and Preine et al. (2022a). Horizon and unit labels as in Figure 5.3. TPF = Thera Pyroclastic Formation. B) High-resolution seismic profile crossing the Anhydros Basin in SW-NE direction. C) Map showing the thickness of Unit 4 and the locations of the profiles.

The Anhydros Basin northeast of Santorini hosts the Kolumbo Volcano and the Kolumbo Volcanic Chain (Fig. 5.1B). As in the previously described basins, we identify a thick, chaotic Unit 4, which is interbedded between Units 3 and 5. Figure 5.5A shows a seismic profile perpendicular to the basin axis terminating on the northwestern flank of the Kolumbo Volcano, while the profile in Figure 5.4B crosses the Anhydros Basin in an SW-NE direction. Both profiles show the previously described Unit 4 and numerous faults including the Ios Fault and Kolumbo Fault. While the Ios Fault is a steep marginal fault, the Kolumbo Fault shows a more complex deformation pattern with at least two auxiliary faults. Unit 4 has a generally chaotic and

weakly reflective appearance, with a pronounced internal reflection and a smooth base (Fig. 5.5A, B). In the upper part of the deposits, we identify a sequence of low-amplitude, stratified reflections (U4d, Fig. 5.2, 5.5A, 5.5B). Unit 4 terminates on the slope of Kolumbo above the early eruptive Kolumbo-Unit K2 (Hübscher et al., 2015; Preine et al., 2022a), where we observe chaotic internal reflections (Fig. 5.5A). Towards the north, the deposit terminates against the Ios Fault, with just a thin sequence extending approximately 1 km further towards the northwest (Fig. 5.5A). Towards the northeast, we identify a stack of internal reflections near the base of Unit 4, which lap onto the Ios Fault (Fig. 5.5B).

5.4.4 Eastern Santorini-Anafi and Anhydros Basins
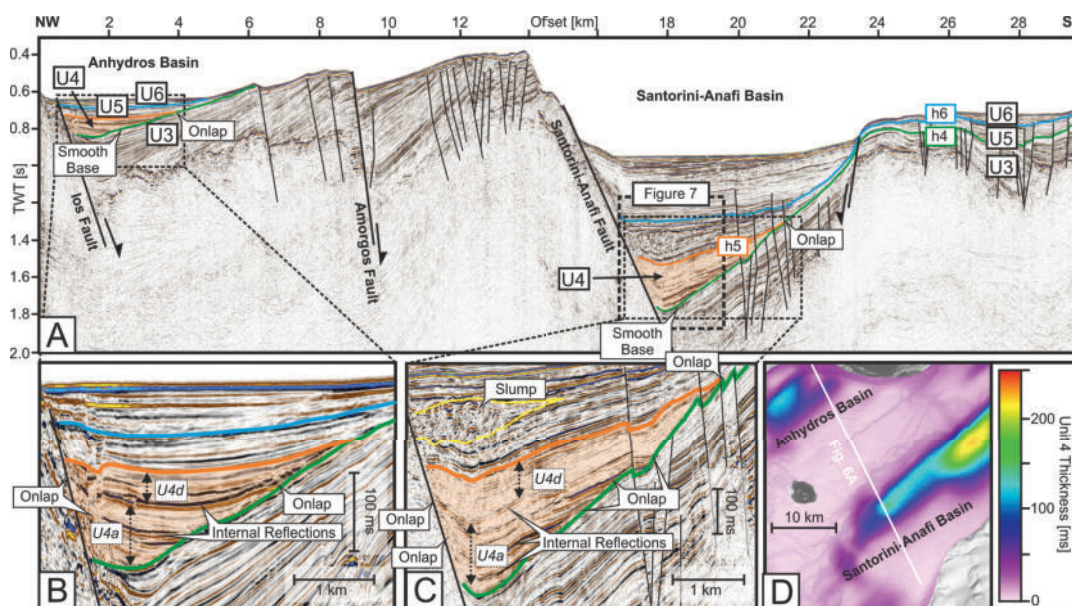
FIGURE 5.6: A) Seismic profile crossing the Anhydros and Santorini-Anafi Basins. Horizon and Unit labels as in Figure 5.3. B, C) Enlargements highlight the internal architecture of Unit 4, which is onlapping the main faults towards the northwest and reflection h4 towards the southeast. D) TWT thickness map of Unit 4 with the location of the seismic profile.

Figure 5.6A shows a seismic profile crossing the eastern Santorini-Anafi and Anhydros Basins. These basins are large graben and half-graben structures with active marginal faults, which have been interpreted by different workers (e.g. Hübscher et al., 2015; Nomikou et al., 2016b; Nomikou et al., 2018b). Our stratigraphic classification can be correlated with that of Nomikou et al. (2018b): Units Sab6/Ab6 and Sab5/Ab5 belong to our Unit 6, while units Sab4/Ab4 correspond to our Unit 5. Unit 4 is part of units Ab4 and Sab4. In the framework of Hübscher et al. (2015), unconformity ab-10 corresponds to horizon h6, and ab-7 corresponds to h4.

Figures 5.6B and C show that Unit 4 thickens significantly toward the marginal faults (the Ios Fault and the Anhydros Fault) while pinching out away from them. In both basins, the upper part of Unit 4 comprises a sequence of low-amplitude, stratified reflections (U4d; Fig. 5.2), while the lower part contains a sequence of internal reflections (U4a; Fig. 5.2, 5.6B, 5.6C). The internal reflections in both basins onlap the basal reflection surface h4. In both basins, Unit 4 is the unit with the most significant

thickness increase towards the marginal faults (Fig. 5.6D). Within Unit 5 we identify a chaotic deposit (marked 'slump') in the hanging wall of the Santorini-Anafi Fault (highlighted by the yellow polyline in Fig. 5.6C).

5.4.5   Distribution and Volume of Unit 4

A comparison of the seismic stratigraphy in all analyzed basins allows correlating Units 3 to 5 based on their internal seismic characteristics (Fig. 5.7). This stratigraphic fit underlines that Unit 4 occurs in all basins at the same stratigraphic position between Unit 5 and Unit 3. The seismic appearance and internal architecture of Unit 4 are broadly similar in all basins, with chaotic and transparent seismic facies (Fig. 5.2) making up most of the deposit and a package of stacked, high-amplitude coherent reflections existing near the base (Fig. 5.7. The upper part of Unit 4 in the East Santorini-Anafi Basin is less chaotic than it is in the other basins.
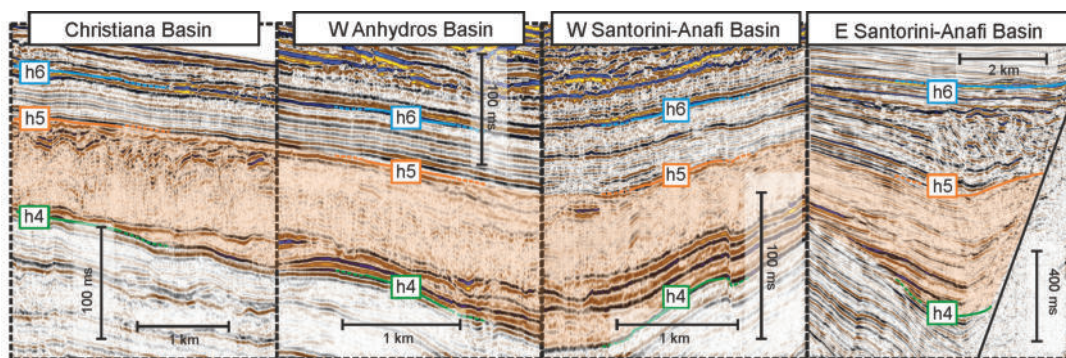
FIGURE 5.7: Enlargements of Unit 4 from each basin illustrating the stratigraphic correlation. The enlargement from the eastern Santorini-Anafi Basin is flipped compared to Fig. 5.6. Horizon and unit labels as in Figures 3-6. For locations, see the boxes in Figures 3-6.

Having identified Unit 4 in all three basins adjacent to Santorini, we mapped its top and base throughout the entire working area and calculated its thickness in TWT. The base of the deposit outlines the general shape of the complex horst and graben structures of the SATZ (Fig. 5.8A). In front of the hanging wall of the Santorini-Anafi Fault in the eastern Santorini-Anafi Basin, the base of Unit 4 forms a deep depression, while it becomes very shallow towards the slope of Santorini, where the Anhydros Horst forms a distinctive topographic high, extending towards Santorini. With our new seismic data, we are able to define three previously unrecognized faults complementing the fault network from Nomikou et al., 2016, 2018b, 2019) (black lines in Fig. 5.8). These additional faults trend SW-NE and extend the fault system from the SATZ towards Santorini. In addition, the Christiana Fault on the northeastern flank of Christiana extends further northeast towards Santorini, suggesting an extension of the SATZ fault system even beneath Santorini.
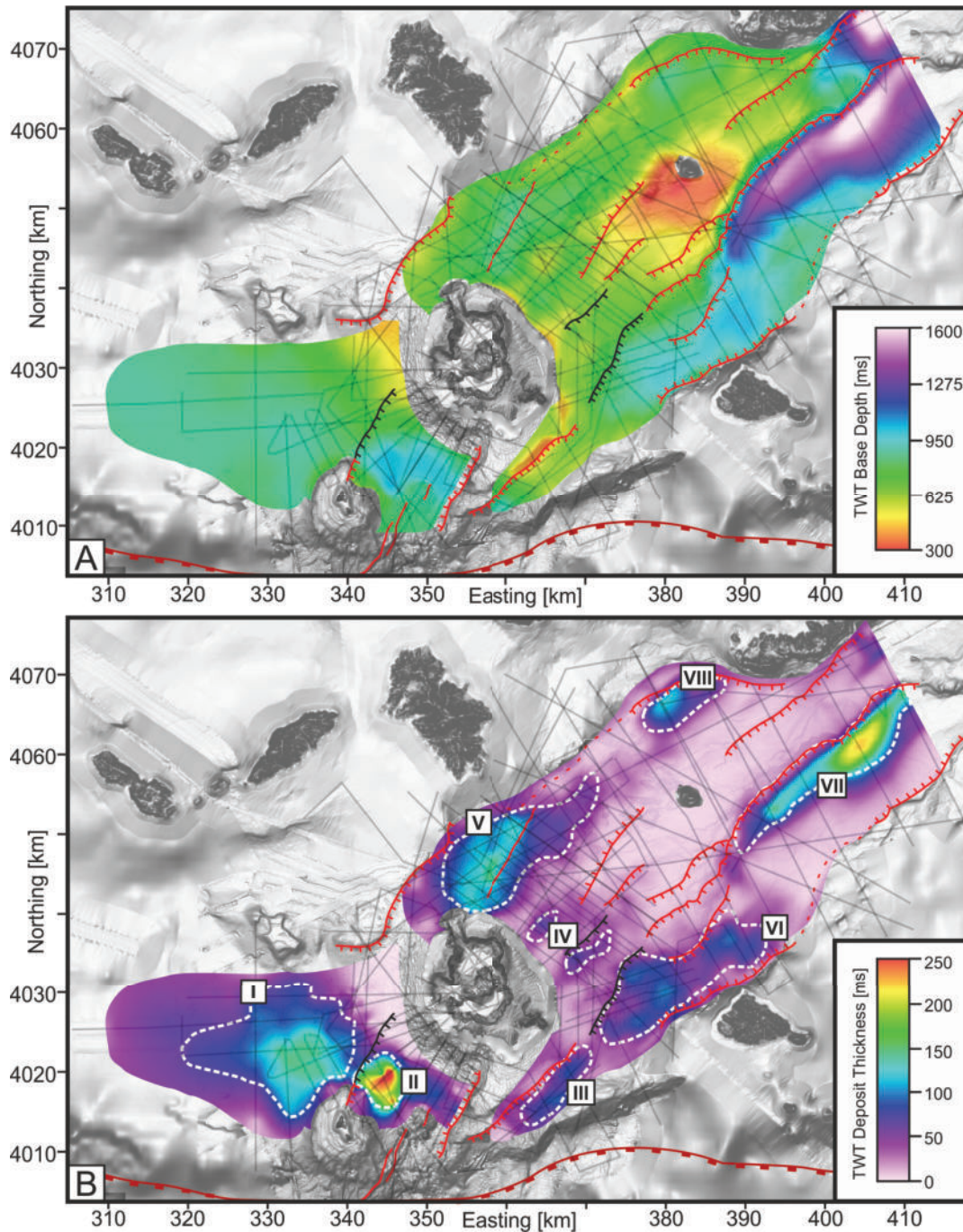
FIGURE 5.8: A) TWT depth map of the base of Unit 4. B) TWT thick-
ness map of Unit 4. Both maps are based on the interpolated seismic
profiles shown in light grey. Red lines indicate faults from Nomikou
et al. (2018b) and Nomikou et al. (2019); black lines indicate faults
from this study. Dashed lines in B indicate individual depo-centers,
labeled I-VIII.

Unit 4 is present in all basins surrounding Santorini and extends far along the rift
basins in the northeast and along the Christiana Basin in the west (Fig. 5.8B). It has
mainly been deposited below the slope break of Santorini and filled up depressions
formed by the adjacent rift basins (Fig. 5.8A and 5.8B). We identify eight specific
depo-centers labeled I-VIII in Figure 5.8B and their locations, extents, volumes, and

relations to faults are summarized in Table 5.1. The entire deposit, including all depo-centers, covers an area of $\sim$1000 km^2 and has a bulk volume of 118 $\pm$ 6.5 km^3.

TABLE 5.1: Summary of characteristics of specific depo-centers of Unit 4. Volumes estimated by interpolating between seismic lines, subtracting the TWT-depth of the top reflection of Unit 4 (h5) from that of the base reflection (h4) and depth-conversion using an interval velocity of 1900 m/s with an uncertainty of $\pm$ 100 m/s. For location of the depo-centers, see Figure 5.8B.

Depo-center	Location	Aprox. Extent [km^2]	Estimated Volume [km^3]	Figures with Crossing Seismic Line	Related Fault
I	Christiana Basin; Northwest of Christiana	360	37 $\pm$ 2	Fig. 5.3A, 5.3B, 5.3E, 5.7, 5.9A	Christiana Fault
II	Christiana Basin; Between Santorini and Christiana	40	9.4 $\pm$ 0.5	Fig. 5.3B, 5.3C, 5.3F	Christiana Fault
III	South of Santorini	30	1.7 $\pm$ 0.1	Fig. 5.4B, 5.4D, 5.4E	Southern Santorini Fault
IV	East of Santorini; Between Santorini and the Anhydros Horst	27	2 +-0.2	Fig. 5.4B	Faults East of Santorini
V	Western Anhydros Basin	200	16.5 $\pm$ 1	Fig. 5.5A, 5.5B, 5.7	Kolumbo and Ios Faults
VI	Western Santorini-Anafi Basin	144	8 $\pm$ 0.5	Fig. 5.4A, 5.7, 5.9, 5.10C	Anafi Fault
VII	Eastern Santorini-Anafi Basin	154	17 $\pm$ 1	Fig. 5.6A, 5.6C, 5.7, 5.10B	Anhydros Fault
VIII	Eastern Anhydros Basin	43	3.5 $\pm$ 0.2	Fig. 5.6A, 5.6B, 5.10A	Ios Fault

5.5 Discussion

5.5.1 Nature of Unit 4

The stratigraphically complex internal architecture of Unit 4 contrasts strongly with that of the well-stratified Units 3 and 5 (Fig. 5.2), which we interpret as the deposits of predominantly hemipelagic sedimentation (Preine et al., 2022a). Generally, the complex chaotic facies and loss of internal stratification within Unit 4 could result from in-situ deformation, e.g., by fluidization without horizontal displacement (e.g. Ogata et al., 2014), or different mechanics of sediment failure and transport. However, the fact that wherever Unit 4 is not present, Unit 5 lies directly on top of Unit 3 without any seismically resolvable intervening sedimentary sequences, indicates deposition within a relatively short time frame and argues against in-situ deformation or fluidization. Therefore, the most likely processes to explain the chaotic nature of Unit 4 are mass failures or large pyroclastic flows (Crutchley et al., 2013; Karstens et al., 2013).

Tsampouraki-Kraounaki and Sakellariou (2018) proposed a pyroclastic origin for Unit 4 in the Christiana Basin since it thickens towards Santorini and there is no distinct scar on the western side of Santorini. The chaotic architecture of Unit 4 shows similarities to the Thera Pyroclastic Formation in some areas (e.g., Fig. 5.4A, 5.5A), which would agree with such an interpretation. However, there is no evidence for any major eruption at that time from nearby onshore outcrops on the Cycladic Islands (e.g. Anafi, Ios, Amorgos, or the basement massif on Santorini), which would be expected due to the abundance and significant volume of Unit 4. Moreover, the internal architecture of Unit 4 shows a strong resemblance to the seismic images of volcanic sector collapse deposits off Montserrat (Lebas et al., 2011; Watt et al., 2012), Ritter Island (Karstens et al., 2019; Watt et al., 2019) and Sakar (Kühn et al., 2021), as well as other non-volcanic mass transport deposits (e.g. Bull et al., 2009; Bull et al., 2020; Posamentier et al., 2011). We identify several instances with features typical

for large mass failures, e.g. the distinct lateral margins in the Christiana Basin (Fig. 5.3C) and Anhydros Basin (Fig. 5.6A), basal erosion and deformation in front of the Christiana edifice (Fig. 5.3B, F) and southeast of Santorini (Fig. 5.4B, C). In general, we observe that the internal reflections within Unit 4 are deformed and complex close to Santorini (Fig. 5.3B, 5.3C, 5.3F, 5.4B, 5.4D, 5.4E), while becoming less chaotic and smoother away from Santorini (Fig. 5.3A, 5.4A, 5.6A-C). This is a pattern that is typical for MTDs and reflects the transition from initial slumps of granular material into more disintegrated, water-saturated, cohesive debris flows and turbidity currents (e.g. Bull et al., 2009; Watt et al., 2019; Watt et al., 2012; Watt et al., 2021; Smit and Stemmerik, 2022).

5.5.2 Emplacement Dynamics

High Energy Emplacement

In the following, we examine different parts of Unit 4 to find indicators for an erosive, high-energy emplacement to determine potential sources of Unit 4. In the Christiana Basin, our seismic data reveal highly deformed, folded reflections (U4b, Fig. 5.2) between Christiana and Santorini (Fig. 5.3A-C) and we observe that parts of Unit 4 are buttressed against an up-bending structure (Fig. 5.3C), which indicates that Unit 4 is frontally confined in this area (Frey-Martínez et al., 2006). The truncation of underlying reflections (e.g. 'Disrupted Base' in Fig. 5.3B, C, F), as well as the internal folding within depo-center II (Fig. 5.8B), imply an erosive emplacement here, whereby the overlying mass transport material scoured into the underlying substrate during transport (Fig. 5.3B, C). The incised morphology of the Christiana Edifice with a horseshoe-shaped scar is a strong indication for a sector collapse towards the northeast (Fig. 5.2G). As visible in Figure 5.3B, the deeper and flatter part of the Christiana scar is directly overlain by Unit 5 and 6, indicating that the formation of the scar corresponds temporally to the emplacement of Unit 4. Consequently, we interpret the folded internal reflections northeast of the Christiana edifice (U4b, Fig. 5.8B) as the slump deposit from that sector collapse event (Fig. 5.3B). Such a NE-directed collapse event would explain the abrupt termination of Unit 4 towards the southeast in Figure 5.3C as being the lateral margin of the collapse deposit. This interpretation is also supported by a comparison of the calculated volume of the deformed strata in front of the Christiana scarp ($\sim$4.9 km^3, Fig. 5.3B, C, F) and the missing volume of the northeast flank of Christiana, which we approximate to be roughly 4.5-5 km^3 from interpolating the missing volume from the bathymetric and seismic data.

We also identify indications for high-energy, erosive emplacement of Unit 4 at the southeastern slope of Santorini (Fig. 5.4B, depo-centers III and IV in Fig. 5.8B). Here, Unit 4 is made up mostly of subunit U4b (Fig. 5.2), with a characteristic blocky topography (Fig. 5.4B). Such blocky deposits are commonly considered to be translated blocks (Bull et al., 2009), which have been widely identified around volcanic islands where they are the result of high-energy slumping and are generally restricted to proximal areas of a mass failure event tending to stop at the slope break (Watt et al., 2012; Watt et al., 2019; Watt et al., 2021; Le Friant et al., 2004; Le Friant et al., 2019). Therefore, we interpret this depo-center as the result of slumping from the southeastern flank of proto-Santorini, which might be associated with activity of the Southern Santorini Fault (Fig. 5.8B). The nearby coast of present-day Santorini is characterized by the outcrop of the pre-volcanic metamorphic basement, which forms the highest elevation of Santorini at Profitis Ilias (Fig. 5.4C). Bell et al. (2013)

noted a distinct horseshoe-shaped structure on the north-eastern side of Profitis Ilias and several large blocks with crustal lithologies located close to the southeastern coast of Santorini. These blocks have been suspected to be the result of large landslide events, which seems to be an old event that is not related to the surficial landslide deposit observed on the seafloor southeast of Santorini (Bell et al., 2013). Whether a large landslide event from this area has contributed to the emplacement of Unit 4, cannot be determined from the seismic data. It is, however, noteworthy that we only observe the distinct blocky nature of Unit 4 on the southeastern flank of Santorini and nowhere else around Santorini.

Low Energy Emplacement
The most voluminous parts of Unit 4 are constituted by depo-centers I, V, VI, VII, and VIII, which lie further away from Santorini than depo-centers II-IV (Fig. 5.8B) and comprise the largely transparent subunit U4c (Fig. 5.2), the weakly reflective subunit U4d (Fig. 5.2), the subparallel internal reflections of U4a (Fig. 5.2) as well as a smooth and laterally continuous base reflection. In contrast to the weak, disrupted and erosional base of Unit 4 observed closer to Santorini (Fig. 5.3B, 5.3C, 5.3F, 4B), the smooth and continuous base implies a lack of basal erosion associated with lower energy emplacement (Watt et al., 2012). The architecture of Unit 4 in these more distal, smoother-shaped deposits fits the definition of frontally emergent MTDs (Frey-Martínez et al., 2006). Such frontally emergent MTDs translate downslope by overthrusting the undisturbed strata and might travel freely over the undeformed slope, evolving into debris and turbidity flows (Frey-Martínez et al., 2006). This mechanism would be in agreement with the internal architecture of Unit 4 in the Christiana Basin (as observed in Fig. 5.3A), but also with the internal architecture of Unit 4 in the Anhydros and Anafi Basins (Fig. 5.4A, 5.5A, 5.5B, 5.6A), suggesting that the transparent, chaotic subunit U4c represents debris flow deposits and the weakly reflective, subparallel subunit U4d represents the turbiditic apron of the deposit (Fig. 5.2).
Further, we interpret the internal reflections at the base of Unit 4 (U4a) as several smaller stacked MTDs that have been deposited before the upper and most voluminous part of Unit 4. These internal reflections occur mostly in areas where the underlying Unit 3 formed depressions (Fig. 5.8A). Towards the margins of Unit 4, e.g., on the flank of Santorini (Fig. 5.3A), the internal reflections disappear and onlap the underlying horizon h4 (Fig. 5.9). As illustrated in Figure 5.9, we find instances where there are several larger transparent subunits (up to 40 ms TWT thick) in between these internal reflections indicating that these precursory events had considerable volumes. The uppermost internal reflection is phase reversed in some instances (PR in Fig. 5.9, which implies the transition from high acoustic impedance to low acoustic impedance. As shown in Sawyer et al. (2009), densification in MTDs plays a major role for the seismic appearance of basal reflections. Typically, densification is greatest near the base and declines upwards (Sawyer et al., 2009). This would imply that the phase-reversed reflection in Unit 4 could be explained by the transition from a more compacted lower part of the upper MTD towards a less compacted upper part of the underlying MTD.
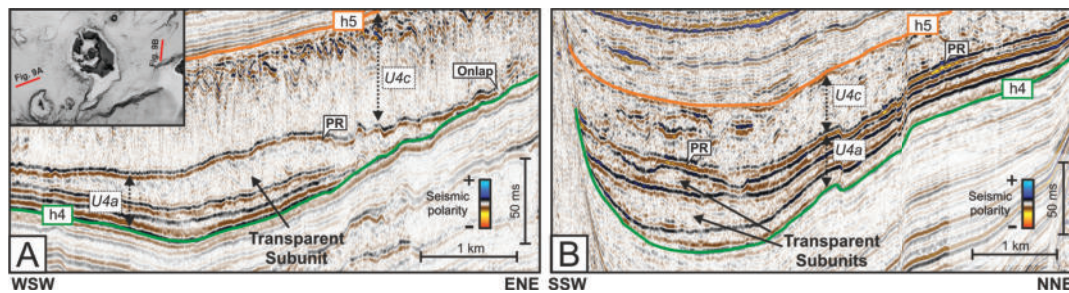
FIGURE 5.9: Enlarged view of internal reflections within Unit 4 (between horizons h5 and h4) in the Christiana (A) and western Santorini-Anafi Basin (B). PR: Phase Reversal. Subunits (U4a, U4c) as introduced in Figure 5.2.

Apart from the horseshoe-shaped scars at Christiana (Fig. 5.3G) and at Profitis Il-ias onshore Santorini (Fig. 5.4C), we did not find other collapse scars sufficiently large to be correlated to the MTDs of the smoother-shaped depo-centers, leaving the sources of these large depo-centers elusive. However, since we find these deposits predominantly in the depressions of the basins surrounding Santorini (Fig. 5.8A), with no evidence of basal erosion, a transport emanating from Santorini seems most reasonable. It is also important to recall that the emplacement of Unit 4 was fol-lowed by 0.7 Myrs of intensive volcanic activity of the CSKVF including at least four caldera collapse events (Druitt et al., 1999; Preine et al., 2022a), which might have obscured even large collapse scars.

An explanation for these voluminous deposits could be widespread secondary sed-iment failure and entrapment, as observed around many other volcanic islands (e.g. Watt et al., 2012; Watt et al., 2021; Le Friant et al., 2019). Failed seafloor sediments contribute up to two-thirds to the entire slide volume of volcanic debris-avalanche deposits offshore Montserrat (Watt et al., 2012). Indications for erosion related to such secondary sediment failures are visible at the steep slope of Santorini, where we find evidence for substantial erosion on the southeastern slope between the blocky depo-centers of Unit 4 (2 km along profile; Fig. 5.4B). Overall, our data show only a thin and rather chaotic sedimentary cover on the slopes of Santorini, which be-longs to the uppermost more recently deposited Units 5 and 6. As early volcan-ism around Santorini was initiated before the emplacement of Unit 4 (Preine et al., 2022a), the flanks of proto-Santorini likely consisted of poorly consolidated sedi-ments with weak volcanic material. Therefore, widespread sediment failures from the slopes of proto-Santorini could have been the source for the lower-energy and voluminous deposits observed in all basins explaining why there are no distinct scars related to Unit 4. The lower-energy deposits make up by far the largest vol-ume of Unit 4. Assuming collapse volumes ~4.9 km^3 for Christiana and ~2.5 km^3 for the southeastern flank of Santorini implies that more than 90 % of the total vol-ume of Unit 4 may be the result of secondary seafloor failures.
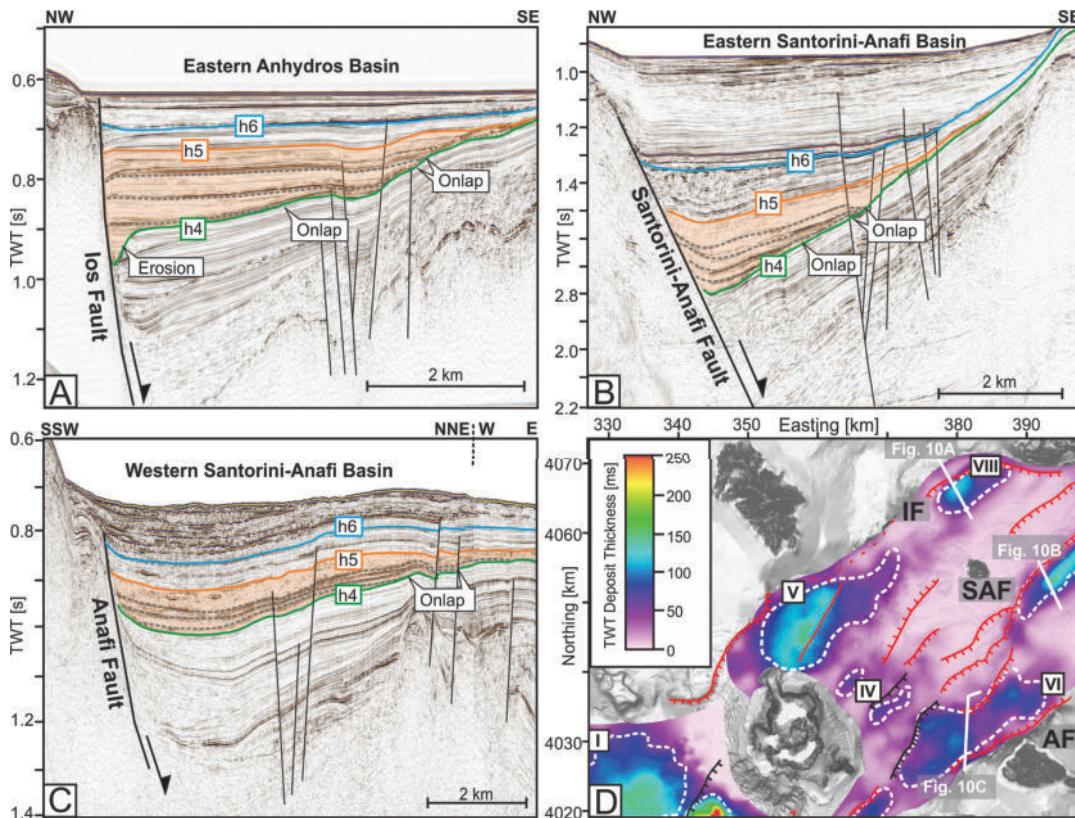
FIGURE 5.10: Enlarged view of Unit 4 (colored semi-transparent orange) in front of the Ios Fault in the Anhydros Basin (A), in front of the Anhydros Fault in the Eastern Santorini-Anafi Basin (B), and in front of the Santorini-Anafi Fault in the Western Santorini-Anafi Basin (C). Horizon and Unit labels as in Figure 5.3. (D) Thickness map as in Figure 5.8B with locations of profiles 10A-C. IF: Ios Fault; AF: Anhydros Fault; SAF: Santorini-Anafi Fault.

5.5.3 Trigger Mechanism

Volcanic sector collapses have been identified in all volcanic settings and their trigger mechanisms range from volcanic intrusions and eruptions, gravitational instabilities, extreme precipitation events, sea-level changes, to earthquakes (Watt et al., 2021). Identifying a specific trigger mechanism is often ambiguous for contemporary sector collapses and becomes even more difficult for an event ~0.7 Myrs ago (Preine et al., 2022a). The timing of the emplacement of Unit 4 marks the transition from a phase of relative volcanic dormancy to a phase of basin-wide emergence of volcanoes in the CSKVF and thus large-scale volcano-tectonic processes represent the most likely trigger mechanisms for the observed large-scale mass-transport events. The tectonic evolution of the CSKVF can be subdivided into four phases that culminated in the evolution of the grabens and half-grabens northeast of Santorini, which formed the previously described basins (Heath et al., 2019; Preine et al., 2022a). Opening of these basins occurred in multiple episodes of enhanced rift activity, so-called 'tectonic pulses', which describe distinct episodes of hanging-wall rotation from the marginal faults in such a short time that no seismically resolvable syn-tectonic deposition occurred (Hübscher et al., 2015). The latest of these episodes

can be linked to horizon h4 and thus to the emplacement of Unit 4. The structural relationship between reflection h4 and the marginal faults in the Anhydros and Santorini-Anafi Basins is characterized by a pronounced dip of the basal reflection h4 toward the marginal faults, which is the result of hanging wall rotation of the Ios, Anhydros, and Santorini-Anafi Faults (Fig. 5.9). In the Anhydros Basin and the western Santorini-Anafi Basin, the internal reflections of Unit 4 have a very different dip compared to the base reflection h4, to which these internal reflections lap onto (Fig. 5.9). This indicates that hanging wall rotation must have occurred before the deposition of Unit 4 and that this Unit filled up a pre-existing accommodation space. These observations combined are indicators that the deposition of Unit 4 was preceded by a rift-pulse in all basins northeast of Santorini, which is in agreement with the temporal framework of rift activity by Hübscher et al. (2015). However, our dataset reveals that tectonic activity during that episode also affected the Christiana Basin and that the southwest-northeast directed fault trend of the rift basins continues underneath present-day Santorini and extends towards Christiana (Fig. 5.8), which is in agreement with seismic tomography results (Heath et al., 2019). The Christiana Fault is directly connected to the scarp of the Christiana edifice, which implies a tectonic control of the sector collapse (Figs. 5.3G).

There are no volcanic deposits correlating to that specific period, while we find a strong indication for enhanced tectonic activity in the entire rift system. Even in phases of regular tectonic activity (as today), the rift is capable of producing energetic earthquakes like the 1956 magnitude 7.4 Amorgos earthquake (Brüstle et al., 2014; Nomikou et al., 2018b) and strong earthquakes have been associated with slumping at Santorini before (Bell et al., 2013). Therefore, a strong rift pulse appears to be the most plausible trigger mechanism and can explain the observed widespread and multi-source mass failures. Whether erosion of the main faults contributed to the smoother deposits farther from Santorini cannot be accurately determined from our data, but the uniform distribution along all depressions of the rift basins, lack of basal erosion, and the lack of major slump deposits rather suggests a dominant transport from the slopes of proto-Santorini towards the basins.

5.5.4 Geohazard Cascade

The complexity of seismic facies observed within Unit 4 indicates that its emplacement occurred as a complex cascade of different processes. To explain its emplacement, we propose a cascade of five processes: rifting, precursory mass-movements, sector collapses, secondary sediment failures, and debris flow deposition, as illustrated in Figure 5.11A-E. In the following, we will refer to Unit 4 as the Santorini Mass-Transport Deposit (SMTD).

As discussed in the previous section, there is evidence that a rift pulse preceded and might have triggered the emplacement of the SMTD. Prior to the main volcanic sector collapse events at Christiana and the southeastern flank of Santorini, we argue that this rift pulse triggered several smaller mass movements, which thus explain the basal subunit within Unit 4 (U4a; Fig. 5.2, 9, 11C). This order of events is particularly evident at the western flank of Christiana (offset km 1-7 in Fig. 5.3B), where basal erosion of the SMTD is accompanied by the sudden disappearance of the internal reflections, which indicates that the major collapse of the Christiana Edifice occurred after the deposition of the material associated with the internal reflections (Fig. 5.9).
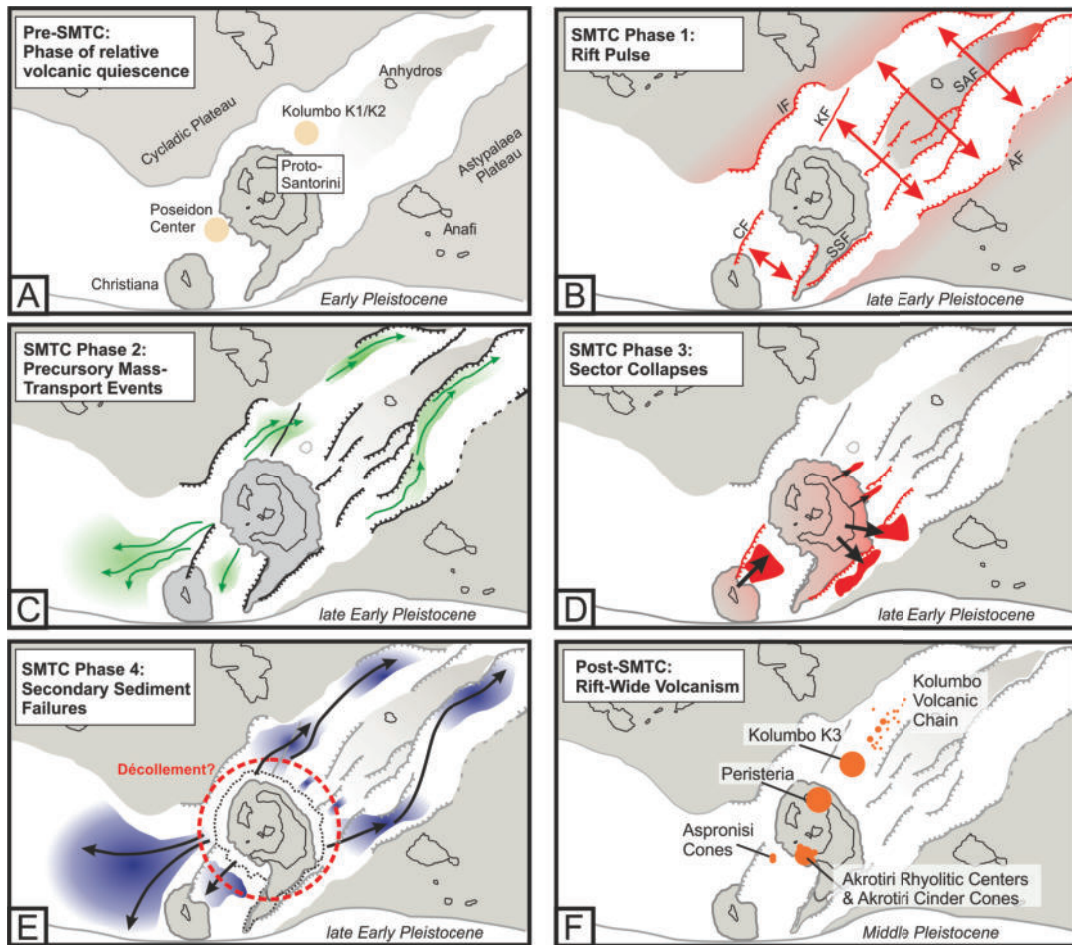
FIGURE 5.11: Schematic Reconstruction of the Santorini Mass Transport Cascade (SMTC) forming the Santorini Mass-Transport Deposit (SMTD). Topographic highs are indicated by the grey areas. Present-day coastlines for approximate reference. Light red color schematically highlights areas with increased tectonic activity or instability. Approximate ages from Preine et al. (2022a). (A) Location of volcanic centers prior to the emplacement of the SMTD. (B) Rift pulse affecting the entire Christiana-Santorini-Kolumbo Field. CF: Christiana Fault; SSF: Southern Santorini Fault; SAF: Santorini-Anafi Fault; KF: Kolumbo Fault; IF: Ios Fault; AF: Anhydros Fault. (C) Precursory Mass-Transport Events (green) occur due to tectonic activity. (D) Catastrophic sector collapses (red) occur at Christiana and the southeastern flank of Santorini. (E) Due to the sudden seafloor loading caused by the sector collapses, a décollement propagates along the flank of Santorini triggering large-scale secondary sediment failures (blue). (F) Emerging volcanic centers (orange, (Preine et al., 2022a)) after the emplacement of the SMTD.

Following the model of Watt et al. (2019) and Watt et al. (2012) and Le Friant et al. (2019), we propose that the sudden loading by the collapse masses (Fig. 5.11C) might have led to the propagation of a décollement, which then triggered large-scale secondary sediment failures from the slopes of proto-Santorini (Fig. 5.11E). We speculate that these failures translated to frontally emergent debris flows, which traveled far throughout the basins filling up the depressions created by the preceding rift pulse. In the last phase of this cascade, turbidites were deposited above the

chaotic unit, both near Santorini (Fig. 5.3B, 5.3C, 5.5A, 5.5B) and further away in the basins (Fig. 5.3A) explaining the low-amplitude, subparallel subunit U4b (Fig. 5.2) observed at the top of Unit 4 in many instances. Each of these phases may or may not have been accompanied by volcanic eruptions from proto-Santorini; the actual role of any eruptions cannot be clarified without scientific drilling.

For the same reason, it is difficult to estimate the duration in which the SMTD has been emplaced. However, since we neither found seismically resolvable layers between Units 3 and 5 at locations where Unit 4 is absent nor syn-tectonic reflections within Unit 4 in the rift basins, the duration of the entire cascade from the rift pulse to the proposed secondary sediment failures can be approximated by the vertical seismic resolution. Assuming a vertical seismic resolution of approx. 4-8 m within Unit 4 (assuming an interval velocity of 1900 m/s) and an average sedimentation rate of 10 cm/kyr (Piper and Perissoratis, 2003; Preine et al., 2022a; Anastasakis and Piper, 2005), the SMTD could have been emplaced over a time period of approx. 40-80 kyrs. However, there are reasons to assume that the timespan of the SMTD emplacement was shorter. We have shown that the rift pulse preceded the deposition of the initial mass-wasting event and most of the hanging-wall rotation occurred before the emplacement of the initial MTDs (Fig. 5.10). It seems reasonable to us that the gap between such a significant tectonic event and the emplacement of large mass wasting deposits was smaller than several tens of thousands of years. Moreover, the propagation of a décollement likely occurred rapidly implying a very short time interval between the sector collapses at Christiana and Santorini and the voluminous secondary sediment failures. However, to exactly determine the timing of the SMTD cascade, scientific drilling is needed.

5.5.5 Impact on the Volcanic Evolution of the CSKVF

Previous studies have shown that landslides may be capable of inducing decompression of subsurface magma storage systems and thus alter eruptive behaviors (Manconi et al., 2009; Pinel and Albino, 2013; Hunt et al., 2018). In the context of the evolution of the CSKVF, it is striking that the emplacement of the SMTD occurred at the transition between two distinctly different volcanic phases (Preine et al., 2022a). While the volcanic phase prior to the emplacement of the SMTD was characterized by two SW-NE aligned volcanic centers with comparably low activity (Poseidon and Early Kolumbo, K1/K2; Fig. 5.11A), the eruptive behavior of the CSKVF changed significantly after the SMTD emplacement with the initiation of basin-wide volcanism (Fig. 5.11F) (Preine et al., 2022a). This subsequent phase saw the construction of the Aspronisi cones SW of Santorini, the eruptions of the Akrotiri rhyolitic centers, the Peristeria stratovolcano, and the monogenetic cinder cones of Aktoriri onshore Santorini, a smaller eruptive sequence at Kolumbo as well as the evolution of the Kolumbo Volcanic Chain (Druitt et al., 1999; Preine et al., 2022a) (Fig. 5.11F). The specific influence of the emplacement of the SMTD sequence on this change in the eruptive behavior cannot be clarified based on the seismic data, since the preceding rift pulse probably also played an important role. However, the relative temporal coincidence of the rift pulse, mass wasting, and the change in eruptive behavior underlines how closely volcanism and crustal tectonics are interconnected at the CSKVF.

5.5.6   Implications for Geohazard Assesment

With a total volume of $118 \pm 6.5 \, \text{km}^3$, the SMTD represents the largest known MTD in the Aegean Sea and the largest known volcanic mass-transport deposit in the entire Mediterranean Sea (Urgeles and Camerlenghi, 2013). It is, for example, five times larger than the largest submarine landslide detected offshore Mt Etna (Pareschi et al., 2006). Also in the context of non-volcanic submarine landslides in the Mediterranean, the volume of the SMTD represents a very large event (Urgeles and Camerlenghi, 2013). However, given the uncertainties in the timing of the proposed cascade, it is difficult to properly access the geohazards associated with the emplacement of the SMTD. For example, it has been shown that even time gaps of a few minutes between separate stages of failure can greatly reduce tsunami magnitudes (Løvholt et al., 2008).

Disaster cascades are worldwide phenomena at volcanic islands and have only recently gained wider attention (Hutchison et al., 2016; López-Saavedra et al., 2021; Walter et al., 2019; Patrick et al., 2020). Prominent examples have been reported from the Canaries, where multistage retrogressive landslides were the trigger for caldera-forming eruptions (Hunt et al., 2018). The Ritter Island sector collapse of 1888, the largest in historic time, also involved a cascade of slow flank movement leading to catastrophic collapse and eruption (Karstens et al., 2019; Watt et al., 2019). Even very recent eruptions such as the eruption of Anak Krakatau in 2018, which was triggered by an eruption and slow flank movements (Walter et al., 2019), and Kilauea in 2018 (Patrick et al., 2020) are prominent examples of cascading geohazards.

It would be insightful to study volcano-tectonic systems comparable to the CSKVF for evidence of similar large-scale cascading geohazards, e.g. the hazardous Krakatau volcanic system at the Sunda strait or the volcano-tectonic Kagoshima graben at the northern end of the Ryukyu Arc in the East China Sea (Kamata and Kodama, 1999; Harjono et al., 1991). Both are volcanic back-arc systems that lie in an extensional marine setting and comprise large volcanoes and calderas (Harjono et al., 1991; Priyanto et al., 2021; Tatsumi et al., 2018).

While cascading effects are an inherent challenge for modeling and forecasting (Zuccaro et al., 2018), increased awareness and further research are crucial to ensure greater resilience of coastal communities towards such catastrophic events, especially for regions as vulnerable as the Mediterranean (Walter et al., 2019; Patrick et al., 2020; López-Saavedra et al., 2021).

5.6   Conclusions

The analysis of an extensive 2D seismic dataset from the Christiana-Santorini-Kolumbo Volcanic Field has allowed us to identify and map the largest volcanic island mass-transport deposit from the Mediterranean Sea, which occurred in the early phase of the evolution of Santorini ∼0.7 Myrs ago. Our results show that emplacement of the Santorini Mass-Transport Deposit (SMTD) likely proceeded as a complex multi-stage cascade, which occurred in all basins surrounding Santorini. We identify five processes that might have contributed to the SMTD cascade: rifting, precursory mass-transport events, catastrophic collapses, secondary sediment failures, and debris flow deposition. Our interpretation is that the emplacement of the SMTD was initiated by an intensive rift pulse, which occurred along SW-NE-directed faults extending from the Christiana Volcano in the southwest towards the island of Amorgos in the northeast (Fig. 5.11A). Smaller precursory mass-transport

events took place before catastrophic frontally confined sector collapses occurred at the northeast flank of the Christiana Volcano and on the southeastern flank of proto-Santorini (Fig. 5.11B). As a consequence, significant secondary sediment failures on the slopes of proto-Santorini were triggered. These secondary sediment failures are frontally emergent and transitioned into debris flows and turbidity flows that transported large amounts of sediment towards the rift basins northeast of Santorini (Fig. 5.11C). Constituting by far the largest portion of the entire SMTD sequence (> 90 %), these secondary failures are additional evidence for the importance of secondary processes in the emplacement of mass movements around volcanic islands, and they highlight the key role of reflection seismic surveys in providing detailed insights into such dynamics. The emplacement of the SMTD correlates with a transition from a phase of relative volcanic dormancy to a phase of basin-wide emergence of volcanoes, highlighting how closely volcanism, tectonism, and mass-transport can interact in rift-hosted volcanic systems.

Acknowledgements

Conflicts of Interest

The authors declare that they have no known competing financial interests or personal relationships that could have appeared to influence the work reported in this paper.

Data Availability

The data that support the findings of this study are available from the corresponding author upon reasonable request.

Chapter 6

Volcano-Tectonic Evolution of the Christiana-Santorini-Kolumbo Rift Zone

Abstract

Located on the Hellenic Arc, the Christiana-Santorini-Kolumbo (CSK) rift zone represents one of the most active and hazardous volcano-tectonic systems in the Mediterranean. Although this rift zone has been intensively studied, its tectonic evolution and the interplay of volcanism and tectonism are still poorly understood. In this study, we use high-resolution reflection seismic imagery to reconstruct the opening of the rift basins. For the first time, we relate the activity of individual faults with the activity of specific volcanic centers in space and time. Our analysis shows a pre-volcanic NNE-SSW-oriented paleo basin underneath the CSK volcanoes, representing a transfer zone between Pliocene ESE-WNW-oriented basins, which was overprinted by a NE-SW-oriented tectonic regime hosting Late Pliocene volcanism that initiated at the Christiana Volcano. All subsequent volcanoes evolved parallel to this trend. Two major Pleistocene tectonic pulses preceded fundamental changes in the volcanism of the CSK rift including the occurrence of widespread small-scale volcanic centers followed by focusing of activity at Santorini with increasing explosivity. The observed correlation between changes in the tectonic system and the magmatism of the CSK volcanoes suggests a deep-seated tectonic control of the volcanic plumbing system. In turn, our analysis reveals the absence of large-scale faults in basin segments affected by volcanism indicating a secondary feedback mechanism on the tectonic system. A comparison with the evolution of the neighboring Kos-Nisyros-Yali volcanic field zone and Rhodos highlights concurrent regional volcano-tectonic changes, suggesting a potential arc-wide scale of the observed volcano-tectonic interplay.

Plain Language Summary

How do regional tectonic movements and large volcanoes interact? Seismological studies indicate complex volcano-tectonic feedback links, but, so far, information on the long-term interactions between tectonics and volcanism is rarely available. The Christiana-Santorini-Kolumbo (CSK) rift zone lies in the Aegean Sea and is notorious for its devastating volcanic eruptions, earthquakes, and tsunamis. This region offers the opportunity to study volcano-tectonic interactions over several million years. In this study, we use high-resolution seismic imagery to reconstruct the evolution of the rift basins and the CSK volcanoes. We find that all volcanoes lie

in a Pliocene transfer zone connecting extensional basins. Volcanism initiated as this older tectonic regime was intersected by a NE-SW-directed fault system. Subsequently, all volcanoes evolved parallel to this trend. Several distinct tectonic reorganizations occurred in the Pleistocene, which had a pronounced influence on the CSK volcanoes. In turn, our analysis indicates that the emergence of volcanism also impacted the tectonic evolution of the rift system hindering the evolution of large-scale normal faults in the volcanic basins. The observed tectonic reorganizations seem to reflect major changes in the stress regime of the Hellenic Arc, potentially also affecting adjacent volcanic centers whose volcano-tectonic evolution is only poorly constrained so far.

6.1   Introduction

The interplay of volcanism and tectonism has shaped many volcanic systems across the world (Acocella, 2021). Regional tectonics weakens the crust through increased faulting and fracturing creating pathways for magmatic fluids to ascend to the surface, although the controlling mechanisms remain elusive (e.g. Hill et al., 2002; Manga and Brodsky, 2006). Our current knowledge of volcano-tectonic feedback mechanisms is based mostly on the interplay of earthquakes and volcanic eruptions on time scales ranging from minutes to decades by direct observations or historic records (e.g. Manga and Brodsky, 2006; Watt et al., 2009). These studies revealed that tectonic movements can change stress levels in the crust and the underlying mantle, influencing production and ascent rates, as well as sizes and explosivities of eruptions. In turn, volcanism can alter the stress of the crust by accommodating extensional strain and inhibiting the formation of faults (Faulds and Varga, 1998) highlighting complex feedback mechanisms between tectonics and volcanism that involve a competition between magmatic and tectonic strain accommodation (e.g. Acocella and Trippanera, 2016; Keir et al., 2006; Wilson et al., 2019). However, the dynamics of long-term interactions (>100 ka) between tectonics and magmatism are less well understood, since they require knowledge of the past dynamics of the tectonic stress field and the volcanic behavior, which are rarely available (Giba et al., 2013). Therefore, our current knowledge about the influence of regional, long-term tectonic stress regimes on volcanic plumbing systems and vice versa remains immature.

Located on the Hellenic Volcanic Arc in the southern Aegean Sea (Fig. 6.1a), the Christiana-Santorini-Kolumbo (CSK) volcanic field (Fig. 6.1c) offers the opportunity to study the interaction of a back-arc rift zone and its volcanic plumbing system over the course of more than 2 million years (Piper et al., 2007; Preine et al., 2022a). Here, the history of volcanism and rift evolution is recorded in the sedimentary basins, which have been the target of numerous geophysical surveys in recent decades. These studies analyzed the seafloor morphology of the area (e.g. Hooft et al., 2017; Nomikou et al., 2018b) as well as the upper crustal structure of the rift zone (Hooft et al., 2019; Heath et al., 2019; Heath et al., 2021; McVey et al., 2020; Schmid et al., 2022), the seismostratigraphy of the rift basins (e.g. Hübscher et al., 2015; Nomikou et al., 2016b; Preine et al., 2022b; Nomikou et al., 2018b; Nomikou et al., 2019), and the spatio-temporal evolution of the CSK volcanic centers (Fig. 6.1b) (e.g. Hübscher et al., 2015; Preine et al., 2022a). However, until now, reconstructions of the tectonic evolution of the rift basins have been lacking, which are crucial to identifying volcano-tectonic feedback mechanisms at the CSK rift zone. Understanding these interactions is critical to enable an accurate hazard assessment for the eastern

Mediterranean to which the CSK field poses a major threat having produced devastating events such as the iconic Minoan eruption approx. 3600 years ago (Nomikou et al., 2016a; Johnston et al., 2014; Druitt et al., 2019b) or the tsunamigenic 1956 magnitude 7.4 Amorgos earthquake (Fig. 6.1c) (Nomikou et al., 2018b; Brüstle et al., 2014).

In this study, we utilize an extensive collection of high-resolution reflection seismic data to map the distribution of seismostratigraphic units and the activity of faults throughout the entire CSK rift zone. In addition, we use horizon flattening to reconstruct the evolution of individual basins. Our objectives are to (i) reconstruct the tectonic evolution of specific rift basins, (ii) relate the tectonic evolution of the rift system to the volcanic evolution of the CSK centers, (iii) investigate volcano-tectonic feedback mechanisms, and (iv) link these findings to the large-scale evolution of the eastern Hellenic Arc.

6.2 Geological Framework

6.2.1 Tectonic Background

The Hellenic Arc in the southern Aegean Sea represents the seismically and volcanically most active region in the Mediterranean Sea (Fig. 6.1a) (Bohnhoff et al., 2006). Formed as the consequence of the subduction of the African plate beneath the Eurasian plate, the Hellenic Arc is an arcuate belt reaching from the Adriatic Sea towards western Anatolia, where it transitions into the Cyprus arc (Fig. 6.1a) (e.g. Royden and Papanikolaou, 2011; Le Pichon and Angelier, 1979). Since the Late Miocene, the Hellenic Arc has stepped southwards and increased in curvature, leading to enhanced extension and intensive internal deformation of the Aegean microplate (e.g. Veen and Kleinspehn, 2002). These processes have been attributed to the rollback of the subducted African slab induced by the downwards pull of the subducted African slab (e.g. Le Pichon and Angelier, 1979; Le Pichon and Kreemer, 2010) gravitational forcing associated with overthickened Alpine crust (e.g. Jolivet, 2001), and westward movement of the Anatolian plate (Taymaz et al., 1991; Le Pichon and Kreemer, 2010). The interplay of these processes produced the complex neotectonic horst and graben structures of the Cycladic islands (Le Pichon and Kreemer, 2010; Royden and Papanikolaou, 2011), where crustal thicknesses range from 20 to 30 km, compared to 40-50 km under mainland Greece and Turkey (Zhu et al., 2006).
The Aegean crust consists of metamorphic rocks belonging to the Attico-Cycladic complex, formed as a result of compressional orogeny in the early Cenozoic (Piper et al., 2007). During Miocene to Pliocene, N-S-directed extension led to basin subsidence in the southern Aegean forming multiple basins bounded by E-W-directed listric normal faults (Anastasakis and Piper, 2005; Piper et al., 2007). Increasing curvature of the Hellenic Arc led to counterclockwise rotation of the eastern segments of the Aegean in the Pliocene and Pleistocene, e.g. at Rhodos (Fig. 6.1a) (Van Hinsbergen et al., 2007). This was accommodated by major arc-normal and arc-parallel extension in the back-arc and forearc Aegean region leading to the formation of NE-SW directed fault systems (e.g. Gautier et al., 1999; Van Hinsbergen and Schmid, 2012; Papazachos, 2019; Bocchini et al., 2018). Prominent examples of these fault systems are the deep Ptolemy, Pliny, and Strabo Trenches in the forearc region (Fig. 6.1a), or the prominent Santorini-Amorgos Tectonic Zone (SATZ) in the back-arc region (Fig. 6.1c) (Nomikou et al., 2018b).
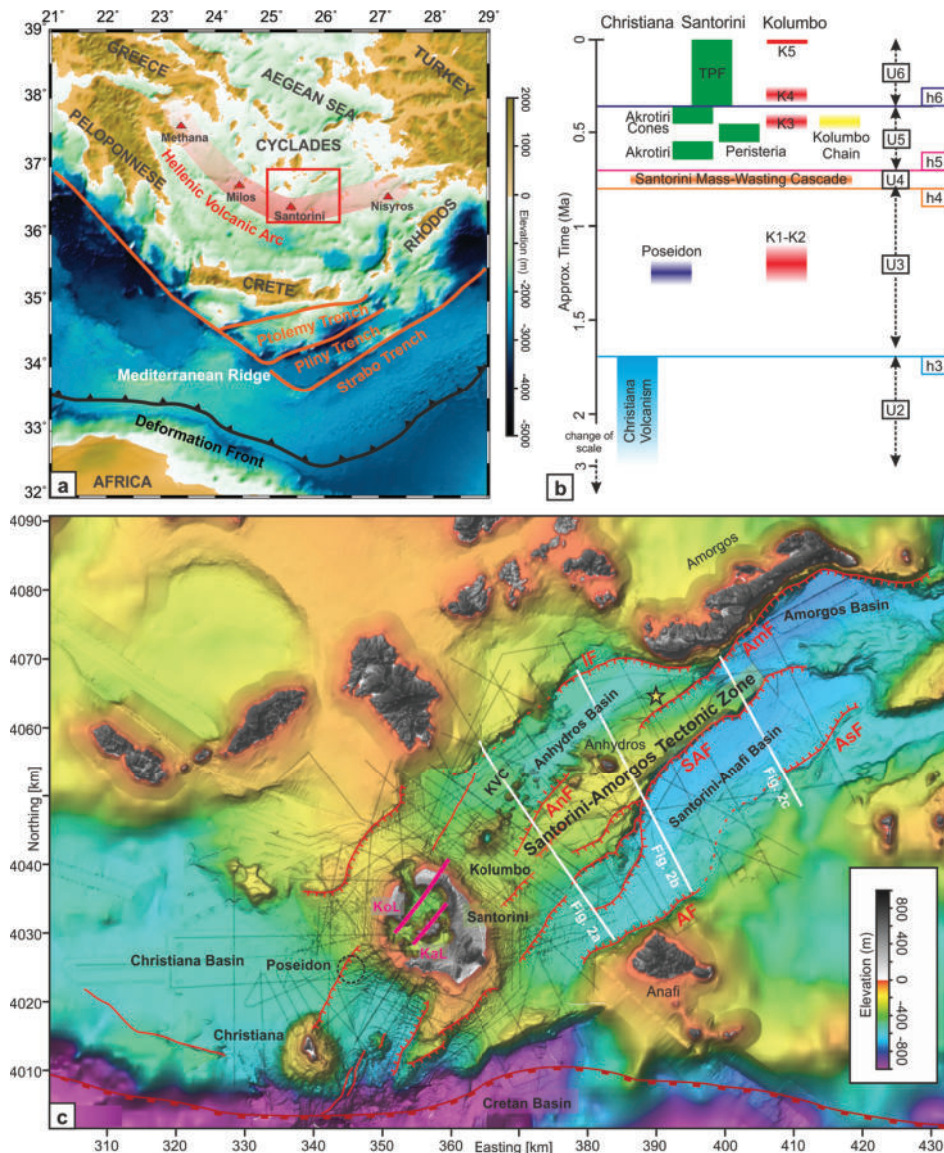
FIGURE 6.1: a) Southern Aegean Sea and major structural features of the Hellenic Arc. Modified from Jolivet et al. (2013), Bocchini et al. (2018), and Preine et al. (2020). Red rectangle shows the study area. b) Illustration of the spatio-temporal evolution of the CSK volcanic field with estimated ages of major volcanic units, unconformities (h1-h6), and seismostratigraphic units (U2-U6). Modified from Preine et al. (2022a). TPF: Thera Pyroclastic Formation; K1-K5: Kolumbo eruptions. c) Morphological map of the CSK rift zone showing islands, basins, volcanic centers, and major extensional structures after Nomikou et al. (2013, 2018a, 2019) and Preine et al. (2022b). Grey lines show all seismic profiles, white lines indicate the locations of seismic profiles shown in Figure 6.1. Red lines indicate faults, purple lines indicate the Kameni and Kolumbo Lines. Yellow star indicates the location of the first Amorgos 1956 earthquake from Okal et al. (2009). Dashed black circle indicate location of buried Poseidon center (Preine et al., 2022a). KVC: Kolumbo Volcanic Chain; KoL: Kolumbo Line; KaL: Kameni Line; AF: Anafi-Fault; AmF: Amorgos Fault; AnF: Anhydros Fault; AsF: Astypalaea Fault; IF: Ios Fault; SAF: Santorini-Anafi Fault.

Located in the center of the Hellenic Arc, the 100 km long and 45 km wide CSK rift zone represents a major structural boundary separating the Hellenic Arc into a volcanically and tectonically active eastern and a quiet western part (Bohnhoff et al., 2006). It is situated at the junction of the Christiana Basin in the west and the SATZ in the east (Fig. 6.1c). The northeastern basins (Anhydros, Santorini-Anafi, and Amorgos) are NE-SW striking grabens and half-grabens with sediment infill up to 1,400 m thick that are bounded by major extensional to transtensional faults with fault throws exceeding 2000 m (Fig. 6.1c) (Bohnhoff et al., 2006; Hübscher et al., 2015; Nomikou et al., 2016b; Nomikou et al., 2018b; Preine et al., 2020)). The Anhydros Basin contains the submarine Kolumbo Volcano and the Kolumbo Volcanic Chain (Fig. 6.1c), whereas the Santorini-Anafi and Amorgos Basins lack volcanoes (Fig. 6.1c). Opening of these basins occurred in multiple episodes of enhanced rift activity, so-called 'tectonic pulses' (Hübscher et al., 2015; Preine et al., 2022b). The Anhydros and Anafi Basins each contain six seismostratigraphic units separated by onlap surfaces while the Amorgos Basin only contains the uppermost four units (Hübscher et al., 2015; Nomikou et al., 2018b; Nomikou et al., 2019; Nomikou et al., 2016b).

Southwest of Santorini lies the Christiana Basin, which hosts the Christiana Volcano and several volcanic domes (Fig. 6.1c) (Nomikou et al., 2013; Hooft et al., 2017). This basin is assumed to have formed prior to the basins NE of Santorini under an older E-W striking fault system (Piper et al., 2007; Preine et al., 2022a; Heath et al., 2019). However, recent studies have shown that the NE-SW-directed fault trend of the northeastern rift basins continues underneath Santorini, with a prominent fault extending from Santorini towards Christiana (Fig. 6.1c) (Preine et al., 2022a; Preine et al., 2022b; Heath et al., 2019). Approx. 0.7 Ma ago, the entire rift system was affected by an intensive tectonic pulse, triggering a cascade of sector collapses and secondary mass-wasting events at Christiana and Santorini (Fig. 6.1b) (Preine et al., 2022b).

6.2.2 Volcanic Background

The present-day Hellenic Volcanic Arc initiated 3-4 Ma ago and stretches from the Gulf of Saronikos in the west through Milos, the CSK field, to the Kos-Nisyros-Yali complex in the east (Fig. 6.1a) (e.g. Piper et al., 2007; Nomikou et al., 2013). The CSK field comprises the extinct Christiana Volcano, the Santorini Caldera, the polygenetic submarine Kolumbo Volcano, as well as the Kolumbo Volcanic Chain (Fig. 6.1c) (Preine et al., 2022a; Nomikou et al., 2019). Having produced over 100 explosive eruptions in the last 360 kyrs, the CSK field is one of the most hazardous volcanic systems in Europe (Druitt et al., 1999). At least four major caldera-forming eruptions have occurred at Santorini, with the most recent caldera-forming eruption, the 3600 ka "Minoan" eruption, being considered one of the largest in the Holocene (e.g. Nomikou et al., 2016a; Johnston et al., 2014; Druitt et al., 1999).
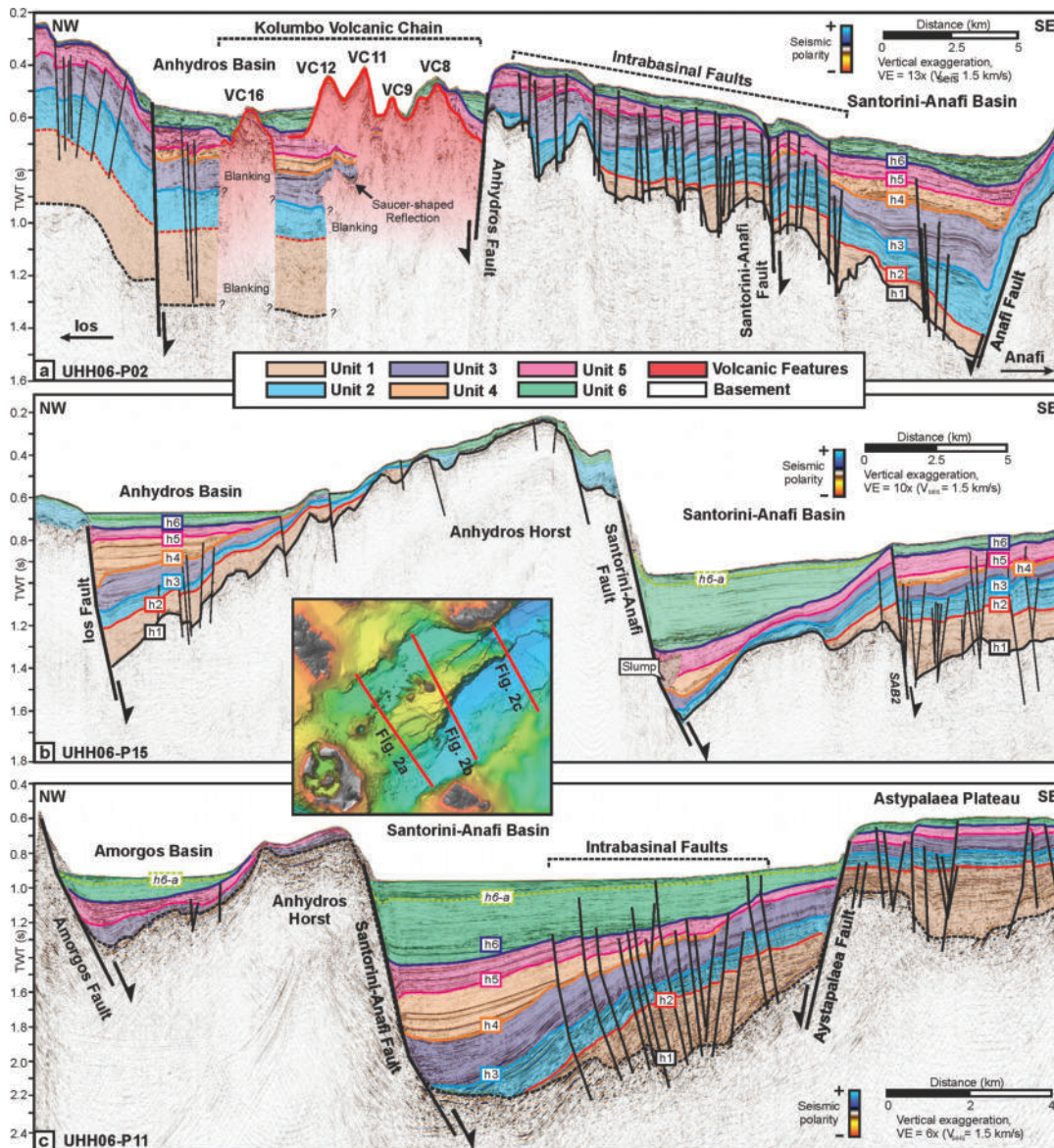
FIGURE 6.2: Seismic profiles crossing the Santorini-Amorgos Tectonic Zone. For locations, see inset map. Semi-transparent colors indicate different seismic (U1-U6) and volcanic units as indicated in the legend on top. VE – vertical exaggeration. (a) Profile UHH06-P02 crossing the western Anhydros Basin, the Kolumbo Volcanic Chain, and the western Santorini-Anafi Basin. SAB2: Major Fault within the Santorini-Anafi Basin. (b) Profile UHH06-P15 profile crossing the eastern Anhydros Basin, the Anhydros Horst, and the central Santorini-Anafi Basin. (c) Profile UHH06-P11 profile crossing the western Amorgos Basin, the Anhydros Horst, and the eastern Santorini-Anafi Basin.

The CSK field is assumed to have evolved during four main phases of volcanic activity (Fig. 6.1b) (Preine et al., 2022a). The first phase initiated in the Pliocene with the formation of the Christiana volcano, which became inactive at approx. 1.6 Ma (Fig. 6.1b) (Preine et al., 2022a; Heath et al., 2019; Piper et al., 2007). In the second phase, volcanism aligned NE-SW and focused on the early Kolumbo and the Poseidon centers (Fig. 6.1b) (Hübscher et al., 2015; Preine et al., 2022a). Both centers

produced volcanoclastic deposits that are intercalated within the sedimentary strata of the hosting Christiana and Anhydros Basins. A distinct change in the volcanic behavior occurred at ∼0.7 Ma after the Santorini mass-wasting cascade occurred that transported up to 125 km³ of sediments from Christiana and Santorini into the surrounding basins (Fig. 6.1b) (Preine et al., 2022b). Afterward, in the third phase, volcanism occurred throughout the entire CSK field forming a series of volcanic cones, as well as the onshore exposed Akrotiri rhyolitic centers, the Peristeria stratovolcano, and the Akrotiri cinder cones (Fig. 6.1b) (Preine et al., 2022a). Another pronounced change in the volcanic system occurred in the fourth phase approx. 360 ka ago, when volcanism focused on the northern part of Santorini and became highly explosive while Kolumbo remained active (Fig. 6.1b). The products of Santorini during this last and ongoing phase are referred to as the Thera Pyroclastic Formation and are largely exposed on the caldera cliffs (Fig. 6.1b) (Druitt et al., 1999). Offshore, these deposits are recognized as a very thick (∼350 m) wedge north of Santorini that thins out towards the Anhydros Basin and the Christiana Basin (Preine et al., 2022a). This latest phase correlates to a distinct change in the primitive-melt diversity that occurred between ∼360 ka and 224 ka (Flaherty et al., 2022). Volcanism during this latest phase focused on the Kolumbo and Kameni Lines (Fig. 6.1c), which bound a low-velocity anomaly interpreted as a shallow magma body at 3 to 5 km depth (Hooft et al., 2019; Heath et al., 2019; McVey et al., 2020).

6.3 Methods

During six cruises between 2006 and 2019, we collected an extensive dataset of over 3,200 km of high-resolution multi- and single-channel seismic data (Fig. 6.1c) (Sigurdsson et al., 2006; Hübscher et al., 2006; Karstens et al., 2020b). For all multichannel seismic profiles, we applied multiple removal by means of surface-related multiple elimination and pre-stack time migration. See Appendix C for more details regarding the acquisition and processing of the seismic data. All processed seismic profiles were combined into an interpretation project using KingdomSuite software. Here, we established the stratigraphic framework (Fig. 6.2) (following the nomenclature in Preine et al. (2022a)), mapped seismic units, and created isochron maps (vertical thickness in two-way travel time) by interpolating between the seismic profiles (Fig. 6.3). We converted the isochron maps to isochore maps in meters by using constant interval velocities derived from diffraction-based wavefront tomography (see Table C.1; Preine et al. (2020)). These interval velocities do not account for lateral velocity changes and should therefore be considered approximations. In addition, we created reconstructions of the rift basin evolution by flattening key horizons (Fig. 6.4). This simple method levels the seismic profile to an interpreted horizon, which allows the effects of fault displacements to be reversed and, thereby, obtain insights into the deformation of the sediments beneath the examined horizons during the time of its deposition (e.g. Nunns, 1991; Jamaludin et al., 2015). Horizon flattening is available as a standard interpretation tool in the KingdomSuite software.

6.4 Results

6.4.1 Seismostratigraphy of the Rift Basins

Different seismostratigraphic interpretations for basins surrounding the CSK field have been presented in previous studies focusing on different parts of the area, e.g.

the Anhydros Basin (Nomikou et al., 2016b; Hübscher et al., 2015) the eastern SATZ (Nomikou et al., 2018b; Nomikou et al., 2019) or the Christiana Basin (Tsampouraki-Kraounaki and Sakellariou, 2018). In the following, we will use a previously de-fined seismostratigraphic framework for the entire CSK rift zone (Preine et al., 2022a; Preine et al., 2022b). This seismostratigraphic framework comprises six units sepa-rated by six key horizons h1-h6 (see Table C.2 for a detailed comparison of the dif-ferent seismostratigraphic frameworks). These horizons are high-amplitude reflec-tions, which lie conformable outside the rift basins but represent major unconformi-ties inside the rift basins. Approximate ages of the seismo-stratigraphic units have been estimated by Preine et al. (2022a) and are based on correlations with onshore volcanic products and the extrapolation of sedimentation rates (for an overview, see Fig. 6.1b). However, due to the lack of direct samples, these ages od deeper units are associated with considerable uncertainties.

The lowermost unit (Unit 1) is characterized by weakly reflective strata with sub-parallel reflections that have been interpreted to be of Pliocene age (Fig. 6.1b) (Preine et al., 2022a). Unit 1 is covered by Unit 2, which comprises a series of well-stratified reflections with medium to high amplitudes and is considered to be of Late Pliocene to Early Pleistocene age (Fig. 6.1b). Unit 3 and Unit 5 consist of a sequence of well-stratified reflections with medium amplitudes, which contrast with the weakly re-flective nature of Unit 4, which has been interpreted as the deposits of the Santorini Mass-Wasting Cascade (Preine et al., 2022b). In the vicinity of Santorini, the upper-most Unit 6 comprises high-amplitude irregular reflections that comprise volcano-sedimentary deposits from the Thera Pyroclastic Formation during the last 0.36 Ma (Fig. 6.1b) (Preine et al., 2022a).

Figure 6.2 shows three seismic profiles crossing the SATZ approx. perpendicular to the NE-SW-directed main fault trend (Nomikou et al., 2018b). Semi-transparent col-ors indicate seismostratigraphic Units 1-6 (for an un-interpreted version of the pro-files, see Figure C.1). Profile A (UHH06-P02) crosses the Kolumbo Volcanic Chain in the Anhydros Basin as well as the Santorini-Anafi Basin and terminates in front of the island of Anafi (Fig. 6.2a). The internal architecture of these two basins dif-fers significantly (Fig. 6.2a). While the Santorini-Anafi Basin represents a SE-ward tilted half-graben bounded to the NW by the Santorini-Anafi Fault with the sedi-mentary infill thickening towards the Anafi Fault, the Anhydros Basin represents a graben bounded by steeply dipping faults and is strongly overprinted by the vol-canism of the Kolumbo Chain masking significant parts of the deeper strata (Fig. 6.2a). The basement reflection h1 is barely visible here, which is in contrast with the Santorini-Anafi Basin, where h1 is a well-defined high-amplitude reflection and the entire sedimentary strata is well-imaged (Fig. 6.2a). While the Anafi Fault has a throw exceeding 1000 m here, the Santorini-Anafi Fault is only a small throw of ~100 m (Fig. 6.2a).

In general, the sedimentary infill of the Anhydros Basin shows a uniform thickness (Fig. 6.2a). While Units 1 and 2 are thick here (> 200 ms TWT / ~250 m), Units 3-6 are rather thin (< 100 ms TWT / ~110 m) (Fig. 6.2a). There are multiple volcanic cones belonging to the Kolumbo Chain, which are labeled VC# according to Nomi-kou et al. (2012) (Fig. 6.2a). Edifice VC16 has distinct high-amplitude reflections at the top reaching the seafloor, while seismic blanking occurs underneath (Fig. 6.2a). Further towards the SE, we identify four volcanic cones VC12, VC11, VC 9, and VC8, which pinch out within Unit 5. While VC8 is buried by Units 6 and 5, volcanic cones VC12, VC11, and VC9 breach the seafloor and are overlain by only a thin sediment cover (Fig. 6.2a). Towards the Anhydros Fault, the underlying strata is strongly disturbed and only some irregular high-amplitude reflections are visible. Beneath

volcanic cone VC12 is a buried volcanic edifice that pinches out within Unit 3 and is marked by a saucer-shaped high-amplitude reflection (Fig. 6.2a). Southeast of the Anhydros Fault is a strongly faulted zone, with many steeply-dipping (~60°) faults that have throws of 10-30 m (Fig. 6.2a). Towards the Anafi Fault, Unit 3 thickens significantly, while having a rather constant thickness elsewhere (Fig. 6.2a). Unit 4 represents a thick deposit in the Santorini-Anafi Basin (~90 ms TWT / ~200 m), but it thins out towards the NW (Fig. 6.2a). While Unit 5 has a rather constant thickness, Unit 6 is thickening towards the Anafi Fault (Fig. 6.2a). Here, we observe high-amplitude irregular reflections representing the volcano-sedimentary deposits from the Thera Pyroclastic Formation (Fig. 6.2a) (Preine et al., 2022a; Preine et al., 2022b).

Profile B (UHH06-P15) crosses the Anhydros and Santorini-Anafi Basins in the central part of the SATZ close to the Anhydros Islet, which is part of the Anhydros Horst (Fig. 6.2b). Here, the Anhydros Basin lacks volcanic structures and represents a typical half-graben bounded by the Ios Fault, which has a throw of ~700 m (Fig. 6.2b) (Hübscher et al., 2015; Nomikou et al., 2018b). We identify all six Units in this basin, with Units 3 and 4 showing a pronounced thickness increase towards the Ios Fault, while Units 5 and 6 have a rather constant thickness (Fig. 6.2b). Reflections h6 and h5 lie flat and onlap reflection h4, which has a distinctly different dip that lies sub-parallel to that of the underlying reflectors h3, h2, and h1 (Fig. 6.2b). The Anhydros horst is overlain by a sequence of thin sediments with some faults piercing the seafloor (Fig. 6.2b).

SE of this horst, the seafloor of the Santorini-Anafi Basin is deeper than that of the Anhydros Basin and the internal architecture of both basins contrasts strongly (Fig. 6.2b). The Santorini-Anafi Fault is associated with a major throw, which offsets the basement up to 1.2 km here (Fig. 6.2b). In the central Santorini-Anafi Basin, Unit 6 is very thick (~350 ms TWT / ~320 m) at the foot of the Santorini-Anafi Fault, while thinning dramatically towards the SE where its thickness is only (~50 ms TWT / ~45 m) (Fig. 6.2b). It comprises a set of low-amplitude reflections that onlap horizon h6 (Fig. 6.2b). At the top of Unit 6, we identify a distinct high-amplitude reflection (h6-a), and at the base, we identify several irregular high-amplitude reflections (Fig. 6.2b). The internal reflections of Unit 6 are mostly sub-parallel to the seafloor while the deeper reflections (h6-h2) show a pronounced dip towards the Santorini-Anafi Fault (Fig. 6.2b). Unit 5 thickens towards the foot of the Santorini-Anafi Fault, where we identify a confined area with irregular reflections interpreted as a slump deposit originated from the Santorini-Anafi Fault (Fig. 6.2b) (Nomikou et al., 2018b; Preine et al., 2022b). Unit 4 is only present at the foot of the Santorini-Anafi Fault and pinches out towards the SE onlapping the underlying unconformity h4 (Fig. 6.2b). Towards the SE on the shoulder of the basin, there is a distinct SE-wards dipping fault (labeled 'SAB2') that marks a distinct change in the internal architecture of the basin infill (Fig. 6.2b). Here, the deeper Units 1-3 are thicker and strongly faulted while thinning out towards the NW (Fig. 6.2b).

Profile C (UHH06-P11) crosses the western tip of the Amorgos Basin and the northeastern Santorini-Anafi Basin, which represents a graben defined by the Santorini-Anafi Fault (throw of > 1.4 km) and the Astypalaea Fault (throw of > 400 m) (Fig. 6.2c) (Nomikou et al., 2018b). The Anhydros Horst, which separates both basins, has a much smaller lateral extent here compared to Profile B (Fig. 6.2b). We identify all six seismostratigraphic units within the Santorini-Anafi Basin while the Amorgos Basin lacks Units 4, 2, and 1 (Fig. 6.2c). Similar to Profile B, Unit 6 is very

thick (∼400 ms TWT / ∼370 m) in the central Santorini-Anafi Basin, while being much thinner on the Astypalaea Plateau (∼60 ms TWT / ∼55 m) (Fig. 6.2c). The internal reflections of this uppermost Unit have low amplitudes, show complex sub-parallel/hummocky internal reflections, and onlap the underlying horizon h6, which represents a major unconformity (Fig. 6.2c). Also here, we identify the high-amplitude reflection h6-a at the top of Unit 6, which defines the base of subunit U6-a that that thickens towards the Santorini-Anafi fault. Both, the Santorini-Anafi Basin and the Astypalaea Plateau, are strongly faulted, but offsets are markedly smaller in Unit 1 with some internal faults fading out at unconformity h6 (Fig. 6.2c). The underlying Units 5-3 are strongly thickening towards the Santorini-Anafi Fault, with Unit 4 pinching out towards the Astypalaea Fault (Fig. 6.2c). In contrast to that, Units 1 and 2 have a uniform thickness in the Santorini-Anafi Basin. The Amorgos Basin also contains a thick sequence of Unit 6 (∼130 ms TWT / ∼120 m), while the underlying Units 5 and 3 are diverging towards the Amorgos Fault (Fig. 6.2c).

6.4.2   Mapping of the Seismostratigraphic Units

Combining all seismic profiles throughout the study area (Fig. 6.1c), we created isochrone maps of all seismostratigraphic units by interpolating between seismic profiles (Fig. 6.3). These isochrones maps reveal a succession of depocenters and deposit-free areas that have been active during different times of the evolution of the rift system. The isochrone maps can be converted to isochore thickness maps by applying interval velocities for each Unit (Preine et al. (2020); see Table C.1). Unit 1 has been deposited in a complex puzzle of depocenters with a main depocenter in the Christiana Basin (Fig. 6.3a). In addition, we identify a large depocenter that extends from the eastern flank of present-day Santorini towards the NNE, which has been crossed by Profile A (Fig. 6.2a). East of the Anhydros islet, we identify a narrow depocenter cross-cutting the present-day Anhydros and Santorini-Anafi Basins (Fig. 6.3a).

Mapping of Unit 2 reveals a main depocenter in the Christiana Basin, as well as a depocenter extending from the NE flank of Santorini towards the island of Ios (Fig. 6.3b). The depocenter in the Christiana Basin is strongly thickening towards the Christiana edifice (Fig. 6.3b), which is mainly due to basin-wards dipping reflections from the Christiana edifice as shown in Preine et al. (2022a). There are two additional depocenters at the western and eastern Santorini-Anafi Basin, which are aligned approx. in NE-SW direction. For Unit 3, we identify two distinct, circular depocenters west and east of Santorini at the locations of the Poseidon and early Kolumbo volcanic centers (Fig. 6.3c) (Preine et al., 2022a). In addition, we identify a depocenter northwest of Anafi (Fig. 6.2a, 6.3c) and a depocenter in front of the eastern Santorini-Anafi Fault (Fig. 6.2c, 6.3c). Both depocenters are aligned NE-SW, parallel to the present-day fault trend (Nomikou et al., 2018b).
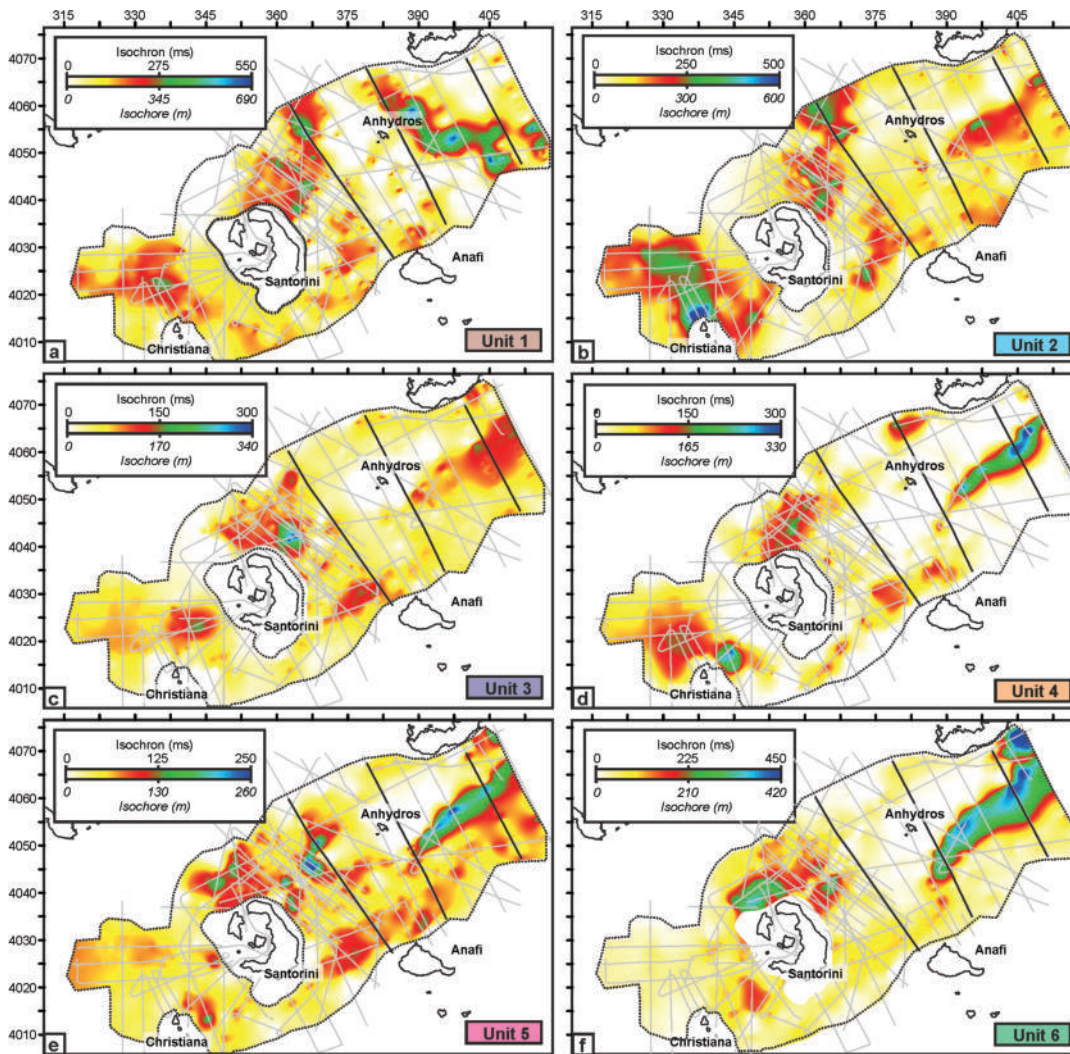
FIGURE 6.3: Isochrone and approximated isochore maps of Units 1-6 as interpolated from seismic lines highlighted in grey. Black lines indicate the location of seismic lines shown in Figure 2. Present-day coastlines for spatial reference.

The isochore map of Unit 4 has already been presented in Preine et al. (2022b)) and comprises eight separated depocenters (Fig. 6.3d). This is well visible in Figure 6.2, where Unit 4 occurs only in the basin centers next to major faults. For Unit 5, we identify a major depocenter at the eastern Santorini-Anafi Basin, where a distinct thickening towards the Santorini-Anafi Fault is observed (Fig. 6.2c, 6.3e). There are several depocenters along the Kolumbo volcanic chain (Fig. 6.3e), which evolved contemporarily to the deposition of Unit 5 (Preine et al., 2022a). The same applies to a distinct depocenter west of Santorini, representing the deposits of the Aspronisi cones (Fig. 6.3e) (Preine et al., 2022a). Additional depocenters are located north of Santorini, between Santorini and Anafi, and east of Christiana (Fig. 6.3e).

The isochore map of Unit 6 reveals a broad depocenter in the Santorini-Anafi Basin (Fig. 6.3f) that has been crossed by Profiles B and C (Fig. 6.2b and c). This depocenter covers the eastern Santorini-Anafi Basin and extends towards the Amorgos Basin in the NE, where it reaches its maximum thickness (> 400 m) (Fig. 6.3f). In addition,

there is a distinct depocenter north of Santorini that is interpreted to be the deposits of the Thera Pyroclastic Formation.

6.5 Discussion

6.5.1 Basin Opening

As described previously, the six key horizons h1-h6 represent major unconformities in the rift basins marking distinct phases of episodic basin-opening. In order to highlight the dynamics of these tectonic episodes, Figure 6.4 illustrates the eastern Anhydros Basin from Profile B (Fig. 6.2b) and the eastern Santorini-Anafi Basin from Profile C (Fig. 6.2c) after successive flattening of key horizons h1-h5 (Fig. 6.3). This method allows to visualize the approximate geological situation during deposition of each flattened horizon and thereby to reconstruct the general basin evolution (Jamaludin et al., 2015). In contrast to methods like structural restoration, horizon flattening does not take into account slip across faults that intersect horizons or compaction during deposition (Nunns, 1991). However, structural restoration requires detailed information about the physical properties of each seismostratigraphic unit, which are typically only available from drilling campaigns.

In general, we distinguish two types of basin-opening in the context of the Santorini-Amorgos Tectonic Zone: continuous hanging-wall rotation vs. tectonic pulses. Continuous hanging-wall rotation implies that the fault-induced subsidence occurs on time scales that allow syn-tectonic deposition, which would manifest as divergent internal reflections. In contrast to that, tectonic pulses are defined by distinct episodes of hanging-wall rotation of the marginal faults, which occur so fast that no seismically resolvable syn- tectonic deposition is detectable. Instead, the subsequently deposited strata laps onto the horizon marking the pulse event. Hübscher et al. (2015) have shown the occurrence of multiple distinct tectonic pulses in the Anhydros Basin, while Preine et al. (2022b) showed that a rift-wide tectonic pulse preceded the emplacement of Unit 4, the Santorini Mass-Transport Deposit.

The tectonics of the Anhydros Basin shows low activity during the deposition of the two uppermost units, 6 and 5, which are well-stratified and only have a minor thickness increase towards the Ios Fault (Fig. 6.4a, c). In contrast to that, there was a distinct tectonic pulse before the deposition of Unit 4. As highlighted in Figure 6.4d, the internal reflections of Unit 4 are parallel to the flattened top of the Unit, while the underlying unconformity h4 reveals a distinct dip, on which the internal reflections onlap. The divergence of internal reflections towards the Ios Fault during deposition of Unit 3 implies a continuous basin opening and tilting (Fig. 6.4g). This also applies to Unit 2, which is generally thin inside the Anhydros Basin but also shows divergence towards the Ios Fault (Fig. 6.4e). For Unit 1, there also seems to be divergence towards the Ios Fault, although imaging becomes more difficult here obscuring the internal architecture of this unit (Fig. 6.4i).
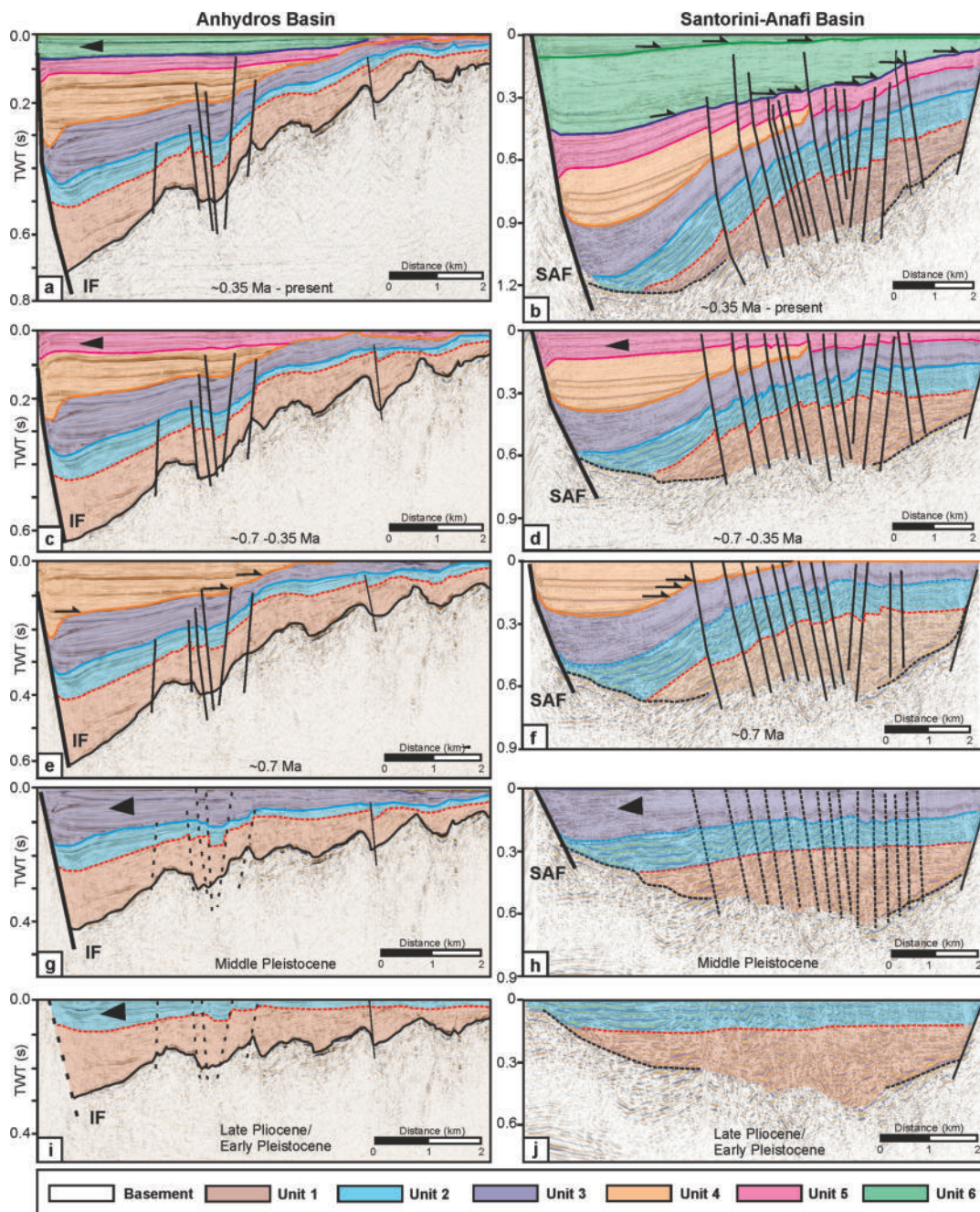
FIGURE 6.4: Reconstruction of the Anhydros Basin (a, c, e, g, i) and the Santorini-Anafi Basin (b, d, f, h, j) by successively flattening the top of each Unit in Figures 6.2b, c. Arrows indicate onlap termination and triangles indicate divergence. Approximate ages of the seismostratigraphic units are from Preine et al. (2022a). SAF: Santorini-Anafi Fault; IF: Ios Fault.

In contrast to the Anhydros Basin, the Santorini-Anafi Basin was highly active during deposition of Units 5 and 6. As shown in Figures 6.2b, c, and 6.4b, Unit 6 is very thick in the Santorini-Anafi Basin while being very thin on the shoulders of the basin. At the top of Unit 6, we identify indications for a recent tectonic event that is marked by the uppermost subunit U6-a, which comprises a set of high-amplitude reflections that contrast with the weakly reflective nature of the rest of Unit 6 (Fig.

6.4b). Internal reflections onlap horizon u6-a indicating that this uppermost subunit might represent a very recent tectonic pulse (Fig. 6.4b). We identify this uppermost subunit U6-a only in the eastern Santorini-Anafi Basin in Profiles B and C and in the Amorgos Basin in Profile C (Fig. 6.2a and 6.2c). This indicates that tectonic deformation in the most recent phase focused on the eastern Santorini-Amorgos Tectonic Zone. Recent tectonic deformation in this area has been underlined by the 1956 Amorgos earthquake whose epicenter has been associated with the Amorgos Fault (Fig. 6.1c) (Nomikou et al., 2018b). However, our seismostratigraphic framework does not allow us to place this unconformity into the age model from Preine et al. (2022a) to tie down the onset of this most recent tectonic pulse.

In addition to that, we identify indications for a major tectonic pulse at the transition of Units 5 and 6 due to the distinct onlap termination of the internal reflections of Unit 6 towards the underlying unconformity h6, which has a markedly different dip (Fig. 6.4b). The irregular high-amplitude reflections at the base of Unit 6 indicate that this tectonic pulse was accompanied by a high-energetic erosional event (Fig. 6.4b) (Preine et al., 2020). In addition, many internal faults have much lower displacements above h6 (< 5 ms TWT / ~5 m) than below it (> 20 ms TWT / ~22 m) indicating that either internal faulting has ceased mostly after the deposition of h6, or that subsequent deposition occurred very rapidly in relation to the rate of faulting. Assuming an age of ~0.36 Ma for unconformity h6 (Preine et al., 2022a) implies a rapid deposition of Unit 6 with sedimentation rates in the order of ~1 m/kyr, which is approx. 5 to 10 times the measured sedimentation rates of the Quaternary across the CSK volcanic rift zone (Anastasakis and Piper, 2005; Piper and Perissoratis, 2003; Kutterolf et al., 2021b). Such enhanced sedimentation rates have also been proposed by previous studies (Piper and Perissoratis, 2003; Perissoratis, 1995) for the Santorini-Anafi region and could be explained by assuming that the Santorini-Anafi Basin has been a major depocenter for volcanoclastic material from Santorini, which has been highly active during the last 0.36 Ma producing the vast Thera Pyroclastic Formation (Druitt et al., 1999). Therefore, the complex internal reflections of Unit 6 in the Santorini-Anafi Basin (Fig. 6.2c, 6.4b) could represent volcanoclastic infill deposits e.g. from pyroclastic flows or remobilized volcanoclastic material.

During deposition of Unit 5, the Santorini-Anafi Fault remained active as indicated by a distinct thickening of the strata towards the NW (Fig. 6.4d). As shown in Figure 6.2b, a major slump deposit is intercalated within Unit 5, which seems to be associated with the activity of the Santorini-Anafi Fault highlighting pronounced tectonic activity during that time. Similar to the Anhydros Basin, we observe that the internal reflections of Unit 4 appear perfectly flat and clearly onlap the underlying unconformity h4 after flattening horizon h5 (Fig. 6.4f). This underlines the concept of a major tectonic pulse happening before the deposition of the mass-transport deposits of Unit 4 (Fig. 6.4f). In contrast, Unit 3 below shows significant divergence towards the Santorini-Anafi Fault indicating that this fault was continuously active during deposition of Unit 3 (Fig. 6.4h). Notably, the offsets between internal faults are mostly leveled after flattening horizon h3, which suggests that these faults formed after the deposition of Unit 3 (Fig. 6.4h). Unit 2 lies flat in the Santorini-Anafi Basin, while Unit 1 seems to be thickening towards the SW, although its internal architecture is difficult to properly image (Fig. 6.4j).

6.5.2 Volcano-Tectonic Evolution of the CSK Rift Zone

Figure 6.5 shows a sketch of the volcano-tectonic evolution of the CSK rift zone as interpreted from our seismostratigraphic framework. Fault activity is inferred from observed thickness differences at individual faults. Ages of different seismostratigraphic Units and the spatio-temporal evolution of the CSK volcanic centers are based on Preine et al. (2022a), whose four major volcanic phases occurred during the deposition of Units 2, 3, 5, and 6 (see Fig. 6.1b for an overview). The lowermost Unit 1 represents the deposits of Early Pliocene marine ingression across the southern Aegean and is considered pre-volcanic (Preine et al., 2022a) (Fig. 6.5a). Our mapping shows that this unit has been deposited in a complex environment with two roughly WNW-ESE striking depocenters in the Christiana Basin and east of the Anhydros Islet (Fig. 6.5a). This fault trend fits the general E-W trend that has been proposed for the Pliocene basins of the southern Aegean (Fig. 6.5a) (e.g. Anastasakis and Piper, 2005; Piper et al., 2007)). Both depocenters are separated by a broader NNE-SSW trending zone, which underlies the present-day centers of Kolumbo and the Kolumbo volcanic chain (termed 'proto-Anhydros Basin', in accordance with Heath et al. (2019)). The presence of a deep proto-Anhydros Basin is supported by deep P-wave seismic tomography indicating that a NE-SW striking basin existed underneath present-day Santorini, Kolumbo, and Christiana (Heath et al., 2019).
Assuming that the dominant extension during that time was oriented NNE-SSW (Fig. 6.5a), implies that this basin might have acted as a transfer zone between WNW-ESE trending fault systems. Similar north-south trending transfer zones have been observed at other centers of the Hellenic Volcanic Arc, e.g. at Milos (Anastasakis and Piper, 2005) or Nisyros (Papanikolaou and Nomikou, 2001), and have also been suggested for Santorini (Piper et al., 2007; Heath et al., 2019). This depocenter might have been a dextral pull-apart basin that accommodated N-S directed strain between the basins west and east of present-day Santorini (Fig. 6.5a). However, the volcanic overprint in the Anhydros Basin prohibits a detailed analysis of fault geometries (e.g. Fig. 6.2a).
During the deposition of Unit 2 in the Late Pliocene / Early Pleistocene, volcanism initiated with the emergence of the Christiana Volcano (Fig. 6.5b) (Preine et al., 2022a). During this time, the Christiana Basin continued to be a major WNW-ESE-oriented depocenter, and the distinct thickening towards Christiana observed in Figure 6.3b represents the volcanoclastic deposits exported from Christiana (Fig. 6.5b). Our mapping of Unit 2 indicates that the Christiana Basin terminates against an NNE-SSW trending boundary (Fig. 6.3a, 6.5e), which fits the trend of the proto Anhydros Basin mapped northeast of Santorini. This can be seen as an indication of a continuation of the proto-Anhydros Basin underneath Santorini as indicated by dotted, orange lines in Figure 6.5b delineated from p-wave tomography (Heath et al., 2019). This fits the trend of our reflection seismic mapping of a proto-Anhydros Basin well. Furthermore, Heath et al. (2019) proposed that the volcanism at Christiana might have been localized by the intersection of the proto Anhydros Basin and the Christiana Basin, which is in agreement with our analysis.
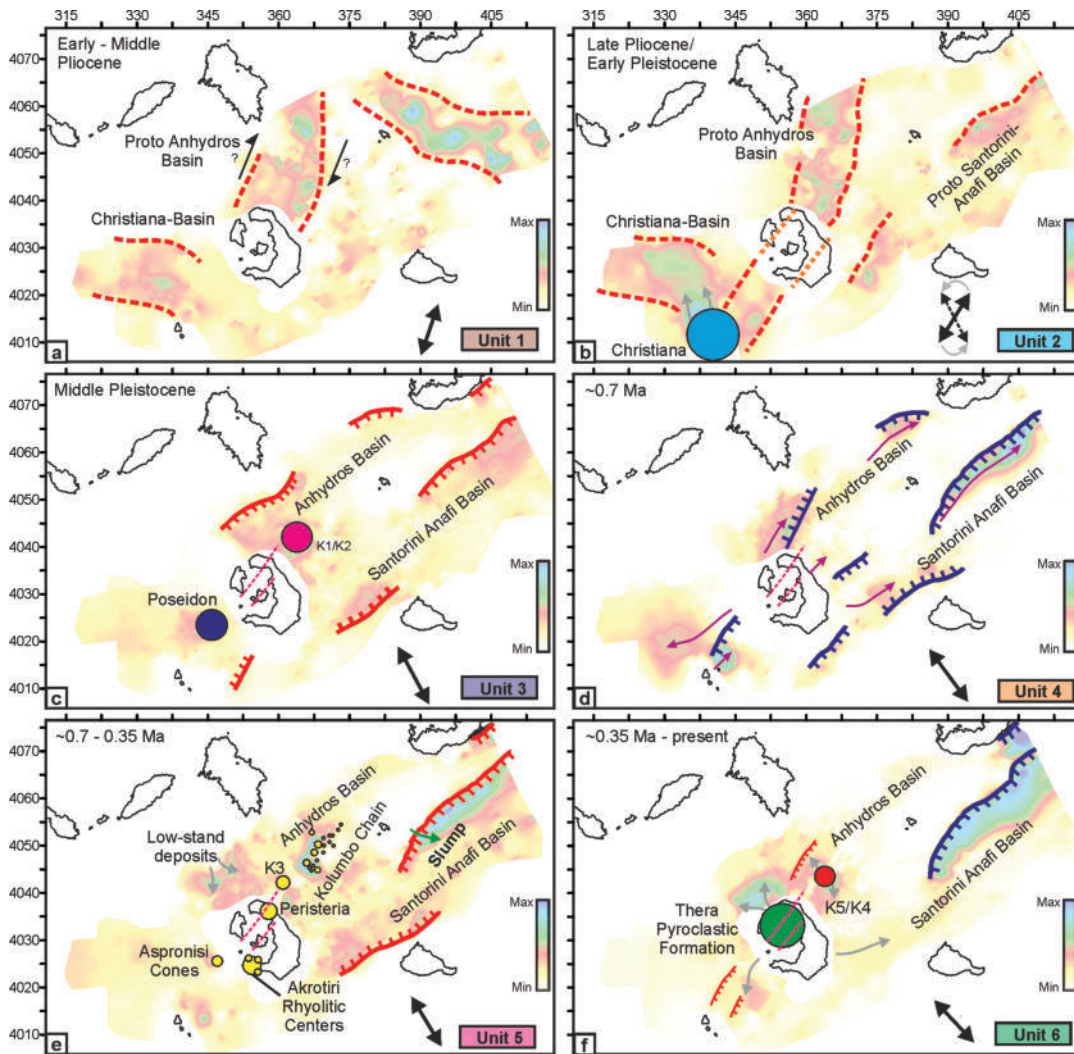
FIGURE 6.5: Schematic reconstruction of the volcano-tectonic evolution of the CSK rift zone. Isochore maps from Figure 3 are plotted in the background. Red toothed lines indicate faults active during deposition of each phase. Blue lines indicate faults that have been affected by tectonic pulses. Dashed lines indicate the outline of depocenters with higher uncertainty. Dashed orange lines indicate the outline of the proto-Anhydros Basin underneath Santorini as defined in Heath et al. (2019). Activity of volcanic centers modified from Preine et al. (2022a). Black arrows indicate approx. direction of extension as inferred from the interpreted faults. Black arrows in F indicate the potential strike-slip movement of the Proto Anhydros Basin. Thin grey arrows indicate the direction of transport of volcanoclastic material and purple arrows indicate the direction of mass-wasting events (Preine et al., 2022b).

East of Santorini, we identify two NE-SW directed depocenters, which we interpret as the early representations of the present-day Santorini-Anafi Basin ('proto Santorini-Anafi Basin', Fig. 6.5b). These depocenters lie parallel to the present-day faults of the SATZ, which suggests that Unit 2 marks a transitional phase where the stress regime rotated counterclockwise from NNE-SSW to NNE-SSE (Fig. 6.5b). Given that the ESE-WNW oriented Pliocene basin mapped with Unit 1 east of Anhydros (Fig. 6.5a) is no longer identifiable in Unit 2, the tectonic nature of the proto

Anhydros Basin during that time remains elusive.

During deposition of Unit 3, the second volcanic phase emerged with the evolution of the early Poseidon and Kolumbo volcanic centers (Fig. 6.5c) (Preine et al., 2022a). Our data clearly show that during that time, NE-SW-oriented depocenters became dominant throughout the entire SATZ including activity of the eastern Santorini-Anafi Fault, the eastern Anhydros Fault, and the Anafi Fault (Fig. 6.4d). This activity seems to have been continuous as indicated by the divergence observed within Unit 3 in the Anafi, Santorini-Anafi and Anhydros Basins (Fig. 6.2, 6.2b, 6.2c, 6.4g, 6.4h). The Poseidon and Kolumbo centers aligned parallel to this new fault trend implying a significant influence of this newly emerging NE-SW-oriented tectonic trend on the magma emplacement. This early NE-SW alignment of volcanic centers could represent an early expression of the present-day Kameni and Kolumbo Lines (dashed line in Fig. 6.5c), which consequently are deep-rooted, old volcano-tectonic lineaments (Preine et al., 2022a).

Initiated by an extensive rift pulse that affected the entire rift system, vast amounts of volcano-sedimentary material from Unit 4 were deposited in the basins surrounding Santorini (Fig. 6.4c; Preine et al. (2022b)). During the deposition of Unit 5 (∼0.7 – 0.36 Ma), volcanism occurred along the entire Christiana-Santorini-Kolumbo field and included the emergence of the Aspronisi cones, the Kolumbo volcanic chain, Kolumbo's Unit K3 as well as the evolution of the Akrotiri rhyolitic centers, the Peristeria stratovolcano, and the Akrotiri cinder cones onshore Santorini (Fig. 6.5e)(Druitt et al., 1999; Preine et al., 2022a). We argue the preceding rift pulse and subsequent mass-wasting cascade had a major impact on the volcanic system due to crustal fracturing in combination with unloading, leading to wide-spread magmatic ascent. The formation of approximately linearly arranged volcanic cones could be related to intra-basinal fault systems such as those observed in the Santorini-Anafi Basin (Fig. 6.2c), which have formed mainly during deposition of Units 3 to 5.

We observe that during deposition of Unit 5, the eastern Santorini-Anafi and Amorgos Faults were continuously active as highlighted by the syn-tectonic growth strata recorded in the sedimentary basin infills (Fig. 6.4c, 6.4d, 6.5e). This continuous activity led to a major slumping event south of the Anhydros Islet as imaged in Profile B (Fig. 6.2b, 6.5e). In addition to that, we identify a depocenter north of Santorini that is not related to any tectonic or volcanic activity but represents a wedge of low-stand deposits likely related to Pleistocene sea-level lowstands (e.g., Marine Isotope Stages 12 and/or 16; see Figure C.2 for an example) Lisiecki and Raymo (2005) (Fig. 6.5e).

After the deposition of Unit 5, another distinct change in the volcano-tectonic system occurred (Fig. 6.4a). At the transition from Unit 5 to 6, volcanism became highly explosive producing the vast Thera Pyroclastic Formation (Druitt et al., 1999; Preine et al., 2022a). During that time also Kolumbo remained active producing two major eruptions (K4/K5). Our seismostratigraphic framework shows that the transition from Unit 5 to 6 is marked by another major tectonic pulse that affected the eastern Santorini-Anafi Basin as indicated by the angular unconformity h6 (Fig. 6.2b, 6.2c, 6.4b). The here proposed h6-rift pulse is in line with a recent study by Flaherty et al. (2022), who showed that a change in melt diversity of the eruptive products of Santorini occurred between ∼360 and 225 ka. This indicates that this tectonic event influenced the deep volcanic plumbing system underneath Santorini e.g. by affecting stresses in the deeper crust and, thus, changing fluxes and proportions of primitive melts from deep supply regions (Flaherty et al., 2022).

In addition, during deposition of Unit 6, the complex Kolumbo and Christiana faults also remained active in the vicinity of Santorini (Fig. 6.5f). However, both show

only minor throws (< 100 m) that decrease from the base of Unit 6 towards the top (Preine et al., 2022b). Furthermore, the tilted uppermost subunit U6-a observed in the eastern basins (Fig. 6.2c) points to yet another recent rift pulse within the eastern Santorini-Anafi Basin. While our seismostratigraphic framework does not allow dating this unconformity, it is noteworthy that another distinct change in melt chemistry of Santorini volcanism occurred 22 ka ago during the caldera-forming Cape Riva eruption (Flaherty et al., 2022). This could correspond to the observed recent tectonic pulse in the eastern SATZ, in which case the age of subunit U6-a would fit the estimated age of Unit A1 from Perissoratis (1995), who correlated related their uppermost seismostratigraphic Unit A1 to the Last Glacial Maximum indicating an approx. age of 20.000 years. However, such temporal correlations remain speculative and the change in melt chemistry after the Cape Riva eruption could also be explained by temporal variations in the supply of slab-derived melts and fluids as well as by caldera collapse (Flaherty et al., 2022).

6.5.3   Volcano-Tectonic Feedback Mechanisms

Having established the temporal correlation of changes in the tectonic system and volcanic behavior, the question remains, whether the tectonic changes triggered the modifications in the volcanic system or vice versa. To answer this with certainty, exact age relations between rifting events and volcanic eruptions are required, which is beyond the temporal resolution of our seismostratigraphic age models. However, there are several reasons to argue that changes in the tectonic system have preceded changes in the volcanic system and, thus, played an important role in the evolution of the CSK volcanic field.

1. The spatial correspondence of the Pliocene proto Anhydros Basin and the major centers of the CSK volcanic field suggests that this early basin represented an initial zone of crustal weakness that facilitated magma ascend. As discussed above, this initial basin seems to have acted as a dextral transfer zone between the WNW-ESE trending depocenters. The spatial correlation between transfer zones and magmatism has been highlighted in previous studies at other volcanoes (Faulds and Varga, 1998; Corti et al., 2003, e.g.[). In the case of the CSK volcanic field, it is noteworthy that the proto Anhydros Basin existed prior to the emplacement of volcanic edifices, which is in contrast to the concept that magmatism causes the formation of transfer zones at the CSK rift as observed in other regions (Faulds and Varga, 1998).

2. Chrono-stratigraphic relations indicate that the evolution of the Poseidon and early Kolumbo centers occurred approx. in the middle of the deposition of Unit 3 (Preine et al., 2022a), which has been deposited under the influence of the newly emerging NE-SW striking fault system (Fig. 6.5c). According to our study the initiation of these faults preceded the emplacement of Poseidon and early Kolumbo volcanism and continued afterward. This suggests that the NE-SW-directed faults guided magma ascent leading to the evolution of the Poseidon and early Kolumbo centers. 3. A major tectonic reorganization occurred at ∼0.7 Ma and preceded the evolution of the widespread emergence of volcanic edifices during deposition of Unit 5. As mentioned above, the sudden fracturing of the Aegean crust during this rift pulse might have generated pathways for the emplacement of volcanic edifices, which follow the NE-SW-directed tectonic trend (Preine et al., 2022a).

4. Our seismostratigraphic framework indicates that the rift pulse at ∼0.36 Ma preceded the deposition of large amounts of volcanoclastic material from Santorini and Kolumbo, indicating that the tectonic change again influenced the volcanic behavior of the CSK rift zone. In this case, this tectonic pulse has been accompanied by a distinct change in melt diversity of the eruptive products of Santorini that might be related to changes in the stresses in the deeper crust (Flaherty et al., 2022).

On the other hand, it is important to note that the non-volcanic basins of the CSK rift zone are characterized by well-defined half-graben and pronounced marginal faults (e.g. at the Santorini-Anafi Basin, the eastern Anhydros Basin, and the Amorgos Basin) with throws of more than 2000 m (Fig. 6.1c, 6.3) (Nomikou et al., 2018b), while the basins hosting the CSK volcanoes (the western Anhydros Basin and the Christiana Basin) lack such distinct tectonic features (Fig. 6.1c, 6.2a). Instead, they are influenced by more complex faults such as the Kolumbo Fault or the Christiana Fault (Fig. 6.5f) (Preine et al., 2022b), which have much lower throws (< 100 m). Also, faults observed within the Thera Pyroclastic Formation in the caldera of Santorini have only minor throws (< 100 m) (Drymoni et al., 2022).

Recent findings by Acocella and Trippanera (2016) offer potential explanations. These authors suggest that amagmatic faulting becomes essentially hindered by the emplacement of dikes, e.g. in Iceland (Acocella and Trippanera, 2016), the northern Ethiopian rift (Keir et al., 2006), and the Costa Rica rift (Wilson et al., 2019), where a competition between magmatic and tectonic strain accommodation has been identified (Corti et al., 2003). Numerous dikes have been identified at the cliffs of Santorini (Drymoni et al., 2020; Drymoni et al., 2022) and also inside the crater of Kolumbo (Nomikou et al., 2012), which are roughly NE-SW aligned (Heath et al., 2019). In addition, the presence of the low-velocity body underneath the northern caldera basin and Kolumbo in 3 to 5 km depth implies that the shallow crust is strongly overprinted by magmatism (Hooft et al., 2019; Heath et al., 2019; McVey et al., 2020; Schmid et al., 2022). The numerous occurrence of magmatic intrusions combined with the concept by Acocella and Trippanera (2016) may suggest that magmatism has accommodated much of the local strain along the proto Anhydros Basin, while the non-volcanic basins accommodated strain by extensive hanging-wall rotation and internal deformation.

Considering that the early volcanic centers of Kolumbo and Poseidon aligned parallel to the NE-SW directed fault trend in Early Pleistocene, magmatic intrusions have likely been abundant along the deeper subsurface throughout the CSK rift zone since the onset of extensive NE-SW directed faulting in Early Pleistocene. An example of the presence of shallow intrusions is the saucer-shaped reflection underneath the Kolumbo Volcanic Chain in Profile A (Fig. 6.2a), which is an indication of sill intrusions (Planke et al., 2005). We propose that the early evolution of large-scale magmatic intrusions since Middle Pleistocene (during deposition of Unit 3) has hindered the formation of extensive marginal faults at Santorini, the western Anhydros Basin, and the Christiana Basin as observed in the other amagmatic basins.

Consequently, our study suggests sensitive volcano-tectonic feedback mechanisms at the CSK rift zone, in which large-scale tectonics seem to have a primary influence both on the evolution of the rift basins and the emplacement of volcanism while, in turn, magmatism seems to have a secondary influence, essentially hindering the evolution of large-scale faults along the CSK volcanic field.

6.5.4 Implications for the Evolution of the Hellenic Arc

While reconstructions of the tectonic evolution of the Hellenic Arc have been presented on broad time scales since Oligocene (e.g. Royden and Papanikolaou, 2011; Jolivet and Brun, 2010; Jolivet et al., 2013; Jolivet and Faccenna, 2000), detailed studies of the tectonic and volcanic evolution of the Arc during the last ~4 Million years are missing so far. However, a few regional studies are available, which enable a qualitative comparison of broader volcano-tectonic changes along the Hellenic Arc since the Pliocene.

Since the volcano-tectonic evolution can be subdivided into distinct phases, it is unclear whether these relate to the local manifestation of the evolving stress regime or to general trends affecting the entire Hellenic Arc. As a proxy for the general tectonic evolution of the eastern Hellenic Arc, Van Hinsbergen et al. (2007) investigated the Plio-Pleistocene tectonic history of the island of Rhodos in the southeastern Aegean Sea (Fig. 6.6) and identified four major tectonic episodes. The first episode occurred between 3.8 and 3.6 Ma and led to a $9 \pm 6°$ counterclockwise rotation of Rhodos (Fig. 6.6a). A second episode occurred between 2.5 and 1.8 Ma tilting Rhodos to the SE while between 1.5 and 1.1 Ma Rhodos tilted to the NW (Fig. 6.6a). The last tectonic phase started at approx. 0.8 Ma when counterclockwise rotation initiated again (Fig. 6.6a). Counterclockwise rotation also affected the western margin of the Rhodos Basin as shown by seismic studies (Fig. 6.6b) (Hall et al., 2009) and has generally been suggested to be the result of the increasing curvature of the Hellenic Arc (Veen and Kleinspehn, 2002). Figure 6.6a shows that the ages of the tectonic events on Rhodos correspond to those of several major unconformities of the CSK rift.

The first counterclockwise rotation event of Rhodes corresponds roughly to the age of unconformity h2 (~3.4 Ma), i.e., the transition from E-W to NE-SW directed extension (Fig. 6.6). The initiation of the second episode of counterclockwise rotation on Rhodes occurred approx. simultaneously to the first tectonic pulse of the CSK rift (~0.7 Ma) indicating that these events represent large-scale tectonic reorganizations affecting the entire southeastern Aegean. Figure 6.6a also shows that both tilting episodes on Rhodos occurred approx. simultaneously to the volcanic activity of Christiana as well as the activity of the Poseidon center and early Kolumbo, suggesting an influence of the arc-wide tectonic regime on the volcanism of the Hellenic Arc. This hypothesis is further supported by comparing the evolution of the CSK volcanic field with that of the Kos-Nisyros-Yali complex on the eastern Hellenic Volcanic Arc (Fig. 6.6). The earliest volcanic activity of the Kos-Nisyros-Yali volcanic complex built dome complexes on southern Kos between 3.4 and 1.6 Ma (e.g. Vougioukalakis et al., 2019) approx. during the same time as Christiana was active and Rhodos tilted first (Fig. 6.6a). Subsequently, volcanic activity became more explosive as demonstrated by the Kefalos Tuff ring that was formed about 0.5 Ma and by the 0.161 ka Kos Plateau Tuff eruption representing one of the largest known explosive eruptions of the Hellenic Arc, which involved a major caldera collapse south of Kos (e.g. Allen et al., 2019; Bachmann et al., 2010). Within the last 100 ka, there were at least two major eruptions with estimated tephra volumes exceeding 10 km3 (Nisyros 1 and Yali 2; Kutterolf et al. (2021b)).
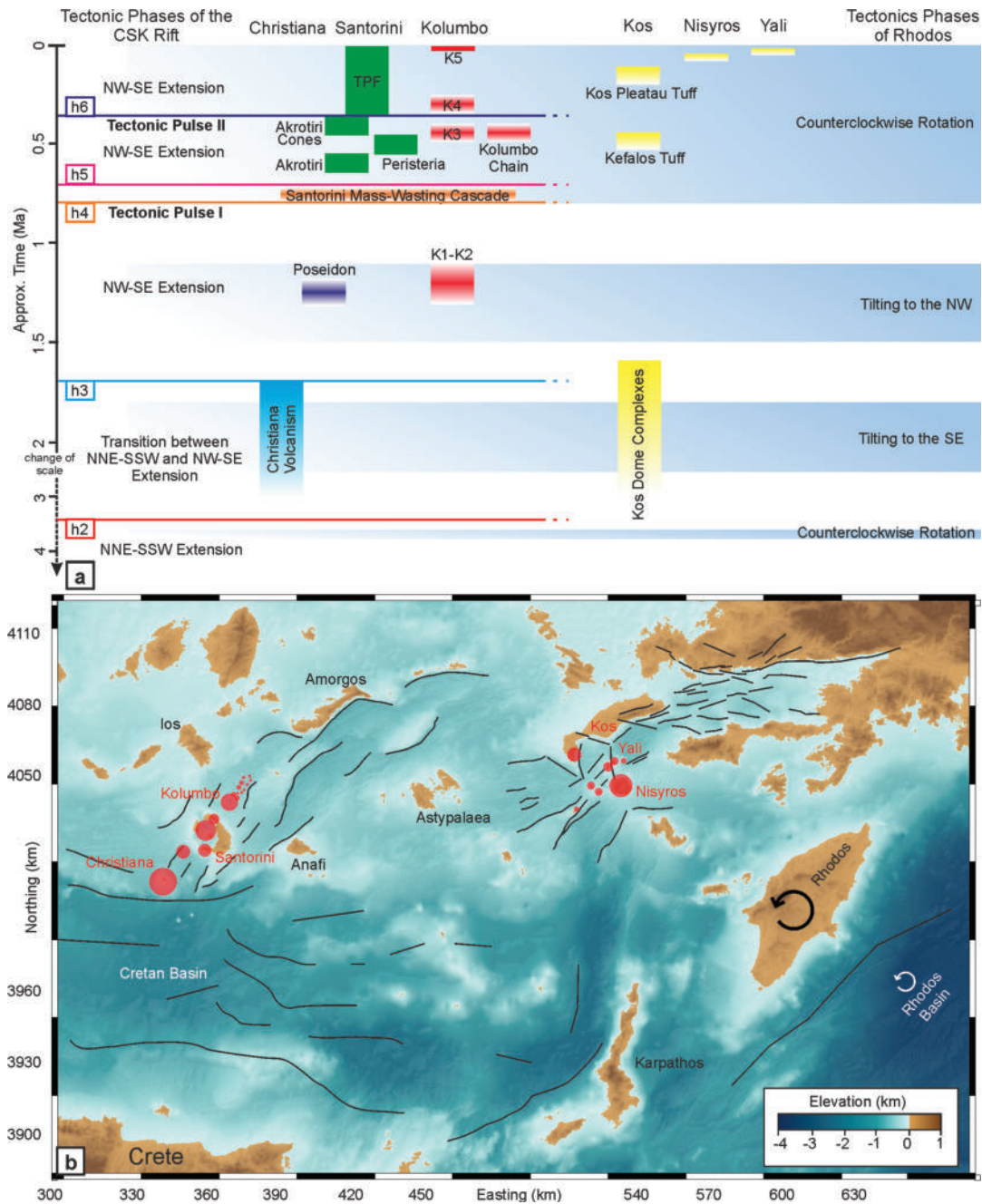
FIGURE 6.6: a) Schematic illustration of the chronology of volcanism and tectonics of the southeastern Aegean Sea. Tectonic phases of the CSK rift are from this study, volcanic ages of the CSK volcanic field from Preine et al. (2022a), volcanic ages of the Kos-Nisyros-Yali Complex from Vougioukalakis et al. (2019) as well as Kutterolf et al. (2021b), and tectonic phases of Rhodos from Van Hinsbergen et al. (2007). b) Morphological map of the southeastern Aegean Sea with volcanic centers marked in red. Major tectonic lines of the CSK field and the Kos-Nisyros-Yali complex are marked in black and have been modified from Nomikou et al. (2013) and Nomikou et al. (2018b) and Preine et al. (2022b). Additional faults have been modified from Ganas et al. (2013).

The similar NE-SW orientation of volcanic and tectonic structures of the Kos-Nisyros-Yali complex (e.g. Tibaldi et al., 2008; Papanikolaou and Nomikou, 2001; Nomikou and Papanikolaou, 2011; Nomikou et al., 2018a; Nomikou et al., 2013) and the CSK field, as well as the general trend from largely effusive volcanism in Late Pliocene / Early Pleistocene toward highly explosive volcanism in Late Pleistocene, highlights volcano-tectonic similarities of both systems (Fig. 6.6a). In addition, Figure 6.6 shows that discrete phases of counterclockwise rotation and tilting at Rhodos correspond not only to distinct phases of volcanism at the CSK field but also at the Kos-Nisyros-Yali complex indicating regional-scale volcano-tectonic feedback links. Similar to the observations of Flaherty et al. (2022) of a distinct change of primitive melt chemistry after the tectonic pulse at ∼0.36 Ma at the CSK field, each of the previous large-scale tectonic episodes may have influenced the stress in the deeper crust of the broader southeastern Aegean changing fluxes as well as proportions of primitive melts from deep magma reservoirs. Such large-scale volcano-tectonic feedback links have hardly been explored so far and the Hellenic Arc offers the opportunity to derive a spatio-temporal reconstruction of an entire Arc System. However, systematic seismic studies are required for this, which are lacking for most parts of the southern Aegean Sea. This is needed to gain a more holistic understanding of volcano-tectonic processes at an arc scale and to improve hazard assessments of the densely populated pan-Aegean realm.

6.6   Conclusions

In this study, we have for the first time consistently linked the evolution of the volcanoes of the Christiana-Santorini-Kolumbo (CSK) volcanic field to the tectonic evolution of the hosting rift basins. Our study shows that distinct volcanic phases correlate with major changes in the tectonic behavior of the rift system. According to our interpretation, a Pliocene NNE-SSW-directed proto basin existed underneath Kolumbo, the Kolumbo volcanic chain, and continued underneath Santorini towards Christiana. This basin acted as a transfer zone between WNW-ESE-oriented Pliocene basins. Volcanism initiated with the onset of NW-SE-directed rifting, which became the main orientation of the emplacement of volcanic edifices in the Pleistocene. Distinct tectonic pulses preceded major changes in the volcanic evolution of the CSK volcanic field. A major rift pulse at approx. 0.7 Ma triggered large-scale mass wasting events, which initiated the emergence of widespread volcanism. Another large-scale tectonic pulse occurred at approx. 0.36 Ma, which corresponds to a distinct shift of Santorini's volcanism marking the transition from effusive to highly explosive eruptions. This transition also corresponds to a change in primitive melt chemistry at Santorini implying deep-seated feedback mechanisms between the regional tectonic regime and the volcanic plumbing system of the CSK field.

We argue that the incremental tectonic reorganizations of the rift might be related to the increasing curvature of the Hellenic Arc that induced counterclockwise rotation and enhanced internal deformation along the entire southeastern Aegean. Vice-versa, our analysis indicates that magmatism at the CSK volcanic field might have hindered the formation of major marginal faults along the CSK volcanic field, which define the morphology of the non-volcanic basins of the rift system. Consequently, the CSK volcanic field reveals volcano-tectonic feedback links in which regional tectonics seem to have had a primary influence on both basin evolution and emplacement of volcanoes, while subsequent magmatism seems to have had a secondary

influence on the tectonic system by accommodating extensional strain in the volcanic basins. Understanding such volcano-tectonic feedback mechanisms is critical to improving future hazard assessments for the Aegean and we strongly encourage similar seismic studies to be conducted for the neighboring volcanic centers of the Hellenic Arc to reconstruct their volcano-tectonic evolution.

Acknowledgments

Open Research

SEG-Y files of the seismic lines shown in Figure 6.2 are available in the Marine Geoscience Data System with data DOI: 10.26022/IEDA/331028.

Chapter 7

Spatio-Temporal Evolution of the Kolumbo Volcanic Chain and its Link to the Volcanic Plumbing System of Santorini

Abstract

The Christiana-Santorini-Kolumbo volcanic field in the southern Aegean Sea is one of the most hazardous volcanic regions in the world. Forming the northeastern part of this volcanic field, the Kolumbo Volcanic Chain (KVC) comprises more than 20 submarine volcanic cones. However, due to their inaccessibility, little is known about the spatio-temporal evolution and tectonic control of these submarine volcanoes and their link to the volcanic plumbing system of Santorini. In this study, we use multichannel reflection seismic imaging to study the internal architecture of the KVC and its link to Santorini. We show that the KVC evolved during two episodes, which initiated at ~1 Ma with the formation of mainly effusive volcanic edifices along a NE-SW trending zone. The cones of the second episode were formed mainly by submarine explosive eruptions between 0.7 and 0.3 Ma and partly developed on top of volcanic edifices from the first episode. We identify two prominent normal faults that underlie and continue the two main trends of the KVC, indicating a direct link between tectonics and volcanism. In addition, we reveal several buried volcanic centers and a distinct volcanic ridge connecting the KVC with Santorini, suggesting a connection between the two volcanic centers in the past. This connection was interrupted by a major tectonic event and, as a result, the two volcanic systems now have separate, largely independent plumbing systems despite their proximity.

Plain Language Summary

In the central Aegean lies the Christiana-Santorini-Kolumbo volcanic system, one of the most volcanically and seismically active regions in Europe. Santorini has had over 200 eruptions in the last 360,000 years. Only 7 km northeast of Santorini lies the underwater volcano Kolumbo, as well as over 20 other smaller underwater volcanoes that form the Kolumbo Volcanic Chain, which have only had 2 major eruptions during this time. In this study, we investigate the history of this volcanic system to understand its relation to Santorini and why volcanoes located so closely together behave so differently. Using seismic reflection data image the internal architecture of the Kolumbo Volcanic Chain and show that it evolved in two episodes along two prominent faults that might continue underneath Santorini. We also identify

a volcanic ridge that lies between Santorini and Kolumbo, indicating a connection between the two systems. Our study suggests that Santorini and the Kolumbo Volcanic Chain evolved as one system in the geological past, but became disconnected from each other during a major tectonic event about 300,000 years ago.

7.1　Introduction

Violent explosive eruptions at volcanic arcs account for ∼95 % of all eruption-related fatalities since 1600 CE, many associated with eruptions of coastal or marine volcanoes (e.g., Krakatau, or Tambora; Auker et al. (2013) and Brown et al. (2017)). As recently demonstrated by the 2022 eruption of Hunga Tonga–Hunga Ha-apai, seawater interaction during shallow eruptions is capable of producing violent phreatomagmatic explosions that generate ocean-scale tsunamis (Carvajal et al., 2022; Lynett et al., 2022). In arc settings, magma is generated by partial melting of the mantle above the subducting slab, and its ascent to the surface is governed by thermodynamic conditions within the crust (e.g. Cashman et al., 2013). Volcanic plumbing systems represent a complex network of vertically extensive melt reservoirs at different depths, developed over long timescales during the growth of a volcano (e.g. Tibaldi and Bonali, 2017). At shallow depths, magma rises along faults and fractures influenced by the regional tectonic stress state, which can lead to the formation of volcanic lineaments (e.g. Tibaldi, 1995). Magma path orientation can be stable over long time scales but modifications in the tectonic stress regime, such as from large earthquakes or modifications in volcano morphology, can influence the volcanic plumbing system (e.g. Hill et al., 2002). This can lead to temporal changes in the eruptive style of individual volcanoes or over short distances from one volcano to another (e.g. Hill et al., 2002).

Investigating the spatio-temporal evolution of the orientation of volcanic plumbing systems is important for understanding the behavior of active volcanoes (e.g. Tibaldi and Bonali, 2017). Being hidden beneath the surface, the deep structure and temporal evolution of volcanic plumbing systems can only be assessed on the basis of geochemical constraints (e.g. Druitt et al., 2012), by studying eroded volcanoes (e.g. Tibaldi et al., 2013) or indirectly via geodetic monitoring (e.g. Bato et al., 2018). However, these methods are difficult to apply to submarine volcanoes due to their inaccessibility for direct sampling and monitoring (Carey and Sigurdsson, 2007; Mitchell, 2012). Here, geophysical methods are required, and recent advances in seismic tomography and full-waveform inversion enable the imaging of shallow melt reservoirs underneath active volcanoes (e.g. Paulatto et al., 2022), but often lack the resolution required to reconstruct the temporal evolution of the system. This critical observational gap can be addressed by high-resolution multichannel seismic imaging, which provides structural images of the subsurface that can be used to reconstruct the relative spatio-temporal evolution of submarine volcanic systems (e.g. Preine et al., 2022a).
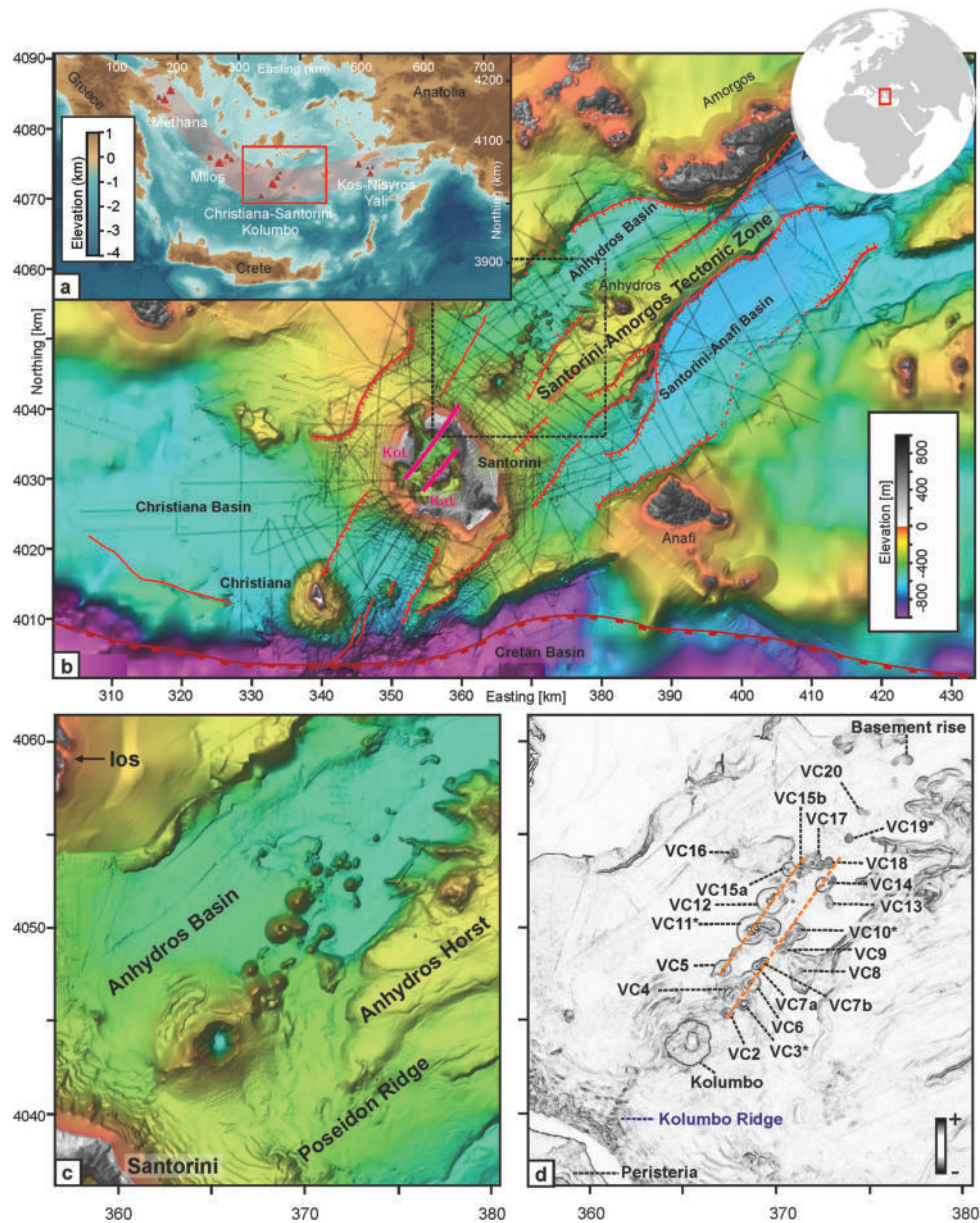
FIGURE 7.1: (a) Regional map of the southern Aegean Sea showing the Hellenic Volcanic Arc (shaded red) with volcanic centers marked by red triangles. The coordinate system here (and in subsequent maps) is UTM Zone 35N, WGS84 datum. The red box indicates the study area shown in (b). (b) Morphological map of the CSK rift zone showing islands, basins, volcanic centers, and major extensional structures (red lines), after Nomikou et al. (2016, 2018, 2019) and Preine et al. (2022b). Grey lines indicate all available seismic profiles. KaL: Kameni Line; KoL: Kolumbo Line (after Heath et al. (2019)). Bathymetry from Nomikou et al. (2012, 2013, 2018, 2019) and Hooft et al. (2017). (c) Close-up of the western Anhydros Basin showing the KVC and major structural elements. Color scale same as (b). (d) Profile curvature from the bathymetric map shown in c. Volcanic cones are labeled according to Nomikou et al. (2012) and Hooft et al. (2017). Asterisks indicate cones with summit craters. A northeast-trending ridge identified in this study is labeled *Kolumbo Ridge*. Orange lines indicate the two main trends of the KVC.

One of the few areas worldwide, where crustal-scale and high-resolution geophysical data as well as detailed petrological analyses are available, is the Christiana-Santorini-Kolumbo (CSK) volcanic field in the southern Aegean Sea (Fig. 7.1) (Nomikou et al., 2019). This 60-km-long volcanic field has produced over 200 eruptions in the last 360 thousand years, including the famous Minoan eruption of Santorini 1600 BCE (e.g. Druitt et al., 1999; Satow et al., 2021; Nomikou et al., 2016a). Located only 7 km northeast of Santorini lies the submarine Kolumbo volcano, which last erupted in 1650 CE, causing ∼70 fatalities on Santorini and generated a tsunami that inundated the nearby Cycladic islands (Fouqué, 1879; Cantner et al., 2014; Karstens et al., In Review_A). This eruption created a 500 m deep and 1500 m wide crater, which hosts an active hydrothermal vent field (Carey et al., 2011; Carey et al., 2013; Fuller et al., 2018). Kolumbo consists of five vertically stacked volcanic units (Hübscher et al., 2015) and is the largest volcano of the Kolumbo Volcanic Chain (KVC), which itself consists of more than 20 submarine volcanoes that are aligned along two NE-SW striking lineaments 16 km northeast of Kolumbo (Nomikou et al., 2012; Hooft et al., 2017).

Since the entire CSK field lies in the same regional rift system, it is subject to a common external tectonic control (e.g. Heath et al., 2019; Heath et al., 2021; Preine et al., 2022c). There is an ongoing discussion regarding the role of regional (> 10 km length) and local (< 10 km length) faults on the emplacement of volcanic features (Hübscher et al., 2015; Heath et al., 2021) and regarding the connection of the plumbing system between the different volcanic centers. While geochemical analyses of the eruption products from both volcanoes suggest independent crustal differentiation (Klaver et al., 2016; Rizzo et al., 2016), seismic tomography showed the presence of a low-velocity anomaly connecting Santorini and Kolumbo at a depth of 3-5 km, interpreted as a zone of magmatic intrusions (Heath et al., 2019; McVey et al., 2020). To date, it is not clear whether there is further evidence for a link between the Santorini volcanic system and the Kolumbo Volcanic Chain, nor is it known how their plumbing systems have evolved in time and space. To address these questions, in this study we investigate the internal architecture of the volcanic edifices from the KVC and explore their relationship to the regional tectonic system using seismic reflection images. Furthermore, we investigate seismic reflection evidence for volcanic features in the area between Santorini and Kolumbo. Based on these analyses, our objectives are to (1) reconstruct the spatio-temporal evolution of the Kolumbo Volcanic Chain, and (2) investigate whether there is a link between the evolution of Santorini and the Kolumbo Volcanic Chain.

7.2   Geological Framework

The KVC is part of the CSK volcanic field, one of the most active volcano-tectonic regions in the Mediterranean Sea (e.g. Bohnhoff et al., 2006; Nomikou et al., 2019). Formed by the partial melting of the subducting African slab beneath the Eurasian plate, volcanism along the CSK field evolved in four phases, which initiated in the Late Pliocene with the emergence of the Christiana Volcano southwest of present-day Santorini (Phase 1;Piper et al. (2007) and Preine et al. (2022a). The subsequent formation of major NE-SW trending fault systems in Middle Pleistocene correlates with the emergence of the early Kolumbo and Poseidon centers (Phase 2), which deposited volcaniclastic material in the Christiana and Anhydros Basins, respectively (Hübscher et al., 2015; Preine et al., 2022a; Preine et al., 2022c). The KVC is thought to

have formed after a major tectonic pulse that triggered a cascade of large-scale mass-wasting events at Santorini and Kolumbo (Phase 3; Preine et al. (2022b,2022c)). This series of events marks the beginning of the third phase, which is thought to include not only the formation of the KVC, but also buried volcanic cones southwest of Santorini, and the evolution of the onshore exposed Akrotiri rhyolitic center, the Peristeria stratovolcano, and the Akrotiri cinder cones (Druitt et al., 1999; Preine et al., 2022a). In the last phase (since ∼360 ka; Phase 4), a major tectonic event occurred in the Santorini-Anafi Basin, followed by the onset of highly explosive volcanism at Santorini, which corresponds to a distinct change in the primitive melt diversity (Flaherty et al., 2022). This explosive volcanism formed the Thera Pyroclastic Formation, while Kolumbo remained active producing two major eruptions (Preine et al., 2022a; Preine et al., 2022c).

Kolumbo's five units (K1-K5) formed over the course of more than 1 million years (Hübscher et al., 2015; Preine et al., 2022a). Seismic reflection data have shown that these volcanic units generally have low-amplitude internal reflections, indicating that they were formed by explosive underwater eruptions (Hübscher et al., 2015). This is consistent with ROV surveys of the crater walls, which show they consist of over 250 m of pumice lapilli and pumice block breccias produced by the historic 1650 CE eruption (Carey et al., 2011). Presently, a hydrothermal vent field is still active in the northern part of the Kolumbo crater (Carey et al., 2011; Carey et al., 2013), and frequent swarms of microseismicity indicate ongoing melt ascent (Schmid et al., 2022) from a melt reservoir at ∼2 to 4 km below the crater (Chrapkiewicz et al., 2022). Northeast of Kolumbo, volcanoes within the KVC occur in water depths of up to 450 m, with summit heights of up to 200 m above the surrounding seafloor (Nomikou et al., 2012). Most of these volcanoes are cone-shaped, with some having characteristic craters at the top, while most have smooth, rounded summits (Fig. 7.1c) (Nomikou et al., 2012; Hooft et al., 2017). The cones of the KVC are aligned along two main trends that are approximately linear and NE-SW oriented (orange dotted lines in Fig. 7.1d), lying parallel to the main fault trend of the CSK rift zone (Nomikou et al., 2012; Hübscher et al., 2015). Only two volcanoes (VC8 and VC16) lie off these main lineaments (Fig. 7.1c). ROV surveys revealed that the volcanoes are sediment-covered and show little to no evidence of recent volcanic activity (Nomikou et al., 2012). Volcanic rock outcrops on the cones consist of fragments of pumice and lava that have been cemented by biological activity, while some show evidence of recent low-temperature hydrothermal activity (Nomikou et al., 2012). In general, the bases of the slopes consist of fine-grained material, while the upper slopes consist of pumice clasts and scattered lapilli (Carey et al., 2011; Nomikou et al., 2012). Previous seismic surveys of some of the volcanic cones revealed low-amplitude reflections within the volcanic cones, which were interpreted as volcaniclastic material from explosive eruptions similar to those that formed the Kolumbo volcano (Hübscher et al., 2015).

An important influence of the local tectonic system on the emplacement of volcanoes at the CSK field has been suggested by previous studies due to the overall linear alignment of volcanic edifices parallel to the NE-SW striking regional rift system (e.g. Druitt et al., 1999; Dimitriadis et al., 2009; Heath et al., 2019; Heath et al., 2021; Feuillet, 2013; Preine et al., 2022c) . The two most prominent volcano-tectonic lineaments are the Kameni and Kolumbo lines, which strike NE-SW intersecting the northern part of the Santorini caldera (Fig. 7.1a) (Druitt et al., 1999; Hooft et al., 2019; Heath et al., 2019; McVey et al., 2020) (Fig. 7.1a). While the Kameni line is defined by a linear alignment of post-Minoan vents in the center of the caldera, the

Kolumbo line connects older volcanic centers in the northern caldera basin and extends towards Kolumbo (Fig. 7.1a). Both lineaments bound a region of isolated caldera collapse (Hooft et al., 2019) as well as a low-velocity anomaly in the depth of 3 to 5 km that extends from the northern caldera basin towards Kolumbo (Heath et al., 2019; McVey et al., 2020).

7.3   Methods

In this study, we utilize an extensive dataset of more than 3,200 km of high-resolution multi- and single-channel seismic data acquired during six cruises between 2006 and 2019 (Fig. 7.1b) (Sigurdsson et al., 2006; Hübscher et al., 2006; Karstens et al., 2020b). For all multichannel seismic lines, we applied multiple removal by means of surface-related multiple elimination and pre-stack time migration to improve the quality of the seismic images. More details on the acquisition and processing of the seismic data can be found in Appendix D. All processed seismic lines were combined into an interpretation project using the Kingdom Suite software. In Figure 7.4, we use instantaneous phase plots (Taner et al., 1979) to highlight low-amplitude but coherent events within the volcanic edifices.

7.4   Seismic Interpretation

7.4.1   Seismostratigraphic Framework

To establish a relative chronology of the evolution of the KVC, we use the seismo-stratigraphic framework established in Preine et al. (2022a) and Preine et al. (2022b). This framework consists of six units separated by six key horizons h1-h6. Unit 1 overlies the acoustic basement and consists of sub-parallel reflections of very low amplitude, which are often difficult to image due to the overprint of the seafloor multiple. The overlying Unit 2 consists of a series of well-stratified reflections with low to medium amplitudes. Units 3 and 5 consist of a series of well-stratified medium amplitude reflections. In contrast, Unit 4 consists of chaotic, weakly reflective material that has been interpreted as the deposits of the Santorini mass wasting cascade (Preine et al., 2022b). Where Unit 4 is missing, Unit 5 directly overlies Unit 3. The uppermost Unit 6 consists of high amplitude reflections that become irregular near Santorini, where they comprise the deposits of the Thera Pyroclastic Formation (Preine et al., 2022a). For the interpretation of the volcanic units of Kolumbo, we follow the nomenclature of Hübscher et al. (2015), who labeled the Kolumbo Units K1-K5.

7.4.2 Kolumbo Volcano and the Kolumbo Volcanic Chain
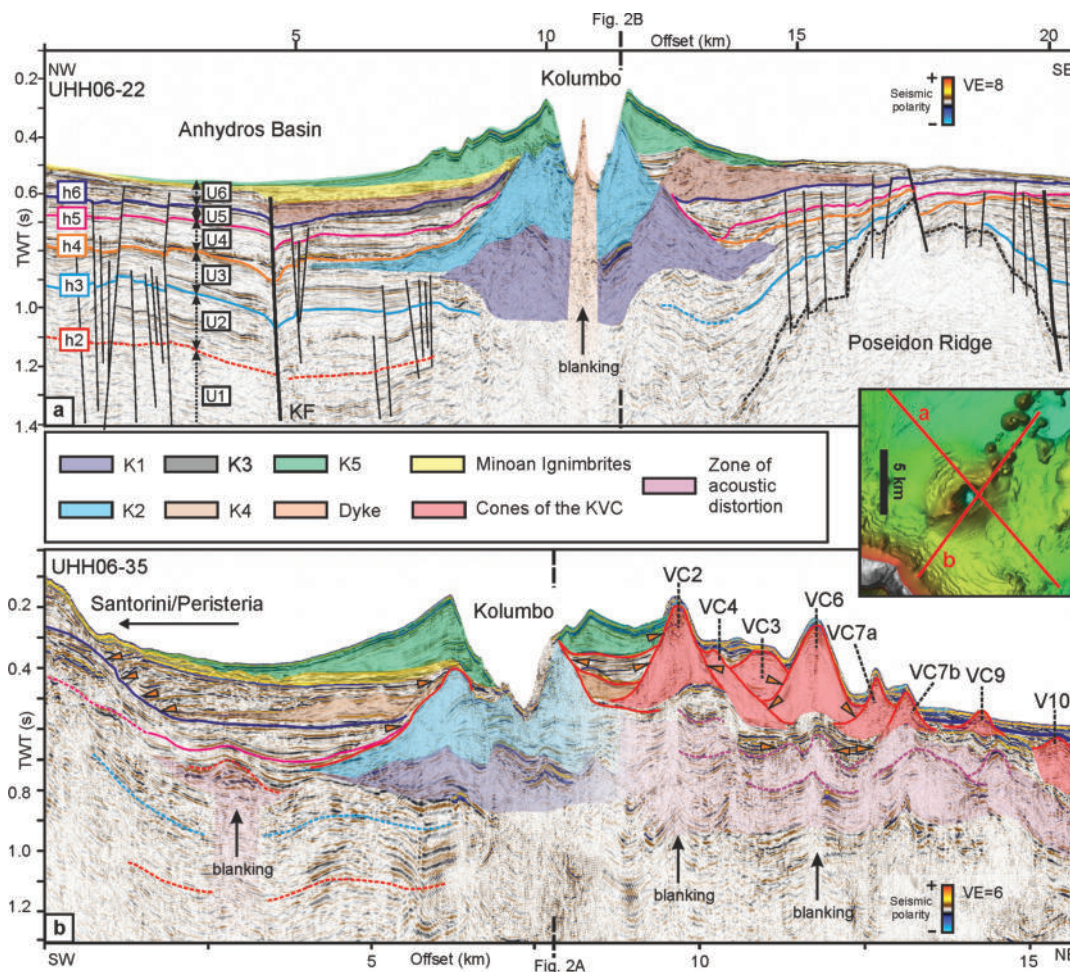
FIGURE 7.2: (a) NW-SE oriented seismic profile HH06-22 crossing the Anhydros Basin and Kolumbo. KF: Kolumbo Fault. (b) SW-NE oriented seismic profile UHH06-35 crossing Kolumbo and several cones of the KVC. Orange triangles mark onlap terminations. Colored horizons h1-h6 mark key reflections separating seismostratigraphic units U1-U6 from Preine et al. (2022a). K1-K5: Kolumbo Units after (Hübscher et al., 2015)). VC: volcanic cone. KF: Kolumbo Fault. Inset map is an extract from Figure 7.1c, showing the locations of the profiles in (a) and (b). See Figure D.1 for an uninterpreted version of the seismic profiles.

Figure 7.2 shows two seismic profiles crossing the Kolumbo Volcano perpendicular to each other. The uppermost profile crosses the Anhydros Basin and Kolumbo in the NW-SE direction (Fig. 7.2a). In the Anhydros Basin, we identify all seismostratigraphic Units, which have relatively constant thicknesses. There are several faults intersecting the strata of the Anhydros Basins, with the Kolumbo Fault being the most prominent (as shown also in Nomikou et al. (2016b) and Preine et al. (2022a)). On top of the uppermost Unit U6, we identify a chaotic subunit, which thickens towards Kolumbo and represents the Minoan ignimbrites (yellow semi-transparent area) (Hübscher et al., 2015; Karstens et al., In Review_B). This Unit is

overlain by Kolumbo's Unit K5, which consists of well-stratified reflections representing the pumice deposits of the 1650 CE eruption (Cantner et al., 2014; Hübscher et al., 2015; Karstens et al., In Review_A). Kolumbo's Unit K4 lies at the basis of Unit U6 and consists of chaotic to transparent internal reflections (Fig. 7.2a). K3 is comparatively small and intercalated within Unit U5, while K2 makes up most of the Kolumbo edifice and is partly exposed on the crater wall (Fig. 7.2b). Both K2 and K1 are intercalated within Unit U3 and separated from each other by prominent high-amplitude reflections (Fig. 7.2a). In the center of the Kolumbo crater, we identify an acoustically transparent structure, which represents a dyke that is exposed on the crater wall (Karstens et al., In Review_B).

The profile in Figure 7.1b starts on the eastern flank of Santorini, crosses the Kolumbo crater, and eight additional cones of the KVC. On the flank of Santorini, we identify the Minoan ignimbrites, which have a wavy topography typical for submarine pyroclastic flow deposits (Pope et al., 2018). Horizon h6 marks a distinct onlap surface, onto which most of the internal reflections of Unit 6 terminate (orange arrows, Fig. 7.2b). Unit 4 is absent in this profile and the deeper Units 1-3 are difficult to interpret since the seismic image is disturbed in the deeper part, especially below the KVC or towards Santorini (Fig. 7.2b). At profile kilometer 2.5, we identify a high-amplitude reflection within Unit 4 (red dashed line, Fig. 7.2b), causing acoustic blanking underneath, which may indicate a small volcanic edifice (Fig. 7.2b).
Beneath Kolumbo, we identify the Kolumbo Units K1, K2, K4, and K5. Unit K4 is relatively small here, while K3 appears to be absent. On the southwest side of Kolumbo, the termination of K2 and K1 is well imaged (∼km 5, Fig. 7.2b). However, the termination towards the northeast below the KVC cannot be constrained as the seismic image becomes highly disturbed below the KVC. The cones of the KVC crossed in this profile decrease in height towards the NE and display complex onlapping relationships with each other (Fig. 7.2b). In general, the cones have an internal architecture similar to that of Kolumbo, consisting of stratified flanks with weak seismic amplitudes and a chaotic, weakly reflective core (Fig. 7.2b). The cones are located on top of weakly reflective strata with several high amplitude reflections (purple semi-transparent area, Fig. 7.2b). Underneath VC2 and VC6, we observe a zone of vertically pervasive blanking and velocity pull-up (marked 'blanking' in Fig. 7.2b), which is a typical effect occurring beneath high-velocity volcanic rocks within a sedimentary sequence (e.g. Jackson, 2012; Reynolds et al., 2018; Magee et al., 2013). Beneath VC6, we observe a sequence of well-stratified reflections that onlap a cone-shaped, acoustically transparent area (orange triangles, Fig. 7.2b).
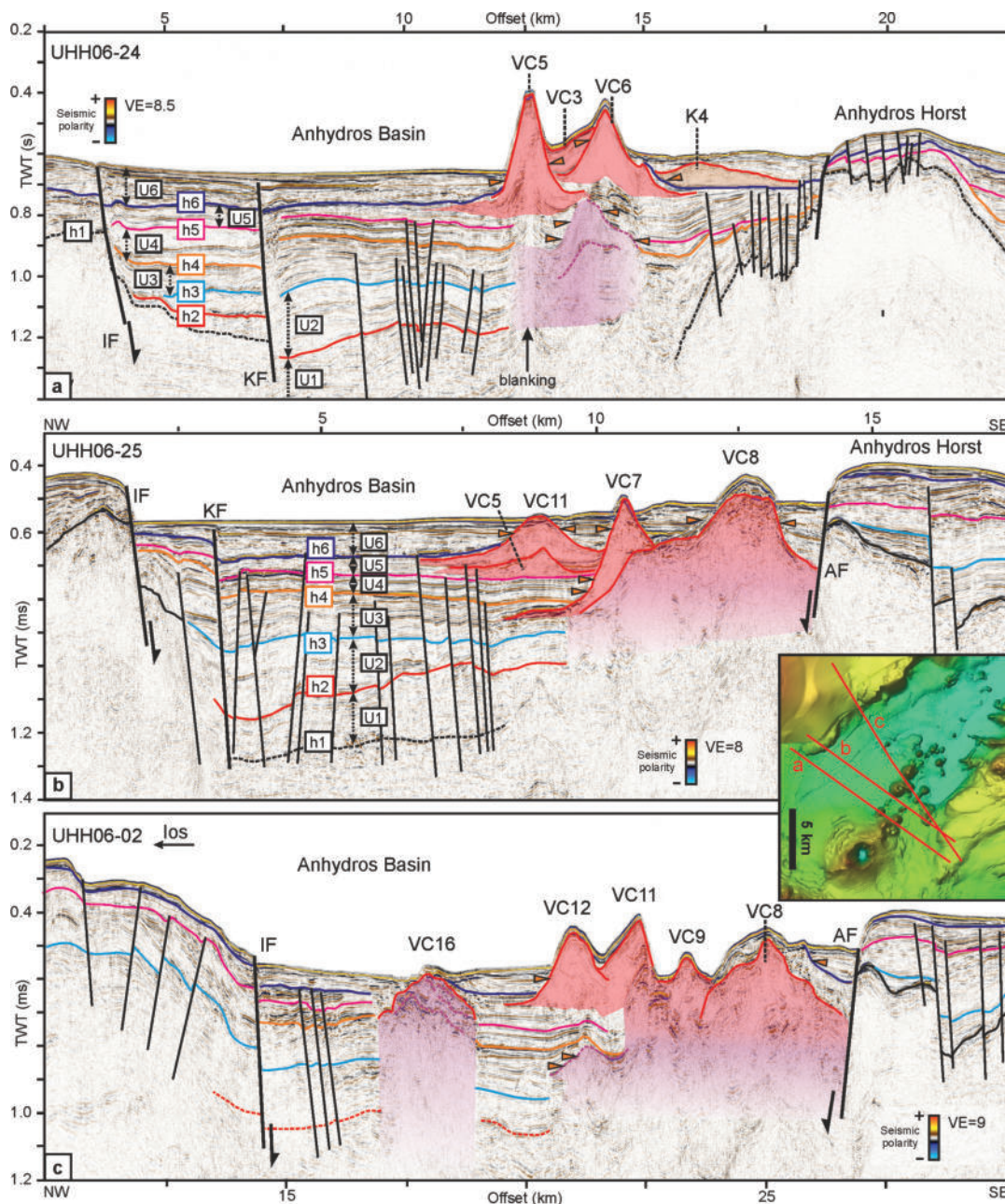
FIGURE 7.3: (a) Seismic profile UHH06-24 crossing the Anhydros Basin and the southwestern part of the KVC. (b) Seismic profile UHH06-25 crossing the Anhydros Basin and the central part of the KVC. (c) Seismic profile UHH06-02 across the Ios shelf, the Anhydros Basin, and the central part of the KVC. Inset map is an extract from Figure 7.1c, showing the locations of the profiles in (a) - (c). See Figure D.2 for an uninterpreted version of the seismic profiles.

Figure 7.3 shows three seismic profiles traversing the central part of the KVC. The uppermost profile crosses the Anhydros Basin and the southwestern part of the KVC including VC6, VC5, and VC3 (Fig. 7.3a). In the Anhydros Basin, we identify all six seismostratigraphic units and the Ios and Kolumbo Faults to the NW of the KVC. Between the Kolumbo Fault and the KVC is a complex fault zone with several small offset internal faults that terminate within Units 3 and 4 (Fig. 7.3a). Southeast of the

KVC, towards the Anhydros Horst, we observe additional internal faults. The flanks of the volcanic cones are all intercalated with Unit 5. There is a zone of pronounced seismic blanking and velocity pull-ups beneath the central part of VC5, while underneath VC6, we identify a zone of chaotic, low amplitude reflections (purple semi-transparent area, Fig. 7.3a). The reflections from Unit 5 overly and/or onlap this cone-shaped area (km 15 in Fig. 7.3a). It is noteworthy that the base of e.g. VC5 lies approximately 130 ms beneath the seafloor, implying that the total height of VC5 is about 115 m greater than the 200 m protruding upwards from the seabed (assuming a velocity of 1750 m/s for unit 6 and 1500 m/s as water velocity, Preine et al. (2022a)).

The seismic profile in Figure 7.3b crosses the Ios Fault and the deep part of the Anhydros Basin, where we find all six seismostratigraphic units and several internal faults (Fig. 7.3b). The profile crosses the flanks of VC5 and VC11 as well as VC7 and VC8. While VC5 and VC11 cause no pull-up or acoustic blanking indicating a moderate internal velocity of the flanks, VC7 and VC8 cause complete blanking of the underlying strata except for some scattered reflection patches (purple dashed lines, Fig. 7.3b). The margin of the Anhydros Basin and the Anhydros Horst is not resolved due to the acoustic blanking (Fig. 7.3b). Figure 7.3a shows that VC7 onlaps VC8, while the northwestern flank of VC7 occurs within Unit 3, suggesting an older age for these two cones compared to the other cones of the KVC, which are within Unit 5 (Preine et al., 2022a) (Fig. 7.3b).

The seismic profile in Figure 7.3c is similarly oriented to the profile crossing the Ios Fault and the Anhydros Basin. Figure 7.3c crosses VC16, which is slightly further west than the rest of the KVC (Figs. 7.1, 7.3c). We identify high amplitude and irregular reflections at the top of this edifice (VC16) and pronounced acoustic blanking underneath (Fig. 7.3c). This is in contrast to the flanks of VC5 and VC11 (Fig. 7.3b) or VC5 and VC6 (Fig. 7.3a), where the acoustic blanking is much less pronounced and we can identify reflections below the cones. On the other hand, the acoustic characteristics of VC16 are similar to those of VC7 and VC8 (Fig. 7.3b), where complete acoustic blanking is observed. Furthermore, Figure 7.1c shows that below VC12, the reflections of Unit 3 onlap a body of chaotic/transparent internal reflections, which is connected to a broad zone of pronounced acoustic blanking beneath VC9 and VC8 (purple semi-transparent area in Fig. 7.3b). Similar to Figure 7.3b, the transition from the Anhydros Basin to the Anhydros Horst is not resolved in this profile (Fig. 7.3c).
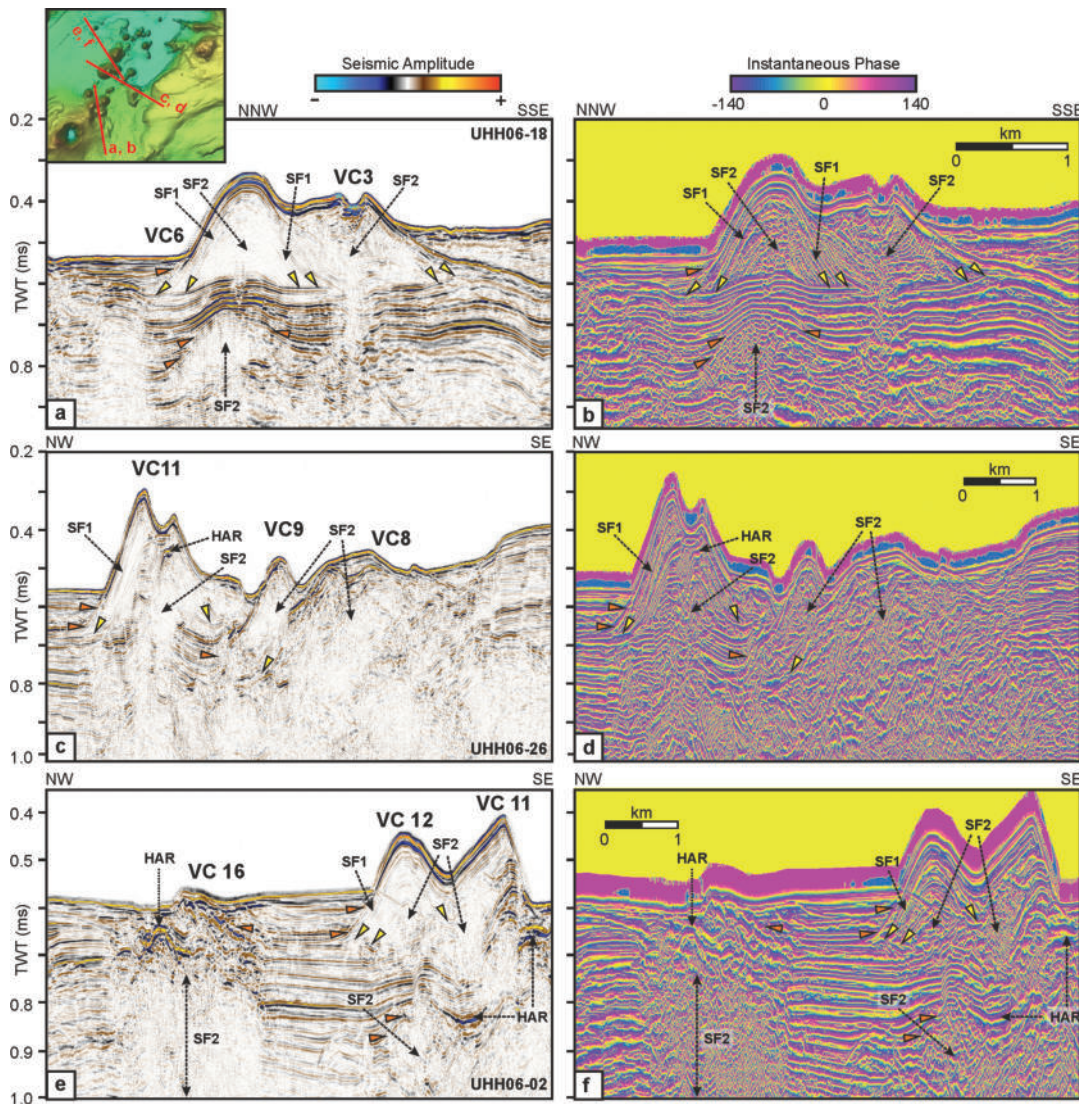
FIGURE 7.4: (a-f) Detailed illustration of the internal architecture of several cones of the KVC. Left panels show seismic amplitude and right panels show instantaneous phase. SF1, SF2: Seismic facies as explained in the text; HAR: High-Amplitude reflection. See Figure D.3 for an uninterpreted version of the seismic profiles.

The profiles shown in Figures 7.2 and 7.3 highlight that the internal architecture of the different volcanic edifices of the KVC is diverse. To examine this in more detail, Figure 7.4 shows enlargements of selected volcanoes from the KVC with their respective instantaneous phase representations, which reveal weak coherent events within the volcanic edifices. We identify the following three main characteristic features:

Seismic Facies 1 (SF1): Many volcanic cones have well-stratified flanks with a pronounced downlap termination towards the base of the edifice (VC3, VC6, VC11, and VC12) (Fig. 7.4). While these reflections have low amplitudes and are barely visible in the amplitude plots (Fig. 7.4a, c, e), they are visible as coherent closely-spaced reflections in the instantaneous phase plots (Fig. 7.4b, d, f). Similar stratified flanks can be observed within Unit K5 of Kolumbo (Fig. 7.2a, b), where they represent stratified

pumice deposits of the explosive 1650 eruption (Hübscher et al., 2015; Karstens et al., In Review_B). Based on the similarity between the stratified flanks of the volcanic cones and the internal structure of Kolumbo's unit K5, we interpret that stratified flanks of the cones are seismic indicators of pumiceous deposits and are thus indicative of explosive eruptions.

Seismic Facies 2 (SF2): All of the volcanic cones investigated in this study exhibit regions of incoherent seismic facies, which we will refer to as SF2. While SF2 is visible as acoustically blanked areas in the amplitude plots (Fig. 7.4a, c, e), the instantaneous phase plots show chaotic, incoherent internal reflections (Fig. 7.4b, d, f). We identify SF2 in the central area of the volcanic cones close to the vents (VC6, VC11) (Fig. 7.4), or within some of the acoustically transparent structures below the cones, e.g., below VC6 or VC12 (Fig. 7.4). In several instances, the incoherency of the strata cannot be explained by velocity effects from the overlying structures alone, as e.g., below VC6, individual horizons can be clearly imaged and traced underneath the volcanic cone, showing a distinct onlap behavior to the underlying incoherent region, which itself has a cone-like shape (Fig. 7.4a, b). This suggests that these features are buried volcanic structures over which newer volcanic cones have developed. This is evident beneath VC12, where the flank of the buried edifice is intercalated within Unit U3 (Fig. 7.3c, 7.4e, 7.4f). This acoustic signature could be explained by the presence of brecciated material and massive hyaloclastites in the near-vent region of volcanic edifices, which has been identified by ROV surveys in the summit regions (Nomikou et al., 2012).
We also identify the incoherent seismic facies along broader areas, e.g., within VC8 and VC16 (Fig. 7.4), where chaotic or acoustic blanking facies extend laterally over an area > 1 km. Below these edifices, there is complete seismic blanking and no coherent reflections can be identified in either the amplitude plot or the instantaneous frequency plot. This is in contrast to other volcanoes of the KVC (e.g., VC3, VC6, and VC12) (Fig. 7.4), where reflections can be identified over wide areas, also below the edifices, suggesting that VC8 and VC16 consist of a different, denser material, e.g. lava flows.

High amplitude reflection (HAR): We identify several reflections with anomalously high amplitudes compared to background reflectivity in the vicinity of several volcanic cones, e.g. next to VC11 (Fig. 7.4c-f), or at VC16 (Fig. 7.4e, f). Some of these reflections, occurring directly beneath volcanic cones, are saucer-shaped and phase-reversed and could be interpreted as sill intrusions (e.g. Planke et al., 2005; Magee et al., 2016) (e.g., Figs. 4e, f). High-amplitude reflections without phase reversals occur e.g. at VC11 directly below the crater (Fig. 7.4a, b), or at VC16 directly above the acoustically blanked area (Fig. 7.4e, f) and could be related to the presence of effusive lava flows as mentioned above.

7.4.3   The Northeastern Section of the Kolumbo Volcanic Chain
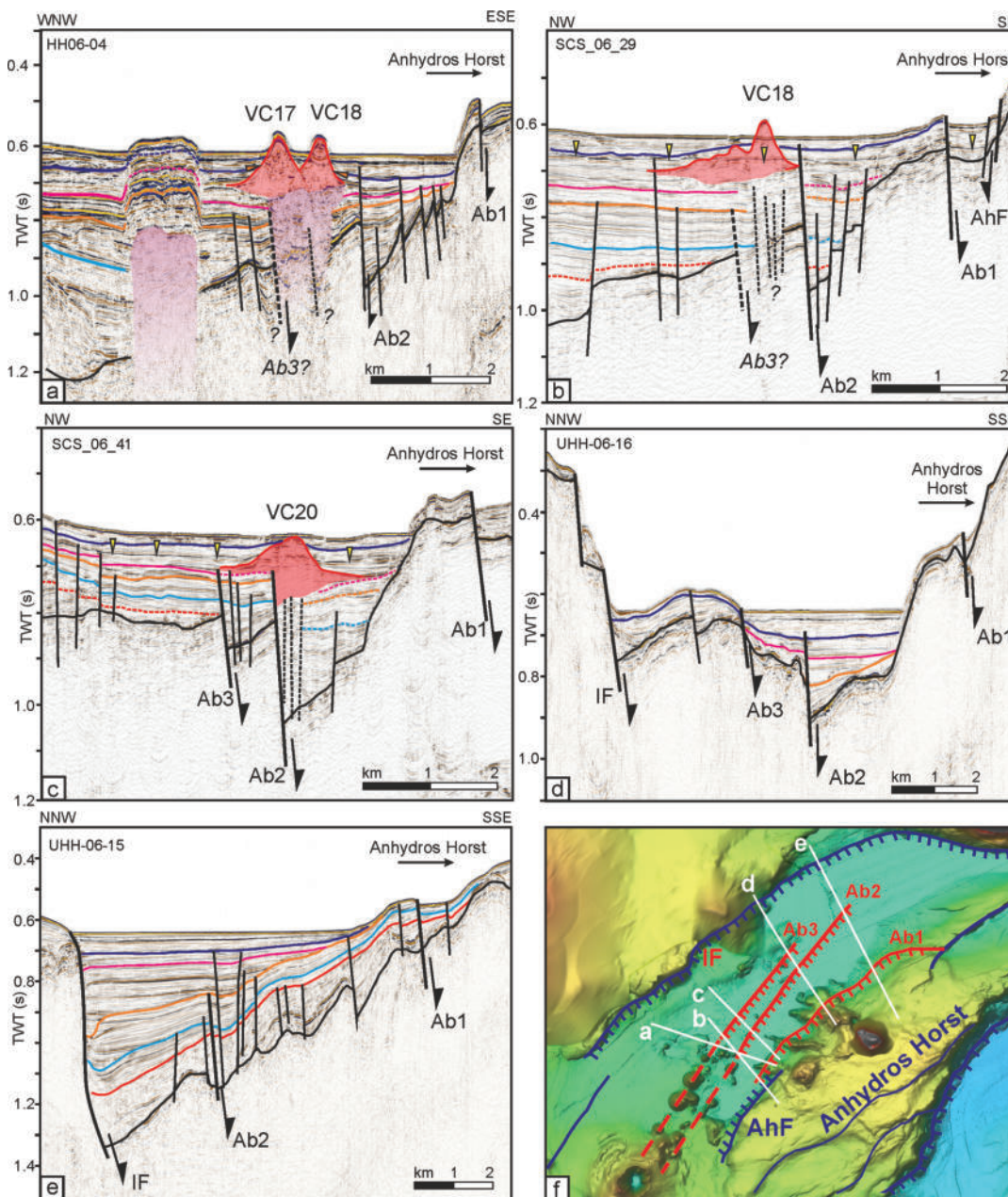
FIGURE 7.5: Seismic profiles across the northeastern KVC and the eastern Anhydros Basin (a-e). Profiles in (b) and (c) are single-channel seismic profiles, in which the yellow arrows indicate the position of the bubble reflection (acquisition artefact). Prominent faults Ab1-Ab3 are highlighted and their location is indicated in the map (f). IF: Ios Fault; AhF: Anhydros Fault. See Figure D.4 for an uninterpreted version of the seismic profiles.

Figure 7.5 shows five profiles crossing the northeastern KVC and the transition to the non-volcanic eastern Anhydros Basin. In all of these profiles, we identify three major normal fault systems Ab1-Ab3, which all dip towards the southeast. The seismic profile shown in Figure 7.5a crosses VC17 and VC18, two of the easternmost cones of the KVC. Northwest of these volcanoes, we identify a broad zone of strong

acoustic blanking that appears to be associated with the northeastern flank of VC16 (Fig. 7.5a). This acoustic blanking zone is overlain by Units 4-6, which appear to be uplifted (Fig. 7.5a). While the thickness of Unit 5 above this zone is constant, Unit 6 is very thin, suggesting that the uplift occurred prior to the deposition of Unit 6. Several faults are visible on the southeastern margin of the Anhydros Basin, including the two prominent faults Ab1 and Ab2, which can be traced along several profiles. Fault Ab1 offsets the seafloor, while Fault Ab2 shows a major throw offsetting the acoustic basement by up to 150 meters, which is also visible in the seismic profiles in Figures 7.5b and 7.5c. The volcanic edifices VC17 and VC18 appear to be located in a zone with several faults that might continue underneath these cones, although these could also be the result of acoustic disturbance due to the overlying volcanic cones (dashed lines and question marks, Fig. 7.5c). This is also the case in the seismic profile in Figure 7.5b crossing VC18, which seems to be located above several faults (dashed lines and question marks, Fig. 7.5b). VC20, which is imaged in the seismic profile in Figure 7.5c, is located further to the NE and we identify Fault Ab2 directly below the edifice, indicating a major structural relationship between the fault and the edifice (Fig. 7.5c).

Overall, the sediment thickness in the profiles in Figures 7.5a-d decreases towards the northeast, and only Units 3-6 are visible in the profile in Figure 7.5e, which is also devoid of volcanic structures. We identify Fault Ab2 and Ab3 in the center of the basin, and towards Fault Ab2, the internal reflections of Unit 3 are divergent (Fig. 7.5d). The seismic profile in Figure 7.5e crosses the eastern Anhydros Basin, which represents a typical half-graben. The internal reflections of Units 2-4 thicken significantly towards the basin-bounding Ios Fault (Fig. 7.5e). We identify Faults Ab1 and Ab2 in the central and eastern part of the Anhydros Basin, while Fault Ab3 appears to be absent here.

7.4.4   The Area between Kolumbo and Santorini

Figure 7.6 shows three seismic profiles traversing the Anhydros Basin between Kolumbo and Santorini. The first profile extends from the northeastern flank of Santorini, crossing Kolumbo and the Anhydros Horst (Fig. 7.6a). Similar to the profiles in Figure 7.2, we identify the Minoan deposits on the flank of Santorini (semi-transparent yellow color; Fig. 7.6a). At profile kilometer 10, there is a cone-shaped area of acoustic blanking (labeled 'Oia cone' in Fig. 7.6a). The internal reflections of Unit 6 onlap this feature and, since we observe a velocity pull-up beneath, we interpret this feature as a small buried volcanic cone similar to the Aspronisi cones southwest of Santorini (Preine et al., 2022a). Continuing towards Kolumbo (at km 12), we observe a high amplitude reflection with acoustic blanking beneath, at the boundary between Units 3 and 4 (red dashed lines, Fig. 7.6a). This feature is very similar to the feature observed on the flank of Santorini in Figure 7.2b. At Kolumbo, we identify all five Kolumbo Units and K3 represents a well-defined volcanic cone within Unit 5. It is noteworthy that the summit of K3 is located about 3 km away from the crater of Kolumbo and there is pronounced acoustic blanking below the center of the cone (km 15 in Fig. 7.6a).
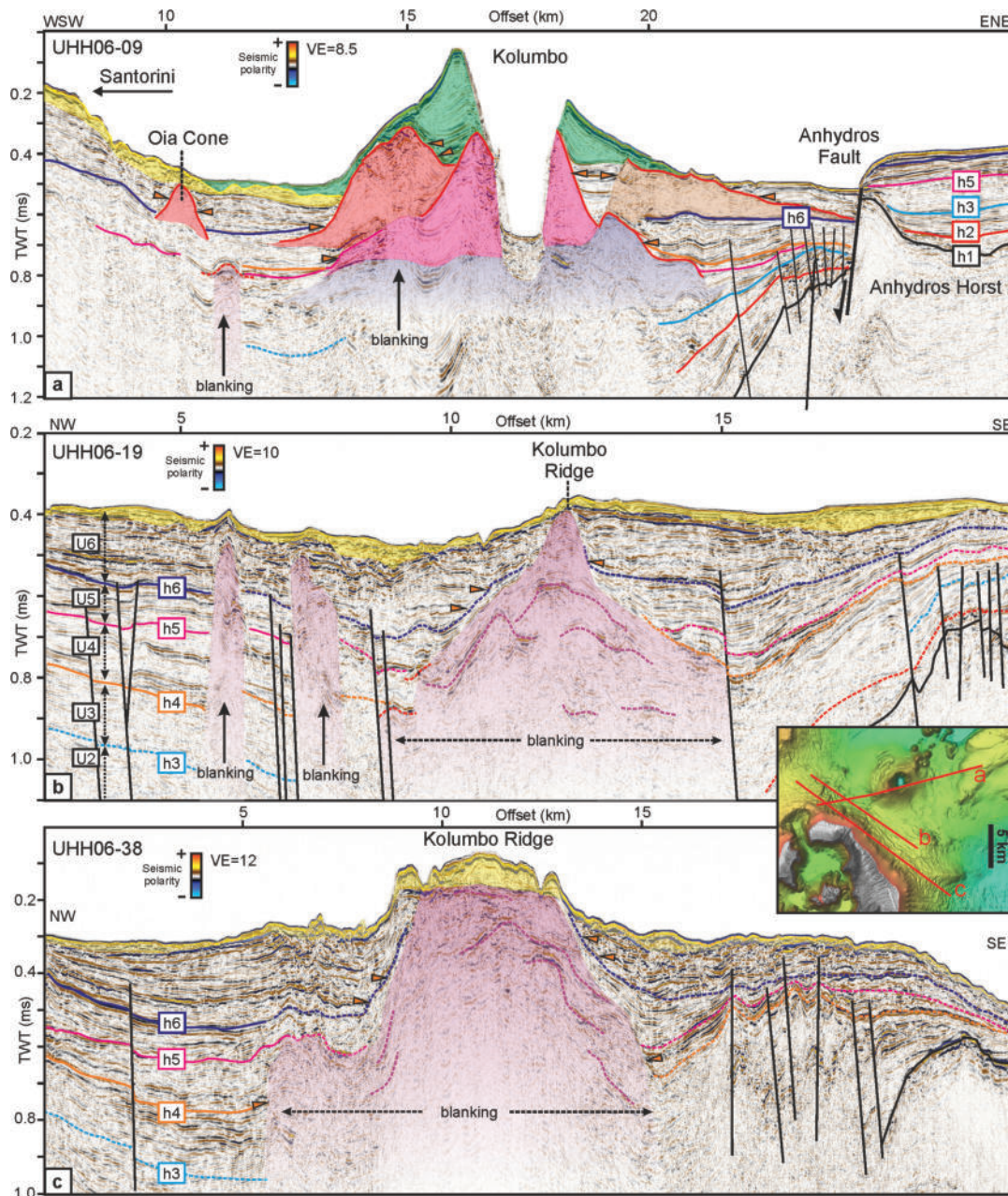
FIGURE 7.6: (a) Seismic profile UHH06-29 traversing the northeast flank of Santorini, Kolumbo, and the Anhydros Horst. (b) Seismic profile UHH06-19 crossing the Anhydros Basin and the Kolumbo Ridge between Santorini and Kolumbo. (c) Seismic profile UHH06-38 crossing the northeastern flank of Santorini. Inset map show the locations of the seismic lines in (a)-(c). See Figure SD.5 for an uninterpreted version of the seismic profiles.

Figures 7.6b and 7.6c show two profiles that are located further to the southwest, traversing the area between Kolumbo and the northeast flank of Santorini. The profiles cross the Kolumbo Ridge, which is a previously unrecognized morphological feature that extends for 6 km from the northeastern flank of Santorini towards Kolumbo (Fig. 7.1c). Compared to the other profiles, the strata here are more irregular, which is why some of the key horizons are indicated by dashed lines (Figs. 6b, c). In both profiles, we identify the Minoan eruption deposits as the shallowest subunit

(Figs. 6b, c). The center of both profiles is dominated by a broad zone of pronounced acoustic blanking (semi-transparent purple area) and upwardly bent reflections with some scattered high amplitude reflections (marked by dashed purple lines in Figs. 6b, c). While the lower units U1-U3 cannot be traced along these zones of strong acoustic blanking, the upper units appear to partially overlie the zone of acoustic disturbance, although it is difficult to trace reflections along these zones. Only for the reflections of Unit 6 can we identify some onlap terminations towards horizon h6.

7.5   Discussion

7.5.1   Spatio-Temporal Evolution of the Kolumbo Volcanic Chain

Using our seismo-stratigraphic framework, we are able to establish a relative spatio-temporal model for the KVC. While the intercalation of the flanks of volcanic cones within the seismo-stratigraphic units allows us to place them in the general stratigraphic framework of the CSK field from Preine et al. (2022a), onlap terminations of individual cones against each other allow us to place them into a relative age context as summarized in Figure 7.7a. For example, the following relative age trend (becoming younger left to right) can be determined from onlap terminations identified in the seismic profile in Figure 7.2b: VC2>VC4>VC6>VC3 (Fig. 7.7a). However, this approach is limited to cones where our seismic data allow us to identify direct onlap terminations. Volcanic edifices that are not imaged by our data or that are too far away from each other cannot be integrated into this relative chronological framework, since internal reflections cannot be reliably traced along the often chaotic or discontinuous intra-volcanic areas.

Our analysis shows that the evolution of the KVC is much more complex than previously thought (Fig. 7.7a). According to the age model from Preine et al. (2022a), the Kolumbo cones evolved in a single phase during the deposition of Unit 5 and are thus between approximately 0.7 and 0.36 Myrs old (phase 3). However, Figure 7.3b clearly shows that VC7 and VC8 occur within Unit 3 and thus evolved during the same phase as K1 and K2 from Kolumbo, implying an age of approximately 1 Myrs (Preine et al., 2022a). The buried edifices, e.g., below VC6 and VC12 (Fig. 7.3a, e) also appear to have developed during this older phase indicating volcanism was widespread at that time. In addition, our seismic images show that the internal architecture of these early volcanic edifices is mainly composed of the incoherent seismic facies SF2 and that there is strong acoustic blanking underneath, which is particularly evident at VC8 (Figs. 3b, 3c, 5c, 5d). As mentioned above, this implies that the edifices from this phase are composed of a very dense, acoustically attenuating material, that could be explained by the presence of thick effusive lava flows. This is in contrast to most of the volcanoes of the younger phase, which were formed during the deposition of Unit 5 ($\sim$0.7-0.35 Ma) (Fig. 7.7a) and appear to have been formed primarily by explosive submarine volcanism, as indicated by the seismically well-imaged flanks (Fig. 7.4) that are very similar to the pumice-bearing crater walls of Kolumbo (Carey et al., 2011).
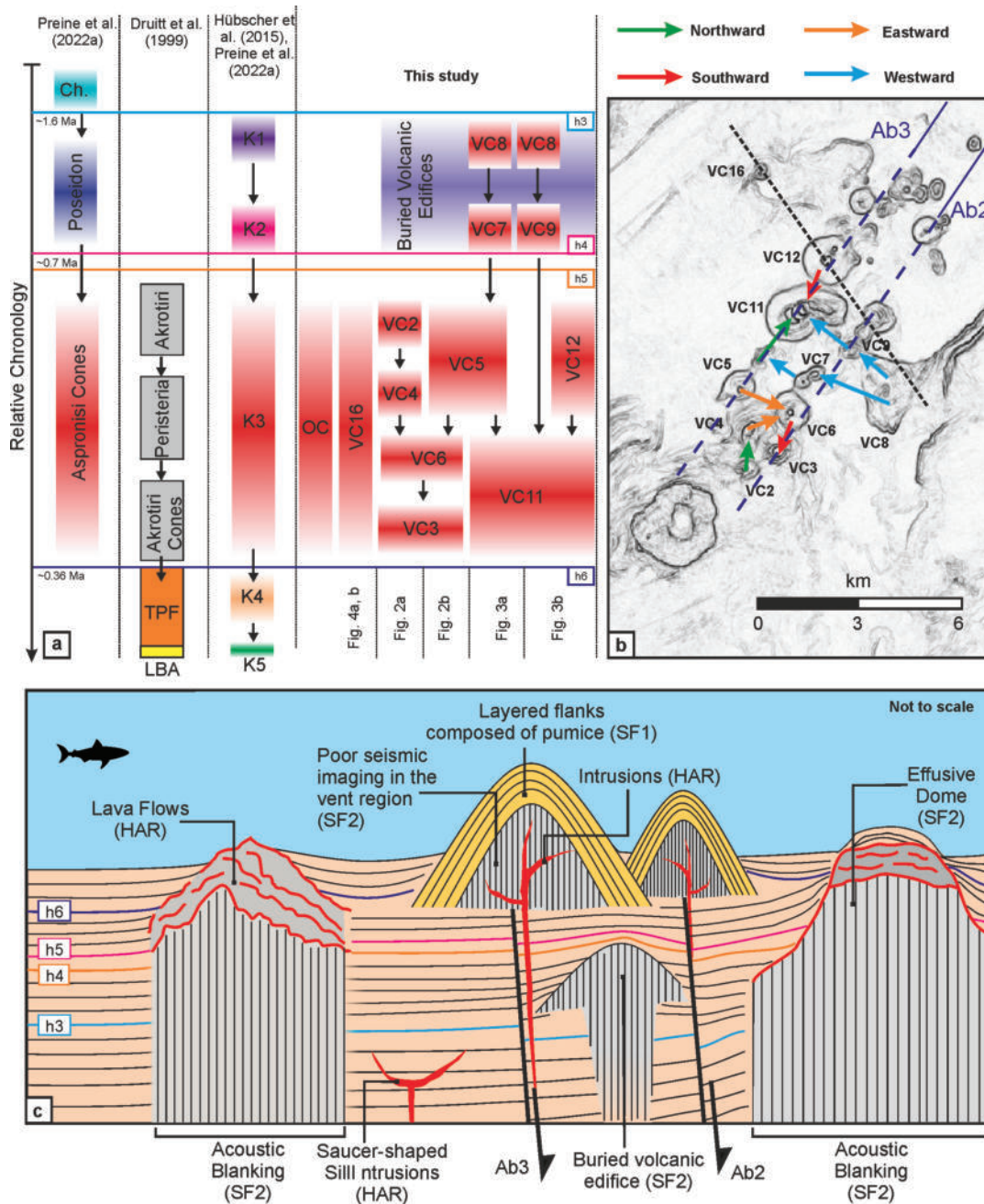
FIGURE 7.7: (a) Relative timeline of the evolution of the CSK volcanic field, placed in the context of the chronostratigraphic framework of (Preine et al., 2022a) – i.e. horizons h3 – h6. Ch.: Christiana, TPF: Thera Pyroclastic Formation, LBA: Late Bronze Age eruption, VC = volcanic cone, OC = Oia Cone. Black arrows indicate increasing age from one volcanic cone to the next. (b) Map of profile curvature showing the direction of onlap terminations from individual cones inferred from the seismic lines. (c) Schematic diagram showing the interpreted internal architecture of exemplary volcanic edifices of the KVC. The approximate location of the sketched section is indicated by the dashed black line in (b). SF: Seismic facies, HAR: High-Amplitude reflection.

Onlap terminations from several cones of the KVC allow us to establish a relative

chronological model of the evolution of the KVC (Fig. 7.7a) and the spatial dimension of onlap terminations is indicated in Figure 7.7b. However, not all volcanoes of this phase seem to have been formed by explosive eruptions, since the seismic image of VC16 is more indicative of effusive volcanism due to the strong acoustic attenuation below and the irregular high-amplitude reflections above (Figure 7.3c, 7.4e, 7.4f). The seismic profile in Figure 7.3c suggests that Unit 6 and parts of Unit 5 lie above VC16. This is also corroborated by Figure 7.6a, where we interpret the acoustically disturbed zone to be an intrusion related to VC16. Here, large parts of Units 4 and 5 appear to be uplifted, with the lack of thickness variation of these units suggesting that this uplift occurred after their deposition (Fig. 7.6a). In contrast, Unit 6 has a much lower thickness above this area, suggesting that it was deposited after the evolution of VC16 (Fig. 7.6a). Thus, our analysis suggests that VC16 was formed during the deposition of Unit 5 and therefore belongs to Phase 3 of Preine et al. (2022a) (Fig. 7.7a), which, accordingly, saw more diverse volcanism than the formation of monogenetic cones only. Figure 7.7c shows a conceptual cross-section through the central part of the KVC, highlighting the different types of volcanic edifices from the two episodes of KVC evolution. The early phase saw the formation of the mainly effusive volcanic edifices such as VC8 and the buried edifices such as those found underneath VC6. The second phase saw the explosive submarine eruptions forming most of the cones of the KVC, in addition to the effusive formation of VC16, which lies off the main trend of the KVC.

7.5.2 The Role of Tectonics

The Kolumbo Chain forms two main trends that lie parallel to the NE-SW striking direction of the basin bounding faults of the Santorini-Amorgos Tectonic Zone (e.g. Hübscher et al., 2015; Nomikou et al., 2018b) related these two trends with two faults that occur in the eastern Anhydros Basin. According to our study, the eastern fault trend is linked to an internal fault zone in the Anhydros Basin, while the western fault trend is connected to the Ios Fault in the Anhydros Basin, implying a direct tectonic control of the KVC. In contrast, a recent study based on seismic anisotropy along the Anhydros Basin concluded that magmatism is not localized in areas of higher fault density, but influenced by the regional-scale tectonic regime (Heath et al., 2021).

The seismic profiles shown in Figure 7.5 indicate that two prominent faults extend the two trends of the KVC towards the northeast into the eastern Anhydros Basin. Fault Ab2 shows a significant throw, offsetting the basement reflection by up to 150 m (Fig. 7.5a-c). This fault can be clearly identified directly underneath VC20, as visible in Figure 7.5c, and seems to continue the strike of the southeastern trend of the KVC far into the Anhydros Basin, where it is expressed as a complex system of intra-basin faults (Fig. 7.5e), in agreement with Hübscher et al. (2015). Fault Ab3 seems to continue the strike of the northwestern trend of the KVC and seems to continue underneath the volcanic cones VC17 and VC18 (Fig. 7.5a, b). However, due to the acoustic disturbances underneath the other cones, we cannot reliably trace faults Ab2 and Ab3 further underneath the KVC. On the other hand, the spatial trend of these faults (Fig. 7.5f) strongly indicates that these faults had an important influence on the volcanic plumbing system of the KVC, with volcanoes evolving both above and in between these faults (Fig. 7.5). Onlap terminations of the volcanic cones do not indicate that one of the two trends is younger than the other, since, as can be seen in Figure 7.7b, there are onlap terminations between individual cones of both trends, indicating that no clear spatial age trend can be derived. Thus, the formation

of the KVC appears to have occurred as a phase of widespread volcanism along both trends of the KVC (Fig. 7.7b).

Figure 7.5 also indicates that the throw of faults Ab2 and Ab3 decreases towards Unit 6, indicating that the main active phase of these faults was the time when Units 3-5 were deposited. This is particularly evident in Figure 7.5d, where Units 4 and 5 show significant divergence towards Fault Ab2. This is consistent with the temporal concept presented in Figure 7.7a, which indicates that the KVC was formed during the deposition of Units 3 and 5. Thus, in addition to the spatial aspect, this also suggests a temporal volcano-tectonic control of the KVC, i.e. that the timing of faulting corresponds to the evolution of the cones along the KVC.

7.5.3 Link between the Kolumbo Volcanic Chain and the Plumbing System of Santorini

Our analysis has shown that the spatio-temporal evolution of the KVC is complex, including both explosive and effusive volcanism over long timescales. This raises the question of how these different phases are related to the volcanic plumbing system of Santorini. While the overprint of the thick Thera Pyroclastic Formation and several caldera collapse events complicate the analysis of the early evolution of Santorini, our seismic data allow the region between Santorini and Kolumbo to be imaged, where the Kolumbo Ridge connects the northeastern flank of Santorini with Kolumbo (Fig. 7.1c).

The seismic profiles in Figures 7.6b and 7.6c illuminate the internal architecture of the Kolumbo Ridge, revealing a zone of acoustic blanking with some scattered high-amplitude reflections beneath, indicating the presence of stacked volcanic edifices or widespread intrusions. The location of the Kolumbo Ridge is consistent with the low-velocity zone from McVey et al. (2020) that extends from Santorini to Kolumbo at 3.5 km depth, which they interpreted as a zone of extensive magmatic intrusions. Figure 7.8a shows the spatial extent of the zone of acoustic blanking underneath the Kolumbo Ridge and the KVC, which has a similar orientation to the deep low-velocity zone of McVey et al. (2020), and its boundaries coincide with the trend of the Kameni and Kolumbo Lines (Fig. 7.8a). Although we cannot trace faults Ab2 and Ab3 underneath the KVC and the Kolumbo Ridge, their orientation also broadly matches the trend of the Kameni and Kolumbo Lines (Heath et al., 2019) suggesting a major volcano-tectonic zone connecting Santorini, the Kolumbo ridge, and the KVC. Onshore geological mapping shows the existence of several NE-SW striking faults as well as numerous dykes on the northeastern flank of Santorini, which could represent the shallowest expression of this large-scale fault zone (e.g. Druitt et al., 1999; Drymoni et al., 2022).

In addition to the Kolumbo Ridge, our seismic data also reveal several smaller volcanic edifices in the area between Santorini and Kolumbo. The seismic profile in Fig. 7.4a shows that the cone forming Kolumbo's Unit K3 had a separate vent located several kilometers southwest of the present-day crater (area of strong acoustic blanking in Fig. 7.6a). We also detect some smaller volcanic features in the area between Santorini and Kolumbo, such as the Oia Cone (Fig. 7.4a) or smaller zones of acoustic blanking, which may be related to shallow intrusions or smaller extrusions (Figs. 2a, 4b, 8). This shows that the area between Santorini and Kolumbo has been volcanically active in the past. Considering that volcanic edifices from Phases 2 and 3 have also been identified southwest of Santorini, such as the Poseidon center and the Aspronisi cones (Preine et al., 2022a), this shows that volcanism in the CSK field was much more widespread in previous phases (Fig. 7.8a). This is supported by

recent findings of Pank et al. (2022)), who sampled submarine lava outcrops in the Santorini caldera and found several samples with ages of ~255 ka and ~309 ± 30 ka (for location, see Pank et al. (2022) and Fig. 7.8a). These samples fill an age gap in the volcanic history of Santorini, as the transition between Peristeria volcanism (550-450 ka) and the onset of the first eruptive cycle is not well constrained (Pank et al., 2022). These authors further show that these samples have a similar Sr-N-Pb isotopic composition to the Peristeria volcano, but argue that the samples belong to a previously unknown stage of Santorini volcanism. Considering the low accuracy of absolute age estimates from seismic stratigraphy, the boundary between phases 3 and 4 (~360 ka) as defined in Preine et al. (2022a) has a considerable error margin. So far, the age model is based on the sedimentation rate extrapolations and the correlation to the onset of the first eruptive cycle on Santorini, which is based on tentative ages for Cape Therma 1 and Cape Therma 2 from Vakhrameeva et al. (2018), Vakhrameeva et al. (n.d.), and Pank et al. (2022). Thus, it is plausible that the lavas of Pank et al. (2022) belong to Phase 3 and thus correspond to the continuation of the widespread volcanism of phase 3, which was subsequently masked by the TPF volcanism and multiple caldera collapses.

Our reconstruction of the spatio-temporal evolution of the KVC in the context of the entire CSK volcanic field and the surrounding tectonic system is illustrated in Figure 7.8b-e. According to this model, after volcanism initiated in Late Pliocene/Early Pleistocene with the emergence of the large Christiana edifice (Phase 1, Fig. 7.8b), it became widespread in the Middle Pleistocene, forming volcanic centers southwest and northeast of present-day Santorini including the first episode of the KVC (Phase 2, Fig. 7.8c). During this period, the tectonic system started to form prominent NE-SW striking faults, including faults Ab2 and Ab3, which appear to have strongly influenced the emplacement of volcanic edifices during this phase (Fig. 7.8d). After a regional tectonic pulse affected the entire CSK rift system and a major mass-wasting cascade occurred at proto-Santorini (Preine et al., 2022b), another episode of wide-spread volcanism took place, which included the onshore exposed Akrotiri and Peristeria centers, the Aspronisi cones SW of Santorini, the newly-discovered Oia Cone between Kolumbo and Santorini, as well as large parts of the younger KVC (Fig. 7.8d). This widespread volcanism, which occurred along a large SW-NE oriented region, suggests that the volcanic plumbing system of the different edifices was laterally connected over a wide area, for example through long dykes systems that are typical for lateral connections along rift systems (e.g. Bato et al., 2018).

The transition from Phase 3 to Phase 4 is marked by another major rifting event, which affected predominantly the northeastern Santorini-Anafi Basin (Fig. 7.1b) (Preine et al., 2022c) This tectonic event had a major influence on the volcanic plumbing system of the KVC since, afterward, volcanism became more spatially isolated and explosive, focusing mainly on the northern caldera basin of Santorini (forming the TPF) and Kolumbo, which had two major eruptions including the 1650 CE K5 eruption (Preine et al., 2022c). This tectonic pulse also corresponds to a change in melt diversity of the eruptive products of Santorini (Flaherty et al., 2022). We argue that the large-scale tectonic event marking the transition from Phase 3 to Phase 4 might have interrupted the connection of the volcanic systems of Santorini and Kolumbo, which seem to have been connected during Phase 3. This could have led to a focusing of volcanic activity on distinct centers during Phase 4. This would explain why there is geophysical evidence for both a deep (McVey et al., 2020) and a shallow (this study) connection between Santorini and the KVC from previous phases, while geochemical analyses of the eruptive products show clear differences

between the two systems (Klaver et al., 2016; Rizzo et al., 2016).
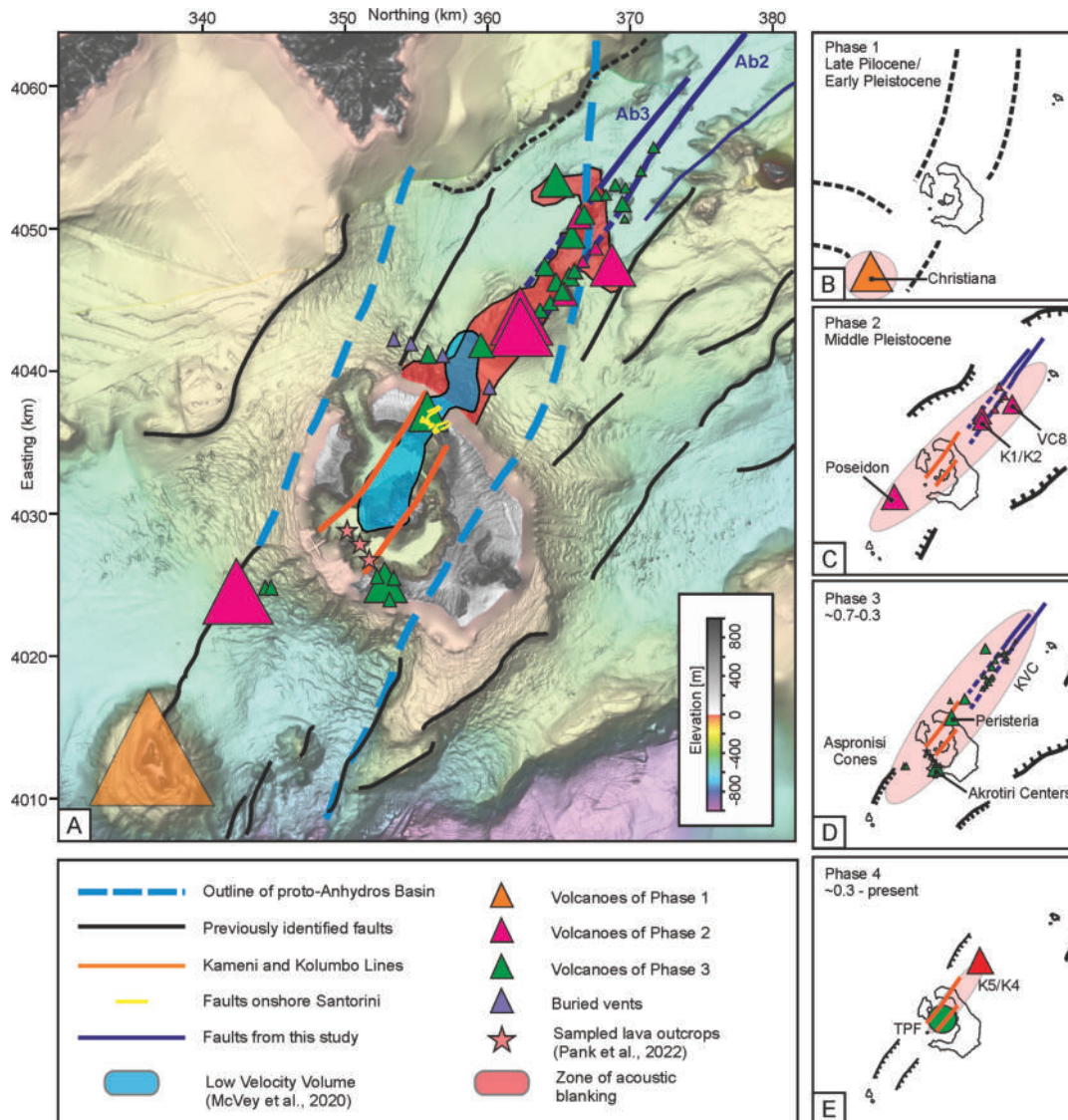
FIGURE 7.8: (a) Morphological map of the CSK rift zone showing major volcano-tectonic features before the onset of the Thera Pyroclastic Formation (TPF, ∼0.3 Ma). Outline of proto-Anhydros Basin taken from Heath et al. (2019) and Preine et al. (2022c)). Previously identified faults from Nomikou et al. (2019) and Preine et al. (2022c). Kameni and Kolumbo Lines according to Heath et al. (2019). Low-Velocity Volume zone from McVey et al. (2020). Locations of cones from Phases 1-3 taken from Preine et al. (2022a)and from this study. Locations of sampled lava outcrops from Pank et al. (2022). (c-e) Sketches of the spatio-temporal evolution of the Kolumbo Volcanic Cones (KVC) in the context of the entire Christiana-Santorini-Kolumbo volcanic field (according to Preine et al. (2022a)). Red semi-transparent color indicates the approximate area of volcanic activity during each phase. Fault evolution according to Preine et al. (2022c). Present-day coastlines for spatial reference.

7.6   Conclusions

In this study, we have used reflection seismic profiles to reconstruct the spatio-temporal evolution of the Kolumbo Volcanic Chain (KVC) and its relationship to the Santorini volcanic system. We show that the KVC evolved in two main episodes. The first episode occurred at approximately 1 Ma and formed volcanic edifices along a broad NE-SW trending zone northeast of Santorini. While most cones of the volcanic edifices of this episode are buried, some have only a thin sedimentary cover or are exposed at the seafloor. These cones seem to have been formed mainly by effusive eruptions, forming thick layers of acoustic blanking in the seismic data. In contrast, volcanoes of the second episode were formed mainly during submarine explosive eruptions between about 0.7 and 0.3 Ma and formed well-stratified pumice cones that generally cause only minimal acoustic disturbances below, although at least one of these younger cones also likely formed during effusive eruptions.

We show that the two main trends of the KVC correspond to two faults that continue towards the eastern Anhydros Basin. Most of the cones formed either on top of or between these faults, indicating a pronounced influence of local tectonism on the volcanic evolution of the KVC. We also identify several buried volcanic centers in the area between Santorini and Kolumbo, as well as a broad zone of acoustic blanking connecting Kolumbo with the northeastern flank of Santorini, which we interpret as a zone of widespread volcanic intrusions. This suggests that volcanism was much more widespread in the early evolution of Santorini, and occurred along a broad NE-SW trending zone that probably continued further beneath present-day Santorini. At some point, a major tectonic event disconnected these systems, explaining the distinct geochemical signatures of the recent eruptive products of Kolumbo and Santorini.

Our study highlights that high-resolution seismic imaging is a versatile tool for studying submarine volcanoes that are difficult to access otherwise. We show that seismic imaging can reveal buried volcanic structures, which would otherwise remain unrecognized, and allows the evolution of volcanic plumbing systems in space and time to be reconstructed. Similar high-resolution seismic surveys at the neighboring volcanic centers of the Hellenic Arc would provide a much clearer picture of the volcanic evolution and tectonic controls of this back-arc system, which is important for a more reliable hazard assessment of the region.

Data availability statement

SEG-Y files of the seismic lines shown in Figure 7.2-7.6 are submitted to the Marine Geoscience Data System and will be publically accessible soon. Link and data DOI will be updated during the revision process.

Acknowledgments

Chapter 8

Revised Minoan Eruption Volume as Benchmark for Large Volcanic Eruptions

Abstract

Volcanic eruptions have caused more than 280,000 fatalities (Auker et al., 2013) since 1600, and large events even affect global climate. Despite their significance, volumes of large-scale eruptions remain poorly constrained (Auker et al., 2013; Self and Gertisser, 2015). The Minoan eruption is considered one of the largest eruptions of the Holocene, with the most recent estimate suggesting a volume of up to 86 km^3 DRE (dense-rock equivalent Johnston et al. (2014)). Here, for the first time, we integrate high-resolution seismic reflection and seismic P-wave tomography datasets with CT (Computed Tomography) derived sedimentological analyses. Our results reveal a total eruption DRE-volume of 31.4 $\pm$ 5.2 km^3 that encompasses an ash-fall DRE-volume of 18.9 $\pm$ 2.2 km^3, an ignimbrite DRE-volume of 6.9 $\pm$ 2 km^3, and an intra-caldera deposit DRE-volume of 5.5 $\pm$ 1 km^3. These volume estimates for different components agree with an independent caldera collapse reconstruction ($\sim$32.5 km^3). Sediment core analyses indicate that the Plinian phase contributed most to the distal ash fall, while seismic observations show that a significantly smaller pyroclastic flow volume than previously assumed was capable of producing the devastating Minoan tsunami. This benchmark reconstruction demonstrates that only complementary geophysical and sedimentological datasets allow reliable eruption volume estimates. The absence of such datasets for most large-scale eruptions precludes more reliable regional and global volcanic risk assessments.

8.1   Introduction

Explosions, tephra fallout, pyroclastic flows, lahars, and tsunamis triggered by volcanic eruptions have a profound impact on society and the environment, while large-scale events can alter Earth's climate (Auker et al., 2013; Self and Gertisser, 2015). Despite the global societal impact of eruptions with a similar magnitude, little is known about fundamental eruption parameters such as volume or mass-partitioning between pyroclastic flows and tephra fall (Self and Gertisser, 2015), thereby limiting hazard assessment. The $\sim$1600 BCE Minoan eruption of Santorini was one of the largest in the Holocene (Johnston et al., 2014) and, owing to its cultural and societal relevance, has been the focus of volcanological and archaeological research since the 19th century. Eruption volume estimates are based either on constraining the caldera

collapse volume or on mapping the eruptive products. Both approaches have limitations, challenges, and associated errors. Caldera collapse volume estimates require a comparison between pre- and post-collapse topographies, which necessitates a detailed understanding of the intra-caldera stratigraphy. However, calderas are often polygenetic and subsequent filling and volcanism can change the primary dimensions, making it difficult to assign precise volumetric changes to a specific eruption (Self and Gertisser, 2015). Eruption volume estimates are based on mapping of eruptive products inside and outside of the caldera and require a combination of techniques dedicated to specific parts and scales of deposits. While cm-thick ash layers cannot be resolved with geophysical methods, sediment coring only reaches the surface of proximal ignimbrite deposits and caldera infill. Determination of the volume of large-scale volcanic events is also complicated by the fact that eruptive products are transported over vast areas and subsequently affected by remobilization or masking by later eruptive activity (Self and Gertisser, 2015). Together, these challenges result in considerable uncertainty regarding the volume of the Minoan eruption, with estimates ranging between 19 and 86 km^3 DRE (Johnston et al., 2014; Heiken and McCoy, 1984).

In contrast to the aforementioned volume uncertainties, the temporal evolution of the Minoan eruption is one of the best understood of all major Holocene eruptions. The cataclysmic event started with precursory explosions some days to weeks before the onset of the main eruption sequence (Heiken and McCoy, 1984; Druitt et al., 1999; Druitt et al., 2019b) which was subdivided into four phases – beginning with subaerial Plinian discharge (Phase 1). After several hours, the eruption vent migrated into a pre-existing flooded caldera, where the interaction with sea-water caused violent phreatomagmatic explosions (Heiken and McCoy, 1984; Druitt et al., 1999; Druitt et al., 2019b) and the emplacement of pyroclastic surges (Phase 2) and low-temperature pyroclastic flows (Phase 3). This phreatomagmatic activity probably formed a tuff cone that filled up the pre-existing caldera, allowing the low-temperature pyroclastic flows to spill over onto Santorini's flanks (Johnston et al., 2014; Bond and Sparks, 1976). Finally, after the connection to the sea was closed and water evaporated, large volumes of hot, fluidized pyroclastic flows ran over the island's slopes forming thick depositional fans (Phase 4), while caldera collapse during and after the eruption formed the island's present-day topography (Johnston et al., 2014; Druitt et al., 2019b; Druitt and Francaviglia, 1992). The entrance of the pyroclastic flows of Phases 3 and 4 into the sea may have triggered tsunamis that impacted coasts around the Aegean Sea (McCoy and Heiken, 2000; Novikova et al., 2011). Thick accumulations of deposits from these pyroclastic flows (termed ignimbrite) occur in the submarine basins surrounding Santorini.

In this study, we reassess the volume of the Minoan eruption with unmatched accuracy by combining high-resolution seismic reflection profiles, seismic P-wave (Vp) tomography, and X-ray Computed Tomography (CT) scans of a selection of marine sediment cores to better constrain the volume of distal tephra, proximal ignimbrite, and intra-caldera deposits. We reconstruct the volume of the caldera collapse based on previously published constraints and compare this estimate with the eruption products, thus providing the first-ever complete volume assessment for a major (>6 magnitude) volcanic eruption.

8.2 Interpretation of Minoan Fall Deposits in Marine Sediment Cores

We identified Minoan eruption fallout ash in 41 gravity cores recovered during research cruise POS513 in 2017 based on their unique geochemical signature (Watkins et al., 1978; Kutterolf et al., 2021a; Kutterolf et al., 2021b). Guided by visual appearance in photographic scans, sedimentological properties, and fabric in X-ray CT-scans, we define three subunits within the Minoan deposits. This tripartition is clearly demonstrated (and representative of the other cores) in the 50-cm-thick sequence of alternating Minoan ash and lapilli layers of core POS513-20, located ∼27 km from the eruptive centre (Fig. 8.1A). The lower subunit consists of 1 to 6 cm thick beds comprising subangular to angular pumice clasts and a low lithic content. Grain size variations are clearly illustrated by grayscale variations in the CT-scan and beds are generally continuous (Fig. 8.1D). A distinct colour change in the photographic scan and a change of the CT-grayscale values mark the boundary with the middle subunit (Fig. 8.1C), which consists mainly of lithic-rich, fine-grained, and laminated deposits with few subrounded to rounded pumice clasts. The CT-scan of the middle unit shows indications of cross-bedding within the partly discontinuous and inclined strata (Fig. 8.1B). The upper unit consists of fine-grained, partly disturbed material, which lacks crystals and lithics. In the CT-scan, the upper unit shows no internal structure, aside from bioturbation, and has an irregular boundary at the base and a diffuse one at the top, which correlates to a distinct porosity decrease (Fig. 8.1B). The lower and middle subunits show pronounced porosity variations correlating with the grain size of beds, while the upper unit shows constant porosity (Fig. 8.1A). The observed tripartition is present in several other cores east of Santorini (Supplement E.1).

Due to its continuous nature of normally graded beds, the angularity of clasts, and the low lithic content, we interpret the lower subunit as Plinian fallout from Phase 1 that was deposited by particles settling through the water column. The cross- and inclined-bedding, the high lithic content, and the non-continuous layering of the middle subunit indicate a more energetic emplacement. Therefore, we interpret the middle subunit as the result of pyroclastic density currents (Phases 2 to 4) that entered the sea and continued as seafloor-bound turbidity currents. Due to its fine grain size, lack of lithics and minerals, and structureless fabric in the CT-scans, we interpret the upper subunit as co-ignimbrite ash fall deposits or dispersed ash, mostly from eruptive Phase 4. However, the middle unit can only be identified in cores obtained from a channel system extending east from Santorini (Supplement E.1), which agrees with its interpretation as turbidites. In cores lacking the middle unit, the boundary between the lower and upper units is characterized by a distinct change in colour and locally in grain size and angularity (Supplement E.1).
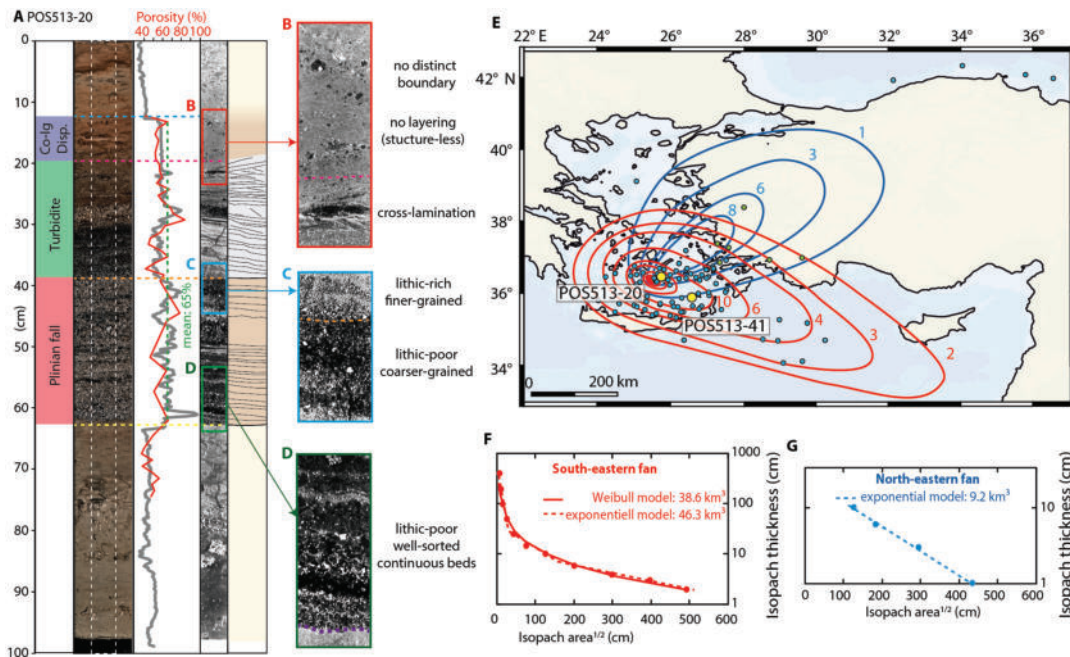
FIGURE 8.1: (A) Photographic scans, porosity measurements, X-ray CT-scan, and stratigraphic interpretation. Co-Ig Disp. Refers to the dispersed co-ignimbrite layer (B) - (D) Enlargements of key intervals of the X-ray CT-scan showing differences between the deposits' sub-units. (E) Isopach maps (cm) for tephra layer 1 (red; Plinian phase) and tephra layer 2 (blue; co-ignimbrite phase). Dots are sediment core locations; yellow dots are cores POS513-20 and POS513-41. (F) Deposit thinning curve for the lower ash layer (Plinian phase). (G) Deposit thinning curve for upper ash layer (co-ignimbrite phase).

8.3   Quantification of Marine Ash Fall Volume

Guided by the described criteria, we identified and measured the thickness of the Plinian layer, the turbidite layer and the co-ignimbrite/dispersed layer. Combined with more distal thickness measurements from the region, we compiled isopach maps for the Plinian and the co-ignimbrite/dispersed ash layers (red in Fig. 8.1E). The thickness distribution of the Plinian layer (lower subunit) agrees well with the thinning trend seen in more distal sediment cores from the Eastern Mediterranean (Watkins et al., 1978) and results in isopachs with a southeast-oriented deposit lobe. The co-ignimbrite/dispersed layer (upper subunit) follows the trend of thickness constraints from Aegean islands, mainland Turkey and the Black Sea (Bonadonna and Costa, 2012), defining a northeast-oriented lobe (blue in Fig. 8.1E). This confirms that the tephra layers were affected by different prevailing wind directions, which has already been documented for the evolution of the first phase (Myers et al., 2021). By plotting the natural logarithm of the isopach thickness against the square root of the isopach area, we determine deposit-thinning trends that we use to estimate total ash fall volumes assuming an exponential decay (Pyle approach (Pyle, 1989); Fig. 8.1F, G) or a Weibull distribution function (Bonadonna and Costa approach (Bonadonna and Costa, 2012); Fig. 8.1F). The latter approach was not possible for the co-ignimbrite/dispersed layer as too few data points were available. The isopach-based volume calculations resulted in bulk deposit volumes of 37.6 to 45.8

km^3 for the southeast-oriented lobe and $\sim$9.2 km^3 for the northeast-oriented lobe (Fig. 8.1F, G). Due to the general Aegean Sea wind pattern (Tyrlis and Lelieveld, 2013; Gerasopoulos et al., 2006), we attribute the northeast-oriented fan lobe to the tropospheric co-ignimbrite from the main ignimbrite-forming phase (mainly Phase 4) and the southeast-oriented lobe to the stratospheric Plinian phase (mainly Phase 1).

To estimate DRE volumes for both lobes, we calculated the deposit porosity for proximal and distal marine ash layers based on cores POS513-20 and POS513-41, deemed representative for proximal and distal Minoan deposits, respectively (Supplement E.1). To this end, we integrated physical grain size and density measurements with CT data as detailed in Supplement E.2. As shown in Fig. 8.1A, both CT-derived and physically measured density estimates capture the same trends in the scanned segments, which we attribute to down-core porosity changes suggested by the strong anti-correlation between density and measured particle size (Supplement E.2). This means that down-core CT grayscale data can be used to refine down-core density and porosity calculations at 500 µm intervals, then transformed into porosity estimates using solid density values for Minoan tephra (Kutterolf et al., 2021a; Kutterolf et al., 2021b) (Supplement E.2).

This integrated analysis results in a mean deposit porosity of 65% for proximal (POS513-20) and 62% for distal (POS513-41) marine tephra deposits. We determine DRE-volumes of 3.2-3.5 km^3 for the northeast-oriented lobe, 13.5-17.6 km^3 for the southeast-oriented lobe, and 18.9 $\pm$ 2.2 km^3 for the total distal fallout tephra deposits of the Minoan eruption. This is consistent with previous estimates (Pyle, 1990; Sigurdsson et al., 1990) that indicated an ash fall DRE-volume of 15 to 19 km^3.

8.4 Minoan Ignimbrites

While Minoan ash fall deposits have been deposited hundreds of kilometres from Santorini, pyroclastic flows extended only several kilometres from the shoreline and were deposited as thick ignimbrites onshore and in the proximal marine area (Sigurdsson et al., 2006). Marine seismic reflection profiles reveal the Thera Pyroclastic Formation (TPF) (Preine et al., 2022a)), which has been formed by explosive volcanism on Santorini during the last 350 kyrs and has been studied in great detail onshore[5,8]. The Minoan deposits form the shallowest stratigraphic unit on Santorini and cover the Cape Riva eruption (22 ka) deposits in many areas on Santorini (Druitt et al., 1999; Druitt and Francaviglia, 1992) including Thera's northwestern cliff (Fig. 8.2A). A seismic profile crossing the northern breach of the caldera wall, in direct proximity to northwestern Thera, shows two chaotic seismic units (Fig. 8.2B). The upper unit (yellow in Fig. 8.2B) is slightly thicker than the underlying unit (brown), and the boundary between them is rugged, resembling the boundary between the Minoan and Cape Riva ignimbrites on Thera (Fig. 8.2A). In addition, the thicknesses of both chaotic units in the seismic profiles are in agreement with the thinning trend of the Minoan and Cape Riva ignimbrites on northern Thera (Fig. 8.2B). Taken together, these observations enable us to correlate the shallowest chaotic seismic units with the Minoan ignimbrites north and east of Santorini.
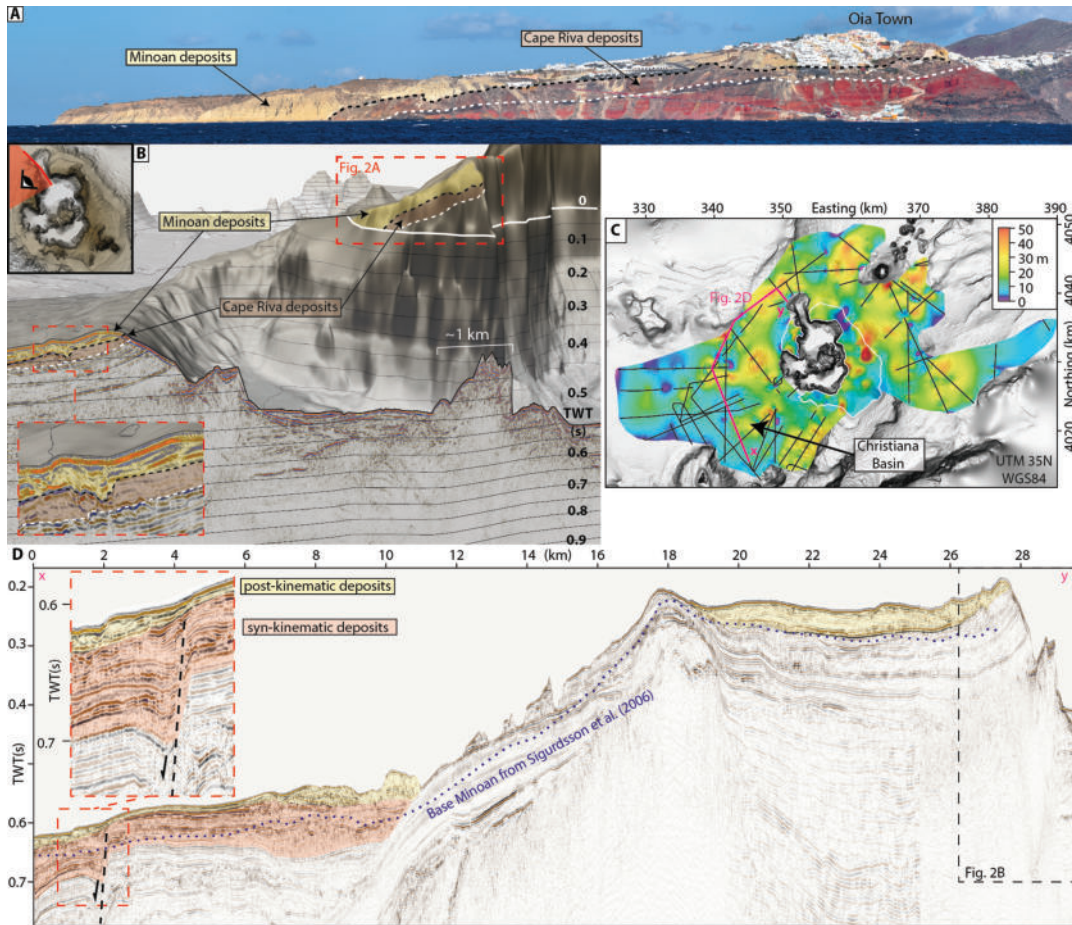
FIGURE 8.2: (A) Photograph of the eastern cliff of Thera from a viewpoint on Therasia with an interpretation of the cliff stratigraphy (Druitt et al., 1999; Druitt and Francaviglia, 1992) showing Minoan deposits atop Cape Riva eruption deposits. (B) Seismic profile combined with a topographic grid of Santorini, including enlargement illustrating the stratigraphic relationship between Minoan and Cape Riva deposits. The viewpoint is also from Therasia. Interpreted seismic units and corresponding subaerial cliff stratigraphy are coloured. (C) Map showing the ignimbrite thickness from seismic mapping combined with onshore deposit mapping (Bond and Sparks, 1976). White line indicates the Santorini coastline. (D) Seismic profile showing the seismic stratigraphy northwest of Santorini. Enlargement shows the Christiana Fault with undeformed, post-kinematic (yellow) deposits interpreted as originating from the Minoan eruption, and offset, syn-kinematic sediments (orange) interpreted as pre-Minoan.

Defining the base of submarine Minoan ignimbrite west of Santorini is more challenging, as the TPF deposits are much thinner there (<100 ms TWT; Fig. 8.2C) than in the north (250 ms TWT) and it is not possible to correlate the onshore and offshore sequences. However, the Christiana Basin southeast of Santorini (Fig. 8.2C) is affected by rifting, offsetting the internal stratigraphy of the TPF by up to 60 ms TWT ($\sim$50 m in Fig. 8.2D, enlargement). The offset increases with depth due to repeated fault activation over the last 350 kyrs, while the shallowest unit (yellow in

Fig. 8.2C) is unaffected by seismically resolvable displacement. This observation enables us to define the youngest (post-kinematic) stratigraphic unit west of Santorini, which includes the Minoan ignimbrite. It is not possible to constrain whether the post-kinematic deposits also include those of the Cape Riva Eruption. Mapping the shallowest stratigraphic unit around Santorini and depth converting with a seismic velocity of 1.78 ± 0.1 km/s (Preine et al., 2022a) yields the thickness map in Fig. 8.2D, indicating a total bulk deposit volume of 14 to 15.7 km^3 for the offshore domain.

Onshore deposits of the four phases of the Minoan eruption have been mapped on the Santorini archipelago, resulting in deposit thickness maps for all four phases[3]. Digitizing the thickness contours results in bulk volumes of 0.28 km^3 for the first phase, 0.34 km^3 for the second phase, 0.45 km^3 for the third phase, 0.36 km^3 for the fourth phase, and a total bulk volume of 1.43 km^3. Minoan ignimbrites deposited offshore are considered to consist primarily of material produced during Phase 4, as deposits from the earlier phases thin-out towards Santorini's coastline (Hooft et al., 2019). Onshore analysis of the lithics-reduced ignimbrite matrix indicates that Phase 4 material consists of pumice (> 2mm) with an average vesicularity of ~78% (Bond and Sparks, 1976; Wilson and Houghton, 1990), while our marine sediment core analysis of the co-ignimbrite ash fall indicates a porosity of ~65% (Fig. 8.1). Assuming a lithic content of 13-26 vol% (based on a wt% of 40-50%) and porosities between 65-78% for the ignimbrite matrix results in a DRE-volume of 0.5 ± 0.1 km^3 for the combined onshore deposits and 6.3 ± 1.8 km^3 for the marine emplaced ignimbrites.
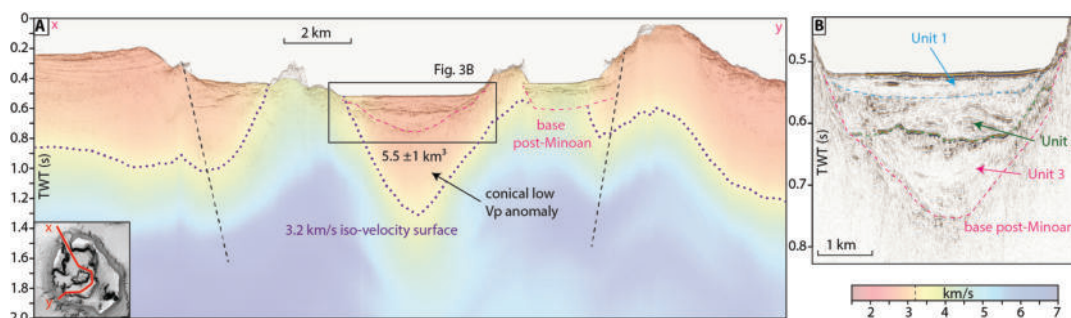
FIGURE 8.3: (A) Seismic profile crossing the Santorini caldera through the northern breach into the northern basin, the western basin, and the southwestern breach. The semi-transparent colours overlaid are from a 3D tomographic Vp model (Hooft et al., 2019). Dashed pink line marks the base of Unit 3, interpreted as the boundary between Minoan and post-Minoan deposits. Dotted purple line is the 3.2 km/s iso-velocity surface, interpreted as the boundary between brecciated and volcanoclastic caldera infill and denser basement. The seismic profile does not cross the centre of the low-Vp anomaly, which is located close to Nea Kameni, and thus does not show its full extent. (B) Enlargement showing the three post-Minoan units in the northern basin.

8.5 Minoan Caldera Infill

Previous studies (Hübscher et al., 2015; Johnston et al., 2015; Nomikou et al., 2016a) identified three seismo-stratigraphic units within the caldera (Fig. 8.3). While the upper two units have been consistently interpreted as post-Minoan deposits, the

lowermost Unit 3 has been interpreted as either down-faulted Minoan deposits (Johnston et al., 2015) or as post-Minoan deposits from the northern breach collapse (Nomikou et al., 2016a). Our new high-resolution data show that the base of Unit 3 defines the boundary between coherent stratified sediments and an incoherent, acoustic basement, and has a funnel-shaped morphology in the northern basin (Fig. 8.3B). Unit 3 shows no indications for internal faulting but reveals on-lapping layers that fill up the funnel-shaped depression beneath the northern basin. This depression correlates spatially with a low-velocity anomaly in Vp-tomography data that formed as a result of the Minoan eruption (Hooft et al., 2019), indicating that Unit 3 was deposited after the collapse and that its base represents the boundary between Minoan and post-Minoan caldera infill.

The seismic reflection data cannot properly image beneath the base of Unit 3. However, Vp-tomography data enable us to reconstruct the seismic velocity distribution of the upper crust beneath the caldera (Hooft et al., 2019). The Vp-tomography reveals a conical, low-Vp anomaly with a diameter of ∼3.0 km extending to ∼2 km depth (Fig. 8.3A). Inherent to the method, the boundary of this low Vp anomaly is not sharp, but 3.2 km/s has been shown to be a well-suited threshold value to distinguish brecciated and volcanoclastic caldera infill from the basement (Hooft et al., 2019). The material underneath the velocity anomaly likely consists of dense volcanic rocks, while the collapse structure itself is bound laterally by metamorphic basement (Hooft et al., 2019). Minoan ignimbrites on Santorini's flank have a Vp of 1.78 km/s, so choosing 3.2 km/s as the threshold value likely overestimates the base of Minoan intra-caldera deposits. With this approach, we estimate a total caldera infill volume of ∼23.4 km^3 (including all Minoan and post-Minoan material between the 3.2 km/s iso-velocity surface and the seafloor). The post-collapse caldera infill (Units 1-3) have a combined bulk volume of 13.6-15.2 km^3, which subtracted from the total caldera infill results in a Minoan caldera infill volume of 8.2 to 9.8 km^3 (i.e. the volume between the 3.0 km/s iso-velocity surface and the base of post-Minoan Unit 3). These deposits have likely been compacted, welded, or hydrothermally altered, and thus applying porosities defined for surface deposits is not feasible. Previous analyses suggested porosity values between 33 and 45% for these deposits (Hooft et al., 2019), which yields a DRE-volume of 5.5 ± km^3.

8.6   Caldera Collapse Reconstruction

The Santorini caldera has been shaped by at least four caldera-forming eruptions over the last 200,000 years (Druitt et al., 1999). Some cliffs surrounding the northern caldera basin predate the ∼1600 BCE eruption, as indicated by a sparse, local cover of Minoan deposits, while the southern and south-eastern cliffs are morphologically fresh and likely formed during the Minoan eruption (Druitt and Francaviglia, 1992) (Fig. 8.4A). This is in agreement with cosmic-ray exposure dating, which indicates that the northern caldera wall existed before the Minoan eruption (Athanassas et al., 2016). The same technique suggests that the northern caldera breach is a long-lived feature, and that the pre-Minoan caldera may have been connected to the sea, while the south-western breach and the western basin were only formed during the Minoan eruption (Athanassas et al., 2016). The Minoan deposits contain lithic fragments of various origins, including geochemically distinctive andesite fragments interpreted as pieces of a pre-Minoan volcanic edifice present inside the ancient caldera (Druitt, 2014; Karátson et al., 2018). The additional presence of stromatolite

fragments in the Minoan tuffs may indicate the presence of a shallow marine lagoon in the pre-Minoan caldera (Anadón et al., 2013). Jointly, these observations enable us to define the approximate shape and size of the pre-Minoan caldera (Druitt et al., 2019b) (Fig. 8.4A). It has been suggested that, during the 3rd phase of the Minoan eruption, this caldera was filled in by a 32-42 km^3 tuff cone before the caldera collapsed anew3 (Fig. 8.4B). However, based on our paleo-topographic reconstruction, as little as 14 km^3 of tuff would have been sufficient to fill up the northern basin, corresponding to a DRE-volume of 4.9 km^3 assuming a deposit porosity of 65%. This DRE-volume is in agreement with our tomography-based caldera infill reconstruction (5.5 ± 1 km^3), suggesting that the entire tuff cone could have collapsed forming the caldera infill. Using the base of Unit 3 as the post-Minoan caldera topography (Fig. 8.4C), we constrain the increase in caldera volume during the Minoan eruption to be ~27 km^3, which combined with the caldera infill indicates a total caldera collapse volume of ~33 km^3.

8.7 Evaluating the Revised Eruption Volume

Combining our DRE-volume estimates for the turbidite layer in the marine sediment cores (~0.1 km^3), the onshore deposits (~0.5 km^3), and marine ignimbrites (3.5 ± 1.3 km^3), yields a pyroclastic current deposit volume of 6.9 ± 2 km^3 for the Minoan eruption (Fig. 8.5). Our estimate is much smaller than the 41 km^3 DRE estimated from previous seismic mapping (Sigurdsson et al., 2006). We attribute this large discrepancy to i) limited resolution of previous seismic data, which led to the erroneous interpretation of large parts of the TPF in the Christiana Basin as Minoan deposits (see dotted line in Fig. 8.2D), and ii) applying a deposit porosity of only 25% compared to the 65-78% we used. Our estimate is also significantly smaller than ignimbrite quantifications based on mass-balance calculations (Pyle, 1990; Sigurdsson et al., 1990) using co-ignimbrite ash volumes in sediment cores, which implied DRE-volumes of 10 to 20 km^3. These estimates were based on attributing 85-98% of the total mapped ash volume to the ignimbrite phase, and quantifying the fine-depleted ignimbrite volume based on mass balance calculations, which assumed mass ratios between ignimbrite and co-ignimbrite ash of 41:59 to 54:46 and co-ignimbrite ash volumes of 15 to 20 km^3 DRE (Pyle, 1990; Sigurdsson et al., 1990). Our sediment core analysis shows a co-ignimbrite ash volume of just 3.4 ± 0.1 km^3 DRE, resulting in an ignimbrite to co-ignimbrite ash volume ratio between 70:30 and 58:42, which is slightly elevated towards the fine-depleted ignimbrite. While our total ash fall estimate of 19 ± 2.1 km^3 DRE (Fig. 8.5) is in line with previous Minoan fall volume estimates of 15 to 19 km^3 DRE (Pyle, 1990; Sigurdsson et al., 1990) (Fig. 8.5), it indicates that the volume of Plinian and phreato-Plinian products (Phases 1 to 3) have been previously underestimated. An increased volume for these earlier phases of the eruption fits well with the formation of the voluminous Phase 3 tuff cone, which was likely accompanied by significant ash production.
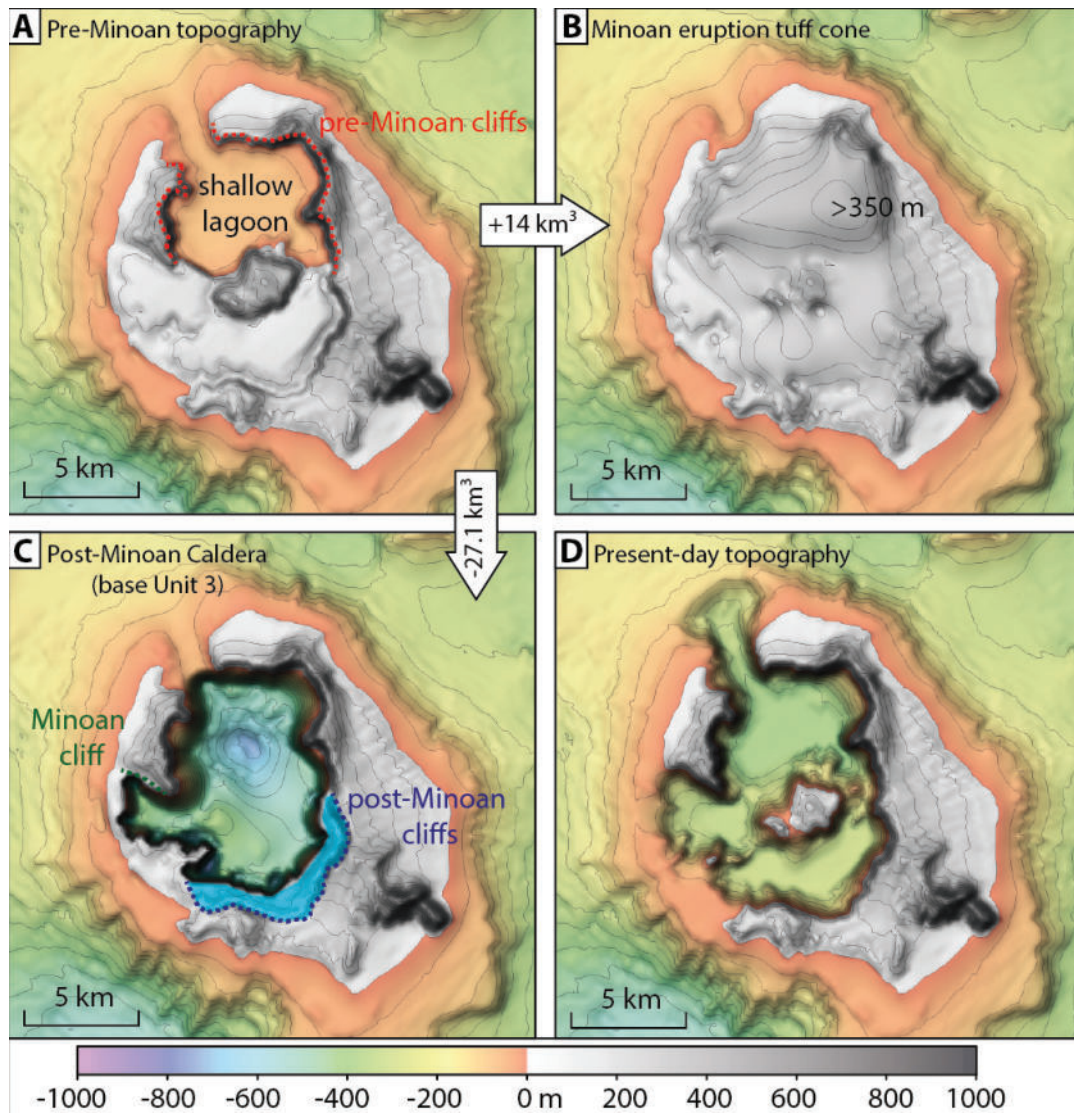
FIGURE 8.4: (A) Pre-Minoan topography with shallow marine northern caldera basin ("shallow lagoon") and pre-Minoan cliffs (dotted red lines) (Druitt and Francaviglia, 1992; Athanassas et al., 2016). (B) Tuff cone formed during the third phase of the Minoan eruption (Heiken and McCoy, 1984; Bond and Sparks, 1976). (C) Post-Minoan caldera based on mapping of the base of Unit 3 (Fig. 8.3) with caldera cliffs ("post-Minoan cliffs") that collapsed after the caldera collapse (marked blue) (Druitt and Francaviglia, 1992). (D) Present-day topography.

Our total eruption volume estimate of ∼31.4 ± 5.2 km³ DRE is in line with Pyle's (1990) estimate of 28-29 km³, which, compared to our calculation, overestimated the ignimbrite phase while not specifically considering the caldera infill (Fig. 8.5). Our caldera infill calculation of 5.5 ± 1 km³ DRE is the least well constrained of our estimates due to uncertainties in defining the base of the Minoan caldera infill and not being able to distinguish between Minoan material and material from earlier collapse events. Nonetheless, it is more robust than the previous estimate of 18-26 km³ DRE3, which was based on a conceptional reconstruction of the Minoan tuff cone that could not be verified in a seismic-based follow-up study (Johnston et al.,

2015). Additional uncertainties in our total volume estimate are i) the possibility that the mapped ignimbrite in Christina Basin may include Cape Riva ignimbrites and failed seafloor material, ii) an underestimate of ultra-distal ash, iii) distally deposited pumice rafts, and iv) post-eruptive erosion. An $\sim$25.7 km^3 turbiditic volcanoclastic megabed in the Cretan Basin has been attributed to the Minoan eruption (Karátson et al., 2018). However, neither seismic data nor sediment cores show indications for such a large mass-transport, making this interpretation highly unlikely. In contrast, our reconstruction of the caldera collapse volume of 32.5 $\pm$ 1 km^3 (Fig. 8.5) demonstrates an internal consistency between two independent approaches, implying high confidence in our estimates. A similar volume consistency has been noted for the $\sim$8.9 km^3 of submarine emplaced deposits of the 1883 Krakatau eruption and the associated $\sim$9 km^3 caldera volume (Self et al., 2004). However, our analysis represents a significantly more detailed and error-constrained approach, by combining a unique dataset of measurements over various scales, from microscopic (sub-millimetre resolution of CT-scans) through (multi)-meter (core stratigraphy and multi-channel seismic data) to shallow crustal scales (P-wave tomography).
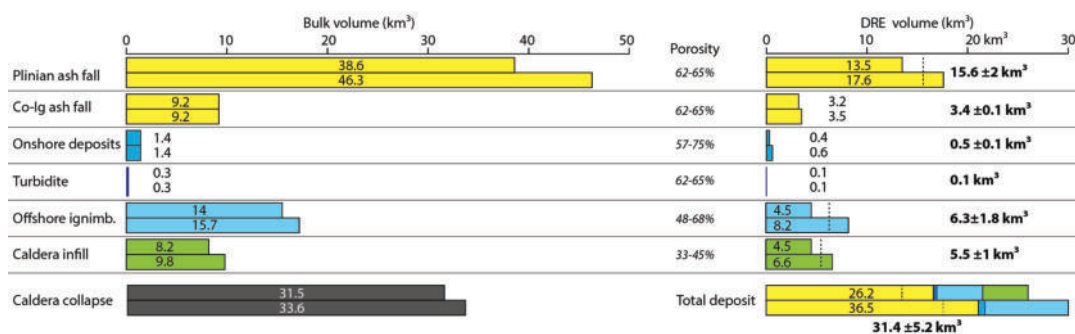
FIGURE 8.5: Minimum and maximum estimates for the bulk and DRE-volumes for the various components of the Minoan eruption deposits. Conversion between bulk and DRE-volumes is based on porosity estimates for each component. Similar caldera collapse volume and the total DRE-volume indicate internal consistency.

8.8 Santorini as a Benchmark for Volcanogenic Geohazard Assessment

Our study yields a marine ignimbrite volume of just 15.7- 17.4 km^3 (6.3 $\pm$ 1.8 km^3 DRE), significantly smaller than previous estimates of 10 - 41 km^3 DRE (Pyle, 1990; Sigurdsson et al., 1990; Sigurdsson et al., 2006) which has broad implications for tsunami hazard assessment. The Minoan marine ignimbrite volume is comparable to the 6.5 km^3 DRE emplaced by the 1883 Krakatau eruption over the course of several hours, which triggered tsunami waves as high as 50 m on the surrounding coasts (Self et al., 2004; Sigurdsson, 1991). Tsunami genesis during both eruptions, and by the marine emplacement of pyroclastic flows in general, are not well understood. Previous numerical simulations of the Minoan tsunami could reproduce reconstructed tsunami run-up heights around the Southern Aegean Sea (Novikova et al., 2011; Pareschi et al., 2006), but these used tsunami source parameters that are not in agreement with our mapping. Regardless, this reduced volume estimate is still large compared to other volcanic flows, like those of historic pyroclastic flows

and volcanic debris avalanches. A dome collapse event on Montserrat in 2003 produced pyroclastic flows over several hours (Herd et al., 2005), with the largest having a bulk volume of 0.016 km^3. The flow entered the sea, triggering a tsunami that was 4 m high on Montserrat's coast and up to 1 m at Guadeloupe (Herd et al., 2005). During the 2018 Anak Krakatau sector collapse, a debris avalanche of only 0.3 km^3 triggered a tsunami up to 13 m high at the coasts of Sumatra and Java, causing 437 fatalities (Grilli et al., 2019). These two events highlight the tsunamigenic potential of shoreline crossing volcanic mass-transport events. Numerical simulations of the 1888 Ritter Island sector collapse revealed that water displacement at the sea surface dominates the tsunami potential of volcanic debris avalanches (Karstens et al., 2020a). It appears likely that this is also true for ground-bound pyroclastic currents, meaning that marine emplaced ignimbrites may have a greater tsunamigenic potential than previously assumed.

To date, Santorini is the only large-scale eruption with a complete coverage of all eruption products. For most eruptions of marine volcanoes, including Tambora (1815), Kuwae (1425) and Samalas (1253), submarine deposit records are incomplete or nonexistent (Monzier et al., 1994; Self et al., 2004; Lavigne et al., 2013; Kandlbauer and Sparks, 2014). While tephra volumes can often be approximated based on onshore tephra thickness measurements (Lavigne et al., 2013; Kandlbauer and Sparks, 2014) reliable ignimbrite volume estimates depend upon the availability of high-resolution seismic reflection imaging. In the absence of such data, total volume estimates have large uncertainties. This limitation is also exemplified by the 1815 eruption of Tambora, where offshore ignimbrite volume estimates vary greatly between 2.8 km^3 DRE (Karstens et al., 2020a) and 21 km^3 DRE (Kandlbauer and Sparks, 2014). To date, most of the largest and most prominent Holocene eruptions, including 1257 Samalas, 1425 Kuwae, 1815 Tambora and 1883 Krakatau, lack reliable (marine) ignimbrite measurements. In the case of Santorini, our results reduce the ignimbrite, caldera infill and total volume estimates significantly, highlighting the large uncertainties introduced by not constraining submarine deposit volumes.

Empirical analyses suggest a correlation between caldera area and the associated eruption volume (Spera and Crisp, 1981). The Santorini caldera ($\sim$83 km^2) is significantly larger than the calderas of Kuwae ($\sim$56 km^2), Tambora ($\sim$37 km^2), and Samalas ($\sim$29 km^2), while volume estimates for their associated caldera-forming eruptions (Monzier et al., 1994; Self et al., 2004; Lavigne et al., 2013; Kandlbauer and Sparks, 2014) are all larger than our revised Minoan eruption estimate. In light of the large uncertainties of volume estimates without seismic datasets and the volume revision for the Minoan eruption, this may point to a systematic overestimation of the volume of the other large-scale Holocene eruptions. However, the polygenetic nature of many calderas, including Santorini, may also have an impact on the reliability of caldera area versus eruption volume correlations. This highlights the necessity of integrated seismic ignimbrite and core-based tephra analyses for other large-scale eruptions. For future analysis of major eruptions, our revised reconstruction of the Minoan eruption represents a framework for estimating eruption volumes. Only improved eruption volume reconstructions can allow reliable hazard and risk assessments for major volcanic eruptions.

Chapter 9

Formation of Undulating Seafloor Bedforms During the Minoan Eruption and their Implications for Eruption Dynamics and Slope Stability at Santorini

Abstract

The Minoan eruption of Santorini is one of the largest Holocene volcanic events, which produced large amounts of pyroclastic flows emplaced on the submerged flanks of the volcano. Marine geophysical surveys reveal a multitude of undulating seafloor bedforms (USBs) around Santorini. While similar structures are known from other volcanoes worldwide, Santorini offers the unique opportunity to relate USB formation with volcanic processes during one of the best-studied volcanic eruptions worldwide. In this study, we combine high-resolution seismic reflection data with multibeam echosounder bathymetry to reveal the internal architecture of USBs around Santorini and to relate their morphological characteristics to formational processes. The USBs around Santorini were formed during the Minoan eruption and represent mass transport deposits. Three types of deposits differ in composition or origin. (1) Depositional USBs, which can only be found to the north of the island, where Minoan eruption ignimbrites reach their maximum thickness and the undulating topography is the result of thrusting within the deposit. (2) USBs related to slope failures of volcaniclastics from the entire Thera Pyroclastic Formation, which can be found east, south, and west of the island. (3) USBs associated with deep-seated deformation, which occurs on the southwest flank along an area affected by rift tectonics and extends to a depth of more than 200 m below the seafloor. In cases (2) and (3), the USBs are formed upslope by block rotation and downslope thrusting. Our study indicates that these processes may have contributed to the generation of the devastating Minoan tsunami. Since Santorini is located in one of the most tectonically active regions in the Mediterranean, capable of producing earthquakes with magnitude M7+, our study has important implications for hazard assessment. A similar event located close to the island may have the potential to reactivate slope instabilities posing a previously undetected but potentially significant tsunami hazard.

9.1   Introduction

The Minoan eruption of Santorini in the Aegean Sea is considered one of the largest explosive volcanic eruptions in the Holocene (Sigurdsson et al., 2006; Johnston et al., 2014). Santorini lies in the center of the Hellenic Arc (Fig. 9.1) and has experienced by at least four caldera-forming eruptions, with the 1600 BCE Minoan eruption being the latest and largest (Druitt et al., 1999; Satow et al., 2021). Within hours to days, Santorini discharged vast amounts of gas-charged magma, sending tephra, pyroclastic flows, aerosols, and tsunamis across the eastern Mediterranean (Druitt et al., 2019a). During the eruption, large parts of the island collapsed, leaving behind a flooded caldera, which dominates Santorini's present-day landscape. The eruption had disastrous consequences for the people that populated the islands of the Aegean Sea in the Late Bronze Age and possibly contributed to the decline of the great Minoan civilization (Druitt et al., 2019a). Deposits of the Minoan eruption cover the seafloor around Santorini (Sigurdsson et al., 2006; Karstens et al., In Review_A), which is characterized by a multitude of Undulating Seafloor Bedforms (USBs) extending up to 25 km from the volcano (Bell, 2011; Hooft et al., 2017). Such undulating bedforms have been identified in a variety of geological settings, ranging from deep-sea fans to continental shelves, and can result from seabed modification by density flows, internal waves, and mass movement (e.g. Lee et al., 2002; Cartigny et al., 2011; Reiche et al., 2018). Extensive fields of USBs have been recognized on the submarine flanks of large-caldera forming volcanic centers, which comprise some of the largest amplitudes ever documented on the seafloor (e.g. Symons et al., 2016). Two recent studies by Pope et al. (2018) and Casalbore et al. (2021) identified two different processes for the formation of USBs at volcanic islands: (1) the deposition of eruption-fed density flows and (2) deformation by slope failure. However, deciphering the different formational processes can be challenging and requires a combination of high-resolution multibeam bathymetry and, most importantly, seismic profiles obtained across the trend of the wave fields (Casalbore et al., 2021).

Santorini has been affected by both major caldera-forming eruptions (Druitt et al., 2019b) and large-scale mass-wasting events (Bell et al., 2013; Nomikou et al., 2016a; Preine et al., 2022b). However, the influence of both processes on the formation of USBs at Santorini has not been resolved. In this study, we use an extensive collection of high-resolution multi-channel seismic data collected onboard R/V Poseidon (Karstens et al., 2020b) and high-resolution bathymetric data to reconstruct the nature and origin of the USBs, as well as the implications for hazard assessment around Santorini. Our first objective is to characterize USBs' morphology and seafloor expression and compare them with bedforms around other volcanic islands. Our second objective is to identify and reconstruct the processes controlling the formation of USBs around Santorini, including the relevance of pyroclastic flow deposition and slope instabilities in the formation of USBs. Finally, our third objective is to discuss the implications of USB formation on slope instabilities and the related hazards for Santorini.
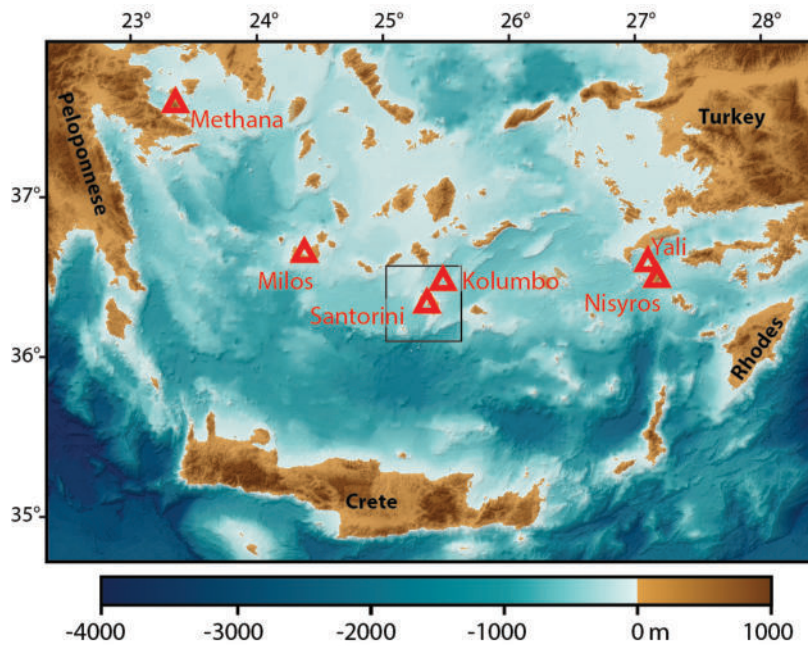
FIGURE 9.1: Map of the Aegean Sea showing the location of volcanic centers of the Hellenic Arc and the study area (box).

9.2 Geological Background

The Hellenic Arc consists of the Methana peninsula, the islands of Poros, Milos, Santorini, Kos, and Nisyros, as well as the submarine volcanoes of the Kolumbo volcanic chain (Fig. 9.1) and has been active from the Late Pleistocene to the Holocene (Sigurdsson et al., 2006; Nomikou et al., 2012). The Santorini caldera in the center of the arc is the most prominent manifestation of the Christiana-Santorini-Kolumbo volcanic field, hosting some of the largest explosive eruptions in the Mediterranean region. Santorini has been active since the early Pleistocene, with periodic cycles of volcanism and dormancy (Preine et al., 2022a). During the most recent volcanic phase of Santorini since ~0.36 Ma, there have been twelve major and numerous minor eruptions, as well as four caldera collapses creating the Thera Pyroclastic Formation (TPF) (Druitt et al., 1999; Druitt et al., 2019b). The last major explosive eruption, known as the Late Bronze Age (LBA) or Minoan eruption, occurred approximately 3600 years before present (Bond and Sparks, 1976; Friedrich et al., 2006; Druitt et al., 2019a) and represents the largest and most prominent event in Santorini's history (Satow et al., 2021). Volume estimates for the Minoan eruption vary significantly between 19 and 86 km^3 dense-rock equivalent (DRE) (Heiken and McCoy, 1984; Johnston et al., 2014), while the latest reconstruction integrating geophysical and sedimentological constraints indicates a volume of 31.4 $\pm$ 5.2 km^3 DRE (Karstens et al., In Review_A) making it one of the largest in the Holocene. The Minoan eruption occurred in a terrestrial to shallow marine setting of a preexisting caldera connected to the sea. It began with explosive eruptions from onshore vents on a pre-Kameni island in the caldera's center (Druitt et al., 1999; Johnston et al., 2014; Druitt et al., 2019a). After several hours, the eruption migrated into the flooded part of the caldera, where the interaction with seawater caused violent phreatomagmatic explosions and the subsequent formation of a tuff cone that filled up the pre-existing caldera and blocked the connection to the sea (Druitt et al., 1999; Johnston et al.,

2014; Druitt et al., 2019a). After all water in the caldera was evaporated, large volumes of pyroclastic flows entered the sea, causing destructive tsunamis. The subsequent caldera collapse formed the archipelago's present-day topography (Druitt et al., 1999; Johnston et al., 2014; Druitt et al., 2019a). Volcanism reemerged with the buildup of Palea and Nea Kameni islands in the caldera's center with the latest eruption in 1950 (Nomikou et al., 2014).
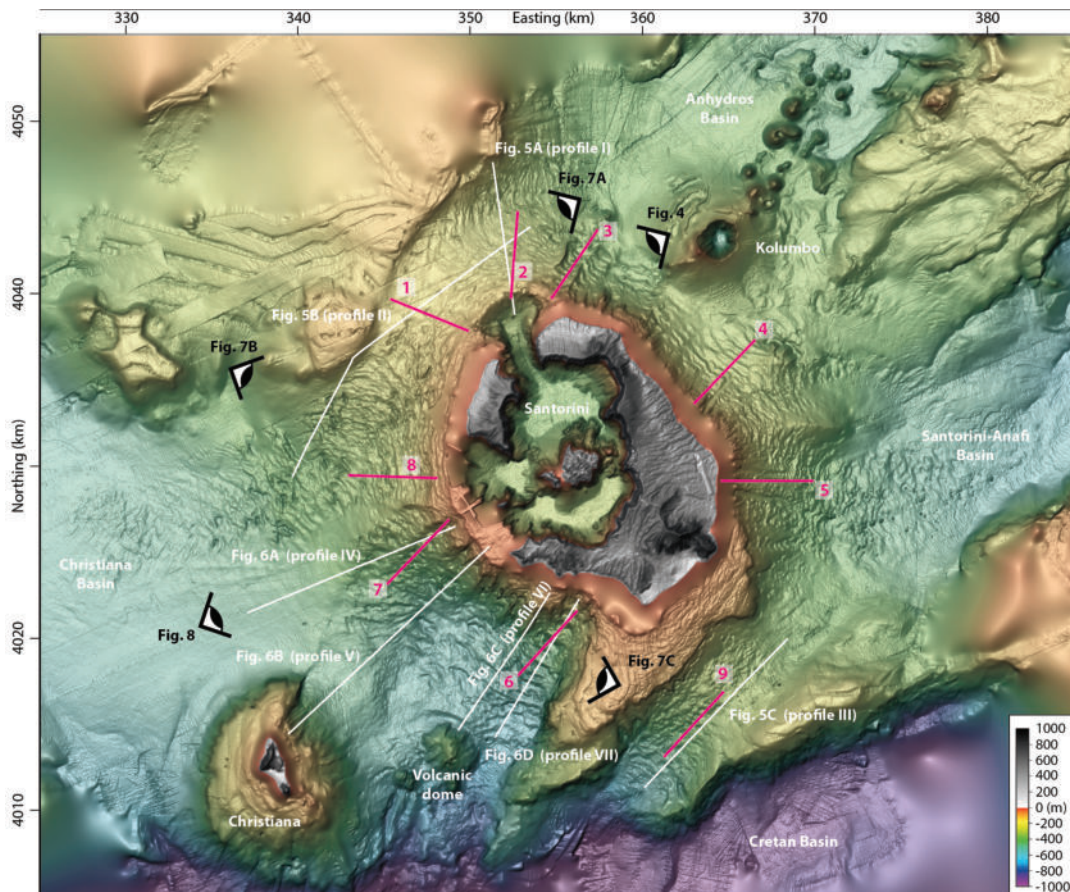
FIGURE 9.2: Shaded bathymetric map of the study area with white lines indicating the location of high-resolution seismic reflection profiles (white lines, Roman numbers) and morphologic profiles (pink lines, Arabic numbers) presented in Fig. 9.3.

9.3   Data and Methods

This study uses high-resolution multi-channel seismic profiles collected during research cruise POS538 on board R/V Poseidon in October 2019 (Karstens et al., 2020b). As the seismic source, we used a GI-airgun in harmonic mode with a primary (Generator) and a secondary (Injector) volume of 45 in3. Seismic signals were recorded by a Geometrics GeoEel streamer with active streamer lengths between 190 m to 250 m. The processing flow included surface-related multiple elimination and pre-stack time migration. The data have a horizontal resolution of ~1.56 m and a vertical resolution of 4-8 m at the seafloor (assuming a seismic velocity of 1,600 m/s). These datasets were analyzed using the seismic interpretation software suites Kingdom Suite by HIS and Petrel by Schlumberger.

The analyzed digital elevation model is a merge (Fig. 9.2) of satellite-derived Advanced Spaceborne Thermal Emission and Reflection Radiometer (ASTER), Community-sourced DEM from European Marine Observation and Data Network (E-MODnet), data acquired on board R/V AEGAEO (Nomikou et al., 2012; Nomikou et al., 2013) during GEOWARN project and R/V Marcus G. Langseth during the PROTEUS project (Hooft et al., 2017; Huff et al., 2021). The swath dataset has a lateral resolution of 20 m and was collected with SEABEAM 2120 20 kHz swath system on R/V Aegaeo and Simrad Kongsberg EM122 12 kHz multibeam echo sounder on R/V Marcus Langseth and processed using the MB-SYSTEM software suite (see Nomikou et al. (2012) and Hooft et al. (2017) for details). In addition, we use bathymetric data collected with an autonomous underwater vehicle (AUV) during cruise POS510 (Hannington, 2018) through seven dives by AUV Abyss that was equipped with the dual frequency (200/400kHz) RESON Seabat 7125 multibeam. The data were processed using the MB-SYSTEM software suite. To combine seismic and bathymetric data, we applied a seismic velocity of 1,500 m/s for the depth-time conversion.

We extracted nine elevation profiles (Fig. 9.3 and Supplement F.1) to constrain the wavelength and amplitude of the undulating seafloor bedforms and compared them with morphometric results from other volcanoes. We calculated regression curves along each profile and subtracted these from the original profiles to highlight undulations and to better constrain mean wave height and wavelengths. Finally, we compare the extracted values for Santorini with weight, height, and wavelength values from other volcanoes on a logarithmic plot (Fig. 9.3D) based on Pope et al. (2018) and Casalbore et al. (2021).

9.4 Results

9.4.1 Seafloor Morphology Around Santorini

USBs occur on all sides of Santorini and are particularly pronounced on the eastern, western, and southwestern flanks (Fig. 9.2). They formed on slopes with average angles of 3.3° and in depths of approx. 100 to 700 m below sea level. They extend up to 25 km from the caldera rim. Three representative bathymetric profiles crossing the northern (A), southwestern (B), and western (C) slopes of Santorini and a logarithmic plot comparing USB wavelengths and wave heights from Santorini derived from nine bathymetric profiles (A-C and supplement F.1) are compared to the USBs of other volcanoes (D) (Fig. 9.3). The USBs around Santorini have heights ranging from 1 to 60 m and wavelengths between 150 and 1,200 m and most of the undulations are asymmetrical (Fig. 9.3). In the logarithmic plot, the USBs arrange linearly and lie in the region of large-scale bedforms (profiles 3, 4, 7, 8, 9) and the intermediate area between large- and small-scale bedforms (profiles 1, 2, 5) (Symons et al., 2016). The smallest wavelengths (130-550 m) and wave heights (1-9 m) appear in the profiles in the north (profiles 1, 2; Fig. 9.3A) and the southeast (profiles 4, 5). These USBs appear in a similar area as bedforms found around Stromboli and Vulcano (Fig. 9.3D). Larger wavelengths (200-800 m) and wave heights (8-38 m) are found in the profiles in the west (profiles 7, 8) (Fig. 9.3B) and the south (profile 9) (Fig. 9.3D). These bedforms plot in a transitional area filling the gap between the Aeolian Island volcanoes and the large caldera-forming eruptions (Fig. 9.3D). Profile 6 in the southwest shows the longest wavelengths (700-1,200 m) and highest wave heights (28-62 m), which are comparable to USBs identified at Macauley, Zavodovski, and Dakataua volcanoes (Fig. 9.3D) (Casalbore et al., 2021).
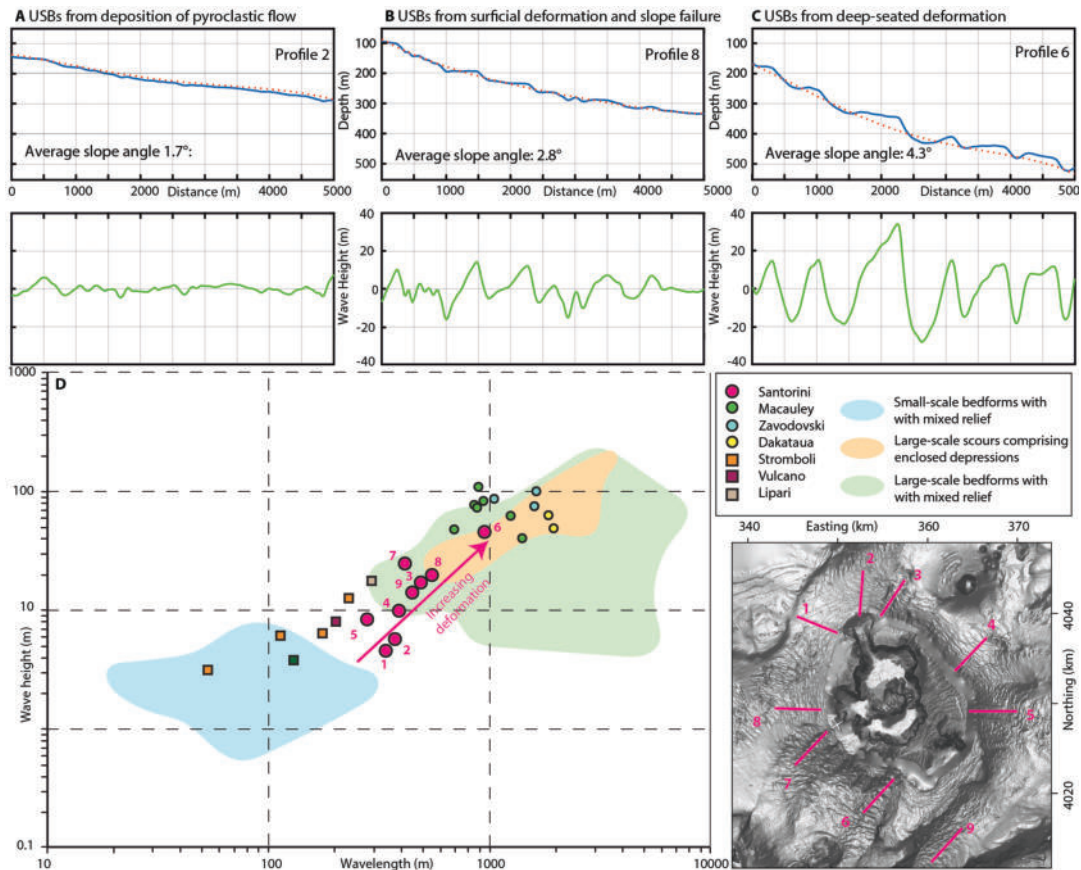
FIGURE 9.3: (A) – (C) Morphological profiles of Santorini's flanks (blue line), regression curves through these profiles (dotted red line), and difference of both (green line) showing the wavelength and wave height of USBs. Profile 2 shows subtle USBs related to pyroclastic flows to the north (A), profile 8 shows medium-scale USBs associated with slope failures to the west (B), and profile 6 shows large-scale USBs associated with deep-seated deformation (C). (D) Comparison of wave height and wavelength of USBs around Santorini versus USBs around other volcanoes based on Pope et al. (2018) and Casalbore et al. (2021).

Ultra-high resolution (2 m) AUV bathymetry allows us to investigate USBs on the northeastern flank of Santorini in great detail (Fig. 9.4). Here, we identify several concave USBs that extend from the shelf of Santorini towards the Anhydros Basin and form several large steps that we interpret as slumps (Fig. 9.4). Toward Santorini, there is a distinct, near-vertical cliff that is variably exposed, which we interpret to be the island shelf break. The USBs lie below this cliff and appear to be the result of mass movement across the cliff, which allows classifying them as type 2 USBs (slope-failure related) following Pope et al. (2018). We identify numerous blocks on the seafloor with sizes ranging from 2-15 m (see enlargements in Fig. 9.4). In addition, we identify several pockmarks with diameters of 20-35 m and depths of ~2 m that could be the result of degassing from the volcanoclastic sediments (Fig. 9.4).
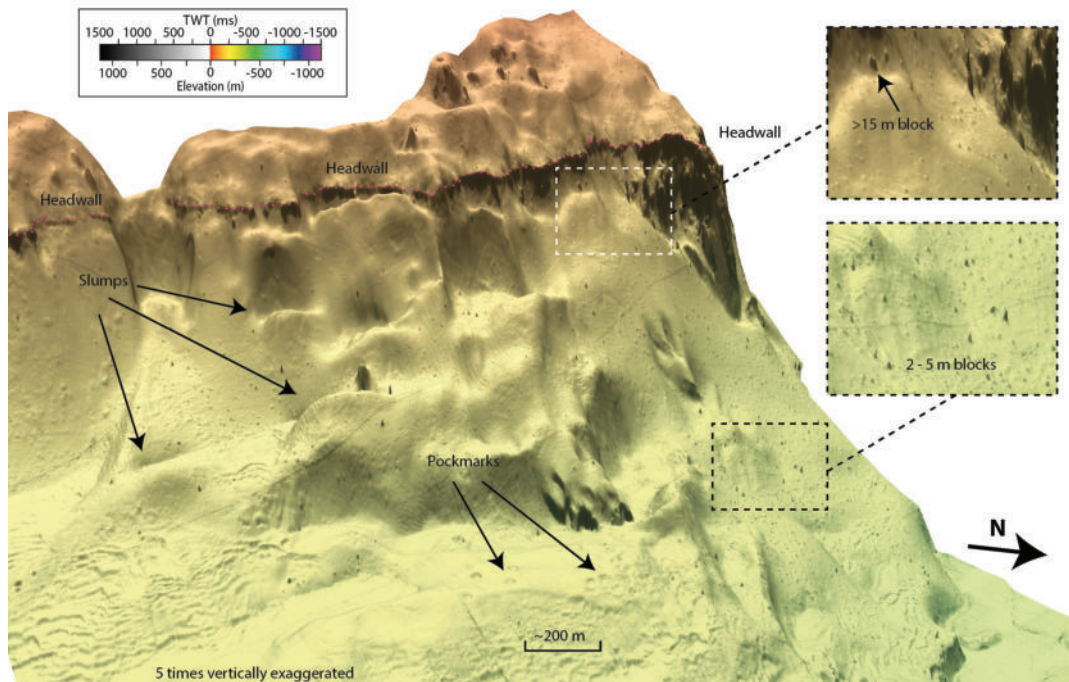
FIGURE 9.4: 3D view of high-resolution AUV bathymetry covering the northeastern slope of Santorini. The bathymetry shows marine ignimbrites from the Minoan eruption slumped from the island's shelf into the neighboring Anhydros Basin. Enlargements show multimeter-scale blocks that have been transported by the pyroclastic flows of the Minoan eruption.

9.4.2 Seismic Interpretation of USB Structures

According to Preine et al. (2022a), the seismic stratigraphy of the basins around Santorini comprises six units of Plio-Pleistocene age (Figs. 9.5, 9.6). The sediments within the uppermost Unit 6 consist of volcaniclastic deposits of the TPF, while Unit 5 is interpreted to consist mainly of hemipelagic sediments (Preine et al., 2022a). Towards the flanks of Santorini, interpretations of the stratigraphy become ambiguous since deeper units fade out. In contrast, the shallowest units have been deposited by the 3.6 ka Minoan and 22 ka Cape Riva caldera-forming eruptions (Karstens et al., In Review_A). Seismic profile I extends from the northern caldera breach of Santorini towards the Ios shelf (Fig. 9.5A). The red horizon marks the shallowest unit around Santorini, interpreted as Minoan ignimbrite, which is erosive at the slope of the caldera but becomes conformable towards the Ios shelf (Karstens et al., In Review_A). The internal reflections are wavy and stacked upon each other, with some internal reflections indicating the thrusting of material (Fig. 9.5A). The blue horizon (h6) marks the base of Unit 6, which consists of a series of wavy or chaotic seismic subunits forming a thick (∼350 m) wedge that comprises the eruptive products of the TPF Preine et al. (2022a); the green horizon marks a prominent internal horizon of Unit 6 (Fig. 9.5A).
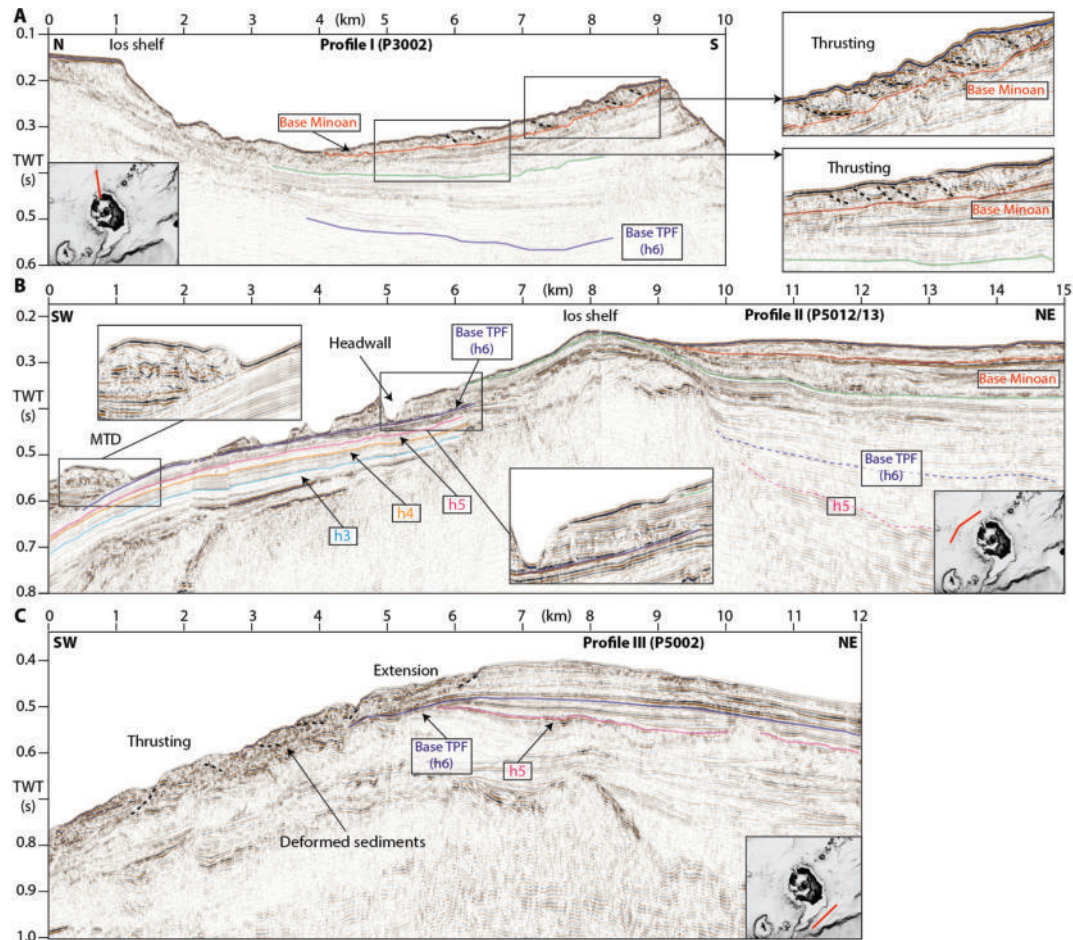
FIGURE 9.5: (A) Seismic profile extending from the northern breach of the caldera towards the Ios shelf with enlargements highlighting the internal architecture of the shallowest seismic subunit. (B) Seismic profile between the northwestern flank of Santorini and the Ios shelf. (C) The seismic profile south of Santorini extending from the Santorini-Anafi Basin towards the Cretan Basin Colored lines indicates key horizons as defined in Preine et al. (2022a) and Karstens et al. (In Review_A).

Seismic profile II extends from the northern flank of Santorini towards the northeastern Christiana Basin (Fig. 9.5B). The Ios shelf forms a ridge separating the profile into two domains. To the east, we identify the same units described for profile I and TPF deposits of Unit 6 reach a thickness of ∼200 m with the Minoan Unit lying conformable on top (Fig. 9.5B). The profile direction is parallel to the local USB trend explaining the lack of surface undulation (Fig. 9.5B). West of the ridge, Unit 6 is significantly thinner (∼50 m) or even absent which is the result of a seafloor failure comprising material of Unit 6 with horizon h6 acting as glide plane (Fig. 9.5B). The failed material was transported from the headwall over several kilometers forming a chaotic mass transport deposit (MTD) on top of undisturbed sediments from Unit 6 (see enlargements in Fig. 9.5B). The exposed glide plane and the translated blocks as well as the MTD cause an undulating seafloor expression (Fig. 9.5B). Seismic profile III covers a 5-km-wide channel connecting the Santorini-Anafi Basin with the Cretan Basin south of Santorini (Fig. 9.5C). Upslope, the shallow stratigraphy comprising Units 5 and 6 is characterized by well-stratified sediments, while Unit 6 is

affected by strong deformation further downslope (Fig. 9.5C). In this area, there is no seismically resolvable layer that can be associated with the Minoan eruption. The deformation causes a highly complex internal structure and appears to be a combination of extensional and compressional deformation leading to the undulating seafloor morphology.

Seismic profile IV extends from the western caldera breach into the Christiana Basin, where the TPF/Unit 6 has a thickness of ~50 m, with the Minoan deposits representing a flat and conformable subunit (Fig. 9.6A). In contrast, towards Santorini, sediments comprising Unit 6 (and possibly 5) are strongly deformed. Further upslope at profile-kilometers 13-15, large-scale USBs appear to be the surface expression of rotated blocks (Fig. 9.6A). Further south, the seismic profile extends from Santorini towards the southeastern part of the Christiana Basin terminating against the Christiana edifice (Fig. 9.6B). Similarly, there is a pronounced contrast of the internal architecture of Unit 6 with well-stratified reflections in the southwestern part and strongly deformed sediments on the foot of the flank of Santorini (profile-km 8-13, Fig. 9.6B). The transition from both facies is highlighted by the enlargements which shows that the deformation affects both Unit 6 and Unit 5. Deformation at the flank is extensional with rotated blocks (profile-km 12-14, Fig. 9.6B), while thrust structures indicate a compressional regime at the toe of the deformed flank segment (Fig. 9.6B).

Profiles VI and VII cross the southeastern margin of the Christiana Basin and highlight the pronounced flank deformation in this area (Fig. 9.6C, D). The profiles are oriented parallel to the slope direction (Fig. 9.6C, D). While profile VI shows an intact and undeformed slope segment (Fig. 9.6C), profile VII covers a failed slope segment less than 2 km apart (Fig. 9.6D). The undeformed slope segment consists of well-stratified sediments on the upper flanks; there is no indication of internal deformation in this flank segment (Fig. 9.6C). In marked contrast, profile VII shows the largest amplitudes of USBs around Santorini (up to 60 m) and the distinctive step-like bedforms show a strong indication of rotational deformation, indicating an extensional regime (Fig. 9.6D). The internal architecture of the step-like bedforms here is complex and backward-tilted layers lying on a well-defined basal shear surface can be identified (h6, Fig. 9.6D).
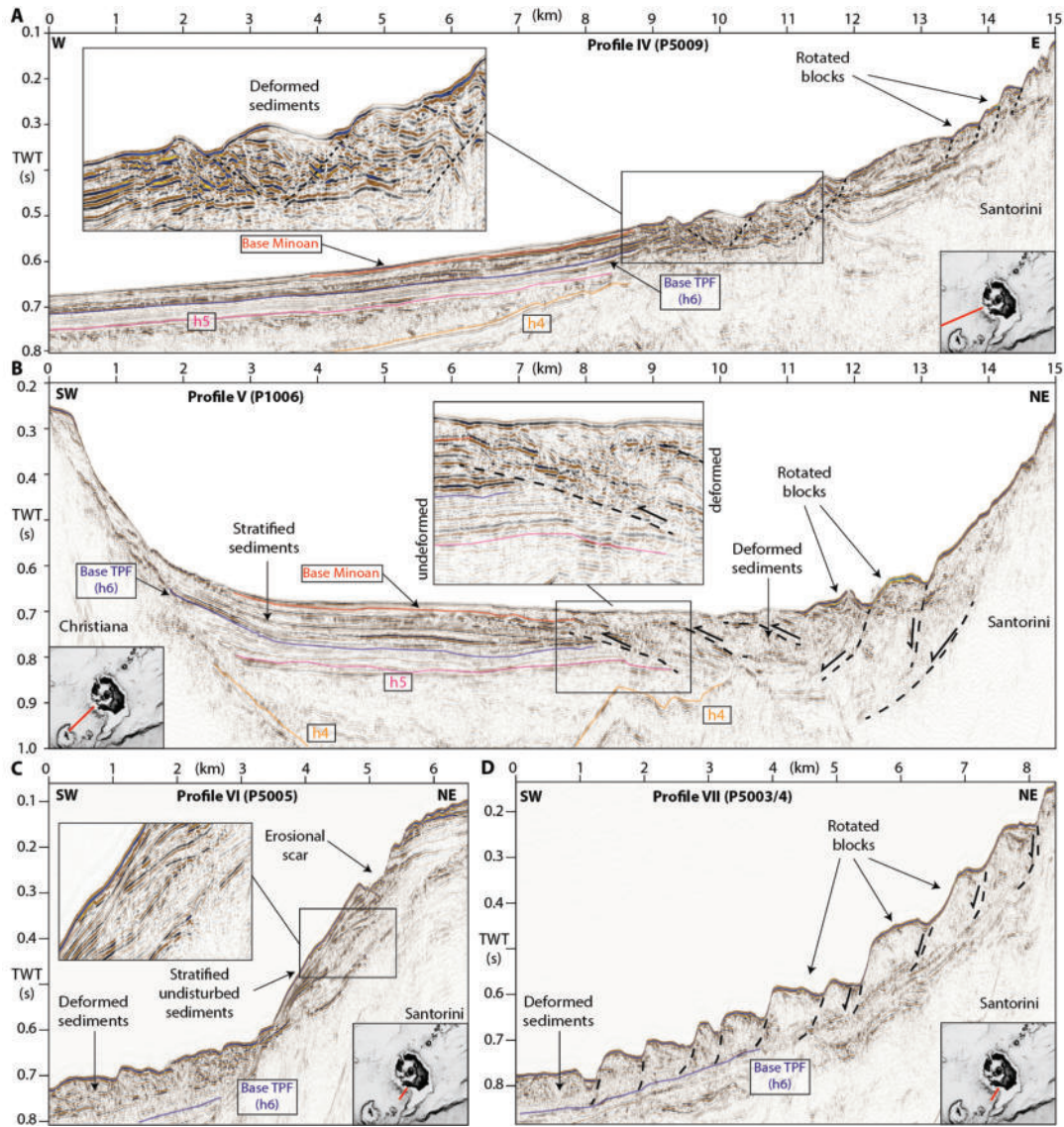
FIGURE 9.6: Seismic profiles from the western and southwestern flanks of Santorini.(A) Seismic profile extending from the western caldera breach towards the Christiana Basin. The enlargement highlights an area of distinct internal deformation. (B) Seismic profile between Santorini and Christiana. The enlargement highlights a transitional zone between laminated and highly disturbed seismic facies of Units 5 and 6. (C), (D) Seismic profiles extending from the southwestern flank of Santorini towards the southwest with little (C) and intense (D) internal deformation.
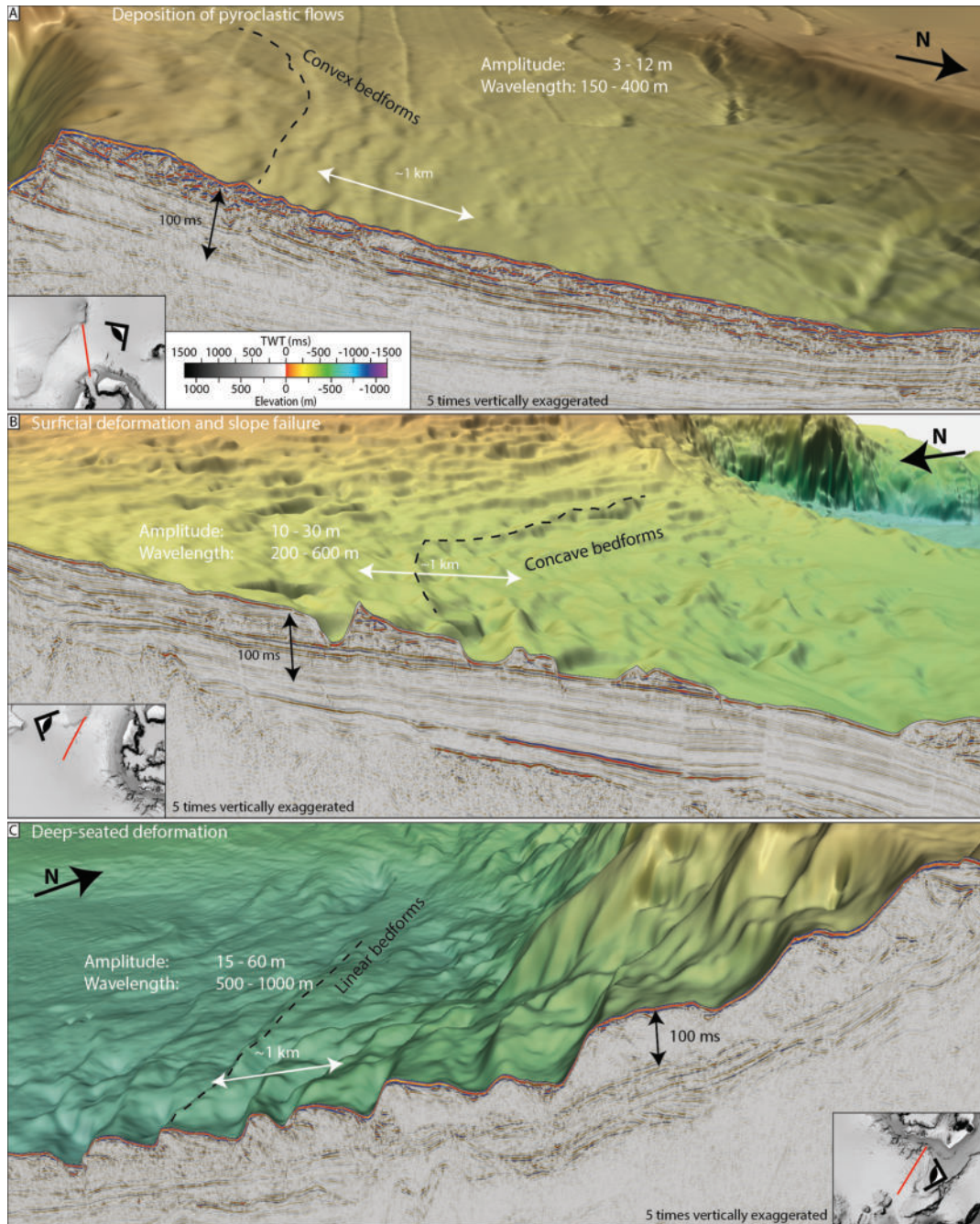
FIGURE 9.7: 3D views on seismic profiles combined with morphological grids of the slopes of Santorini. (A) Northern slope of Santorini viewed from the east. The rim of the northern caldera breach is visible on the left side. Small-scale USBs extend behind the breach. Seismic profile corresponds to Figure 9.4A. (B) Northwestern flank of Santorini viewed from the northwest. Irregular USBs are related to slope failures of the TPF. Seismic profile corresponds to Figure 9.4B. (C) Southwestern flank of Santorini viewed from the south. USBs are related to rotated blocks. Seismic profile corresponds to Figure 9.5D

9.4.3   Combination of Bathymetric and Seismic Reflection Data

We combine seismic profiles with the multibeam bathymetry to show a 3D view of the northern flank of Santorini between the northern caldera breach and the Ios shelf (Fig. 9.7A). USBs are limited to the area just behind the caldera breach, with comparably small amplitudes (3-12 m) and wavelengths (150-400 m, Fig. 9.7A). The bathymetry highlights that the USBs have a convex shape and extend radially along the northern caldera breach (Fig. 9.7A). On the northwestern slope of Santorini towards the Christiana Basin, USBs show a concave shape and are related to the erosive surface observed in the seismic profile (Fig. 9.7B, 9.5B). These features have larger amplitudes (10-30 m) and larger wavelengths (200-600 m) compared to the northern flank of Santorini. Where Unit 6 is absent, the seafloor is a smooth surface, indicating that horizon h6 marks a major lithological boundary separating consolidated sediments from Unit 5 (comprising mainly hemipelagic sediments) from Unit 6 (comprising mainly volcaniclastic material from the TPF; Preine et al. (2022a)). On the southwestern flank of Santorini, the rotated blocks affect large areas along the slope and mid-slope areas (Fig. 9.7C). This internal deformation affects the entire strata of Unit 6, and, strikingly, none of these large USBs are covered by seismically resolvable sediment, indicating a young formation or reactivation age of these features (Fig. 9.7C).

9.5   Discussion

9.5.1   Characterization of Large-Scale Undulating Seafloor Bedforms Around Santorini

Pope et al. (2018) have identified the deposition of volcanogenic flows and gravitationally-driven slope failure as the main processes controlling the formation of USBs on the submarine flanks of volcanic complexes. According to their classification, depositional bedforms (type 1) are associated with a convex planform shape and a relatively undisturbed internal stratigraphy. Slope failure-related bedforms (type 2) have a concave to linear planform shape. They are characterized by a chaotic internal architecture with thrust faults, indicating compression at the toe of the MTD, and normal faults, indicating extension further upslope (Pope et al., 2018).
USBs are known from many other submarine volcanoes, including Macauley, Dakataua, Zavodovski, the Aeolian Islands, and the Azores (Pope et al., 2018; Casalbore et al., 2021; Chang et al., 2022). Macauley, Dakataua, and Zavodovski volcanoes are similar in size to Santorini, approximately 5-15 km in diameter, lie in island arc settings, and have had caldera-forming eruptions that discharged ∼10 to 100 km^3 of tephra with pyroclastic flow generation as at least one phase of each eruption (Siebert, 2002). USBs around these volcanoes have the largest wavelengths and wave heights (Fig. 9.3D). On the other end of the spectrum are USBs from the Aeolian Islands, which have smaller wavelengths and wave heights (Fig. 9.3D). While volcanism at the Aeolian Islands is mainly effusive, pyroclastic flow generating eruptions are known from Lipari, Vulcano, and Stromboli (Lucchi et al., 2013).
USBs at Santorini cover a comparably wide range of the spectrum with wave heights between 1 and 80 m and wavelengths between 150 and 1,200 m and plot between the Aeolian Island USBs and those associated with large caldera-forming centers suggesting that there is likely a continuum of USBs in the wave height/wavelength domain that defines a broadly linear trend on a log/log plot (Fig. 9.3D). The smallest USB wavelengths and wave heights around Santorini are found on the northern

slopes, where USBs have a convex bedform (Figs. 9.2, 9.5, 9.6, 9.7). The north flank of Santorini has been the main depocenter of volcaniclastics from the TPF, and it is possible to identify the base of Minoan eruption ignimbrite (Fig. 9.5A, 9.7A) (Preine et al., 2022a; Karstens et al., In Review_A), that were likely deposited by pyroclastic flows (Druitt et al., 1999; Johnston et al., 2014; Druitt et al., 2019a). Therefore, this deposit and its surficial USBs are flow-derived depositional structures per definition (type 1 following Pope et al. (2018)). However, their internal architecture and seismic characteristics differ significantly from typical type 1 units as the Minoan ignimbrite has a somewhat chaotic internal architecture with coherent internal reflections indicating thrust faults that control the extent and location of surface undulations. There is no evidence of internal anti-dune-like structures resulting from bedload deposition (Figs. 9.5A, 9.7A). Therefore, USBs north of Santorini define a new sub-class of bedforms (e.g., type 1B) that should be added to the classification scheme of Pope et al. (2018).

Along Santorini's northeastern, western, and southwestern slopes, the USBs' wavelengths and wave heights increase, and seismic profiles show a significant deepening of deformation beneath the USBs (Fig. 9.8A-C). To the southwest of Santorini, linear USBs have the largest wavelengths and wave heights (Figs. 9.3D, 9.6C, 9.7C) and have similar dimensions as those found around other volcanoes affected by caldera-forming eruptions (Fig. 9.3D). USBs in this area are the surface expression of km-scale rotated blocks, thrust structures, and heavily deformed sediments. To the south, east, and west of Santorini, the planform shape of the USBs is concave to linear (Fig. 9.2), and the deformation affects mainly the TPF with normal faults indicating extension in the upper slope of the profiles (Figs. 9.5C, 9.6). Their seismic stratigraphy and planform shape indicate slope failure as the governing formation process following the classification scheme of Pope et al. (2018). The AUV bathymetry underscores this interpretation from the northeastern flank of Santorini, where we can identify a distinct headwall and related slumps (Fig. 9.4). This scar seems to be related to a former shelf break, likely consisting of lava flows from the Peristeria volcano, which defines the morphology of the northeastern side of Santorini (Fig. 9.2) (e.g. Druitt et al., 1999).

Profile V covers an area within the northwestern USBs resulting from a slope failure with upslope extension and compression at the toe (Fig. 9.6B). The fact that a seismically resolvable unit covers neither this area nor the USBs elsewhere suggests that the observed slope instabilities were active during or after the deposition of the Minoan ignimbrite, which is also highlighted by the presence of large blocks in the AUV bathymetry (Fig. 9.4). The USBs to the south (profile 9; Fig. F.1I), east (profile 8, Fig. 9.3B) and west (profile 4, Fig. F.1D) of the island have intermediate wavelengths and wave heights (Fig. 9.3D) and have concave surface bedforms.

The comparison of USBs at Santorini indicates that USBs become larger with increasing amounts of internal deformation (Fig. 9.3D). In addition, there is a correlation between the average slope angle and USB dimensions, suggesting that increasing slope angles influence type 2 USB formation (Fig. 9.3), which agrees with observations from other geological settings indicating that slope angle is the dominant factor for slope stability (Miramontes et al., 2018).
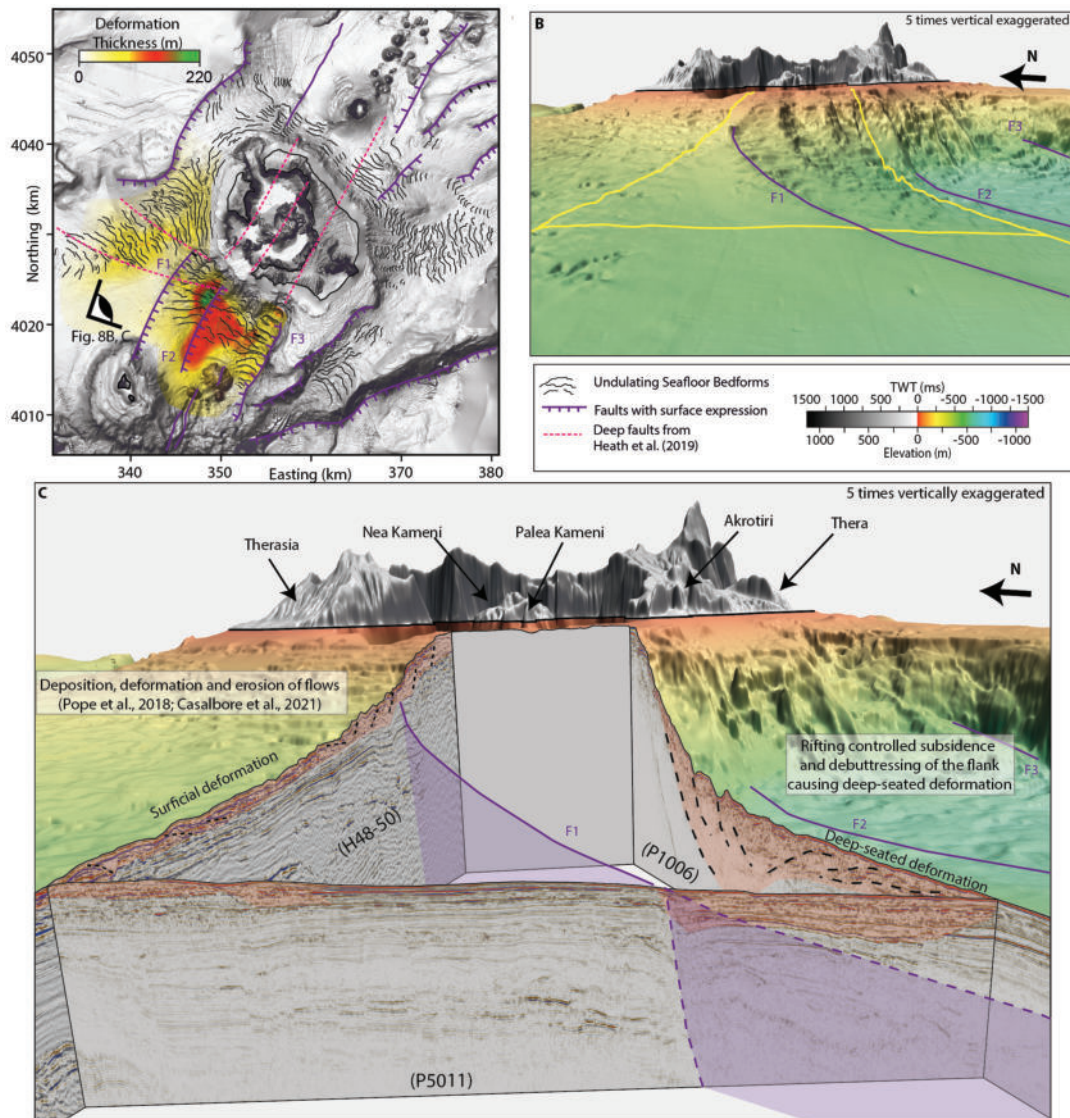
FIGURE 9.8: (A) Morphological map of Santorini highlighting USBs, major surficial faults from Nomikou et al. (2018b) and Nomikou et al. (2019) and Preine et al. (2022a), deep faults from Heath et al. (2019), as well as the thickness of the deformation. 3D view on the southwestern flank of Santorini from the Christiana basin with major faults and seismic profiles shown in (C). (C) 3D view from the same viewpoint combining seismic profiles and bathymetry illustrating how deformation deepens towards the southeast correlating with major faults. Profile H48-50 is from another survey (POS 338; Hübscher et al. (2006)).
See Preine et al. (2022b) for acquisition and processing details.

9.5.2 Formation of Undulating Seafloor Bedforms During the Minoan Eruption

Entrance of Pyroclastic Flows into the Sea

Caldera-forming eruptions like the Minoan event can generate enormous volumes of volcaniclastic sediment reaching up to hundreds of cubic kilometers of material (e.g. Carey and Sigurdsson, 1989; Legros and Druitt, 2000; Freundt, 2003). The material can be delivered to the marine environment by fallout through the water column,

or sediment gravity flows that typically originate as pyroclastic flows and surges (Carey and Schneider, 2011). The 1883 eruption of the Krakatau volcano in Indonesia serves as an essential guide to the potential sedimentological impact on the marine environment and as an analogue for the Minoan eruption of Santorini. Over the period of approximately one day, the Krakatau eruption discharged 14 km^3 of dacitic magma in the form of pumice and ash, with about 10 km^3 deposited into the marine environment surrounding the volcano, and principally by the entrance of hot pyroclastic flows into the sea (Sigurdsson et al., 1991). There is only inferred information about the timing and duration of pyroclastic flow discharge at Santorini. Still, a recent seismic analysis suggests that the volume may have been as much as 4.5 to 8.2 km^3 DRE of pyroclastic material (Karstens et al., In Review_A). Such a large volume of volcaniclastics entering the sea, essentially instantaneously, would have had a significant impact on the seafloor. The analysis of sediment cores around Santorini indicates the presence of ground-based flow deposits extending tens of kilometers towards the east of Santorini, deposited before co-ignimbrite ash settled on top (Karstens et al., In Review_A). This suggests that pyroclastic flow discharge occurred over hours rather than weeks indicating that pyroclastic flow discharge rates of the Minoan and 1883 Krakatau eruptions likely were similar.

At Krakatau, major underwater pyroclastic flows formed a deposit up to 80 m high that extended up to 80 km from the volcano (Carey et al., 1996). Submarine deposits were laid down in all directions around the volcano due to pyroclastic flows being unconfined during their runout from large-scale subaerial eruption column collapse (Sigurdsson et al., 1991). The presence of USBs at Krakatau is currently unknown due to a lack of high-resolution bathymetric data. An omnidirectional deposition of pyroclastic flows during the Minoan eruption can be inferred from the great thicknesses of onshore pyroclastic flow deposits on the coasts of Santorini, where enormous volumes of pumice and ash must have entered the sea (Druitt et al., 2019b). This agrees with analogue volcanic jet experiments of the collapse of a particle-laden plume to simulate pyroclastic flow formation resulted in the deposition of concentric sediment ridges around the plume source resembling the USBs observed at Santorini (Gilchrist and Jellinek, 2021). These authors suggested that the sediment waves surrounding Santorini may have formed by concentric discharge of material during plume collapse.

The seismic stratigraphy of Minoan deposits to the north of Santorini allows an analysis of the depositional processes controlling USB formation (Figs. 9.5A and 9.7A). USBs of the northern deposit fan correlate with internal thrust structures, indicating a compressional regime at the toe of the slide (Frey-Martínez et al., 2006). Such structures are often found in spatially confined MTDs worldwide (e.g., Sakar Island, Kühn et al. (2021) or offshore Montserrat, (Watt et al., 2012). However, the Minoan ignimbrite was emplaced unconfined, and we suggest that thrusting developed as the result of loss of kinematic energy during emplacement (Frey-Martínez et al., 2006), causing the leading flow segment to decelerate due to interaction with the substrate and the following material to push into it (Fig. 9.8B).
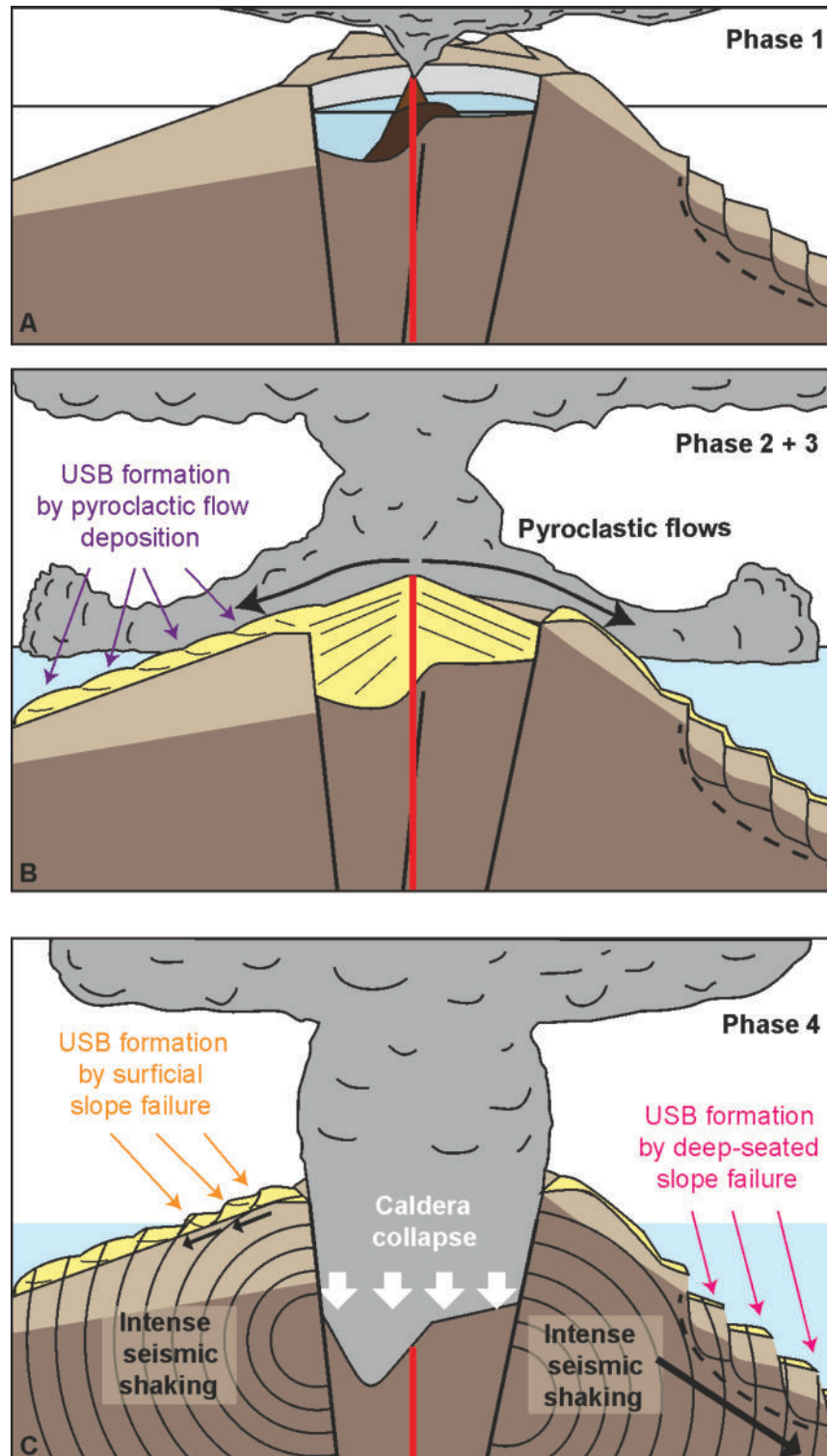
FIGURE 9.9: Illustration of the development of USBs on Santorini's flank. (A) Phase 1 of the eruption initiated with a subaerial eruption from an onshore vent in the Caldera (Druitt et al., 2019a) with pre-exiting deep-seated deformation at the southern flank. (B) Deposition of pyroclastic flows during Phases 2 and 3 of the eruption forming depositional USBs on the northern flank of the island. (C) Caldera collapse during Phase 4 of the eruption triggering slope instabilities and reactivating deep-seated deformation.

Instability of Volcaniclastic Deposits

Apart from the northern flank, nearly all USBs around Santorini result from deformation processes, i.e., slope failures. Earthquakes generate horizontal and vertical accelerations that increase shear and normal stresses and therefore are possible triggers for such deformation (Hampton et al., 1996). Strong, shallow earthquakes are a common feature associated with large-scale explosive eruptions, especially when the foundering of the volcanic edifice leads to the generation of a caldera (Yokoyama, 2001). Earthquakes with magnitudes of 7 have been inferred for the 1815 eruption of Tambora in Indonesia and the 1912 eruption of Mt. Katmai in Alaska (Abe, 1992; Yokoyama, 2001). More recently, the smaller eruption of Mt. Pinatubo in 1994 was associated with an earthquake of magnitude 5.7 (Mori et al., 1996), and a correlation between earthquake magnitude and caldera collapse volume has been suggested (Abe, 1980). During the Minoan eruption, the caldera floor dropped by almost 600 m (Johnston et al., 2014) with a caldera collapse volume of $\sim$33 km^3 (Karstens et al., In Review_A). Significant earthquakes likely accompanied this event.

Hürlimann et al. (2000) analyzed the magnitude of an earthquake necessary to generate significant slope failure on the sides of a caldera-forming volcanic center. They calculated that even a comparably small earthquake with magnitude Mw 5 centered at a caldera could trigger slope failures. Although such calculations are difficult to generalize or to transfer to Santorini directly, it appears plausible that seismic shaking was a contributing factor in the formation of deformational USBs at Santorini. Type 2 USBs, including those around Santorini, share morphological characteristics known from subaqueous MTD affected by spreading (e.g., the Storegga Slide), which in many cases are triggered by earthquakes causing liquefaction or strain softening along a lithological defined glide plane (Micallef et al., 2007; Bucci et al., 2022). The boundary between the TPF and the underlying hemipelagic sediments northwest (h6 in Fig. 9.5B; (Preine et al., 2022a)) or older lava flows northeast of Santorini (Fig. 9.4) appears to have acted as glide planes for USBs related to surficial deformation around Santorini. The mainly pyroclastic deposits of the TPF are expected to have a low effective stress governed by the low density of pumice clasts (Wiemer and Kopf, 2017). The combination of intense seismic shaking and rapid deposition of large amounts of material on top of deposits of low shear strength on steep slope gradients can explain the formation of slope instabilities and the creation of deformational USBs around Santorini during the Minoan eruption (Fig. 9.9B, C). Evidence for this process can be observed to the south, east, and west of Santorini, where slope failure, even locally, caused an evacuation of the slide plane (Figs. 9.5B, 9.7B) or exposed the headwall (Fig. 9.4).

Deep-Seated Deformation of the Volcanic Edifice

In terms of sediment depth, the deformation of volcanic deposits on the western flank of Santorini is comparably shallow to that in the northwest but becomes significantly deeper towards the southeastern margin of the Christiana Basin (Fig. 9.8A). The lateral extent of this deep-seated deformation correlates with the Christiana Fault (F1 in Fig. 9.8B), which stretches from the sidewall of a sector collapse at Christiana (Preine et al., 2022b) towards the northeast and continues on the western slope of Santorini. This fault correlates with a topographic step in the seafloor (Figs. 9.2, 9.8). It defines the boundary between an area with smooth morphology

with minor USBs to the NW and a significantly more rugged terrain with large amplitude/wavelength USBs to the SE in the Christiana Basin (Figs. 9.2, 9.8). This morphology results from extension along rotational normal faults on Santorini's slope and a compressional regime leading to thrusts in the Christiana Basin (Figs. 9.6B, 9.6C). Towards the southwest, an additional morphological step coincides with faults (F2) controlling the segmentation of Christiana Basin sedimentary infill (Preine et al., 2022b). A major normal fault (F3) defines the southeastern boundary of the Christiana Basin (Fig. 9.8) following the regional SW-NE fault trend (Hooft et al., 2017; Nomikou et al., 2018b; Preine et al., 2022c). This suggests that rift tectonics affect the slopes of Santorini and control the deep-seated deformation, which is only observed in front of the southwestern flanks of the volcanic edifice. Strikingly, this area between Santorini and Christiana marks the intersection of the former Pliocene ESE-WNW striking tectonic regime and the new NE-SW directed fault trend that emerged in Early Pleistocene and shaped the Santorini-Amorgos Tectonic Zone northeast of Santorini (Heath et al., 2019; Preine et al., 2022c). This new fault trend seems to continue underneath Santorini, and the intersecting fault trends define the area affected by deep-seated deformation (Fig. 9.8) (Heath et al., 2019; Preine et al., 2022c)).

Deep-seated deformation within volcanic edifices is known from many volcanoes worldwide, including Mount Etna, Kilauea, and Piton de Fournaise, where the interplay between volcanic rifts, gravitational instability, and regional tectonics appear to play a significant role (Poland et al., 2017). In the case of Etna, deformation controlled by major fault systems is an active process measured in the onshore and offshore domains that appear to occur (at least temporally) independent from volcanic activity (Urlaub et al., 2018). Deep-seated deformation of volcanic edifice received major attention with the 2018 sector collapse of Anak Krakatau, for which the analysis of Interferometric Synthetic Aperture Radar (InSAR) revealed that the volcanic edifice slowly deformed before the catastrophic collapse (Walter et al., 2019). Similar observations have been made for the 1888 Ritter Island sector collapse based on seismic data (Karstens et al., 2019), where deep-seated deformation caused instability of the volcanic edifice that formed USBs with thrust structures similar to those observed in the Christiana Basin. At Ritter Island, a small volcanic cone buttressed the actively deforming flank and caused the formation of a stable toreva block separating the two catastrophically failed flank segments (Karstens et al., 2019). The active opening and thus extensional regime of the Christiana Basin likely has had a contrasting effect, resulting in debuttressing and facilitating structural instability of Santorini's southwestern flank.

While the increase of deformation with depth suggests that deep-seated deformation at Santorini is a long-term process that took place before the Minoan eruption, likely, ground acceleration by major earthquakes and the readjustment of structural elements had a significant impact on the development of the observed slope instabilities (Fig. 9.9C). Since there is no evidence for seismically resolvable draping of the USBs their formation or reactivation occurred during or after deposition of the Minoan deposits. This suggests that a major pulse of deep-seated deformation likely accompanied caldera collapse during the Minoan eruption

Implications for Slope Stability and Geohazard Assessment at Santorini

The Minoan eruption is associated with a significant tsunami, whose deposits have been identified on the surrounding islands, on the northern coast of Crete, and as

far as Turkey and Israel (Bruins et al., 2008; Novikova et al., 2011; Lespez et al., 2021; Paris et al., 2022) There is an ongoing debate about the tsunami source mechanisms during the Minoan eruption, with caldera collapse and the emplacement of pyroclastic flows being the primary candidates in the publications above. At the same time, slope instabilities have not received much attention because they were not resolved before this study. Here, we suggest that the slope instabilities on the flank of Santorini formed or have been reactivated during the Minoan eruption. Such widely distributed deformation likely would have had a significant tsunami potential as demonstrated by the sector collapse of Anak Krakatau in 2018, during which a comparably small slide volume of $\sim$0.3 km^3 triggered a devastating tsunami at the coasts surrounding the Sunda Strait (Grilli et al., 2019). The deep-seated deformation between F2 and F3 alone affects sediments with a volume of $\sim$2 km^3 (Fig. 9.7). Considering that type 2 USBs are found on all sides of Santorini in shallow water depths of less than 500 m and that these have formed (or been reactivated) implies a significant tsunami potential during USB formation. We suggest that a combination of slope instabilities and the potential simultaneous deposition of 4.5 to 8.2 km^3 DRE of pyroclastic material (Karstens et al., In Review_A) could explain the large size of the Minoan tsunami.

Except for a phase of unrest accompanied by inflation from 2011 to 2012, the Santorini caldera floor is experiencing subsidence (Parks et al., 2015). It is considered unlikely that Santorini will host another caldera-forming event in the near future, as the last major eruption occurred only 3,600 years ago (Satow et al., 2021). However, catastrophic collapses of unstable volcanic flanks are not always related to volcanic activity (Vries and Francis, 1997). Santorini is located in one of Europe's most tectonically-active regions, which hosted the tsunamigenic 1956 Mw 7.5 and 7.2 earthquakes (Brüstle et al., 2014). If an earthquake with a similar magnitude occurred in the direct vicinity of the Santorini edifice, ground acceleration could reactivate the surficial slope instabilities surrounding Santorini, particularly on the southwest flank. At Kilauea, intense slip along the detachment of the Hilina slump was repeatedly associated with large-scale earthquakes like the 2018 Mw 6.9 and the tsunamigenic 1975 Mw 7.7 earthquakes (Lin and Okubo, 2020). The reactivation of the deep-seated deformation at Santorini's southwestern flank might have a significant, so far unrecognized tsunamigenic potential. As the zone of instability is entirely submerged, it cannot be monitored using satellite-based InSAR measurements. Additional marine seismic measurements and seafloor-based geodetic measurements like those applied at the submerged flank of Mt Etna (Urlaub et al., 2018) are required to evaluate the current state of the flank.

9.6 Conclusions

An integrated analysis of high-resolution seismic reflection profiles and bathymetric data led to the differentiation of three types of undulating seafloor bedforms (USBs) and their formational processes around the Santorini volcanic complex in the Aegean Sea. USBs to the north of the islands have the lowest amplitudes and wavelengths and formed within pyroclastic flow deposits from the 3.6 ka Minoan eruption. The undulations likely result from thrusting, caused by deceleration of the leading part of submarine flows during emplacement. This represents a new sub-type of depositional bedforms, adding to the classification scheme by Pope et

al. (2018). USBs to the west and northeast of Santorini are associated with slope failures that include Minoan deposits and volcaniclastic material from the entire Thera Pyroclastic Formation. These USBs and related collapse structures are not covered by material from the Minoan eruption, indicating that they have formed after the main phase of pyroclastic flow discharge. Southwest of Santorini in the Christiana Basin, USBs have the highest amplitudes and wavelengths and are associated with deep-seated deformation extending to at least 200 m below the seafloor. The deep-seated deformation spatially correlates with the intersection between Pliocene and present-day rift structures. A lack of mantling of the deep-seated USBs by Minoan deposits indicates that they have been formed, or more likely reactivated, during the Minoan eruption.

The common occurrence of USBs on the seafloor surrounding submarine and partially emergent calderas, particularly in subduction zone environments, suggests that specific volcanological and tectonic processes favor their formation. A characteristic feature of the undulating bedforms found on the slopes of large calderas is their radial distribution around the entire volcanic complex. Large-volume explosive eruptions that generate calderas in submarine/subaerial arc settings, such as Santorini's Minoan eruption, provide insights into the origin of concentrically distributed USBs. We suggest that a cascading series of events favor their formation during caldera-forming eruptions that include rapid loading of loose, unconsolidated pyroclastic material on submarine flanks, contemporaneous failure of such material due to associated large-scale seismic activity, and the activation of deeper-seated structural elements of complex caldera centers that are geodynamically controlled by local tectonics. The occurrence of large-scale USBs encircling a submarine or partially emergent caldera is likely to be a signature of previous large-scale explosive eruptions that have discharged tens to hundreds of cubic kilometers of magma. From a hazard perspective, pyroclastic flow emplacement and slope failures are fundamental tsunami source mechanisms during volcanic eruptions. While the devastating tsunami associated with the Minoan eruption of Santorini has previously been attributed to the submarine emplacement of several cubic kilometers of pyroclastic flows, widespread slope failures have not been considered a tsunami source mechanism. It appears most plausible that both processes acted synchronously during the Minoan eruption, which most likely increased the magnitude of the resulting tsunami. This also highlights the potential of USBs as indicators of tsunamigenic processes during past eruptions. Further combined seismic and morphologic surveys of large-scale marine volcanoes are necessary to evaluate whether the observations from Santorini can be applied to other major eruptions.

Acknowledgments

Chapter 10

Set up to Fail – Cascading Events During the 1650 Tsunamigenic Eruption of Kolumbo Volcano

Abstract

Volcanogenic tsunamis have caused more than 55,000 fatalities since the late 18th century (Auker et al., 2013). Tsunami generation is often due to a combination of processes including submarine explosions, pyroclastic flows, caldera subsidence, and flank failures (Paris et al., 2014). The 1650 eruption of Kolumbo submarine volcano triggered a tsunami causing major destruction on surrounding islands in the Aegean Sea (Cantner et al., 2014). However, the source mechanisms behind the Kolumbo tsunami remain disputed due to difficulties in sampling and imaging submarine volcanoes. Here, we show that it was the collapse of Kolumbo's northwestern flank that triggered both a highly explosive eruption phase and the tsunami. High-resolution three-dimensional seismic data reveal internal deformation and slumping of the flank that depressurized the magma feeding system and caused an initial catastrophic explosion. Kolumbo's volcanic cone was notoriously unstable as it consisted almost entirely of highly vesicular pumice from local fallout and volcaniclastic flows. Tsunami simulations constrained by the new data suggest that flank movement was the primary tsunami source mechanism followed by submarine explosive eruptions. Our analysis represents the first integrated quantitative reconstruction of a cascading sequence of natural hazards and suggests that monitoring of submarine flank movements should be used in early warning for tsunamigenic volcanic events.

10.1   Introduction

The 2022 Hunga Tonga-Hunga Ha'apai (HTHH) eruption in Tonga (Cronin et al., 2022) and the 2018 Anak Krakatau sector collapse in Indonesia demonstrated the devastating tsunami hazard of volcanic eruptions in shallow marine environments and at the land-sea-boundary (Grilli et al., 2019). While little is known so far about the processes preceding the HTHH eruption, Anak Krakatau has been a focus site for volcanological research in recent years. The 2018 tsunami of Anak Krakatau hit neighboring coasts without any warning and caused hundreds of casualties (Grilli et al., 2019). Satellite altimetry data from more than ten years before the event indicated deformation within the volcanic edifice (Chaussard and Amelung, 2012). However, it was only after the collapse that these observations were interpreted as

revealing prolonged, deep-seated deformation in the build-up to the collapse (Walter et al., 2019). Internal deformation of a volcanic flank preceding catastrophic failure has also been demonstrated for the 1888 Ritter Island sector collapse (Karstens et al., 2019; Watt et al., 2019) and episodic gravity-driven movement along deep decollements is known from several large volcanoes including Mt Etna (Puglisi and Bonforte, 2004; Urlaub et al., 2018) and Kilauea (Segall et al., 2006).
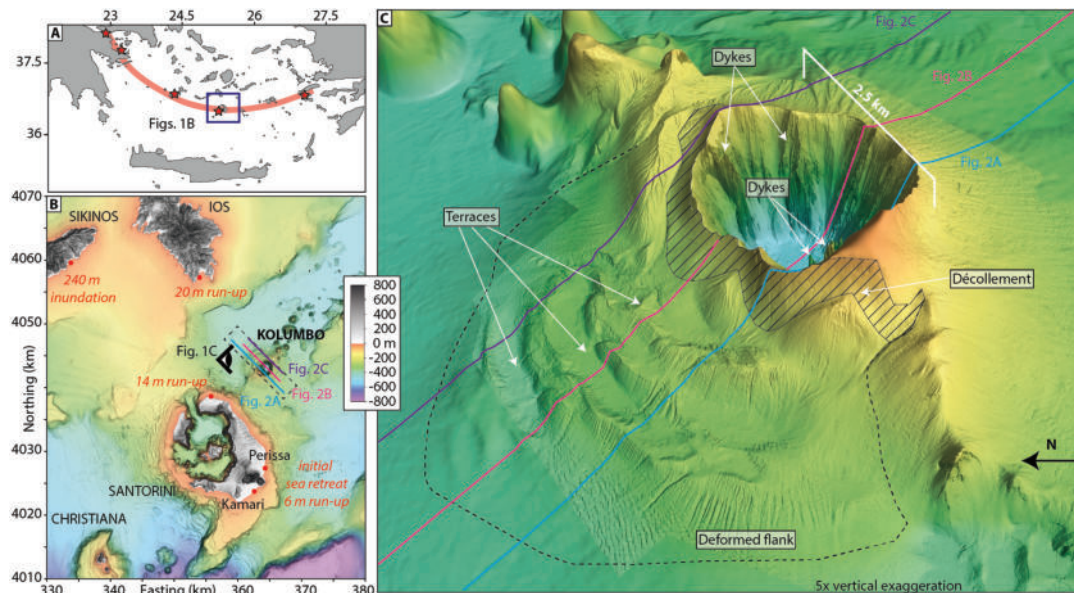
FIGURE 10.1: (A) Map of the Hellenic Volcanic Arc (red) with active volcanoes (stars) and the location of this study area (blue box). (B) Topographic map of the Christiana-Santorini-Kolumbo volcanic zone and neighboring islands of Sikinos and Ios with historical tsunami eyewitness accounts. (C) Perspective view of high-resolution (2 m) bathymetry data (Hannington, 2018; Nomikou et al., 2022) showing Kolumbo's deformed northwestern flank with terrace morphology, exposed part of the décollement, and the 1650 crater with morphological expression of dykes. Eye symbol in (B) shows viewing direction.

Kolumbo is a fully submerged volcano 7 km northeast of Santorini and part of the Hellenic Volcanic Arc. It is by far the largest volcano of the Kolumbo Volcanic Chain consisting of 24 volcanic cones formed 350 ka (Nomikou et al., 2012; Preine et al., 2022a)(Fig. 10.1). Kolumbo's edifice was created by at least five eruptive cycles, the earliest dating back more than 1 Myrs (Hübscher et al., 2015; Preine et al., 2022a). The most recent eruption, in 1650, formed a cone consisting of up to 260 m-thick stratified pumice deposits, which breached the sea surface before being destroyed by a violent explosive eruption that formed a 500 m-deep and 1500 m-wide crater (Fouqué, 1879; Cantner et al., 2014). The eruption deposits consist of highly vesicular rhyolitic pumice with cm-size mafic inclusions, likely reflecting an eruption triggered by mafic replenishment into a cooler silicic reservoir (Cantner et al., 2014; Klaver et al., 2016). The 1650 eruption triggered a tsunami causing major destruction on the neighboring islands of Santorini, Ios and Sikinos. Historical eyewitness accounts reported maximum run-up heights of 20 m on the southern coast of Ios, 240 m inundation on Sikinos, and flooding of up to 2 km^2 of land on the western coast of Santorini which caused major destruction in the towns of Kamari and Perissa (Fouqué,

1879; Dominey-Howes et al., 2000; Ulvrova et al., 2016) (Fig. 10.1B). Flooding at Kamari and Perissa was preceded by sea retreat, indicating a negative-amplitude leading wave (Ulvrova et al., 2016). Onshore tsunami deposits have been identified up to 14 m above sea level on the north coast of Santorini, 6 m above sea level in Kamari and up to 360 m inland in Perissa as well as on Ios and Sikinos (Ulvrova et al., 2016). Previous analyses of the 1650 tsunami proposed the submarine emplacement of pyroclastic flows, caldera collapse and underwater explosions as potential singular source mechanisms (Ulvrova et al., 2016).

However, the movement of Kolumbo's northwestern flank (Fig. 10.1C) has not been considered as a source mechanism in previous simulations. In this study, we use new high-resolution 3D reflection seismic data and numerical tsunami simulations to reconstruct the mechanisms that caused the tsunami waves recorded in 1650. We investigate Kolumbo's flank deformation and evaluate its tsunamigenic potential, as well as its role in triggering the violent explosion.

10.2 Structural Architecture of Kolumbo

New high-resolution (2 m) bathymetry data reveal intricate morphological detail of the cone formed by the 1650 eruption of Kolumbo (Fig. 10.1C). The northwestern flank of the volcano is characterized by a distinctive terraced morphology, in stark contrast to the smooth flanks to the south and east. 3D seismic reflection data reveal the subsurface architecture of this structural asymmetry (Fig. 10.2). While the southeastern flank comprises undeformed, sub-parallel strata (Fig. 10.2A), the northwestern flank displays pronounced internal deformation (Fig. 10.2A). This deformed sedimentary unit lies directly above the 1600 BCE Minoan eruption ignimbrites (Hübscher et al., 2015). Aside from the 1650 eruption, there is no evidence for other recent explosive eruptions in sediment cores (Kutterolf et al., 2021a; Kutterolf et al., 2021b). Therefore, the deformation affects solely volcanic sediments deposited by the 1650 eruption. Mapping of the top and base of the deformed sediments yields a volume of 1.2 km³, assuming a seismic velocity of 1700 m/s based on refraction seismic data (Preine et al., 2022a). The bathymetric data show elongate ridges that strike slope parallel around the northern flank of the volcanic edifice (Fig. 10.1C). Detailed analysis of the 3D seismic data reveals that they are the surface expression of anticlinal folds that form above thrust faults that detach onto a shallow décollement (Fig. 10.2). Their curved shapes in planform, their relative steepness, and the fact that internal thrusting can be observed in some sections of the 3D data, show unequivocally that these ridges are the result of compression and not contourite sedimentation. Deformation at the toe of the flank is complex and segmented (manifesting itself in the terrace-like morphology), while a distinct décollement can be observed toward the top of the remnant cone (hatched region, Fig. 10.1C, 10.3A). The exposed décollement has a slope angle of 19°, while the underlying strata dip at 11°, which is significantly steeper than strata within the southwestern flank that dip at 6° (Fig. 10.2A). The steeper stratigraphic dips beneath the northwestern flank are likely due to deposition onto a pre-existing remnant cone (Fig. 10.2A), which is not present beneath the southeastern flank. Additionally, there is a morphological step between the two slopes, as the base of the 1650 cone lies 50 m deeper on the northwestern side of the edifice (Fig. 10.2). The remnant cone (K3 based on Preine et al. (2022a)) and the morphological step cutting through the edifice likely control the instability

of the northwestern flank.
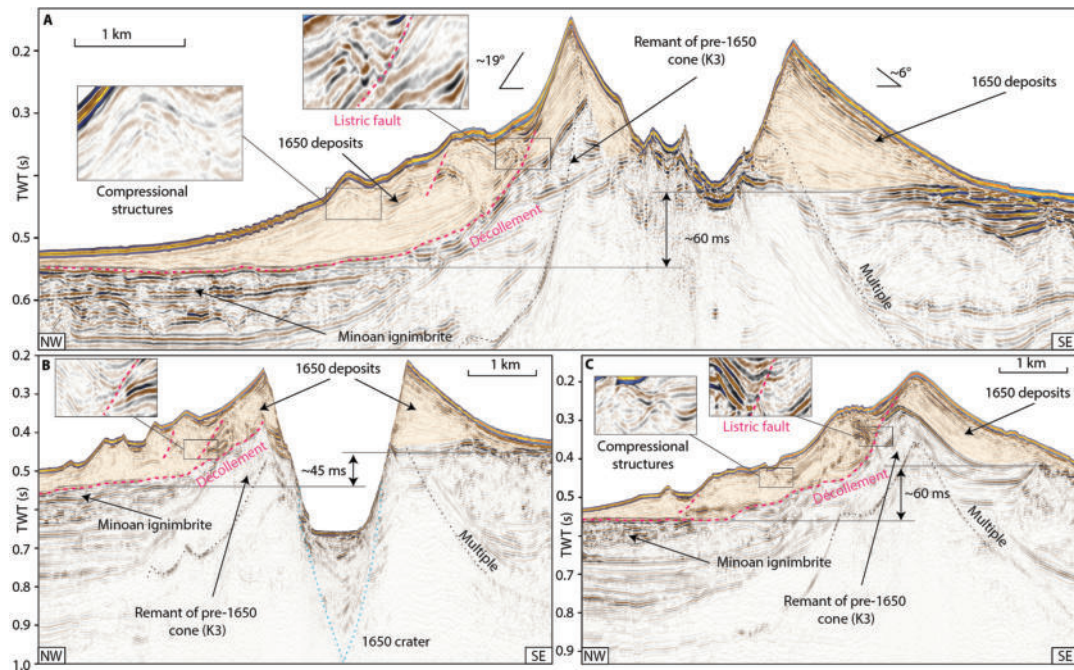
FIGURE 10.2: Reflection seismic profiles of the Kolumbo edifice. Profiles from the 3D seismic dataset showing Kolumbo's deformed edifice. Orange regions represent material deposited by the 1650 eruption. Enlargements highlight deformation (folding) in the sub-seafloor.

Previous numerical simulations (Ulvrova et al., 2016) suggested a violent explosion, pyroclastic flow emplacement, and caldera subsidence as potential tsunami source mechanisms during the 1650 eruption. However, the 3D seismic data show neither indications for sizable pyroclastic flow deposits (Fig. 10.2A), nor for ring faults that would accommodate caldera collapse (Fig. 10.2B). Therefore, we rule out pyroclastic flow emplacement and caldera collapse as potential tsunami source mechanisms. The existence of a 2500-m-wide and 500-m-deep crater, however, provides clear evidence for a highly explosive eruption phase. The seismic and bathymetric datasets suggest a link between this explosion and the flank deformation. At the top of the remnant cone, the décollement intersects prominent ridges that are the seafloor expression of feeder dykes (Fig. 10.3A, D). Their present exposure is probably due to their higher mechanical stability relative to the surrounding tephra deposits, which have been eroded since the 1650 eruption. While the explosion represents an obvious tsunami source mechanism, the previously unconsidered tsunamigenic potential of the flank deformation requires careful evaluation.
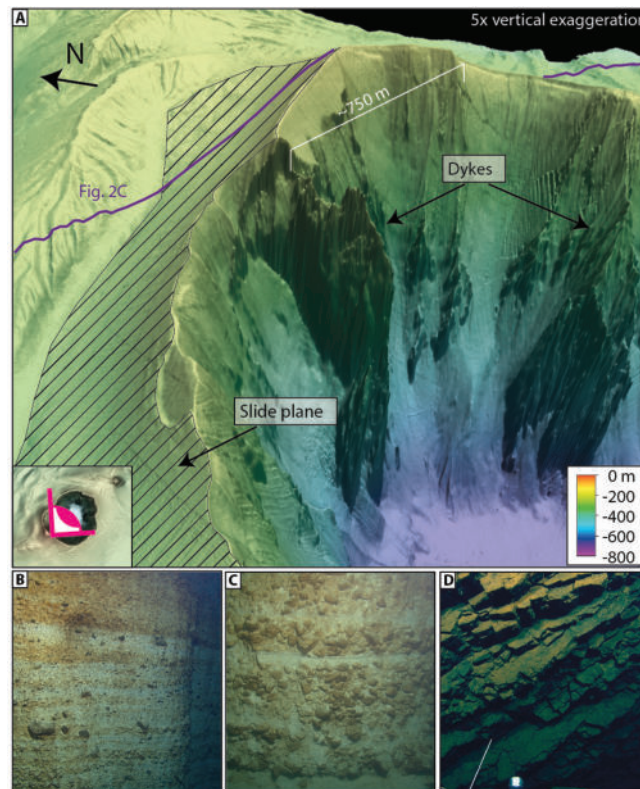
FIGURE 10.3: 3D view on Kolumbo's northeastern crater wall with exposed dykes and exposed slide plane. (B) and (C) ROV image of pumice layering representative of the 1650 cone's lithology. (D) ROV image of exposed dyke within the crater.

10.3 Reassessment of the 1650 Tsunami

Historical eyewitness accounts of tsunamis can be used to test the feasibility of tsunami simulations. For Kolumbo, the observations of higher tsunami run-up at Ios than at Santorini, and sea retreat preceding inundation in eastern Santorini (Fouqué, 1879; Dominey-Howes et al., 2000; Ulvrova et al., 2016), suggest a northwesterly directed wave propagation. Previous numerical simulations of the explosive eruption assumed a radial-symmetric initial waveform with a steep positive amplitude leading wave, followed by a trough that mimics the crater (Ulvrova et al., 2016). By assuming a peak wave amplitude of 250 m, these simulations could reproduce tsunami run-up heights at Santorini. However, the simulations could not reproduce the initial sea retreat at Kamari and Perissa, and they underestimated the 20 m run-up height at Ios by a factor of four. Therefore, it appears unlikely that an underwater explosion was the primary source of the 1650 tsunami.

To evaluate the tsunami potential of flank deformation, we extrapolated the present-day southeastern flank slopes toward the sea surface to reconstruct a cone that just breaches the sea surface (Figure G.1 in Appendix G), to be consistent with eyewitness accounts (Fouqué, 1879; Cantner et al., 2014). This pre-explosion topography, and the seismically-imaged décollement, were used as input surfaces for numerical tsunami simulations using VolcFlow (Kelfoun et al., 2010). Kolumbo's cone consists of poorly consolidated pumice with a median dry density of 0.725 g/cm^3 and median vesicularity 67.5 (Cantner et al., 2014), which, depending on the inter-pore

porosity, results in a bulk deposit density of 1,250 to 1,500 kg/m^3. This density is significantly lower than values used in previous volcanic landslide tsunami simulations, e.g., 1,900 kg/m^3 at Anak Krakatau (Grilli et al., 2019), 2000 kg/m^3 at Ritter Island (Karstens et al., 2020a) and 2,600 kg/m^3 at Tenerife (Giachetti et al., 2011). In VolcFlow simulations, the slide material density, in combination with its yield strength, controls the dynamics of flank deformation. We tested a large parameter space (Appendix G) with yield strengths between 2,000 and 75,000 Pa, and densities between 1,250 and 2,000 kg/m^3. We compared the resulting flank deformation and tsunami heights with the geophysical observations and the eyewitness reports.
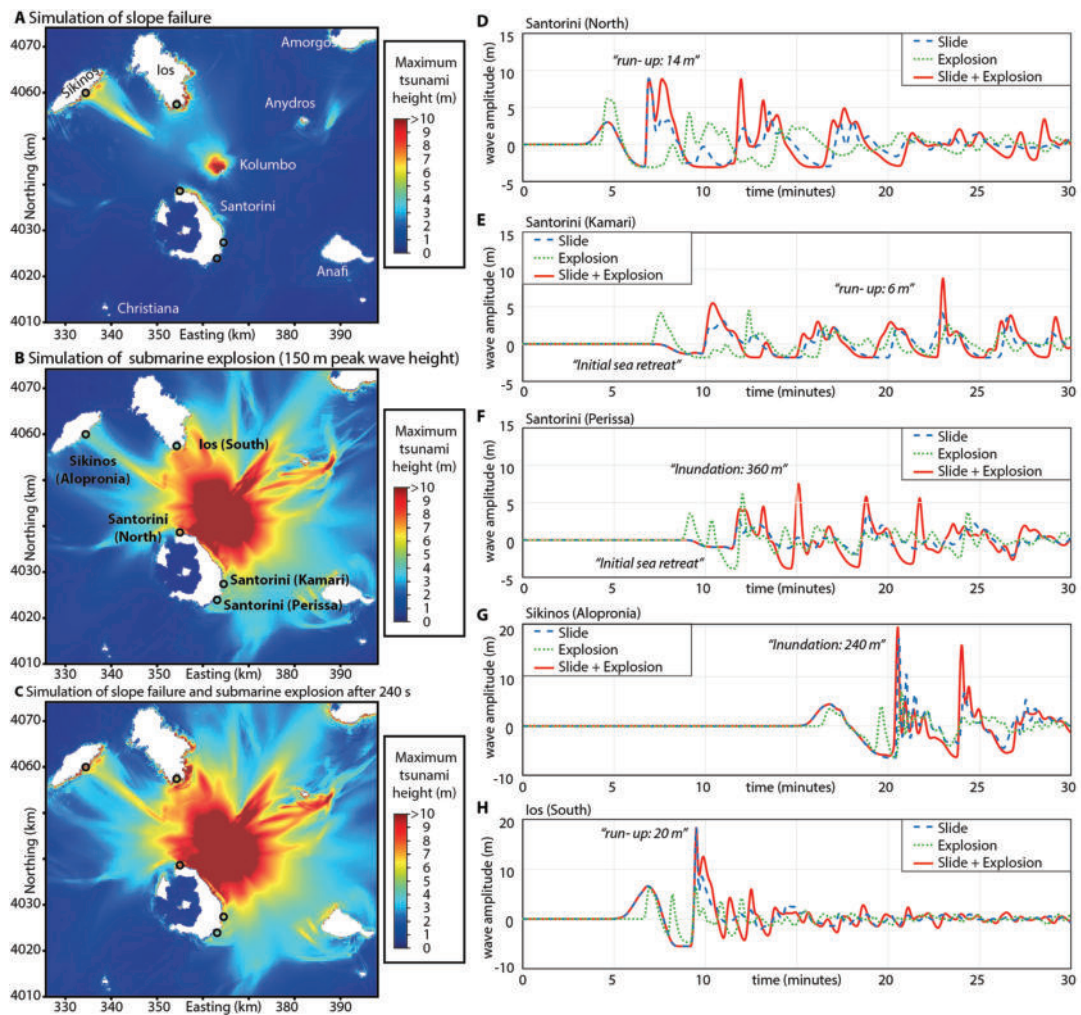
FIGURE 10.4: Map showing the maximum tsunami heights of the simulation assuming a slide density of 1,500 kg/m³ and a yield strength of 7,500 Pa. (B) Map showing the maximum tsunami heights of the simulation assuming an explosion with a peak tsunami height of 150 m. (C) Map showing the maximum tsunami heights of the simulation assuming a slide density of 1,500 kg/m³ and a yield strength of 7,500 Pa and an additional explosion at 4 minutes after the initiation of the slide with a peak tsunami height of 150 m. (D) - (H) Virtual tide gauges showing the tsunami waveforms up to 30 minutes after the beginning of the flank deformation.

Our analyses reveal that a range of yield strength-density pairs can reproduce the

observed tsunami run-up heights at Ios, Sikinos, and northern Santorini (Fig. 10.4A, Appendix G). Given the deposit density range defined by the pumice sample analysis (1,250 - 1,500 kg/m3), it is possible to reproduce the tsunami observations with simulations using a yield strength between 5,000 and 20,000 Pa, which is the same value range used in previous VolcFlow simulations of Anak Kraktau (Giachetti et al., 2012) and Ritter Island (Karstens et al., 2020a). At Perissa and Kamari, the important observation of sea retreat is reproduced, but runup heights are underestimated (blue dashed line in Fig. 10.4D-H).

In addition, we simulated an explosion-induced tsunami, which requires an estimate of the peak wave amplitude, previously assumed to be in the range of 150-240 m to be able to reconstruct tsunami observations at Santorini (Ulvrova et al., 2016). However, considering the crater rim lies in an average water depth of only 135 m, the initial wave height by the explosion is unlikely to have exceeded this. Our simulations of an explosion-induced tsunami with a peak wave height of 150 m can neither reproduce the wave height observed at southern Ios and Sikinos nor the reported initial sea retreat at Kamari and Perissa (green dotted line in Fig. 10.4C-G).

Since the seismic data clearly show that both source mechanisms could have contributed to tsunami genesis and neither the slope failure nor the explosion-induced tsunami simulations alone could reproduce eyewitness accounts, we performed additional model runs to simulate the effects of a combination of both source mechanisms, superimposing the wavefield of an explosion onto that caused by flank deformation. The lag time between flank deformation and the explosion is unknown. However, we attribute the explosion to depressurization of a critical, erupting system or exposure of the feeder system, which requires a lateral translation on the order of 500 - 1000 m. Given a simulated flank deformation velocity of 3 to 4 m/s, this equates to a lag time of 2 to 5 minutes from the initiation of the slope instability. Our results show that assuming a lag time of 4 minutes from the beginning of flank deformation to the explosion, and an explosion-derived initial wave height of 150 m, we are able to reproduce all historic tsunami observations (red solid line in Fig. 10.4). In addition, various combinations of lag time and explosion-derived initial wave height show good agreement with the run-up heights at Ios and Sikinos as well as the initial sea retreat and subsequent run-up heights on the eastern Santorini coastline (Appendix G). This gives high confidence in our combined simulation approach and highlights the complexity of tsunami generation during the cascading chain of events during volcanic eruptions (Fig. 10.5).

10.4 Chain of Events During the 1650 Eruption

The combination of high-resolution marine geophysical datasets and historical eyewitness accounts offers the unique opportunity to reconstruct the sequence of volcanic processes that triggered the 1650 explosion and tsunami. The 1650 cone consists of highly vesicular pumice, which was deposited as fallout from the eruption column, where many of the large pumice clasts floated at the sea surface before becoming water-saturated and sinking3 (Fig. 10.5A, B). The 1650 cone had a volume of approximately 5 to 7 km^3, which was deposited in a very short timeframe of only two weeks, based on the onset of visually detectable eruption products in eyewitness accounts (Cantner et al., 2014; Fouqué, 1879). This rapid deposition has likely precluded significant consolidation of the pumice deposits covering the pre-1650 topography. The pre-1650 topography was characterized by the remnants of a cone on

the northwestern side of Kolumbo from the previous eruptive cycle (K3 in Fig. 10.2) as well as a topographic step cutting through the volcanic edifice. Consequently, deposits from the 1650 eruption were deposited on steep slopes on the northwestern side of Kolumbo, while the southwestern side was relatively flat (Figs. 2, 5B). ROV-dives targeting neighboring cones from the Kolumbo chain have revealed pronounced biogenic cementation of volcanic material (Nomikou et al., 2012; Tucker et al., 2020), thereby forming a stark material contrast with the overlying 1650 eruption products, which is indicated by a positive polarity reflection (Fig. 10.2).

Slope stability is governed by the sub-seafloor effective stress profile and material strength properties. The 1650 pumice deposits were sensitive to slope failure triggered by dynamic loading because a) rapid deposition precluded the development of cohesion and b) the exceptionally low deposit density (1250 to 1500 kg/m^3) resulted in low effective stress within the cone. We suggest that the pronounced material contrast between the cone and the older, underlying volcanic material, as well as the steeper northwestern slope (19° compared to 6° elsewhere), explains why failure occurred on the northwestern flank. Eruptive activity was accompanied by earthquakes noted in the eyewitness reports (Cantner et al., 2014), which caused strong ground acceleration and the associated dynamic pore pressure increase. Ultimately, this caused the development of a listric failure surface that cuts through the northwestern flank of the cone and soles out on to the pre-1650 material, defining the décollement of the slope instability (Fig. 10.2, 10.5C).

The associated water displacement not only triggered a tsunami, as demonstrated by our numerical simulations, but also directly affected the dynamics of the ongoing eruption. The failure will have exposed deeper levels in the vent directly to sea-water, while crack formation allowed phreatomagmatic interactions still deeper within the edifice (Fig. 10.5D). Likewise, instantaneous decompression of the magma by unroofing from the slope failure will have led to near-instantaneous expansion of the magmatic fluid phase within the critical system, followed by rapidly enhanced internal (closed-system) degassing and associated further pressure buildup. Based on the geometry of the décollement, the slope failure removed up to 200 m of material from the underlying system. Assuming a bulk density of 1,300 to 1,500 kg/m^3, this may have resulted in a pressure reduction of up to 2.6 to 3 MPa, affecting the underlying feeder system and magma reservoir at a depth as shallow as 2 km, as indicated by seismic full-waveform inversion (Chrapkiewicz et al., 2022).

The deduced flank failure happened during an ongoing eruption, meaning that there was a hydraulic connection in the form of a highly vesicular magma (Cantner et al., 2014) between the summit region and the deeper magma feeding system. A decompression of 3 MPa in the conduit at e.g. 10 MPa ambient pressure would lead to a sudden volume increase of about 50% for bubbles existing in the magma, and thus produce efficient fragmentation in the upper vent region (Cashman and Blundy, 2000). The pressure release upwards in the open conduit would be sufficient to increase the internal bubble pressure above the typical yield strength of about 5 MPa for a felsic magma (Papale, 1999), leading to magma fragmentation at shallow conduit levels. The magma strain rate would suddenly exceed a critical limit (Gonnermann, 2015), and efficient magma fragmentation would commence at shallow levels. The increased fragmentation rates lead to a rapid downward migration of the fragmentation level, thereby initiating a chain reaction of accelerated decompression, producing increased eruption rates, which further decompresses the deeper parts of the magma feeding system leading to a runaway process of magma ascent and subsequent depressurization. The result is rapid (catastrophic) degassing in the

magma reservoir, causing a highly explosive eruption. Decompression experiments (Burgisser et al., 2005) suggest a lag time of 180 s between initial rapid decompression and accelerated degassing caused by bubble coalescence, which would be in agreement with the assumed slope failure dynamics. As the volatile pressure in the magma system increases rapidly, a runaway explosive eruption is initiated, further enhanced by increased magma-water interaction and thus phreatomagmatic explosions (Cas and Simmons, 2018). Potential evidence of enhanced phreatomagmatic fragmentation of Kolumbo magma may lie in the abundance of very fine grained tephra found in close proximity to the volcano in box cores and chemically correlated to the products of the 1650 event (Fuller et al., 2018).

Depressurization by unroofing is known to have triggered violent explosive eruptions such as the 1980 Mount St. Helens eruption, multiple caldera-forming eruptions at Tenerife (Hunt et al., 2018), and initial results suggest that this process may have triggered the 2022 HTHH eruption (Cronin et al., 2022). The up to 2500 m-wide crater of Kolumbo is the result of one or multiple violent explosions, which agrees well with historical reports that the explosion was heard at least 400 km away at the Dardanelles (Cantner et al., 2014). The analysis of marine tephra in sediment cores (Kutterolf et al., 2021a) indicates that the 1650 eruption produced 4.4 km^3 (dense-rock equivalent (DRE) volume of 2.5 km^3) of tephra. Considering the large amounts of pumice forming the 1650-cone (5 km^3) and the reported pumice rafts floating throughout the southern Aegean Sea (Cantner et al., 2014), the total eruption volume was larger than 10 kg^3 (5 km^3 DRE). In comparison, the 1980 Mount St. Helens eruption produced only 1.1 km^3 of tephra, while first mass flow rate based estimates suggest an eruption volume of 1.9 km^3 for the 2022 HTHH eruption (Yuen et al., 2022).
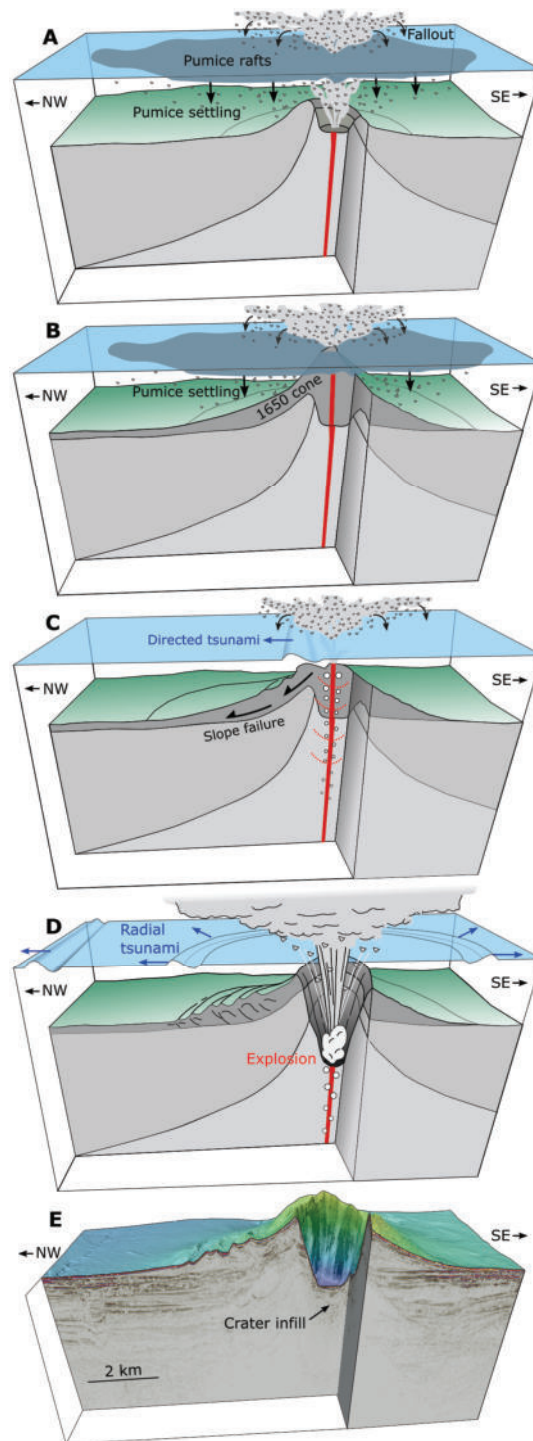
FIGURE 10.5: (A) Eruption initiates, producing large amounts of pumice that float on the sea surface before settling to the seafloor (Cantner et al., 2014). (B) On-going eruption and pumice settling results in establishment of the 1650 cone, which breaches the sea surface (Cantner et al., 2014). (C) Northwestern flank deforms and moves downslope, causing a directed tsunami and resulting in depressurisation of the underlying volcanic system. (D) Depressurisation leads to degassing and expansion which triggers the violent explosion. (E) High-resolution bathymetry and 3D seismic data reveal the present-day architecture of Kolumbo.

10.5 Towards Improved Flank Stability Monitoring and Volcanogenic Tsunami Early-Warning Systems

The 3D seismic analysis of Kolumbo highlights the complexity of tsunami genesis during volcanic eruptions, with flank deformation being the nucleus of a chain of events in a supercritical system. Internal deformation within volcanic flanks can progress over long periods, as seen by 3D seismic data of Ritter Island's failed flank (Karstens et al., 2019) and pre-collapse InSAR data for Anak Krakatau (Walter et al., 2019). The most prominent historical sector collapse triggered the 1980 eruption of Mount St. Helens, whichwas preceded by intrusion-controlled flank deformation. Although not all deformation of a volcanic flank will lead to a catastrophic collapse, deformation was a key precursor to these historical volcanic collapse events. Current monitoring strategies targeting the detection of flank deformation are based on satellite data and repeated photogrammetric imaging (Walter et al., 2019), methods that cannot be used to survey submerged volcanic edifices. Submarine geodetic networks have proven capable of detecting periodic slip events at Mount Etna11, indicating that submarine deformation monitoring is possible. However, neither remote sensing-based subaerial approaches nor submarine geodetic monitoring techniques allow real-time observations of flank deformation. This may not be a problem for detecting prolonged deformation as a precursory warning signal, but would be unsatisfactory in the case of rapidly developing systems like Kolumbo, or for detecting and characterizing the transition from slow to fast (tsunamigenic) flank movement. It is not yet known whether unroofing by a slope failure played a key role in triggering the 2022 HHTH eruption, nor whether the edifice underwent longer-term (weeks to months) deformation prior the eruption.

There are several active (sub) marine volcanoes that have been affected by repeated slope failures in the past, but which are currently not monitored. Kick'em Jenny (Lesser Antilles) is highly active and has been affected by repeated small-scale cone collapses in recent decades (Allen et al., 2018). While these collapses have not resulted in significant tsunami events in recent history, the shallow water depth of the active vent (190 m), and its formation on the scar of a major sector collapse, highlight the potential hazard. Slope stability analyses and numerical simulations indicate a significant tsunami hazard associated with a potential sector collapse (Dondin et al., 2017), which would be amplified further by a phase of explosive eruptive activity, as indicated by the 1650 Kolumbo and 2022 HHTH eruptions. Another candidate for future submarine flank monitoring is the Myojinsho submarine volcano in Japan (Fiske et al., 1998). Its 1952-1953 explosive eruptions bore many similarities to the evolution of Kolumbo, by forming a 4 km diameter symmetrical volcaniclastic cone, which breached the sea surface before being destroyed by violent explosions (Fiske et al., 1998). While there is no evidence for past slope deformation in the available low-resolution bathymetry data, the steeply sloped cone (21°) formed on the northeastern rim of a larger pre-existing caldera. Renewed activity could result in a flank collapse of the volcaniclastic cone and depressurization of the underlying magmatic system, similar to the Kolumbo eruption, with the potential for the generation of much larger tsunamis than those caused by the 1952-1953 cone building activity. Finally, Kolumbo itself poses a significant hazard to the densely populated northern and western coasts of Santorini. A low P-wave velocity zone at 2 to 4 km depth indicates a shallow melt reservoir beneath Kolumbo, and repeated earthquake swarms may indicate fracturing associated with ascending melts (Chrapkiewicz et

al., 2022; Schmid et al., 2022). Renewed volcanic activity or a strong earthquake may reactivate the deep-seated deformation of the northwestern flank, with the potential to trigger tsunami waves that would arrive at Santorini within 5 minutes (Fig. 10.4). Bottom waters in Kolumbo's crater are highly acidic (Carey et al., 2013), and even a minor slope failure could potentially trigger a limnic eruption releasing large amounts of CO_2 and other toxic trace gases like SO_2. Given that most fatalities from the 1650 eruption of Kolumbo were associated with toxic gases (Cantner et al., 2014), this scenario deserves particular attention. However, currently available submarine monitoring systems require long lead-in times (often several years) and costly infrastructure, which would have precluded monitoring efforts even if subaerial precursors had been identified. Local populations, decision-makers and scientists are currently unprepared for the threats posed by submarine eruptions and slope failures, as has been demonstrated by the recent 2018 sector collapse of Anak Krakatau and the 2022 HHTH eruption. Therefore, new shore-line crossing monitoring strategies are required that are capable of being deployed as part of rapid response initiatives during volcanic unrest, and which enable real-time observation of slope movement.

Chapter 11

When Zhere is No Offset: A Demonstration of Seismic Diffraction Imaging and Depth-Velocity Model Building in the Southern Aegean Sea

Abstract

A vast majority of marine geological research is based on academic seismic data collected with single-channel systems or short-offset multi-channel seismic cables, which often lack reflection moveout for conventional velocity analysis. Consequently, our understanding of earth processes often relies on seismic time sections, which hampers quantitative analysis in terms of depth, formation thicknesses, or dip angles of faults. In order to overcome these limitations, we present a robust diffraction extraction scheme that models and adaptively subtracts the reflected wavefield from the data. We use diffractions to estimate insightful wavefront attributes and perform wavefront tomography to obtain laterally resolved seismic velocity information in depth. Using diffraction focusing as a quality control tool, we perform an interpretation-driven refinement to derive a geologically plausible depth-velocity-model. In a final step, we perform depth migration to arrive at a spatial reconstruction of the shallow crust. Further, we focus the diffracted wavefield to demonstrate how these diffraction images can be used as physics-guided attribute maps to support the identification of faults and unconformities. We demonstrate the potential of this processing scheme by its application to a seismic line from the Santorini-Amorgos Tectonic Zone, located on the Hellenic Volcanic Arc, which is notorious for its catastrophic volcanic eruptions, earthquakes, and tsunamis. The resulting depth image allows a refined fault pattern delineation and, for the first time, a quantitative analysis of the basin stratigraphy. We conclude that diffraction-based data analysis has a high potential, especially when the acquisition geometry of seismic data does not allow conventional velocity analysis.

Plain Language Summary

The active seismic method is a standard tool for studying and imaging the Earth's lithosphere. Proper imaging of complex geological targets requires seismic data of excellent quality, which are typically only acquired with expensive industrial surveys. Academic surveys, however, are often restricted to marine seismic equipment

with limited illumination, which compromises imaging and interpretation. While most of the contemporary processing and interpretational routines are tailored to the reflected wavefield, recent research suggests that the often overlooked diffracted wavefield might help to overcome the gap between academic and industrial seismic imaging. Wave diffraction is the response of the seismic wavefield to small-scale subsurface structures and allows to estimate velocities even from single-channel seismic data.

In this study, we use an academic seismic profile from the southern Aegean Sea and extract a rich diffracted wavefield from the data. We utilize these diffractions to estimate a velocity model that permits a reconstruction of the subsurface in depth and specifically highlight discontinuous features related to past dynamic processes. Such depth images allow us to reliably measure thicknesses and fault angles. We conclude that diffraction-based data analysis has a high potential for academic research and strongly encourage its application in future studies.

11.1 Introduction

Most marine geological research during the last 50 years is based on academic seismic reflection data, collected with single-channel systems or multi-channel seismic cables with an offset-depth ratio too small for velocity analysis based on common-midpoint (CMP) processing. Without doubt, the scientific outcome from those studies is impressive, yet seismic depth sections would be required in order to test them by quantitative modeling. In recent works, it has been shown that diffractions possess unique properties which bear the potential to overcome these characteristic limitations of academic studies (e.g. Bauer et al., 2017; Schwarz and Gajewski, 2017; Fomel et al., 2007). Wave diffraction occurs at geodynamically important structures like faults, pinch-outs, erosional surfaces, or other small-scale scattering objects and encodes sub-wavelength information on the scattering geometry (e.g. Landa and Keydar, 1998). Diffracted waves do not obey Snell's Law and provide superior illumination compared to reflected waves. Moreover, due to their passive-source like radiation, they encode their full multi-channel response in prominent data subsets like the zero-offset section (e.g. Bauer et al., 2017; Schwarz and Gajewski, 2017).

Separating the diffracted wavefield has high potential: on the one hand, it principally allows to image and analyze fault systems as well as the small-scale heterogeneity with sub-wavelength resolution (Berkovitch et al., 2009; Silvestrov et al., 2015; Decker et al., 2015). On the other hand, diffractions illuminate the subsurface in such a way that laterally resolved velocity information can be obtained. Consequently, and without the need for expensive industry-style acquisitions, diffractions offer the possibility to measure curvatures in the zero-offset section, which allows automatic depth-velocity model building by means of wavefront tomography (Bauer et al., 2017; Duveneck, 2004). However, apart from Bauer et al. (2018), no example of data-driven depth-velocity model building based on diffraction-only data in the zero-offset domain has been published so far.

In this work, we use an academic seismic profile from the Santorini-Amorgos Tectonic Zone (SATZ), located in the South Aegean Sea, to explore the diffracted wavefield and to estimate an interval velocity model for depth-conversion. The SATZ is a typical example for the aforementioned dilemma academic science is often facing. While this area is notorious for its catastrophic volcanic eruptions, earthquakes, and tsunamis, the acting tectonic forces are not completely understood to this day. One reason is that previous studies have been based on single-channel or low-fold

seismic vintage data with short streamers (Perissoratis 1995; Hübscher et al., 2006; Nomikou et al., 2018), thus handicapping the estimation of interval-velocities for depth migration. Hübscher et al. (2015) and Nomikou et al. (2018) have shown that the SATZ is characterized by a high degree of local heterogeneity, e.g. in the form of abundant fault systems and volcanic intercalations which makes this area a natural laboratory for studying diffractions.
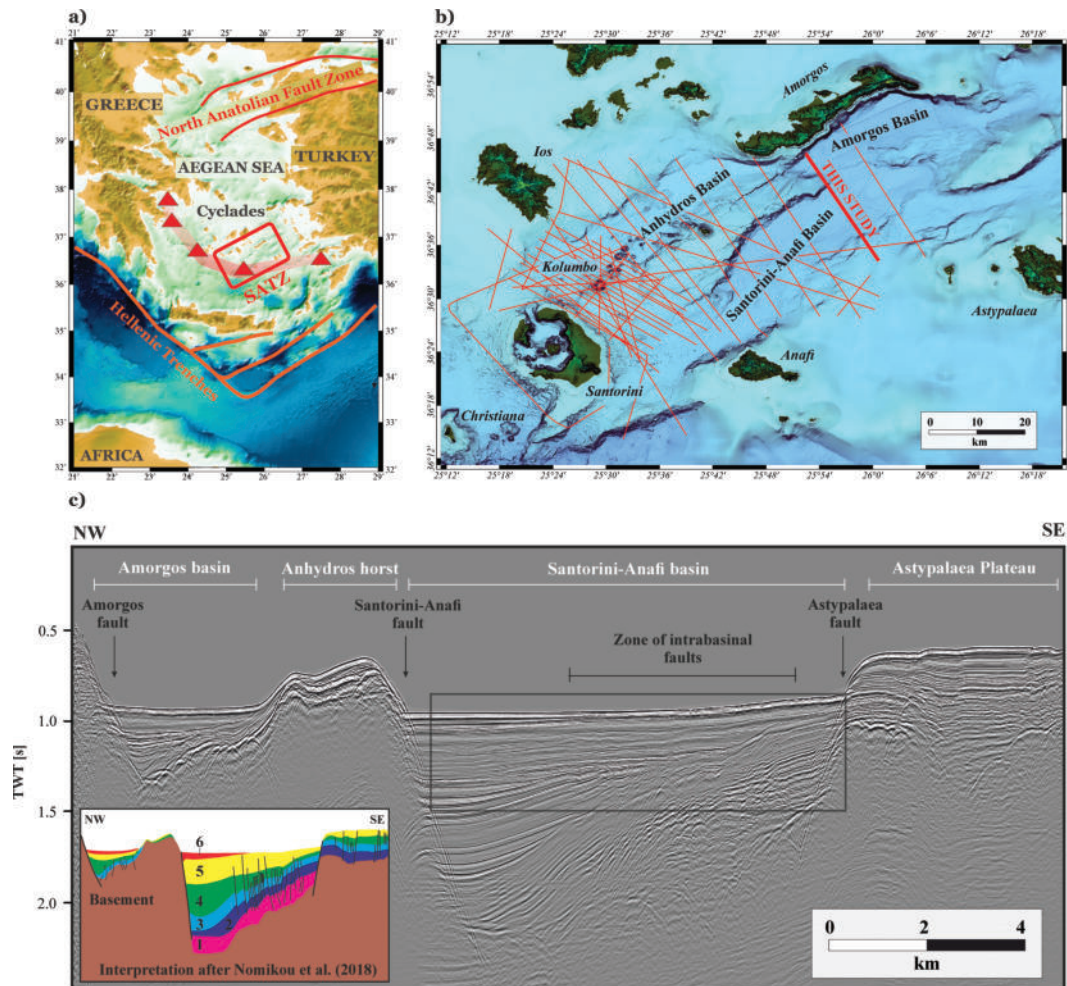
FIGURE 11.1: (a) Aegean Sea and major geological features. The semi-transparent red area marks the Hellenic Volcanic Arc and the red box indicates the working area. (b) Morphological map of the study area based on swath bathymetry. Thin red lines illustrate the location of the seismic profiles acquired during research cruise POS338 (Hübscher et al., 2006). The thick red line indicates profile 11 which is the focus of this study. (c) CMP Stack of seismic profile 11 after multiple elimination with the interpretation by Nomikou et al. (2018b). The black rectangle indicates the location of the blow-up highlighted in Figure 11.3.

11.2 Geological Setting

The Santorini-Amorgos Tectonic Zone (SATZ) represents a zone of NE-SW oriented en-echelon rifts located in the center of the Hellenic Volcanic Arc in the south Aegean Sea (Figure 11.1a) (Nomikou et al., 2019). Driven by the rollback of the Nubian slab,

the southern Aegean Sea has experienced substantial extension (e.g. Le Pichon and Angelier, 1979; Cossette et al., 2016; Bocchini et al., 2018). The SATZ represents one of the most prominent morphotectonic features of the Cycladic Islands and separates the Cycladic plateau towards the North and the minor Anafi-Astypalaea plateau towards the South (Nomikou et al., 2019; Le Pichon and Kreemer, 2010). Bathymetric and available tectonic data of the SATZ most recently published by Nomikou et al. (2019) and Hooft et al. (2017) reveal a system of ridges and basins which has been interpreted as an extensional complex of tectonic grabens and horsts. To the south-west, the SATZ is characterized by the volcanic centers of Christiana, Santorini, and Kolumbo which are responsible for numerous volcanic eruptions, including the well-known Minoan eruption of Santorini approx. 3600 years ago (Druitt and Francaviglia, 1992; Druitt et al., 1999; Nomikou et al., 2016a; Hooft et al., 2019). The remarkably linear alignment of the volcanic edifices highlights the fundamental control that crustal structure and tectonics have on the location of volcanic activity (Nomikou et al., 2013; Nomikou et al., 2019; Hooft et al., 2019; Heath et al., 2019).

North-east of Santorini, three distinct basins have been identified by Nomikou et al. (2018b): the Anhydros basin, the Santorini-Anafi basin, and the Amorgos basin (Figure 11.1b). Seismic reflection data show that the opening of these basins most likely occurred in sudden tectonic pulses (Hübscher et al., 2015; Nomikou et al., 2016b). The regional geological setting comprises alpine formations forming the basement rocks and overlying post-alpine sediments which are restricted to offshore areas between the islands and are thought to consist of marine sediments comprising turbidites, hemipelagic sediments, and volcaniclastics (Perissoratis, 1995; Hübscher et al., 2015; Nomikou et al., 2016b; Nomikou et al., 2018b). These sediments have transgressed the former Cycladic land and volcanic intercalations have been identified close to the volcanic centers of Santorini and Kolumbo (Hübscher et al., 2015; Nomikou et al., 2016b). Each basin is bounded by active marginal normal faults and characterized by extensive internal fault systems (Hübscher et al., 2015; Nomikou et al., 2018b).

Based on a recent active seismic tomography experiment, Heath et al. (2019) and Hooft et al. (2019) obtained tomographic P-wave velocity models for the upper-crustal structure across Santorini volcano and the surrounding region. In agreement with the previous tectonic models, they conclude that tectono-magmatic lineaments control magma emplacement at Santorini and Kolumbo and that the initiation of basin-formation pre-dates the onset of volcanism. Heath et al. (2019) inferred that the Anhydros Basin is of maximum 1.5 km thickness and the Santorini-Anafi Basin of maximum 2 km thickness.
There is an ongoing debate about the role of strike-slip deformation in the SATZ. Based on the investigation of microseismic activity, Bohnhoff et al. (2006) concluded that the SATZ is currently influenced by a right-lateral transtensional tectonic regime. Sakellariou et al. (2010) proposed the concept that the whole SATZ represents a shear zone characterized by dextral strike-slip to oblique faults. Direct seismic indicators like flower structures, however, have not been presented so far. Also recent publications by Hübscher et al. (2015) and Nomikou et al. (2018b) did not find direct indicators for strike-slip faulting in the presented multi-channel reflection seismic data. While the possibility of strike-slip faulting was not ruled out, these authors concluded that normal faulting as a result of the regional extensional to transtensional movement represents the main tectonic mechanism.

11.3 Imaging Challenges

In order to further investigate the role of strike-slip tectonics and to understand the dynamics of the basin formation, seismic imaging in depth is necessary to properly estimate sedimentary thicknesses, calculate fault angles, and quantify horizontal strain. To arrive at accurate reconstructions in depth, precise velocity models, which require borehole information and lateral illumination, are in demand. Typically, this is achieved by means of of deploying long streamers as they are used e.g. in hydrocarbon industry. Academic surveys, however, are often very limited in terms of budget and, therefore, mostly smaller streamer systems with lower channel-counts are used aggravating the estimation of interval velocities.

This dilemma also applies to the SATZ. On the one hand, there are no exploitable boreholes in the area that could serve as a reliable source for velocity information. On the other hand, available academic reflection seismic data from the SATZ are generally of poor quality. Pioneering work by Perissoratis (1995) was based on analog data acquired with a single-channel streamer and even recent studies by Sakellariou et al. (2010) and Tsampouraki-Kraounaki and Sakellariou (2018) were based on digital single-channel seismic data. In contrast, the stratigraphic studies by Hübscher et al. (2015) and Nomikou et al. (2016b), Nomikou et al. (2018b), and Nomikou et al. (2019) were based on multi-channel seismic data collected in 2006 during research cruise POS338 with RV Poseidon using a streamer of 600 m length (Hübscher et al., 2006). While the resulting data-quality was superior compared to previous studies, the relatively large channel spacing of 25 m limited a detailed investigation of internal reflection and fault patterns and the limited streamer length hampered the estimation of velocities from the data. Another source of uncertainty of these data regarding the estimation of interval velocities is the fact that no birds were used during the measurement to control the depth of the streamer.

Therefore, the only available velocity information from the SATZ are the tomographic P-wave velocity models presented by Heath et al. (2019) and Hooft et al. (2019). While these models are well suited to study the large-scale structure of the upper <3 km crust, they do not resolve the small-scale velocity distribution and do not account for the high degree of local complexity in the rift basins. Consequently, these velocity models cannot be used directly for depth migration.

Figure 11.1c shows a CMP stack of seismic line 11 from the POS338 data-set after the application of surface-related multiple elimination (SRME) (Verschuur et al., 1992). This profile has been interpreted by Nomikou et al. (2018b) and runs NW-SE crossing the Amorgos basin, the Anhydros Horst as well as the Santorini-Anafi basin and the Astypalaea plateau. The Amorgos basin is interpreted as a semi-graben produced by the activity of the Amorgos fault, whereas the Santorini-Anafi basin represents an asymmetric graben bounded by the important Santorini-Anafi fault and the Astypalaea fault (Nomikou et al., 2018b). Six sedimentary units were identified within the Santorini-Anafi basin and major internal deformation is indicated by extended fault systems in the sedimentary strata of the Santorini-Anafi basin within the hinge-zone of the marginal Santorini-Anafi fault and the Astypalaea fault (see small illustration in Figure 11.1c). These fault systems are associated with a high number of diffractions which are overprinted by the dominant reflected wavefield. The abundance of diffractions makes this seismic profile a highly suitable example to test how the diffracted wavefield can contribute to the processing and interpretation of offset-limited academic seismic data.

11.4   Methods

In recent decades, detail-rich seismic wavefields have been captured on land and on the sea. Owing to its first development and extensive utilization in the prospection of oil and gas, until the early 2000s, the seismic method put most emphasis on the reflected portion of this wavefield, which resulted in many important discoveries in industry and academia. With the advent of full-waveform inversion, the desire to record low-frequency diving waves led to a spectacular yet cost-intensive shift in data acquisition (Virieux and Operto, 2009; Warner et al., 2013; Morgan et al., 2013). As a result, the promised resolution of such reconstructions remains largely intractable in expeditions where academic objectives are concerned. To arrive at maximally resolved seismic subsurface reconstructions when academic low-fold and short-offset acquisitions were recorded, we make use of the still largely unexplored diffracted component of the wavefield (e.g. Schwarz, 2019a). As illustrated in Figure 11.2a, diffractions are unique in that they exclusively occur when subsurface properties change abruptly. More precisely, in contrast to reflections and diving waves, these signatures are only caused, when the local curvature of a material contrast is comparable to or even smaller than the prevailing seismic wavelength.
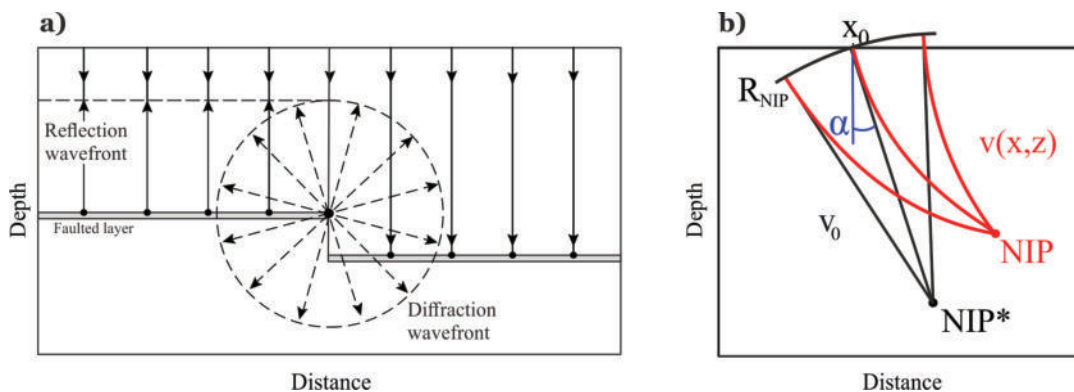
FIGURE 11.2: (a) Zero-Offset rays hitting a faulted layer. While reflected wavefronts obey Snell's Law, diffracted wavefronts are scattered radially when encountering the truncated end of the faulted layer. (b) Illustration of the concept of wavefront tomography. Black lines indicate the optical image space with a medium of constant velocity v_0, in which the apparent location of the normal incident point (NIP*) is found by straight-ray projection. Determining the true velocity model $v(x,z)$ and finding the true normal incidence point (NIP) location (red) is the goal of wavefront tomography.

11.4.1   Diffraction Separation and Focusing

Owing to the effect of geometrical spreading, diffractions are generally characterized by very low amplitudes and often remain masked by more prominent higher-amplitude reflections (Figure 11.2a). For that reason, accessing the diffracted wavefield has been and still remains a major challenge to confront. In recent years, a range of methods has been introduced to arrive at approximate diffraction-only images based e.g. on modified versions of Kirchhoff's diffraction integral (e.g. Moser and Howard, 2008; Dafni and Symes, 2017; Yin and Nakata, 2017), specific versions of the Radon transformation and plane-wave destruction filters (e.g. Fomel, 2002; Karimpouli et al., 2015) or multi-dimensional stacking (Dell and Gajewski, 2011; Bauer et al., 2016; Bakhtiari et al., 2018). While the latter has the advantage of being

directly applicable in the time domain without the need for specific data transformations and not requiring a detailed velocity model, the quality of the separation depends on the quality of the performed coherence measurements and the pre-stack data.

A different approach to the problem was introduced by Schwarz and Gajewski (2017) and extended by Schwarz (2019b). In contrast to previous attempts, these works specifically target the reflected rather than the diffracted wavefield, with the potential benefit of leaving weak diffracted signatures largely unharmed in the separated result. Likewise, in contrast to workflows directly incorporating Kirchhoff migration, the separation is performed directly in the un-migrated (data) domain, leading to the applicability of a multitude of conventional imaging and inversion algorithms. The first step of this non-invasive strategy, very much like in surface-related multiple suppression (Verschuur et al., 1992), constitutes in a targeted *modeling* of the interfering noise – in our case, the reflected contributions. This is achieved by means of coherence analysis, in which the local fit of a curved traveltime operator

$$\Delta t(x_0, t_0) = \sqrt{\left(t_0 + 2\frac{\sin\alpha}{v_0}\Delta x\right)^2 + \frac{2t_0\cos^2\alpha}{v_0}\left(\frac{\Delta x^2}{R_{\mathrm{N}}} + \frac{h^2}{R_{\mathrm{NIP}}}\right)} - t_0 \qquad (11.1)$$

is optimized for neighboring traces (with midpoints laterally separated by Δx and half the source-receiver distance h), by repeatedly evaluating the semblance norm (Neidell and Taner, 1971). Written as above, the estimated propagation time $t_0/2$, the emergence angle α, and the curvature radius R_{NIP} represent one-way properties of a wavefront emitted by a fictitious source placed either at the normal-incidence point (NIP) or the diffractor location (compare Figure 11.2). While for reflections, this wavefront is fully conceptual and expresses a symmetry in the common-midpoint gather ($h \neq 0$), for diffractions and passive events ($R_{\mathrm{N}} = R_{\mathrm{NIP}}$) it describes the shape of the actual physical wavefield stemming from the localized scatterer or the passive source (Bauer et al., 2017; Diekmann et al., 2019). As a result, for reflections, sufficient offset (h) information is needed, whereas, for diffractions, wavefront curvatures can be fully determined in the zero-offset ($h = 0$) section. Forming a by-product of coherence analysis, these wavefront attributes, in addition to velocity inversion, permit the formulation of supportive diffraction filters that can additionally constrain the separation (Schwarz and Gajewski, 2017; Schwarz, 2019b).
Following this procedure of constructing a reflection model by means of local coherent data summations, a successful separation requires an adaptation step, which like the summation itself should be performed within an aperture to preserve weak interfering energy. Such an adaptation of the reflection stack is achieved by introducing local scaling coefficients γ_0 and time shifts τ_0. Following the superposition principle, the interference of reflections and diffractions can, in good approximation be *reversed*, if the estimated coherent reflection model is reasonably accurate. Expressing the coherent reflection stack as C_{ref}, and the raw input data as $\mathcal{D}$, the adaptive separation procedure can thus be expressed as

$$C_{diff} \approx D(x_0, t_0) - \gamma_0 C_{ref}(x_0, t_0 + \tau_0), \qquad (11.2)$$

where $(\mathbf{x}_0, t_0)$ is the central data point under consideration and C_{diff} denotes the diffracted wavefield. For more details on the estimation of the necessary amplitude weights and time shifts and applications in seismic and ground-penetrating-radar data, we refer to Schwarz (2019b).

After their successful extraction, uncorrelated noise that was suppressed in the reflection model will likewise remain in the data, thereby setting natural limits on the detectability of diffracted signatures. However, as diffractions, despite their weakness, possess the property of coherence, the aforementioned coherence analysis can be carried out for the separated dataset.

11.4.2   Wavefront Tomography

Based on the concept of wavefront attributes, Duveneck (2004) introduced wavefront tomography, an efficient and robust scheme for the estimation of smooth depth-velocity models, which has been applied successfully to industrial multi-channel data (Bauer et al., 2017) as well as diffraction-only data (Bauer et al., 2017; Bauer et al., 2018) and passive-seismic measurements (Schwarz et al., 2016; Diekmann et al., 2019). In this study, due to limited offsets in the academic seismic data, the reflected measurements are hardly usable for velocity inversion. Accordingly, wavefront attributes have to be extracted from the diffraction-only data C_{diff} obtained during the previous step. This is done by means of coherence analysis, during which the hyperbolic traveltime moveout approximation (11.1) is locally fitted to the data (e.g. Jäger et al., 2001). The input for wavefront tomography consists of numerous sets of wavefront attributes that can be picked in an automatic fashion in the resulting zero-offset sections based on their coherence,

$$\mathbf{d}_i = (\xi, T, \alpha, R_{\mathrm{NIP}})_i \, , \qquad \text{with } i = 1, \dots, n_{picks} \, , \qquad (11.3)$$

where n_{picks} denotes the total number of picked data points, $T = t_0/2$ the one-way zero-offset traveltime and ξ the position on the recording surface. The model parameters $\mathbf{m}$ are the B-spline velocity coefficients $v(x, z)$ on a pre-defined grid of $n_x \times n_z$ knots and localizations $(x, z)_i$ and ray-takeoff angles θ_i associated with each data point. The initial localizations and ray-takeoff angles are obtained by downward kinematic ray tracing into the initial model (which in our applications merely consists of the constant near-surface velocity v_0, compare Figure 11.2b) starting from ξ_i under the angles α_i until the remaining traveltime vanishes. Subsequently, upwards dynamic ray tracing from $(x, z, \theta)_i$ yields the modelled data points $\tilde{\mathbf{d}}$. The misfit between the measured and modelled data points $\Delta\mathbf{d} = \mathbf{d} - \tilde{\mathbf{d}}$ defines the cost function,

$$\Psi(\mathbf{m}) = \frac{1}{2}\|\mathbf{d} - \tilde{\mathbf{d}}\|_2^2 + \Lambda\left(\partial_{xx}v(x, z)), \partial_{zz}v(x, z)\right) \, , \qquad (11.4)$$

where Λ constitutes a regularisation term that ensures a smooth velocity model. During the inversion, the cost function is minimized iteratively in a damped-weighted least-squares sense until a velocity model and localizations $(x, z)_i$ are found that are most consistent with the measured wavefront attributes (compare Figure 11.2b). For stability, we apply the inversion algorithm in a cascaded fashion, starting from a coarse grid and then successively increasing the number of B-spline knots.

11.5 Data-Driven Results

11.5.1 Diffraction Separation
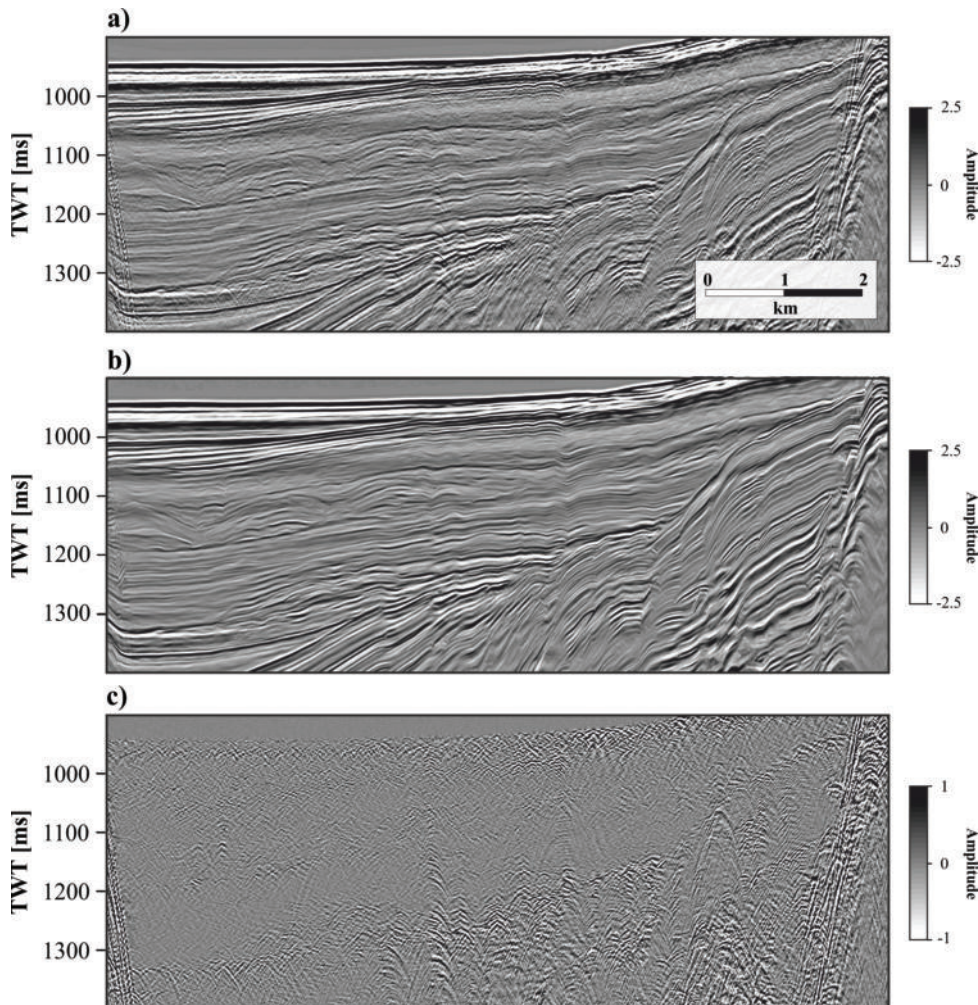
FIGURE 11.3: Results of the coherent stacking and subtraction scheme for diffraction separation illustrated on a zoomed section from seismic line 11: (a) the input CMP Stack, (b) the reflection-only data, and (c) the diffraction-only data.

In order to reveal the faint diffracted wavefield, we perform diffraction separation based on the approach by Schwarz (2019b). As input, we use the CMP stack of seismic line 11 with a CMP-spacing of 12.5 m from the POS338 data-set (Figure 11.1 and Figure 11.3a). With the purpose of recovering as much of the diffracted wavefield as possible, pre-processing for the separation was kept to a minimum comprising only simple bandpass filtering for the removal of low-frequent swell noise, SRME for multiple elimination in addition to the application of a top mute and trace mute. The processing flow is illustrated in Figure H.1.

In the first step, we carry out coherent wavefield summation using planar beamforming in order to estimate the reflection-only data. With a lateral aperture of 100 m and a coherence time window of 20 ms, supported by a wavefront filter with a maximum angle of $10°$ to search for, we obtain the reflection-only section illustrated in

Figure 11.3b. As demonstrated by Schwarz (2019b), the lateral aperture plays an important role in the success of the modeling of the reflected wavefield as it controls the number of traces used for the coherent stacking and, consequently, how discriminative the separation is. The more traces are considered, the more of the crossing diffraction energy is neglected in the reflection-only data, and the better the diffraction-subtraction works later on. However, as too large apertures tend to smear the reflections, the proper aperture choice can bee seen as a trade-off and, consequently, requires parameter testing (Schwarz, 2019b). As Figure 11.3b demonstrates, the reflection-only section has a higher lateral continuity compared to the input CMP stack (Figure 11.3a) and, more importantly, is free of diffractions.

In the next step, the diffraction-only data are generated by performing coherent beam subtraction. Also here, the lateral aperture is an important parameter and several tests showed that using 400 m is the best trade-off value. An example of the effect of different apertures used for the separation is provided in the supplementary information (Figure H.2). The resulting diffraction-only section is illustrated in Figure 11.3c. This section is generally free of reflections and a rich, complex diffracted wavefield is revealed. Diffractions can be identified throughout the section, but seem to cluster around distinctive structures. Not only vertical structures that seem to represent faults but also horizontal structures that seem to represent unconformities are highly *diffractive*. Note e.g. the high number of diffractions along the faults in the center of the basin and towards the marginal Astypalaea fault. This illustration highlights that most of the diffractions at faults are created at the tips of the faulted horizons. Consequently, faults seem only diffractive when reflection-horizons are present.

The numerical cost of the whole diffraction separation routine can be considered as fairly reasonable. The seismic line under consideration comprises 2022 CMPs and was acquired with a sampling rate of 1 ms and a recording length of 3 s. On a conventional computer with a quad-core processor, the coherence analysis for deriving the reflection-only data took approx. 10 minutes and the adaptive subtraction for generating the diffraction-only data approx. one hour.

11.5.2 Wavefront Tomography
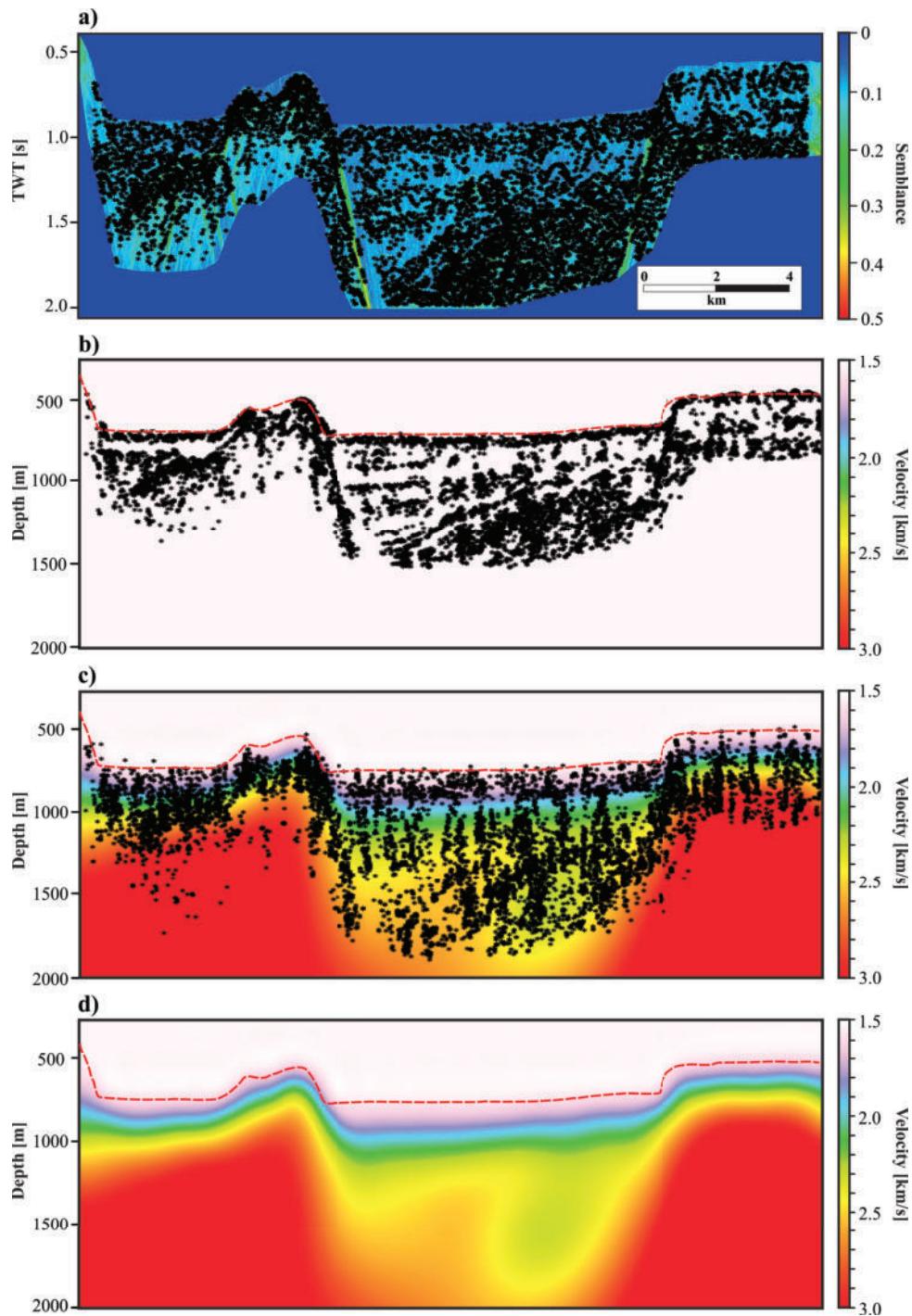
FIGURE 11.4: Results of diffraction-based wavefront tomography. (a) All 11,866 automatically picked data points plotted into the semblance section. (b) The constant initial model for the inversion overlain by the initial scatterer localizations. (c) Final velocity model overlain with final scatterer localizations. (d) Final velocity model. The dashed red line indicates the location of the seafloor horizon.

In order to derive a depth-velocity model, we apply the previously introduced wavefront-tomographic scheme based on the separated zero-offset diffraction response. In the

first step, we estimate the wavefront attributes and the diffraction coherence using the semblance norm. Figure 11.4a illustrates the resulting semblance section overlain by 11,866 automatically picked data points, which consist of sets of wavefront attributes that form the input of the inversion algorithm. These data points are scattered over the whole section ensuring the needed illumination for velocity inversion. In order to avoid contributions from the faint multiple remnants, we mute the diffraction coherence below the arrival time of the seafloor multiple before the automatic picking. In the next step, we calculate the initial model without assuming any a priori information other than the near-surface velocity $v_0 = 1.52\,\text{km/s}$ which corresponds to the regional water velocity. The resulting initial model is displayed in Figure 11.4b together with the initial ray starting locations associated with each data point, which are obtained by downward kinematic ray tracing into the constant initial model. During the inversion, we applied two grid refinements, the first nine iterations with 11×5 B-spline knots and a spacing of 2500 m in x- and 625 m in z-direction, followed by eight iterations with 21×9 B-spline knots (1250 m in x- and 312.5 m in z-direction) and seven iterations with 41×17 B-spline knots (625 m in x- and 156.25 m in z-direction). The resulting velocity model overlain with the final scatterer locations after a total of 24 iterations is illustrated in Figure 11.4c. While the scatterer locations were distributed quite broadly in the semblance section, the final scatterer locations seem to be more focussed after the inversion. We identify several areas where the final scatterer locations organize in vertical structures following the outline of faults.

Figure 11.4d shows the velocity distribution inferred from the diffracted wavefield. The inverted velocities range from 1.5 km/s to 3.0 km/s. The basement is estimated at approx. 3.0 km/s while for the sedimentary strata a rather smooth velocity increase from 1.5 km/s to approx. 2.5 km/s has been inverted. In general, the velocity model acknowledges the expected velocity contrast from the sedimentary strata to the basement very well. Especially the elevated basement of the Anhydros Horst is distinctly expressed in the velocity model. The velocity distribution in the Santorini-Anafi basin is characterized by a lateral velocity increase between the left and the right part of the basin. While the inverted velocities in the right part do not exceed 2.5 km/s, high velocities of over 2.9 km/s can be found within the sedimentary strata of the left part of the basin. In contrast to that, the velocity distribution for the Astypalaea plateau and the Amorgos basin show no comparable lateral velocity variations.
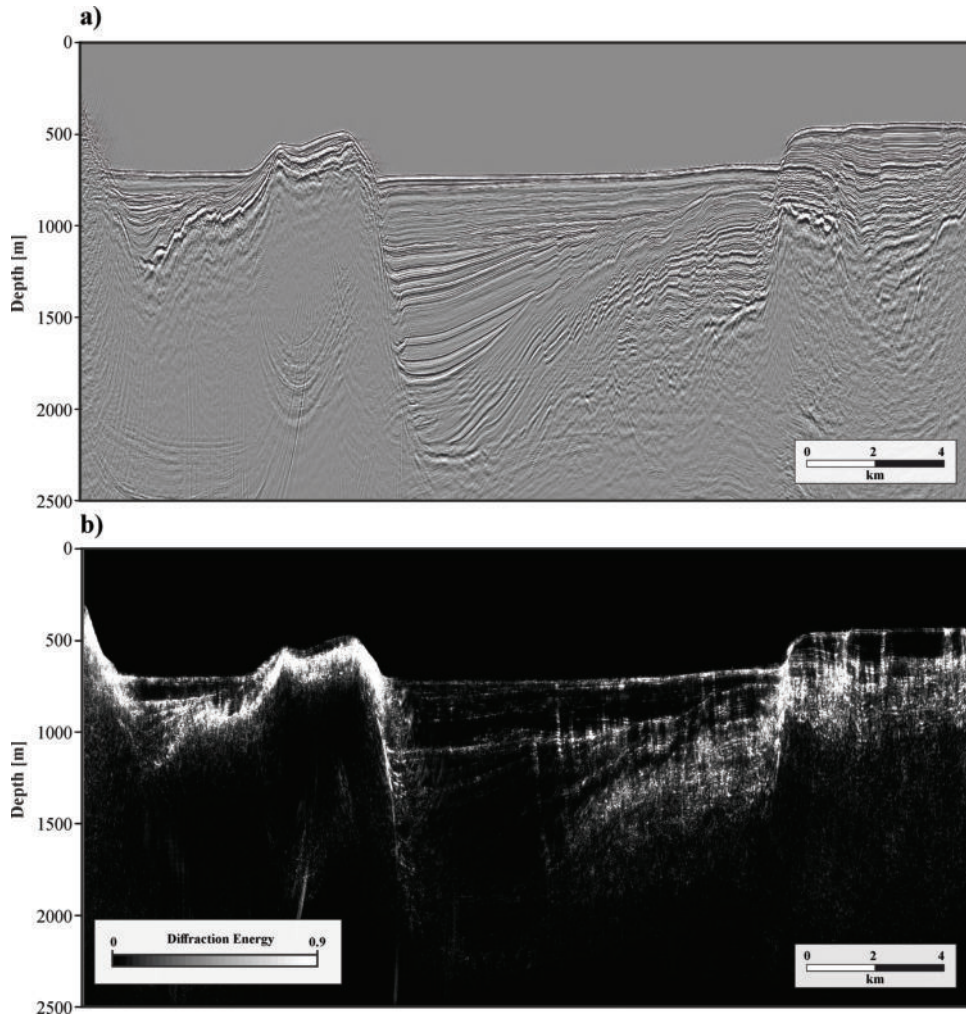
FIGURE 11.5: (a) Finite-differences depth migration of the full wavefield using the velocity model illustrated in Figure 11.4d. (b) Diffraction energy calculated from the finite-differences depth-migrated diffraction-only data using the inverted velocity model illustrated in Figure 11.4d.

11.5.3 Depth Imaging

In the next step, we use the data-derived velocity model for finite-difference (FD) depth migration. As input for the migration, we use the zero-offset section after multiple elimination which has also been used as input for diffraction separation (see Figure H.1). The result is displayed in Figure 11.5a and a comparison of the migration result with the depth-stretched CMP stack is provided in Figure H.3 in the supplementary information. In general, the quality of the depth image seems good as most faults are sharply focussed and there are no obvious artifacts. Also the rugged basement reflection is well imaged and all of its many edges are sharply focused. While the margins of the Santorini-Anafi basin are reconstructed reasonably well, we observe a slight down-bending of the seafloor-reflections towards the Anhydros horst and the Astypalaea plateau which could be explained as a consequence of the smoothness of the velocity model.

In addition, we present a diffraction depth image of the profile obtained by means of FD depth migration of the diffraction-only data using the inverted velocity model. By calculating the squared envelope of the migrated diffractions, we arrive at an

image that illustrates the *diffraction energy* (Figure 11.5b). Such a diffraction depth image provides highly-resolved structural detail. In particular, it highlights the complex system of internal faults in the center of the Santorini-Anafi basin and on the Astypalaea plateau. These faults are expressed as linear, slightly curved features and can be traced nicely through the seismic section and seem to penetrate the seafloor on the Astypalaea plateau. Furthermore, we observe that the Anhydros horst is associated with a high degree of diffractivity, possibly as a consequence of tectonic exposure or erosion. Interestingly, some unconformities can be clearly delineated in the diffraction image, while others are expressed as faint or even transparent events which suggests a different roughness associated with these horizons.

11.6   Interpretation-Driven Refinement

11.6.1   Quality Control
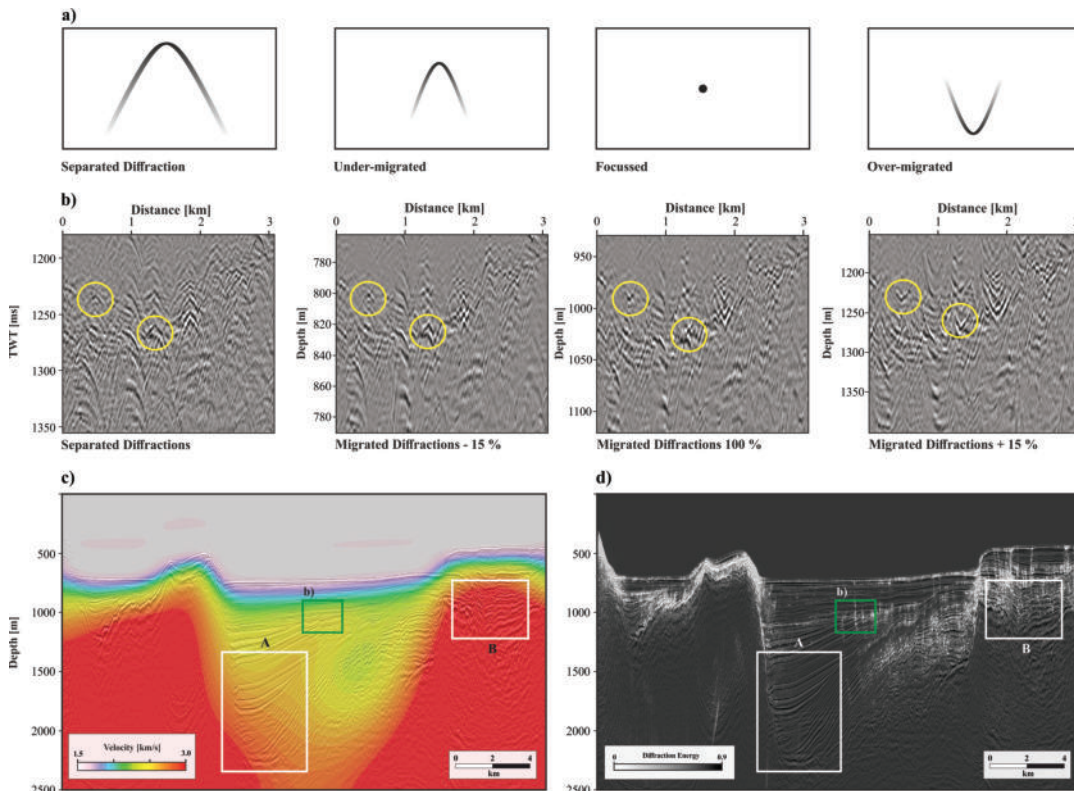
FIGURE 11.6: (a) Schematic illustration of how migration with different velocities affects the shape of diffractions. (b) A small excerpt of the seismic section after diffraction separation. Migration with different velocities results in under-migration (-15 %), focusing (100 %) or over-migration (+15 %). Two prominent instances are highlighted by the yellow circles. (c) FD migrated seismic section overlain with the inverted velocity model and (d) the diffraction depth image. White rectangles indicate areas of unexpected high velocities within the sedimentary strata. The green rectangle indicates the location of the small excerpt shown in (b).

As mentioned in the previous section, the data-derived velocity model presented in Figure 11.4d depicts the expected velocity distribution of the profile quite well. The

sedimentary strata is generally associated with a rather gentle velocity increase from approx. 1.5 km/s to 2.5 km/s while the basement is associated with higher velocities in the order of 3.0 km/s. These values are mostly in agreement with the regional tomographic model presented by Heath et al. (2019), who attribute metamorphic basement and sedimentary strata with to velocities higher or lower than 3.0 km/s, respectively (compare their Figure 11.5). However, a more detailed comparison of their results is not feasible as the presented velocity models are too coarsely resolved considering the high complexity of the data under consideration.

In order to further assess the quality of our velocity model, we (i) analyze the focusing of diffractions after migration and (ii) evaluate the geological plausibility of the inverted velocities. In a similar way to the velocity analysis of conventional long-offset data, where the flatness of common-image-gathers (CIG) is used for quality control, we visually assess the focusing behavior of diffractions to evaluate the quality of the velocity model. Figure 11.6a shows a schematic illustration of how diffractions appear after the migration with different velocities. If too low velocities are used, the diffractions will be under-migrated and have downwards-bent tails. If the velocity used for the migration is correct, the diffractions will be focussed. Using too high a velocity results in over-migration and upwards-bent diffraction tails.

Following this strategy, we evaluated the behavior of the separated diffractions after migration with the inverted velocity model with velocity models perturbed by $\pm$ 15%, respectively. An excerpt from the result containing numerous diffractions is illustrated in Figure 11.6b (see Figure 11.6c for the location within the profile). Two prominent instances are emphasized by the yellow circles. Migrating the separated diffractions with a velocity model of -15 % of the inverted velocity model leads to a narrowing of the diffraction tails but they remain visible in the section. In contrast to that, the migration of the diffractions with the inverted velocity model leads to an overall focusing and the section appears generally free of diffraction tails. The migration with +15 % leads to an over-migration of the diffractions and we can identify numerous upwards-bent diffraction tails within the seismic section. These observations show that the inverted velocity model fits the data quite well and can be validated at least with an approximate confidence interval of $\pm$ 15 %.

By applying this quality control procedure throughout the seismic section, we were able to validate the inverted velocities for most of those areas, in which distinct diffractions are present e.g. along faults. In areas where the diffracted wavefield is more complex, however, focussing is more complicated to assess quantitatively. Especially in the vicinity of the alpine basement, we can not be certain that we take only point diffractions into account as we might encounter lenticular objects (Malehmir et al., 2009). In addition, the focusing of diffractions is only an appropriate quality control tool if scattering occurs in or close to the acquisition plane. However, in case of out-of-plane scattering, diffraction focusing is not an appropriate measure for quality control. As such diffractions appear with distorted curvatures, they will also affect the quality of the velocity inversion. As shown by Malehmir et al. (2009), such out-of-plane diffractions can contribute from considerable distances from the acquisition plane. The identification of out-of-plane contributions still constitutes a challenge and we have to assume that our estimates are affected by them. We argue, however, that the inverted velocities from the diffracted wavefield can be expected to be reliable when a high density of diffractions e.g. from elongated faults are encountered. It is reasonable to assume that such structures are most likely to be located in the acquisition-plane and, consequently, diffraction focusing can be used for quality control in these areas. In contrast, inverted velocities in areas that are constrained by few events should be assessed with caution.

Therefore, we use a second criterion for evaluating the quality of the inverted velocity model: the geological plausibility. Figure 11.6c illustrates the depth-migrated section overlain with the inverted velocity model and Figure 11.6d shows the depth-migrated section overlain with the diffraction depth image. We observe considerable lateral velocity variation within the Santorini-Anafi basin. In the right part of the basin, the velocities of the sedimentary strata are generally lower than 2.5 km/s while in the left part of the basin, we observe a zone with high velocities exceeding 2.9 km/s as highlighted by Rectangle A. Those velocities can be considered geologically implausible for the expected marine sediments (Nomikou et al., 2018). As can be seen in Figure 11.6d, this area is mostly free of diffraction events. This lack of illumination might explain why implausibly high velocities have been inverted here. If an area is not properly constrained by diffractions, the inverted velocity model is more likely to suffer from interpolation artifacts or wrongly-fitted events. However, the right part of the basin is characterized by a high degree of diffractivity, which makes the respective velocity better supported by data.

Furthermore, Rectangle B highlights an area with high velocities in the center of the Astypalaea plateau. Here, the contact of the basement and the sediments is not properly acknowledged by the inverted velocity model and the lower sedimentary strata are associated with velocities of approx. 3.0 km/s, which, again, seems not plausible here. The margins of the plateau, however, are associated with lower velocities and honor the contact of the basement and the sediments more accurately. In contrast to the region denoted by Rectangle A, Figure 11.6d indicates that the area within Rectangle B is actually constrained by numerous diffractions. However, we know from Nomikou et al. (2018) that the Astypalaea plateau is a complex region with a highly varying sedimentary thickness and a very rugged basement. Therefore, the probability of out-of-plane contributions is high in this area, which could explain why unrealistically high velocities have been inferred.

These observations highlight the two main limitations of the proposed velocity inversion workflow for 2D seismic acquisitions: the lack of diffractions in some regions and out-of-plane contribution. However, if 3D data are considered, the problem of out-of-plane can be addressed. Other limitations of the data-driven velocity estimation are the fact that it does not account for anisotropy and that smoothing does not account for the strong velocity contrasts e.g. at the contact of the basement and the sedimentary strata. This could explain e.g. the previously mentioned down-bending of the seafloor reflection close to the Anhydros horst in the migrated section (Figure 11.5a).
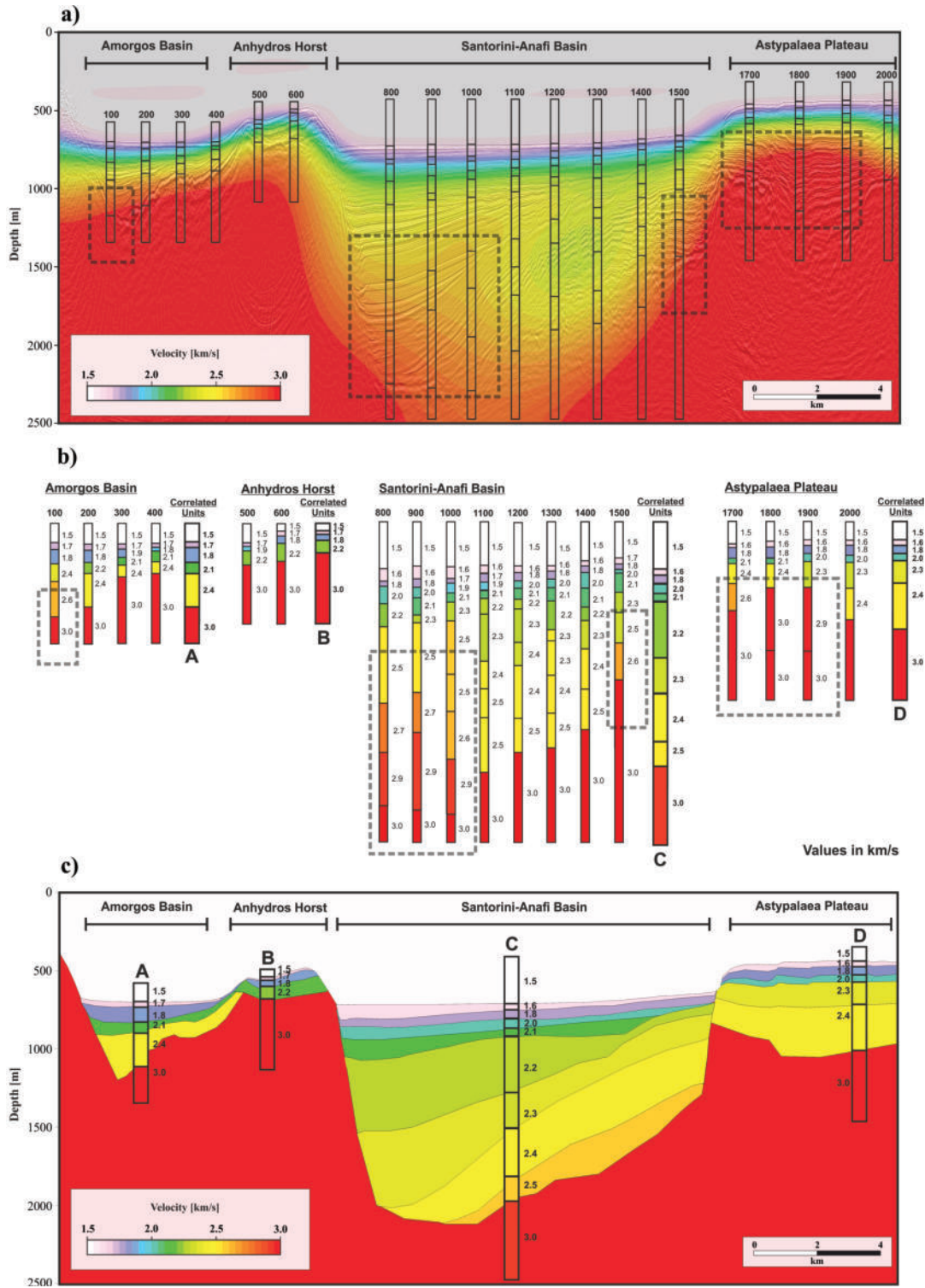
FIGURE 11.7: Illustration of the interpretation-driven velocity refinement. (a) FD migrated seismic section overlain with the inverted velocity model and our sampling points. (b) Extracted velocity values for each stratigraphic layer and the correlated units. The dashed rectangles highlight those areas where our quality control indicated implausible velocities. (c) Refined velocity model.

11.6.2   Velocity Model Refinement

Although our quality control showed that the data-derived velocity model is reliable in extended regions, in certain areas the velocities are implausible for the previously explained reasons. In order to derive a velocity model that is geologically consistent throughout, we suggest an interpretation-driven refinement that utilizes the strengths of the data-driven velocity inversion to compensate for its weaknesses. Therefore, our strategy is to extract 1D velocity profiles for every 100th CMP from the inverted velocity model and to assign the extracted velocities to stratigraphic units. This procedure is illustrated in Figures 11.7a and b. The dashed rectangles highlight those areas, where our quality control indicated zones of implausible velocities. For each layer, we estimate the average value of the extracted velocity and round this estimate to the second decimal place. Afterwards we correlate the units within each compartment of the seismic profile and determine a mean value for the respective stratigraphic layer, while excluding all values within the pre-defined zones of uncertainty. The resulting correlated units for each compartment are illustrated in Figure 11.7b.

In the next step, we assemble a velocity model for the whole seismic section based on the correlated units. The resulting model is depicted in Figure 11.7c. Apart from the zones of high uncertainty, the resulting velocity model is comparable to the original data-driven inversion. For each compartment, the refined velocity model fits the stratigraphic interpretation by Nomikou et al. (2018) reasonably well. In general, the velocity model consists of an upper layer with rather low-velocities of approx. 1.6 - 1.7 km/s underlain by a layer with an interval velocity of approx. 1.8 km/s. Below these upper units, we identify several intermediate units with velocities in the order of 2.0 - 2.2 km/s which are comparably thin for most parts of the profile but have a large thickness in the Santorini-Anafi basin. The lowermost units comprise velocities of approx. 2.4 km/s. Although a comparison is only partially feasible, this refined velocity model is in general agreement with the regional tomographic model presented by Heath et al. (2019) while remaining geologically plausible. However, just like any other means of interpretation, the whole refinement process is subject to a certain degree of subjectivity and does not account for lateral velocity variations within the compartments of the seismic section e.g. as a result of compaction. It might be stressed at this point that the proposed interpretational guide is informed by the lateral continuity of the reflected wavefield, which emphasizes the distinct yet complementary nature and synergetic potential of reflections and diffractions for imaging.
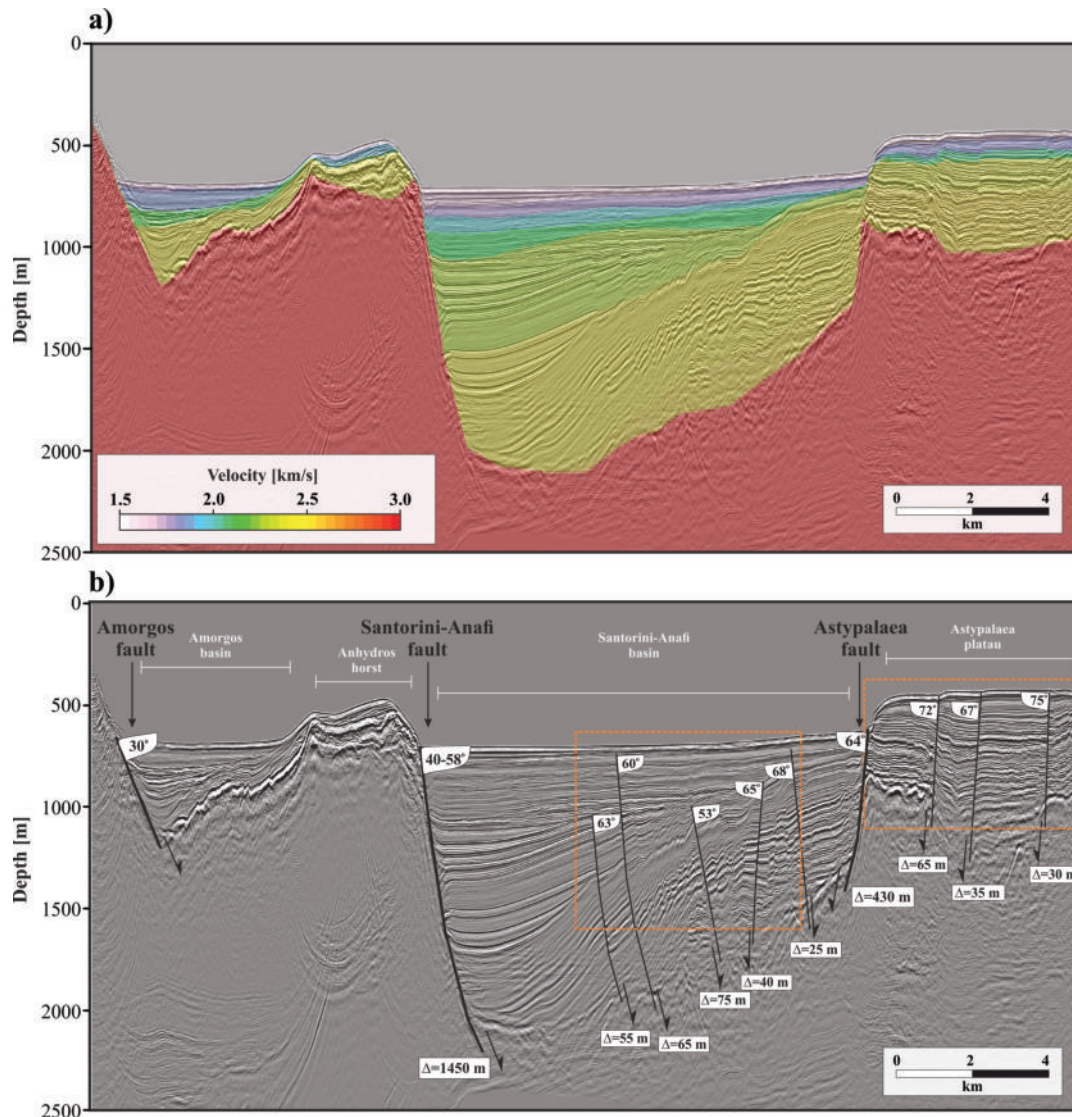
FIGURE 11.8: (a) Full-wavefield depth image superimposed by re-
fined velocity model used for migration. (b) Depth image as in (a)
but shown with dipping angles and throws estimated for the most
prominent faults. Orange rectangles announce two sections that are
highlighted in Figure 11.9.

11.6.3 Geological Implications

Figure 11.8a shows the FD depth-migrated seismic section overlain with the refined
velocity model. This illustration highlights the geological plausibility of the velocity
model. Since the refined velocity model takes into account the high velocity contrast
between the metamorphic basement and the sedimentary strata, the depth-migrated
image is now free of artifacts such as the warping of the seafloor reflection, which
had been observed after the migration with the data-driven velocity model (Figure
11.5a). A comparison of the FD depth-migrated image using the refined velocity
model and the velocity model derived from wavefront tomography can be found in
figures H.4 and H.5 in the supporting information. The overlay of the velocity model
and the seismic section further suggests a stratigraphic relationship of the lowermost
units of the Amorgos basin, the Santorini-Anafi basin, and the Astypalaea Plateau.
Figure 11.8b illustrates the refined FD depth-migrated image as well as the dipping

angles and throws of the most significant faults. Based on this depth image, we infer the total thickness of the sedimentary strata to be approx. 1.4 km, which is remarkable considering that the marine sediments of the SATZ are considered to be of Plio-Quaternary age (Perissoratis, 1995). In order to understand the acting forces responsible for the formation and the evolutionary history of this rift-zone, it would be very helpful to estimate the amount of extension. Having derived a depth-converted seismic section, we encourage the application of structural restoration (Nunns, 1991) in future studies in order to reconstruct and measure the extension in the Santorini-Anafi basin.

Using the interpretation-software KINGDOM, we measure the angles and throws of the most significant faults as illustrated in Figure 11.8b. Compared to the estimates by Nomikou et al. (2018), our study indicates smaller angles for the marginal Amorgos-fault ($30°$ compared to $38°$) and the listric Santorini-Anafi fault ($40 - 58°$ compared to $68°$) and a larger angle for the Astypalaea fault ($64°$ compared to $45°$) but still indicate normal faulting to be the main tectonic mechanism responsible for basin formation. While the throw of the marginal faults is very significant (approx. 1450 m for the Santorini-Anafi fault and approx. 430 m for the Astypalaea fault), the throw of the most important internal faults ranges from 25 to 75 m. Their fault angles lie between $53°$ and $75°$. As indicated in Figure 11.8b, the sense of displacement of the internal faults within the center of the Santorini-Anafi basin changes from NW to the SE forming narrow subsided zones in the center. In order to further analyze the internal fault systems, we utilize the diffraction depth image derived with the refined velocity model. As shown in Figure 11.5b, such diffraction images highlight small-scale heterogeneity and seem to be good indicators for faulting, tectonic overprint or erosion.

As already mentioned by Schwarz (2019a), diffraction images are highly suitable to be used as an alternative to conventional attributes for fault interpretation as e.g. image coherence or image curvature (Bahorich and Farmer, 1995; Marfurt et al., 1998; Chopra and Marfurt, 2007). Following this notion, we combine the diffraction depth images and the refined depth images to arrive at physically informed laterally resolved discontinuity maps. Two examples of these maps are illustrated in Figure 11.9 for the Astypalaea plateau (a-c) and the intrabasinal fault system of the Santorini-Anafi basin (d-f). By blending the diffraction image with the depth-migrated images, we are able to combine the strengths of both the reflected and the diffracted wavefield to facilitate the identification of faults. Especially when considering highly complex fault systems such as the the intrabasinal faults in the Santorini-Anafi basin (Figure 11.9d-f), the diffraction maps provide a powerful guide for the systematic delineation of individual faults.
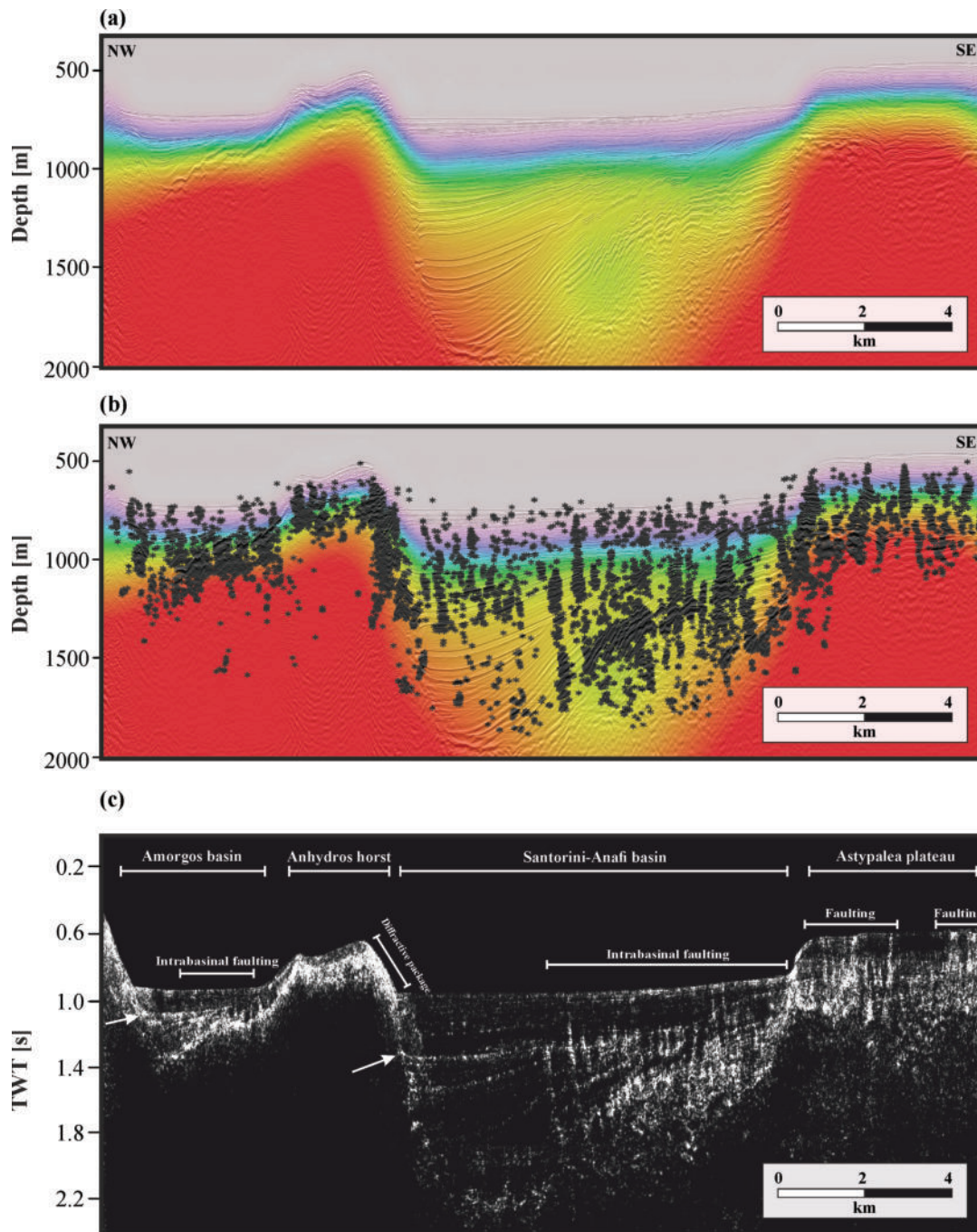
FIGURE 11.9: Excerpts of the final depth image of the Astypalaea plateau and the Santorini-Anafi basin (a,d), the respective fault attribute maps (b,e) and the corresponding fault interpretation (c,f). For location see Figure 11.8b.

Based on these images we present a sketch of the outline of the identified fault systems on the Astypalaea plateau (Figure 11.9c) and in the Santorini-Anafi basin (Figure 11.9f). In both sections, we identify zones in which the sense of displacement of the faults changes from the NW to the SE forming narrow subsided zones in the center (see arrows in Figure 11.9c and f). On the one hand, these subsidiary faults could be interpreted as forming a part of negative flower structures. Such negative flower structures would be an indication for some form of strike-slip movement (Harding, 1990). On the other hand, the shape of the subsidiary faults could also be explained

as the result of antithetic faulting with respect to the marginal Santorini-Anafi fault. In order to further analyze these narrow zones, however, adjacent seismic lines need to be considered. It is interesting that faulting within the Santorini-Anafi basin is mostly restricted to the strata below the unconformity highlighted by the dashed line in Figure 11.9f. This is clearly visible both in the presented diffraction images (Figure 11.5b) and the fault image (Figure 11.9e). Only a few faults penetrate the strata above and their displacement is significantly smaller above than below this unconformity (several meters vs. several tens of meters). This indicates that this unconformity marks a significant change in the tectonic behavior of the fault system. Either the internal faulting within the Santorini-Anafi basin has ceased mostly after the formation of this unconformity or the deposition of the upper units has happened very rapidly with regard to the rate of faulting.

In order to further investigate the timing, orientation, and nature of the identified faults, however, adjacent profiles from the POS338 data-set have to be taken into account. The internal consistency of the presented results suggests that the proposed diffraction-based workflow for depth imaging is practically feasible and its application to other profiles recorded in the working area is strongly recommended. It was demonstrated that no offset information is required, which makes the vast range of vintage seismic profiles from the SATZ new candidates for resolving the debate on strike-slip deformation in the SATZ shedding new light on the volcano-tectonic evolution of this remarkable morphotectonic zone.

11.7   Conclusions and Outlook

In this study, we have shown how the diffracted wavefield can be utilized to enable depth-conversion of academic seismic data without the need for offset information. Using an offset-limited academic seismic line from the Santorini-Amorgos Tectonic Zone (SATZ), we reveal a rich diffracted wavefield by means of a robust separation scheme that models and adaptively subtracts the reflected wavefield from the data. We use the separated diffractions to estimate insightful wavefront attributes and perform wavefront tomography to, for the first time in the study area, derive a depth-velocity model which we use for finite difference depth migration. The diffraction-based velocity model reliably honors the most prominent features of the seismic profile and accounts for the expected sudden velocity increase at the sediment-basement interface.

We further analyze the quality of the inverted velocity model by examining the focusing of diffractions in a similar manner as common-image-gathers are used in reflection-based processing. Founded on this quality-control scheme, we show that the inverted velocity model is reliable where distinct diffractions from elongated faults are considered as these structures are most likely to lie within the acquisition plane. Here, we were able to validate the inverted velocities at least with an approximate confidence interval of $\pm\,15\,\%$ which we consider acceptable in the context of low-budget academic data. Due to the effect of possible out-of-plane contributions and the partial absence of illumination, however, we identify some areas of the inverted model with geologically implausible velocities. Based on the partial lateral continuity of reflection events, we suggest a complementary knowledge-guided refinement that remains geologically plausible across the full investigated study area. In addition, we also perform a depth migration of the separated diffracted wavefield to derive spatial diffraction images. These highly resolved reconstructions provide detailed insight into processes like erosion (diffraction at unconformities) or tectonic

overprint (diffraction at faults). Following the notion of using the diffraction images as physical attribute maps, a combination with full-wavefield depth images is demonstrated to facilitate the identification of faults and other discontinuous features in depth. Led by these findings, we encourage using the diffracted wavefield for the direct imaging of complicated fault and fracture systems in depth.

The presented depth image allows the first data-based quantification of the thickness distribution of the sedimentary strata as well as fault angles and throws within the SATZ. We estimate a maximum sedimentary thickness of approx. 1400 m and angles of the marginal faults that indicate normal faulting. Several narrow fault systems identified by means of the unique diffraction depth images in the Santorini-Anafi basin and on the Astypalaea plateau appear to be of flower-like assembly. We hypothesize that these features are caused either by zones of narrow strike-slip deformation or antithetic faulting with regard to the listric marginal faults. This movement appears to have been a long-lasting process in the SATZ and is less expressed in the younger sedimentary units.

In conclusion, we strongly encourage the application of the proposed diffraction-based workflow for high-resolution imaging and depth conversion in future studies. Since the presented scheme is likewise applicable to single-channel data, we consider its potential to be very promising, e.g. in the context of scientific drilling where velocities prior to drilling are often only poorly constrained. As was demonstrated by Bauer et al. (2019), diffraction focussing can be directly invoked in wavefront tomography with the benefit of automated quality control and increased stability in complex subsurface settings. Moreover, the challenge of correctly identifying out-of-plane scattering becomes obsolete, if 3D data are considered. Cost-effective limited-offset P-cable data are geared towards enabling affordable 3D seismic imaging in academic investigations, which makes this emerging data resource an ideal candidate for diffraction imaging and inversion across scales and communities.

Acknowledgements

Chapter 12

Synthesis and Outlook

12.1 Summary of the Main Results

This thesis has demonstrated that seismic reflection imaging is a very valuable tool for studying the internal structure and evolution of volcanic systems and can provide fundamental new insights even in an area as well studied as the Christiana-Santorini-Kolumbo volcanic field. Chapters 4-10 have shown that seismic reflection data can be used to study various facets of volcanology, from the reconstruction of the spatio-temporal evolution and volcano-tectonic interactions on scales of millions of years (Chapters 4, 5, 6, 7), to the estimation of the volume and emplacement dynamics of large-scale volcanic eruptions (Chapters 8, 9), the reconstruction of cascading events leading to a vast mass-transport-deposit (Chapter 5) or a major historical volcanogenic tsunami (Chapter 10). For each of these chapters, it has been key to integrate the seismic data into the geological and volcanological context of the study area in order to develop models that are consistent across different disciplines. Thus, the concepts presented in this thesis are consistent not only with the volcano-stratigraphy onshore Santorini (e.g Druitt et al., 1999) but are also consistent with recent studies based on sediment cores (Kutterolf et al., 2021a; Kutterolf et al., 2021b) or studies of the shallow crust (Hooft et al., 2019; Heath et al., 2019; McVey et al., 2020). In addition, this thesis demonstrated the potential of diffraction extraction as a tool to derive interval velocity models and unique diffraction images from offset-limited academic seismic data (Chapter 11).

12.1.1 Volcano-Tectonic Evolution of the CSK Volcanic Field

One of the main objectives of this thesis was to reconstruct the spatio-temporal evolution of the CSK field and how it is related to the evolution of the regional tectonic system. Previous analyses of the offshore realm have been able to image the internal structure of the eastern rift basins (e.g. Nomikou et al., 2016b; Nomikou et al., 2018a; Nomikou et al., 2019) or the Kolumbo Volcano (Hübscher and Gohl, 2016). What has been lacking so far, is a seismo-stratigraphic framework that links the rift basins to the volcanic centers and consistently incorporates the onshore volcanic stratigraphy (e.g. Druitt et al., 1999). Such a model was presented in Chapter 4, consisting of six units U1-U6, separated by six key reflectors h1-h6. These units were identified in the Christiana Basin west of Santorini and the Anhydros and Santorini-Anafi Basins east of Santorini, thus enabling a link of the stratigraphy of the basins on all sides of Santorini. Subsequently, this seismo-stratigraphic framework was used to place major volcanic deposits from the CSK centers in a chronological order, resulting in the first consistent spatio-temporal model for the entire CSK field.

According to this model, the CSK volcanic field developed in four phases, roughly

dated based on sedimentation rates and correlations with the onshore stratigraphy of Santorini and Christiana. The first phase began in the Pliocene with the evolution of the Christiana Volcano, before the early Kolumbo Volcano and the newly discovered Poseidon Center emerged in the second phase. The third phase was a period of widespread volcanic activity that saw the evolution of the newly discovered Aspronisi cones SW of Santorini and the evolution of the Kolumbo Volcanic Chain. During the fourth phase, volcanism focused on the Santorini Caldera, while Kolumbo remained active. With the exception of Chapter 11, all other chapters of this thesis are based on this seismo-stratigraphic framework and successively extended it.

Chapter 5 examined the internal structure and emplacement mechanisms of Unit 4. This unit has been identified in all basins surrounding Santorini and based on its internal seismic architecture, it represents the deposits of multiple mass-wasting events that occurred in a relatively short time both on the Christiana Volcano and on Santorini. Triggered by a major rifting event, large-sector collapses occured on both volcanoes, causing secondary sediment failures that transitioned into debris and turbidity flows, which traveled far into the rift basins. With a total volume of up to 125 km^3, this event produced one of the largest volcanic island mass-transport deposits in the Mediterranean Sea.

The tectonic evolution of the CSK rift system and its relation to the CSK volcanic field was further investigated in Chapter 6. For this purpose, the entire seismic dataset was used to map the thickness of each seismo-stratigraphic unit over the entire area spanning from the Christiana Basin, through the volcanic centers towards the eastern Santorini-Anafi Basin. The resulting volcano-tectonic model, together with some further details from Chapter 7, is illustrated in Figure 12.1, while Figure 12.2 shows the corresponding timeline. According to this model, the CSK volcanic field evolved on an NNE-SSW trending paleo basin, which may have acted as a transfer zone between Pliocene ESE-WNW-oriented basins (Fig. 12.1a). Volcanism at Christiana initiated as a new NE-SW-oriented tectonic regime emerged in the Late Pliocene/Early Pleistocene (Fig. 12.1b). Subsequently, all volcanic structures evolved parallel to this trend (Fig. 12.1c). Two major Pleistocene tectonic pulses were identified, each of which triggered changes in the behavior of the volcanic field. The first event at approx. 0.7 Ma, triggered the Santorini-Mass-Wasting Cascade as described in Chapter 5 (Fig. 12.1d). Afterwards, widespread volcanism occurred along a distinct NE-SW directed zone crosscutting present-day Santorini (Fig. 12.1e). A more recent tectonic pulse at about 0.35 Ma led to major subsidence in the Santorini-Anafi Basin, while volcanism focussed on Santorini and became highly explosive forming the Thera Pyroclastic Formation (Fig. 12.1f). Further, this chapter discusses this volcanic-tectonic model in the wider context of the southern Aegean (Figure 12.2), especially in comparison with the Kos-Nisyros-Yali field to the east and the tectonic evolution of Rhodes. This comparison highlights regional changes in volcanic behavior of the CSK field and the Kos-Nisyros Yali field at the same approximate times, suggesting large-scale volcano-tectonic interactions between both volcanic centers.
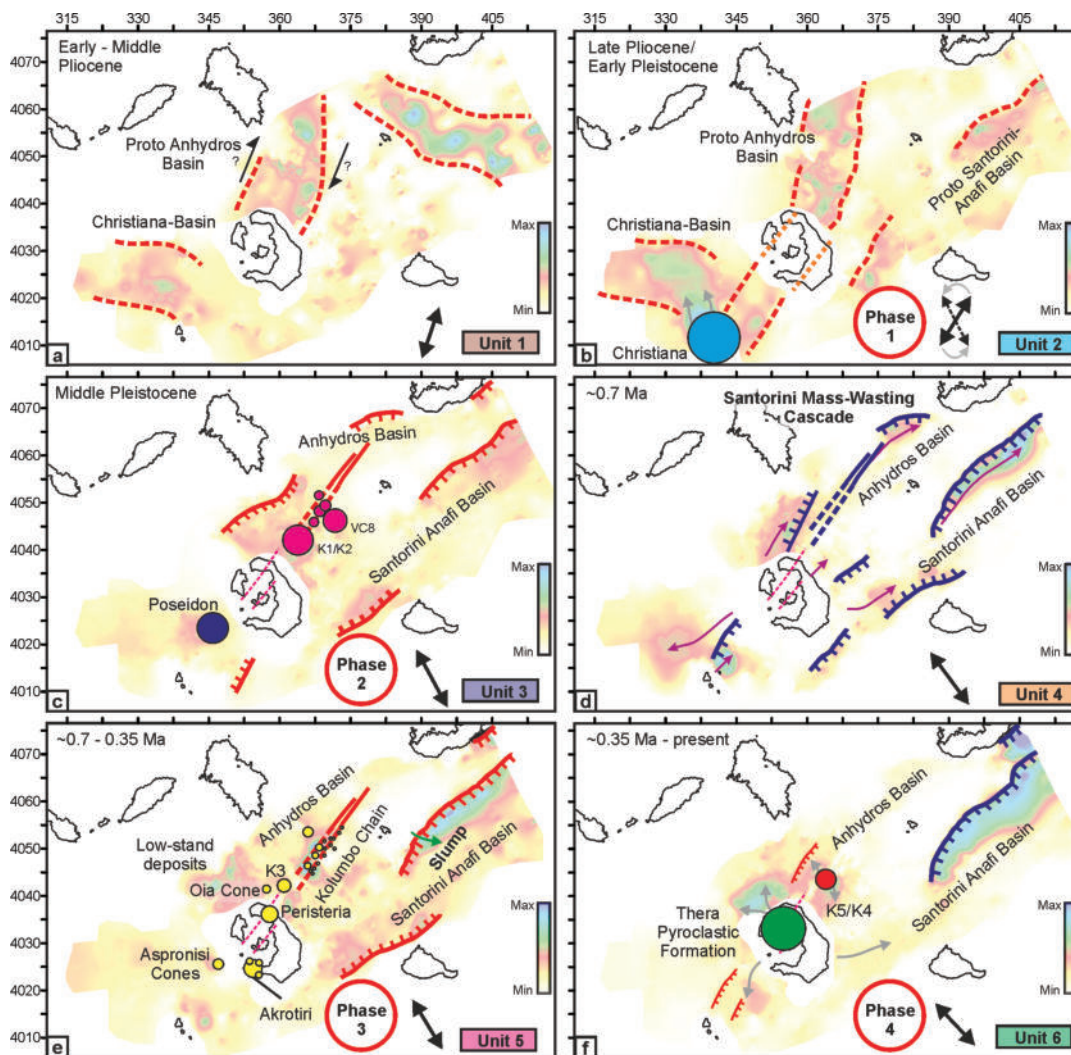
FIGURE 12.1: Schematic reconstruction of the volcano-tectonic evolution of the CSK rift zone. Modified from Chapters 6 and 7. Relative isochore maps of the different units are plotted in the background. Red lines indicate faults active during deposition of each phase. Blue lines show faults that have been affected by tectonic pulses. Dashed lines depict the outline of depocenters with higher uncertainty. Dashed orange lines indicate the outline of the proto-Anhydros Basin underneath Santorini as defined by Heath et al. (2019). Volcanic phases (red circles) are modified from Chapters 4 and 7. Black arrows show approx. direction of extension as inferred from the interpreted faults. Black arrows in F indicate the potential strike-slip movement of the proto-Anhydros Basin. Thin grey arrows highlight the direction of transport of volcanoclastic material and purple arrows indicate the direction of mass-wasting events (Chapter 5).

Chapter 7 examined the area between Santorini and the Kolumbo Volcanic Chain in more detail. It was found that the Kolumbo Volcanic Chain was not formed in a single phase, but that parts of this Volcanic Chain are much older and were formed during the same time as the early Kolumbo deposits and the Poseidon Center (Fig. 12.1c). Volcanism was diverse and evidence of both explosive and effusive volcanism has been found occurring at different times. One of the main findings is that the Kolumbo Volcanic Chain developed along two normal faults, which can be traced

beneath individual volcanoes in the northeast (Fig. 12.1c, d, e). Towards Santorini, other smaller volcanic centers, such as the Oia Cone, were discovered, as well as a volcanic ridge connecting Kolumbo with Santorini (Fig. 12.1e). This suggests a connection between both volcanic systems, e.g. during Phases 2 and 3. This link got probably disconnected after the tectonic pulse before Phase 4, leading to a focus of volcanism mainly on Santorini with increasing explosivity (Fig. 12.1, 12.2).
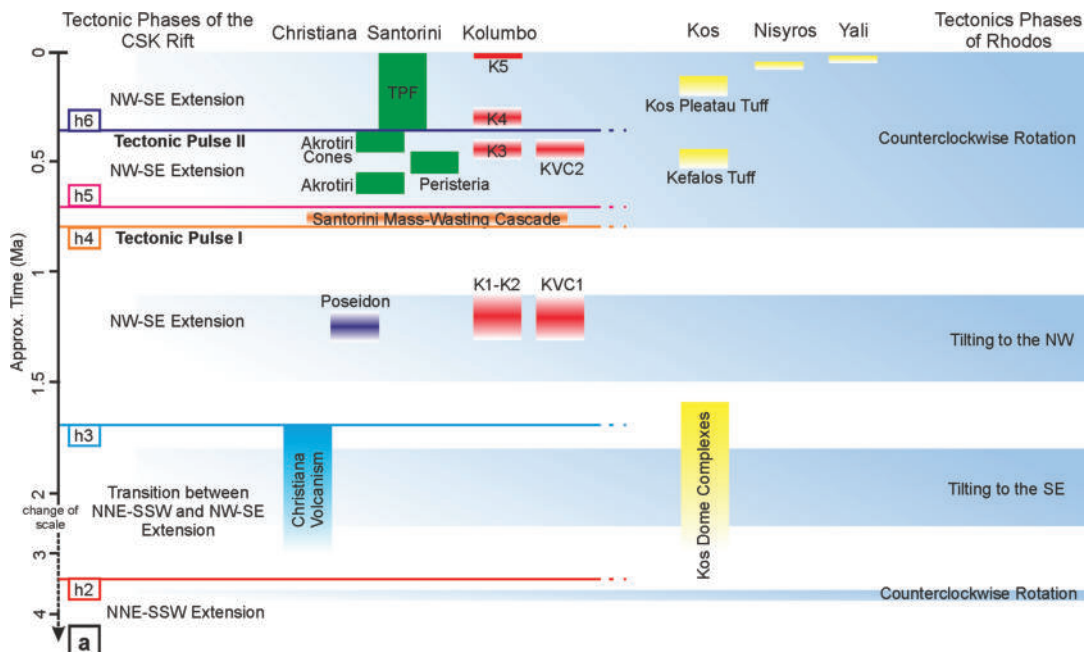
FIGURE 12.2: Schematic illustration of the chronology of volcanism and tectonics of the southeastern Aegean Sea. Tectonic phases of the CSK rift are from Preine et al. (2022c), volcanic ages of the CSK volcanic field from Preine et al. (2022a), volcanic ages of the Kos-Nisyros-Yali Complex from Vougioukalakis et al. (2019) as well as Kutterolf et al. (2021b), and tectonic phases of Rhodos from Van Hinsbergen et al. (2007). KVC: Kolumbo Volcanic Chain.

12.1.2   The Minoan Eruption and its Influence on the Seafloor Morphology

The Minoan eruption of Santorini is probably one of the best-studied large-scale (VEI > 7) volcanic eruptions and has been the focus of volcanological and archaeological research since the 19th-century (Fouqué, 1879; Druitt et al., 1999). The temporal evolution of this eruption has been reconstructed from numerous volcanological studies of the onshore deposits, but are large uncertainties about the volume of this eruption with previous estimates ranging from 19 to 86 km^3 (Heiken and McCoy, 1984; Johnston et al., 2014). In particular, the volume of the offshore deposited ignimbrites and ash-fall deposits has previously been a large source of uncertainty, as they range from (multi-) meter thick deposits proximal to the source to fine-grained deposits several kilometers away from the source, which can only be assessed by multidisciplinary research efforts. This also means that little has been known so far about how vast amounts (> several km^3) of pyroclastic material deposited in a relatively short time as well as caldera collapse events affected the seafloor morphology around Santorini.

In order to address the large uncertainties regarding the volume of the Minoan Eruption, Chapter 8 provided the first holistic reconstruction of any large-scale volcanic eruption worldwide by combining geophysical and sedimentological datasets from various scales, ranging from microscopic (sub-millimeter resolution of computed tomography scans) to (multi-) meter (sediment core and multi-channel seismic data) up to shallow crustal scales (P-wave tomography). This joint analysis resulted in a total DRE-volume estimate of 31.4 ± 5.2 km^3 for the Minoan eruption, which comprises an ignimbrite DRE volume of 6.9 ± 2 km^3, an ash-fall DRE-volume of 18.9 ± 2.2 km^3, and an intra-caldera deposit DRE-volume of 5.5 ± 1 km3. This estimate is significantly smaller than the previous estimate of 86 km^3 (Johnston et al., 2014) but is consistent with an independent caldera collapse reconstruction of $\sim$32.5 km^3.

One of the main factors that have led to this volume reduction is that the new high-resolution seismic data has allowed to identify and map the submarine ignimbrites. This was also the key to Chapter 9, which investigated the formation of undulating sediment bedforms (USBs) during the Minoan eruption. These seafloor bedforms have been identified in previous studies and extend up to 25 km from the volcano. However, the mechanisms of their formation and their relationship to the Minoan eruption have been unclear. Based on seismic interpretation, this chapter showed that the USBs around Santorini were formed during the Minoan eruption and represent mass-transport deposits, although three different formation processes were identified. (1) Flow-derived ignimbrites from the Minoan eruption are found north of Santorini. Undulating sediment bedforms are the result of syn-depositional thrusting. (2) Slope failures of material from the entire TPF were identified east, south, and west of Santorini. (3) Deep-seated tectonic deformation occurred on the southwestern flank of Santorini leading to a steepening and debuttressing of the flank of Santorini triggering multiple mass failure events of the entire TPF. In both cases, USBs are the result of block rotation in the extensional upslope domain, while downslope, thrusting formed undulating morphologies. As the USBs are not overlain by seismically resolvable material, these processes took place during the Minoan eruption as a result of intensive ground movements due to the caldera collapse and/or as a result of a syn-eruptive rifting event.

12.1.3 Cascading Hazards

A key element of this thesis is that different geological processes interact in the form of cascades during extreme events. As shown in Chapter 9, several processes interacted during the Minoan eruption, where the rapid loading of loose, unconsolidated pyroclastic material on submarine flanks, the simultaneous failure of such material due to large-scale seismic activity, and the reactivation of deep-seated tectonic deformation led to the formation of the USBs on the flanks of Santorini. Therefore, in addition, to the emplacement of pyroclastic flows, the formation of these USBs due to slope failures, probably also had an important influence on the resulting tsunami that affected large parts of the eastern Mediterranean.

The reconstruction of the historic Kolumbo eruption in Chapter 10 highlighted the hazard potential of such disaster cascades during submarine explosive eruptions. Using high-resolution three-dimensional seismic data and bathymetry, it was shown that the catastrophic explosion and tsunami were triggered by the collapse of Kolumbo's northwest flank. The failure of the flank depressurized the magma feeding system and triggered the catastrophic explosion, and is the result of the instability of the flanks of Kolumbo, which almost entirely consist of highly vesicular pumice from

local fallout and volcaniclastic flows. Tsunami reconstructions have shown that eye-witness accounts of the tsunami can be explained by the fact that the tsunami was first triggered by the flank movement and then amplified by the explosion.

In addition, Chapter 5 showed that disaster cascades have also played a crucial role in the more distant past of the CSK field. The seismic reflection profiles were used to reconstruct the deposition of Unit 4, which occurred at about 0.7 Ma as a complex cascade of five processes: rifting, precursory mass movements, sector collapses, secondary sediment failures, and debris flow deposition. A major rift pulse affecting the entire CSK rift system triggered initial mass-wasting events, which were followed by sector collapses of the Christiana edifice and the flanks of proto-Santorini. The sudden loading of these events led to the propagation of a décollement, which triggered large-scale secondary sediment failures that account for more than 90 % of the entire volume of Unit 4. These sediment failures transitioned into turbidity flows that traveled far into the rift basins. This complex cascade affected the volcanic plumbing system of the CSK field and triggered a phase of rift-wide volcanism highlighting the important volcano-tectonic feedback mechanisms along this volcanic system.

12.1.4   Diffraction Imaging

Chapter 11 presented a new, innovative way to convert offset-limited seismic data to the depth domain using diffraction separation. This approach uses seismic stacks before migration and first models the reflected wavefield before adaptively subtracting it from the input data. Subsequently, wavefront attributes are computed from the separated diffractions and used for wavefront tomography, which was used to produce depth velocity models. An interpretation-driven refinement of the velocity field was necessary to compensate for out-of-plane effects and thus to obtain a geologically plausible velocity field. This was then used for post-stack depth migration, for which diffraction focusing was used as a quality control tool.

In addition, this chapter has shown that the use of focused diffraction images in combination with full wavefield images allows the identification of small-scale heterogeneities that can be very useful in seismic interpretation. This can play an important role in the interpretation in volcano-tectonic settings as demonstrated in Figure 12.3, which shows an overlay of a focussed diffraction energy image on the full-wavefield image of a profile along the Kolumbo Volcanic Chain and western Santorini-Anafi Basin. The focused diffraction energy highlights not only faults, but also the presence of MTDs such as Unit 4, or the ignimbrites close to the sea surface (Fig. 12.3). On the other hand, the volcanic structures of the Kolumbo Volcanic Chain also show high diffraction energy, clustered mainly along the cones interpreted as effusive deposits. Future studies should further investigate how the use of these diffraction images can support seismic data interpretations and how they compare to other interpretation attributes such as the similarity or chaotic reflection attributes.
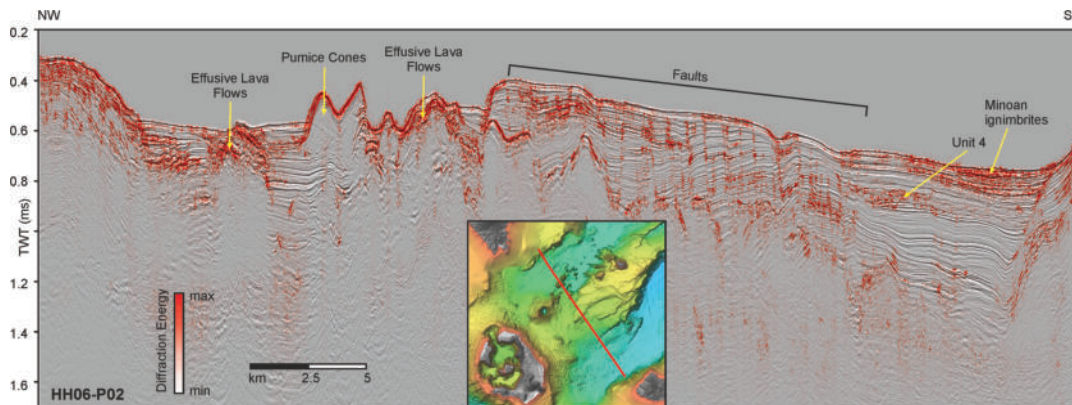
FIGURE 12.3: Time-migrated seismic image of a profile across the Santorini-Anafi Basin and the Kolumbo Chain superimposed with an image of focused diffraction energy highlighting several small-scale discontinuities.

12.2 Outlook

12.2.1 IODP Expedition 398

Most of the results of this thesis are largely based on the interpretation of the seismic data. However, these interpretations are limited by a number of uncertainties that cannot be resolved without ground-truthing by drilling (Chapter 3). While the relative chronology of volcanic episodes is confirmed by a robust correlation of seismic facies in the different basins, the precise ages for different volcanic events or seismo-stratigraphic units estimated in this thesis (Chapter 4) have large error margins because they were calculated assuming constant sedimentation rates (Chapter 3), which introduces a significant amount of uncertainty. In addition, there also remain uncertainties about the exact nature of buried deposits such as the nature of the Poseidon deposit (Chapter 4) or the nature of Unit 4 (Chapter 5), that need to be tested by scientific drilling. Although there are a number of other exciting questions in the CSK volcanic field that can be further investigated using seismic lines (e.g. regarding the nature and timing of the large volcanic edifices northeast of the Christiana edifice (Fig. 12.4) or the exact nature of the intra-caldera deposits), the uncertainties mentioned above cannot be resolved with seismic data alone. However, all these open questions will be addressed during IODP Expedition 398 *Hellenic Arc Volcanic Field* that is scheduled from December 2022 to February 2023 (Druitt et al., 2022). This expedition plans to drill six primary sites at the CSK volcanic rift, of which two sites are inside the Santorini Caldera and four outside in the rift basins (Fig. 12.4; all IODP sites are labeled as CSK-XY) (Druitt et al., 2022).
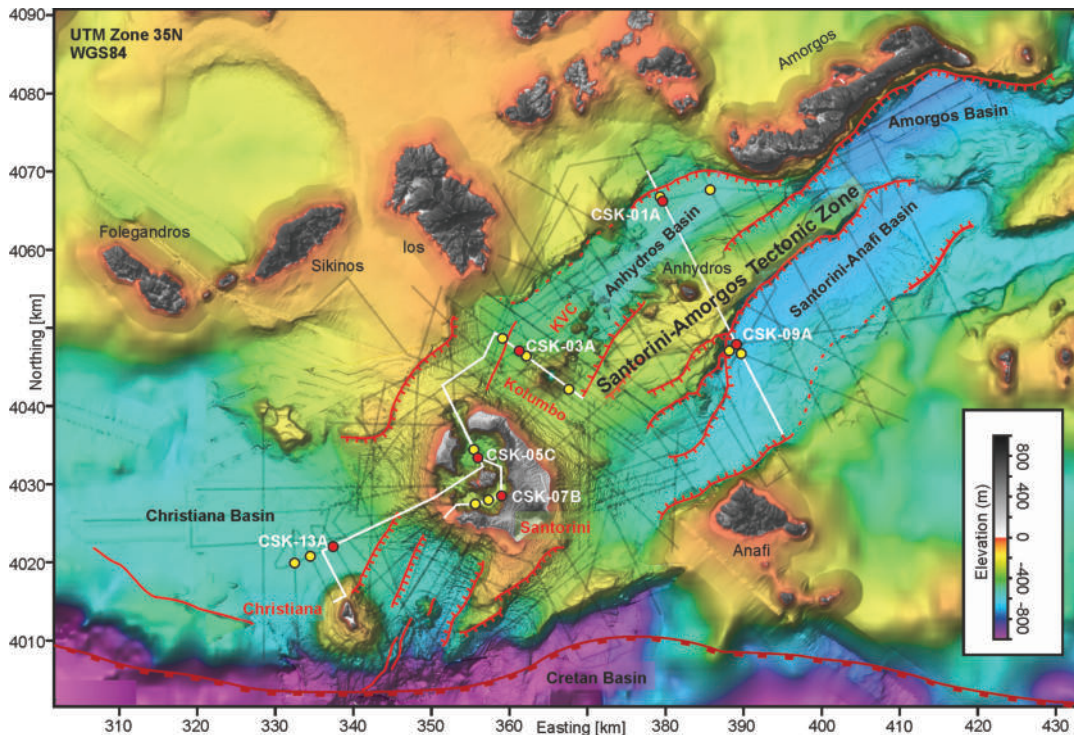
FIGURE 12.4: Morphological map of the CSK rift zone showing islands, basins, volcanic centers, and major extensional structures (red lines) (Nomikou et al., 2019). Grey lines indicate seismic lines; white lines indicate seismic profiles shown in Figure 12.5. Circles indicate primary (red) and alternate (yellow) sites for IODP Expedition 398. Modified from Preine et al. (2022c). Coordinate system is UTM Zone 35N, WGS84.

IODP Expedition 398 has five main goals (Druitt et al., 2022):

1. Reconstruct the volcanic history of the CSK volcanic tectonics and volcanism

2. Reconstruct subsidence and tectonic histories of the rift basins and study the relation of tectonics and volcanism

3. Document magma petrogenesis at the CSK volcanic field in space and time

4. Unravel the iconic caldera-forming Minoan eruption

5. Study the histories, dynamics, and hazards of the CSK volcanoes.

The seismic lines processed and homogenized in this thesis will play a key role in the evaluation of this expedition. The borehole and logging data from Expedition 398 will provide detailed stratigraphic, physical property, and age data recorded at depth. However, to address the main objectives of Expedition 398, especially Objectives 1, 2, 4, and 5, it is necessary to extend the constrained 1D stratigraphic model from the wells regionally throughout the rift basins and the caldera to constrain the sources, distribution, and volumes of individual volcano-sedimentary units. This can only be achieved by means of core-log seismic integration (e.g. Riedel et al., 2020; Crutchley et al., 2022), which will be carried out as part of the DFG-funded project HU698/27 at the University of Hamburg.

Core-log seismic integration during IODP Expedition 398 will provide the unique

opportunity to test, refine and extend most of the concepts presented in this thesis. As shown in Figure 12.5A, the CSK-13A and CSK-03A sites will allow the main concepts of Chapter 4 to be tested, and in particular, will allow estimating the ages of the Units U1-U6. Core-log seismic integration will enable a gapless reconstruction of the volcanic history of the Christiana-Santorini-Kolumbo volcanic field. In addition, Figure 12.5C shows that sites CSK-01A and CSK-09A are ideally located to reconstruct the tectonic evolution of the eastern rift basin at a much higher resolution than it was possible during this thesis (Chapter 6). Core-log seismic integration here will enable the temporal relationship of tectonic pulses and volcanic episodes of CSK volcanism to be quantified.

Another key area of the CSK volcanic field is the Santorini Caldera. To understand the internal architecture of the caldera, the CSK-07B and CSK-05C sites will allow the unraveling of the intra-caldera deposits(Fig. 12.5E). In Chapter 8, the volume of intra-caldera deposits from the Minoan eruption was estimated using deep tomographic data, which is associated with a large error margin. Core-log seismic integration in the caldera will allow the nature of individual units within the caldera to be determined and their volumes to be calculated. This also has important implications for the evolution of the Kameni volcano, which so far is only constrained by onshore sampling, eyewitness accounts, and bathymetric mapping (e.g. Nomikou et al., 2014).

In addition, IODP Expedition 398 will also allow for a much more detailed understanding of the nature and emplacement dynamics of Unit 4, the 'Hidden Giant' (Chapter 5). All sites outside the caldera cross the deposits of the Santorini Mass-Wasting Cascade, which will allow drilling different components of Unit 4, such as proximal deposits close to Christiana or Kolumbo (e.g. at site 03-A and 13-A) or distal deposits in the rift basins (e.g. at site 01-A and 09-A) (Fig. 12.5).

Another important aspect of IODP Expedition 398 will be to test the velocity model and thus the method of diffraction-based velocity inversion presented in Chapter 11. Core-log seismic integration at each site will allow the assignment of the velocity information from sonic logs or vertical seismic profiles to individual seismo-stratigraphic units. These velocity models can then be compared with the diffraction-based models to test and further calibrate the method. Once reliable velocity models have been established, they can be used to perform depth migration for all profiles across the rift basins to estimate fault angles, and formation thicknesses, as well as to perform structural restoration to estimate extension rates.

The processed and homogenized dataset that has emerged from this thesis will be one of the keys to the evaluation of IODP Expedition 398. In addition, the results presented in chapters 4-11 allow to sharpen the research questions during the evaluation of IODP Expedition 398 and to place the 1D results from the boreholes directly into the seismo-stratigraphic framework of this thesis in order to spatially extrapolate the findings.
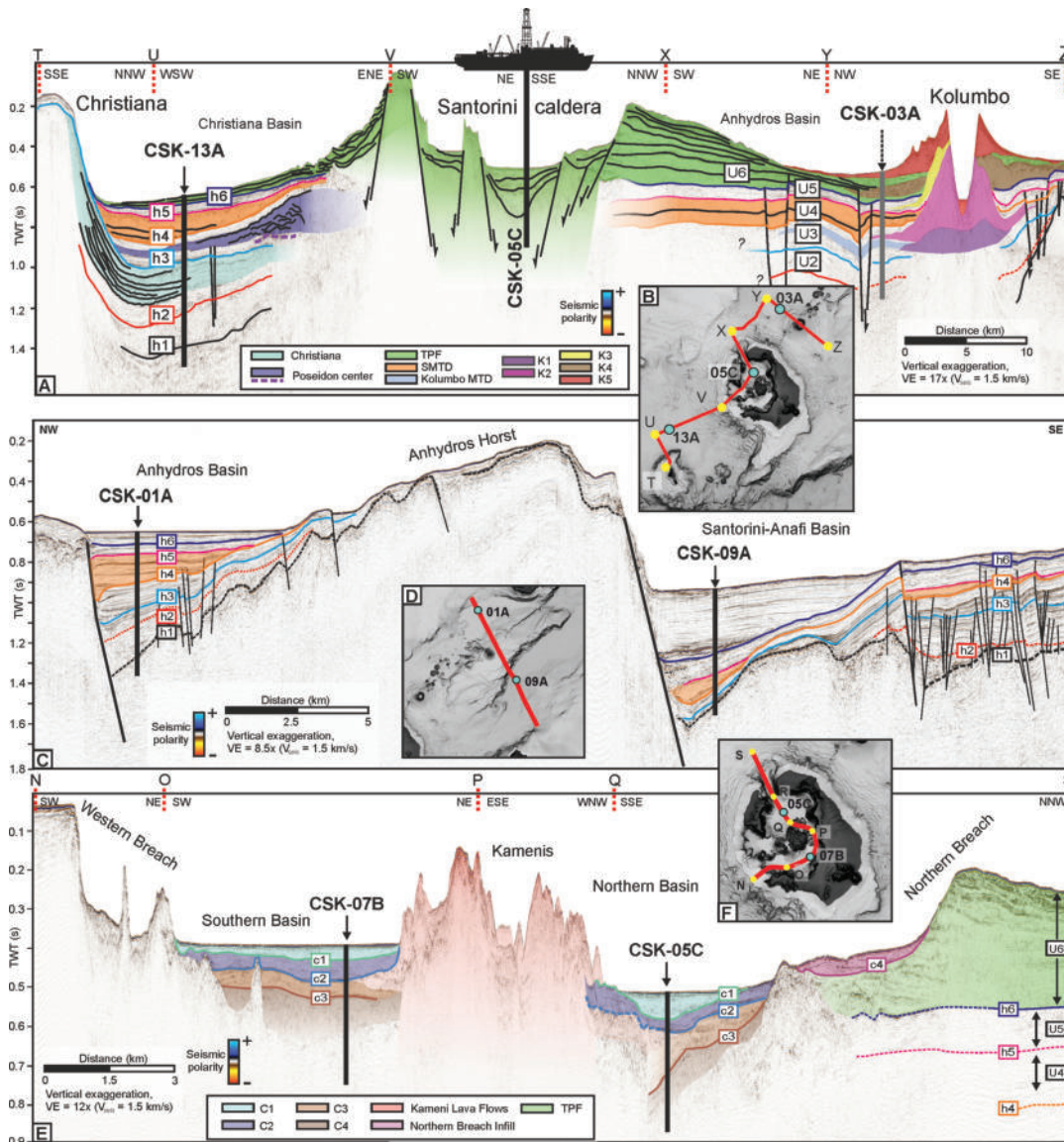
FIGURE 12.5: Seismic profiles crossing all six primary sites of IODP
Expedition 398 (A, C, E). Their locations are shown on the maps (B,
D, F). Modified from Preine et al. (2022a) and (Druitt et al., 2022).
TPF: Thera Pyroclastic Formation; SMTD: Santorini Mass-Transport
Deposit; MTD: Mass-Transport Deposit

12.2.2   Towards Reconstructing the Volcano-Tectonic Evolution of the Entire Hellenic Volcanic Arc

As outlined in the introduction, understanding the past of volcanic systems is key to better anticipate future hazard scenarios. The CSK volcanic field is only one of four major volcanic centers of the Hellenic Volcanic Arc, as shown in Figure 12.6. All of these centers are located near the densely populated islands of the Aegean Sea or close to the coast of mainland Greece and Turkey, with many large cities lying close to the shoreline at low elevations making them particularly vulnerable to tsunami events (Fig. 12.6). For example, the Aegina-Poros-Methana Volcanic Field is located in the Gulf of Saronikos, directly on the opposite side of the Piraeus, which has a population of ~450,000 million (Fig. 12.6). On the other side of the Hellenic Volcanic

Arc, the Kos-Nisyros-Yali Volcanic Field lies close to the coast of Anatolia, near the towns of Bodrum, Didim, and Marmaris, which together have a population of over 300,000 (Fig. 12.6). Having produced the Kos Plateau Tuff eruption 161,000 years ago, one of the largest explosive eruptions of the Hellenic Arc, the Kos-Nisyros-Yali Volcanic Field poses a significant hazard to these cities (Vougioukalakis et al., 2019). Also, the cities of Heraklion and Chania on Crete (> 300,000 people) are at risk from tsunamis from the volcanic field, given that the Minoan tsunami, for example, had a major impact on the northern coast of Crete (e.g. Lespez et al., 2021).
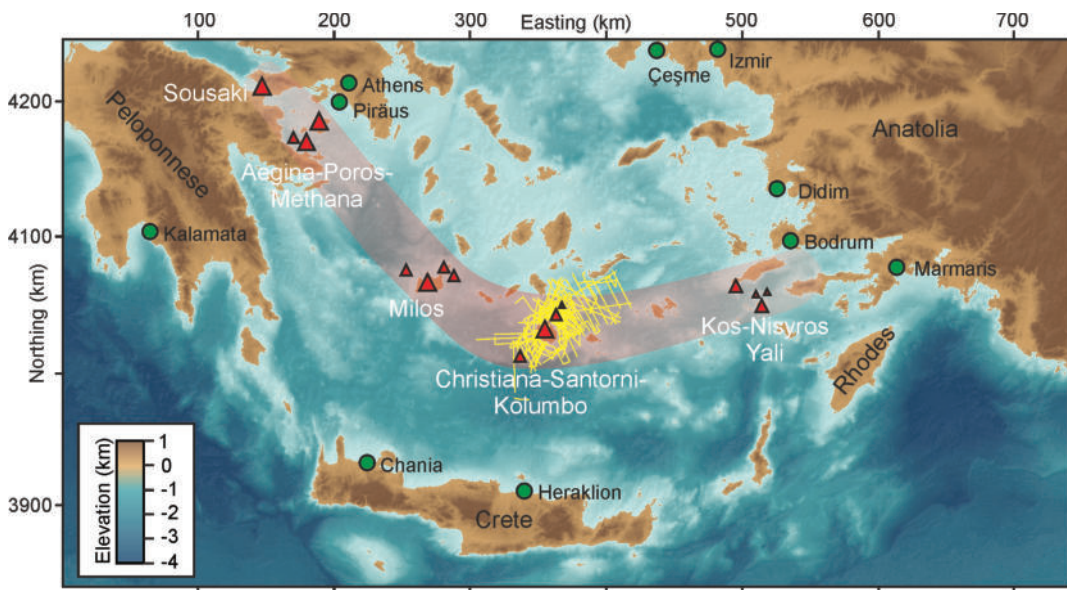

FIGURE 12.6: Morphological map of the southern Aegean Sea with the volcanic centers of the Hellenic Volcanic Arc marked by the red triangles. Yellow lines indicate seismic lines used in this study. Green circles indicate major cities in the southern Aegean Sea.

Except for the Christiana-Santorini-Kolumbo volcanic field, no high-resolution reflection seismic data have been acquired along the other volcanic centers of the Hellenic Arc, so that the internal architecture of these systems remains unknown, leaving questions about the structural evolution, and the relationship between volcanism and tectonics largely unresolved. As shown in this thesis, reflection seismic data can also be used to discover previously unknown volcanic centers and to unravel the volume of large-scale eruptions and mass-wasting events. For example, an important question is where exactly the source of the Kos Plateau eruption is located. So far, it is thought that the caldera is located somewhere between the islands of Kos, Nisyros, and Yali, but this remains to be verified (e.g. Allen et al., 2019). Seismic surveys may solve this puzzle.

As discussed in Chapter 6, volcano-tectonic interactions could potentially operate on a large scale, affecting multiple volcanic systems of the arc, but this needs to be tested by extending the coverage of seismic data (Fig. 12.6). Thus, the Hellenic Arc offers the unique opportunity to reconstruct the volcano-tectonic evolution of an entire volcanic arc, and, being easily accessible even for smaller research vessels, represents an ideal natural laboratory to study back-arc volcanic systems. The interdisciplinary combination of reflection seismic data with deep seismic tomography, sediment and drill cores in combination with onshore volcanic stratigraphy, has the

potential to unravel such volcano-tectonic interactions on scales from kilometers to sub-millimeters over times of millions of years. Lessons learned here may be important for understanding other back arc volcanic systems around the world, such as the Sunda Arc, which produced the devastating Krakatau and Tambora eruptions, or the Tonga–Kermadec Volcanic Arc, which recently produced the Hunga-Tonga eruption (e.g. Lynett et al., 2022; Poli and Shapiro, 2022).

12.3   Implications for Hazard Assesments

The new insights gained as part of this thesis have important implications for hazard assessments for the eastern Mediterranean, but also for other major marine volcanic systems around the globe. Chapter 8 provided the first integrated reconstruction of the volume of a major volcanic eruption making the Minoan eruption the only large-scale eruption with complete coverage of all eruption products. For most of the world's major (VEI > 7) marine eruptions, such as Krakatau (1883), Tambora (1815), Kuwae (1425), or Samalas (1253), the submarine record is incomplete and especially the volume of offshore ignimbrites is unconstrained. However, reliable estimates of volumes and reoccurrence rates of large-scale eruptions are crucial for improving statistical models used to assess volcanic hazards (Self and Gertisser, 2015). Future research should systematically explore and integrate all eruption archives, from reconstructing caldera volumes to mapping onshore deposits, as well as proximal and distal marine deposits. Chapter 8 has outlined a multidisciplinary approach that should now be adopted for other large eruptions to better tie down the global eruption risk (Self and Gertisser, 2015).

While it is important to continue to increase our knowledge of the evolutionary history of volcanic systems, the next step must also focus on translating this knowledge into concrete recommendations for hazard mitigation strategies. In a region such as the southern Aegean, which is threatened by a whole range of geohazards, the development, and deployment of monitoring and early warning systems are essential to prevent the next major event from becoming a disaster. This is particularly important for Santorini, which receives around 70,000 people per day during peak tourist seasons on an area of just 76 km^2 (Fig. 12.7) (Sarantakou and Terkenli, 2021).

Large-scale volcano-tectonic interactions shaped the CSK volcanic system during its evolution (Chapters 4-7) and these interactions continue to exert an important influence on Santorini, as demonstrated during the period of magmatic inflation at Santorini in 2011-12 when stress changes caused by magma intrusion beneath the Santorini Caldera triggered earthquakes at the margin of the Cretan Basin (Feuillet, 2013; Kiratzi, 2013). In addition, regional tectonics also have a major influence on the stability of the southwestern flank of Santorini, which is affected by deep-seated deformation, as is known from other volcanoes worldwide (e.g. Mt Etna, Kilauea, and Piton de Fournaise) (Urlaub et al., 2018; Poland et al., 2017) as shown in Chapter 9. Large-scale earthquakes (Mw > 7), such as those that occurred in the recent past in the Santorini-Amorgos Tectonic Zone (e.g. Okal et al., 2009), could reactivate these instabilities and trigger disaster cascades, the effects of which are difficult to estimate so far. For this reason, special attention should be paid to shoreline crossing monitoring strategies, in particular on the southwestern and northeastern flanks of Santorini.

FIGURE 12.7: There are few places in the world where the proximity of tourist hot spots and volcanic centers is as evident as on Santorini. This photo shows of a church and a hotel terrace in front of the Kameni lava shield (Photo: J. Preine).

Furthermore, emphasis should be placed on the monitoring of the Kolumbo Volcano. Chapter 10 has shown how a disaster cascade led to the explosive eruption of Kolumbo and the generation of a destructive tsunami, the nucleus of which was the flank movement of Kolumbo. The flanks of Kolumbo are made of unstable material and in the future, another slide on its flanks might occur. The bottom waters within Kolumbo's crater are currently highly acidic (Carey et al., 2013) and frequent swarms of microseismicity indicate ongoing melt ascent from a reservoir that is located at 2.1-4.0 km depth below sea level (Schmid et al., 2022; Chrapkiewicz et al., 2022). Future slope failures could potentially trigger a limnic eruption releasing large amounts of CO_2 and other toxic gases like SO_2. Since flank deformation has been a key element in other historical tsunamigenic events on volcanic islands such as Ritter Island or Anak Krakatau (Karstens et al., 2019; Walter et al., 2019), a focus of future research should be the continuous monitoring of Kolumbo's flanks. This requires technological innovations that are also urgently needed at other submarine volcanoes around the world, such as Kick'em Jenny (Lesser Antilles) or the Myohinsho submarine volcano in Japan, both of which have also been affected by slope failures in the past (Fiske et al., 1998; Allen et al., 2018). A promising project underway in this regard is the SANTORY (SANTORini's seafloor volcanic observatorY) observatory, which will monitor the activity of the Kolumbo Volcano by establishing a long-term observatory that will be integrated into a hazard monitoring platform aimed at identifying precursors for potentially explosive volcanic eruptions, earthquakes, landslides, and hydrothermal emissions of toxic elements into the water (Nomikou et al., 2022). This will involve developing a monitoring protocol and advising policymakers on scenario planning and hazard mitigation strategies (Nomikou et al., 2022).

Such projects, which seek to bridge the gap between science, local stakeholders, and

policymakers, are urgently needed to pave the way toward global mitigation of the effects of volcanic eruptions. In the next century, the likelihood of a catastrophic volcanic eruption to occur is hundreds of times greater than the probability of an asteroid or comet impact (Trilling et al., 2017; Cassidy and Mani, 2022). Hundreds of millions of dollars are spent annually on planetary defense, yet there is no coordinated approach to assessing and mitigating the global risk of eruptions (Cassidy and Mani, 2022). This must change.

Acknowledgements

This thesis has been written with the support of many wonderful people, without whom I would never have been able to complete it. Although my doctoral project began a month before the Corona pandemic and has largely taken place from my home office, I have been fortunate to have had support, advice and mentorship from many inspiring people (online and offline) over the past three years, for which I am very grateful.

First of all, I would like to thank **Christian Hübscher** wholeheartedly for your trust, your supervision, your foresight, your support at all levels, and for the great moments on land and at sea. Christian, you ignited my fascination for research, and for that, I will always be grateful. From the first day onboard RV Alkor during the student cruise in my fourth bachelor semester, I knew I wanted to become a marine geophysicist and you gave me that opportunity. After more than twelve seagoing expeditions, I can't say I've had nearly enough. The seven years I spent in your working group were formative on many levels and you showed me how important it is to never lose curiosity. You introduced me to the treasure trove of data from RV Poseidon cruise POS338 (I will never get tired of these profiles) and offered me the opportunity to work on them during my PhD project. During that time, you taught me to always have the big picture in mind, to question existing knowledge, but also how important it is to bring projects to the finishing line. Thank you for the opportunities to participate in several scientific conferences and for an amazing field trip to Iceland. In a few days, we will set off together for IODP Expedition 398 to test fundamental concepts of this thesis, which is scientifically the most exciting project of my career. I am grateful for the opportunity to have contributed to the proposal, and for your support and encouragement to apply to become a participant. I already look forward to the next two years evaluating the new data from this expedition.

I want to thank **Paraskevi Nomikou** for being my co-supervisor during my PhD. Evi, I am very grateful that you introduced me to the fascinating world of the southern Aegean, and for the different projects, we worked on together. I will never forget the anxious hours together at sea off Samos when we weathered storms and other adversities together and were rewarded with great data (and great Greek food) in the end. Your enthusiasm for science and for Santorini is contagious. Thank you also for making the excursion to Santorini and Christiana happen earlier this year, which was absolutely stunning. I look forward to learning more about the CSK volcanic field together on the Joides Resolution.

My special thanks go to **Jens Karstens**. This work is largely based on the data we collected on RV Poseidon cruise POS538, which you led as PI. I am extremely grateful for the opportunity to work with this fascinating data and for the opportunity to work together on the interpretation of this dataset. Without the countless hours we spent on the phone or on Zoom discussing new ideas, my thesis would have taken a different course. You have always pushed me to think outside the box and question existing knowledge, and this had a significant impact on my approach to science. In the three years, there were also times of conflict, but we were always able to overcome these, and I am very grateful for that. When others were already satisfied with the results, you always tried to go one step further, include more data, and involve other disciplines. This process certainly took time, but it was absolutely worth it. That impressed me very much. I would also like to thank you for proofreading this

help.

Furthermore, I want to thank **Katharina Pank, Steffen Kutterolf, Ralf Gertisser** and **Carole Berthod** for an amazing week of fieldwork on Santorini and Christiana, where I learned an awful lot. I am looking forward to working more together during and after IODP Expedition 398.

I would like to express my sincere thanks to my working group, with whom I spent a fantastic time in the office as soon as the Corona situation allowed it again. Whether at sea, having coffee together, playing darts, or having a beer at the end of the day, you made the time at the office worthwhile for me. So thanks to **Arne, Bene, Carina, Charly, Elli, Karo, Ingra, Laura, Matthias, Tobias** and, **Wiebke**.

I would like to thank the other participants of cruise POS538: **Judith Elger, Michel Kühn, Giacomo Dalla Valle, Thies Bartels** and **Gero Wetzel**. Further, I would like to thank the captains, crews, and scientific parties of RV Poseidon POS338 and RV Aegeo THERA expeditions.

Many days of this thesis I spent in the home office and that I didn't go crazy, I owe to **Charlotte**. You supported me a lot during this time and helped me to get back on track when things weren't going so well, or when there were conflicts on a personal level. The last few months before submitting this thesis were very intense and you always supported me in every way during this time and also helped a lot with proofreading. I'm deeply grateful for that.

Last but not least, I want to thank my family and my friends for their love and support throughout the last three years, which have been a very demanding but also very fulfilling time.

Appendix A

Appendix for Chapter 4

A.1 Acquisition and Processing Parameters of Reflection Seismic Data

In this study, we utilize an extensive dataset of seismic profiles comprising single-channel seismic (SCS) data acquired in 2006 (Sigurdsson et al., 2006), multichannel data acquired during cruise POS338 in 2006 (Hübscher et al., 2006), and recently acquired high-resolution multichannel seismic data from cruise POS538 (Figure 4.1) (Karstens et al., 2020b). While the entire dataset was used to establish the stratigraphic framework, our study is focused on the data acquired in 2019 (Figure 4.2A-F, 4.3A) and 2006 (Figure 4.2G). Figures 4.2A and 4.3A show a seismic line that connects seismic profiles 5007, 5009, 3004, 1006, 1007, and 3001 (Karstens et al., 2020b). Figure 4.2F shows seismic line 5004 (Karstens et al., 2020b) and Figure 4.2G seismic line HH06-26 (Hübscher et al., 2006).

For the acquisition of the 2019 multichannel reflection seismic data, a GI-Pulser was used and operated in harmonic mode with a primary (Generator) and a secondary (Injector) volume of 45 in3. The shot distance approximates to 6.2 m given a shot interval of 4 s and a ship speed of 4.5 kn. Seismic energy was recorded by multiple concatenated Geometrics GeoEel streamer segments, resulting in active streamer sections ranging from 190 m to 250 m length. Given a channel spacing of 1.56 m and the comparably small shot interval, a very dense CMP spacing of 1.56 m was achieved, ensuring a high lateral resolution. With a main frequency of 125 Hz, the vertical resolution can be approximated to approx. 3-6 m (using the $\lambda/4$- or $\lambda/2$-approximation) at the seafloor (v=1500 m/s) to 5-10 m in the deeper sedimentary strata (v=2400 m/s).

Processing comprised trace-editing, simple frequency filtering (15-1500 Hz), and multiple suppression by means of surface-related multiple elimination (SRME). This was followed by spherical divergence correction, time-variant frequency filtering, pre-stack time migration, top-muting, and white-noise removal.

The 2006 data were acquired by means of a GI-Pulser operated in true GI mode with a primary volume of 45 in3 and a secondary volume of 105 in3 and a 600 m analog streamer with 24 channels. We achieved a CMP-spacing of 12.5 m with an average fold of 24. These data have a main frequency of 60 Hz indicating a vertical resolution of approx. 6-12 m close to the seafloor (v=1500 m/s) or 10-20 m within the deeper sedimentary strata (v=2400 m/s). PProcessing of this data set comprised trace-editing, simple frequency filtering (10-500 Hz), suppression of a receiver-ghost by means of predictive deconvolution, suppression of surface-related multiples by means of SRME as well as pre-stack time migration followed by top-muting and white-noise removal. More details regarding the processing of these data have been provided by Preine et al. (2020). General information about the seismic method and

processing can be found, e.g. Hübscher and Gohl (2016).

All processed seismic lines were combined into a single interpretation project using the Kingdom software. Here, we established the stratigraphic framework and created the figures that are shown in this study.
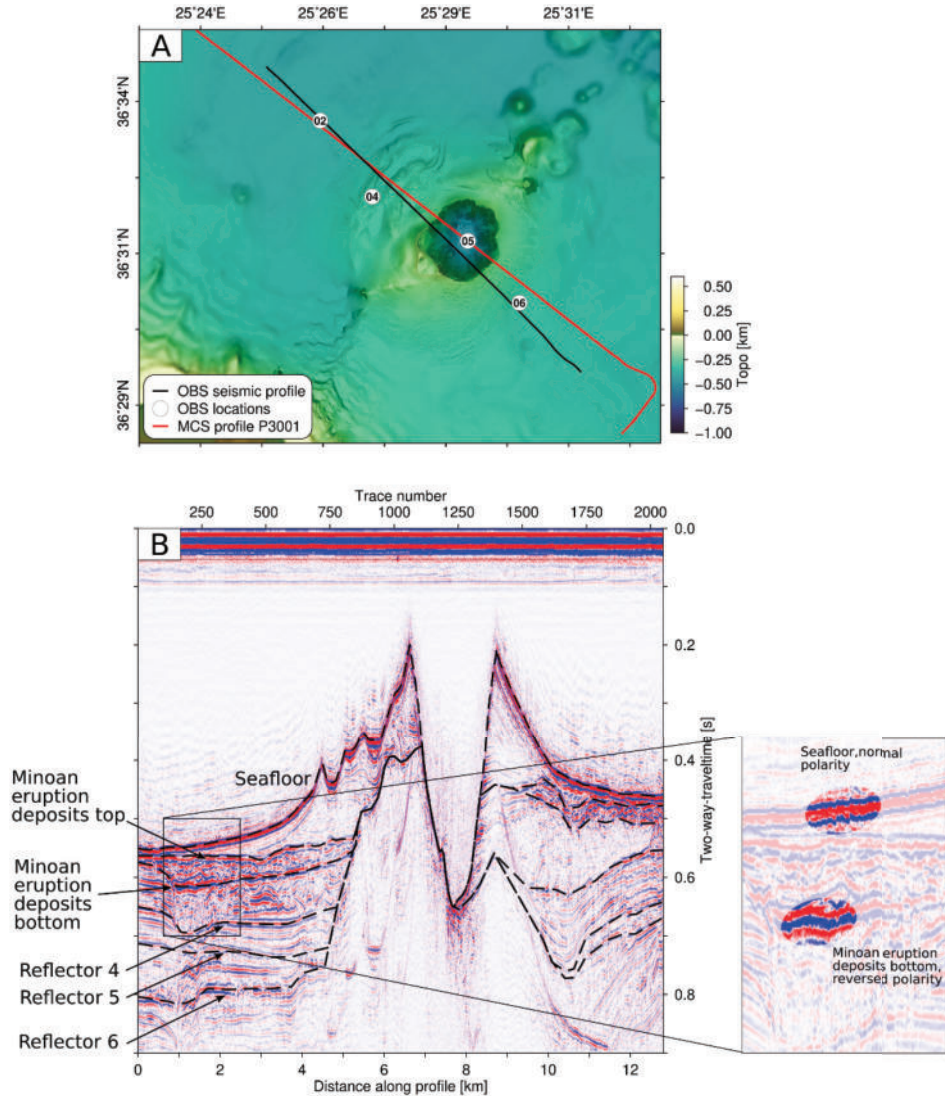
FIGURE A.1: A) Bathymetry of the Kolumbo region with the location of the 2D velocity model (profile P41, solid black line) constructed from OBS data. Numbered, white circles represent OBS locations. The red, solid lines represent multi-channel seismic line P3001, which was used to tie the identified seismoacoustic units into the larger regional stratigraphic framework. B) MCS data section along profile P41, extracted from the 3D seismic cube. Dashed black lines show the geometry of reflectors incorporated in the initial P-wave velocity model. As a requirement of the RAYINVR software (Zelt and Smith, 1992) the reflectors are continuous throughout the model and pinch out underneath the volcano, where the sedimentary deposits from outside Kolumbo are absent. LBA = Late Bronze AgeMinoan eruption deposits, as described in Hübscher et al. (2015).

A.2 Velocity Estimation

Construction of a 2D P-wave velocity model for sediment deposits in the Kolumbo region Six Ocean Bottom Seismometers (OBS) were deployed during RV Poseidon cruise POS538 around the Kolumbo Volcano and in the Anhydros Basin to constrain subsurface P-wave velocities (Vp) (Karstens et al., 2020b). We constructed a 2D Vp-model (profile P41 hereafter) that strikes in NNE to SSW direction and crosses the Kolumbo crater (Figure A.1A). Profile P41 is subparallel with the 2D MCS line P3001 (Y-Z; Figure 4.2A and 4.3A) and locates within the extent of the 3D seismic cube acquired during cruise POS538 (Figure A.1A).

We use the reflected and refracted phase observations from four OBS (stations 02, 04, 05, 06) for forward velocity modeling. At first, we used all available a priori information to establish an initial 2D Vp-model along profile P41. The shallow part of the initial velocity model was constructed by incorporating the geometry of six prominent reflectors identified in a 2D MCS data section along profile P41, which was extracted from a processed and time-migrated 3D seismic cube crossing the Kolumbo Volcano (Figure A.1B) (Karstens et al., 2020b). The six reflectors are indicated by dashed black lines in Figure A.1B and correspond to the units of the stratigraphic framework presented in this manuscript. Noteworthy is the strong reflector marking the top and bottom of the Late Bronze AgeMinoan eruption of Santorini (LBA) (Druitt, 2014). The LBA Minoan bottom reflector shows a negative polarity in comparison to the seafloor reflector, which is indicative of a negative impedance contrast at this layer boundary, Figure A.1B. Based on the reflectors, six layers were defined which are summarized in Table A.1. To establish the initial velocity model, the reflectors were converted from two-way travel time into depth with a velocity of 1.52 km/s, resembling the average identified water velocity in this area (Karstens et al., 2020b).

TABLE A.1: Velocities and lithological relation of the uppermost layers in the final velocity model.

Layer number	Vp top [km/s]	Vp bottom [km/s]	Comment/Stratigraphy	Stratigraphic Unit
1	1.52	1.52	Water	
2	1.68	1.68	Deposits of the 1650 Kolumbo eruption	K5 (within U6)
3	1.78	1.78	Minoan deposits	U6
4	1.72	1.72	Deposits from an older Kolumbo eruption	K4 (within U6)
5	1.9	1.9	Well-stratified deposits	U5
6	1.92	2.0	Stratified, partially chaotic deposits	U4
7	2.2	2.70	Lower boundary is defined by Vp=2.7 km/s contour of the 3D vp-model from Hooft et al. (2019)	U3, U2, U1

The lower part of the initial velocity model (where Vp is larger than 2.7 km/s) was

adapted from the regional 3D Vp model of Hooft et al. (2019). It should be noted that the refraction seismic survey of Hooft et al. (2019) – project PROTEUS – included only one receiving OBS in the vicinity of profile P41 which impedes a sparse ray coverage in the shallow subsurface in this region. Accordingly, the shallow part of the Hooft et al. (2019) 3D model is not well-constrained in the region of our profile P41. The initial velocity model was then used as starting model for iterative forward modeling with ray-tracing, utilizing the methods of Zelt and Ellis (1988) and Zelt and Smith (1992). The layer velocities and interface depths in the initial 2D Vp-model were iteratively updated to minimize the misfit of theoretical and observed travel times. We started this procedure with the uppermost sedimentary layer and proceeded layer-by-layer downwards. In our approach, we used constant layer velocities for the five uppermost layers, listed in Table A.1. These velocities are in good agreement with the diffraction-based velocity model presented by Preine et al. (2020) for the Santorini-Anafi basin further NE of the study area.
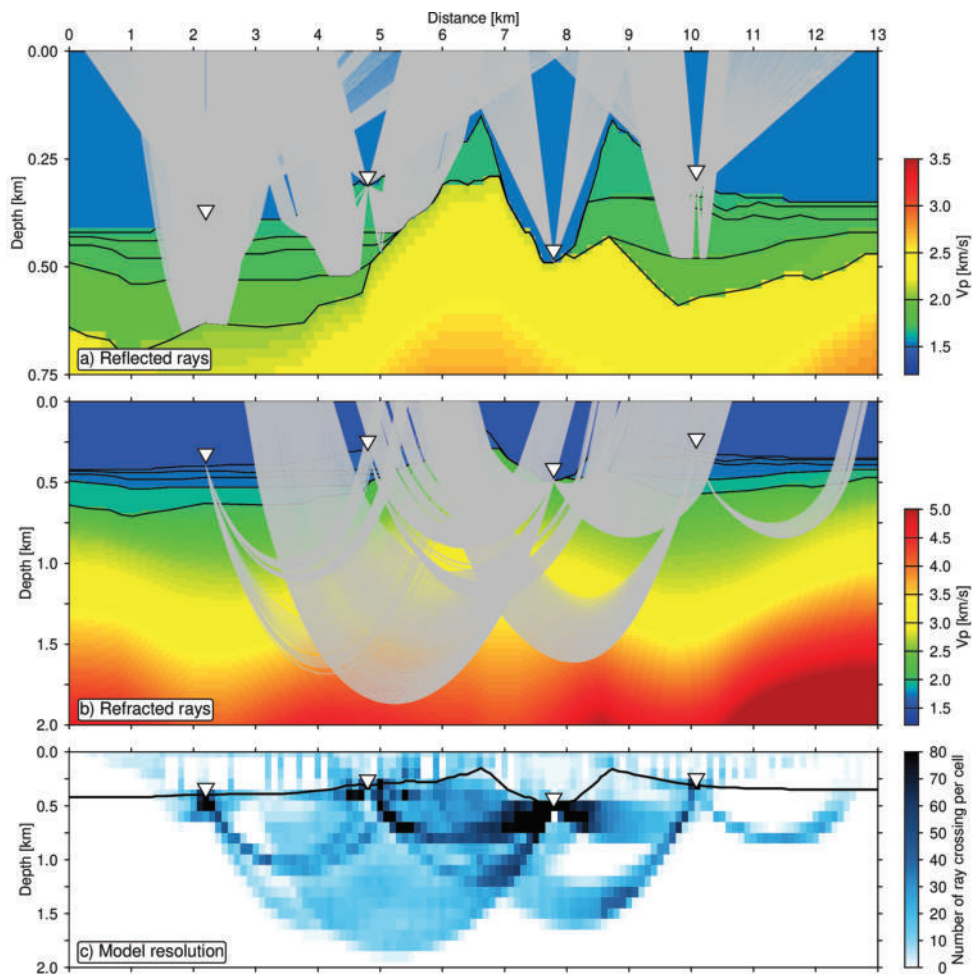
FIGURE A.2: A) Final velocity model with reflected rays superposed. B) Final velocity model with refracted rays superposed. C) Resolution plot with the number of ray-crossings per cell of 0.1×0.1 km size. Inverted triangles in all panels indicate OBS locations.

The final velocity model includes 6684 travel-time picks, which are associated with

incertainties between 0.005 and 0.017 s. The average misfit of theoretical and observed travel-times in the final model is 0.014 s and the Chi squared value is 1.84. Figure A.2 shows the final velocity model together with reflected rays (panel a) and refracted rays (panel b) used in the forward modeling. The resolution (panel c) is best in the central part of the model. Figure A.3 shows a seismic shot-gather for station 02 together with the theoretical and observed reflected arrivals from sedimentary layers.
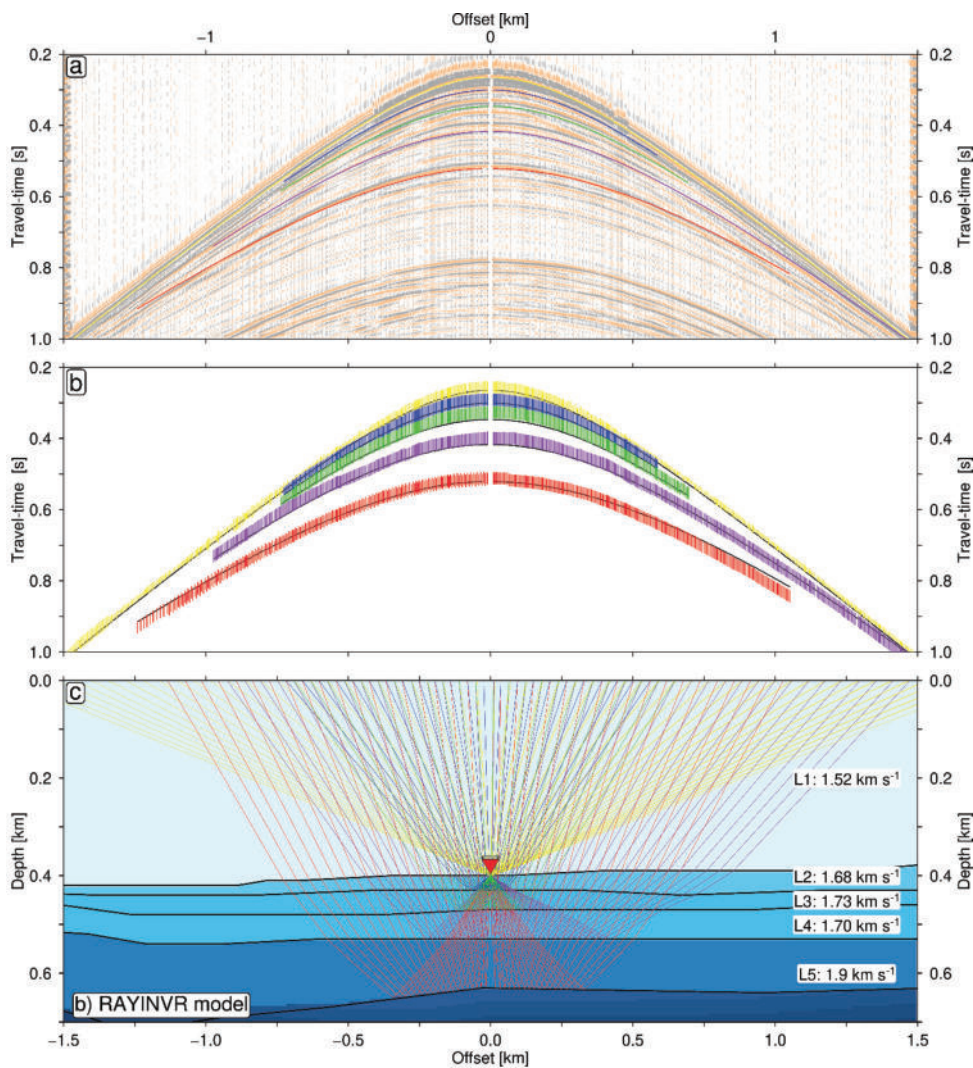
FIGURE A.3: A) Shot gather of the hydrophone channel from OBS02 deployed 4.5 km to the northeast of the Kolumbo crater. Colored lines show theoretical phase arrivals from the layered model in panel c. B) Vertical colored bars show picked phase arrivals and black lines show theoretical arrivals from the layered model in panel c. C) Final Vp-model of the subsurface around OBS02 (red triangle). Rays are indicated by colored lines (corresponding to colors in panels A, B). Layer velocities are indicated near the right boundary of the panel.

A.3   Thickness and Age Estimation

We approximate the ages of the identified unconformities uch1-6 and the identified volcanic deposits by first estimating the thicknesses of the stratigraphic units U1-U6 and then dividing these thicknesses by an approximate sedimentation rate known from the CSKVF. This approach has been used by previous authors in the Southern Aegean Sea to approximate ages (Piper and Perissoratis, 2003; Anastasakis and Piper, 2005; Piper et al., 2007).

Piper and Perissoratis (2003) presented a large collection of sediment cores from the southern Aegean Sea and estimated a mean sedimentation rate of 10 cm/ka for the area. They further argued that, away from the volcanic centers, sedimentation rates have remained reasonably uniform in the Quaternary in the Aegean Sea. Close to the volcanic centers, however, they observed higher sedimentation rates (> 20 cm/ka). This is in agreement with our observations from the seismic data across the CSKVF. Our data clearly show that especially close to Santorini, there are significant thickness variations of the uppermost unit U6, which we interpret as the deposits from the Thera Pyroclastic Formation deposited since ∼0.35 Ma. As illustrated in Figure 4.3A, this unit has a thickness of over 350 m north of the caldera, where it represents a wedge of alternating low-amplitude, chaotic, and wavy reflections that resemble the stratified flanks of the caldera cliffs of the Santorini Caldera (Figure 4.2C). In contrast to that, U6 has a thickness of only ∼40 m towards the Christiana basin while being less chaotic and more stratified. This thickness remains approx. constant away from Santorini across the Christiana basin indicating that the influence of pyroclastic deposits is small here and suggesting a rather constant sedimentation rate (Figure 4.3A). The underlying unit U5 represents a well-stratified unit with a constant thickness across the whole working area, which is not thickening towards Santorini (Figure 4.3A). Unit U4 is interpreted as a large mass-transport or pyroclastic deposit derived from present-day Santorini and is significantly varying in thickness (Figure 4.3A). The thickness of unit U3 is influenced by the presence of the Poseidon deposit and the lowermost units from Kolumbo (K1 and K2) as well as the smaller Kolumbo MTD (Figure 4.3A). Apart from these volcanic units, unit U3 comprises well-stratified reflections, which generally have a constant thickness. Unit U2 is thickening towards Christiana but has a rather constant thickness away from Christiana (Figure 4.3A). The lowermost unit U1 is hardly discernable in the Anhydros basin but represents a major unit in the Christiana basin. This shows that approximating ages using sedimentation rates is challenging in this environment and must exclude volcanoclastic formations, mass-transport deposits, and thickening strata.

Figures A.4 A and B show seismic profiles from the Christiana and Anhydros basins with five sites P1-P5 for which we estimated the thickness of each stratigraphic unit. MTDs and volcaniclastic units are highlighted by semi-transparent areas. The estimated TWT thicknesses of P1-P5 are shown in Figure A.5 and Table A.2. We indicated in Table A.2, whether divergence (DIV) was observed within a unit at one of our sample sites and neglected those values for the thickness and age calculation. In addition, we estimated the thicknesses of the Poseidon deposit in the Christiana basin and the Kolumbo MTD in the Anhydros basin as well as their difference to the overlying unconformity h4 (Poseidon/Kolumbo MTD) in order to approximate the ages of these volcanic deposits.
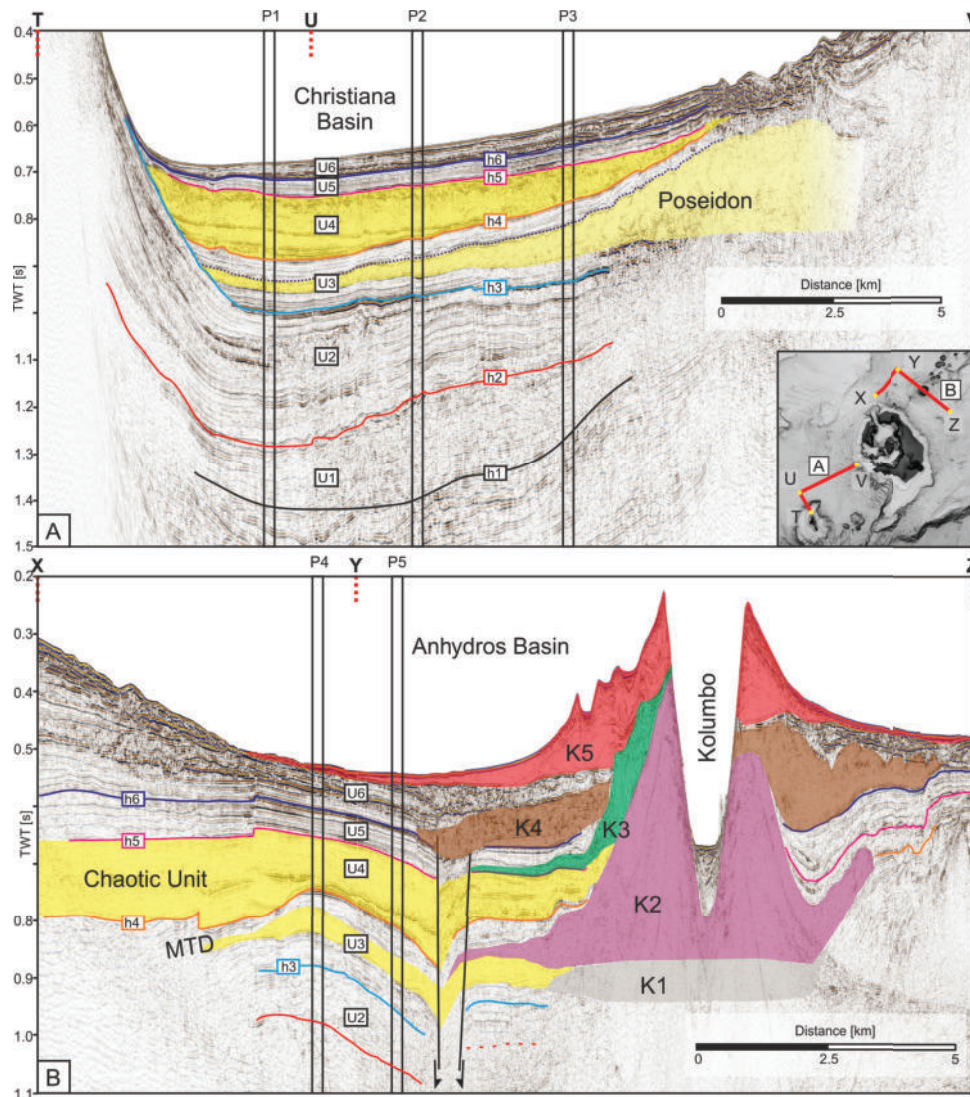
FIGURE A.4: Seismic profile across the Christiana Basin (A) and
the Anhydros Basin (B) with sample points for thickness estima-
tion. Semi-transparent units indicate volcanic and mass-transport de-
posits. For location, see inlet map.

Table A.3 shows the mean TWT-thicknesses for the main units, their estimated inter-
val velocities (see the previous section) as well as the estimated thicknesses in me-
ters. The age of the base of each of these units is estimated by dividing the estimated
thicknesses by the approx. sedimentation rate of 0.10 cm/ka (Piper and Perissoratis,
2003).
Even though we neglect MTDs and volcanoclastic formations, the assumption of
a constant sedimentation rate introduces considerable uncertainty to the age esti-
mates, which increases with depth. While our estimates are in agreement with pre-
vious authors Piper et al. (2007) and Hübscher et al. (2015), they remain yet to be
verified by scientific drilling. So far, only one scientific drilling campaign has been
conducted in the vicinity of our working area: DSDP hole 378 in the Cretan Basin
several kilometers southwest of Christiana (Hsu et al., 1978). Based on an old vin-
tage seismic profile, Hsu et al. (1978) define an uppermost unit as "ponded facies"

with numerous horizontal reflectors, which they correlate with hemipelagic nan-
nofossil marls and oozes of Quaternary age with some intercalated tephra layers.
Below that, they identified a "transparent facies", which was correlated to nanno-
fossil marlstones of Pliocene age. These units overlay a unit consisting of gypsum
related to the Messinian salinity crisis. The description of the "ponded facies" fits
our observations of the well-stratified units U2-U6 from the CSKVF, while the "trans-
parent facies" fits our observation of the lowermost weakly reflective unit U1 from
the CSKVF. The ages would fit well since we date the uppermost units U2-U6 to ap-
prox. 0-3.4 Ma implying a mostly Pleistocene Age and unit U1 to approx. 3.4 - 5.3
Ma, which corresponds to a Pliocene Age. Since we have no direct ties to the DSDP
drill site, this comparison remains speculative but shows that our age approxima-
tions generally fit with the regional geological constraints.
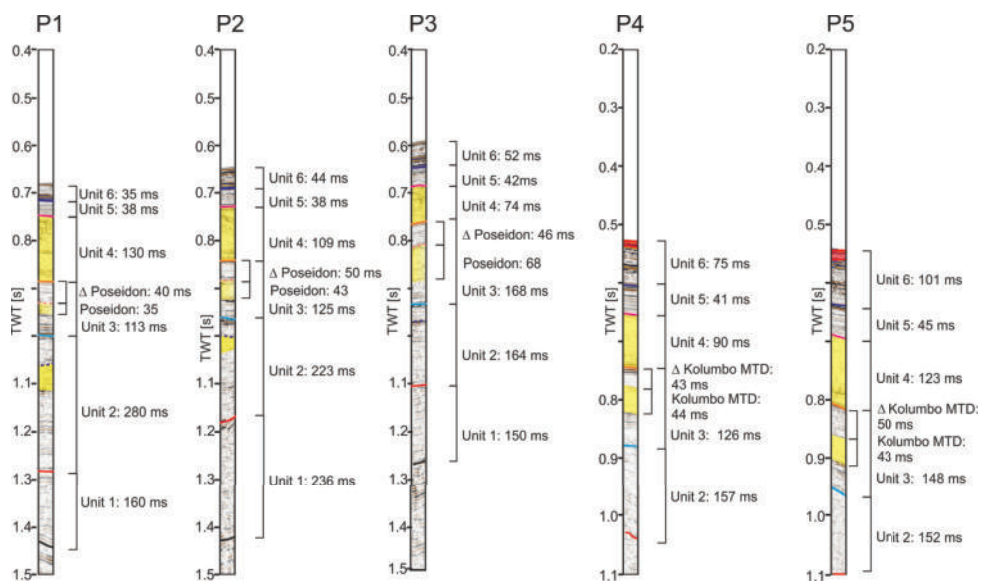
FIGURE A.5: TWT Thicknesses of the five sample points shown in
Figure A.4.

TABLE A.2: TWT-Thicknesses of the main stratigraphic units as well as volcanic units measured at the sites P1-P5. For location, see Figure A.4.

Units Christiana	P1 [ms]	P2 [ms]	P3 [ms]	Units Anhydros	P4 [ms]	P5 [ms]
Unit 6	35	44	52 (DIV)	Unit 6	75 (DIV)	101 (DIV)
Unit 5	38	38	42	Unit 5	41	45
Unit 4	130	109	74	Unit 4	90	123
Unit 3	113	125	168 (DIV)	Unit 3	126	148 (DIV)
Poseidon	35	43	68	Kolumbo MTD	44	43
Δ Poseidon	40	50	46	Δ Kolumbo MTD	43	50
Unit 3 - Poseidon	78	82	100 (DIV)	Unit 3 - Kolumbo MTD	82	103 (DIV)
Unit 2	280 (DIV)	233 (DIV)	164	Unit 2	157	152
Unit 1	160	236 (DIV)	150	Unit 1	-	-

TABLE A.3: Median TWT-Thicknesses of the main stratigraphic units and volcanic units, their interval velocities, estimated thicknesses and approximate ages.

Units	Tickness [TWT]	Velocity [km/s]	Thickness [m]	Age at Base [Ma]
Unit 6	40	1.72 - 1.78	35 ± 1	0.35
Unit 5	41	1.90	39 ± 1	0.7
Pre-Poseidon	45	2.0 - 2.2	48 ± 3	1.2
Pre-Kolumbo	43	2.0 - 2.2	45 ± 2	1.2
Unit 3	81	2.0 - 2.2	85 ± 4	1.6
Unit 2	160	2.2 - 2.4	181 ± 8	3.4
Unit 1	155	2.4 - 2.7	198 ± 12	5.4

Appendix B

Appendix for Chapter 5

The seismic data used in this study are from three cruises between 2006 and 2019 (Sigurdsson et al., 2006; Hübscher et al., 2006; Karstens et al., 2020b). Single-channel seismic data were acquired in 2006 during the THERA project on RV Aegaeo. As the seismic source, a G-pulser was used with a volume of 10 in3. The general processing comprised simple bandpass filtering (15-500 Hz), de-spiking, predictive deconvolution for the suppression of a strong bubble signal, and spherical divergence correction. In order to migrate the data, we binned the shot points into a regular spacing of 10 m. After migration, we applied a top-mute and white-noise removal. The vertical resolution of these data can be approximated to 8-15 m (using the $\lambda/4$- or $\lambda/2$-approximation) within Unit 4 (v=1900 m/s). For the cruise POS338 with RV Poseidon, a GI-pulser was used and operated in true GI mode with a primary (Generator) volume of 45 in3 and a secondary (Injector) volume of 105 in3. Using a 600 m analog streamer with 24 Channels, we defined a CMP-spacing of 12.5 m. Processing of these data comprised trace-editing, simple frequency filtering (10-500 Hz), suppression of a receiver-ghost signal by predictive deconvolution, surface-related multiple elimination as well as spherical divergence correction, pre-stack time migration followed by top-muting and white-noise removal. These data have a main frequency of 60 Hz indicating a vertical resolution of approx. 8-15 m within Unit 4. During the most recent cruise POS538 in 2019, we acquired seismic data with a much higher lateral resolution (CMP spacing of 1.56 m). As a seismic source, we used a GI-pulser that was operated in harmonic mode with primary and secondary volumes of 45 in3. Seismic energy was recorded by multiple concatenated Geometrics GeoEel streamer segments, resulting in active streamer sections ranging from 190 m to 250 m in length. Processing comprised trace-editing, simple frequency filtering (15-1500 Hz), and multiple suppression by means of surface-related multiple elimination (SRME). This was followed by spherical divergence correction, time-variant frequency filtering, pre-stack time migration, top-muting, and white-noise removal. With a main frequency of 125 Hz, the vertical resolution can be approximated to approx. 4-8 m within Unit 4.

Appendix C

Appendix for Chapter 6

Here we present supporting information for the paper titled "Volcano-Tectonic Evolution of the Christiana-Santorini-Kolumbo Rift Zone". Contained in this file is a description of the processing of the used multi-channel data (Text S1), an uninterpreted version of the seismic profiles shown in Figure 6.2 (Figure C.1), a table describing approximate interval velocities used for depth approximations, and a table comparing different seismo-stratigraphic classifications for the Christiana-Santorini-Kolumbo rift zone. Figure C.2 shows a seismic profile crossing the low-stand deposits indicated in Figure 6.5.

Text S5-1

The seismic data used in this study are from three cruises between 2006 and 2019 (Sigurdsson et al., 2006; Hübscher et al., 2006; Karstens et al., 2020). Single-channel seismic data were acquired in 2006 during the THERA project on RV Aegaeo. As the seismic source, a G-pulser was used with a volume of 10 in^3. The general processing comprised simple bandpass filtering (15-500 Hz), de-spiking, predictive deconvolution for the suppression of a strong bubble signal, and spherical divergence correction. In order to migrate the data, we binned the shot points into a regular spacing of 10 m. After migration, we applied a top-mute and white-noise removal. The vertical resolution of these data can be approximated to 8-15 m (using the $\lambda/4$- or $\lambda/2$-approximation) within the shallow sediments (v=1900 m/s).

For the cruise POS338 with RV Poseidon, a GI-pulser was used and operated in true GI mode with a primary (Generator) volume of 45 in^3 and a secondary (Injector) volume of 105 in^3. Using a 600 m analog streamer with 24 Channels, we defined a CMP-spacing of 12.5 m. Processing of these data comprised trace-editing, simple frequency filtering (10-500 Hz), suppression of a receiver-ghost signal by predictive deconvolution, surface-related multiple elimination as well as spherical divergence correction, pre-stack time migration followed by top-muting and white-noise removal. These data have a main frequency of 60 Hz indicating a vertical resolution of approx. 8-15 m. During the most recent cruise POS538 in 2019, we acquired seismic data with a much higher lateral resolution (CMP spacing of 1.56 m). As a seismic source, we used a GI-pulser that was operated in harmonic mode with primary and secondary volumes of 45 in^3. Seismic energy was recorded by multiple concatenated Geometrics GeoEel streamer segments, resulting in active streamer sections ranging from 190 m to 250 m in length. Processing comprised trace-editing, simple frequency filtering (15-1500 Hz), and multiple suppression by means of surface-related multiple elimination (SRME). This was followed by spherical divergence correction, time-variant frequency filtering, pre-stack time migration, top-muting, and white-noise removal. With a main frequency of 125 Hz, the vertical resolution can be approximated to approx. 4-8 m.

FIGURE C.1: Uninterpreted version of the seismic profiles shown in Figure 6.2.

TABLE C.1: Interval velocities used for converting isochore maps to isochrone maps in Figure 6.3.

Seismostratigraphic Unit	Interval velocity from Preine et al. (2020)
Unit 1	2500 m/s
Unit 2	2400 m/s
Unit 3	2300 m/s
Unit 4	2200 m/s
Unit 5	2100 m/s
Unit 6	1850 m/s

TABLE C.2: Comparison of different seismostratigraphic classifications for the basins of the Christiana-Santorini-Kolumbo rift system.

	Preine et al. (2022a, 2022b) & this study	Hübscher et al. (2015)	Nomikou et al. (2016b)	Nomikou et al. (2018, 2019)	Tsampouraki-Kaounaki & Sakellariou (2018)	Piper et al. (2007)
Study Focus	Chrsitiana Basin, Anhydros Basin, Santorini-Anafi Basin	Anhydros Basin	Anhydros Basin	Anhydros Basin & Santorini-Anafi Basin	Christiana Basin	Christiana Basin, Anhydros Basin, Santorini-Anafi Basin
Seismo-stratigraphic Units	Unit 1	-	Ab1	Sab1/Ab1	Unit 5	-
	Unit 2	-	Ab2	Sab2/Ab2	Unit 4/2	-
	Unit 3	Sk1	Ab3	Sab3/Ab3	Unit 2	-
	Unit 4	Sk2	Ab4	Sab4/Ab4	Unit 1	-
	Unit 5	Sk3	Ab5	Ab5 & Sab4/Ab4	Unit 1	-
	Unit 6	Sk4	Ab6	Sab6/Ab6 & Sab5	Unit 1	-
Key reflectors / unconformities	h1	ab1	ab-0	Base Sab1/Ab1	Base Unit 5	-
	h2	ab2	ab-1	Base Sab2/Ab2	Base Unit 4	1
	h3	-	ab-2	Base Sab3/Ab3	-	C
	h4	ab7	ab-3	Base Sab4/Ab4	Base Unit 1	B
	h5	-	ab-4	-	-	-
	h6	ab10	ab-6	Base Sab5/Ab5	-	A

FIGURE C.2: Seismic profile crossing the Ios shelf north of Santorini. Towards Santorini, we identify a characteristic sequence of low-stand deposits.

Appendix D

Appendix for Chapter 7

Here we present supporting information for the paper titled "Spatio-temporal evolution of the Kolumbo Volcanic Chain and its link to the volcanic plumbing system of Santorini". Contained in this file is a description of the processing of the seismic reflection data (Text S1), and uninterpreted versions of the seismic profiles shown in Figures 7.2-7.6 (Figure D.1-D.5).

Text S6-1

The seismic data used in this study are from two cruises between from 2006 (Sigurdsson et al., 2006; Hübscher et al., 2006). Single-channel seismic data were acquired in 2006 during the THERA project on RV Aegaeo. As the seismic source, a G-pulser was used with a volume of 10 in^3. The general processing comprised simple band-pass filtering (15-500 Hz), de-spiking, and spherical divergence correction. In order to migrate the data, we binned the shot points into a regular spacing of 10 m. After migration, we applied a top-mute and white-noise removal. The vertical resolution of these data can be approximated to 8-15 m (using the $\lambda/4$- or $\lambda/2$-approximation) within the shallow sediments (v=1900 m/s).

For the cruise POS338 with RV Poseidon, a GI-pulser was used and operated in true GI mode with a primary (Generator) volume of 45 in^3 and a secondary (Injector) volume of 105 in^3. Using a 600 m analog streamer with 24 Channels, we defined a CMP-spacing of 12.5 m. Processing of these data comprised trace-editing, simple frequency filtering (10-500 Hz), suppression of a receiver-ghost signal by predictive deconvolution, surface-related multiple elimination as well as spherical divergence correction, pre-stack time migration followed by top-muting and white-noise removal. These data have a main frequency of 60 Hz indicating a vertical resolution of approx. 8-15 m.

FIGURE D.1: Uninterpreted version of the seismic profiles shown in Figure 7.2.
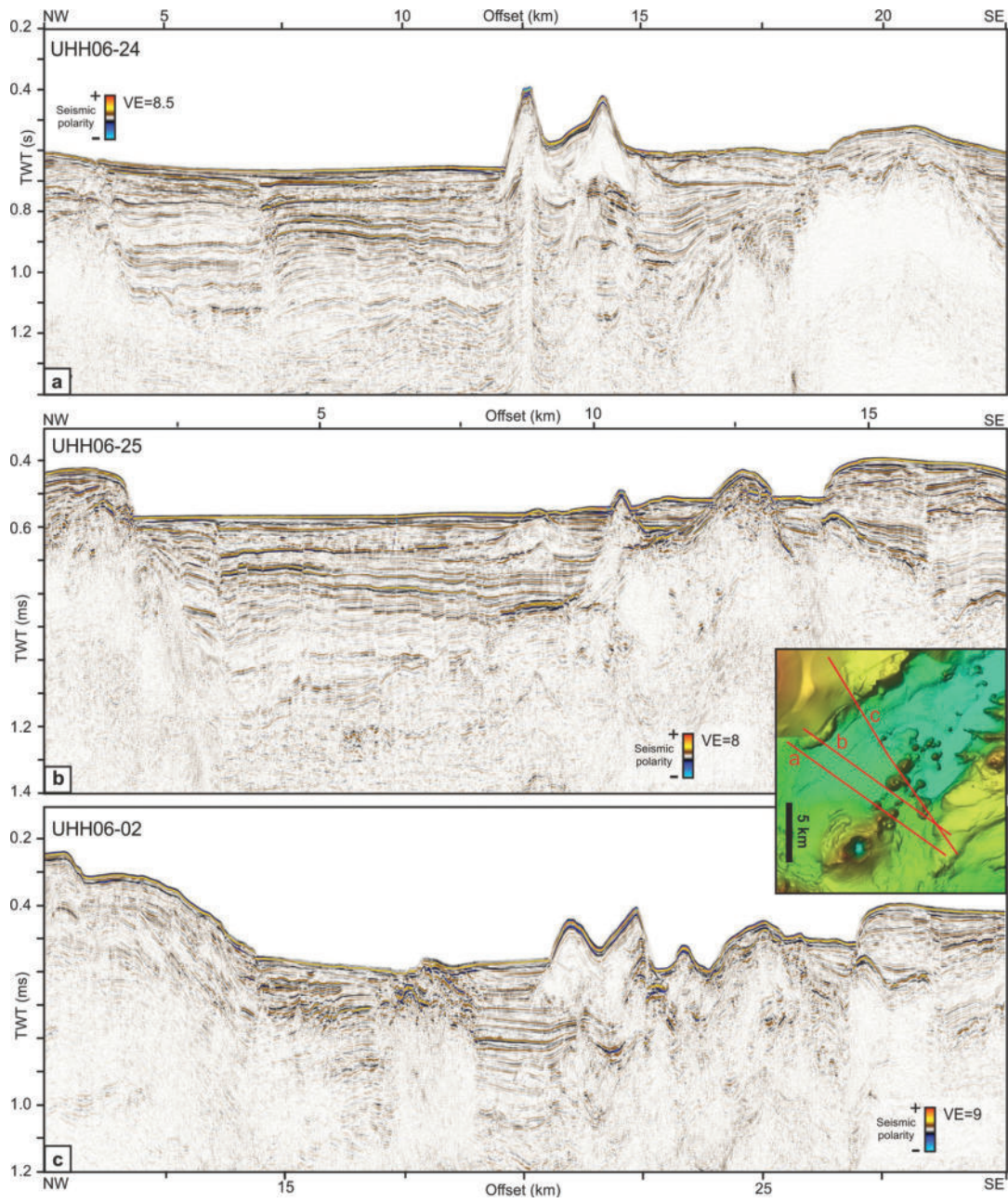
FIGURE D.2: Uninterpreted version of the seismic profiles shown in
Figure 7.3.
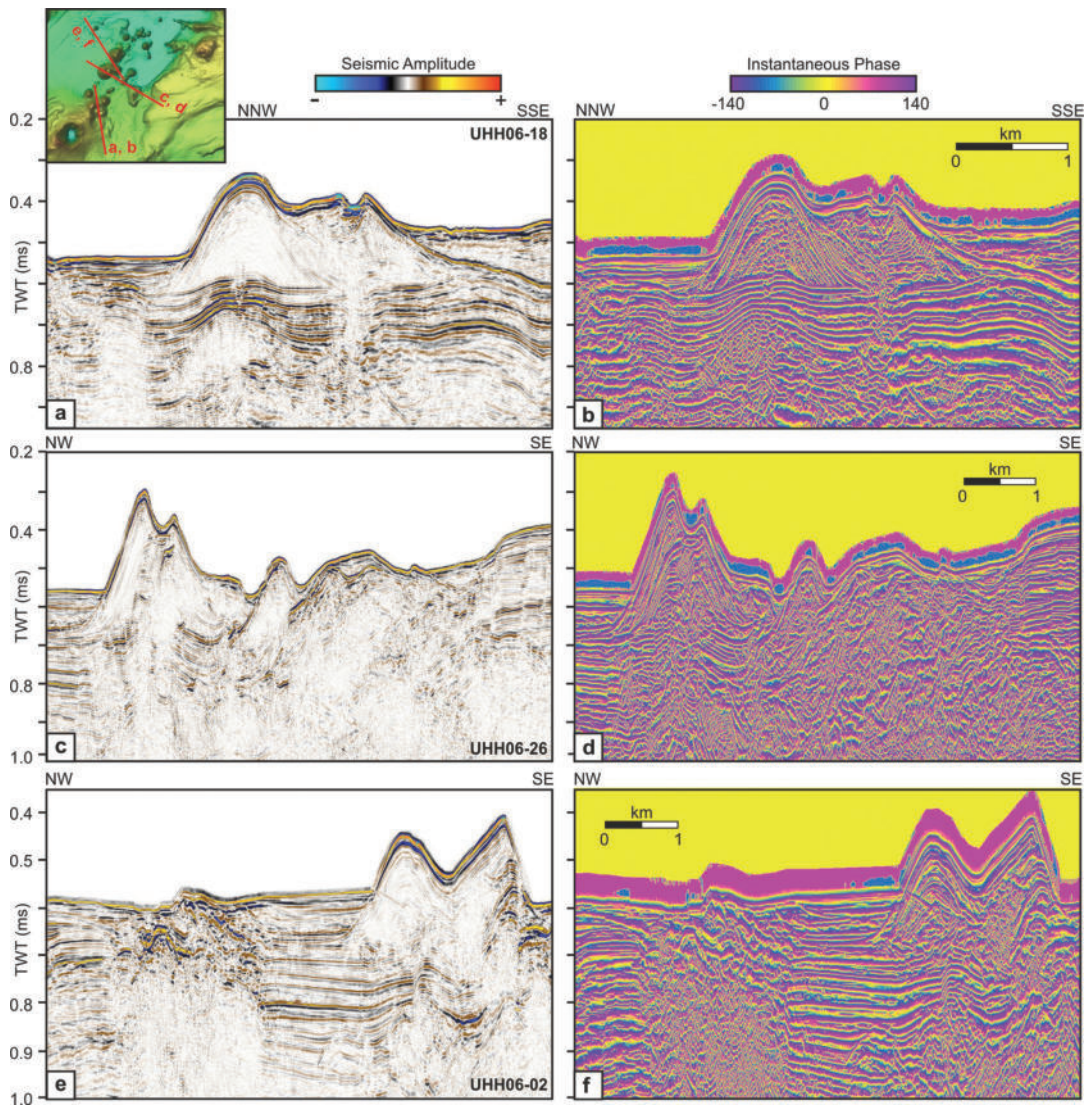
FIGURE D.3: Uninterpreted version of the seismic profiles shown in
Figure 7.4.
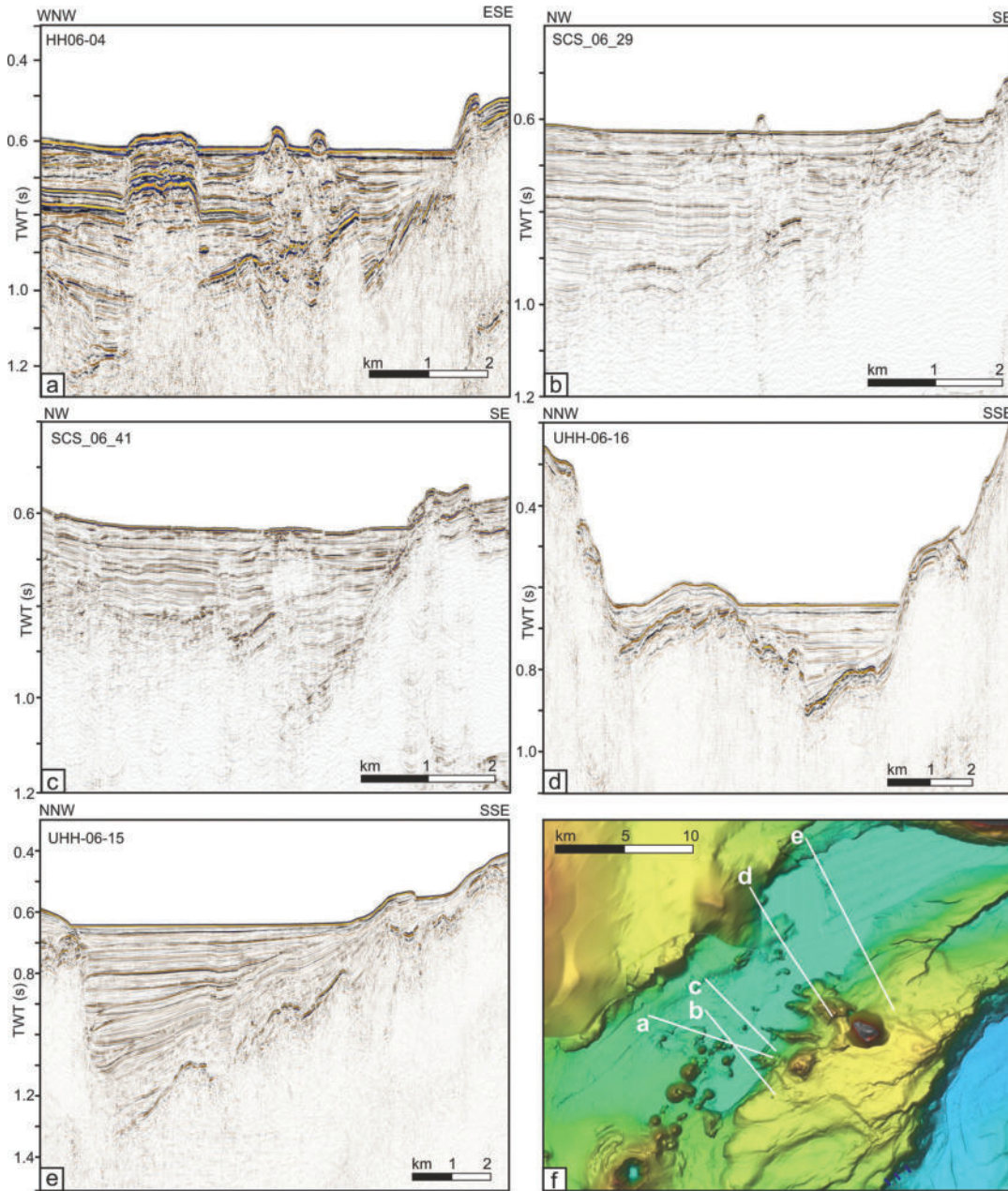
FIGURE D.4: Uninterpreted version of the seismic profiles shown in
Figure 7.5.
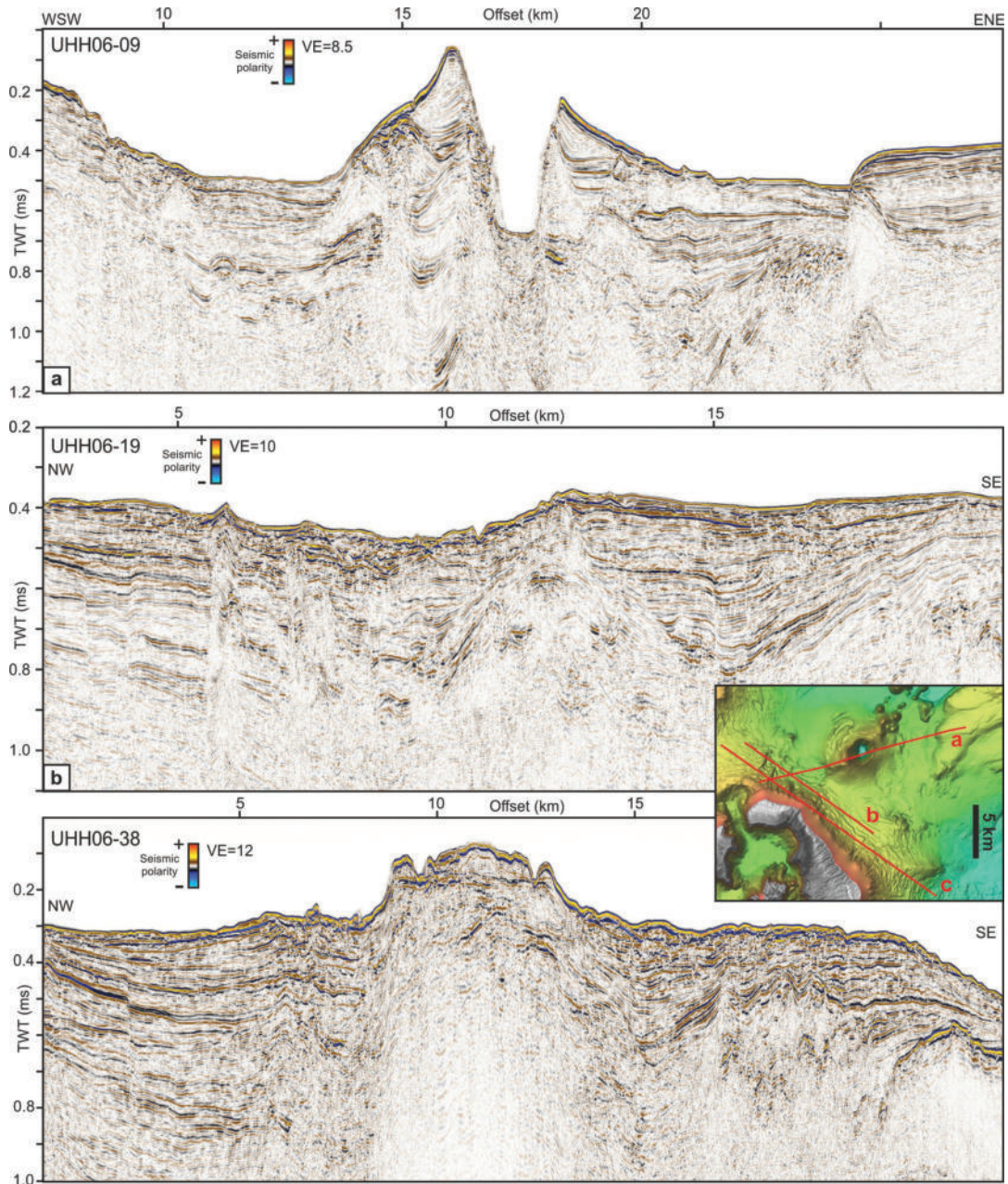
FIGURE D.5: Uninterpreted version of the seismic profiles shown in
Figure 7.6.

Appendix E

Appendix for Chapter 8

E.1   Supplement 8-1 – Sediment Core Analysis

The tripartite nature of core POS513-20 is also present in the 66-cm-thick Minoan deposits in core POS513-41, obtained 140 km from the eruptive centre (Fig. E.1). Due to the greater distance from source, grain size is generally smaller, and individual beds are thinner than in POS513-20. The lower subunit shows normally graded beds of medium ash overlain by a more massive sequence with faint lamination. The boundary of the lower subunit to the underlying hemipelagic sediments is unconformable (Fig. E.1), which is the result of the comparably dense ash material sinking into the substrate causing the development of a flame structure. As in core POS513-20, prominent colour and grayscale changes mark the boundary to the middle subunit, which indicate a higher lithic and crystal content and an increase in grain size (Fig. E.1C). Cross-lamination characterizes the fabric of the middle section and the boundary to the upper unit is defined by a transition to structureless material (of similar grain size) in the upper unit (Fig. E.1C), which consists of fine ash. Again, the diffuse transition to hemipelagic sediments is indicated by porosity change (Fig. E.1A).
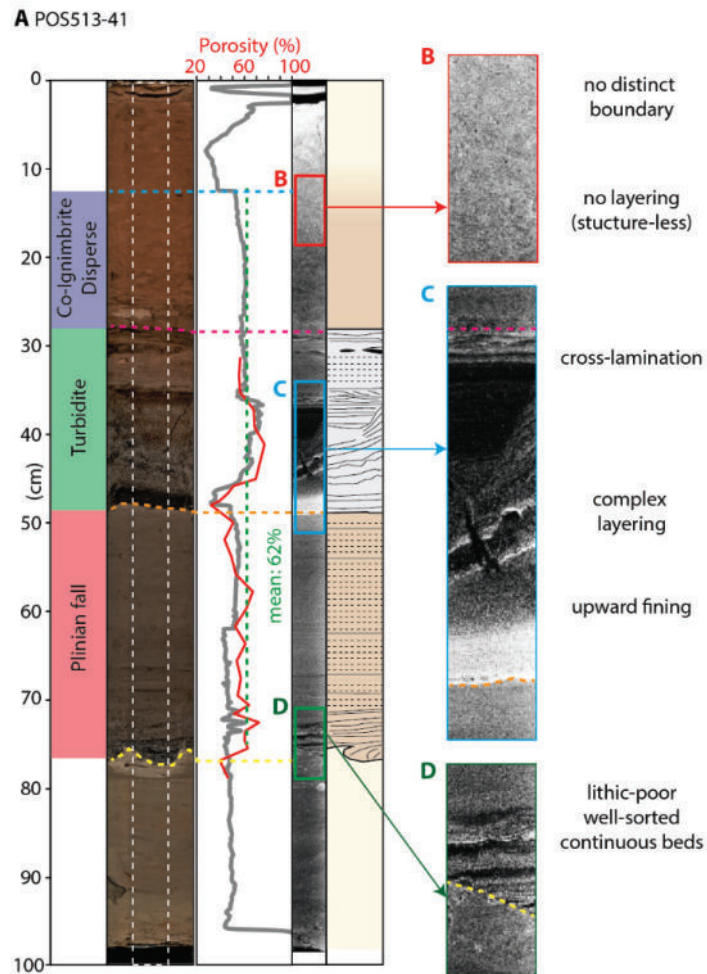
FIGURE E.1: (A) Photographic scans, porosity measurements, X-ray CT-scan and stratigraphic interpretation. (B) - (D) Enlargements of key intervals of the X-ray CT-scan showing differences between the deposit subunits.
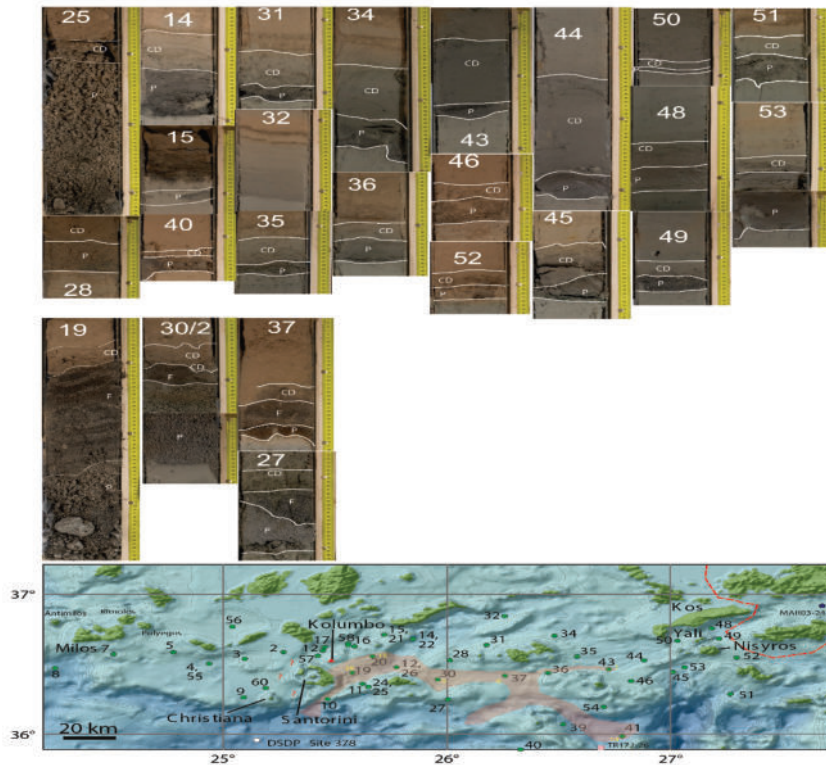
FIGURE E.2: Upper panel shows interpreted core photographs indicating Plinian ash fall deposits (P) and co-ignimbrite ash fall deposits/dispersed ash portion (CD) from marine Minoan tephras in selected cores east of Santorini from research cruise POS513. Middle panel shows the interpreted core pictures indicating tripartition of the marine Minoan tephra sequence into basal Plinian Fall deposits (P), middle flow-related deposits (F), and co-ignimbrite ash fall deposits/dispersed ash portion (CD) from selected cores east of Santorini from research cruise POS513. Lower panel indicates the position of all POS 513 cores that show tripartition of the marine Minoan tephra sequence and respective thickness in cm of the turbidite unit (yellow numbers) as well as the estimated areal distribution of the flow deposits following bathymetric depressions

E.2 Supplement 8-2 – Correlation between CT-Gray-Scale Value Analysis and Measured Porosity

As seen in Figs. 8.1 and E.1, both CT-derived and physically measured density estimates capture the same trends in the scanned sections of POS 513-20 and POS 513-41. Based on the homogenous geochemistry and solid density reported for both Minoan tephra deposits by Kutterolf, et al. (Kutterolf et al., 2021b; Kutterolf et al., 2021a), we attribute these variations to down-core porosity changes. This interpretation is furthermore supported by the strong anti-correlation (R = -0.64, p = 0.0003, n= 34) between density and particle size measured on samples from both investigated cores (see methods).

Following from the above, we argue that our down-core CT grayscale data can be used to revise MT ash fall volume estimates by refining density and porosity calculations. To do so, we i) harness the afore-mentioned relation between CT-derived

and physically measured density estimates to model density variations at 500 μm down-core intervals as shown in Fig. E.3, ii) transform these to porosity estimates using the Minoan tephra solid density values reported by Kutterolf, et al. (ref. 1) as well as the formula by Caffrey (1995): porosity = 1 – (bulk density/solid density), and 3) validate this approach using independent CT-derived pore volume estimates (see methods). The latter effort is, however, hampered by scanning resolution limits that prevent us from resolving pores smaller than 100 μm (see methods). But while this drawback greatly affects CT porosity estimates for the distal fine-grained ash in POS 513-41, the results for the sand-sized MT deposit in proximal POS 513-20 are far more encouraging and support the validity of our approach (Fig. E.3).
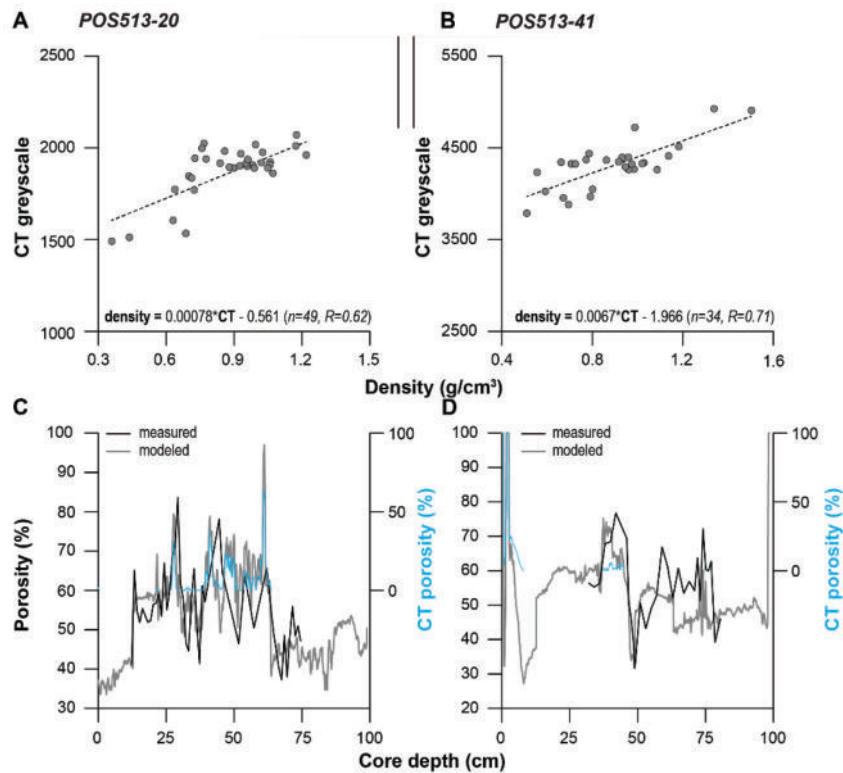
FIGURE E.3: Correlation between CT-gray-scale value analysis and measured porosity.

Appendix F

Appendix for Chapter 9
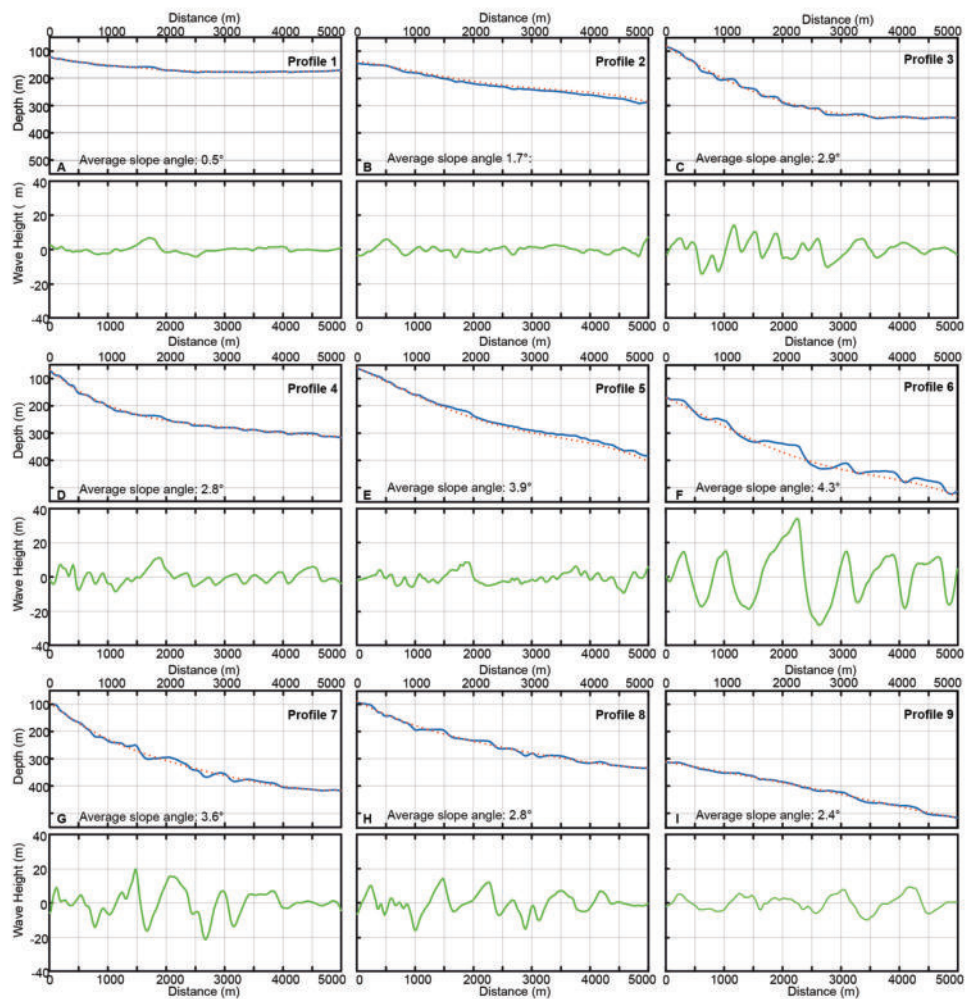
FIGURE F.1: (A) – (I) Morphological profiles of Santorini's flanks (blue line), regression curves through these profiles (dotted red line), and difference of both (green line) showing the wavelength and wave height of USBs.

Appendix G

Appendix for Chapter 10

G.1 Cone and Slide Plane Reconstructions Used as Simulation Input
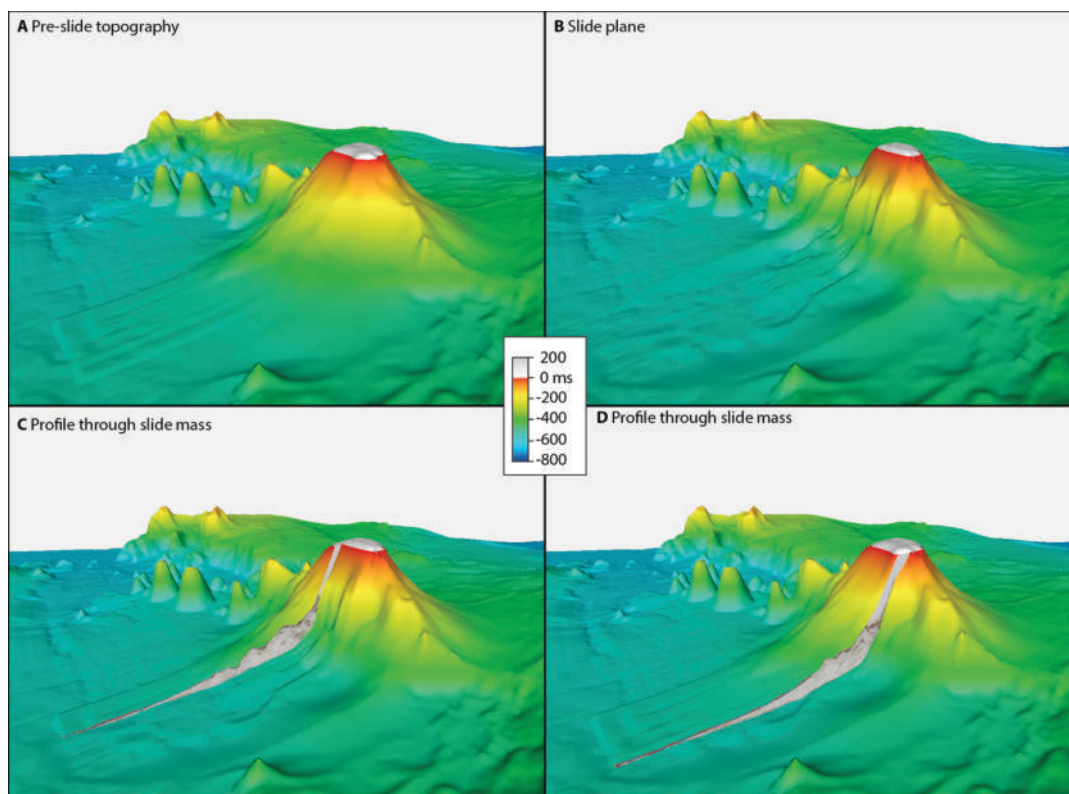
FIGURE G.1: Cone and slide plane reconstructions used as simulation input.

G.2 Sensitivity Analysis

To test the effects of simulation parameters and the interaction between wave fields produced by the slope failure and the explosion, we performed 44 numerical simulation runs with VolcFlow. The simulations sim 01 to sim 20 were dedicated to parameter tests for the slope failure. We used the slide plane defined in Supplement S1 and tested density values of 1,250 kg/m^3, 1,500 kg/m^3, 1,750 kg/m^3, and 2,000 kg/m^3 and yield strengths of 5 kPa, 7.5 kPa, 10 kPa, 20 kPa, and 50 kPa, resulting in

20 parameter combinations (Fig. G.2). The simulations showed a general trend toward higher tsunami waves for greater densities and smaller yield strengths, which is expected as these control the kinetic energy of the sliding mass that is transferred into the water column. It should be noted that density values of 1,750 kg/m^3 and 2,000 kg/m^3 are too high, according to the analysis of pumice samples obtained from Kolumbo's cone (Cantner et al., 2014), which indicated a bulk deposit density between 1,250 and 1,500 kg/m^3. All simulations using a density of 1,250 kg/m^3 resulted in too small a wave field (Fig. G.2). Likewise, simulations using a density of 1,500 kg/m^3 and yield strengths of 20 kPa and 50 kPa resulted in too small a wave field (Fig. G.2). The simulations assuming a density of 1,500 and yield strengths of 5 kPa, 7.5 kPa, 10 kPa, and 20 kPa were the best-suited simulations. In the absence of direct constraints of the slide kinematics, we adopted a density of 1,500 kg/m³ and a yield strength of 7.5 kPa for further simulations combining the slope failure with an explosive eruption (described below).
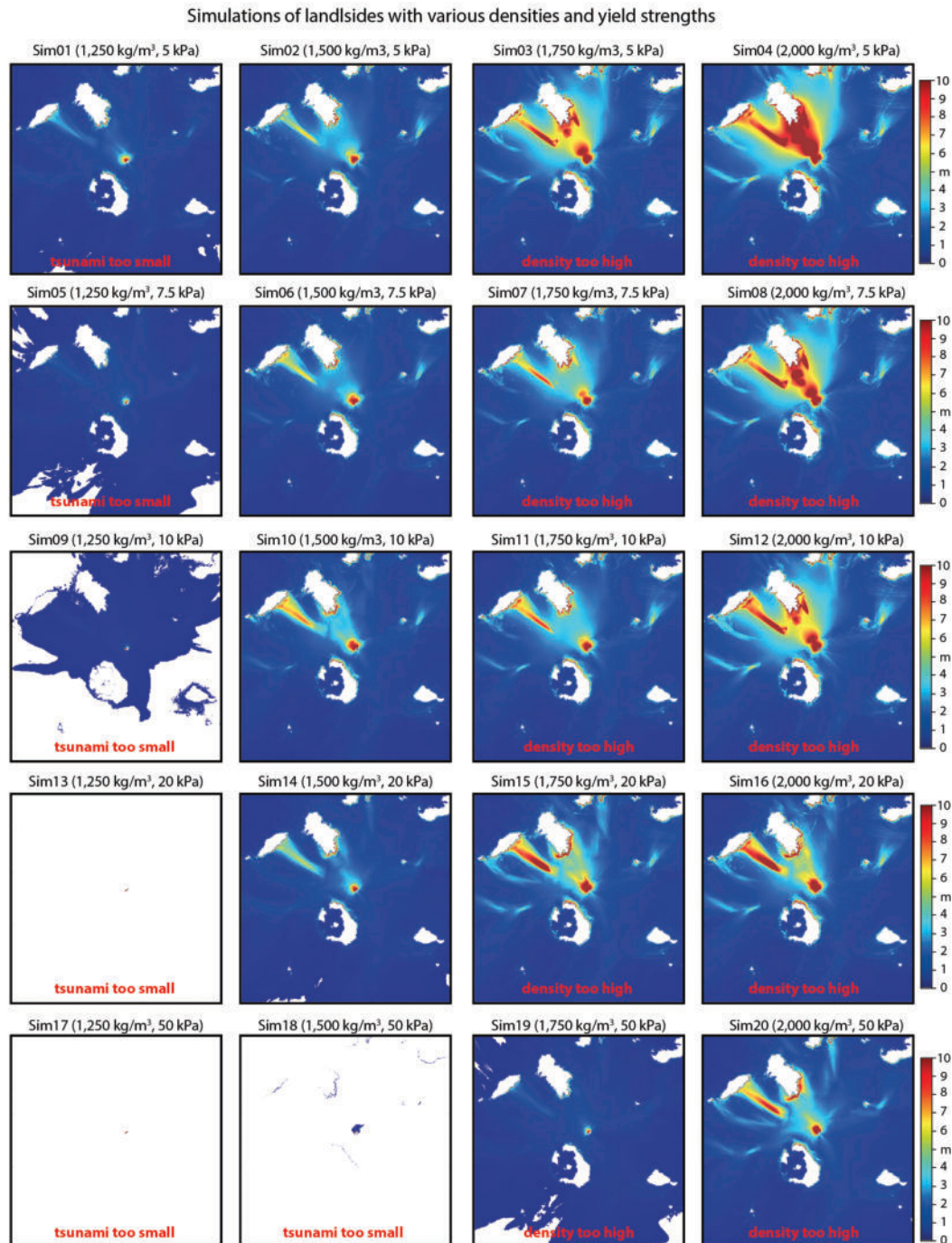
FIGURE G.2: Maximum tsunami heights for simulations of a slope failure (sim 001 to sim 020). Parameter combinations tested are density (in kg/m3) and yield strength (in kPa).

We performed four simulations for the tsunami genesis by an explosive eruption, following the approach by Ulvrova et al. (2016), which requires an estimation of the peak wave height. We simulated peak wave heights of 100 m, 125 m, 150 m, and 240 m. The simulations demonstrate how greater peak wave heights resulted in higher tsunami wave fields, as expected (Fig. G.3).

Simulations of explosive eruptions with various peak wave heights
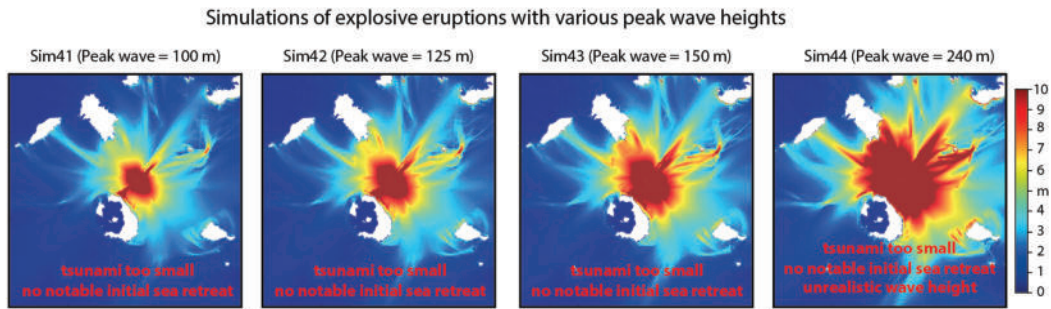
FIGURE G.3: Maximum tsunami heights for simulations of an explosive eruption (sim 041 to sim 044).

We then performed 20 additional simulations of a combined slope failure and explosion source mechanism. As mentioned earlier, we adopted a best estimate for density (1,500 kg/m^3) and yield strength (7.5 kPa) for the slope failure, and combined this scenario with an explosion with peak wave heights of 100 m, 125 m, 150 m, and 240 m (Fig. G.3). As the wave fields from both source mechanisms will superimpose themselves, the time delay between slope failure and the explosion is important, but unknown. Therefore, we simulated a broad range of 1 to 5 minute time delays, resulting in 20 parameter combinations. Since the average crater rim depth is 135 m, the simulations assuming a peak wave height of 240 m have to be considered unrealistic. As expected, the time delay between slope failure and explosion is critical in determining whether an initial sea retreat (caused by the slope failure induced tsunami) at Kamari and Perissa is observed or not. To validate the results, we defined threshold tsunami heights that should be reached to be consistent with historic observations. The precise locations of these historic observations are unknown, and the locations of the tsunami tide gauges do not always represent the location of maximum wave height for a given region (this location varies slightly from simulation to simulation). Therefore, we defined threshold tsunami heights that are smaller than the maximum observed wave heights: 7.5 m at northern Santorini, 5 m at Perissa and Kamari, and 10 m at southern Ios and Sikinos. Following these criteria, and the required initial sea retreat at Perissa and Kamari, only simulations sim 024, sim 028, sim032, sim 038, and sim 039 fulfill all requirements. This highlights the importance of the time delay between different interacting tsunami source mechanisms.

Appendix H

Appendix for Chapter 11

Here we present supporting information for the paper titled "When there is no offset - a demonstration of seismic diffraction imaging and depth velocity model building in the southern Aegean Sea." Contained in this section is a figure illustrating the proposed processing flow for the academic reflection seismic data (Figure H.1) and a figure illustrating the effect of different apertures used for the diffraction separation (Figure H.1).

Further, Figure H.3 compares the depth-stretched CMP stack and the seismic section after FD depth migration using the velocity model derived from wavefront tomography. Figure H.4 compares the depth-stretched CMP stack with the seismic section after FD depth migration using the refined velocity model. In addition, Figure H.5 compares the FD depth migrated section using the velocity model derived by wavefront tomography and the FD depth migrated section using the refined velocity model. These Figures allow to access and compare the quality of the presented depth migrations.
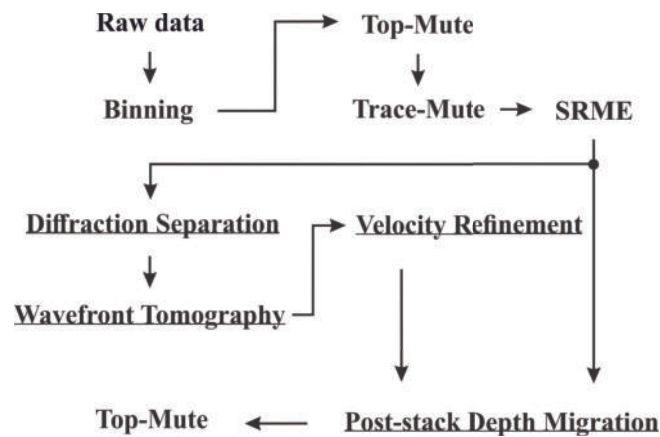
FIGURE H.1: Illustration of the processing flow. Processing steps related to diffraction and depth imaging are underlined.
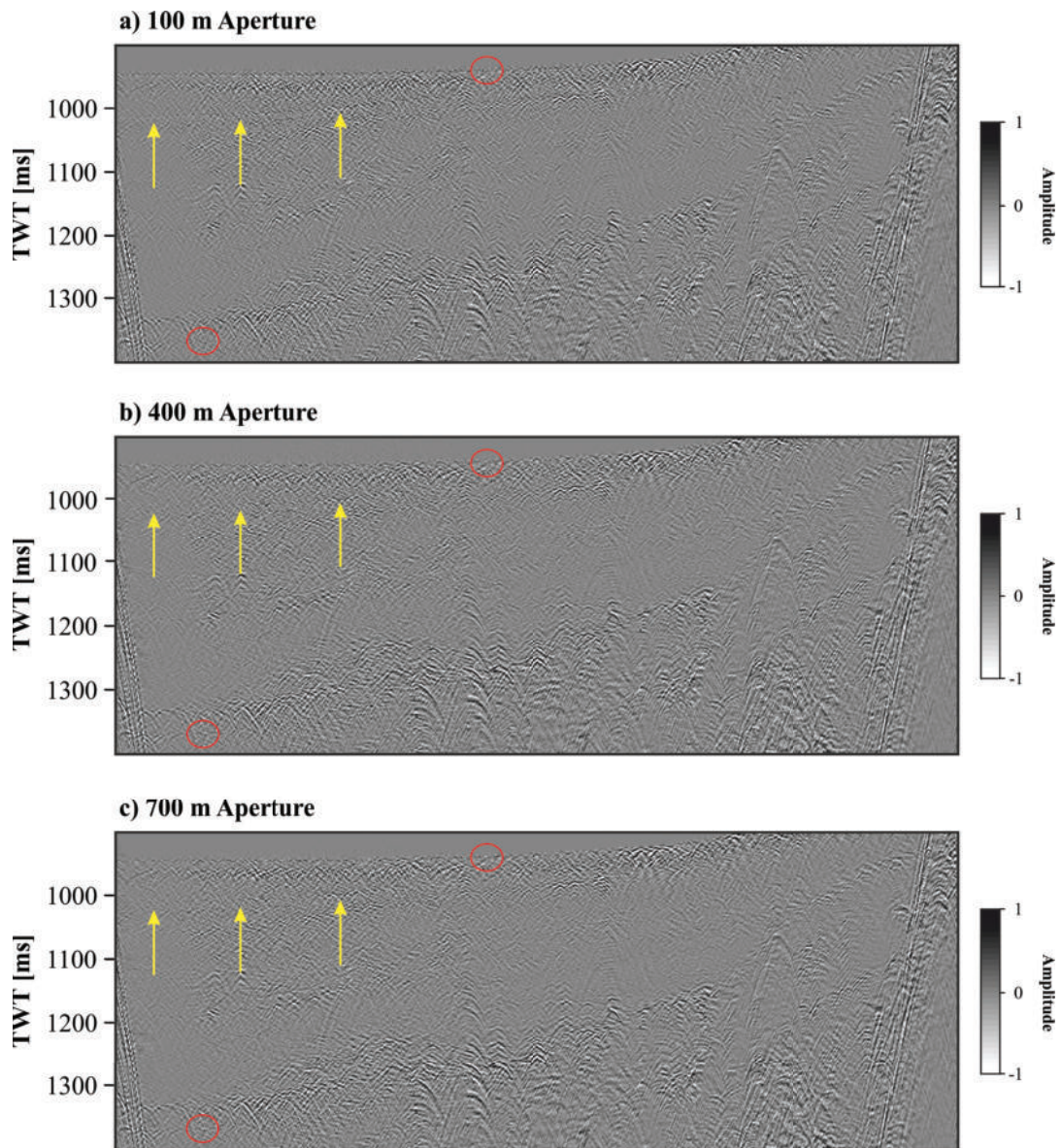
FIGURE H.2: Illustration of how different apertures for the coherent beam subtraction affect the separation result. Yellow arrows indicate a reflection horizon that remains in the separation derived with smaller apertures. Red circles indicate artefacts introduced when using higher apertures.
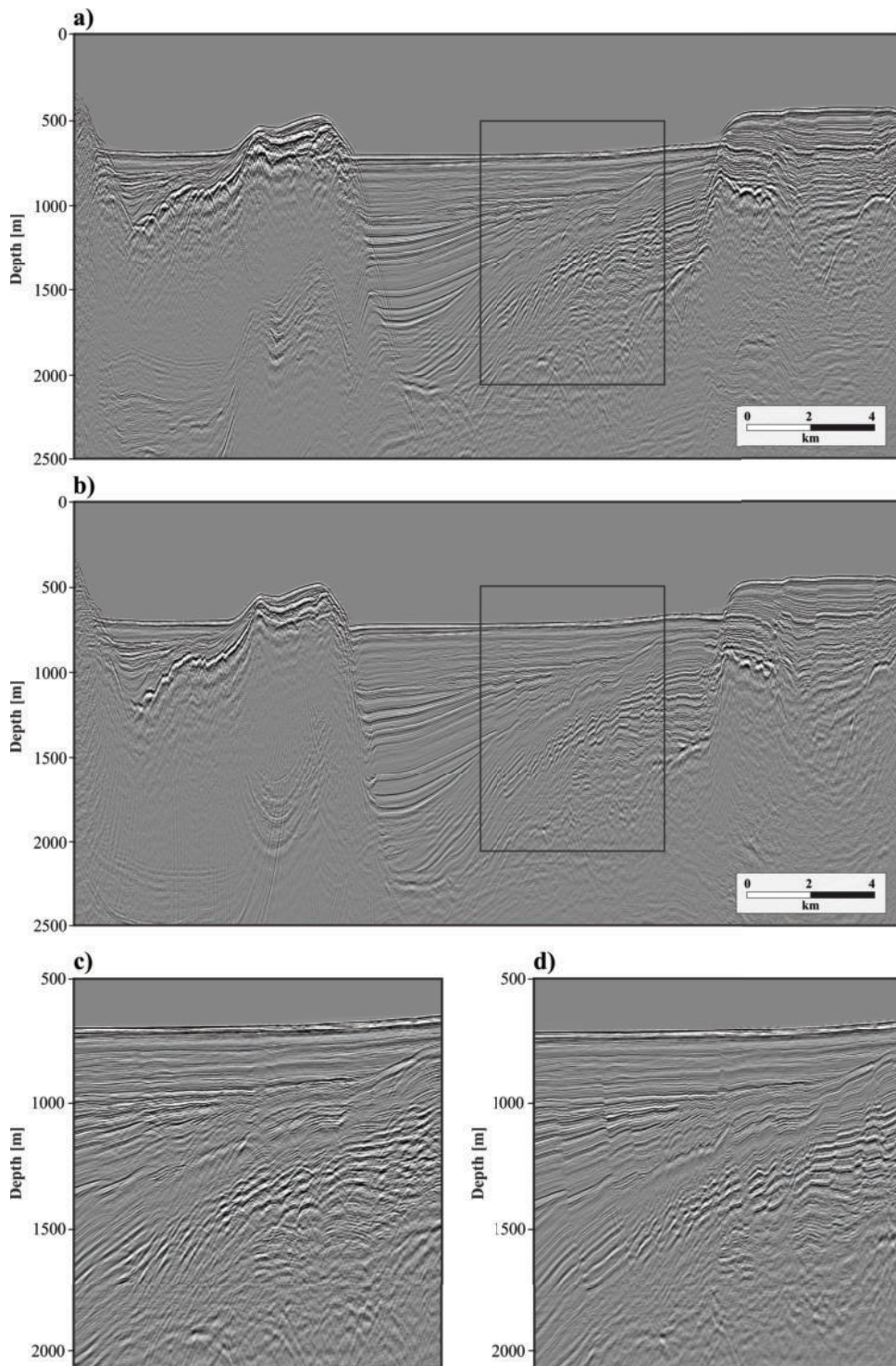
FIGURE H.3: (a) Depth-stretched CMP stack. (b) FD depth migration using the velocity model derived from wavefront tomography. (c) Zoomed section of the depth-stretched CMP stack. (d) Zoomed section of the FD depth migrated section derived with the velocity model from wavefront tomography.
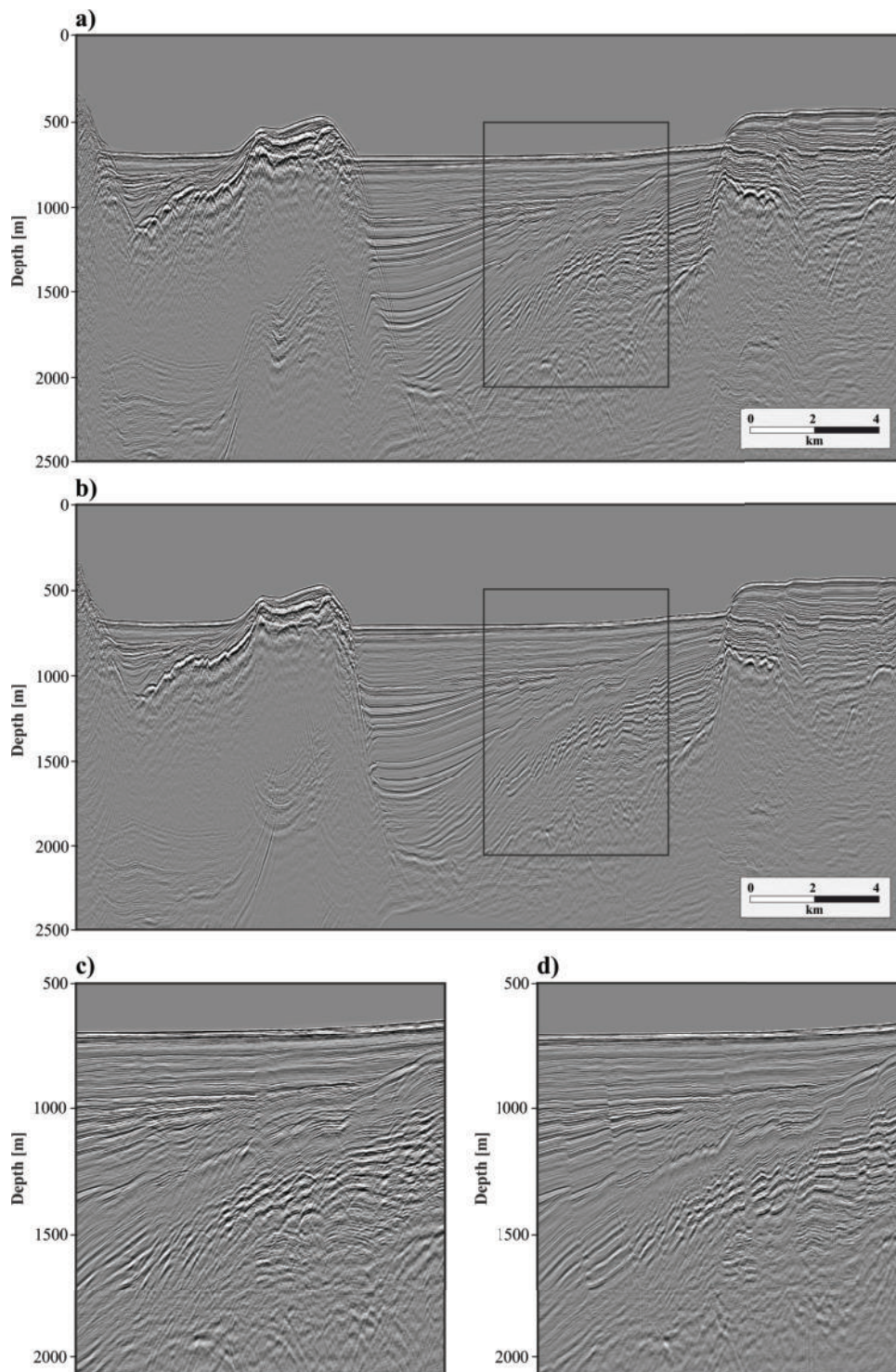
FIGURE H.4: (a) Depth-stretched CMP stack. (b) FD depth migration using the refined velocity model. (c) Zoomed section of the depth-stretched CMP stack. (d) Zoomed section of the FD depth Migration derived with the refined velocity model.
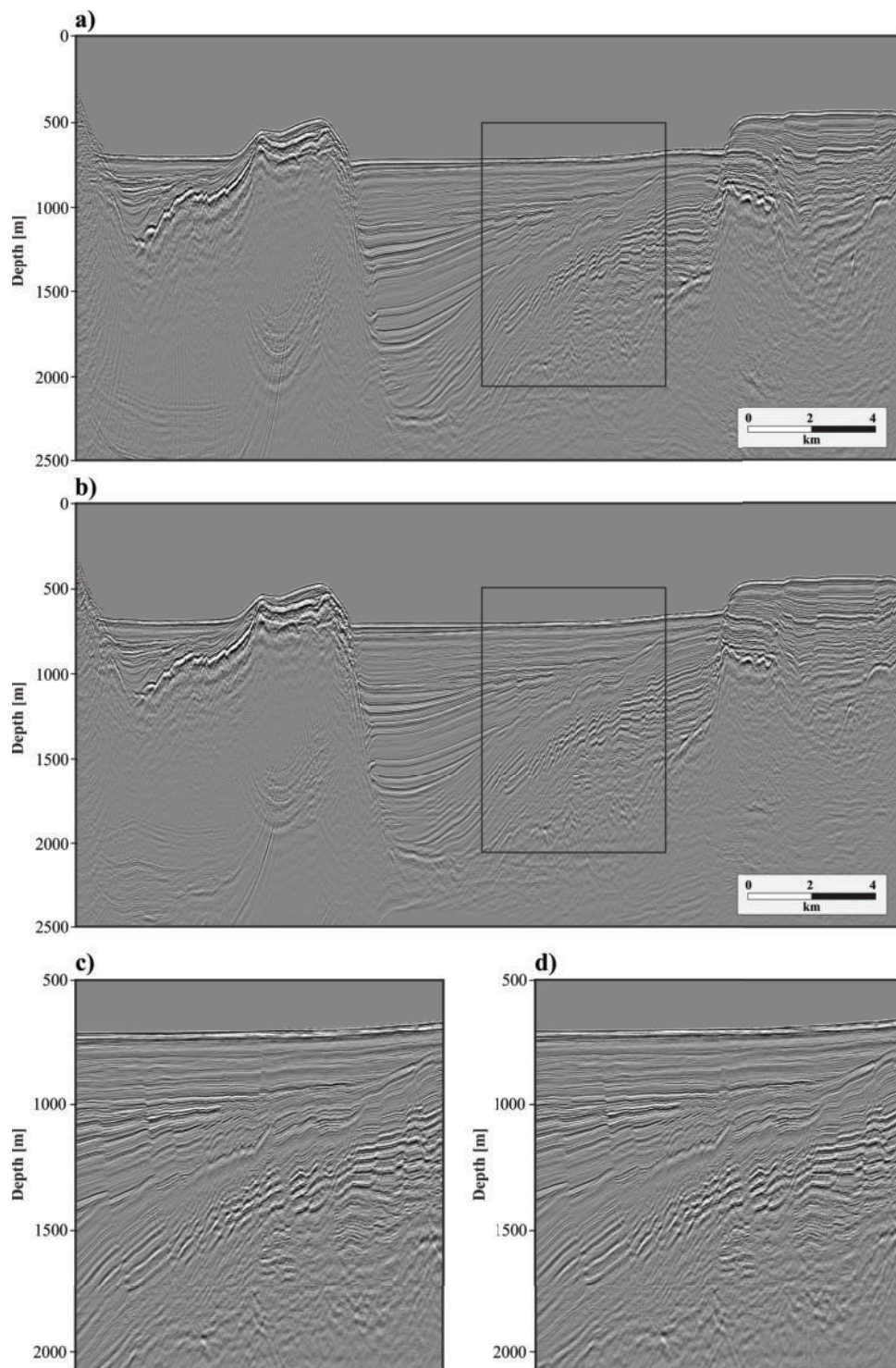
FIGURE H.5: (a) Result of FD depth migration using the velocity model derived from wavefront tomography. (b) Result of FD depth migration using the refined velocity model. (c) Zoomed section of the FD depth migration derived with the velocity model from wavefront tomography. (d) Zoomed section of the FD depth migration derived with the refined velocity model.

List of Abbreviations

Ab1-3:   Anhydros Basin Faults 1-3
AF: Anafi Fault
AhF: Anhydros Fault
AmF: Amorgos Fault
AsF: Astypalaea Fault
BCE: Before Common Era
CE: Common Era
CIG: Common Image Gather
CMP: Common Midpoint
Co-Ig: Co-Ignimbrite
CSK: Christiana-Santorini-Kolumbo
CSKVF: Christiana-Santorini-Kolumbo Volcanic Field
CT: Computed Tomography
DIV: Divergence
DRE: Dense-Rock Equivalent
ENE: East North East
ESE: East South East
FD: Finite Difference
h1-h6:   Horizons 1-6
HAR: High-Amplitude Reflection
IF: Ios Fault
InSAR: Interferometric Synthetic Aperture Radar
IODP: International Ocean Discovery Program
GI: Generator Injector
GPS: Global Positioning System
K1-K5:   Kolumbo Units 1-5
ka: Kilo Annum (Thousand Years Ago)
KaL: Kameni Line
KoL: Kolumbo Line
KVC: Kolumbo Volcanic Chain
kyrs: Thousand years
LBA: Late Bronze Age
Ma: Mega Annum (Million Years Ago)
MCS: Multi-Channel Seismic
MTD: Mass-Transport Deposit
Myrs: Million Years
NE: North East
NIP: Normal Incidence Point
NMO: Normal Moveout
NNE: North-northeast
NNW: North North West

NW:	North West
OC:	Oia Cone
PSTM:	Pre-Stack Time Migration
RV:	Research Vessel
SAF:	Santorini-Anafi Fault
SANTORY:	SANTORini's seafloor volcanic observatorY
SATZ:	Santorini-Amorgos Tectonic Zone
SCS:	Single-Channel Seismic
SE:	South East
SF1-2:	Seismic Facies 1-2
SMTD:	Santorini Mass-Transport Deposit
SW:	South West
SRME:	Surface-Related Multiple Elimination
SSE:	South South East
SSW:	South South West
TPF:	Thera Pyroclastic Formation
TWT:	Two-Way Traveltime
U1-U6:	Units 1-6
USB:	Undulating Seafloor Bedform
UTM:	Universal Transverse Mercator
VEI:	Volcanic Explosivity Index
VC:	Volcanic Cone
VE:	Vertical Exaggeration
Vp:	P-wave Velocity
WGS:	World Geodetic System
WNW:	West North West
WSW:	West South West

Bibliography

Abe, K (1980). "Magnitudes of major volcanic earthquakes of Japan 1901 to 1925". In: *Journal of the Faculty of Science, Hokkaido University. Series 7, Geophysics* 6.1, pp. 201–212.

– (1992). "Seismicity of the caldera-making eruption of Mount Katmai, Alaska in 1912". In: *Bulletin of the Seismological Society of America* 82.1, pp. 175–191.

Acocella, V (2021). *Volcano-tectonic processes*. Springer Nature.

Acocella, V and D Trippanera (2016). "How diking affects the tectonomagmatic evolution of slow spreading plate boundaries: Overview and model". In: *Geosphere* 12.3, pp. 867–883.

Allen, L, A O'Connell, and V Kiermer (2019). "How can we ensure visibility and diversity in research contributions? How the Contributor Role Taxonomy (CRediT) is helping the shift from authorship to contributorship". In: *Learned Publishing* 32.1, pp. 71–74.

Allen, RW et al. (2018). "30 Years in the Life of an Active Submarine Volcano: A Time-Lapse Bathymetry Study of the Kick-'em-Jenny Volcano, Lesser Antilles". In: *Geochemistry, Geophysics, Geosystems* 19.3, pp. 715–731.

Anadón, P, C Canet, and WL Friedrich (2013). "Aragonite stromatolitic buildups from Santorini (Aegean Sea, Greece): geochemical and palaeontological constraints of the caldera palaeoenvironment prior to the Minoan eruption (ca 3600 yr bp)". In: *Sedimentology* 60.5, pp. 1128–1155.

Anastasakis, G and D Piper (2005). "Late Neogene evolution of the western South Aegean volcanic arc: sedimentary imprint of volcanicity around Milos". In: *Marine Geology* 215.3-4, pp. 135–158.

Athanassas, CD et al. (2016). "Evidence from cosmic ray exposure (CRE) dating for the existence of a pre-Minoan caldera on Santorini, Greece". In: *Bulletin of Volcanology* 78.5, pp. 1–13.

Auker, MR et al. (2013). "A statistical analysis of the global historical volcanic fatalities record". In: *Journal of Applied Volcanology* 2.1, pp. 1–24.

Bachmann, O et al. (2010). "The 40Ar/39Ar and U/Pb dating of young rhyolites in the Kos-Nisyros volcanic complex, Eastern Aegean Arc, Greece: Age discordance due to excess 40Ar in biotite". In: *Geochemistry, Geophysics, Geosystems* 11.8.

Bahorich, M and S Farmer (1995). "3-D seismic discontinuity for faults and stratigraphic features: The coherence cube". In: *The leading edge* 14.10, pp. 1053–1058.

Bakhtiari, P et al. (2018). "Common-reflection-surface-based prestack diffraction separation and imaging". In: *Geophysics* 83.1, S47–S55.

Bato, MG et al. (2018). "Possible deep connection between volcanic systems evidenced by sequential assimilation of geodetic data". In: *Scientific reports* 8.1, pp. 1–13.

Bauer, A, B Schwarz, and D Gajewski (2016). "Enhancement of prestack diffraction data and attributes using a traveltime decomposition approach". In: *Studia Geophysica et Geodaetica* 60.3, pp. 471–486.

– (2017). "Utilizing diffractions in wavefront tomography". In: *Geophysics* 82.2, R65–R73.

Bauer, A et al. (2019). "Wavefront tomography with enforced diffraction focusing". In: *81st EAGE Conference and Exhibition 2019*. Vol. 2019. 1. European Association of Geoscientists & Engineers, pp. 1–5.

Bauer, AB, BS Schwarz, and DG Gajewski (2018). "Diffraction wavefront tomography-efficient automated velocity inversion for multi-fold and single-channel data". In: *80th EAGE Conference & Exhibition 2018 Workshop Programme*. European Association of Geoscientists & Engineers, cp–556.

Bell, KLC (2011). *On the origin of submarine sediment features in the southern Aegean Sea*. University of Rhode Island.

Bell, KLC et al. (2013). "Submarine evidence of a debris avalanche deposit on the eastern slope of Santorini volcano, Greece". In: *Tectonophysics* 597, pp. 147–160.

Bellefleur, G et al. (2006). "Comparison of single-and multichannel high-resolution seismic data for shallow stratigraphy mapping in St. Lawrence River estuary, Quebec". In: *Geol. Surv. Can. D* 2, pp. 1–10.

Berkovitch, A et al. (2009). "Diffraction imaging by multifocusing". In: *Geophysics* 74.6, WCA75–WCA81.

Bischoff, A et al. (2019). "Stratigraphy of architectural elements of a buried monogenetic volcanic system". In: *Open Geosciences* 11.1, pp. 581–616.

Bischoff, A et al. (2021). "Seismic geomorphology, architecture and stratigraphy of volcanoes buried in sedimentary basins". In: *Updates in Volcanology-Transdisciplinary Nature of Volcano Science*. IntechOpen.

Bocchini, GM et al. (2018). "Tearing, segmentation, and backstepping of subduction in the Aegean: New insights from seismicity". In: *Tectonophysics* 734, pp. 96–118.

Bohnhoff, M et al. (2006). "Microseismic activity in the Hellenic Volcanic Arc, Greece, with emphasis on the seismotectonic setting of the Santorini–Amorgos zone". In: *Tectonophysics* 423.1-4, pp. 17–33.

Bonadonna, C and A Costa (2012). "Estimating the volume of tephra deposits: a new simple strategy". In: *Geology* 40.5, pp. 415–418.

Bond, A and RSJ Sparks (1976). "The minoan eruption of Santorini, Greece". In: *Journal of the Geological Society* 132.1, pp. 1–16.

Brown, SK, MR Auker, and RSJ Sparks (2015). "Populations around Holocene volcanoes and development of a Population Exposure Index". In: *Global volcanic hazards and risk*, pp. 223–232.

Brown, SK et al. (2017). "Volcanic fatalities database: analysis of volcanic threat with distance and victim classification". In: *Journal of Applied Volcanology* 6.1, pp. 1–20.

Bruins, HJ et al. (2008). "Geoarchaeological tsunami deposits at Palaikastro (Crete) and the Late Minoan IA eruption of Santorini". In: *Journal of Archaeological Science* 35.1, pp. 191–212.

Brunet, M et al. (2016). "Composition, geometry, and emplacement dynamics of a large volcanic island landslide offshore M artinique: From volcano flank-collapse to seafloor sediment failure?" In: *Geochemistry, Geophysics, Geosystems* 17.3, pp. 699–724.

Brüstle, A et al. (2014). "Focal mechanism and depth of the 1956 Amorgos twin earthquakes from waveform matching of analogue seismograms". In: *Solid Earth* 5.2, pp. 1027–1044.

Bucci, MG et al. (2022). "A global review of subaqueous spreading and its morphological and sedimentological characteristics: A database for highlighting the current state of the art". In: *Geomorphology*, p. 108397.

Bull, S, J Cartwright, and M Huuse (2009). "A review of kinematic indicators from mass-transport complexes using 3D seismic data". In: *Marine and Petroleum Geology* 26.7, pp. 1132–1151.

Bull, S et al. (2020). "Influence of mass transport deposit (MTD) surface topography on deep-water deposition: an example from a predominantly fine-grained continental margin, New Zealand". In: *Geological Society, London, Special Publications* 500.1, pp. 147–171.

Burgisser, A, GW Bergantz, and RE Breidenthal (2005). "Addressing complexity in laboratory experiments: the scaling of dilute multiphase flows in magmatic systems". In: *Journal of Volcanology and Geothermal Research* 141.3-4, pp. 245–265.

Caffrey, JM (1995). "Spatial and seasonal patterns in sediment nitrogen remineralization and ammonium concentrations in San Francisco Bay, California". In: *Estuaries* 18.1, pp. 219–233.

Cantner, K, S Carey, and P Nomikou (2014). "Integrated volcanologic and petrologic analysis of the 1650 AD eruption of Kolumbo submarine volcano, Greece". In: *Journal of Volcanology and Geothermal Research* 269, pp. 28–43.

Carey, S and H Sigurdsson (1989). "The intensity of plinian eruptions". In: *Bulletin of Volcanology* 51.1, pp. 28–40.

– (2007). "Exploring submarine arc volcanoes". In: *Oceanography* 20.4, pp. 80–89.

Carey, S et al. (1996). "Pyroclastic flows and surges over water: an example from the 1883 Krakatau eruption". In: *Bulletin of Volcanology* 57.7, pp. 493–511.

Carey, S et al. (2011). "Exploration of the Kolumbo volcanic rift zone". In.

Carey, S et al. (2013). "CO2 degassing from hydrothermal vents at Kolumbo submarine volcano, Greece, and the accumulation of acidic crater water". In: *Geology* 41.9, pp. 1035–1038.

Carey, SN and JL Schneider (2011). "Volcaniclastic processes and deposits in the deep-sea". In: *Developments in Sedimentology*. Vol. 63. Elsevier, pp. 457–515.

Cartigny, MJB et al. (2011). "A comparative study of sediment waves and cyclic steps based on geometries, internal structures and numerical modeling". In: *Marine Geology* 280.1-4, pp. 40–56.

Cartwright, J and M Huuse (2005). "3D seismic technology: the geological 'Hubble'". In: *Basin Research* 17.1, pp. 1–20.

Carvajal, M et al. (2022). "Worldwide signature of the 2022 Tonga volcanic tsunami". In: *Geophysical Research Letters* 49.6, e2022GL098153.

Cas, RAF and JM Simmons (2018). "Why deep-water eruptions are so different from subaerial eruptions". In: *Frontiers in Earth Science* 6, p. 198.

Casalbore, D et al. (2021). "Bedforms on the submarine flanks of insular volcanoes: New insights gained from high resolution seafloor surveys". In: *Sedimentology* 68.4, pp. 1400–1438.

Cashman, K and J Blundy (2000). "Degassing and crystallization of ascending andesite and dacite". In: *Philosophical Transactions of the Royal Society of London. Series A: Mathematical, Physical and Engineering Sciences* 358.1770, pp. 1487–1513.

Cashman, KV, R Stephen, and R Sparks (2013). "How volcanoes work: A 25 year perspective". In: *Bulletin* 125.5-6, pp. 664–690.

Cassidy, M and L Mani (2022). "Prepare now for big eruptions". In: *Nature* 608, pp. 469–71.

Chang, YC et al. (2022). "Asymmetric abundances of submarine sediment waves around the Azores volcanic islands". In: *Marine Geology* 449, p. 106837.

Chaussard, E and F Amelung (2012). "Precursory inflation of shallow magma reservoirs at west Sunda volcanoes detected by InSAR". In: *Geophysical Research Letters* 39.21.

Chopra, S and KJ Marfurt (2007). *Seismic attributes for prospect identification and reservoir characterization*. Society of Exploration Geophysicists, European Association of Geoscientists, and Engineers.

Chrapkiewicz, K et al. (2022). "Magma chamber detected beneath an arc volcano with full-waveform inversion of active-source seismic data". In: *Geochemistry, Geophysics, Geosystems*, e2022GC010475.

Corti, G et al. (2003). "Analogue modelling of continental extension: a review focused on the relations between the patterns of deformation and the presence of magma". In: *Earth-Science Reviews* 63.3-4, pp. 169–247.

Cossette, E et al. (2016). "Structure and anisotropy of the crust in the Cyclades, Greece, using receiver functions constrained by in situ rock textural data". In: *Journal of Geophysical Research: Solid Earth* 121.4, pp. 2661–2678.

Cronin, S et al. (2022). "The 15 January 2022 Hunga eruption, Tonga-first petrographic and geochemical results". In: *EGU General Assembly Conference Abstracts*, EGU22–13584.

Crutchley, GJ et al. (2013). "Insights into the emplacement dynamics of volcanic landslides from high-resolution 3D seismic data acquired offshore Montserrat, Lesser Antilles". In: *Marine Geology* 335, pp. 1–15.

Crutchley, GJ et al. (2022). "Investigating the basal shear zone of the submarine Tuaheni Landslide Complex, New Zealand: a core-log-seismic integration study". In: *Journal of Geophysical Research: Solid Earth* 127.1.

Dafni, R and W Symes (2017). "Diffraction imaging by prestack reverse-time migration in the dip-angle domain". In: *Geophysical Prospecting* 65, pp. 295–316.

Decker, L, X Janson, and S Fomel (2015). "Carbonate reservoir characterization using seismic diffraction imaging". In: *Interpretation* 3.1, SF21–SF30.

Dell, S and D Gajewski (2011). "Common-reflection-surface-based workflow for diffraction imaging". In: *Geophysics* 76.5, S187–S195.

Diekmann, L et al. (2019). "Source localization and joint velocity model building using wavefront attributes". In: *Geophysical Journal International* 219.2, pp. 995–1007.

Dimitriadis, I et al. (2009). "Seismicity and active tectonics at Coloumbo Reef (Aegean Sea, Greece): Monitoring an active volcano at Santorini Volcanic Center using a temporary seismic network". In: *Tectonophysics* 465.1-4, pp. 136–149.

Dominey-Howes, D (2004). "A re-analysis of the Late Bronze Age eruption and tsunami of Santorini, Greece, and the implications for the volcano–tsunami hazard". In: *Journal of Volcanology and Geothermal Research* 130.1-2, pp. 107–132.

Dominey-Howes, DTM, GA Papadopoulos, and AG Dawson (2000). "Geological and historical investigation of the 1650 Mt. Columbo (Thera Island) eruption and tsunami, Aegean Sea, Greece". In: *Natural Hazards* 21.1, pp. 83–96.

Dondin, F et al. (2017). "Flank instability assessment at Kick-'em-Jenny submarine volcano (Grenada, Lesser Antilles): a multidisciplinary approach using experiments and modeling". In: *Bulletin of Volcanology* 79.1, pp. 1–15.

Druitt, TH (2014). "New insights into the initiation and venting of the Bronze-Age eruption of Santorini (Greece), from component analysis". In: *Bulletin of Volcanology* 76.2, pp. 1–21.

Druitt, TH and V Francaviglia (1992). "Caldera formation on Santorini and the physiography of the islands in the late Bronze Age". In: *Bulletin of Volcanology* 54.6, pp. 484–493.

Druitt, TH, S Kutterolf, and TW Höfig (2022). "Expedition 398 Scientific Prospectus: Hellenic Arc Volcanic Field". In: *Scientific prospectus* 398.

Druitt, TH, FW McCoy, and GE Vougioukalakis (2019a). "The Late Bronze Age eruption of Santorini volcano and its impact on the ancient Mediterranean world". In: *Elements* 15.3, pp. 185–190.

Druitt, TH, DM Pyle, and TA Mather (2019b). "Santorini volcano and its plumbing system". In: *Elements: An International Magazine of Mineralogy, Geochemistry, and Petrology* 15.3, pp. 177–184.

Druitt, TH et al. (1999). "Santorini volcano". In: *Geological Society Memoir* 19.

Druitt, TH et al. (2012). "Decadal to monthly timescales of magma transfer and reservoir growth at a caldera volcano". In: *Nature* 482.7383, pp. 77–80.

Drymoni, K, J Browning, and A Gudmundsson (2020). "Dyke-arrest scenarios in extensional regimes: Insights from field observations and numerical models, Santorini, Greece". In: *Journal of Volcanology and Geothermal Research* 396, p. 106854.

– (2022). "Spatial and temporal volcanotectonic evolution of Santorini volcano, Greece". In: *Bulletin of Volcanology* 84.6, pp. 1–18.

Duveneck, E (2004). "Velocity model estimation with data-derived wavefront attributes". In: *Geophysics* 69.1, pp. 265–274.

Faulds, HE and RJ Varga (1998). "The role of accommodation zones and transfer zones in the regional segmentation of extended terranes". In: *Geological Society of America Special Papers* 323, pp. 1–45.

Feuillet, N (2013). "The 2011–2012 unrest at Santorini rift: stress interaction between active faulting and volcanism". In: *Geophysical Research Letters* 40.14, pp. 3532–3537.

Fiske, RS et al. (1998). "Tephra dispersal from Myojinsho, Japan, during its shallow submarine eruption of 1952–1953". In: *Bulletin of Volcanology* 59.4, pp. 262–275.

Flaherty, T et al. (2022). "Temporal variations in the diversity of primitive melts supplied to the Santorini silicic magmatic system and links to lithospheric stresses". In: *Contributions to Mineralogy and Petrology* 177.8, pp. 1–21.

Fomel, S (2002). "Applications of plane-wave destruction filters". In: *Geophysics* 67.6, pp. 1946–1960.

Fomel, S, E Landa, and MT Taner (2007). "Poststack velocity analysis by separation and imaging of seismic diffractions". In: *Geophysics* 72.6, U89–U94.

Fouqué, F (1879). *Santorin et ses éruptions*. G. Masson.

Freundt, A (2003). "Entrance of hot pyroclastic flows into the sea: experimental observations". In: *Bulletin of Volcanology* 65.2, pp. 144–164.

Frey-Martínez, J, J Cartwright, and D James (2006). "Frontally confined versus frontally emergent submarine landslides: A 3D seismic characterisation". In: *Marine and Petroleum Geology* 23.5, pp. 585–604.

Friedrich, WL et al. (2006). "Santorini eruption radiocarbon dated to 1627-1600 BC". In: *Science* 312.5773, pp. 548–548.

Fuller, S, S Carey, and P Nomikou (2018). "Distribution of fine-grained tephra from the 1650 CE submarine eruption of Kolumbo volcano, Greece". In: *Journal of Volcanology and Geothermal Research* 352, pp. 10–25.

Galland, O et al. (2018). "Storage and transport of magma in the layered crust — Formation of sills and related flat-lying intrusions". In: *Volcanic and igneous plumbing systems*. Elsevier, pp. 113–138.

Ganas, A et al. (2013). "GPS-derived estimates of crustal deformation in the central and north Ionian Sea, Greece: 3-yr results from NOANET continuous network data". In: *Journal of Geodynamics* 67, pp. 62–71.

Gautier, P et al. (1999). "Timing, kinematics and cause of Aegean extension: a scenario based on a comparison with simple analogue experiments". In: *Tectonophysics* 315.1-4, pp. 31–72.

Gerasopoulos, E et al. (2006). "A complex case study of down to the surface intrusions of persistent stratospheric air over the Eastern Mediterranean". In: *Atmospheric Environment* 40.22, pp. 4113–4125.

Giachetti, T et al. (2011). "Numerical modelling of the tsunami triggered by the Güìmar debris avalanche, Tenerife (Canary Islands): comparison with field-based data". In: *Marine Geology* 284.1-4, pp. 189–202.

Giachetti, T et al. (2012). "Tsunami hazard related to a flank collapse of Anak Krakatau Volcano, Sunda Strait, Indonesia". In: *Geological Society, London, Special Publications* 361.1, pp. 79–90.

Giba, M et al. (2013). "Investigation of the spatio-temporal relationship between normal faulting and arc volcanism on million-year time scales". In: *Journal of the Geological Society* 170.6, pp. 951–962.

Gilchrist, JT and AM Jellinek (2021). "Sediment waves and the gravitational stability of volcanic jets". In: *Bulletin of Volcanology* 83.10, pp. 1–59.

Gonnermann, HM (2015). "Magma fragmentation". In: *Annual Review of Earth and Planetary Sciences* 43, pp. 431–458.

Gray, SH et al. (2001). "Seismic migration problems and solutions". In: *Geophysics* 66.5, pp. 1622–1640.

Grilli, ST et al. (2019). "Modelling of the tsunami from the December 22, 2018 lateral collapse of Anak Krakatau volcano in the Sunda Straits, Indonesia". In: *Scientific reports* 9.1, pp. 1–13.

Hall, J et al. (2009). "Structural architecture of the Rhodes Basin: a deep depocentre that evolved since the Pliocene at the junction of Hellenic and Cyprus Arcs, eastern Mediterranean". In: *Marine Geology* 258.1-4, pp. 1–23.

Hampton, MA, HJ Lee, and J Locat (1996). "Submarine landslides". In: *Reviews of geophysics* 34.1, pp. 33–59.

Hannington, MD (2018). "RV POSEIDON Fahrtbericht/Cruise Report POS510-ANYDROS: Rifting and Hydrothermal Activity in the Cyclades Back-Arc Basin, Catania (Italy)–Heraklion (Greece) 06.03.-29.03. 2017". In.

Harding, TP (1990). "Identification of wrench faults using subsurface structural data: criteria and pitfalls". In: *AAPG bulletin* 74.10, pp. 1590–1609.

Harjono, H et al. (1991). "Seismicity of the Sunda Strait: evidence for crustal extension and volcanological implications". In: *Tectonics* 10.1, pp. 17–30.

Heap, MJ and BM Kennedy (2016). "Exploring the scale-dependent permeability of fractured andesite". In: *Earth and Planetary Science Letters* 447, pp. 139–150.

Heath, BA et al. (2019). "Tectonism and its relation to magmatism around Santorini Volcano from upper crustal P wave velocity". In: *Journal of Geophysical Research: Solid Earth* 124.10, pp. 10610–10629.

Heath, BA et al. (2021). "Relationship Between Active Faulting/Fracturing and Magmatism Around Santorini: Seismic Anisotropy From an Active Source Tomography Experiment". In: *Journal of Geophysical Research: Solid Earth* 126.8, e2021JB0218 bibrangedash 98.

Heiken, G and F McCoy (1984). "Caldera development during the Minoan eruption, Thira, Cyclades, Greece". In: *Journal of Geophysical Research: Solid Earth* 89.B10, pp. 8441–8462.

Herd, RA, M Edmonds, and VA Bass (2005). "Catastrophic lava dome failure at Soufrière Hills volcano, Montserrat, 12–13 July 2003". In: *Journal of Volcanology and Geothermal Research* 148.3-4, pp. 234–252.

Hill, DP, F Pollitz, and C Newhall (2002). "Earthquake-volcano interactions". In: *Physics Today* 55.11, pp. 41–47.

Hooft, EEE et al. (2017). "Backarc tectonism, volcanism, and mass wasting shape seafloor morphology in the Santorini-Christiana-Amorgos region of the Hellenic Volcanic Arc". In: *Tectonophysics* 712, pp. 396–414.

Hooft, EEE et al. (2019). "Seismic imaging of Santorini: subsurface constraints on caldera collapse and present-day magma recharge". In: *Earth and Planetary Science Letters* 514, pp. 48–61.

Hsu, K et al. (1978). "DSDP site 378". In: *DSDP* 42, pp. 321–357.

Hübscher, C and K Gohl (2016). "Reflection/refraction seismology". In: *(Encyclopedia of Earth Sciences Series)*. Springer, pp. 721–731.

Hübscher, C, M Ruhnau, and P Nomikou (2015). "Volcano-tectonic evolution of the polygenetic Kolumbo submarine volcano/Santorini (Aegean Sea)". In: *Journal of Volcanology and Geothermal Research* 291, pp. 101–111.

Hübscher, C et al. (2006). "Toward a risk assessment of central Aegean volcanoes". In: *Eos, Transactions American Geophysical Union* 87.39, pp. 401–407.

Huff, AE et al. (2021). "Applying planetary mapping methods to submarine environments: onshore-offshore geomorphology of Christiana-Santorini-Kolumbo Volcanic Group, Greece". In: *Journal of Maps* 17.3, pp. 111–121.

Hunt, JE, M Cassidy, and PJ Talling (2018). "Multi-stage volcanic island flank collapses with coeval explosive caldera-forming eruptions". In: *Scientific Reports* 8.1, pp. 1–11.

Hürlimann, M, J Martí, and A Ledesma (2000). "Mechanical relationship between catastrophic volcanic landslides and caldera collapses". In: *Geophysical research letters* 27.16, pp. 2393–2396.

Hutchison, AA et al. (2016). "The 1717 eruption of Volcán de Fuego, Guatemala: cascading hazards and societal response". In: *Quaternary International* 394, pp. 69–78.

Ida, Y and B Voight (1995). "Models of magmatic processes and volcanic eruptions". In: *Journal of volcanology and geothermal research* 66.1-4.

Jackson, CAL (2012). "Seismic reflection imaging and controls on the preservation of ancient sill-fed magmatic vents". In: *Journal of the Geological Society* 169.5, pp. 503–506.

Jäger, R et al. (2001). "Common-reflection-surface stack: Image and attributes". In: *Geophysics* 66.1, pp. 97–109.

Jamaludin, SN Fathiyah, AH Abdul Latiff, and DP Ghosh (2015). "Structural balancing vs horizon flattening on seismic data: example from extensional tectonic setting". In: *IOP Conference Series: Earth and Environmental Science*. Vol. 23. 1. IOP Publishing, p. 012003.

Johnston, EN et al. (2014). "Revised estimates for the volume of the Late Bronze Age Minoan eruption, Santorini, Greece". In: *Journal of the Geological Society* 171.4, pp. 583–590.

Johnston, EN et al. (2015). "Stratigraphic relations of Santorini's intracaldera fill and implications for the rate of post-caldera volcanism". In: *Journal of the Geological Society* 172.3, pp. 323–335.

Jolivet, L (2001). "A comparison of geodetic and finite strain pattern in the Aegean, geodynamic implications". In: *Earth and Planetary science letters* 187.1-2, pp. 95–104.

Jolivet, L and JP Brun (2010). "Cenozoic geodynamic evolution of the Aegean". In: *International Journal of Earth Sciences* 99.1, pp. 109–138.

Jolivet, L and C Faccenna (2000). "Mediterranean extension and the Africa-Eurasia collision". In: *Tectonics* 19.6, pp. 1095–1106.

Jolivet, L et al. (2013). "Aegean tectonics: Strain localisation, slab tearing and trench retreat". In: *Tectonophysics* 597, pp. 1–33.

Kamata, H and K Kodama (1999). "Volcanic history and tectonics of the Southwest Japan Arc". In: *Island Arc* 8.3, pp. 393–403.

Kandlbauer, J and RSJ Sparks (2014). "New estimates of the 1815 Tambora eruption volume". In: *Journal of Volcanology and Geothermal Research* 286, pp. 93–100.

Karátson, D et al. (2018). "Towards reconstruction of the lost Late Bronze Age intracaldera island of Santorini, Greece". In: *Scientific Reports* 8.1, pp. 1–8.

Karimpouli, S et al. (2015). "Automated diffraction delineation using an apex-shifted Radon transform". In: *Journal of Geophysics and Engineering* 12.2, pp. 199–209.

Karstens, J et al. (2013). "Emplacement of pyroclastic deposits offshore Montserrat: Insights from 3D seismic data". In: *Journal of Volcanology and Geothermal Research* 257, pp. 1–11.

Karstens, J et al. (2019). "From gradual spreading to catastrophic collapse - Reconstruction of the 1888 Ritter Island volcanic sector collapse from high-resolution 3D seismic data". In: *Earth and Planetary Science Letters* 517, pp. 1–13.

Karstens, J et al. (2020a). "Combining 3D seismics, eyewitness accounts and numerical simulations to reconstruct the 1888 Ritter Island sector collapse and tsunami". In: *International Journal of Earth Sciences* 109.8, pp. 2659–2677.

Karstens, J et al. (2020b). "R/V Poseidon Cruise Report 538-THESEUS Tsunami hazard of explosive submarine eruptions, 7th October–28th October 2019, Cartagena (Spain)-Heraklion (Greece)". In.

Karstens, J et al. (In Review_A). "Set up to fail – cascading events during the 1650 tsunamigenic eruption of Kolumbo volcano." In: *Nature Communications*.

Karstens, J et al. (In Review_B). "Revised Minoan eruption volume as benchmark for large volcanic eruptions". In: *Nature Communications*.

Kearey, P, M Brooks, and I Hill (2002). *An introduction to geophysical exploration*. Vol. 4. John Wiley & Sons.

Keir, D et al. (2006). "Strain accommodation by magmatism and faulting as rifting proceeds to breakup: Seismicity of the northern Ethiopian rift". In: *Journal of Geophysical Research: Solid Earth* 111.B5.

Kelfoun, K, T Giachetti, and P Labazuy (2010). "Landslide-generated tsunamis at Réunion Island". In: *Journal of Geophysical Research: Earth Surface* 115.F4.

Kiratzi, A (2013). "The January 2012 earthquake sequence in the Cretan Basin, south of the Hellenic Volcanic Arc: Focal mechanisms, rupture directivity and slip models". In: *Tectonophysics* 586, pp. 160–172.

Klarner, S and O Klarner (2012). "Identification of paleo-volcanic rocks on seismic data". In: *Updates in volcanology—a comprehensive approach to volcanological problems. Intech, Rijeka*, pp. 181–206.

Klaver, M et al. (2016). "A distinct source and differentiation history for Kolumbo submarine volcano, Santorini volcanic field, Aegean arc". In: *Geochemistry, Geophysics, Geosystems* 17.8, pp. 3254–3273.

Kopp, Heidrun et al. (2021). *Marine geohazards: Safeguarding society and the Blue Economy from a hidden threat*.

Kühn, M et al. (2021). "Seismic reconstruction of seafloor sediment deformation during volcanic debris avalanche emplacement offshore Sakar, Papua New Guinea". In: *Marine Geology* 439, p. 106563.

Kutterolf, S et al. (2021a). "The Medial Offshore Record of Explosive Volcanism Along the Central to Eastern Aegean Volcanic Arc: 1. Tephrostratigraphic Correlations". In: *Geochemistry, Geophysics, Geosystems* 22.12.

Kutterolf, S et al. (2021b). "The medial offshore record of explosive volcanism along the central to eastern Aegean Volcanic Arc: 2. Tephra ages and volumes, eruption magnitudes and marine sedimentation rate variations". In: *Geochemistry, Geophysics, Geosystems* 22.12, e2021GC010011.

Landa, E and S Keydar (1998). "Seismic monitoring of diffraction images for detection of local heterogeneities". In: *Geophysics* 63.3, pp. 1093–1100.

Lavigne, F et al. (2013). "Source of the great AD 1257 mystery eruption unveiled, Samalas volcano, Rinjani Volcanic Complex, Indonesia". In: *Proceedings of the National Academy of Sciences* 110.42, pp. 16742–16747.

Le Friant, A et al. (2004). "Geomorphological evolution of Montserrat (West Indies): importance of flank collapse and erosional processes". In: *Journal of the Geological Society* 161.1, pp. 147–160.

Le Friant, A et al. (2015). "Submarine record of volcanic island construction and collapse in the L esser A ntilles arc: First scientific drilling of submarine volcanic island landslides by IODP E xpedition 340". In: *Geochemistry, Geophysics, Geosystems* 16.2, pp. 420–442.

Le Friant, A et al. (2019). "Submarine landslides around volcanic islands: A review of what can be learned from the Lesser Antilles Arc". In: *Submarine Landslides: Subaqueous Mass Transport Deposits from Outcrops to Seismic Profiles*, pp. 277–297.

Le Pichon, X and J Angelier (1979). "The Hellenic arc and trench system: a key to the neotectonic evolution of the eastern Mediterranean area". In: *Tectonophysics* 60.1-2, pp. 1–42.

– (1981). "The Aegean Sea". In: *Philosophical Transactions of the Royal Society of London. Series A, Mathematical and Physical Sciences* 300.1454, pp. 357–372.

Le Pichon, X and C Kreemer (2010). "The Miocene-to-present kinematic evolution of the Eastern Mediterranean and Middle East and its implications for dynamics". In: *Annual Review of Earth and Planetary Sciences* 38, pp. 323–351.

Lebas, E et al. (2011). "Multiple widespread landslides during the long-term evolution of a volcanic island: Insights from high-resolution seismic data, Montserrat, Lesser Antilles". In: *Geochemistry, Geophysics, Geosystems* 12.5.

Lee, HJ et al. (2002). "Distinguishing sediment waves from slope failure deposits: field examples, including the 'Humboldt slide', and modelling results". In: *Marine Geology* 192.1-3, pp. 79–104.

Legros, F and TH Druitt (2000). "On the emplacement of ignimbrite in shallow-marine environments". In: *Journal of Volcanology and Geothermal Research* 95.1-4, pp. 9–22.

Lespez, L et al. (2021). "Discovery of a tsunami deposit from the Bronze Age Santorini eruption at Malia (Crete): impact, chronology, extension". In: *Scientific reports* 11.1, pp. 1–14.

Lin, G and PG Okubo (2020). "Seismic evidence for a shallow detachment beneath Kīlauea's south flank during the 2018 activity". In: *Geophysical research letters* 47.15, e2020GL088003.

Lin, J et al. (2022). "Magnitude, frequency and climate forcing of global volcanism during the last glacial period as seen in Greenland and Antarctic ice cores (60–9 ka)". In: *Climate of the Past* 18.3, pp. 485–506.

Lisiecki, LE and ME Raymo (2005). "A Pliocene-Pleistocene stack of 57 globally distributed benthic δ18O records". In: *Paleoceanography* 20.1.

López-Saavedra, M et al. (2021). "Cascading Effects of Extreme Geohazards on Tenerife (Canary Islands)". In: *Journal of Geophysical Research: Solid Earth* 126.9, e2021JB02 bibrangedash 2294.

Løvholt, F, G Pedersen, and G Gisler (2008). "Oceanic propagation of a potential tsunami from the La Palma Island". In: *Journal of Geophysical Research: Oceans* 113.C9.

Lucchi, F et al. (2013). "The Aeolian islands volcanoes". In: Geological Society of London.

Lynett, P et al. (2022). "Diverse tsunamigenesis triggered by the Hunga Tonga-Hunga Ha'apai eruption". In: *Nature* 609.7928, pp. 728–733.

Magee, C, E Hunt-Stewart, and CAL Jackson (2013). "Volcano growth mechanisms and the role of sub-volcanic intrusions: Insights from 2D seismic reflection data". In: *Earth and Planetary Science Letters* 373, pp. 41–53.

Magee, C et al. (2016). "Lateral magma flow in mafic sill complexes". In: *Geosphere* 12.3, pp. 809–841.

Malehmir, A et al. (2009). "3D constraints on a possible deep > 2.5 km massive sulphide mineralization from 2D crooked-line seismic reflection data in the Kristineberg mining area, northern Sweden". In: *Tectonophysics* 479.3-4, pp. 223–240.

Manconi, A et al. (2009). "The effects of flank collapses on volcano plumbing systems". In: *Geology* 37.12, pp. 1099–1102.

Manga, M and E Brodsky (2006). "Seismic triggering of eruptions in the far field: Volcanoes and geysers". In: *Annu. Rev. Earth Planet. Sci* 34, pp. 263–291.

Marfurt, KJ et al. (1998). "3-D seismic attributes using a semblance-based coherency algorithm". In: *Geophysics* 63.4, pp. 1150–1165.

Marinatos, S (1939). "The volcanic destruction of Minoan Crete". In: *Antiquity* 13.52, pp. 425–439.

Masson, DG et al. (2002). "Slope failures on the flanks of the western Canary Islands". In: *Earth-Science Reviews* 57.1-2, pp. 1–35.

McCoy, F W and G Heiken (2000). "Tsunami generated by the Late Bronze age eruption of Thera (Santorini), Greece". In: *Pure and Applied Geophysics* 157.6, pp. 1227–1256.

McGuire, WJ (1996). "Volcano instability: a review of contemporary themes". In: *Geological Society, London, Special Publications* 110.1, pp. 1–23.

McVey, BG et al. (2020). "Magma accumulation beneath Santorini volcano, Greece, from P-wave tomography". In: *Geology* 48.3, pp. 231–235.

Meier, T et al. (2007). "A model for the Hellenic subduction zone in the area of Crete based on seismological investigations". In: *Geological Society, London, Special Publications* 291.1, pp. 183–199.

Micallef, A et al. (2007). "Morphology and mechanics of submarine spreading: A case study from the Storegga Slide". In: *Journal of Geophysical Research: Earth Surface* 112.F3.

Miramontes, E et al. (2018). "Morphological control of slope instability in contourites: a geotechnical approach". In: *Landslides* 15.6, pp. 1085–1095.

Mitchell, N (2012). "Hot, cracking rocks deep down". In: *Nature Geoscience* 5.7, pp. 444–445.

Mitchum, RM, Peter R Vail, and Samuel Thompson III (1977). "Seismic stratigraphy and global changes of sea level: Part 2. The depositional sequence as a basic unit for stratigraphic analysis: Section 2. Application of seismic reflection configuration to stratigraphic interpretation". In.

Monzier, M, C Robin, and JP Eissen (1994). "Kuwae (1425 AD): the forgotten caldera". In: *Journal of Volcanology and Geothermal Research* 59.3, pp. 207–218.

Moore, JG, WR Normark, and RT Holcomb (1994). "Giant hawaiian landslides". In: *Annual Review of Earth and Planetary Sciences* 22, pp. 119–144.

Moore, JG et al. (1989). "Prodigious submarine landslides on the Hawaiian Ridge". In: *Journal of Geophysical Research: Solid Earth* 94.B12, pp. 17465–17484.

Morgan, J et al. (2013). "Next-generation seismic experiments: wide-angle, multi-azimuth, three-dimensional, full-waveform inversion". In: *Geophysical Journal International* 195.3, pp. 1657–1678.

Mori, J et al. (1996). "Volcanic earthquakes following the 1991 climactic eruption of Mount Pinatubo: Strong seismicity during a waning eruption". In: *Fire and Mud: Eruptions and Lahars of Mount Pinatubo, Philippines*, pp. 339–350.

Moser, T and C Howard (2008). "Diffraction imaging in depth". In: *Geophysical Prospecting* 56.5, pp. 627–641.

Myers, ML et al. (2021). "Evolution of magma decompression and discharge during a Plinian event (Late Bronze-Age eruption, Santorini) from multiple eruption-intensity proxies". In: *Bulletin of Volcanology* 83.3, pp. 1–17.

Neidell, NS and MT Taner (1971). "Semblance and other coherency measures for multichannel data". In: *Geophysics* 36.3, pp. 482–497.

Nicol, A, A Barrier, and H Wang (2019). "Characterization of a Middle Miocene Monogenetic Volcanic Field Buried in the Canterbury Basin, New Zealand–Part I". In.

Nomikou, P, C Hübscher, and S Carey (2019). "The Christiana–Santorini–Kolumbo Volcanic Field". In: *Elements: An International Magazine of Mineralogy, Geochemistry, and Petrology* 15.3, pp. 171–176.

Nomikou, P and D Papanikolaou (2011). "Extension of active fault zones on Nisyros volcano across the Yali-Nisyros Channel based on onshore and offshore data". In: *Marine Geophysical Research* 32.1, pp. 181–192.

Nomikou, P, D Papanikolaou, and VJ Dietrich (2018a). "Geodynamics and volcanism in the Kos-Yali-Nisyros volcanic field". In: *Nisyros Volcano*. Springer, pp. 13–55.

Nomikou, P et al. (2012). "Submarine volcanoes of the Kolumbo volcanic zone NE of Santorini Caldera, Greece". In: *Global and Planetary Change* 90, pp. 135–151.

Nomikou, P et al. (2013). "Submarine volcanoes along the Aegean volcanic arc". In: *Tectonophysics* 597, pp. 123–146.

Nomikou, P et al. (2014). "The emergence and growth of a submarine volcano: The Kameni islands, Santorini (Greece)". In: *GeoResJ* 1, pp. 8–18.

Nomikou, P et al. (2016a). "Post-eruptive flooding of Santorini caldera and implications for tsunami generation". In: *Nature communications* 7.1, pp. 1–10.

Nomikou, P et al. (2016b). "Tectono-stratigraphic evolution through successive extensional events of the Anydros Basin, hosting Kolumbo volcanic field at the Aegean Sea, Greece". In: *Tectonophysics* 671, pp. 202–217.

Nomikou, P et al. (2018b). "Expanding extension, subsidence and lateral segmentation within the Santorini-Amorgos basins during Quaternary: Implications for the 1956 Amorgos events, central-south Aegean Sea, Greece". In: *Tectonophysics* 722, pp. 138–153.

Nomikou, P et al. (2022). "SANTORY: SANTORini's Seafloor Volcanic ObservatorY". In: *Frontiers in Marine Science*, p. 421.

Novikova, T, Gerassimos A Papadopoulos, and Floyd W McCoy (2011). "Modelling of tsunami generated by the giant late Bronze Age eruption of Thera, South Aegean Sea, Greece". In: *Geophysical Journal International* 186.2, pp. 665–680.

Nunns, AG (1991). "Structural Restoration of Seismic and Geologic Sections in Extensional Regimes (1)". In: *AAPG bulletin* 75.2, pp. 278–297.

Ogata, K et al. (2014). "Shear zone liquefaction in mass transport deposit emplacement: a multi-scale integration of seismic reflection and outcrop data". In: *Marine Geology* 356, pp. 50–64.

Okal, EA et al. (2009). "The 1956 earthquake and tsunami in Amorgos, Greece". In: *Geophysical Journal International* 178.3, pp. 1533–1554.

Pank, K et al. (2022). "Mineralogy and geochemistry of lavas from the submarine lower caldera walls of Santorini Volcano (Greece)". In: *Journal of Volcanology and Geothermal Research* 427, p. 107556.

Papale, P (1999). "Strain-induced magma fragmentation in explosive eruptions". In: *Nature* 397.6718, pp. 425–428.

Papanikolaou, D and P Nomikou (2001). "Tectonic structure and volcanic centers at the eastern edge of the Aegean volcanic arc around Nisyros island". In: *Bulletin of the Geological Society of Greece* 34.1, pp. 289–296.

Papazachos, CB (2019). "Deep structure and active tectonics of the South Aegean volcanic arc". In: *Elements: An International Magazine of Mineralogy, Geochemistry, and Petrology* 15.3, pp. 153–158.

Pareschi, MR et al. (2006). "Large submarine landslides offshore Mt. Etna". In: *Geophysical Research Letters* 33.13.

Paris, R et al. (2014). "Volcanic tsunami: a review of source mechanisms, past events and hazards in Southeast Asia (Indonesia, Philippines, Papua New Guinea)". In: *Natural Hazards* 70.1, pp. 447–470.

Paris, R et al. (2022). "A Minoan and a Neolithic tsunami recorded in coastal sediments of Ios Island, Aegean Sea, Greece". In: *Marine Geology* 452, p. 106908.

Parks, MM et al. (2015). "From quiescence to unrest: 20 years of satellite geodetic measurements at Santorini volcano, Greece". In: *Journal of Geophysical Research: Solid Earth* 120.2, pp. 1309–1328.

Patrick, Matthew R et al. (2020). "The cascading origin of the 2018 Kīlauea eruption and implications for future forecasting". In: *Nature Communications* 11.1, pp. 1–13.

Paulatto, M et al. (2022). "Advances in seismic imaging of magma and crystal mush". In.

Perissoratis, C (1995). "The Santorini volcanic complex and its relation to the stratigraphy and structure of the Aegean arc, Greece". In: *Marine Geology* 128.1-2, pp. 37–58.

Pinel, V and F Albino (2013). "Consequences of volcano sector collapse on magmatic storage zones: Insights from numerical modeling". In: *Journal of Volcanology and Geothermal Research* 252, pp. 29–37.

Piper, DJW and C Perissoratis (2003). "Quaternary neotectonics of the South Aegean arc". In: *Marine Geology* 198.3-4, pp. 259–288.

Piper, DJW et al. (2007). "Distribution and chronology of submarine volcanic rocks around Santorini and their relationship to faulting". In: *Geological Society, London, Special Publications* 291.1, pp. 99–111.

Planke, S et al. (2000). "Seismic volcanostratigraphy of large-volume basaltic extrusive complexes on rifted margins". In: *Journal of Geophysical Research: Solid Earth* 105.B8, pp. 19335–19351.

Planke, S et al. (2005). "Seismic characteristics and distribution of volcanic intrusions and hydrothermal vent complexes in the Vøring and Møre basins". In: *Geological Society, London, Petroleum Geology Conference series*. Vol. 6. 1. Geological Society of London, pp. 833–844.

Planke, S et al. (2009). "P-Cable high-resolution seismic". In: *Oceanography* 22.1, p. 85.

Poland, MP et al. (2017). "The spectrum of persistent volcanic flank instability: A review and proposed framework based on Kīlauea, Piton de la Fournaise, and Etna". In: *Journal of Volcanology and Geothermal Research* 339, pp. 63–80.

Poli, P and NM Shapiro (2022). "Rapid characterization of large volcanic eruptions: Measuring the impulse of the Hunga Tonga Ha'apai explosion from teleseismic waves". In: *Geophysical Research Letters* 49.8, e2022GL098123.

Pope, EL et al. (2018). "Origin of spectacular fields of submarine sediment waves around volcanic islands". In: *Earth and Planetary Science Letters* 493, pp. 12–24.

Pörtner, HO et al. (2022). "Climate change 2022: Impacts, adaptation and vulnerability". In: *IPCC Sixth Assessment Report*.

Posamentier, HW, OJ Martinsen, and RC Shipp (2011). "The character and genesis of submarine mass-transport deposits: insights from outcrop and 3D seismic data". In: *Mass-transport deposits in deepwater settings. Tulsa: SEPM, Special Publication* 96, pp. 7–38.

Preine, J et al. (2020). "When There Is No Offset: A Demonstration of Seismic Diffraction Imaging and Depth-Velocity Model Building in the Southern Aegean Sea". In: *Journal of Geophysical Research: Solid Earth* 125.9, e2020JB019961.

Preine, J et al. (2022a). "Spatio-temporal evolution of the Christiana-Santorini-Kolumbo volcanic field, Aegean Sea". In: *Geology* 50.1, pp. 96–100.

Preine, J et al. (2022b). "The Hidden Giant: How a rift pulse triggered a cascade of sector collapses and voluminous secondary mass-transport events in the early evolution of Santorini". In: *Basin Research*.

Preine, J et al. (2022c). "Volcano-Tectonic Evolution of the Christiana-Santorini-Kolumbo Rift Zone". In: *Tectonics*, e2022TC007524.

Priyanto, WS et al. (2021). "Bathymetry and shallow seismic imaging of the 2018 flank collapse of Anak Krakatau". In: *Frontiers in Earth Science* 8, p. 577448.

Puchelt, H et al. (1977). "Geochemical and peterological studies of lavas, pyroclastica, and associated xenoliths from the Christiana islands, Aegean Sea". In.

Puglisi, G and A Bonforte (2004). "Dynamics of Mount Etna Volcano inferred from static and kinematic GPS measurements". In: *Journal of Geophysical Research: Solid Earth* 109.B11.

Pyle, DM (1989). "The thickness, volume and grainsize of tephra fall deposits". In: *Bulletin of Volcanology* 51.1, pp. 1–15.

– (1990). "New estimates for the volume of the Minoan eruption". In: *Thera and the Aegean world III* 2, pp. 113–121.

Reiche, S et al. (2018). "The role of internal waves in the late Quaternary evolution of the Israeli continental slope". In: *Marine Geology* 406, pp. 177–192.

Reid, A and T Mountain (2015). "Lessons of Tambora ignored, 200 years on". In: *East Asia Forum, Australian National University*. Vol. 25.

Reilinger, R et al. (2010). "Geodetic constraints on the tectonic evolution of the Aegean region and strain accumulation along the Hellenic subduction zone". In: *Tectonophysics* 488.1-4, pp. 22–30.

Reynolds, P et al. (2018). "The architecture of submarine monogenetic volcanoes–insights from 3D seismic data". In: *Basin Research* 30, pp. 437–451.

Riedel, M et al. (2020). "Physical properties and core-log seismic integration from drilling at the Danube deep-sea fan, Black Sea". In: *Marine and Petroleum Geology* 114, p. 104192.

Rizzo, AL et al. (2016). "Kolumbo submarine volcano (Greece): An active window into the Aegean subduction system". In: *Scientific reports* 6.1, pp. 1–9.

Rohrman, M (2007). "Prospectivity of volcanic basins: Trap delineation and acreage de-risking". In: *AAPG bulletin* 91.6, pp. 915–939.

Romer, RHW et al. (2021). "The evolution of central volcanoes in ultraslow rift systems: Constraints from D. João de Castro seamount, Azores". In: *Tectonics* 40.7.

Royden, L and D Papanikolaou (2011). "Slab segmentation and late Cenozoic disruption of the Hellenic arc". In: *Geochemistry, Geophysics, Geosystems* 12.3.

Sakellariou, D et al. (2010). "Active tectonics in the Hellenic Volcanic Arc: the Kolumbo submarine volcanic zone". In: *Bulletin of the Geological Society of Greece* 43.2, pp. 1056–1063.

Sarantakou, E and TS Terkenli (2021). "Non-institutionalized forms of tourism accommodation and overtourism impacts on the landscape: the case of Santorini, Greece". In: *Travel and Tourism in the Age of Overtourism*. Routledge, pp. 59–81.

Satow, C et al. (2021). "Eruptive activity of the Santorini Volcano controlled by sea-level rise and fall". In: *Nature Geoscience* 14.8, pp. 586–592.

Sawyer, DE et al. (2009). "Retrogressive failures recorded in mass transport deposits in the Ursa Basin, Northern Gulf of Mexico". In: *Journal of Geophysical Research: Solid Earth* 114.B10.

Schmid, F et al. (2022). "Heralds of Future Volcanism: Swarms of Microseismicity Beneath the Submarine Kolumbo Volcano Indicate Opening of Near-Vertical Fractures Exploited by Ascending Melts". In: *Geochemistry, Geophysics, Geosystems* 23.7, e2022GC010420.

Schofield, N et al. (2012). "Seismic imaging of 'broken bridges': linking seismic to outcrop-scale investigations of intrusive magma lobes". In: *Journal of the Geological Society* 169.4, pp. 421–426.

Schwarz, B (2019a). "An introduction to seismic diffraction". In: *Advances in Geophysics* 60.

– (2019b). "Coherent wavefield subtraction for diffraction separation". In: *Geophysics* 84.3, pp. V157–V168.

Schwarz, N, A Bauer, and D Gajewski (2016). "Passive seismic source localization via common-reflection-surface attributes". In: *Studia geophysica et geodaetica* 60.3, pp. 531–546.

Schwarz, N and D Gajewski (2017). "Accessing the diffracted wavefield by coherent subtraction". In: *Geophysical Journal International* 211.1, pp. 45–49.

Segall, P et al. (2006). "Earthquakes triggered by silent slip events on Kīlauea volcano, Hawaii". In: *Nature* 442.7098, pp. 71–74.

Self, S and R Gertisser (2015). "Tying down eruption risk". In: *Nature Geoscience* 8.4, pp. 248–250.

Self, S et al. (2004). "Magma volume, volatile emissions, and stratospheric aerosols from the 1815 eruption of Tambora". In: *Geophysical Research Letters* 31.20.

Seward, D, GA Wagner, and H Pichler (1980). "Fission track ages of Santorini volcanics (Greece)". In: *Thera and the Aegean world* 2, pp. 101–108.

Siebert, L (1984). "Large volcanic debris avalanches: characteristics of source areas, deposits, and associated eruptions". In: *Journal of volcanology and geothermal research* 22.3-4, pp. 163–197.

– (2002). "Volcanoes of the world: An illustrated catalogue of Holocene volcanoes and their eruptions in Smithsonian Institution, Global Volcanism Program Digital Information Series GVP-3". In: *http://www. volcano.si.edu/world/*.

Sigurdsson, H (1991). "Submarine pyroclastic flows of the 1883 eruption of Krakatau volcano". In: *Nat. Geog. Res. Explor.* 7, pp. 310–327.

Sigurdsson, H, S Carey, and JD Devine (1990). "Assessment of mass, dynamics and environmental effects of the Minoan eruption of Santorini volcano". In: *Thera and the Aegean world III* 2, pp. 100–112.

Sigurdsson, H et al. (1991). "Pyroclastic flows of the 1883 Krakatau eruption". In: *Eos, Transactions American Geophysical Union* 72.36, pp. 377–381.

Sigurdsson, H et al. (2006). "Marine investigations of Greece's Santorini volcanic field". In: *Eos, Transactions American Geophysical Union* 87.34, pp. 337–342.

Silvestrov, I, R Baina, and E Landa (2015). "Poststack diffraction imaging using reverse-time migration". In: *Geophysical Prospecting* 64.1, pp. 129–142.

Smit, FWH and L Stemmerik (2022). "Seismic geomorphology of submarine landslides in the Chalk Group of the Danish Central Graben: implications for reservoir potential". In: *Geological Society, London, Special Publications* 525.

Smith, H (2017). "Santorini's popularity soars but locals say it has hit saturation point". In: *The Guardian* 28.

Sørensen, MB et al. (2012). "Probabilistic tsunami hazard in the Mediterranean Sea". In: *Journal of Geophysical Research: Solid Earth* 117.B1.

Spera, FJ and JA Crisp (1981). "Eruption volume, periodicity, and caldera area: relationships and inferences on development of compositional zonation in silicic magma chambers". In: *Journal of Volcanology and Geothermal Research* 11.2-4, pp. 169–187.

Stothers, RB (1984). "The great Tambora eruption in 1815 and its aftermath". In: *Science* 224.4654, pp. 1191–1198.

Symons, WO et al. (2016). "Large-scale sediment waves and scours on the modern seafloor and their implications for the prevalence of supercritical flows". In: *Marine Geology* 371, pp. 130–148.

Taner, MT, F Koehler, and RE Sheriff (1979). "Complex seismic trace analysis". In: *Geophysics* 44.6, pp. 1041–1063.

Tatsumi, Y et al. (2018). "Giant rhyolite lava dome formation after 7.3 ka supereruption at Kikai caldera, SW Japan". In: *Scientific Reports* 8.1, pp. 1–9.

Taymaz, T, J Jackson, and D McKenzie (1991). "Active tectonics of the north and central Aegean Sea". In: *Geophysical Journal International* 106.2, pp. 433–490.

Tibaldi, A (1995). "Morphology of pyroclastic cones and tectonics". In: *Journal of Geophysical Research: Solid Earth* 100.B12, pp. 24521–24535.

Tibaldi, A and FL Bonali (2017). "Intra-arc and back-arc volcano-tectonics: Magma pathways at Holocene Alaska-Aleutian volcanoes". In: *Earth-Science Reviews* 167, pp. 1–26.

Tibaldi, A et al. (2008). "Tectonics of Nisyros Island, Greece, by field and offshore data, and analogue modelling". In: *Journal of Structural Geology* 30.12, pp. 1489–1506.

Tibaldi, A et al. (2013). "Structure of regional dykes and local cone sheets in the Midhyrna-Lysuskard area, Snaefellsnes Peninsula (NW Iceland)". In: *Bulletin of volcanology* 75.11, pp. 1–16.

Trilling, DE et al. (2017). "The size distribution of near-earth objects larger than 10 m". In: *The Astronomical Journal* 154.4, p. 170.

Tsampouraki-Kraounaki, K and D Sakellariou (2018). "Seismic stratigraphy and geodynamic evolution of Christiana Basin, South Aegean arc". In: *Marine Geology* 399, pp. 135–147.

Tucker, ME et al. (2020). "Carbonate crusts around volcanic islands: Composition, origin and their significance in slope stability". In: *Marine Geology* 429, p. 106320.

Tyrlis, E and J Lelieveld (2013). "Climatology and dynamics of the summer Etesian winds over the eastern Mediterranean". In: *Journal of the Atmospheric Sciences* 70.11, pp. 3374–3396.

Ulvrova, M et al. (2016). "Source of the tsunami generated by the 1650 AD eruption of Kolumbo submarine volcano (Aegean Sea, Greece)". In: *Journal of Volcanology and Geothermal Research* 321, pp. 125–139.

Urgeles, R and A Camerlenghi (2013). "Submarine landslides of the Mediterranean Sea: Trigger mechanisms, dynamics, and frequency-magnitude distribution". In: *Journal of Geophysical Research: Earth Surface* 118.4, pp. 2600–2618.

Urlaub, M et al. (2018). "Gravitational collapse of Mount Etna's southeastern flank". In: *Science Advances* 4.10, eaat9700.

Vakhrameeva, P et al. (n.d.). "Eastern Mediterranean volcanism during marine isotope stages 9 to 7e (335–235 ka): insights based on cryptotephra layers at Tenaghi Philippon, Greece". In: ().

Vakhrameeva, P et al. (2018). "The cryptotephra record of the Marine Isotope Stage 12 to 10 interval (460–335 ka) at Tenaghi Philippon, Greece: Exploring chronological markers for the Middle Pleistocene of the Mediterranean region". In: *Quaternary Science Reviews* 200, pp. 313–333.

Van Hinsbergen, DJJ and SM Schmid (2012). "Map view restoration of Aegean–West Anatolian accretion and extension since the Eocene". In: *Tectonics* 31.5.

Van Hinsbergen, DJJ et al. (2007). "Discrete Plio-Pleistocene phases of tilting and counterclockwise rotation in the southeastern Aegean arc (Rhodos, Greece): early Pliocene formation of the south Aegean left-lateral strike-slip system". In: *Journal of the Geological Society* 164.6, pp. 1133–1144.

Veen, JH ten and KL Kleinspehn (2002). "Geodynamics along an increasingly curved convergent plate margin: Late Miocene-Pleistocene Rhodes, Greece". In: *Tectonics* 21.3, pp. 8–1.

Verschuur, DJ, AJ Berkhout, and CPA Wapenaar (1992). "Adaptive surface-related multiple elimination". In: *Geophysics* 57.9, pp. 1166–1177.

Viesca, R C and James R Rice (2012). "Nucleation of slip-weakening rupture instability in landslides by localized increase of pore pressure". In: *Journal of Geophysical Research: Solid Earth* 117.B3.

Virieux, J and S Operto (2009). "An overview of full-waveform inversion in exploration geophysics". In: *Geophysics* 74.6, WCC1–WCC26.

Voight, B (2000). "Structural stability of andesite volcanoes and lava domes". In: *Philosophical Transactions of the Royal Society of London. Series A: Mathematical, Physical and Engineering Sciences* 358.1770, pp. 1663–1703.

Vougioukalakis, GE, Christopher G Satow, and Timothy H Druitt (2019). "Volcanism of the South Aegean volcanic arc". In: *Elements: An International Magazine of Mineralogy, Geochemistry, and Petrology* 15.3, pp. 159–164.

Vries, B Van Wyk de and PW Francis (1997). "Catastrophic collapse at stratovolcanoes induced by gradual volcano spreading". In: *Nature* 387.6631, pp. 387–390.

Walter, TR et al. (2019). "Complex hazard cascade culminating in the Anak Krakatau sector collapse". In: *Nature communications* 10.1, pp. 1–11.

Warner, M et al. (2013). "Anisotropic 3D full-waveform inversion". In: *Geophysics* 78.2, R59–R80.

Watkins, ND et al. (1978). "Volume and extent of the Minoan tephra from Santorini Volcano: new evidence from deep-sea sediment cores". In: *Nature* 271.5641, pp. 122–126.

Watt, Sebastian FL, David M Pyle, and Tamsin A Mather (2009). "The influence of great earthquakes on volcanic eruption rate along the Chilean subduction zone". In: *Earth and Planetary Science Letters* 277.3-4, pp. 399–407.

Watt, SFL, J Karstens, and C Berndt (2021). "Volcanic-island lateral collapses and their submarine deposits". In: *Volcanic Debris Avalanches*. Springer, pp. 255–279.

Watt, SFL et al. (2012). "Combinations of volcanic-flank and seafloor-sediment failure offshore Montserrat, and their implications for tsunami generation". In: *Earth and Planetary Science Letters* 319, pp. 228–240.

Watt, SFL et al. (2019). "From catastrophic collapse to multi-phase deposition: flow transformation, seafloor interaction and triggered eruption following a volcanic-island landslide". In: *Earth and Planetary Science Letters* 517, pp. 135–147.

Weiß, BJ et al. (2015). "Submarine explosive volcanism in the southeastern Terceira Rift/São Miguel region (Azores)". In: *Journal of Volcanology and Geothermal Research* 303, pp. 79–91.

Wiemer, G and A Kopf (2017). "On the role of volcanic ash deposits as preferential submarine slope failure planes". In: *Landslides* 14.1, pp. 223–232.

Wilson, CJN and BF Houghton (1990). "Eruptive mechanisms in the Minoan eruption: evidence from pumice vesicularity". In: *Thera and the Aegean world III* 2, pp. 122–128.

Wilson, DJ et al. (2019). "Does intermediate spreading-rate oceanic crust result from episodic transition between magmatic and magma-dominated, faulting-enhanced spreading?—The Costa Rica Rift example". In: *Geophysical Journal International* 218.3, pp. 1617–1641.

Yilmaz, Ö (2001). *Seismic data analysis: Processing, inversion, and interpretation of seismic data*. Society of exploration geophysicists.

Yin, J and N Nakata (2017). "Diffraction imaging with geometric-mean reverse time migration". In: *SEG Technical Program Expanded Abstracts 2017*. Society of Exploration Geophysicists, pp. 974–979.

Yokoyama, I (2001). "The largest magnitudes of earthquakes associated with some historical volcanic eruptions and their volcanological significance". In: *Annals of Geophysics* 44.5-6.

Yuen, DA et al. (2022). "Under the surface: Pressure-induced planetary-scale waves, volcanic lightning, and gaseous clouds caused by the submarine eruption of Hunga Tonga-Hunga Ha'apai volcano". In: *Earthquake Research Advances*, p. 100134.

Zelt, CA and RM Ellis (1988). "Practical and efficient ray tracing in two-dimensional media for rapid traveltime and amplitude forward modeling". In: *Canadian journal of exploration geophysics* 24.1, pp. 16–31.

Zelt, CA and RB Smith (1992). "Seismic traveltime inversion for 2-D crustal velocity structure". In: *Geophysical journal international* 108.1, pp. 16–34.

Zhu, L et al. (2006). "Crustal thickness variations in the Aegean region and implications for the extension of continental crust". In: *Journal of Geophysical Research: Solid Earth* 111.B1.

Zuccaro, G, D De Gregorio, and MF Leone (2018). "Theoretical model for cascading effects analyses". In: *International journal of disaster risk reduction* 30, pp. 199–215.

Eidesstattliche Versicherung | Declaration of Oath

Hiermit erkläre ich an Eides statt, dass ich die vorliegende Dissertationsschrift selbst verfasst und keine anderen als die angegebenen Quellen und Hilfsmittel benutzt habe.

I hereby declare upon oath that I have written the present dissertation independently and have not used further resources and aids than those stated.

Hamburg, 20.11.23
Ort, den | City, date

Jonas Preine
Unterschrift | Signature